THE TRANSITION FROM HYPOGENE TO SUPERGENE MINERALISATION AT THE MASHITU SOUTH Cu-Co DEPOSIT, KATANGA, DEMOCRATIC REPUBLIC OF THE CONGO

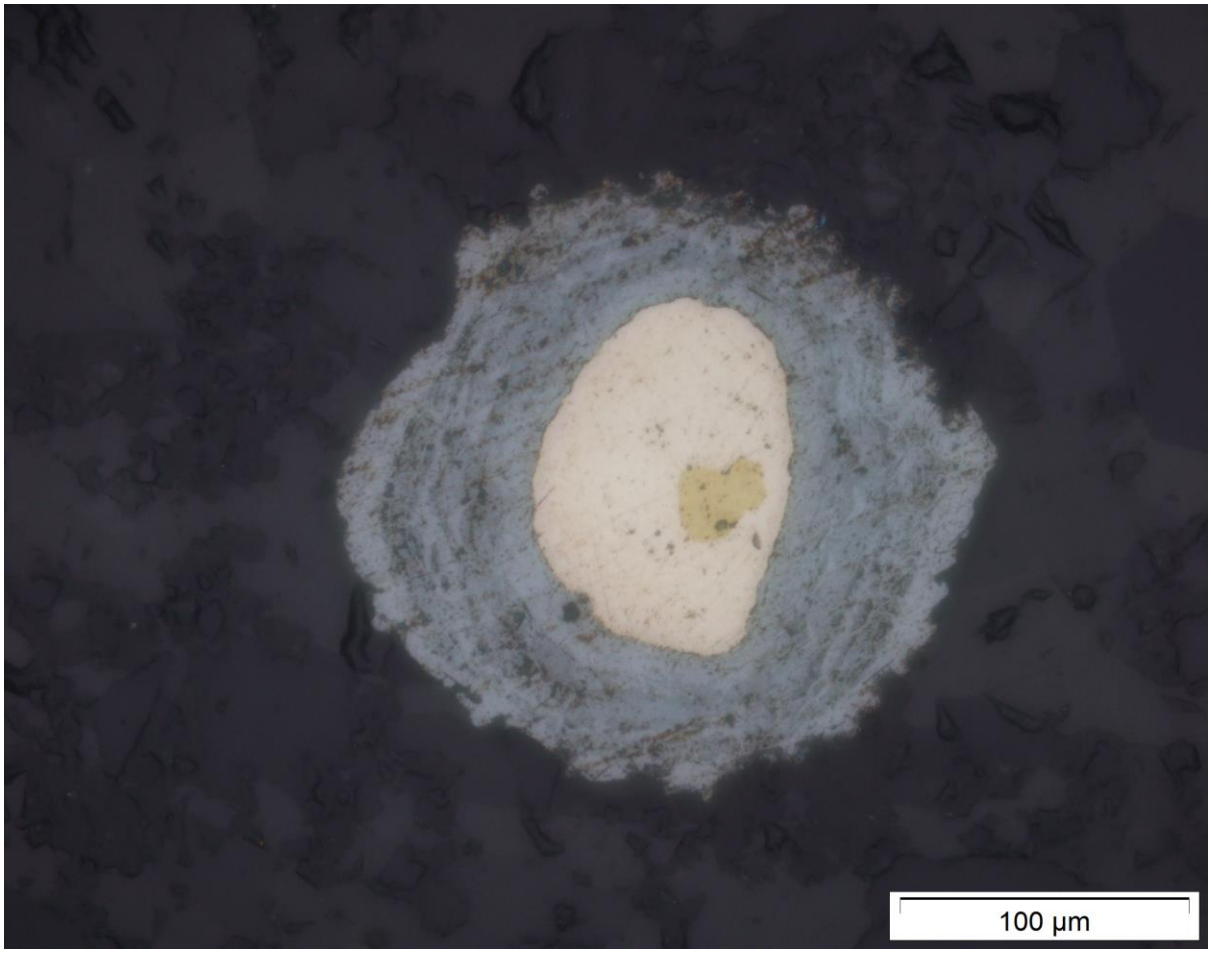

Gruffudd Morgan Gigler

A Dissertation submitted to the Faculty of Science, University of the Witwatersrand, Johannesburg, in fulfilment of the requirements for the degree of Doctor of Philosophy.

October 2018

DECLARATION

I declare that this dissertation is my own, unaided work. It is being submitted for the degree of Doctor of Philosophy at the University of the Witwatersrand, Johannesburg. It has not been submitted before for any degree or examination in any other University.

_____

Signature of Candidate

_____28th _____ day of _____October_____ 2018

ABSTRACT

Mashitu South is a Cu-Co deposit situated in the Katanga Province of the Democratic Republic of the Congo (DRC), about 25km to the east of the city of Kolwezi. It lies within the northwestern portion of the Central African Copperbelt (CAC), an arcuate region with a world-class abundance of copper deposits that straddles the external-fold-and-thrust-belt and the Domes region of the Lufilian arc, an orogenic belt that formed during the ~600-500Ma Pan-African orogeny. Cu-Co mineralisation at Mashitu South is hosted in the rocks of the Mines Series and Roches Argillo-Talceuses (RAT) subgroups of the Roan Group, deposited during the early stages of the opening of the Katangan basin, which is constrained to a maximum age of ~880Ma.

This study characterises the mineralisation stages and geochemistry of Mashitu South through a combination of core logging, geostatistical and petrographic techniques. The mineralogical and geochemical changes which occurred to the deposit throughout its paragenetic history are also explored. This is done with the purpose of linking the mineralisation at the deposit to regional metallogenic and geodynamic events, as well as developing vectors to Cu-Co mineralisation.

Mineralisation at Mashitu South occurred in four stages. The first stage is characterised by the development of stratiform-disseminated, zoned Cu-Co sulphides restricted to the rocks of the Mines Series, in a manner comparable to the sedimentary-hosted stratiform copper (SSC) deposit model. A protracted, syn-diagenetic timing is inferred for this stage, which caused the formation of hypogene, stratiform orebodies, primarily in the Kamoto Formation. Metals emplaced during the first stage were remobilised during the second mineralisation stage, which resulted in the development of vein-hosted hypogene Cu-Co sulphides, but does not appear to have concentrated metals into significant orebodies at Mashitu South. The second period of mineralisation is inferred to be early/syn-orogenic in age. Hypogene mineralisation at Mashitu South is found to have an element association of Cu + Co + Bi + Ni + V + S ± Mo ± As ± Fe ± Zn. The deposit was subsequently affected by two discrete stages of supergene alteration and mineralisation. Supergene alteration has resulted in the in-situ oxidation of hypogene Cu-Co sulphides, and also the leaching and remobilisation

of metals from hypogene mineralisation. The leaching and remobilisation process formed supergene, malachite-dominated orebodies which have an element association of Cu + Be + P ± Zn, the location of which is primarily controlled by metal availability and permeability of the host rocks. The RAT Subgroup is frequently host to such orebodies, underneath leached and eroded away Mines Series strata. These orebodies are usually found at a depth of ~30-50m.

An occurrence of bacillus-shaped features composed of Cu-Co sulphides was discovered in the lower Shales Dolomitique du Base (SDB) unit of the Mines Subgroup, and investigated with respect to the potential biogenicity and antiquity of the features as candidate microfossils. Further study found these features to be pseudofossils formed primarily by the replacement of diagenetic rutile crystals by sulphides, during the primary, stratiform mineralisation stage.

The various elements of the hypogene geochemical association are shown to have different mobilities in the supergene leaching environment, with Cu being relatively mobile and Co + Bi + Ni + V ± Mo being relatively refractory. This variation in mobility between elements, which are associated with Cu in the hypogene environment, suggests a zonation of these elements around Cu in the supergene environment, controlled by the hydrological gradient. At Mashitu South, this has resulted in the relative enrichment of Bi, Mo, V and Co in the upper 10m of the rock profile. Nickel is not as depleted in this interval as Cu, which is strongly depleted in the near-surface environment. It is therefore hypothesised that Bi, Mo, V, Co and Ni would make better surface vectors towards buried Cu-Co mineralisation than Cu, in regions where the supergene leaching process is particularly effective. 'Cobalt caps' above Cu-Co deposits in Katanga are well known, but this study suggests that Bi, Mo and V may make even better surface vectors to mineralisation than Co.

ACKNOWLEDGEMENTS

This thesis is the result of a true melting pot of ideas with provenances from a great many people, whose assistance I could not have done without. To begin with, Eurasian Resources Group (ERG) S.A.R.L. and the Centre of Excellence for Integrated Mineral and Energy Resource Analysis (CIMERA) are to be thanked for funding this project through the Economic Geology Research Institute (EGRI), School of Geosciences, University of the Witwatersrand.

The first, vital input was from John Lauderdale, with whom the concept of the project was hammered out. All of the staff at Comide S.P.R.L. have bent over backwards to accommodate my research, including Joseph Chimvinga, John Robertson, John Zvorufura and Marx Besa. The core shed staff, headed by Jacques Maloba and including Monsieurs Toto, Robert, Alphonse, Patient, Ernest and Mack did all the hard work, and I'm grateful for their patience in helping me to practice my very rusty French, and non-existent Swahili! Loni Gallant, Kennedy Mtetwa, Helen Twigg and Arturo Digdigan were also helpful to me during my stays at other ERG projects in Congo. Big thanks are due to Joseph, John, Sagren, Owen, Benson, Fred, Boniface, Talent, Mussa and Adolf (The Knights of the Square Table) as well as John, Omer, Oded and the two Ronnies for their hospitality at Comide. Tony Martin has been a mentor to the project, in terms of geology, dietary advice and philosophy, and without him I might never have been introduced to the term 'toothpaste tectonics'!

Consultants Pete Cheshire and Keith Kenyon have played important advisory roles. Pete's ability in the field has been extremely instructive, and the murky world of geostatistics has been greatly illuminated by Keith's course on geochemistry.

From Colorado School of Mines, Grainne Byrne, Steffan Ball and Murray Hitzman have shared interesting ideas and opinions on the Copperbelt with me and have contributed greatly towards the 'melting pot'. In particular, Murray's course on sedimentary-hosted stratiform copper was invaluable in helping me to understand the primary mineralisation processes at work.

My colleagues, Kevin Dalton and Marta Sośnicka, have kept me sane through the trials and tribulations of the project. I'm grateful for their scientific advice, patience, endless renditions of 'Back to Black' and such pearls of wisdom as "Boys are stupid". Thanks also to

all the many occupants and not-cupants of Room 120 during my time there and to Ben, Yassus, Hannah and Bump, who've offered their scientific help and advice while keeping me thoroughly entertained.

From the University of the Witwatersrand, my thanks are due to Caiphas Majola, Musa and Sam from the cutting lab, and to Jacques Gerber, Alexander Ziegler and Rudolph Erasmus at the MMU. Paul Nex and Sharad Master have provided useful insight into many aspects of my work and on the Copperbelt in general. Cameron Penn-Clarke, Zubair Jinnah, Pierre Durand and Jessica Judkins have helped to plug the gaps in my knowledge on palaeontology and microfossils. Special thanks must be given to Guy Charlesworth for casting an editorial eye over this thesis in demanding circumstances (and for putting up with my annoying grammatical habits). No acknowledgement could be complete without referring to Judith Kinnaird, whose supervision, advice and encouragement has been invaluable, and who has inspired a sense of urgency in me to learn Welsh!

My parents, Janet and Jeffrey Gigler, have my eternal gratitude for their editing suggestions, for supporting me throughout this project, for giving me what I needed to excel in trying conditions, and for everything else besides. I thank God for a good life and an enquiring mind.

TABLE OF CONTENTS

LIST OF FIGURES 1

LIST OF ABBREVIATIONS AND TERMINOLOGY 32

CHAPTER 1: INTRODUCTION 36

1.1 Overview 36

1.2 Geography and Mining History of the Central African Copperbelt 37

1.3 Stratigraphy 39

1.3.1 Basin Setting: The Katangan Supergroup 39

1.3.2 The Roan Group 42

1.3.2.1 R1: The R.A.T. 42

1.3.2.2 R2: The Mines Series.....44

1.3.2.3 R3: The Dipeta Subgroup.....47

1.3.2.4 R4: The Mwashya Subgroup.....48

1.3.3 The Nguba Group 48

1.3.3.1 Ng1. The Likasi Subgroup. 49

1.3.3.2 Ng2. The Monwezi Subgroup. 50

1.3.4 The Kundelungu Group 50

1.3.4.1 K1: The Kalule Subgroup.....50

1.3.4.2 K2: The Kiubo Subgroup 51

1.3.4.3 K3: The Plateaux Subgroup 51

1.3.5 Comparison to the Zambian Copperbelt 51

1.4 Structure and Tectonics..... 54

1.4.1 The Katangan Rift..... 55

1.4.2 The Lufilian Orogeny 56

1.4.3 Post Lufilian Deformation..... 60

1.4.4 The 'Roan Megabreccia' Debate 61

1.4.4.1 The 'traditional tectonic'/'fold and thrust' model.....62

1.4.4.2 The salt tectonic model *63*
1.4.4.3 The olistostrome complex model *65*
1.5 Metamorphism **66**
1.6 Magmatism and Igneous Rocks **68**

CHAPTER 2: REGIONAL MINERALISATION **69**
2.1 Cu-Co Mineralisation in the Central African Copperbelt **69**
2.1.1 Stratiform Mineralisation **70**
2.1.2 Vein-Type Mineralisation **83**
2.1.3 Supergene Mineralisation **87**
2.2 Related Deposit Types **97**
2.2.1 'Zambian-Type' Cu **97**
2.2.2 'Domes Region Cu (± Co, Ni, Au, Mo, U) **99**
2.2.3 Zn-Pb-Cu Deposits **101**
2.2.4 Cu-Ag (± Zn, Pb, As) deposits in the Lufilian Foreland **102**
2.2.5 Copperbelt Uranium Deposits **103**
2.3 Synthesis **105**

CHAPTER 3: FIELD WORK AND CORE LOGGING **106**
3.1 Introduction to Mashitu South **106**
3.1.1 Geography **106**
3.1.2 Regional Geology **108**
3.1.3 Structure of the Mashitu Complex **110**
3.1.3.1 Brecciation at Mashitu North and the other deposits of the Complex *113*
3.1.4 Stratigraphy of Mashitu South **114**
3.1.5 Mineralisation, Metasomatism and Mineralogy at Mashitu South **114**
3.1.6 Objectives of Fieldwork and Core Logging **116**
3.2 Methods **116**
3.2.1 Field Excursions **116**
3.2.2 Core Logging **117**
3.3 Results **119**

3.3.1 Field Excursions **119**
3.3.2 Core Logging **119**
3.3.2.1 MSSD075, MSSD080 and MSSD083 ..... *120*
3.3.2.2 MSSD140 ..... *140*
3.4 Discussion **145**
3.4.1 Stratigraphy **145**
3.4.2 Structure – Nature of the Mashitu Complex Breccias **149**
3.4.3 Alteration **155**
3.4.4 Mineralisation **156**
3.4.4.1 Hypogene mineralisation: distribution and zonation *156*
3.4.4.2 Supergene mineralisation: distribution and zonation *160*
3.4.4.3 The transition from hypogene to supergene mineralisation *167*
3.5 Conclusions from Fieldwork and Logging **168**

CHAPTER 4: PETROGRAPHY **170**
4.1 Introduction – Aims and Objectives **170**
4.2 Methods **170**
4.2.1 Optical Microscopy **171**
4.2.2 Scanning Electron Microscopy **171**
4.2.3 Sulphur Isotope Ratio Analysis **172**
4.3 Results **174**
4.3.1 Ore Mineral Paragenesis **174**
4.3.2 Ore Mineral Distribution **211**
4.3.3 Gangue Mineralogy **211**
4.3.3.1 Type 1 and Type 2 veins *225*
4.3.4 Sulphur Isotope Ratio Analyses **229**
4.4 Discussion – Cu-Co mineralisation **230**
4.4.1 The Pre-Ore Diagenetic Stage **231**
4.4.2 The Early Hydrothermal SSC Stage **233**
4.4.3 The Late Hydrothermal Ore Stage **244**
4.4.4 The Early Supergene Stage **246**
4.4.5 The Late Supergene Stage **249**

4.4.6 Sources of Sulphur 252
4.5 Conclusions from Petrography and Paragenesis 253

CHAPTER 5: GEOCHEMISTRY 255
5.1 Introduction – Aims and Objectives 255
5.2 Methods 256
5.2.1 Study of the Whole Mashitu South Deposit: Combining the Databases 256
5.2.2 Study of MSSD075, 080, 083 and MSSD140 259
5.2.3 Data splitting 259
5.2.4 Univariate Statistics 259
5.2.5 Pearson's Correlation Matrices 259
5.2.6 Bivariate Scatter Plots 262
5.2.7 Ternary Plots 263
5.2.8 Data Normalisation 266
5.2.9 Depth Profiles 270
5.2.10 Other techniques 270
5.3 Results 270
5.3.1 Overall Geology and Geochemistry of the Mashitu South Deposit 270
5.3.1.1 Lithology 270
5.3.1.2 Stratigraphy 272
5.3.1.3 Geochemistry 273
5.3.2 Splitting the Data for Mashitu South by Lithostratigraphy 280
5.3.2.1 C.M.N. Unit 280
5.3.2.2 S.D.S. Unit 283
5.3.2.3 S.D.2d Unit 285
5.3.2.4 S.D.B. Unit 287
5.3.2.5 R.S.C. Unit 289
5.3.2.6 R.S.F. Unit 291
5.3.2.7 D.Strat Unit 293
5.3.2.8 R.A.T. Gris Unit 295
5.3.2.9 R.A.T. Rouge Unit 297
5.3.2.10 Undifferentiated Breccias 299

5.3.3 Splitting the Data for Mashitu South by Depth **301**
5.3.3.1 Variation from depth to surface *301*
5.3.3.2 Near-surface variation *304*
5.3.4 Analysing the four logged holes: MSSD075, 080, 083 and 140 ..... **307**
5.3.4.1 Stratigraphy – the Sr : Sc ratio *307*
5.3.4.2 Alteration *310*
5.3.4.3 Cu Mineralisation: geochemical associations *316*
5.3.5. U Mineralisation: Distribution and Geochemical Associations **318**
5.4 Discussion **323**
5.4.1 Lithostratigraphy and Sedimentary Processes **323**
5.4.2 Alteration **324**
5.4.2.1 Magnesian Alteration *324*
5.4.2.2 Silicification *326*
5.4.2.3 Potassic alteration *326*
5.4.2.4 Argillic/supergene/surficial alteration *327*
5.4.3 Cu-Co Mineralisation **329**
5.4.3.1 Variation by lithostratigraphy *329*
5.4.3.2 Variation by depth *335*
5.4.3.3 The transition from hypogene to supergene mineralisation *340*
5.4.3.4 Surface vectors towards buried Cu-Co mineralisation *342*
5.4.3.5 Implications for geochemical exploration *345*
5.4.4 U Mineralisation **346**
5.5 Conclusions from Geochemistry **347**

CHAPTER 6: SOIL GEOCHEMISTRY **349**
6.1 Introduction – Aims and Objectives **349**
6.2 Methods **351**
6.3 Results **353**
6.4 Discussion **366**
6.4.1 Copper Distribution in Soil **366**
6.4.1.1 Cu anomalies which are not found over known Cu deposits *368*
6.4.2 Titanium Distribution in Soil **371**

6.4.3 Limitations in the Remaining Data 372
6.4.4 Comparison of Regional Soil to the Top of the Mashitu South Profile 376
6.5 Conclusions from Soil Geochemistry 381

CHAPTER 7: BACILLIFORM PSEUDOFOSSILS 382

7.1 Introduction 382
7.2 Methods 384
7.2.1 Optical Microscopy 385
7.2.2 Scanning Electron Microscopy (SEM) 385
7.2.3 Raman Spectroscopy 386
7.3 Results 387
7.3.1 Groundmass Mineralogy 387
7.3.2 Vein Mineralogy 387
7.3.3 Bacilliforms 389
7.4 Discussion 394
7.4.1 Rock History 394
7.4.2 Prokaryotic Microfossils? 396
7.4.2.1 Antiquity 396
7.4.2.2 Biogenicity 397
7.4.2.3 Potential mode of life and preservation 399
7.4.3 Abiogenic Pseudofossils? 402
7.4.4 Pseudofossils or Microfossils? 406
7.5 Conclusions from Bacilliform Pseudofossils 408

CHAPTER 8: DISCUSSION AND SYNTHESIS 409

8.1 Structure of the Mashitu South Deposit 409
8.2 Stratigraphy and Sedimentology of the Mashitu South Deposit 410
8.3 Metasomatic Alteration at the Mashitu South Deposit 413
8.4 Mineralisation at the Mashitu South Deposit 414
8.4.1 The Pre-Ore Diagenetic Stage 417
8.4.2 The Early Hydrothermal SSC Stage 417

8.4.3 The Late Hydrothermal Ore Stage 421
8.4.4 The Early Supergene Stage 424
8.4.5 The Late Supergene Stage 425
8.4.6 Implications for the Surface Geochemistry of Cu-Co Deposits 429
8.5 Further Work: Exploration Considerations 432

CHAPTER 9: CONCLUSIONS 435
9.1 Structure 435
9.2 Sedimentology and Stratigraphy 435
9.3 Mineralogy and Alteration 436
9.4 Mineralisation 436
9.5 Surface Geochemistry 439

REFERENCES 441

APPENDICES 477
Appendix 1 478
Appendix 2 479
Appendix 3 480
Appendix 4 501
Appendix 5 505
Appendix 6 506
Appendix 7 507
Appendix 8 513
Appendix 9 516
Appendix 10 521
Appendix 11 527

LIST OF FIGURES

Figure 1.1: The study area (Mashitu) in relation to key locations and deposit groups (crossed hammers) in the Central African Copperbelt (CAC). Data ©2014 Google Maps 37

Figure 1.2: Regional geological map of the Congolese Copperbelt (after François; 2006), with key deposits and the cities of Lubumbashi and Likasi illustrated. Mashitu is represented as a star. 39

Figure 1.3: Theoretical diagram of the aulacogenic orientation of the Katangan and Zambian basins relative to their bounding cratons during Neoproterozoic rifting. After Hitzman (2009a). 40

Figure 1.4: Stratigraphic summary for the R1, R2, R3 and R4 subgroups. The colours are those used for each stratigraphic unit in the Gecamines (a Congolese para-statal mining company) local geological maps of the Katangan Copperbelt, which are adopted for geological maps and figures in this thesis. Approx. thicknesses are those witnessed in the vicinity of the Mashitu group of deposits (Chimvinga, 2014, pers. comm.). 45

Figure 1.5: Stratigraphic summary (after Cailteux, 1994) for the Katangan Supergroup. The colours are those used for each stratigraphic unit in the Gecamines regional geological maps of the Katangan Copperbelt – which are adopted for geological maps and figures in this thesis..... 48

Figure 1.6: Traditional correlation of the Katangan across the DRC and Zambia from Cailteux et al. (1994). Authors such as Bull et al. (2010) consider the Zambian Roan to occupy a lower stratigraphic level than the Congolese Roan. The Upper and Lower Kundelungu Groups refer to the Kundelungu and Nguba Groups respectively, according the updated stratigraphic nomenclature..... 53

Figure 1.7: Sketch map of the structural zones of the Lufilian Arc and surrounding terranes. The approximate extent of known Central African Copperbelt mineralisation is outlined in dashed yellow. Zone 1: Katanga High; Zone 2: Synclinorial Belt; Zone 3: Domes Region; Zone 4: External Fold and Thrust Belt. Modified from Kampunzu and Cailteux (1999); Porada and Berhorst (2000) and Selley et al. (2005). 55

Figure 1.8: Location of the Central African Copperbelt (yellow star) within the regional geotectonic setting of cratons and orogenic belts. Modified from Syamujaye (2014). 58

Figure 1.9: Conceptual sketch of the three deformation stages of the Lufilian Orogeny described by Kipata et al. (2013), with the inferred convergence of the three cratons involved. The yellow belt is a sketch of the Lufilian Arc whereas the orange represents the Lufilian Foreland. D1: Collision of the Congo and Kalahari cratons causes overturned folding, thrusting and northward transport of thrust sheets. D2: Collision by the Bangweulu Block results in clockwise rotational deformation and 'orogenic bending' of the Arc. D3: Further advancement of the Bangweulu Block results in sinistral strike-slip reactivation of thrust faults formed during D1. Not to scale. D1 represents the 'Kolwezian' phase of deformation whereas D2 and D3 represent the 'Monwezi' phases of deformation described by Kampunzu and Cailteux (1999). 60

Figure 1.10: Disaggregated blocks of Mines Subgroup stratigraphy in the Tenke-Fungurume area, some 40km to the east of the Mashitu group of Cu-Co deposits. Modified from Zientek et al. (2014) and Jackson et al. (2003)..... 62

Figure 1.11: Model showing the hypothesised distribution of evaporite deposition throughout the Katangan Basin. From Jackson et al. (2003)..... 64

Figure 1.12: Model showing the role of salt diapirism in the brecciation and disaggregation of the Roan Group and the Mines Subgroup. From Hitzman et al. (2012). 65

Figure 2.1: Location of a selection of economically or academically significant Copperbelt mineral deposits, modified from Muchez et al. (2008). Mashitu is shown as a star while the three major (>15 Mt) Congolese deposits – Kamoa, Kolwezi and Tenke-Fungurume – are symbolised by enlarged circles. 70

Figure 2.2: Cu-Co distribution within the Upper and Lower Orebodies of the Mines Subgroup. From: Nilsson et al. (2011). 71

Figure 2.3: Eh-pH stability field diagrams for A.: the Cu-O-H-S system at 25°C, ΣS=10-4 and for B: the Cu-O-H-S-Cl system at 25°C, ΣS=10-4 and Cl-=0.5m as NaCl. In the saline system B., copper is stable in the soluble, transportable forms of $CuCl_3^{2-}$ and $CuCl^{2-}$ ions at near neutral pH's and only mildly oxidising Eh's. This is in contrast to the non-saline system A., where copper is stable only as soluble, transportable Cu^{2+} at low, acidic pH and in oxidising Eh conditions..... 73

Figure 2.4.: Generalised model for the generation and transport of copper-rich fluids responsible for forming S.S.C. deposits. Evaporitic, Cl^--bearing fluids descend into redbeds where they circulate in a closed system and strip copper from labile minerals. In the Copperbelt, circulation of these fluids within the basement as well as the redbeds is thought to have been important in mobilising the quantities of copper observed in the stratiform deposits. From Hitzman et al. (2010)..... 75

Figure 2.5.: Model for the lateral transport of primary ore fluids through the R.S.C. and deposition of the Upper and Lower Orebodies above and below this unit. From: Fay and Barton (2012). . 76

Figure 2.6: Conceptual illustration of the relationship between mineralisation, sulphide zonation, and lithological redox horizons in S.S.C. type mineralisation. In the Katangan Copperbelt, the R1 Subgroup serves as the redbeds and the R2 Subgroup serves as the greybeds creating a major regional reduction front. 78

Figure 2.7: Generalised paragenesis for sulphides and associated metasomatism related to the stratiform mineralisation stage of the Katangan Copperbelt. Compiled based on information from: Dejonghe and Ngoyi (1995), Dewaele et al. (2006a), El Desouky et al. (2010), Hitzman et al. (2010), Fay and Barton (2012), Hitzman et al. (2012), Schmandt et al. (2013). 81

Figure 2.8: Generalised summary of the paragenesis of 'vein-type' Cu-Co mineralisation from the Katangan Copperbelt described by Dewaele et al. (2006a). A timeline is not included because many vein type Cu-Co mineralising events with a similar paragenetic history appear to have occurred at different periods in the history of the Copperbelt..... 86

Figure 2.9: Conceptual illustration of the generalised depth-profile-zonation of supergene alteration in Katanga, showing the various alteration zones together with their dominant ore mineralogy. The depth to the Primary Sulphide Zone, where meteoric fluids have ceased to percolate (or have lost their oxidising potential by the time they arrive) is typically anywhere between 100-200m. 89

Figure 2.10: Eh-pH diagram showing copper mineral stability at surface conditions and at low f(CO2) (from Taylor, 2011; c.f. Anderson, 1982)..... 91

Figure 2.11: Conceptual illustration of the process of Cu-Co decoupling in the supergene environment, to form 'cobalt caps' over supergene copper deposits. The lateral dispersal of residual cobalt through physical weathering is also illustrated. Modified from Decree et al. (2010). 93

Figure 2.12: Photographs of anthropogenic supergene copper minerals (some form of verdigris) near a tailings pond for the Kipushi Mine, Katanga, D.R.C.. A: anthropogenic construction cement with overgrowth of copper verdigris. Pen for scale. B: Cross-sectionally-split dolomite road cobble showing the surficial nature of the copper minerals. Thumb and finger-tips for scale. 96

Figure 3.1: Regional map showing the location of the Mashitu Complex. Imagery from Google Maps: ©2016 CNES/Astrium, Map data ©2016 Google. 107

Figure 3.2: Map showing the location of Mashitu South within the Mashitu Complex and in the context of local infrastructure. ©2016 CNES/Astrium, Map data ©2016 Google 107

Figure 3.3: Regional Geology Map of the Camrose Concession. Map supplied by Comide S.P.R.L. and modified from Francois (1973). 109

Figure 3.4: Local geology of the Mashitu Complex. Map supplied by Comide S.P.R.L. and based on work by P. Cheshire (2014). Structural interpretations of fold axes creating a dome-and-basin architecture are modifications made by the author. See Appendix 2 for a descriptive summary of the stratigraphy. 111

Figure 3.5: East-west cross section through the eastern margin of the Mashitu South Deposit, showing an Upper Block of Mines Series juxtaposed over a Lower Block of Mines Series, along what appears to be a thrust-fault plane of dislocation. A breccia of irregular thickness, found along this plane of dislocation, may be related to rheid flow processes caused by evaporite mobilisation along the fault plane, with local diapirism occurring where evaporites became concentrated enough. The stratigraphic boundaries (black lines), position of the fault and 'para-diapiric structure' have been interpreted during the present study, while the cross section has been supplied by Comide S.P.R.L.. 112

Figure 3.6: Ore assemblages from the Mashitu South deposit. Mal=malachite, hm=haematite, ga=gangue, cc=chalcocite, car=carrollite, bn=bornite. A: Malachite-haematite ore from a supergene vein in an argillaceous silicate mudstone. B: Carrollite-bornite-chalcocite stratiform-disseminated hypogene ore from an argillaceous silicate mudstone. Images and interpretations taken from McLaren (2011). 115

Figure 3.7: Red-circled locations of field visits to various deposits in the area of Mashitu South. For a key to the geology and the location of the Pungulume Principal deposit (shown on the inlay), refer to Figure 3.3. Map provided by Comide S.P.R.L. and modified in this study. 117

Figure 3.8: Geological Map of the Mashitu South Mines Series fragment (outlined in thick black). The locations of the four holes which were logged as part of this study (MSSD075, MSSD080, MSSD083, and MSSD140) are indicated and circled in dark blue. 118

Figure 3.9: Logging template used in the present study to log MSSD075, 080, 083 and MSSD140. . 119

Figure 3.10: Photo of monomictic dolomite-vein-supported protobreccia. H.Q. core size for scale. 121

Figure 3.11: Polymictic, matrix-supported breccia. H.Q. core size for scale. 121

Figure 3.12: Reddish sandy siltstone. H.Q. core size for scale. 122

Figure 3.13: Greenish sandy siltstone with enterolithic dolomite (top left). H.Q. core size for scale. 122

Figure 3.14: Bedded micritic dolomite with cherty layers. H.Q. core size for scale. 123

Figure 3.15: Wavy-laminated silicified micritic dolomite. H.Q. core size for scale. 124

Figure 3.16: Stromatolitic, silicic, vuggy crystalline dolomite. N.Q. core size for scale. 124

Figure 3.17: Lower mottled red-green dolomitic argillite. H.Q. core size for scale. 126

Figure 3.18: Black carbonaceous shale, cross-cut by veins of dolomite. H.Q. core size for scale. 126

Figure 3.19: Upper mottled red-green dolomitic argillite, cross-cut by a wide variety of orientations of dolomite veins. H.Q. core size for scale. 127

Figure 3.20: Silicified stromatolitic unit in the upper micritic dolomite. H.Q. core size for scale. 129

Figure 3.21: Carbonaceous grey micritic dolomite with laminations. H.Q. core size for scale. 129

Figure 3.22: Fine-medium grained crystalline blue dolomite. H.Q. core size for scale. 130

Figure 3.23: Algal-laminated micritic dolomite . H.Q. core size for scale. 130

Figure 3.24: 'Cauliflower shape' elongate dolomite nodules, reminiscent of chicken wire texture. H.Q. core size for scale. 131

Figure 3.25: Silicification overprint to an originally carbonaceous micritic dolomite. H.Q. core size for scale. 131

Figure 3.26: White rock affected by surficial advanced argillic alteration. P.Q. core size for scale. .. 132

Figure 3.27: Red-brown near-surface saprolite. P.Q. core size for scale. 132

Figure 3.28: Type 1 dolomite veins cutting through the upper micritic dolomite. H.Q. core size for scale. 134

Figure 3.29: Type 2 dolomite veins cutting through dolomitic argillite. H.Q. core size for scale. 134

Figure 3.30: Vein-hosted and stratiform chalcocite-bornite-carrollite in the wavy-laminated silicified micritic dolomite. Chalcocite and bornite are visible as an iridescent blue. N.Q. core size for scale. 136

Figure 3.31: Dolomite vein-hosted chalcopyrite and chalcocite in the black carbonaceous shale. H.Q. core size for scale. 136

Figure 3.32: Pervasive green malachite in the lower crystalline silicic dolomite. Small amount of chalcocite and heterogenite are also visible in the picture. H.Q. core size for scale. 137

Figure 3.33: Fracture-filling blue chrysocolla in crystalline blue dolomite. H.Q. core size for scale. . 138

Figure 3.34: Euhedral fracture-fill cobaltoan dolomite on heterogenite base. H.Q. core size for scale. 138

Figure 3.35: Native copper in the lower crystalline silicic dolomite. N.Q. core size for scale. 139

Figure 3.36: Carrollite (bright-silver), chalcocite (dark-silver-grey), heterogenite (black), cobaltoan dolomite (pink) and uranium-oxide (yellow) in the lower silicic dolomite. N.Q. core size for scale. 139

Figure 3.37: Resistant, weathered, laminated silica-and-clay rock. P.Q. core size for scale. 141

Figure 3.38: Red sandy siltstone. H.Q. core size for scale. 142

Figure 3.39: Layer sub-parallel vein of specular haematite (top left) and monomictic dolomite-vein-supported in-situ protobrecciation of the red sandy siltstone (centre right). P.Q. core size for scale. 142

Figure 3.40: Grey, shaly argillite. H.Q. core size for scale. 143

Figure 3.41: Fracture-hosted botryoidal malachite in the red sandy siltstone. P.Q. core size for scale. 144

Figure 3.42: Interpreted correlation of Mines Series stratigraphy between the MSSD075, MSSD080 and MSSD083 drill-holes arranged in order (left to right, SSE to NNW) of their collar position on the Mashitu South Mines Series fragment. Collar locations of these holes are given in Figure 3.8. This interpretation is based on logs of these holes presented in Appendix 3, using lithological similarities, the Sr:Sc ratio (see Chapter 4) and clast/grain size of the rock units. Red lines indicate correlation between different stratigraphic units across the holes, the blue line indicates Sr:Sc ratio of samples taken from the drill core, which was found to be a useful tool for correlating stratigraphy (see Chapter 4) and the black line represents grain/clast size. The blue line is broken in MSSD080 at intervals where the core was not sampled. Stratigraphic units are represented by colours on the graph: see Figures 1.4 and 3.4 for a key. These units are, from bottom to top, the RAT Rouge (yellow), the RAT Gris (green), the DStrat (orange), the RSF (red), the RSC (pale blue), the SDB (beige), the SD2d (brown), the SDS (dark blue) and the CMN (maroon). Note that a repetition of the stratigraphy in MSSD083 exists, probably induced by tectonic stacking, that cuts out the CMN unit from the lower stratigraphic fragment. 147

Figure 3.43: A rock face on the north side of Mashitu Principal pit showing multiple generations of breccia. There is a clast supported monomictic breccia (top) above a deformed lithic fragment (middle) and a clast-supported polymictic breccia (bottom). Camera case for scale. 151

Figure 3.44: A rock face on the north side of Mashitu Principal pit showing a large unit of polymictic, matrix-supported breccia. Hammer for scale. 152

Figure 3.45: Multiple generations and types of breccia from a hole from Mashitu North. Complex cross-cutting relations are observable, and different generations of breccia are included as clasts within other breccia generations. H.Q. sized core for scale. 153

Figure 3.46: Conceptual illustration for the origin of the Roan megabreccias at the Mashitu Complex. Strain is concentrated in the less-competent, evaporite-interbedded units of the Dipeta and the R.AT. during orogenesis, causing the brittle fragmentation and dislocation of the more competent Mines Series in between. 155

Figure 3.47: Stratiform mineralisation in the R.S.F. unit in MSSD075. Disseminated chalcocite is visible with a metallic lustre and dark-blue-to-violet sheen. H.Q. core size for scale. 157

Figure 3.48: Stratiform mineralisation model for Kambove West from van Langendonck et al. (2013) This model fits the distribution of carrollite at Mashitu South well (but not other Cu sulphides). 157

Figure 3.49: Stratiform-disseminated pyrite and chalcopyrite cross-cut by Type 2 dolomite veins which host chalcopyrite and possibly carrollite, within the S.D.B. of MSSD080. H.Q. core size for scale. 159

Figure 3.50: Stratiform-disseminated pyrite in the SD2d of MSSD083. Note the bedding-sub-parallel type 1 veinlets in the bottom left-hand corner. 159

Figure 3.51: Speleothems of breccia-hosted malachite in the Mashitu Principal pit. Pencil for scale. 160

Figure 3.52: Sub-botryoidal heterogenite in the Mashitu Principal pit. Hammer for scale. 161

Figure 3.53: Fracture-hosted malachite and chrysocolla in the Mashitu North pit. Hammer for scale. 161

Figure 3.54: Black-shale hosted azurite in the Kabolela pit. Hammer for scale. 162

Figure 3.55: Kolwezite (green) and heterogenite (black) in the RSF unit at the Anticline deposit, near the Mashitu Complex. Pen for scale. Photo courtesy of Joseph Chimvinga. 162

Figure 3.56: Libethenite from the Mashitu North pit. Fingers for scale. 163

Figure 3.57: Pseudomalachite and malachite from the Kakanda North pit. Fingers for scale. 163

Figure 3.58: Model for the distribution of supergene mineralisation in and around the R.S.C. stratigraphic unit at Tenke-Fungurume. This model can be applied equally to other permeable lithological units, such as permeable breccias. From Fay and Barton (2012). 164

Figure 3.59: Nodular D.Strat with in-situ malachite from the Nzilo deposit. Hammer for scale..... 166

Figure 3.60: In-situ malachite and heterogenite mineralisation in stromatolitic R.S.C. from the Kii deposit. This photo is taken perpendicular to an exposed bedding surface, showing the domal tops of fossilised stromatolite mounds. Hammer for scale. 166

Figure 3.61: Cu-Co zoning in the supergene environment in the western face of Kakanda North pit. Fluids, travelling down a south-dipping breccia, have infiltrated the country rock, precipitating heterogenite in proximity to the breccia and malachite further away. Benches are 3m high for scale. 167

Figure 4.1: FEI Quanta 400 FEG-ESEM and EDS setup at the MMU, University of the Witwatersrand. 172

Figure 4.2: Summary of sample material subjected to sulphur isotope ratio analysis..... 173

Figure 4.3: 'Para-framboidal' clusters of pyrite 1 (Py1) disseminated through the groundmass. Some replacement of pyrite 1 by grey haematite 1 (Hm1) has taken place. Optical image taken in reflected PPL from sample MSSD080_21_1. 175

Figure 4.4: Euhedral laths of disseminated, reddish haematite 1 (Hm1) surrounded by later ore phases. Note the abutment of the chalcocite 1 phase against haematite 1. Optical image taken in reflected PPL of sample MSSD083_16_1. 176

Figure 4.5: Euhedral, cubic, disseminated pyrite 2 crystal. Optical image taken in reflected PPL of sample MSSD083_23_3. 177

Figure 4.6: Pyrite 2 crystals around earlier-formed Hm1 laths. Optical image taken in reflected PPL of sample MSSD083_22_2. 177

Figure 4.7: Pyrite 3 crystals associated with Type 1 quartz-carbonate veins, with minor rimming by chalcocite 1, in proximity to nodules/boudins within the DStrat unit. Optical image taken in reflected PPL from sample MSSD080_20_2. 178

Figure 4.8: SEM-EDS element mapping images of a pyrite 3 crystal, which is roughly 600 µm in length, at the edge of a quartz-carbonate nodule. A: SEM image of site. B: Site map of S concentration. C: Site map of Fe concentration. D: Site map of Co concentration. Fe and S are concentrated, as would be expected, within pyrite (FeS2). As shown by (D), Co is concentrated as a trace element in pyrite 3, with the Co element map faintly mirroring the shape of the pyrite crystal.

Additionally, the element map reveals the presence of two Cu-Co sulphide crystals rimming the pyrite 3 crystal, which were confirmed as carrollite (Car1) by spot analysis. Sample MSSD083_23_4. 179

Figure 4.9: SEM image of a Type 1 vein-hosted sulphide assemblage. A large bleb of chalcopyrite (Cpy1) is rimmed and replaced by bornite (Bn1). Sphalerite (Sph1) is the pale, dull grey phase mantled by the slightly lighter bornite. The results of an EDS spot analysis (Spectrum 2) confirm the identity of the crystal as sphalerite. Sample MSSD083_21_4. 180

Figure 4.10: Stratiform, disseminated pyrite 3 and chalcopyrite 1 masses within the siliciclastic groundmass of the SD2d. Optical image taken in reflected PPL of sample MSSD083_22_2. 181

Figure 4.11: A disseminated mass of chalcopyrite 1 surrounding earlier pyrite (Py1) and haematite (Hm1) phases. Optical image taken in reflected PPL of sample MSSD083_22_2. 181

Figure 4.12: Type 1 vein-hosted chalcopyrite 1 rimmed by bornite (purple, Bn1). Digenite (Dg1, deep blue) forms exsolution textures within the bornite. The Bn1-Dg1 is itself rimmed by carrollite 1 (grey-white). Optical image taken in reflected PPL of sample MSSD083_21_4. 182

Figure 4.13: Stratiform disseminated chalcocite 1 masses. Optical image taken in reflected PPL of sample MSSD075_16_3. 183

Figure 4.14: Disseminated chalcocite 1 mass mantled by carrollite1. Bornite 1 is barely visible as purple remnants within the replacing mass of blue Cc1. Optical image taken in reflected PPL of sample MSSD083_23_2. 183

Figure 4.15: Carrollite (Car1) rimmed and replaced by chalcocite (Cc3) within a Type 1 antitaxial dolomite vein. Main optical image is taken in transmitted XPL, inset image is taken in reflected PPL, from sample MSSD083_20_1. 184

Figure 4.16: Carrollite 1 as a mantling, replacing phase to an earlier chalcopyrite-bornite-chalcocite disseminated sulphide bleb (bornite, Bn1, is barely visible as purple remnants within chalcocite 1). Note that carrollite 1 does not appear to be replacing pyrite 2. Optical image taken in reflected PPL of sample MSSD083_23_2. 185

Figure 4.17: Near total replacement of a sulphide bleb such as the one in Figure 4.15, progressively by chalcocite 1 and then by carrollite 1. Optical image, reflected PPL of sample MSSD083_23_2. 185

Figure 4.18: Replacement of chalcopyrite 1 by a crystal of CoPy1 (cobaltoan pyrite), itself replaced by concentrically banded chalcocite 3 and haematite 2. Optical image taken in reflected PPL of sample MSSD080_13_2. 186

Figure 4.19: SEM image of the sulphide bleb in Figure 4.17, showing an EDS spot analysis of the cobaltoan pyrite (CoPy1). The crystal is primarily Fe and S but contains ~5 wt.% Co. 186

Figure 4.20: Type 2 vein-hosted carrollite 2, mantled and replaced by bornite 2. Optical image taken in reflected PPL from sample MSSD083_06_5. 187

Figure 4.21: Tiny crystals of type 2 vein-hosted chalcopyrite 2; one crystal is mostly replaced by bornite 2. Optical image taken in reflected PPL from MSSD083_26_2. 188

Figure 4.22: Type 2 vein-hosted sulphide bleb of bornite 2 mantling a small remnant of carrollite 2, with chalcocite 2 apparently exsolving from bornite 2. Optical image taken in reflected PPL from sample MSSD083_06_5. 189

Figure 4.23: Type 2 vein-hosted bleb of chalcocite 2, which is replaced around the rims by closely-intergrown mixture of malachite and haematite (Mal and Hm). Optical image taken in reflected PPL from sample MSSD080_14_1. 189

Figure 4.24: Type 2 vein-hosted chalcocite 2 cross-cutting stratiform-disseminated chalcocite 1. Optical image taken in reflected PPL from sample MSSD083_14_1_M. 190

Figure 4.25: Chalcopyrite 2 being progressively replaced by chalcocite 2 and then digenite 2 within a Type 2 dolomite vein. Optical image taken in reflected PPL from sample MSSD083_06_1. 191

Figure 4.26: Mass of native copper 1 mantled by chalcocite 3. Optical image taken in reflected PPL from sample MSSD080_18_1. 192

Figure 4.27A: SEM image showing the locations of EDS spot analyses. Spectra, shown in Figure 4.26B, indicate that spectrum 1 = chrysocolla 1, spectrum 2 = malachite 1, spectrum 3 = tenorite 1 and spectrum 4 = cuprite 1. These phases occur in the paragenetic order of cuprite 1, tenorite 1, malachite 1 and finally chrysocolla 1, generally appearing to fill voids in the rock from the

outside inwards, with chrysocolla 1 filling the last remaining space during crystallisation. Sample MSSD080_18_1. 193

Figure 4.27B: Results of EDS spot analyses conducted on Spectra 1-4 as shown in Figure 4.25A. Spectrum 1 represents chrysocolla. Spectrum 2 represents malachite. Note that carbon in the malachite chemical formula (Cu2CO3(OH)2) is not represented in the quantitative analysis of malachite, due to the carbon coating of the sample. Spectrum 3 represents tenorite. Spectrum 4 represents cuprite, which contains less oxygen by proportion than tenorite and is also brighter in the SEM image (Figure 4.25A). Si is included in the results for cuprite and tenorite, due to overlapping analysis of nearby chrysocolla within the area of electron-gathering during EDS spot analyses..... 194

Figure 4.28: Chalcocite 3, concentrically banded with haematite 2 around cobaltoan pyrite 1, and replacing it. Optical image taken in reflected PPL from MSSD080_13_2. 195

Figure 4.29: SEM image of chalcocite 3 and haematite 2 intergrown, or forming exsolution textures with each other (see inset – haematite is the darker of the two phases). This mixture appears to be replacing a chalcocite 2 crystal in situ, which is wrapped around a euhedral apatite (Apa) - barite (Bar) crystal within a Type 2 vein. Sample MSSD075_19_2. 196

Figure 4.30: Bornite 3 and haematite 3 rimming and replacing chalcopyrite 1 and chalcocite 1. Optical image taken in reflected PPL of MSSD075_15_1. 197

Figure 4.31: Carrollite replaced by a complicated assemblage of chalcocite 3, digenite 3, and covellite 3, with later haematite 2 and malachite 1. Optical image taken in reflected PPL from sample MSSD080_10_2. 197

Figure 4.32: A groundmass-disseminated crystal of pyrite 2 being replaced by haematite 2. Optical image taken in reflected PPL from sample MSSD083_07_2..... 198

Figure 4.33: Haematite 2 replacing a crystal of pyrite 2. A vein of later chalcocite 4 and haematite 3 abuts against the rim of haematite 2. Optical image taken in reflected PPL of sample MSSD083_20_1. 199

Figure 4.34: Haematite 2 crystals in a Type 2 dolomite vein mantled by concentrically zoned spherocobaltite (Sct) and cobaltoan dolomite. The faint pink colour of the vein dolomite belies a slight Co content making it cobaltoan dolomite (CoDol). Optical image taken in transmitted PPL of sample MSSD083_17_1. 200

Figure 4.35: SEM image of the haematite (Hm2) crystal on the right in Figure 4.33. EDS analyses suggest minute amounts of spherocobaltite in contact with Hm2, mantled by cobaltoan magnesite (CoMag), followed by high-Co cobaltoan dolomite (HiCoDol), and finally low-Co cobaltoan dolomite (CoDol) making up the bulk of the vein. The phases are arranged in order of decreasing-outwards Co-content perhaps suggesting the progressive breakdown and replacement of a central Co mineral. 200

Figure 4.36: SEM image of heterogenite 1 intergrown with apatite and quartz. EDS analysis of the phase shows that heterogenite 1 contains up to 10 wt.% Cu (Spectrum 1). The Si content of the Spectrum 1 analysis is caused by intergrown quartz. Note the concentrically zoned botryoids of heterogenite 1 towards the upper left of the image. Malachite 1 can be seen abutting against these heterogenite 1 botryoids. Sample MSSD080_18_1. 201

Figure 4.37: SEM image of azurite 1 rimming and replacing euhedral cuprite 1, while chrysocolla 1 forms rims to azurite 1. Spectrum 1 is the result of an EDS analysis of azurite 1. Note the carbon content of azurite (Cu3(CO3)2(OH)2) is not represented by the analysis, as the sample has been carbon coated. The Cu content of the analysis is too high for the mineral to be malachite, which has a similar signature but contains less wt.% Cu. This is diagnostic of azurite, supported by the deep blue tinge to the portion of the slide from which this image was taken. Sample MSSD080_18_1. 202

Figure 4.38: SEM image of malachite 1, chrysocolla 1, malachite 2 and chrysocolla 2 filling voids in a Type 2 dolomite vein. Malachite 1 and chrysocolla 1 occur as earlier veins which terminate at the void in which malachite 2, followed by chrysocolla 2, grow as outwards-in void fills. Sample MSSD080_10_2. 203

Figure 4.39: Void filling bands of chalcocite 4 and haematite 3. Optical image taken in reflected PPL from sample MSSD083_20_1. 204

Figure 4.40: Replacement of a carrollite 1 crystal in two stages: first by chalcocite 3, and then by chalcocite 4 which appears to be intergrown with an unidentified mineral, possibly haematite. Optical image taken in reflected PPL from sample MSSD083_24_2. 204

Figure 4.41: Fracture-fill veins with haematite 3 forming first at the vein margins followed by malachite 2. Optical image taken in reflected PPL from sample MSSD083_07_1. 205

Figure 4.42: Replacement of dolomite (Dol) along a Type 1 vein by cobaltoan carbonate (CoCarb2). Optical image taken in transmitted PPL of sample MSSD083_17_1. 206

Figure 4.43: Chaotic distribution of quartz (Qtz), micrite (Mct) and a mixture of chlorite (Chl) and mica (Mic) in the RSC unit. Heterogenite (Het2) occurs pervasively as amorphous masses distributed through the micaceous portion of the rock. Optical image taken in transmitted XPL from sample MSSD075_17_1. 207

Figure 4.44: Dendritic heterogenite 2 growing through the groundmass of the Schistes Dolomitique Superieur unit (SDS). EDS analysis shows that heterogenite 2 is intergrown with apatite. Later malachite 2 grows around the Het2 dendrites. Optical image taken in transmitted PPL from sample MSSD080_14_2. 207

Figure 4.45: Radial-fibrous malachite 2 within a fracture-fill vein in the RAT Rouge. The earlier haematite 3 phase can be seen around the vein-margins. Optical image taken in transmitted PPL from sample MSSD140_07_1. 208

Figure 4.46: Anhedral malachite 2 forming in voids and fracture-fill veins, with later-formed chrysocolla 2 forming the centres to these voids and veins. Optical image taken in transmitted PPL from sample MSSD080_10_2. 209

Figure 4.47: Botryoidal pseudomalachite 1 growing out from earlier-formed botryoids of malachite 2. Optical image taken in transmitted PPL from sample MSSD140_07_1. 210

Figure 4.48: SEM image of an assembly of euhedral laths of haematite 3, radial fibrous malachite 2 and botryoidal pseudomalachite 1, formed in that paragenetic order. Sample MSSD140_07_1. 210

Figure 4.49: Table showing the distribution of mineralisation-related phases identified in MSSD057, 080 and 083, in each of the stratigraphic units at Mashitu South. The number in each cell shows how many samples from a particular unit carried a particular mineralisation phase. Each cell has a corresponding bar representation, the thickness of which is proportional to the number of samples identified. The 'Stages' into which all the phases are grouped will be discussed in Section 4.4. 212

Figure 4.50: SEM image of a detrital zircon (Zir) grain within the quartz (Qtz), mica (Mic) and chlorite (Chl) groundmass of the RSC unit, showing EDS spot analysis of the grain (Spectrum 1). Sample MSSD075_17_2. 213

Figure 4.51: SEM image of a calcite (Cal) vein cutting through a nodule of magnesite (Mag) within a groundmass of dolomite (Dol) and quartz (Qtz), in the DStrat unit. An EDS spot analysis of the vein shows a high Ca:Mg ratio indicative of calcite (carbon is not represented in the analysis as the sample has been carbon coated). Some, if not all of the Mg indicated by the results may come from overlap of the adjacent magnesite into the analysis. Sample MSSD083_26_1. 214

Figure 4.52: SEM image of magnesite (Mag) nodules within a dolomite (Dol) and quartz (Qtz) groundmass, with disseminated pyrite (Py), in the DStrat unit. Sample MSSD083_26_1. ... 215

Figure 4.53: SEM image of magnesite (Mag) and apatite (Apa) in a Type 2 dolomite vein. Sample MSSD080_10_1. 215

Figure 4.54: SEM image of euhedral spars of chlorite (Chl) between crystalline quartz (Qtz). Heterogenite (Het) fills the space between chlorite crystals. Sample MSSD075_17_2. 216

Figure 4.55: Foliated muscovite mica (elongate crystals and high birefringence colours: purple and orange) within the siliciclastic groundmass of the SD2d black shale stratigraphic unit. Optical image taken in transmitted XPL of MSSD083_21_4. 217

Figure 4.56: SEM image of laths of iron-rich biotite (Bio) in a siliciclastic quartz (Qtz)-chlorite (Chl) groundmass, with later apatite (Apa). The lack of Mg in the EDS analysis (Spectrum 4) suggests that this crystal is the iron-rich end-member, annite. Sample MSSD080_14_2. 218

Figure 4.57: SEM image and EDS analysis of an authigenic rutile (Rut) crystal. Sample MSSD075_22_2. 219

Figure 4.58: SEM image and EDS analysis of a euhedral rhombic monazite (Mon) crystal within a chloritic, siliciclastic (Chl+Qtz) groundmass. Sample MSSD075_22_2. 220

Figure 4.59: SEM image and EDS analysis of a euhedral lath of apatite (Apa) within a Type 2 dolomite (Dol) vein. The apatite has later barite (Bar) growing within cavities in it, and is mantled and cross-cut by chalcocite (Cc) and haematite (Hm). Sample MSSD075_19_2. 221

Figure 4.60: SEM image and EDS analysis of an anhedral mass of barite (Bar), rimmed and replaced by haematite (Hm) and apatite (Apa), in the silicic, chlorite-rich RSC unit. Sample MSSD075_17_2. 222

Figure 4.61: SEM image and EDS analysis of a skeletal halite (Hal) crystal within a Type 2 vein, in proximity to monazite (Mon), apatite (Apa), quartz (Qtz) and magnetite (Mag). The skeletal

crystal structure of the halite appears to be in high relief on the sample. This is unusual, as one would not expect halite, with a low hardness, to survive the polishing process in high relief. It is possible that halite crystal growth could have occurred on the surface of the sample sometime after polishing due to contamination. Sample MSSD080_10_1. 223

Figure 4.62: SEM image and EDS analyses of sulphate phases as inclusions within authigenic quartz. Tiny inclusions of gypsum (Gy) or anhydrite (Anh) and a Sr-bearing mineral that could be celestine (Cel) (Spectrum 3 is mixed and may include analysis of nearby quartz and barite as well as celestine) are replaced along fractures in the quartz (Qtz) by later barite (Bar). Sample MSSD075_22_2. 224

Figure 4.63: Photograph of a quarter-core sample MSSD075_19_2, from the DStrat. Within this sample a Type 2 dolomite vein, which hosts chalcocite (grey blebs within the vein), can be seen to cross-cut a network of Type 1 dolomite veins. Type 1 and Type 2 veins are outlined in red and blue, respectively. Scale bar at the left of the sample is in centimetres. 225

Figure 4.64: Euhedral quartz (Qtz) at the margin of a Type 1 vein. Optical image taken in transmitted XPL of sample MSSD083_21_3. 226

Figure 4.65: Optical images of various different paragenetic phases of Type 1 veins, taken from the same viewpoint. A: subhedral apatite (Apa). Transmitted, PPL. B: Euhedral quartz (Qtz) and anhedral dolomite (Dol). Transmitted, XPL. C: Anhedral chalcopyrite 1 (Cpy1) which is hosted at the margins of the Type 1 vein, and unrelated pyrite 2 (Py2) which is groundmass-hosted. Reflected, PPL image of MSSD083_21_4. 227

Figure 4.66: SEM image of a Type 2 dolomite (Dol) vein containing early magnesite (Mag) and later apatite (Apa) and halite (Hal). Sample MSSD080_10_1. 228

Figure 4.67: SEM image of tiny inclusions of chlorite (Chl) within Type 2 vein-hosted chalcocite (Cc). The EDS Spectrum 4 presents a mixed analysis which captures some of the chalcocite surrounding the tiny chlorite grains. Sample MSSD080_10_1. 229

Figure 4.68: Summary of sulphur isotope results from this study, compared against selected ranges of $\delta^{34}S$ values for different sources of sulphur (Thode, 1991). Meteoric sulphur refers to sulphur dissolved in rain and snow, evaporites refer to evaporitic sulphates such as gypsum and sedimentary sulphides refers to authigenic, diagenetic sulphides such as pyrite. Typical values in this range are represented by a solid black line and uncommon values are represented by a

dashed line. Arrows at the margins of the graphs show that the range of $\delta^{34}S$ values for this category extends beyond the area shown by the graph 230

Figure 4.69: Pyrite 2 (Py2) being replaced in-situ by chalcocite 1 (Cc1), within a region of microcrystalline quartz silicification in the DStrat. Optical image taken in reflected PPL from sample MSSD075_19_1. 233

Figure 4.70: Type 1 veins composed of quartz (Qtz), minor dolomite and pyrite 3 (Py3) 'breaking through' layers of the rock within the micritic groundmass of the DStrat unit. It seems likely that this veining occurred pre-lithification and was caused by fluid overpressure, inducing soft-sediment deformation. Optical image taken in XPL from sample MSSD075_19_1. 236

Figure 4.71: Red-Green-Blue EDS map of a stratiform-disseminated sulphide bleb. Red=Fe, Green=Cu, Blue=Co. Note the blue-green carrollite (Car1) phase rimming all earlier-formed stratiform sulphides, including pyrite (Py2), chalcopyrite (Cpy1) and chalcocite (Cc1). Sample MSSD083_23_2. 238

Figure 4.72: Red-Green-Blue EDS map of a Type 1 vein-hosted sulphide bleb. Red=Fe, Green=Cu, Blue=Co. Carrollite 1 (Car1) rims chalcocite 1 (Cc1) and in some cases pyrite 3 (Py3), and occurs along grain boundaries and in veins cutting chalcocite 1. A remnant of bornite (Bn1) exists in the middle of the chalcocite. Red streaks within some of the Car1 'veins' are haematite which is thought to have exploited the same fractures in the grains as the Car1 phase, at a later time. Sample MSSD075_16_2. 239

Figure 4.73: Comparison of the paragenetic phases present in all high-grade (>1%/10,000ppm Cu) samples from MSS075, 080 and 083, ranked in order of Cu grade. This figure was compiled by taking the grade of the closest assay interval to the sample. Note that the carrollite 1 (Car1) and chalcocite 3 (Cc3) phases are present in more high grade samples than other phases, and appear to make a significant contribution to Cu grades at Mashitu South. 243

Figure 4.74: Eh-pH diagram showing copper mineral stability at surface conditions and at low f(CO2) (modified from Taylor, 2011). Paths 1 and 2 reflect trends of variation in Eh and pH required to form the paragenetic order of mineralisation observed in the Early Supergene Stage at Mashitu South. 248

Figure 4.75: Genetic summary of the 5 mineralisation stages at Mashitu South. Bracketed numbers in bold are references to literature: (1): Sillitoe et al. (2015); (2): Jensen and Dechow (1962); (3):

El Desouky et al. (2009); (4): Brown et al. (2014); (5): Hitzman et al. (2010); (6): Selley et al. (2010); (7): De Putter et al. (2010); (8): Armstrong et al. (2005); (9) Selley et al. (2006); (10): Decree et al. (2014); (11): Kampunzu et al. (1991); (12): Decree et al. (2010). 251

Figure 5.1: List of attributes assigned to each sample from the combined database..... 258

Figure 5.2: Detection limits for the various assay techniques, provided by Comide S.P.R.L..... 258

Figure 5.3: Example of part of a correlation matrix completed for a geochemical dataset. The colour coding of cells is a result of the conditional formatting described above, it allows for a quick and simple assessment of strong positive (warm colours) and negative (cold colours) correlations. In this example we see that the strongest positive correlation is between Ti and Al, while Ca:Sr, Be:Ti, Be:Zn and Ni:Co also correlate well with each other. Strong negative correlations are observed between Ca:Fe and between Ca:Be. This example is from the whole 12,058 sample combined database. 261

Figure 5.4: Example of a scatter plot of two attributes created from one of the datasets. This particular example shows a strong positive correlation between titanium and aluminium within all the samples in the core of MSSD083. The R-value for these variables is 0.9096. 262

Figure 5.5: Atomic and molecular weights of the components used to calculate the A, C and F variables, to one decimal point. Atomic weights from Winter (2016)..... 263

Figure 5.6: Triangular ACF diagram showing fields where different rock types typically plot, after Eskola (1915) and taken from Nelson (2011)..... 265

Figure 5.7: Example of multiple datasets compared by their ACEMS-normalised-mean-values. Shown here are 6 lithostratigraphically split datasets (left, in rows) and the respective elements by which they are compared (top, in columns). Anomalously high values are in yellow and orange, close-to-average values are in green while anomalously low values are in blue and purple (refer to text). 267

Figure 5.8: Average Concentration of Elements at Mashitu South (ACEMS) normalising values calculated by finding the mean concentration of each element within the entire 12,058 assayed sample combined database. 268

Figure 5.9: Example of the application of the normalising-to-ACEMS process. The split dataset comprising the Lithology of 'Shale and Massive Sulphide' is used, a small, 2m interval

consisting of 3 samples from hole MSSD182. Table A: ACEMS normalising values. Table B: Mean concentrations of elements within the dataset. Table C: Normalised-to-ACEMS values (Norm.), which are calculated by dividing the values in B by the values in A and plotted on the multi-element plot below. Values in Table C are colour coded; Orange: Norm. ≥ 10; Yellow: 10 > Norm. ≥ 2; Green: 2 > Norm. ≥ 0.5; Blue: 0.5 > Norm. It is evident by Table C and the spider plot that S, Ca, Cu, K, V, Zn, Mo and Cd are anomalously high in 'Shale and Massive Sulphide', while Mn, Ni and Ag are anomalously low. 269

Figure 5.10: Pie chart of the various different logged lithologies corresponding to geochemical samples at the Mashitu South deposit, out of a total of 12,058 samples. The number next to each lithology name is the amount of samples which were logged as this lithology. 271

Figure 5.11: Pie chart of the various different logged stratigraphies corresponding to geochemical samples at the Mashitu South deposit, out of a total of 12,058 samples. The number next to each stratigraphy name is the amount of samples which were logged as this stratigraphy. 272

Figure 5.12: Logarithmic line chart showing the Average Concentration of Elements at Mashitu South (ACEMS) calculated by taking the mean concentration of each element in all 12,058 geochemical samples from the deposit. 273

Figure 5.13: Frequency distributions for A: Magnesium and B: Aluminium, the two most abundant elements out of the 28 analysed in the Mashitu South samples. Low skewness in both cases indicates that these are rock-forming elements at the deposit, but both histograms suggest a multi-modal frequency distribution (bimodal for Mg, trimodal for Al) suggesting that both contain multiple populations, some close-to-normally distributed and some with a skewed distribution..... 274

Figure 5.14: Frequency distributions for A: Copper and B: Cobalt. Both distributions appear unimodal and highly skewed, typical of ore elements. 275

Figure 5.15: Ranked skewness of the frequency distributions of elements analysed at Mashitu South. 276

Figure 5.16: Pearson correlations of elements with depth at Mashitu South. 277

Figure 5.17: Scatter plot of depth vs. element concentration for Cu and Co in the samples from Mashitu South. There are two zones of enrichment, one at depth (demarcated by brackets) and one

near-surface (indicated by arrows). Note that the near-surface zone of enrichment is higher for Co than for Cu. 278

Figure 5.18: Table of R-values for element vs. element concentration for Cu and Co at Mashitu South. 279

Figure 5.19: Pie chart showing the lithological composition of the CMN unit. 281

Figure 5.20: Spider diagram showing the ACEMS-normalised mean concentrations of different elements in the CMN. 282

Figure 5.21: Summary table showing the ACEMS-normalised mean concentrations of different elements in various lithologies within the CMN. 282

Figure 5.22: Pie chart showing the lithological composition of the SDS unit. 283

Figure 5.23: Spider diagram showing the ACEMS-normalised mean concentrations of different elements in the SDS. 284

Figure 5.24: Summary table showing the ACEMS-normalised mean concentrations of different elements in various lithologies within the SDS. 284

Figure 5.25: Pie chart showing the lithological composition of the SD2d unit. 285

Figure 5.26: Spider diagram showing the ACEMS-normalised mean concentrations of different elements in the SD2d. 286

Figure 5.27: Summary table showing the ACEMS-normalised mean concentrations of different elements in various lithologies within the SD2d. 286

Figure 5.28: Pie chart showing the lithological composition of the SDB unit. 287

Figure 5.29: Spider diagram showing the ACEMS-normalised mean concentrations of different elements in the SDB. 288

Figure 5.30: Summary table showing the ACEMS-normalised mean concentrations of different elements in various lithologies within the SDB. 288

Figure 5.31: Pie chart showing the lithological composition of the RSC unit. 289

Figure 5.32: Spider diagram showing the ACEMS-normalised mean concentrations of different elements in the RSC. 290

Figure 5.33: Summary table showing the ACEMS-normalised mean concentrations of different elements in various lithologies within the RSC. 290

Figure 5.34: Pie chart showing the lithological composition of the RSF unit. 291

Figure 5.35: Spider diagram showing the ACEMS-normalised mean concentrations of different elements in the RSF. 292

Figure 5.36: Summary table showing the ACEMS-normalised mean concentrations of different elements in various lithologies within the RSF. 292

Figure 5.37: Pie chart showing the lithological composition of the DStrat unit. 293

Figure 5.38: Spider diagram showing the ACEMS-normalised mean concentrations of different elements in the DStrat. 294

Figure 5.39: Summary table showing the ACEMS-normalised mean concentrations of different elements in various lithologies within the DStrat. 294

Figure 5.40: Pie chart showing the lithological composition of the RAT Gris unit. 295

Figure 5.41: Spider diagram showing the ACEMS-normalised mean concentrations of different elements in the RAT Gris. 296

Figure 5.42: Summary table showing the ACEMS-normalised mean concentrations of different elements in various lithologies within the RAT Gris. 296

Figure 5.43: Pie chart showing the lithological composition of the RAT Rouge unit. 297

Figure 5.44: Spider diagram showing the ACEMS-normalised mean concentrations of different elements in the RAT Rouge. 298

Figure 5.45: Summary table showing the ACEMS-normalised mean concentrations of different elements in various lithologies within the RAT Rouge. 298

Figure 5.46: Pie chart showing the lithological composition of Undifferentiated Breccias. 299

Figure 5.47: Spider diagram showing the ACEMS-normalised mean concentrations of different elements in Undifferentiated Breccias. 300

Figure 5.48: Summary table showing ACEMS-normalised mean concentrations of different elements in various lithologies within Undifferentiated Breccias. 300

Figure 5.49: Summary of ACEMS-normalised mean element concentration at different depth-intervals. 303

Figure 5.50: Spider diagram showing the data presented in Figure 5.49. 303

Figure 5.51: Summary of ACEMS-normalised mean element concentrations within 1m depth intervals from the top 10 of core from Mashitu South. 304

Figure 5.52: Spider-graph of ACEMS-normalised concentrations of elements at different depth intervals in the top 10m of drill core at Mashitu South. 305

Figure 5.53: Line graph showing variation of the mean concentrations of selected elements normalised to ACEMS (represented as line series) at different depth intervals. 306

Figure 5.54: Downhole Sr:Sc ratios (blue line) plotted against clast/grain size (black line) and interpreted stratigraphy (see stratigraphic key), for MSSD080, 083, 075 and 140. 309

Figure 5.55: ACF ternary diagram for CMN samples in MSSD075, 080 and 083 showing a trend from originally calcareous rocks towards increasing values of F. Fields in which calcareous rocks (blue), basic rocks (green), quartzo-feldspathic rocks (orange) and pelitic rocks (brown) would be expected to plot are shown on the diagram. 311

Figure 5.56: Scatter plot of Mg and Ca concentration in CMN samples in MSSD075, 080 and 083 showing three different trends of Ca and Mg variation. Trends are explained in the text... 311

Figure 5.57: Scatter plot of Mg and Ca concentration in SDS samples in MSSD075, 080 and 083 showing two different trends of Mg and Al variation. 312

Figure 5.58: ACF ternary diagram for RSC samples in MSSD075, 080 and 083 showing a trend from originally calcareous rocks towards decreasing values of C, with little change in the F proportions. Fields in which calcareous rocks (blue), basic rocks (green), quartzo-feldspathic rocks (orange) and pelitic rocks (brown) would be expected to plot are shown on the diagram. 313

Figure 5.59: Evidence for potassic alteration in the Mines Series at Mashitu South. A: high positive correlation between K and Al in hole MNWR016, with nearly a 1:1 relationship between concentrations of the two elements. B: AKF diagram showing a trend of alteration of S.D. samples towards higher K and A values. C: depth profile for K with stratigraphy in MSSD075. D: Average K contents of each stratigraphic unit in MSSD075, 080, 083 and 140. 314

Figure 5.60: ACF ternary diagram for RSF samples in holes MSSD075, 080 and 083 (symbolised as red dots) and MSSD140 (red bars), showing progressive silicification and subsequent argillic alteration. 315

Figure 5.61: Table of correlations between Cu and other elements in the various lithologies of MSSD075, 080, 083 and 140. R-values for the Pearson value for each correlation with Cu are displayed along the rows corresponding to each element. These values are colour coded as explained in Section 5.2.5. The sum of the R-values in each stratigraphic unit are included in the 'Sum of R-values' column, and these are ranked and colour coded separately in the right-most column. It can be observed that Co, Bi, Ni, Be, V, S, Fe, Mo, P, As and Zn correlate significantly over all of the stratigraphic datasets. Assessing the RAT Rouge stratigraphic column, we see that Be, P and K correlate well with Cu. Be and P are inferred to be associated with supergene Cu mineralisation in the RAT, while Co, Bi, Ni, V, S, Fe, Mo, As and Zn are inferred to be associated with hypogene Cu mineralisation in the Mines Series. 317

Figure 5.62: Map of the eastern portion of the Mashitu South deposit (see Figures 3.4 and 3.8) showing the distribution of drill holes from which samples were taken with levels of uranium concentration over 0.01% U. On the circular icons above U-bearing holes, the colours represent the maximum grade of uranium found in a sample and the numbers represent the number of samples in each hole which contain >0.01% U. 319

Figure 5.63: Down-hole profile of uranium concentration in MSSD083 combined with stratigraphy. As we can see, U-grade is particularly pronounced within, or directly adjacent to, the RSC stratigraphic unit..... 320

Figure 5.64: W-E cross section through the eastern flank of the Mashitu South deposit. Intersections with significant grades of U (>100ppm) are circled in red, note that these correspond to the RSC stratigraphic unit. Each square on the grid is 100m x 100m. 321

Figure 5.65: Correlations between U and various other elements within the whole Mashitu South combined database. U correlates well with Ni and Co, and less well with S, As and V. 322

Figure 5.66: ACF ternary diagram for samples from MSSD075, 080, 083 and 140. Geochemical trends in the samples suggest the presence of a number of different alteration types changing the primary geochemistry of these sedimentary rocks, including magnesian alteration, argillic alteration and silicification. 325

Figure 5.67: Table of average copper concentration in the various stratigraphic units of Mashitu South. The 'predominant lithology' column represents the most commonly logged primary lithology of each stratigraphic unit. The 'equivalent in %' column is the result of multiplying the ACEMS value for Cu (0.64%) with the ACEMS-normalised value for each dataset. The 'primary correlator' column represents the element in each dataset which shows the highest Pearson r-value correlation with Cu. The data show that the SD2d and the RSF represent significant stratigraphic orebodies, with Bi and Mo associated with copper in these two units. 330

Figure 5.68: Table of average cobalt concentration in the various stratigraphic units of Mashitu South. The 'predominant lithology' column represents the most commonly logged primary lithology of each stratigraphic unit. The 'equivalent in %' column is the result of multiplying the ACEMS value for Co (0.16%) with the ACEMS-normalised value for each dataset. The 'primary correlator' column represents the element in each dataset which shows the highest Pearson r-value correlation with Co. The RSF is the most significant orebody for Co. Ni correlates with Co very consistently in most of the stratigraphic units. 330

Figure 5.69: Table of average copper concentration in the various lithological units of Mashitu South. The 'equivalent in %' column is the result of multiplying the ACEMS value for Cu (0.64%) with the ACEMS-normalised value for each dataset. Cu concentration tends to be high in breccia lithologies and low in 'clay' or 'saprolite' lithologies. 332

Figure 5.70: Table of average copper concentration in the various lithostratigraphic units of Mashitu South. The 'equivalent in %' column is the result of multiplying the ACEMS value for Cu (0.64%) with the ACEMS-normalised value for each dataset. The 'primary correlator' column represents the element in each dataset which shows the highest Pearson r-value correlation with Cu. Lithologies from the RSF and SD2d appear to have the highest concentrations of Cu, and 'breccia' lithologies also tend to have high Cu concentrations. 'Saprolite' and 'Clay' lithologies tend to be poor in Cu, by comparison..... 334

Figure 5.71: Table of Pearson correlation coefficient R-values for each different element, in the 5 designated depth intervals, ranked. The elements Co, Bi, Ni, V, S, Mo, As and Fe, which appear to be associated with copper in deeper datasets, are highlighted in orange, while Be and P,

which seem to be associated with copper in shallow datasets, are highlighted dark green. Zn, which shows a loose association with copper in both deep and shallow datasets, is highlighted in yellow. Different elements can be observed to have different correlations with Cu at different depth intervals. 336

Figure 5.72: Table of Pearson correlation coefficient R-values for each different element in the 5 designated depth intervals, which have been assigned a number 1-5 with increasing depth. The right hand column shows the 'correlation of the correlation of an element with copper, with depth'. These results are summarised in the bottom sub-table. The 'correlation of the correlation of an element with copper, with depth' is most positive in Co, while it is most negative in P, with the order Co, Fe, V, Mo, Bi, Ni, As, S, Zn, Be, and P of affinity with Cu at depth vs. near the surface. 337

Figure 5.73: Downhole element plots of Cu, Co, Bi, Ni, V and S within MSSD075. The variation in sample concentration for each element (black line) is shown alongside the logged stratigraphy through each hole, which is represented by shading as follows: CMN: maroon; SDS: dark blue; SD2d: brown; SDB: beige; RSC: light blue; RSF: red; DStrat: orange; RAT Gris: green; RAT Rouge: yellow. Each element shows good spatial correspondence with each other in zones of Cu mineralisation, particularly at depth, and especially within the RSF and SDB stratigraphic units which are known to be regional stratiform Cu-Co orebodies. 339

Figure 5.74: Scatter plot of Cu vs P in the Mashitu South combined database. Most of the data is relatively scattered, however a very distinct linear trend exists (marked by the dashed black arrow) between the two elements within certain data, with a Cu:P ratio of 5:1 (shown by the red lines). This consistent trend in the data would suggest the growth of a Cu-P mineral with the same elemental ratio of Cu:P. 341

Figure 5.75: Downhole element plot of Cu, P, and Be in MSSD140. Stratigraphy is represented by the colour shading on the graph: the RAT Rouge is shaded yellow, the RSF is shaded red, and unknown/unassigned stratigraphy is left unshaded. Cu, P and Be all appear in greatly elevated concentrations between a depth of 30-50m, corresponding to a region of breccia-hosted, malachite-dominated supergene remobilised mineralisation. 342

Figure 5.76: Comparative Cu and Co soil geochemistry maps for the Mashitu and Anticline complexes. At this scale (1:30,000), Co gives a more focussed anomaly, nearer to the mineralised Mines Series fragments than Cu, which is more broadly distributed by comparison. Cu also seems to

have concentrated along the bed of a nearby tributary, which Co has not done to such an extent. Modified from Siebel et al. (2013)..... 344

Figure 6.1: Depth profile for Cu, Bi, Co, V, Mo and Ni concentration in MSSD140. The 30-50m zone of Cu enrichment is overlain by a region in the top 10m where Bi, V, Co, Mo and Ni are enriched. 350

Figure 6.2: Map of the extent of the Comide sampling program (outlined in red) overlain on the regional geology, an expanded view of which is shown in Figure 3.3. The grid squares are 5km x 5km for scale. 351

Figure 6.3: Exemplary values used for the calculation of the CoCoNiBiVMo index for fictional sample X. See text above for explanation. 352

Figure 6.4: Soil geochemical contour map for Cu, overlain on regional geology 354

Figure 6.5: Soil geochemical contour map for Co, overlain on regional geology 355

Figure 6.6: Soil geochemical contour map for Ni, overlain on regional geology 356

Figure 6.7: Soil geochemical contour map for Bi, overlain on regional geology 357

Figure 6.8: Soil geochemical contour map for V, overlain on regional geology 358

Figure 6.9: Soil geochemical contour map for Mo, overlain on regional geology..... 359

Figure 6.10: Soil geochemical contour map for Ca, overlain on regional geology 360

Figure 6.11: Soil geochemical contour map for Ti, overlain on regional geology 361

Figure 6.12: Soil geochemical contour map for the CuCoNiBiVMo index, overlain on regional geology 362

Figure 6.13: Soil geochemical contour map for the CoNiBiVMo index, overlain on regional geology 363

Figure 6.14: Soil geochemical contour map for the CoNiBi index, overlain on regional geology 364

Figure 6.15: Soil geochemical contour map for the CoBi index, overlain on regional geology 365

Figure 6.16: Inflated portion of the SE corner of the Cu soil geochemistry map presented in Figure 6.4, with locations of Cu-Co deposits/Mines Series fragments in the vicinity of Mashitu South. While appreciable Cu anomalies exist over the Kinshasa and Anticline deposit groups, the Mashitu and Kalukundi groups of deposits are not marked by such focussed anomalies. See Figure 6.4 for key. 367

Figure 6.17: Inflated portion of the SW portion of the Cu soil geochemistry map presented in Figure 6.4, with locations of Cu-Co deposits. Significant Cu anomalies exist over the Pungulume Principal, Pungulume East, Bona North and Bona South deposits. An unidentified, possibly deposit-related anomaly which exists towards the Southeast of this map is indicated. See Figure 6.4 for key. 368

Figure 6.18: Inflated portion of the NW portion of the Cu soil geochemistry map presented in Figure 6.4. Several Cu anomalies exist within a region mapped as 'Undifferentiated Roan' (outlined in red). This region is effectively an inlier surrounded by Nguba and Kundelungu Group rocks. An additional, lone anomaly exists further towards the West, at the boundary between the Nguba and Kundelungu Groups. See Figure 6.4 for key. 369

Figure 6.19: Inflated portion of the south-central portion of the Cu soil geochemistry map presented in Figure 6.4. A series of indicated Cu anomalies are found in close proximity to a river bed. Another Cu anomaly is indicated over a tight inlier of Roan Group between two faulted contacts with the Kundelungu Group, which could possibly be related to an undiscovered Cu deposit. See Figure 6.4 for key. 370

Figure 6.20: Map of Ti concentration in soil over the Camrose concession. Limits of the Ng1.1 (Grand Conglomerat) stratigraphic unit are outlined in red. The Ng1.1 unit appears to be characterised by broad anomalies of high Ti-in-soil. 371

Figure 6.21: Inflated portion of the map of Ti concentration in soil over the Camrose concession shown in Figure 6.20. Negative Ti anomalies (indicated) surround the Pungulume and Bona deposits. 372

Figure 6.22: Co concentration in soil maps from the Anticline-Mashitu area. Data collected by Africo Resources is displayed on the left (modified from Siebel et al., 2013) and the Comide dataset is displayed on the right. A pronounced Co anomaly exists over the deposits in the Africo data but not in the Comide data. 373

Figure 6.23: Inflated portion of the Ni concentration in soil map from Figure 6.6, showing a rectangular region where all Ni-in-soil values are 0. See Figure 6.6 for key. 374

Figure 6.24: Inflated portion of the Bi concentration in soil map from Figure 6.7, showing a rectangular region where most Bi-in-soil values are 0, with a few isolated exceptions. See Figure 6.7 for key. 374

Figure 6.25: Inflated portion of the Mo concentration in soil map from Figure 6.9, showing a rectangular region outside of which all Mo-in-soil values are 0. See Figure 6.9 for key. 375

Figure 6.26: Inflated portion of the V concentration in soil map from Figure 6.8, showing a pronounced linear anomaly of V which is likely to be a data-artefact created by error. See Figure 6.8 for key. 375

Figure 6.27: Table and line graph showing the enrichment factors for the concentration of elements in soil at Mashitu South (MSS), relative to the concentration of elements in the regional soil data. Values above 1 mean that an element is relatively enriched in the soil at Mashitu South compared to the regional abundance, and values below 1 mean that an element is relatively depleted at Mashitu South compared to the regional abundance in soil. 379

Figure 7.1: Lithostratigraphic column of a portion of borehole MSSD083, showing the location of sample MSSD083_16_1 and including Cu and Co assays. 383

Figure 7.2: Photograph of sample MSSD083_16_1 and the polished original thin-section which was cut from it. The thin section is taken from the corner of the sample indicated by the red rectangle. 384

Figure 7.3: Summary of the material used in this study. 385

Figure. 7.4. Optical photomicrographs of groundmass and vein mineralisation textures in thin sections cut from sample MSSD083_16_1 (A, B and D: reflected PPL; C: transmitted PPL). Py=pyrite, cc=chalcocite, carr=carrollite, gdms=groundmass, qtz=quartz, ap=apatite and rt=rutile. A: Para-framboidal pyrite band mantled by chalcocite and carrollite. B: Early subhedral pyrite within a quartz-rich band of groundmass, mantled by chalcocite, which is itself rimmed by carrollite. C: dilated portion of apatite-rutile vein which cuts through the siliciclastic groundmass of MSSD083_16_1. These dilated portions of apatite-rutile veins are host to bacilliforms. D: Rutile from a constricted portion of an apatite-rutile vein, overgrown by groundmass-hosted chalcocite and carrollite. 388

Figure 7.5. Optical photomicrographs of bacilliforms within sample MSSD083_16_1; all images taken in reflected PPL. A: two conjoined bacilliforms composed of a central chalcocite region (navy blue-grey) and an external carrollite rim (white). B, C: hollow bacilliforms consisting of just a carrollite rim. D: Pyrite crystal (bright yellow-white) within the internal cavity of a hollow carrollite bacilliform. E, F: bacilliforms exhibiting curvature against the contacting apatite substrate. G,H: clusters of conjoined bacilliforms. 390

Figure 7.6A. Optical photomicrographs of bacilliforms taken in reflected PPL, showing the spot analysis locations for the corresponding spectra (a, b, c, d and e) in Figure 7.6B. Figure provided by Sosnicka (pers. comm., 2016) and reproduced with permission. 391

Figure 7.6B. Band-intensity-normalised Raman spectra corresponding to the spot analysis locations denoted in Figure 7.6A (a, b, c, d and e), together with spectra collected for Epofix resin, Akapaste diamond paste and haematite from sample MSSD083_16_1 for comparative purposes. The 'D' and 'G' markers denote the position of, respectively, the disorder (~1350 Δ cm-1) and graphite (~1600 Δ cm-1) modes of elemental carbon. All 5 spectra indicate traces of relatively disordered carbonaceous material at the site of analysis. Figure provided by Sosnicka (pers. comm., 2016) and reproduced with permission. 392

Figure 7.7. Size distribution of the population of 64 counted bacilliforms shown by which section cut from sample MSSD083_16_1 they were identified in. 394

Figure 7.8. Optical photomicrographs of bacilliforms from sample MSSD083_16_1, taken in reflected PPL. A: several bacilliforms occupying different cavities within an apatite vein. B: a number of bacilliforms occupying a single partially-haematite-filled cavity. C, D: examples of bacilliforms conjoined at the ends in a manner reminiscent of cell division. 398

Figure 7.9. Back-Scattered-Electron (BSE) electron microscopy images of a number of bacilliforms existing within a cavity in slide 16_1_A. B shows a magnified portion of the field of view in A, with both images taken of roughly the same area of the slide shown by the photomicrograph in Fig. 7.8B. 398

Figure 7.10. Optical photomicrograph of a bacilliform-hosting cavity within an apatite vein, taken in reflected PPL. Cavities within the apatite (ap) were coated, but not totally filled by an early phase of haematite (hm1). The carrollite (carr) bacilliform then grew/was emplaced, followed by a second phase of botryoidal haematite (hm2) which abuts against the bacilliforms. ... 400

Figure 7.11. Band-intensity-normalised Raman Spectra of spot analyses made in close proximity to bacilliforms within sample MSSD083_16_1. Spectra a and b correspond to the respective points on the reflected PPL photomicrographs. The 'D' and 'G' markers denote the position of, respectively, the disorder (~1350 Δ cm-1) and graphite (~1600 Δ cm-1) modes of elemental carbon. Both spectra show the presence of carbonaceous material outside of the boundaries of the bacilliforms themselves (in spectrum a the 'D' carbon mode is obscured by the disorder mode of haematite at ~1320 Δ cm-1). 404

Figure 7.12. Optical photomicrographs of abiogenic features within MSSD083_16_1, taken in reflected PPL. Ap= apatite, hm=haematite, carr=carrollite, rt=rutile, py=pyrite, gdms=groundmass and cc=chalcocite. A: an angular carrollite bacilliform in contact with a rutile crystal. B: lath-shaped elongate rutile crystals within the groundmass, some of which are sub-rounded at their ends. C: an acicular carrollite bacilliform, the long end of which runs parallel to a radial trend of fibrous apatite crystals, suggesting that the carrollite may be a pseudomorph of an apatite crystal. D: chalcocite and carrollite appearing to replace a lath-shaped crystal of rutile within an apatite vein. 406

Figure 8.1: Paragenesis table for the various mineralisation-related phases and alteration types at Mashitu South. Speculative ages are by reference to the literature as follows: (1): Maximum age of Roan depositions by age of detrital zircons from the Nchanga granite (Armstrong et al., 2005). (2): Re-Os date for stratiform sulphides at Konkola, Zambia (Barra et al., 2004). (3): Re-Os dates for stratiform and stratiform-remobilised hypogene sulphides at the Kamoto deposit (Muchez et al., 2015). (4): End of a period of U (and likely, other metals) circulation in the Katangan Copperbelt (Decree et al., 2014). (5): Re-Os date for vein-type sulphides at Konkola, Zambia (Selley et al., 2005). (6): Age of syn-metamorphic Cu-U mineralisation in the Domes Region, Zambia (Eglinger et al., 2014a; Turlin et al., 2015). (7): Age of two periods of supergene heterogenite formation in Katanga (Decree et al., 2010). The three phases indicated in red (Car1, Cc3 and Mal2 – see Chapter 5) are those which have contributed most significantly to the formation of high-grade Cu-Co ore at Mashitu South. 415

Figure 8.2: Conceptual model for the development of each of the mineralisation stages present at Mashitu South. A: Deposition of the R1 and R2 units. B: Development of Py in reducing and Hm in oxidising environments of deposition, as part of the Pre-Ore Diagenetic Stage. C: Formation of zoned, stratiform Cu- sulphides during the Early Hydrothermal SSC stage. D: RSC-focussed distribution of stratiform carrollite in the later part of the Early Hydrothermal SSC stage. E: Development of Type 2 vein-hosted sulphides of the Late Hydrothermal Ore Stage, focussed along faults and breccias. F: Formation of supergene oxides and sulphides of the Early and Late Supergene Stages: at the top of the profile, along breccias, and along the RSC unit. 416

Figure 8.3: Conceptual model for the dissociation of hypogene ore-associated elements during supergene alteration at Mashitu South. A hypogene orebody with an association of Cu+Co+Ni+Bi+V+Mo (left) is exposed to the surface environment and meteoric fluids (middle), producing a vertical pattern of enrichment zonation (right) based on the relative mobility of each element in meteoric fluids. Data from Mashitu South shows that Cu, the most mobile metal of the association, descends to a depth of between 10-50m where it is enriched as Late Supergene malachite-pseudomalachite ore, whereas Bi, the least mobile, is most enriched within the top <1m of the profile, remaining behind as a trace element in some residual phase such as haematite. 428

Figure 8.4: Conceptual model for the development of lateral element zonation around a fictional Cu deposit with a Cu-Co-Bi hypogene association. Bi, the least mobile element in meteoric fluid, remains proximal to the location of the orebody, while the more mobile Co and Cu are redistributed and enriched hydrologically and topographically downstream of the deposit in accordance with their mobility. Topographic map is from Apollo Mapping (2016) and is only used for conceptual purposes. 431

LIST OF ABBREVIATIONS AND TERMINOLOGY

AUTHOR-DEFINED TERMS

ACEMS.....Average Concentration of Elements at Mashitu South.

Normalisation factor created by the averaging of all available geochemical element-concentration data for the Mashitu South deposit, as described in section 4.2.8.

Bacilliform.....

Having the form of a 'bacillus', the Latin word for 'rod', which is typified by the 'bacilli' shape and 'Bacillus' genus of bacteria. See Chapter 7.

Para-Exotic.....

A descriptive term for supergene copper mineralisation which is found at some distance vertically below the source of metals, which is usually from the original position of hypogene mineralisation.

GENERAL

CAC.....Central African Copperbelt

CCB.....Congolese/Katangan Copperbelt

DRC.....Democratic Republic of the Congo

EDS..... Energy-Dispersive X-ray Spectroscopy

EGRI.....Economic Geology Research Institute

ENRC.....Eurasian Natural Resources Group

ICP-AES.....Induced-Coupled-Plasma Atomic-Emission-Spectroscopy

LA-ICP-MS..... Laser-Ablation Induced-Coupled-Plasma Mass-Spectroscopy

MSS..... Mashitu South

PPL..... Plane-Polarised Light

SEM..... Scanning Electron Microscope

SSC.....Sedimentary-hosted Stratiform Copper

XPL..... Cross-Polarised Light

XRF .....X-ray Fluorescence

ZCB ..... Zambian Copperbelt

MINERALOGICAL

Anh ..... Anhydrite

Apa ..... Apatite

Azu .....Azurite

Bar ..... Barite

Bio ..... Biotite

Bn ..... Bornite

Car ..... Carrollite

Cc..... Chalcocite

Cel ..... Celestine

Chl ..... Chlorite

CoCarb.....Cobaltoan Carbonate

CoDol.....Cobaltoan Dolomite

CoMag .....Cobaltoan Magnesite

CoPy ..... Cobaltoan Pyrite

Cov ..... Covellite

Cpy .....Chalcopyrite

Cry .....Chrysocolla

Cu .....Native Copper

Cup ..... Cuprite

Dg .....Digenite

Dol ..... Dolomite

Gy .....Gypsum

Hal .....Halite

Het.....Heterogenite

Hm ..... Haematite

Mag ..... Magnesite

Mal ..... Malachite

Mon ..... Monazite

Mus ..... Muscovite

Psm ..... Pseudomalachite

Py ..... Pyrite

Qtz ..... Quartz

Rut ..... Rutile

Sph ..... Sphalerite

Ten ..... Tenorite

Zir ..... Zircon

STRATIGRAPHIC

See section 1.3 for a systematic description of stratigraphic units. Entries here are presented in stratigraphic, rather than alphabetical order.

K ..... Kundelungu Group

K3 ..... Plateaux Subgroup

K2 ..... Kiubo Subgroup

K1 ..... Kalule Subgroup

Ng ..... Nguba Group

Ng2 ..... Monwezi Subgroup

Ng1 ..... Likasi Subgroup

R ..... Roan Group

R4 ..... Mwashya Subgroup

R3 ..... Dipeta Subgroup

R.G.S. ..... Roches Gréseuses Superieur

R2 ..... Mines Subgroup

CMN .....Calcaire et Mineraux Noire Unit, equivalent to the 'Kambove Formation'

SD ..... Schistes Dolomitique Unit, equivalent to the 'Dolomitic Shales Formation'

SDS ..... Shales Dolomitique Superieur Unit

SDB..... Shales Dolomitique du Base Unit

Kamoto Formation.....Consists of the RSC, RSF and DStrat units

RSC .....Roches Siliceuse et Cellulaire Unit

RSF ..... Roches Siliceuse et Feiulletées Unit

DStrat..... Dolomies Stratifée Unit

R1 ..... RAT Subgroup

RAT..... Roches Argileuse et Talceuse

RAT Gris ..... 'Grey' RAT, in contact with R2

RAT Rouge .....'Red' Rat generally found beneath the RAT Gris

CHAPTER 1: INTRODUCTION

1.1 Overview

This study has been carried out at the Mashitu South Cu-Co deposit, in the Katanga province, Democratic Republic of Congo (DRC) (Figure 1.1). It forms part of a research programme established between Professor J. Kinnaird of the Economic Geology Research Institute (EGRI), School of Geosciences, University of the Witwatersrand, and Eurasian Natural Resources Corporation (ENRC), now called Eurasian Resources Group (ERG). The work has also been supported by the Centre of Excellence for Integrated Mineral and Energy Resource Analysis (CIMERA).

The focus of this research is to categorise and understand the processes behind local primary sulphide mineralising events and the paragenetic transition to secondary oxide mineralising processes, with the aim of developing local geochemical and mineralogical indicators of, and vectors to, Cu-Co mineralisation. It was also developed with the aim of describing the paragenesis behind mineralisation at the deposit and fitting this paragenesis within the geological evolution of the Lufilian Arc.

The study area comprises the Camrose concession operated by ENRC and managed by the Comide (S.P.R.L) enterprise. The Mashitu deposit group is situated approximately 25km East of Lac Nzilo and the city of Kolwezi, in the Katangan province of the DRC. A regional map is provided (Figure 1.1) and a map of the Comide licence is included as Appendix 1. This area occurs in the northwestern side of the Central African Copperbelt (CAC), specifically within the Katangan (Congolese) portion.

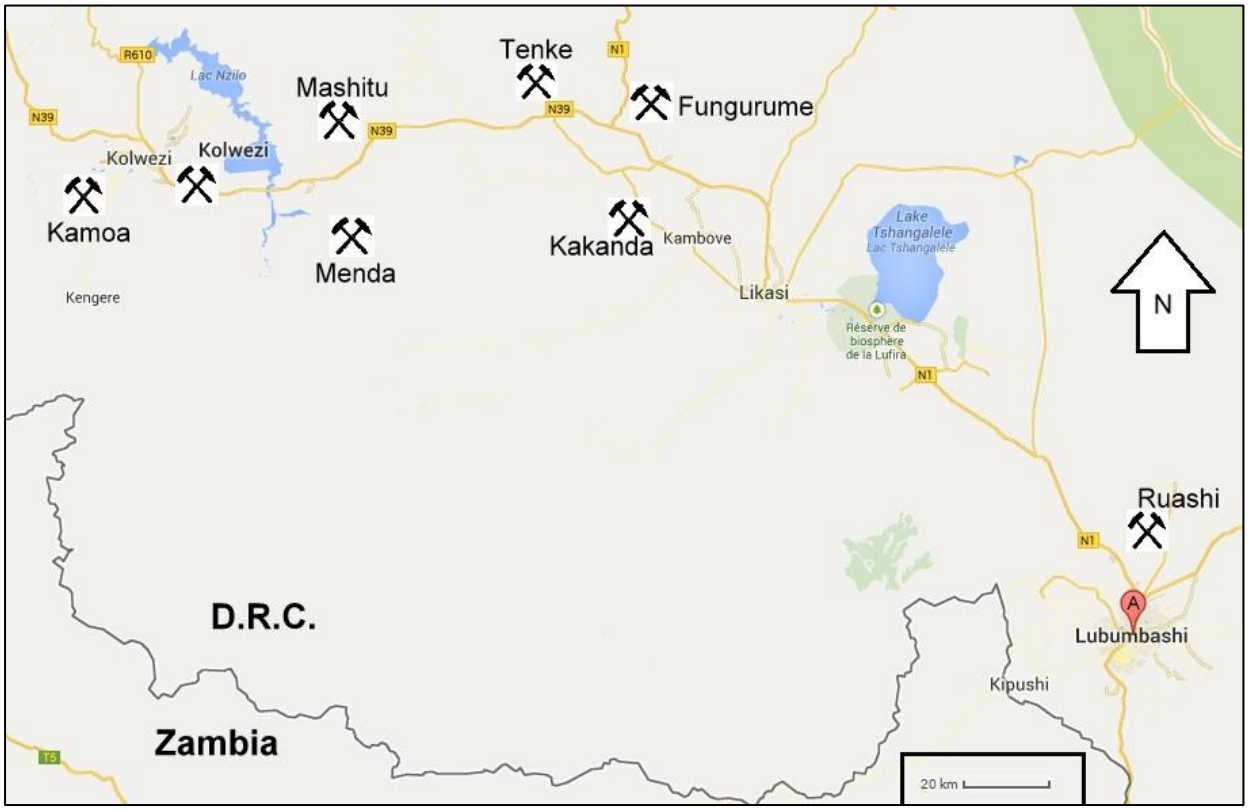

***Figure 1.1**: The study area (Mashitu) in relation to key locations and deposit groups (crossed hammers) in the Central African Copperbelt (CAC). Data ©2014 Google Maps*

1.2 Geography and Mining History of the Central African Copperbelt

The Central African Copperbelt (CAC) is a metallogenic province that spans the countries of the DRC and Zambia. It lies at the northernmost edge of the southern African or 'Huila' plateau giving it an elevation of around 1,200m on average. The climate varies from 'Humid Subtropical' to 'Subtropical Highland' according to the Köppen Climate Classification (Peel *et al.*, 2007), with average annual precipitation of around 120cm mostly in summer during the rainy season between October and April. The temperature range is between 16 and 28°C, the average being 20.6°C (Jobin-Bevans *et al.*, 2006). The present-day climate differs markedly from Northern Congo and the Congo River Basin, which have a Tropical Rainforest to Tropical Monsoon climate with higher temperatures and precipitation rates. Population centres of note within the Copperbelt include Lubumbashi, Kolwezi (DRC), Ndola and Kitwe (Zambia).

Exploitation of the CAC in the form of artisanal digging dates back to at least the 4th Century A.D. in Katanga (de Maret, 1982; 1986). However, late 19th-early 20th Century Belgian colonialism initiated copper mining on an industrial scale. Political instability in the region over the past 60 years, including the transition from colonial to independent governments under Patrice Lumumba/Joseph Kasa-Vubu and Mobutu Sese Seko, attempted secession of the State of Katanga, and the First and Second Congo Wars, have contributed to wildly varying copper production with a general downwards trend over this period, aided by chronic mismanagement and corruption.

However, recent recovery and investment in the past decade under Joseph Kabila place the DRC 7th and Zambia 8th in terms of global copper producers (Brininstool, 2014), and the DRC 1st and Zambia 6th as cobalt producers (Shedd, 2014), almost exclusively as a result of mining in the Copperbelt. CAC reserves are thought to add up to something in the order of 40,000,000 tonnes Cu and 3,670,000 tonnes of Co (Brininstool, 2014; Shedd, 2014) and high grades relative to many deposits around the world make the CAC Cu-Co deposits attractive for exploitation, despite the lack of infrastructure that make deposits in the region of lower grade difficult to mine economically. The CAC has clear and rising global significance in the production of copper and cobalt.

The name 'Copperbelt' refers to the regional prevalence of copper deposits and the area is considered by Hitzman *et al.* (2010) to be one of the word's three 'supergiant' Sedimentary Stratiform Copper (SSC) districts, the other two being the Kupferschiefer of northeast Europe and the Udokan district of Siberia. The CAC is confined to the Neoproterozoic Lufilian tectonic arc and surrounding areas (see section 1.4. Structure) and can be broadly divided into the Congolese/Katangan portion (North and West) and the Zambian portion (South and East) by variation in stratigraphic facies, metamorphic grade and mineralisation. Unusually for SSC deposits, within the Congolese or Katangan portion of CAC, cobalt is concentrated in economically exploitable quantities in many cases and is commonly extracted as a by-product alongside copper. Most Katangan deposits are thus referred to as Cu-Co. This chapter focusses on the Katangan portion of the CAC in which the study area resides, with a regional geological map shown in Figure 1.2.

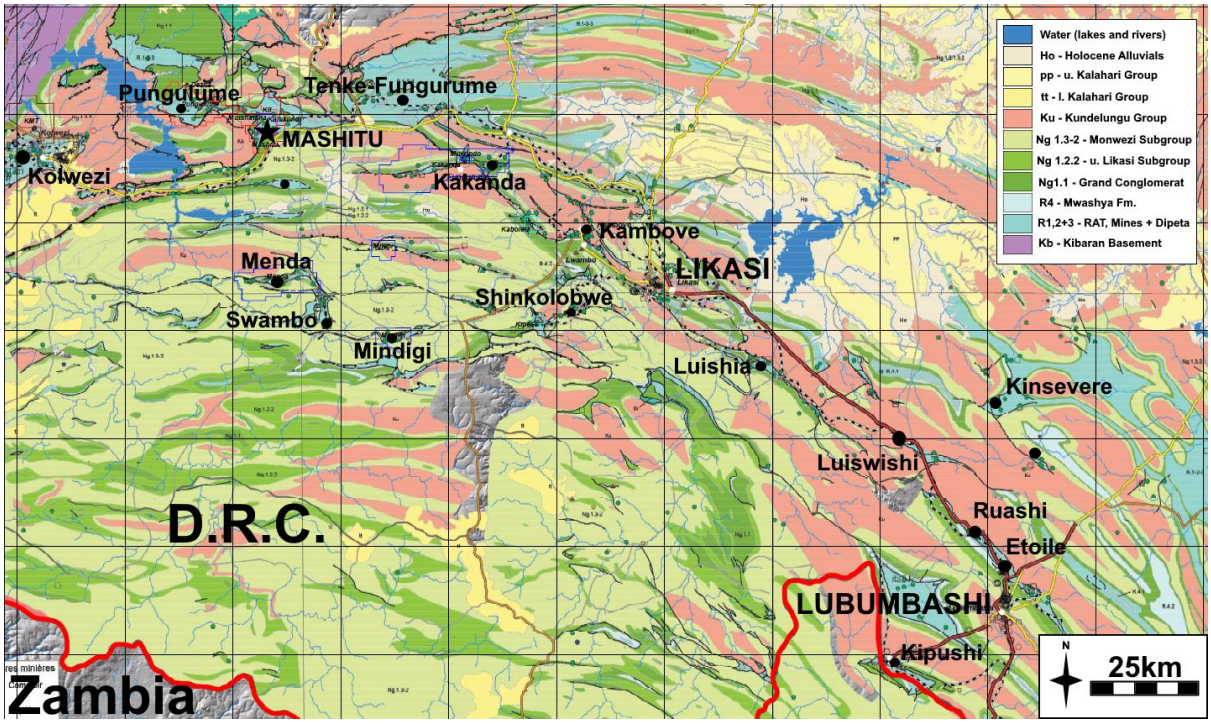

***Figure 1.2**: Regional geological map of the Congolese Copperbelt (after François; 2006), with key deposits and the cities of Lubumbashi and Likasi illustrated. Mashitu is represented as a star.*

1.3 Stratigraphy

1.3.1 Basin Setting: The Katangan Supergroup

The Cu-Co deposits of the Copperbelt are hosted in the rocks of the Katangan Supergroup which was deposited in the Katangan Basin between maximum ages of ~880Ma (Armstrong *et al.*, 2005) and ~575Ma (Master *et al.*, 2005), during a Wilson cycle of rifting and basin closure ending in the Lufilian orogeny, a stage of the Pan-African orogenic assembly of the Gondwanan supercontinent. This cycle began with aulocogenic, two-stage rifting between the Bangweulu, Congo and Kalahari cratons. The resulting basin had a trap-door architecture, hinged to the south, with the Zambian portion forming a graben-like sub-basin south of the hinge possibly separated by a basement high (Hitzman, 2009a) (see Figure 1.3). Sedimentary fill underwent a fairly standard intracratonic basin evolution from syn-rift continental clastics (red-beds), through sabkha chemical sediments (carbonates and evaporites), with pelitic shallow marine sediments making up the upper Katangan

Supergroup. For more details on the regional setting of the Katangan basin, see section 1.4: Structure and Tectonics.

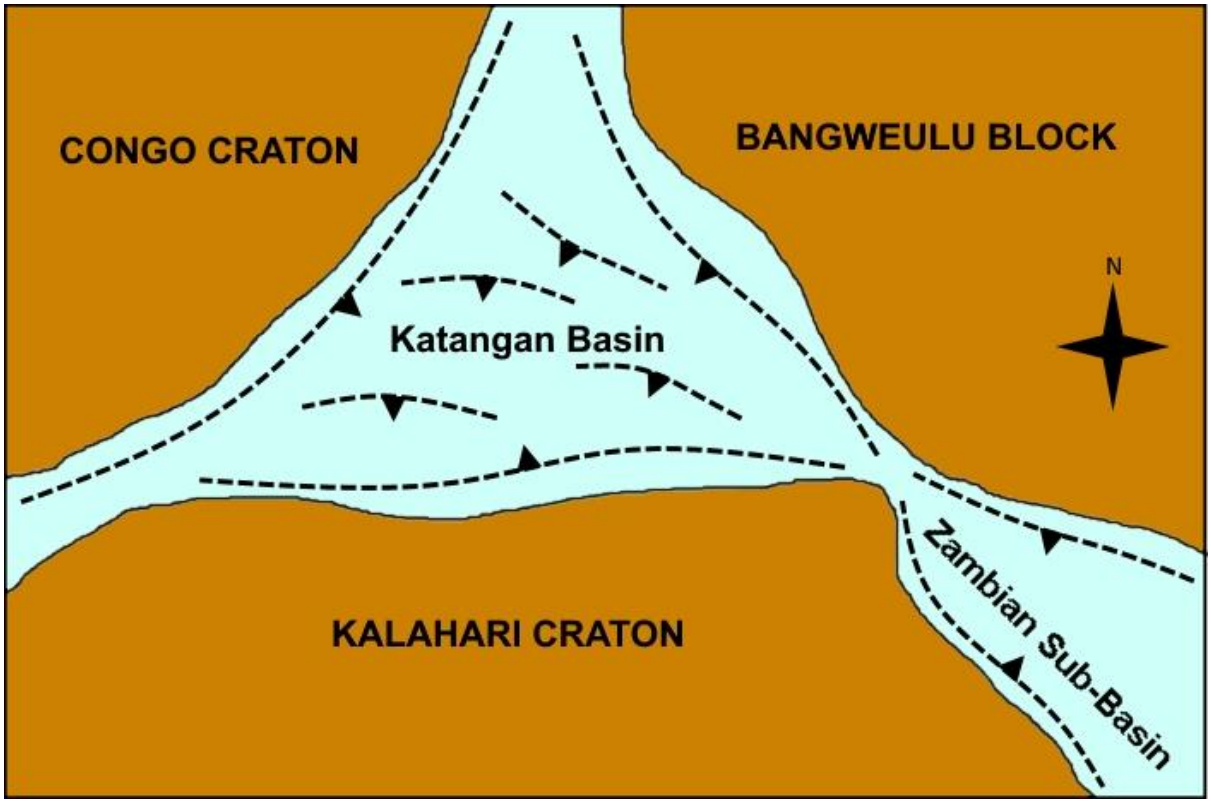

Figure 1.3*: Theoretical diagram of the aulacogenic orientation of the Katangan and Zambian basins relative to their bounding cratons during Neoproterozoic rifting. After Hitzman (2009a).*

There is debate as to whether the Katangan remained an intracratonic, Red-Sea style proto-oceanic basin over the course of its existence (Daly, 1986; Hanson *et al.*, 1994; Stern, 1994; Condie, 2003), or whether it evolved into a full ocean basin in the order of 1000's of km's width, as was present in the wider Zambezi belt to the South (Coward & Daly, 1984, Porada & Berhorst, 2000). Based on the age correlation of regional eclogites to the Lufilian orogeny and the necessity of such rocks to be old, cold and dense, as well as MORB style geochemistry of some Katangan-rift associated crust and the presence of highly metamorphosed and altered 'ophiolites' (John, 2001; John *et al.*, 2003) a long-lived, wide ocean basin between the Congo and Kalahari cratons is postulated to have existed, into which the Katangan Supergroup sediments were deposited. However, the veracity of these eclogites, whiteschists and other subduction-related rocks in the Katangan Basin is questioned by authors such as Hitzman (2015a, pers. comm.) who consider the unusual

mineralogy and chemistry of the apparent subduction-related metamorphism to reflect its production through extensive hydrothermal alteration, rather than through deep subduction-related burial. There is certainly convincing evidence for a full oceanic basin within the Zambezi belt, although whether sea-floor spreading extended into the Katangan basin appears less certain and is still a matter of confusion (certainly, mafic igneous rocks from the Katangan may be found within the basin). Most SSC-type metallogenic provinces in other part of the world formed in intracratonic basins (Hitzman, 2015b), so perhaps the metallogenic signature of the basin itself suggests that seafloor spreading is unlikely to have initiated in the Central African Copperbelt.

The rifted basement rocks which underlie the Katangan Supergroup in the CAC are exposed in Zambia and consist of a 2050-1800 Ma Palaeoproterozoic magmatic arc terrane (Rainaud, 1999), but in the DRC there is only exposure of the basement to the northwest of and in the south-eastern part of the Copperbelt, and no confirmed interception of the basement beneath the Katangan Supergroup in boreholes from the central Congolese Copperbelt to date. Porphyry-type hydrothermal systems in this basement terrane may have contributed towards the Cu-fertility of the region (Dejonghe and Ngoyi, 1995; see *Mineralisation and Metasomatism*). The CAC is flanked to the NW and SE respectively by the Kibaran and Irumide Mesoproterozoic orogenic belts, which may also have been sources of sedimentary input into the Katangan basin. In addition, Rainaud *et al.* (2003) recognise a possible Mesoarchaean terrane (3169-3225 Ma) beneath the CAC based on age dating of detrital zircons from the Katangan Supergroup in Zambia and the DRC.

The Katangan Supergroup itself is between ~5km (Cailteux *et al*., 1994) and ~9km (Unrug, 1988) thick, covers the majority of the Lufilian Arc over an area of approximately 250,000km^2, and is made up of 3 groups, from bottom to top: the Roan, Nguba and Kundelungu Groups. Katangan rifting proceeded in two stages, with the lower Roan (R1-3) deposited in the first stage and the upper Roan (R4), Nguba and Kundelungu deposited in the second stage (Cailetux, 1994; Bull *et al*., 2010). A stratigraphic column for the Katangan (previously Shaban) Supergroup is presented as Appendix 2. This thickness of sediment, while significant, is less than expected when considered in terms of the period during which the basin was active - roughly 300 million years. Given rates of deposition in even the slowest-filling basins of recent geological history it would suggest that significant, unrecognised unconformities exist (or recognised unconformities account for huge gaps in

the sedimentary record) within the Katangan sequence marking a turbulent basin history (Bull *et al.*, 2010).

The Congolese/Katangan, Zambian and Northwest Province portions of the Lufilian Arc are quite different not only in stratigraphic terms but also in metamorphic grade, structure, and mineralisation styles, even though they all reside within the same basin system. This section focuses on the stratigraphy of the Congolese portion of the Copperbelt.

1.3.2 The Roan Group

The Roan Group is perhaps the best studied portion of the Katangan Supergroup because it hosts the majority of the traditional SSC mineralisation. The Roan sedimentary sequence, assumed to be basal fill of the Katangan Basin, consists of (from bottom to top) the Roches Argillo-Talceuses [R.A.T. (R1)] Mines (R2), Dipeta (R3) and Mwashya (R4) Subgroups, of which the R2 or 'Mines Subgroup' is again best studied because of its often-mineralised nature. The Roan Group is primarily a dolomitic sequence which becomes more siliciclastic towards the top within the Dipeta and particularly Mwashya Subgroups (see Appendix 2). It is bounded chronologically by the Grand Conglomerat at the base of the overlying Nguba Group, with an age of between 712 and 770 Ma (Key *et al.*, 2000; Bull *et al.*, 2011), and by detrital zircons towards the base of the group, thought to be derived from the unconformably underlying Nchanga Granite dated at 883±10 Ma (Armstrong *et al.*, 2003). Three sea-level transgression events are recorded in the Roan: the first at the R1-R2 transition, the second within the C.M.N. of the R2 Subgroup, and the third at the R.G.S.-Mofya transition within the R3 (Bull *et al.*, 2010).

1.3.2.1 R1: Les Roches Argillo-Talceuses (R.A.T.) Subgroup

The R1 Subgroup, or R.A.T., as it is known from the original French designation of 'les Roches Argillo-Talceuses' (argillic talc-bearing rocks), is a thick unit of red-bed continental clastics. Thicknesses of hundreds of metres are recorded in many locations including Mashitu, however due to the unit's highly brecciated nature, a continuous stratigraphic section is difficult to discern. It consists primarily of siltstones with subsidiary mudstones and sandstones and occasional carbonates and shales, the mineralogy being primarily quartz, K-feldspar, haematite, Mg-chlorite and muscovite (Hitzman, 2015b). Haematite gives

most of the unit a distinct red colour. Evaporite textures such as enterolithic carbonate veining, carbonate 'nodules' that may be after evaporites, and 'chicken wire' veining are common and are likely to reflect the presence of sedimentary or diagenetic evaporites before hydrothermal or kinetic mobilisation.

The R.A.T. is brecciated in many cases (see section 1.4. Structure), making a complete sedimentary section through the unit difficult to find – additionally the base of the R.A.T. Subgroup has never been drilled or found exposed at the surface. Interpretations for these breccias range from sedimentary conglomerates, debridites and mass flows (Grujenschi, 1978; Wendorff, 2000), to collapse breccias formed by evaporite dissolution and diapirism (François, 1974; Bell, 1989; Jackson, 2003), to 'slush' breccias related to hydrothermal or kinetic evaporite mobilisation (Martin, 2014, pers. comm.), to cataclastic, fault-related breccias and the damage envelopes surrounding them (Demesmaker *et al.*, 1963). There are clearly a variety of types of breccia and all of the processes mentioned above may be responsible for different breccia occurrences. In addition, a 'Poudinage' unit described as a 'transgression conglomerate' is sometimes recognised at the base of the RAT. The prevalence of brecciation, position in the stratigraphic sequence and frequency of former evaporite textures lead some authors to consider the R1 Subgroup as having previously contained huge thicknesses of evaporite, since mobilised during halokinesis (Bell, 1989; Jackson, 2003; Hitzman *et al.* 2010; 2012) (see 1.4. Structure). This model postulates hundreds of metres, perhaps up to a kilometre of salt to have existed in a layer or layers within the R.A.T. before halokinesis, although units of evaporite are not present within the R.A.T. today.

A common division at deposit scale is a distinction between the 'R.A.T. Rouge/Lilac' (Red R.A.T.) and the sometimes overlying 'R.A.T. Gris' (Grey R.A.T.) at the base of the Mines Subgroup. The R.A.T. Gris shares the same sedimentary textures and primary mineralogy as the R.A.T. Rouge, although it is a mottled greeny-grey and occasionally contains primary copper sulphides, whereas the R.A.T. Rouge is red and is never reported to contain primary copper sulphides. The R.A.T. Gris, confusingly, is often grouped with the R2 Mines rather than R1 with the R.A.T. Rouge, however authors such as Cailteux (1994) and Broughton (2014) consider the R.A.T. Gris and Rouge to be the same unit, altered differentially, with reduced iron present in the R.A.T. Gris responsible for its green-grey colour.

The R1 Subgroup is considered to represent the very onset of deposition into the Katangan Basin – a syn-rift continental siliciclastic red-bed sequence (Hitzman, 2015b) deposited in what could be considered a lowstand systems tract (Bull *et al.*, 2010).

1.3.2.2 R2: The Mines Subgroup

The Mines Subgroup or 'Mines Series' as it is traditionally known is a sequence of rocks consisting of 3 formations and 6 units. Compared to other stratigraphic units the Mines Subgroup is well studied and constrained and generally displays the most consistent, predictable stratigraphic relationships as a result. This high level of understanding is perhaps due to the subgroup hosting the majority of Cu-Co mineralisation throughout the Congolese Copperbelt (see Chapter 2: Regional Mineralisation). The R2 Mines Subgroup does not form a consistent stratigraphic horizon across the Lufilian Arc, but is rather broken into a large number of 'fragments' or 'rafts' set within other fragments, or large, sometimes homogenised, melange-like masses of the other subgroups (mostly R1 but also R3 and R4) of the Roan Group. It should be noted that these masses of R1, 3 and 4 between the R2 fragments are poorly understood because of their usual lack of mineralisation. The cause of this fragmentation is not clearly understood and will be discussed in Section 1.4: Structure. A stratigraphic summary for the R2 Mines Subgroup is presented in Figure 1.4. The R2 consists of (from bottom to top) the Kamoto Dolomite Formation, the Dolomitic Shales Formation and the Kambove Formation. The Mines Subgroup represents the transition from syn-rift siliciclastic basin fill (the R1) to post-rift carbonate shelf and continental slope sedimentation.

Group	Subgroup	Formation	Unit	Approx. Thickness (m)
Roan	Mwashya R4			100
	Dipeta R3	Mofya	Mofya	500
		Roches Gréseuses Superieur (R.G.S.)	R.G.S.	150
	Mines R2	Kambove	Calcaire et Mineraux Noire (C.M.N.)	100
		Dolomitic Shales	Shales Dolomitique Superieur (S.D.S.)	50
			Shales Dolomitique du Base (S.D.B.)	50
		Kamoto	Roches Siliceuse Cellulaire (R.S.C.)	10
			Roches Siliceuse Feiulletées (R.S.F.)	5
			Dolomies Stratifieé (D.Strat)	5
	Roches Argillo-Talceuse (R.A.T.) R1		R.A.T. Gris	5
			R.A.T. Rouge	?

***Figure 1.4**: Stratigraphic summary for the R1, R2, R3 and R4 subgroups. The colours are those used for each stratigraphic unit in the Gecamines (a Congolese para-statal mining company) local geological maps of the Katangan Copperbelt, which are adopted for geological maps and figures in this thesis. Approx. thicknesses are those witnessed in the vicinity of the Mashitu group of deposits (Chimvinga, 2014, pers. comm.).*

At the base of the Kamoto Formation, overlying the R.A.T. Gris of R1, is the 'Dolomies Stratifiées' or D.Strat, a grey banded dolomite unit with beds usually a few centimetres in width. Its most distinctive feature is the presence of cm-scale 'blebs' or 'nodules' which are now composed of chert or microcrystalline silica. These 'blebs' may be silicified evaporite casts, or some remnant of silica-fixing stromatolitic organisms, although there is no universal consensus on their true nature. Gypsum casts on the bedding surfaces of the D.Strat are common. The Roches Siliceuse Feuilletées or R.S.F. occurs conformably above the D.Strat. This is a unit of laminated dolomite where the banding of the D.Strat becomes

more wavy and thinner (going from cm to mm scale). The R.S.F. lacks the 'blebs' found in the D.Strat and is usually almost totally silicified, a result of its proximity to the overlying R.S.C. or perhaps by syn-depositional silica fixed by algae. Out of any unit of the Mines Subgroup, the R.S.F. tends to be the most heavily and consistently mineralised with copper. The Roches Siliceuse Cellulaire (R.S.C.) occurs at the top of the Kamoto Formation and consists of chaotically bedded, heavily silicified dolomite. Domal stromatolite structures and wavy-laminated algal beds comprise the majority of the unit. Primary silicification was likely the result of depositional silica-fixing by the stromatolites, a common feature of stromatolitic rocks (Kremer *et al.*, 2012). However, diagenetic and metasomatic silicification events may have occurred too. The Kamoto Formation records primary carbonate deposition in a transgressive sequence of water deepening, transitional from a shore-face intertidal environment to a back-reef lagoonal environment in the D.Strat and R.S.F. units, with the R.S.C. recording the reef environment itself (Cailteux, 1994).

The Dolomitic Shales Formation consists of the Shales Dolomitiques du Base (S.D.B.) overlain by the Shales Dolomitiques Superieur (S.D.S.) unit. The whole formation is a sequence of laminated or bedded dolomitised siliciclastic shales. The upper S.D.S. unit tends to be more massive, less calcareous and less bedded than the lower S.D.B. unit, representing further transgression and water deepening from the calcareous Kamoto Formation, into a continental slope environment. The Dolomitic Shales (or S.D.) Formation is also divided into 9 subzones on the basis of layers of black graphitic shale units that punctuate the usual green, red or blue of the S.D. shales. However, these subzones can rarely be convincingly traced along great lateral distances and at Mashitu, in the author's opinion, only the S.D.S. and S.D.B. can be separated from each other on the basis of a more consistent graphitic shale marker horizon between them which is equated with the S.D.2d. subzone. This graphitic shale records deep, anoxic water conditions and is considered to be a maximum flooding surface by Bull *et al.* (2010) with the remainder of the S.D.S. therefore deposited in a highstand systems tract.

The Kambove Formation – equivalent to the Calcaire et Mineraux Noire (C.M.N.) unit of the traditional mining nomenclature (Figure 1.4) - transitions from the shales of the S.D. into a sequence of deep and then shallow-water carbonates in a sequence of regression, transgression, and another regressive event (Bull *et al.*, 2010). These carbonates are distinct from the underlying Kamoto by virtue, firstly, of their thickness: the Kamoto is often 20m

thick or less whereas the C.M.N. is usually close to 100m. The Formation/unit is quite laterally variable in nature and attempting to subdivide the C.M.N. into units over this 100m thickness is difficult, but there are general trends in sedimentation. Overall, the unit comprises dark grey-blue-white dolomites and carbonates with darker graphitic beds, lighter coloured cherty or silicified layers, abundant wavy (algal) bedding, disrupted storm wave base beds, and nodular, chicken-wire-bearing horizons that are suggestive of evaporites. The base and top of the C.M.N. both contain more abundant wavy algal laminations and evaporites, with the more graphitic and cherty beds occurring in between. This reflects Bull *et al.*'s (2010) assertion that another, small transgressive event is recorded within the C.M.N., marking a change from the deep-water maximum flooding surface of the S.D., regression to supra-tidal C.M.N. carbonates, transgression to sub-tidal C.M.N. carbonates, and subsequent regression back to supra-tidal carbonates in the upper C.M.N.

1.3.2.3 R3: The Dipeta Subgroup

The Dipeta Subgroup is divided into two units, the Roches Gréseuses Superieur (R.G.S.) and overlying Mofya (see Figure 1.4). The R.G.S. is a sequence of red-to-purple-to-green siltstones, mudstones and sandstones with subsidiary calcareous layers, recording continued sea-level regression from the shelf carbonates of the C.M.N. to near-shore or even sub-aerial facies. Gypsum casts are abundant in the R.G.S. at Pungulume (west of Mashitu) hinting at the presence of subaerial evaporites. It has, in many ways, characteristics that are quite similar to the R1 R.A.T., even to the frequency of breccias, making it, together with the R.A.T., another suspect location for the theoretically large thicknesses of evaporite required for the halokinetic theory of Copperbelt tectonics (Bell, 1989; Jackson, 2003; Hitzman, *et al.*, 2010; 2012) (see 1.4. Structure).

The Mofya unit, an incompletely known succession overlying the RGS, consists of a calcareous algal limestone-dolomite sequence, with dolomitic shales comprising small to considerable portions of the unit (usually towards the top with more calcareous rocks at the bottom). Domal stromatolites and evaporite casts after gypsum are common towards the base. This unit corresponds in facies to the Kambove and Kamoto Formations (Hitzman, 2015b) recording the third sea level transgression in the Roan Group from the sub-aerially deposited R.G.S. in a manner mirroring to the R.A.T. – Kamoto transition; in this repetition

of facies, another redox horizon is found that results in SSC mineralisation at the Pungulume Cu-Co deposit some 20km west of Mashitu.

1.3.2.4 R4: The Mwashya Subgroup

Siliciclastic shales with minor interbedded siltstones, sandstones and carbonates make up the majority of the Mwashya, with frequent intervals of black graphitic shales which are usually pyritic and sometimes host Cu sulphides. These rock types are indicative of deep water facies and represent continuing sea-level transgression from the lagoonal/reef facies found in the R3 Mofya unit. At more marginal locations around the Katangan Basin, the Mwashya is made up primarily of fluvial-deltaic sequences of greywacke sandstone with locally distributed pebble channel-beds and lenses of anoxic black shales (Schmandt *et al.,* 2013). These shale lenses, and the contact with the largely anoxic diamictites of the overlying Grand Conglomerat (Figure 1.5), are also significant redox horizons and prospective for mineralisation such as that found at Kamoa (Schmandt *et al.*, 2013).

Group	Subgroup	Noteworthy Units	Approx. Thickness (m)
Kundelungu	Plateaux		100
	Kiubo		
	Kalule	Pink Limestone (Calcaire Rose)	
		Petit Conglomerat	
Nguba	Monwezi		500
	Likasi	Katontwe Limestone	
		Grand Conglomerat	
Roan	Mwashya		1000
	Dipeta		
	Mines		
	R.A.T.		?

Figure 1.5*: Stratigraphic summary (after Cailteux, 1994) for the Katangan Supergroup. The colours are those used for each stratigraphic unit in the Gecamines regional geological maps of the Katangan Copperbelt – which are adopted for geological maps and figures in this thesis.*

1.3.3 The Nguba Group

The Nguba Group consists mostly of weakly dolomitic shales and is separated from the underlying Roan Group by a major unconformity, and a regional diamictite known as the

‘Grand Conglomerat’, depositionally constrained between 735 +/- 5 Ma and 765 +/- 5 Ma based on zircon ages in the boundary units (Key *et al.*, 2002). However, Bull *et al.* (2010; 2011) infer the unit to correlate with the Sturtian glacial event at 712 Ma through litho and chemo-stratigraphy. Stratigraphically the Nguba Group is composed of the basal Likasi and overlying Monwezi Subgroups, and was previously known as the ‘Lower Kundelungu’ or ‘Ki’ Group. Neither the Nguba nor the Kundelungu Groups appear to be extensively affected by the ‘megabrecciation’ experienced by the Roan Group. Figure 1.5 summarises the stratigraphy of the Nguba Group.

1.3.3.1 Ng1. The Likasi Subgroup

The Likasi Subgroup contains the Grand Conglomerat at its base. The Grand Conglomerat appears to conformably overly the Mwashya towards the middle of the Katangan Basin, but towards the basin margins it unconformably overlies several different lithologies including Kibaran basement, marking it as the top of a significant unconformity (François, 1974). It is a polymicitic matrix-supported conglomerate consisting of sub-rounded clasts of limestones, shales, sandstones and even granite clasts presumed to be from the basement exposed at the margins of the basin during deposition. These clasts are contained in a dark, fine-grained matrix of silt and mud. The proportion of clasts varies laterally and vertically, with some units being mostly mudstone and others with up to 50% clasts, although the unit is always matrix supported. The clast to matrix ratio generally reduces towards the top of the unit. Depositionally this unit is thought to be a glacial diamictite, although the lack of dropstone and other textures expected of a diamictite led some to question whether it is in fact the result of basin-scale turbidite flows carrying glacial moraine from the basin margins towards the centre of the basin (Binda and van Eden, 1972; Hitzman, 2015b). Bull *et al.* (2010; 2011) correlate this unit with the Sturtian glacial event dated at ~712 Ma.

The Kakontwe Limestone unit commonly overlies the Grand Conglomerat as a ‘cap carbonate’ sequence consisting of massive limestones and dolomite, laminated algal carbonates and dolomitic siltstones (Cailteux *et al.*, 1994). It occasionally hosts sporadic mineralisation (Hitzman, 2015b). Above the Kakontwe Limestone, the top of the Likasi Subgroup gives way to siliciclastic shales and the sequence from the top of the Grand Conglomerat represents a gradual sea level transgression.

1.3.3.2 Ng2. The Monwezi Subgroup

The Monwezi Subgroup is a continuation of the upper Likasi, comprising micaceous siliciclastic shales of a variety of colours and sometimes dolomitic in composition. It represents continuing sea-level transgression or a highstand phase of deep water deposition (Bull *et al*., 2010). Dolomitisation of these shales is likely to have occurred epigenetically through metasomatism (Cailteux *et al*, 1994).

1.3.4 The Kundelungu Group

The Kundelungu Group consists mostly of siliciclastic sediments and is marked at the base by another basal diamictite known as the 'Petit Conglomerat'. This unit is correlated by Master and Wendorff (2011) to the Ghaub diamictite of the Otavi Group in the Damara orogenic belt, thought to be a tillite representing the Marinoan glacial event and dated at 635.5±1.2 Ma by Hoffman *et al.* (2004). A maximum age from detrital muscovite for the upper Kundelungu sediments is given by Master *et al.* (2005) at ~573 Ma, suggesting that deposition continued well into the convergence of the Kalahari and Congo cratons. The Kundelungu Group is made up of K1 Kalule Subgroup, the K2 Kiubo Subgroup, and the K3 Plateaux Subgroup. Figure 1.5 summarises the stratigraphy of the Kundelungu Group.

1.3.4.1 K1: The Kalule Subgroup

This unit, like the Likasi Subgroup of the underlying Nguba, has a basal diamictite known as the Petit Conglomerat which differs from the Grand Conglomerat by being generally more matrix-dominated and containing smaller clasts. As mentioned above, it is correlated with the Marinoan glacial event (Master and Wendorff, 2011) and may also represent an unconformity due to a glacial cessation of deposition. This diamictite is also capped by a carbonate unit referred to as the 'Pink Limestone/Calcaire Rose', a massive to algally-laminated haematitic carbonate, which gives way up-section to oolitic carbonate layers and then to calcareous shales (Cailteux, 1994).

1.3.4.2 K2: The Kiubo Subgroup

The Kiubo sequence overlies the carbonates of the upper K1. The Kiubo Subgroup (K2) consists of siliciclastic sandstones, siltstones, shales and mudstones with occasional carbonate shales.

1.3.4.3 K3: The Plateaux Subgroup

The Plateaux Subgroup is a dominantly terrestrial sequence of sediments mostly comprising texturally immature arkosic sandstones, with minor conglomerates and siliciclastic shales. The sequence continues the pattern of sea level regression that began in the K1 Subgroup, and, as the last unit present in the geological record that was deposited in the Katangan Basin, it is likely that this final regression records basin inversion and the onset of the Lufilian Orogeny. Master *et al.* (2005) have dated detrital zircons from the Plateaux Subgroup which yield ages of ~573 Ma, giving a lower limit for the age of the inverting Katangan Basin. Wendorff (2000) suggests that before K3 was deposited, thrust sheets from the advancing orogenic front began calving into the basin, forming the 'Roan megabreccias' found lower in the stratigraphy and that the R1 R.A.T. Subgroup is actually a conglomerate complex deposited between the deposition of K2 and K3 as a result of the break-up of these thrust sheets. This theory is explored further in section 1.4. Structure.

It should be noted that Cailteux *et al.* (2007) propose a different, more comprehensive stratigraphic classification of the Nguba and Kundelungu Groups, with the Subgroups named Muombe (Ng1), Bunkeya (Ng2), Gombela (Ku1), Ngule (Ku2) and Biano (Ku3). These Subgroups were themselves split into 14 different formations. Although the classification of Cailteux *et al.* (2007) was comprehensive in scope, it has not been universally accepted by later researchers or mining companies. Thus, for the purposes of this thesis, the older, Gecamines-age stratigraphic classifications are discussed for the sake of continuity.

1.3.5 Comparison to the Zambian Copperbelt

Debate exists over the correlation of the Roan in Zambia and the Roan in the DRC and has been traditionally based on correlation of the mineralised horizons of the Congolese Mines Subgroup and the Zambian Ore Shale (e.g. Cailteux *et al.*, 2005; 2007). However, the

Zambian Roan exhibits more shoreward carbonate facies whereas the DRC seems to be more basinward and siliciclastic (Figure 1.6). Bull *et al.* (2010; 2011) recognise seven stratigraphic sequences within the Roan Group of Zambia, the uppermost of which are correlated by them through carbon and oxygen isotope chemostratigraphy, as well as lithostratigraphy with the Subgroups R2, R3 and R4. This leads them to conclude that, rather than the Zambian 'Ore Shale' member being equivalent to the Congolese 'Mines Series', that the Ore Shale occupies a lower stratigraphic level in Congo, somewhere in the RAT Subgroup. They infer that perhaps a deeper sequence of sediments equivalent to the Zambian 'Copperbelt Orebody Member', potentially host to copper, exists below the current level of exposure in the Congolese/Katangan Copperbelt. This conclusion is supported by Hitzman *et al.* (2012). Work by Hitzman (2015b) suggests another possibility: that the Zambian Copperbelt was formed in a sub-basin extending off from the main Katangan Basin, separated by a basement high, and that the contrasting depositional styles are a result of the resulting difference in source regions and accommodation space. If this is the case, it is clear that the basins combined by Nguba/Kundelungu times (i.e. ~712 Ma), either as a result of continued basin 'unzipping' or by basin inversion and closure, with relative stratigraphic unity between the Zambian and Congolese Copperbelts achieved by the time of deposition of these groups.

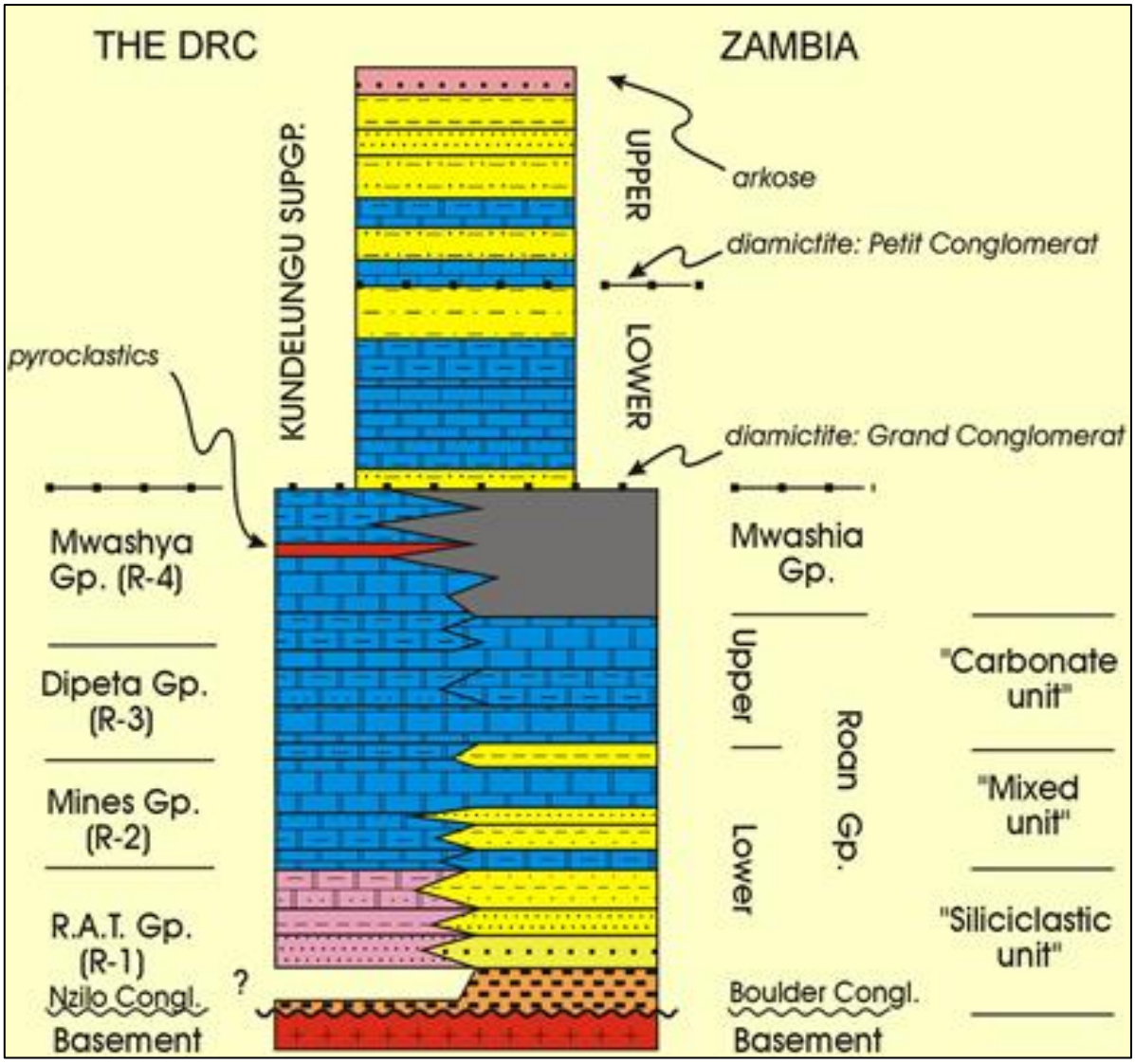

Figure 1.6*: Traditional correlation of the Katangan across the DRC and Zambia from Cailteux et al. (1994). Authors such as Bull et al. (2010) consider the Zambian Roan to occupy a lower stratigraphic level than the Congolese Roan. The Upper and Lower Kundelungu Groups refer to the Kundelungu and Nguba Groups respectively, according the updated stratigraphic nomenclature.*

1.4 Structure and Tectonics

The Central African Copperbelt (CAC) itself straddles two structural zones of the four-zoned (Unrug, 1988) Lufilian Arc, an arcuate orogenic belt sandwiched between the Congo, Kalahari and Bangweulu block cratons in the Lufilian stage of the Pan-African Orogeny. The four zones of the arc are differentiated by structural and metamorphic styles and comprise (from South to north) the 'Katanga High', a thin Katangan sediment cover over granitic basement, the 'Synclinorial Belt' containing deep, tightly folded upper Katangan sediments, the 'Domes Region' so named for its domal basement highs onlapped by the Katangan Supergroup (this is the only region that is significantly metamorphosed – greenschist-amphibolite, and even controversial blueschist-eclogite facies (John, 2001; John *et al.*, 2003) and can be considered the 'centre' of the Lufilian orogeny) and finally the 'External Fold-and-Thrust Belt', a highly folded and faulted region of the arc containing the Roan megabreccias. Beyond these four structural zones, to the northeast, is the Lufilian Foreland (see Figure 1.7).

The Domes Region and the External Fold and Thrust Belt are the primary two structural zones host to Copperbelt mineralisation (Hitzman *et al.,* 2012), with the Zambian Copperbelt lying mostly within the Domes Region and the Congolese Copperbelt mostly within the External Fold and Thrust Belt. The substantial metamorphism and presence of basement in the Domes Region, compared to the megabreccias and thrust sheets of the External Fold and Thrust Belt, influence the contrasting styles of mineralisation between Zambia and Congo.

The structure of the Copperbelt is largely defined by Katangan rifting and the events of the Lufilian orogeny as described below. Subsequent post-Lufilian extensional events related to far-field stresses of Gondwana breakup and the East African Rift can also be distinguished (Kipata *et al.*, 2013), but play a seemingly peripheral role in the geology of the region. In this introduction the main focus is on the structure of the External Fold and Thrust Belt, the structural zone that contains the Mashitu deposits and the majority of Congolese Copperbelt mineralisation.

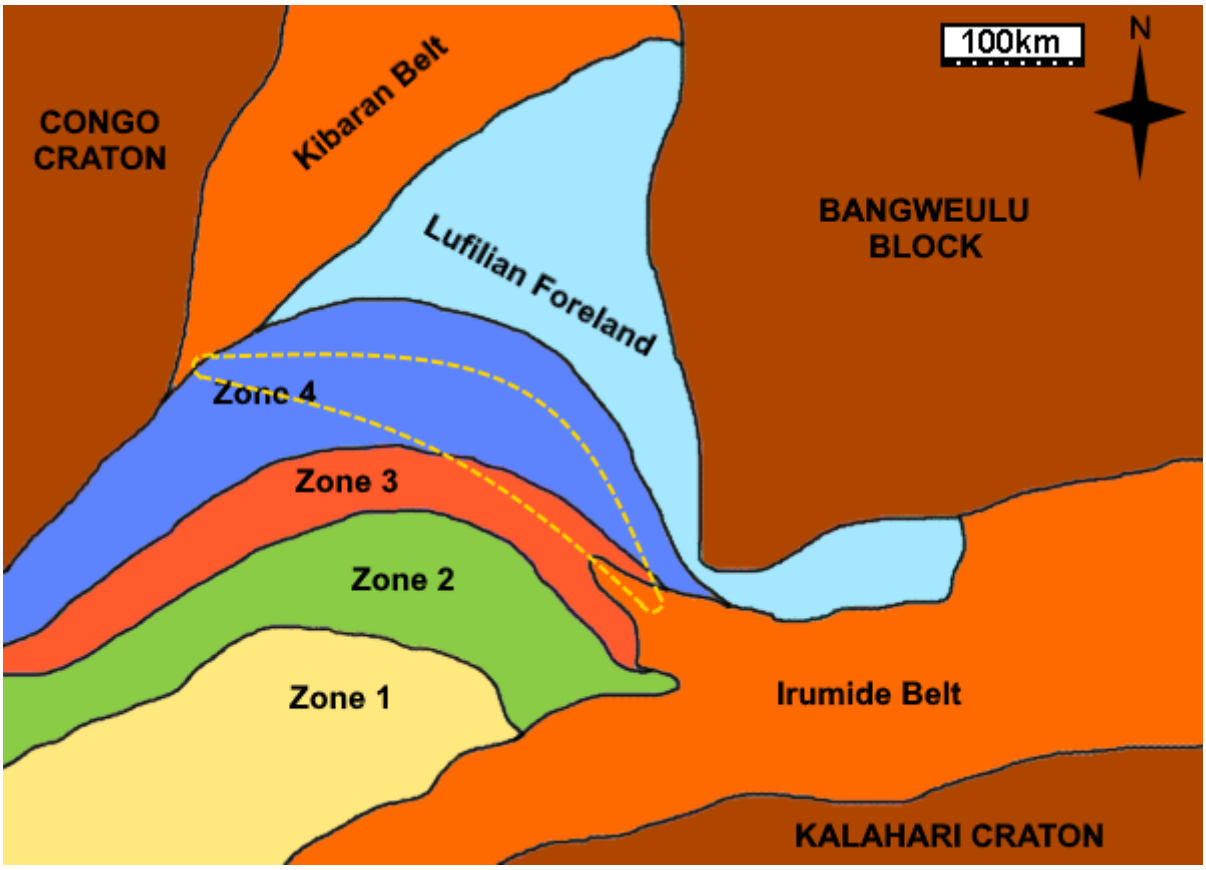

Figure 1.7: *Sketch map of the structural zones of the Lufilian Arc and surrounding terranes. The approximate extent of known Central African Copperbelt mineralisation is outlined in dashed yellow.* ***Zone 1****: Katanga High;* ***Zone 2****: Synclinorial Belt;* ***Zone 3****: Domes Region;* ***Zone 4****: External Fold and Thrust Belt. Modified from Kampunzu and Cailteux (1999); Porada and Berhorst (2000) and Selley et al. (2005).*

1.4.1 The Katangan Rift

Aulocogenic rifting between the Congo, Kalahari and Bangweulu block cratons (see Figure 1.3) caused the opening of the Katangan basin system (Kampunzu and Cailteux, 1999), creation of normal fault-bounded sub-basins and deposition of the Katangan supergroup (see section 1.3: Stratigraphy). The orientation of Katangan structures is highly variable and difficult to reconstruct both due to the aulocogenic nature of the original rift and subsequent deformation during the Lufilian orogeny, although a group of such extensional structures can be distinguished, often reactivated (Selley *et al.,* 2005; Kazadi-Banza, 2012; Kipata *et al.*, 2013). The first deposition in the basin may be as old as 880 Ma (Armstrong *et*

al., 2005) however the onset of extensional magmatism/crustal generation does not begin until 846±19 Ma (Kampunzu *et al.*, 1991), placing the onset of the rifting process between these dates.

The traditional view on the Katangan Basin is that rifting remained essentially intracratonic, with true seafloor spreading never having occurred before basin inversion in the following Lufilian Orogeny (Daly, 1986; Hanson *et al.*, 1994; Stern, 1994; Tembo *et al.*, 1999; Condie, 2003; Eglinger, 2013). John (2001) and John *et al.* (2003) present evidence that rifting proceeded into a full open-ocean basin of perhaps >1000kms width with associated subduction, however later work by Wood *et al.* (2014) and Hitzman (2015b) questions the veracity of whiteschist assemblages interpreted to be subduction related – saying instead that kyanite-bearing assemblages in the Domes Region are formed by saline hydrothermal fluids rather than subduction to high P/T conditions.

Whatever the lateral extent of the basin, discontinuous extension occurred over a period of almost 300 million years with normal faults accommodating this extension and encouraging syn-rift redbed sedimentation on a number of occasions. Three discrete 1st order extension events are inferred from the facies changes between the Kundelungu, Nguba and Roan Groups, each of which consists of a series of 2nd order depositional sequences (Bull *et al.*, 2011). During basin inversion, many of these normal faults formed the loci for reverse/thrust reactivation and also nucleation points for folds (Hitzman, 2015b).

Jackson *et al.* (2003), in their salt tectonic model (see section *1.4.4.2*), place the onset of salt diapirism during the Katangan rift extensional phase, which is refined by Selley *et al.* (2010a) to around the time of the deposition of the Ng1.1. Grand Conglomerat (roughly 712 Ma). According to this model passive diapirism continued throughout Nguba and Kundelungu times due to loading disturbances caused by continued extension (with diapirs often forming along normal faults) and progressive sediment loading.

1.4.2. The Lufilian Orogeny

Re-convergence of the Kalahari and Congo cratons during the Lufilian/Pan-African orogeny occurred contemporaneously with Katangan deposition and it is likely that localised extension and deposition continued throughout the early stages of the orogeny within an overall compressive tectonic regime; early Lufilian syn-tectonic granites are reported by

Hanson *et al.* (1994) in central Zambia and dated at c. 820 Ma, long before peak orogenic metamorphism at 540-535 Ma (Kröner and Stern, 2005). This contradicts the suggestion of Kampunzu *et al.* (1991) that convergence was rapid and limited crustal stacking occurred (as an explanation for the lack of subduction-related magmatism). John (2001) suggests that rare eclogite and whiteschist metamorphism of Katangan rocks in North and Central Zambia indicates that the crust was indeed buried to great depths. However, if the open-ocean hypothesis is correct, its great age and cold temperature would have kept it from melting. The system can be explained by a high degree of crustal thickening during the orogeny, at the base of which would be cold Katangan-ocean crust. However, low metamorphic grades in the Katangan of DRC do not fit comfortably with this hypothesis. The best explanation for the seemingly contradictive tectonic observations across the Lufilian Arc may be in the model of Daly (1986) that envisages that a 'zipper' collision occurred between the two cratons, beginning in the (modern) southeast and proceeding northwesterly, with implicit differences in metamorphic grade and deformation intensity along the suture.

The open ocean theory of John (2001) is not widely accepted. Wood *et al.* (2014), Hitzman (2015b) and other authors have questioned the interpretation of kyanite in the Domes Region and the North-West Province as necessarily being a product of high P/T conditions. Instead, highly saline metasomatic fluids at lower pressure and temperature are invoked to produce the talc-kyanite-quartz-phlogopite assemblages observed by Wood *et al.* (2014), who find fluid inclusions within such assemblages that record temperatures of 330-415°C (too low for subduction) and salinities of 40-70 wt.% NaCl, suggesting a high evaporite content and perhaps related to the salt tectonic model of Jackson *et al.* (2003). The metasomatic hypothesis for kyanite in the Lufilian Arc argues for a lack of subduction during the orogeny, which has academic merit for explaining the lack of observed arc magmatism or the usual metamorphic facies patterns that one would expect during subductive convergence. Eglinger *et al.* (2016) and Turlin *et al*. (2015) investigate different kyanite-garnet assemblages in the Domes Region and present a metamorphic, rather than metasomatic model for their formation, estimating them to have formed at 40-50km depth. However, this study explains the burial through syn-orogenic crustal thickening rather than through subduction.

Whatever the nature of the re-convergence, the Congo, Kalahari and Bangweulu Block cratons came together again as part of the Pan-African orogenic episode, inverting the

Katangan Basin, and causing the Lufilian orogeny. Figure 1.8 shows a map of tectonic domains in Africa, giving the location of the Central African Copperbelt (CAC) and the Lufilian Arc relative to cratons and other orogenic belts.

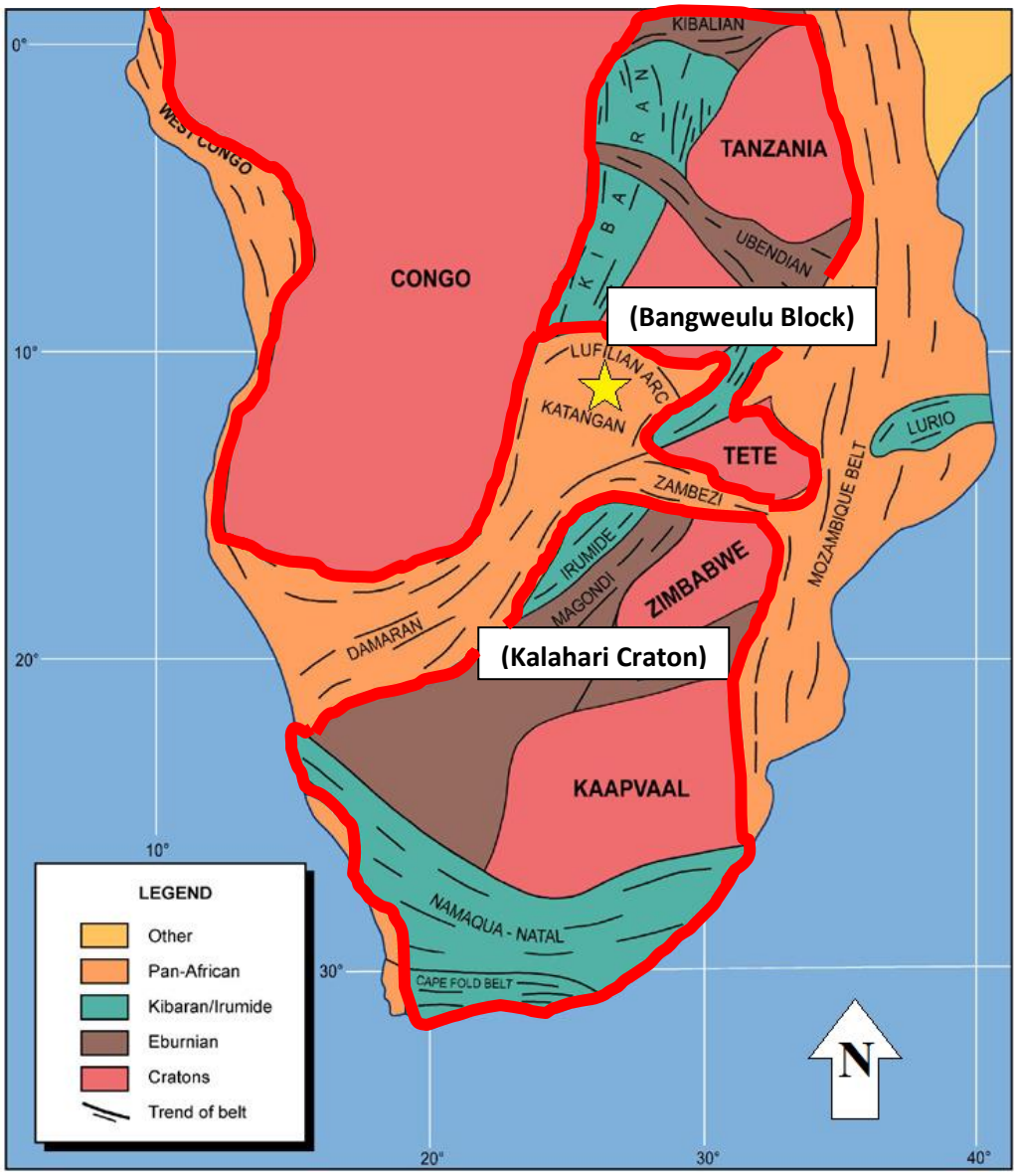

Figure 1.8: *Location of the Central African Copperbelt (yellow star) within the regional geotectonic setting of cratons and orogenic belts. Modified from Syamujaye (2014).*

Most authors infer a series of deformational events within the orogeny. Kampunzu and Cailteux (1999) distinguish 3 tectonic phases: D1, the 'Kolwezian Phase' is characterised by recumbent folding, thrusting and backfolding with a northward transport direction. D2, the 'Monwezi Phase', resulted in left-lateral/sinistral strike slip faulting and clockwise rotation of

the Lufilian Arc, and finally D3, the 'Chilatembo Phase' is marked by structures transverse to the Lufilian Arc and can be thought of as essentially post-Lufilian. Selley *et al.* (2005) note that many of these structures are compressive/transpressive reactivations of extensional faults formed during Katangan rifting. The D1 and D2 phases are well agreed upon and recognised widely by studies such as at Kinsevere (Kazadi-Banza, 2012) and Ruashi (Johnson, 2014). Kipata *et al.* (2013), using Delvaux and Sperner (2003) stress-tensor analysis, attributes 3 compressive deformations to the orogeny: the first a brittle, reverse/thrust fault period with northwards transport of thrust sheets; the second a largely ductile 'orogenic bending' causing the arcuate shape of the modern belt with a N-S to NNE-SSW direction of compression; and the third a NE-SW transpressive event in which many older Lufilian faults were re-activated in a sinistral strike-slip sense. These three compressive events can be interpreted as a more detailed reassignment of Kampunzu and Cailteux (1999)'s D1 and D2 phases, with the 'Monwezi' D2 phase comprising the two 'orogenic bending' and transpressive faulting phases of Kipata *et al.* (2013).

The transpressive, rotational element of the D2 event of Kampunzu and Cailteux (1999) is perhaps a result of the 3-craton convergence involved in the orogeny. The slightly later arrival of the Bangweulu Block subsequent to Congo-Kalahari collision could explain the 'orogenic bending' and resulting arcuate shape of the Lufilian (Figure 1.9). Two periods of extension are recognised by Kipata *et al.* (2013) relating to subsequent orogenic collapse, one transtensional and the latter fully extensional. These two periods of collapse resulted in structures trending with the same orientations as those created in the compressive phase and are not to be confused with the D3 event of Kampunzu and Cailteux (1999), which is probably equivalent to post-Lufilian deformation. These orogenic collapse features may have played an important role in controlling epigenetic stratabound mineralisation (see Chapter 2: Regional Mineralisation). A summary diagram of the Lufilian orogeny is given in Figure 1.9.

It should be noted that there has been very little work completed to date in terms of regional-scale structural analysis of the Lufilian Arc. The present, limited understanding is mostly based on analyses of isolated deposits (e.g. Kazadi-Banza, 2012; Kipata *et al*., 2013, Johnson, 2014), which are typically restricted to the inconsistently-and-implacably-deformed Mines Subgroup, and to broader studies of geological map patterns (Kampunzu and Cailteux, 1999).

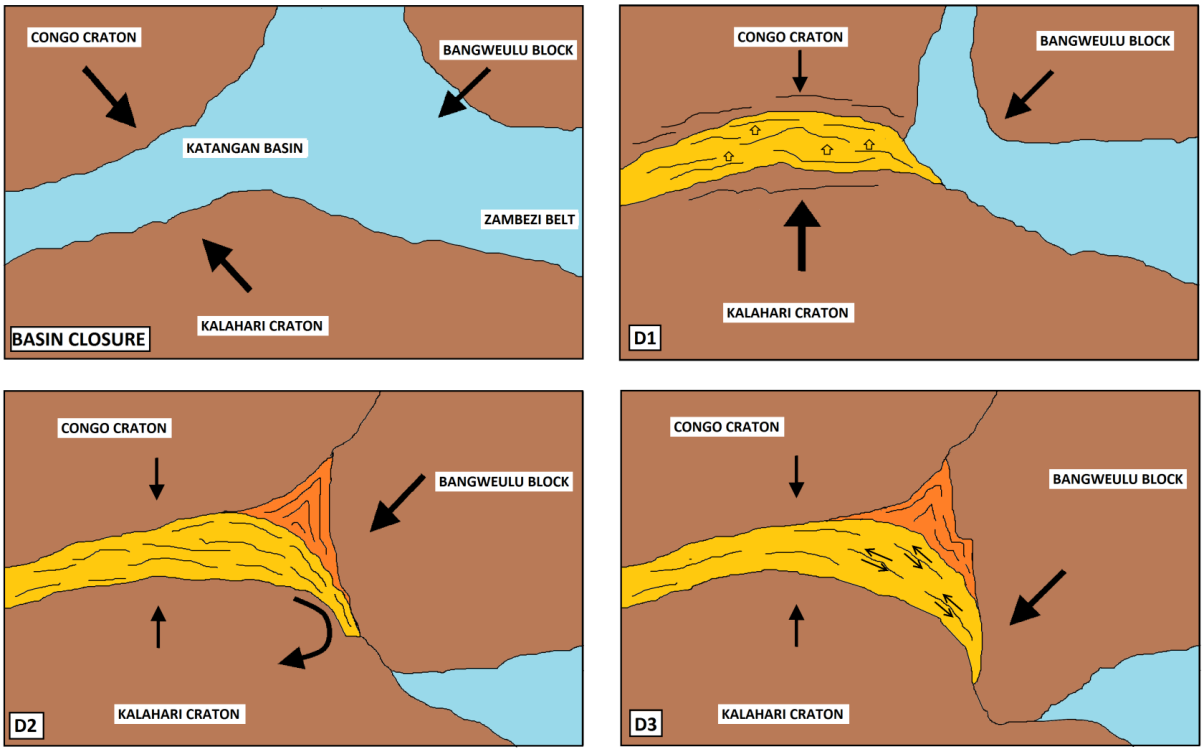

Figure 1.9*: Conceptual sketch of the three deformation stages of the Lufilian Orogeny described by Kipata et al. (2013), with the inferred convergence of the three cratons involved. The yellow belt is a sketch of the Lufilian Arc whereas the orange represents the Lufilian Foreland.* ***D1****: Collision of the Congo and Kalahari cratons causes overturned folding, thrusting and northward transport of thrust sheets.* ***D2****: Collision by the Bangweulu Block results in clockwise rotational deformation and 'orogenic bending' of the Arc.* ***D3****: Further advancement of the Bangweulu Block results in sinistral strike-slip reactivation of thrust faults formed during D1. Not to scale. D1 represents the 'Kolwezian' phase of deformation whereas D2 and D3 represent the 'Monwezi' phases of deformation described by Kampunzu and Cailteux (1999).*

1.4.3. Post Lufilian Deformation

Most structures that post-date the Lufilian orogeny are formed by Mesozoic NW-SE transpressional inversion related to Gondwana break-up, and two phases (one NE-SW and the latter NW-SE) of extension related to the East African Rift (Kipata *et al.*, 2013). All three post-Lufilian deformation phases are relatively weak and are caused by far-field stresses peripheral to extensional tectonic events. Most authors infer pre-and-syn-Lufilian timings of hypogene mineralisation (e.g. Dewaele *et al.,* 2006a; Kipata *et al.*, 2013; Eglinger *et al.,* 2013; 2014a; 2014b; Turlin *et al.,* 2015; Muchez *et al.,* 2015; Sillitoe *et al.,* 2015), although

Muchez *et al.* (2015) report a period of volumetrically minor sulphide remobilisation at 230 ± 36 Ma at the Kamoto deposit. In the external fold-and-thrust belt, no known economic Cu-Co deposits are reported to have post-Lufilian ages and post-Lufilian deformation is likely to have played little part in hypogene mineralisation. However, post-Lufilian deformation may have played some role in controlling climate and topographic factors in the development of secondary supergene mineralisation. Certainly, regional uplift in the Late Miocene was responsible for accelerating physical erosion and exposing hypogene mineralisation to meteoric fluids, resulting in the earlier of two periods of supergene enrichment (Decree *et al.*, 2010).

1.4.4. The 'Roan Megabreccia' Debate

A curious, economically important and much debated feature of the orogeny is the final orientation of the Roan Group sedimentary rocks. Rather than forming a coherent stratigraphic horizon, as generally seen in the Nguba and Kundelungu Group sediments, outcrops of the Roan Group are often disaggregated from each other into discrete 10^2 or 10^3m scale 'blocks' (François, 1974). These blocks are generally bounded by faults, which may place them adjacent to other Roan Group blocks, coherent stratigraphic packages of other groups or to expansive units of highly variable breccias (Figure 1.10). The blocks themselves are often deformed within these complexes. There are three prevailing theories as to the origin of the Roan 'megabreccias' as they are commonly known. The longest held theory is that they are simply the product of traditional fold-and-thrust-belt tectonics; that during the brittle phase of compression the Roan was transported >100km to the North by thrust sheets, over the basement, creating a disaggregated series of broken up blocks bounded by cataclastic breccias (e.g. Demesmaeker *et al.* 1963; Unrug, 1988, François, 1974; Cailteux and Kampunzu, 1995). Secondly, more recent studies, aided by a developing understanding of the importance of salt dissolution (and the Cl^- ion) in the transport of Cu (e.g. Rose, 1976) drew comparisons to tectonic provinces with similar 'megabreccia' features around the world such as the Wernecke Mountains of Canada and the Flinders Range of Australia (Bell, 1989). In this model large bodies of salt were deposited within the Roan Group which have since diapirically migrated out of the system through overlying units, causing the disaggregation of the Roan blocks witnessed today (Jackson *et al.*, 2003)

in a para-autochthonous manner (Bull *et al.*, 2011). The third genetic model for the megabreccias, proposed by Wendorff (2000) involves thrust-sheet-driven olistrosome complexes, from which mega-clasts gravitationally disaggregated and were incorporated into an erosionally driven mass-flow dominated sedimentary sequence, effectively a tectono-sedimentary origin for the breccias.

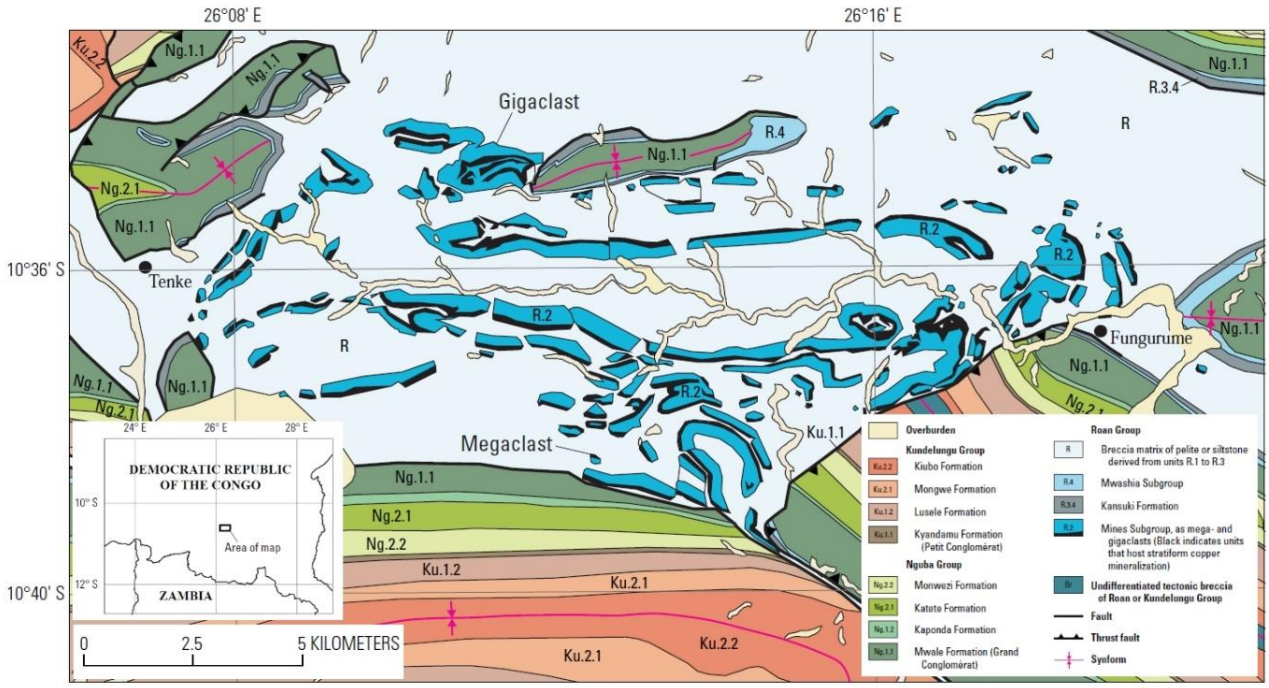

***Figure 1.10**: Disaggregated blocks of Mines Subgroup stratigraphy in the Tenke-Fungurume area, some 40km to the east of the Mashitu group of Cu-Co deposits. Modified from Zientek et al. (2014) and Jackson et al. (2003).*

1.4.4.1 The 'traditional tectonic'/'fold and thrust' model

Early authors on the Copperbelt e.g. (Demesmaker *et al.*, 1963) took a more traditional tectonic approach to the structural observations made at deposits around the region. Both layer-parallel and layer-discordant breccias in Congo and Zambia were interpreted as of tectonic origin (François, 1974; 1987; 1993), primarily formed in the creation of allochthonous thrust sheets generated during the Lufilian Orogeny where transport over large distances (>100km to the northeast (Porada, 1989)) has caused the disaggregation of large blocks of stratigraphy. The role of evaporites in the earlier literature was recognised but largely limited to aiding the transport of these thrust sheets by fluidisation (Cailteux and Kampunzu, 1995, Cailteux *et al*., 2018). Analogies were drawn by Kampunzu and Cailteux

(1999) to fluidised, thrust related breccias of the Damaran Naukluft Nappe complex (Behr *et al.*, 1981; 1983; Porada and Behr, 1988), the decollements of the Alpine Orogeny external zone (Malavieille and Ritz, 1989) and the Himalayan frontal thrust zone (Gee, 1983; Baker *et al.*, 1988).

1.4.4.2 The salt tectonic model

Authors as early as François (1987) and De Magnee and François (1988) recognised folding in certain areas of the Copperbelt as possibly related to diapirism rather than ductile folding tectonics – noting that certain anticlines were cored with megabreccia and Roan Group fragments. The region has since been likened to other sedimentary basins of the world where salt diapirism plays an important role in the regional tectonic structure, such as the Wernecke Mountains of Canada and the Flinders Range of Australia (Bell, 1989). However, these interpretations of diapirism tended to be construed by their authors as limited in extent, with traditional fold-and-thrust tectonism being responsible for most of the deformation witnessed and the Katangan Basin being interpreted as mostly allochthonous. Jackson *et al.* (2003) subsequently presented a model which advocated for widespread diapirism in Roan (pre-Lufilian) times followed by allochthonous thrust-sheet tectonics, again fluidised by salt. This model placed the majority of the salt in the western Congolese portion of the Katangan Basin, with thinner beds of evaporite and accordingly less diapirism eastwards towards the Zambian portion where tectonics are more thrust-sheet-controlled (Figure 1.11).

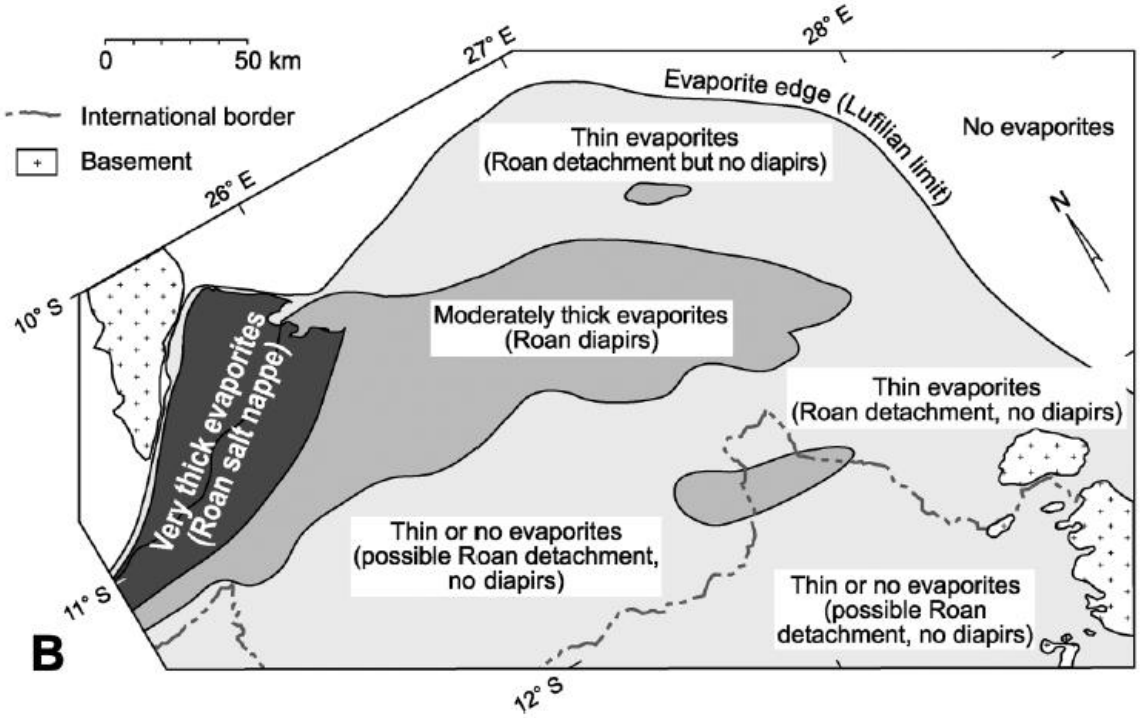

Figure 1.11*: Model showing the hypothesised distribution of evaporite deposition throughout the Katangan Basin. From Jackson et al. (2003).*

Subsequently, this model has been championed by many authors and has been refined to suggest that pre-orogenic diapirism as well as evaporite dissolution with subsequent void collapse is the dominant factor in western-Katangan brecciation, without significant lateral displacement of the basin during the Lufilian orogeny (e.g. Bull *et al.*, 2010; Bull *et al.*, 2011; Hitzman *et al.*, 2012). Hitzman *et al.* (2012) have argued for a para-autochthonous Katangan Basin and have suggested that the disaggregation of the Roan Group can be explained solely by pre-orogenic halokinesis, as shown in Figure 1.12. In this model, great thicknesses of evaporite are postulated to have been deposited stratigraphically between the mid and upper-R.A.T. (~750m of evaporites) and between the Mines Subgroup and Dipeta Subgroups (~400m of evaporites), with thinner units of evaporite scattered throughout the Roan (Hitzman *et al.*, 2015b). Loading of sediments above these two thicker main evaporite units is thought to have caused them to move diapirically, mobilising away from their sites of deposition and causing the brittle fragmentation and ductile transport of the more competent unit of Mines Subgroup sediments in between. The salt would have since extruded and been eroded away, leaving little direct evidence of its presence in the stratigraphic sequence (Jackson *et al.*, 2003; Hitzman, 2015b).

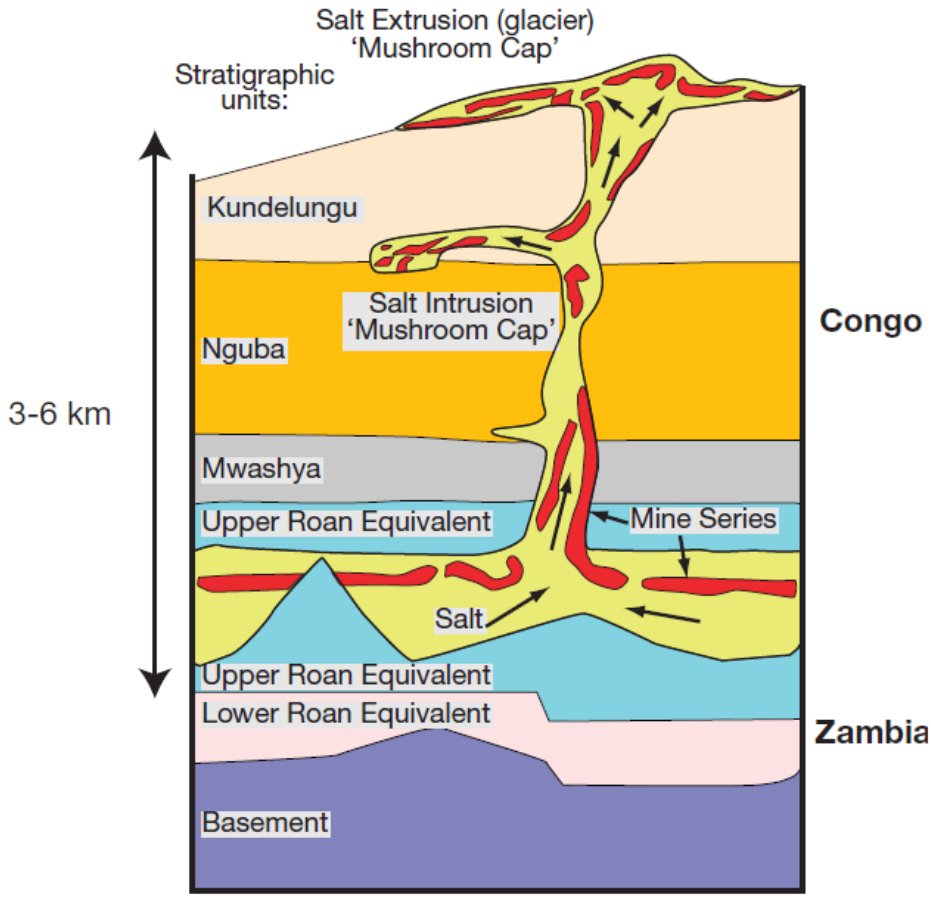

***Figure 1.12**: Model showing the role of salt diapirism in the brecciation and disaggregation of the Roan Group and the Mines Subgroup. From Hitzman et al. (2012).*

1.4.4.3. The olistostrome complex model

The majority of Katangan breccias in the region occur within the R1 (R.A.T.) Subgroup of the Roan Group, a thick sequence of largely immature continentally derived redbed sediments (see section *1.3.2.1. – R1: The R.A.T.*). Many of these breccias are layer parallel and have many features which are decidedly reminiscent of conglomeratic sedimentary units. A sedimentary origin for the megabreccias of the Katangan Basin was first proposed by Grujenschi (1978), but was largely discounted. Later work by Wendorff (1995) and Binda and Porada (1995) suggested that the megabreccias could be large 'olistostrome' complexes – a melange of clastic breccias including megaclasts of more competent stratigraphy such as the Mines Subgroup, which broke off, eroded and were amalgamated into the complex at the front of advancing thrust sheets, propelled to the northeast by the Lufilian orogeny. This amalgamation would have happened in a surficial, sedimentary environment, and later

refinements to the model by Wendorff (2000; 2003; 2005) would advocate for the stratigraphy to be rewritten to include two new sedimentological groups, the Fungurume and Plateaux Groups. These two new groups would comprise those concordant 'breccias' which draw source material from all three predating Roan, Nguba and Kundelungu Groups of the Katangan Supergroup, postdating them all at <575 Ma (Master *et al.*, 2005). These are classified as tectonic or halokinetic breccias of the Roan Group by other models.

All three models have local merit in explaining observations of deformation-related features, sedimentation patterns and mineralisation, and at a regional scale a combined model seems the most likely explanation, with different processes acting at different places and times across the Lufilian Arc. Many of the more recent studies of the Copperbelt at a regional scale (e.g. Hitzman *et al.*, 2010; 2012; Jackson *et al.*, 2003; Koziy *et al.*, 2009; Muchez *et al.*, 2008; 2010; Selley *et al.*, 2005; 2010a), due to more cross-disciplinary integration of traditionally 'petroleum geology' aligned study techniques with Copperbelt geology, have increasingly advocated for the importance of the salt tectonic model and this model appears to be emerging as the dominant one in many author's recent interpretations.

The study area of the Camrose concession appears to exhibit features best explained by a combined salt/traditional-tectonic model; this hypothesis will be investigated further in this dissertation.

1.5 Metamorphism

Metamorphism across the Central African Copperbelt is heterogeneous and again reflects the difference between the Zambian and Congolese Copperbelts. Whereas the rocks of the Congolese Copperbelt generally reached no higher than lower greenschist facies P-T, with chlorite being the dominant metamorphic mineral described, Zambian rocks commonly reached up to lower amphibolite facies with metamorphic biotite and phlogopite (Ramsay and Ridgway, 1977). Rocks of the Domes Region of Zambia's North West Province, where Katangan Supergroup rocks abut against domes of Kibaran-age basement, were subjected to even higher peak metamorphic conditions which created garnet-kyanite metamorphic

assemblages (Cosi *et al.*, 1992; Eglinger *et al*., 2016). With the exception of these garnet-kyanite schists of the Domes Region, which were subjected to P/T conditions of ~9-10 kilobars at 550-650°C and exhibit migmatite textures (Eglinger *et al*., 2016), most of the rocks of the Katangan Supergroup retain their sedimentary textures. Ramsay and Ridgway (1977) showed that much of the Katangan Supergroup underwent a typical orogenic clockwise P/T path caused by the Lufilian Orogeny, which ended at around 500 Ma.

Scapolite is also common in the Zambian part of the Lufilian Arc, to the extent that it can be considered "one of the major scapolite provinces of the world" according to Ramsay and Ridgway (1977). This attests to the former presence of significant quantities of evaporite minerals in the basin, as scapolite is recognised as frequently being the product of the metamorphism of evaporitic halite (Ramsay and Ridgeway, 1970; Serdyuchenko, 1975). In the Congo, scapolite is not such a common component because metamorphic conditions did not reach P-T conditions high enough to cause its formation (Hitzman *et al.*, 2012). Gypsum, anhydrite, celestine and barite are more commonly found in the rocks of the Congolese Copperbelt, where scapolite is rare.

In addition to this orogenic P-T path of regional metamorphism, John (2001) and John *et al.* (2003) have postulated that the talc-kyanite whiteschists of the Domes Region are eclogite facies rocks formed during Lufilian-age High P/T subduction (and subsequently exhumed). This is cited as evidence that the Katangan Basin opened to the extent of an open, long-lived ocean basin rather than an intracratonic, Red Sea-style proto-oceanic basin (Coward and Daly, 1984; Cosi *et al.*, 1992; Porada and Berhorst, 1998; John *et al.*, 2004). However, the eclogitic, high P-T metamorphic nature of the whiteschists in the Domes Region is refuted by Wood *et al.* (2014) and Halley *et al.* (2016), who demonstrated that they could instead have been formed by highly saline metasomatic fluids. Eglinger *et al.* (2016) and Turlin *et al.* (2015) propose that kyanite-garnet assemblages in the Domes region are indeed metamorphic, but were buried due to crustal thickening rather than subduction. Extensive metasomatism throughout the basin confuses the issue of distinguishing metamorphic assemblages from metasomatic ones.

1.6 Magmatism and Igneous Rocks

Hyaloclastites, hyaloclastic breccias, pillow lavas, basalt flows, dolerites and gabbros (in order of abundance) are recorded throughout the Lufilian arc, however, volumetrically they do not comprise a significant proportion of the rocks in the Katangan Basin and magmatic activity does not seem to have been extensive (Auger, 1975; Lefebvre, 1975; Kampunzu *et al.*, 1991). Igneous activity in the Lufilian Arc is mostly limited to syn-Katangan rift volcanics and intrusions, which evolved from continental tholeiite to alkaline tholeiite to E-MORB tholeiite affinity, inferred by some authors to mark full transition from intracratonic rift to proto-ocean (e.g. Cosi *et al.*, 1992; Tembo *et al*., 1999; Kampunzu *et al.*, 2000).

Calc-alkaline magmatism and other subduction related petrogenetic processes expected of the early stages of the Lufilian orogeny are curiously absent (Kampunzu *et al.*, 1991) although collision-related S-type granitoids are a rare, but present feature of the arc (Hanson *et al.*, 1994). Igneous rocks and derived detrital sediments have an important role to play in dating of the Katangan rocks.

Magmatism in the Copperbelt is not thought to have played a direct role in the development of Cu-Co mineralisation, although igneous rocks, mostly in the form of basement granites, are thought to be the main source of metals for the deposits on a regional scale (Koziy *et al.*, 2009; Brown, 2014; van Wilderode *et al.*, 2014). Authors have long speculated that copper deposits in the granitic basement might be responsible for the great fertility of the Copperbelt (Wakefield, 1978; Dejonghe and Ngoyi, 1995). A study by Sillitoe *et al.* (2015) found evidence for a mineralising event in the basement rock at 1084 to 1059 ± 5 Ma, coincident with the Irumide orogeny, from Re-Os ages of molybdenite in Cu-Fe-Mo sulphide assemblages. This finding supports earlier speculation that the basement of the Copperbelt was mineralised before the opening of the Katangan Basin. Additionally, mafic igneous intrusions and volcanics are considered to be a potential source of cobalt in Copperbelt Cu-Co deposits (Annels *et al*., 1983; Annels and Simmonds, 1984), an unusual component in most Sedimentary-Hosted Stratiform Copper (S.S.C.) systems (Hitzman *et al.*, 2012; van Wilderode *et al.*, 2014). There are other types of deposit associated with igneous activity in the region, for example the suspected Iron-Oxide-Copper-Gold (IOCG) deposits of the Hook Granite Suite at the extreme southern limits of the Zambian Lufilian Arc.

CHAPTER 2: REGIONAL MINERALISATION

Scientific interest in the geology of the Lufilian Arc has largely been motivated by the great metal endowment of the Copperbelt. The region has the world's largest reserves of cobalt with ~50% and contains ~15% of the world's copper resources (Cox *et al.*, 2007; Sillitoe, 2012; Brininstool, 2014; Shedd, 2014). The Central African Copperbelt (C.A.C.) is described by Hitzman *et al.* (2012) as "the world's largest and highest-grade sedimentary copper province" and the region is only surpassed by the porphyry-copper districts of the Andean Volcanic Belt in terms of significance to global copper mining (Sillitoe, 2012). Hitzman *et al.* (2012) make three distinctions between Sedimentary-Hosted Stratiform Copper (S.S.C.) mineralisation styles in the C.A.C. based on geography: 'Congolese-type' Cu-Co mineralisation, 'Zambian type' Cu, and copper mineralisation of the North West Province (Domes Region) of Zambia. These mineralisation styles are supplemented in the C.A.C. by economic concentrations of Pb, Zn, Ag, Ge, U, Ni, and Mo, which in many cases are related to S.S.C. mineralisation, either through their direct co-occurrence with economic Cu/Co or by a number of similarities in deposit style which link them to S.S.C. type mineralisation. This thesis will focus on Congolese type Cu-Co as it is the primary recognised mineralisation style at Mashitu South.

2.1 Cu-Co Mineralisation in the Central African Copperbelt

The Cu-Co geochemical association of a large quantity of S.S.C. type mineralisation in the Copperbelt is known as 'Congolese type' because the majority of it exists in the Congolese portion of the Lufilian Arc, a region distinct from the Zambian Lufilian Arc in stratigraphy, structure and metamorphic grade as discussed in Chapter 1. In terms of tonnage, three major Cu-Co deposits containing >15 Mt Cu exist in the Congolese (or Katangan) Copperbelt. These are Kamoa (which lacks associated Co mineralisation), Kolwezi and Tenke-Fungurume (Hitzman *et al.*, 2012), together with numerous smaller deposits (e.g. Kambove, Kamoya, Ruashi, Luiswishi, Kinsevere, Kakanda, Mashitu, Pungulume, Menda, Luishia). The tectonic disaggregation of the Mines Subgroup has complicated the definition of distinct deposits and many deposits are grouped in clusters of several individual 'rafts' of Mines Subgroup

rocks. Other sedimentary-hosted deposit types exist within the Katangan Copperbelt which will be discussed in section 2.2: on related deposit types. The locations of a selection of important Copperbelt mineral deposits are shown in Figure 2.1. Ore minerals which are commonly mined in the Katangan Copperbelt include chalcopyrite ($CuFeS_2$), bornite (Cu_5FeS_4), chalcocite (Cu_2S), carrollite $Cu(Co,Ni)_2S_4$, malachite ($Cu_2CO_3(OH)_2$) and heterogenite (CoOOH). Dewaele *et al.* (2006a) genetically classify the Katangan Cu-Co deposits into three main types based on their mineralisation style: stratiform, vein-type and supergene.

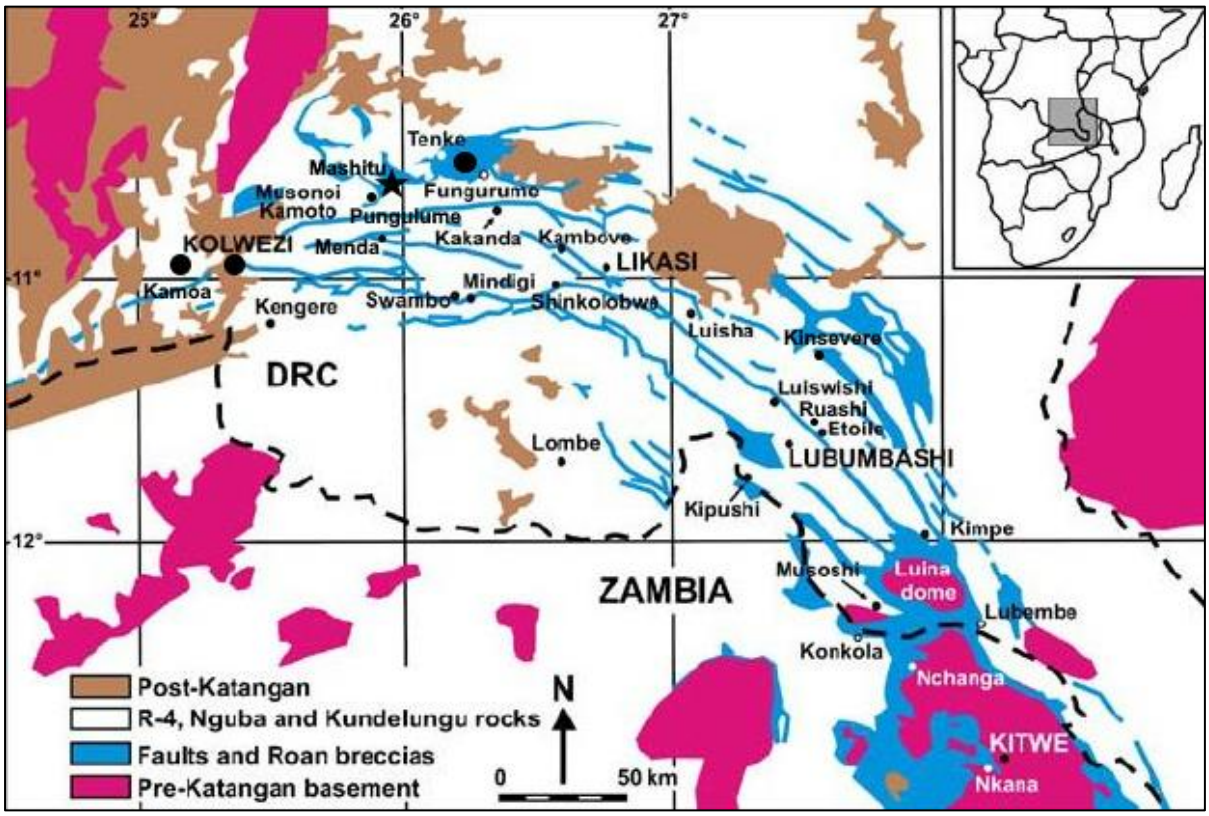

***Figure 2.1**: Location of a selection of economically or academically significant Copperbelt mineral deposits, modified from Muchez et al. (2008). Mashitu is shown as a star while the three major (>15 Mt) Congolese deposits – Kamoa, Kolwezi and Tenke-Fungurume – are symbolised by enlarged circles.*

2.1.1 Stratiform Mineralisation

The stratiform mineralisation type is characterised by disseminated stratiform hypogene sulphides, predominantly pyrite, chalcopyrite, bornite, chalcocite and carrollite, of which the

latter three are important ore minerals. These phases are primarily deposited within km-scale 'megaclasts' of the Mines (R2) Subgroup (Oosterbosh and Schuiling, 1951), however examples of this mineralisation type exist in other stratigraphic units such as the Dipeta (R3) (Chimvinga, pers. comm., 2014) the Mwashya (R4) and the Grand Conglomerat (Ng1) (Broughton and Rogers, 2010). The majority of Mines Subgroup stratiform mineralisation in the Congolese Copperbelt is contained in the 'Lower Orebody', hosted in the D.Strat and R.S.F. units of the Kamoto Dolomite Formation, and the 'Upper Orebody' in the lowermost S.D.B. unit of the Dolomitic Shales Formation (Hitzman *et al.*, 2012). The two orebodies are separated by the mostly barren, silicified dolomite of the R.S.C. unit which is usually no more than 5-10m in thickness. Figure 2.2 shows the generalised distribution of mineralisation within the Mines Subgroup stratigraphy.

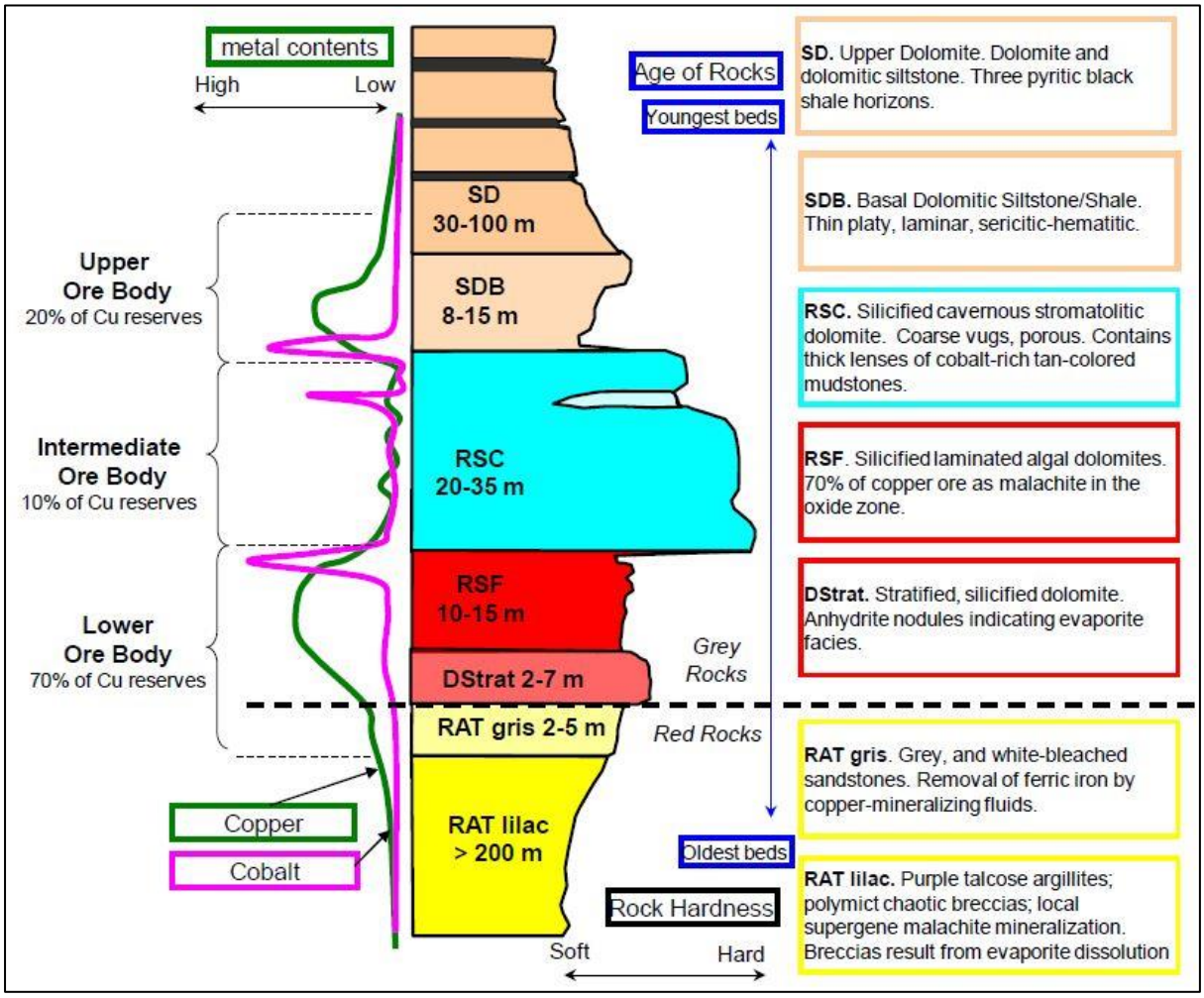

***Figure 2.2**: Cu-Co distribution within the Upper and Lower Orebodies of the Mines Subgroup. From: Nilsson et al. (2011)*

The source of copper in the stratiform deposits of Katanga is debated. An early model by Unrug (1988) suggested large volumes of Nguba Group volcanic rocks were leached of copper along graben blocks, with copper-bearing fluids expelled from these grabens into adjacent Roan Group stratigraphy. However, this model does not take into account an early diagenetic timing for stratiform mineralisation (which will be discussed later). In many S.S.C. systems the majority of copper is derived from thick oxidised 'redbed' sequences that underlie reduced 'greybed' facies (often carbonates or deep marine shales) into which the copper is precipitated under changing redox conditions (Hitzman *et al.*, 2010; Brown, 2014). However, the necessary volumes of redbeds required to source all of the copper are not observed in the Katangan Supergroup (Hitzman 2000; Cailteux *et al.*, 2005), and authors cite instead the granitic basement (Muchez *et al.*, 2008; Koziy *et al.*, 2009; van Wilderode *et al.*, 2014), and perhaps even ancient porphyry-type deposits within the basement (Dejonghe and Ngoyi, 1995) as being the main source of metals. In a recent discovery, Sillitoe *et al.* (2015) have dated molybdenite from Cu-Mo mineralisation in the Zambian Mwombezhi Dome to 1084-1059 ± 5 Ma, contemporaneous with the (pre-Lufilian) Irumide orogeny. This finding strengthens the case for mineralisation events increasing the Cu-fertility of the basement <u>before</u> the onset of Katangan rifting (maximum age 883 ± 10 Ma: Armstrong *et al.;* 2010) and perhaps contributing to the metal endowment of the Copperbelt. Cobalt is an unusual component to be concentrated economically in most S.S.C. systems (Hitzman *et al.*, 2010) and may have been sourced from Katangan-rift-related mafic rocks (Annels *et al.*, 1983; Annels and Simmonds, 1984; Unrug, 1988; Annels, 1989; Koziy *et al.*, 2009; Muchez and Corbella, 2012; van Wilderode *et al.*, 2014) or from anomalous concentrations of cobalt in the granitic basement (van Wilderode *et al.*, 2014), though its provenance is not well understood.

In general, the fluids responsible for stratiform Cu-Co mineralisation give low-moderate temperatures (75-250°C) and reasonably high salinities (10-25 wt. % NaCl) in fluid inclusion studies consistent with formational water brines circulating during diagenesis and basin evolution (Muchez *et al.*, 2008; El Desouky *et al.*, 2009; Kampunzu *et al.*, 2009; Schmandt *et al.*, 2013). The salinities suggest a component of dissolved evaporitic material in the mineralising fluids. Indeed, the Cl^- ion provided by the dissolution of halite and sylvite is a well-recognised carrier of Cu^{2+} in the form of $CuCl_2^-$ and $CuCl_3^{2-}$ (Rose, 1976) and is

implicated in many global SSC systems as being the primary cause of copper mobilisation (Brown, 2014). Reactive transport modelling by Muchez and Corbella (2012) shows that Co is also carried by hydrous and chloride complexes in the form of $CoCl(H_2O)^{5+}$, $CoCl_4^{2-}$ and $CoCl_2(H_2O)_2(aq)$. Dissolution of salt from the large evaporite sequences postulated to exist within the R1 by proponents of the salt tectonic model of Jackson *et al.* (2003), as well as less voluminous evaporites within the R2, would have contributed to the observed salinities of fluid inclusions associated with stratiform mineralisation. In such a high salinity environment, copper is mobile in near-neutral pH and moderately oxidising Eh conditions (Rose, 1967), as illustrated in Figure 2.3. These brines would have descended into the lower R1 and the basement, where, during circulation in hydrologically closed basins (Hitzman *et al.*, 2010), they would have stripped copper from labile minerals Brown (2014). A study by Walker (1989) gives average Cu concentrations for these minerals, with the more mafic ones containing higher concentrations of copper (pyroxene:~120ppm; biotite:~86ppm; amphibole:~78ppm; magnetite:~76ppm; plagioclase:~62ppm; K-feldspar:~1-20ppm); the copper leached from these common minerals would have potentially been supplemented by copper sulphide mineralisation in the basement (Sillitoe *et al.*, 2015).

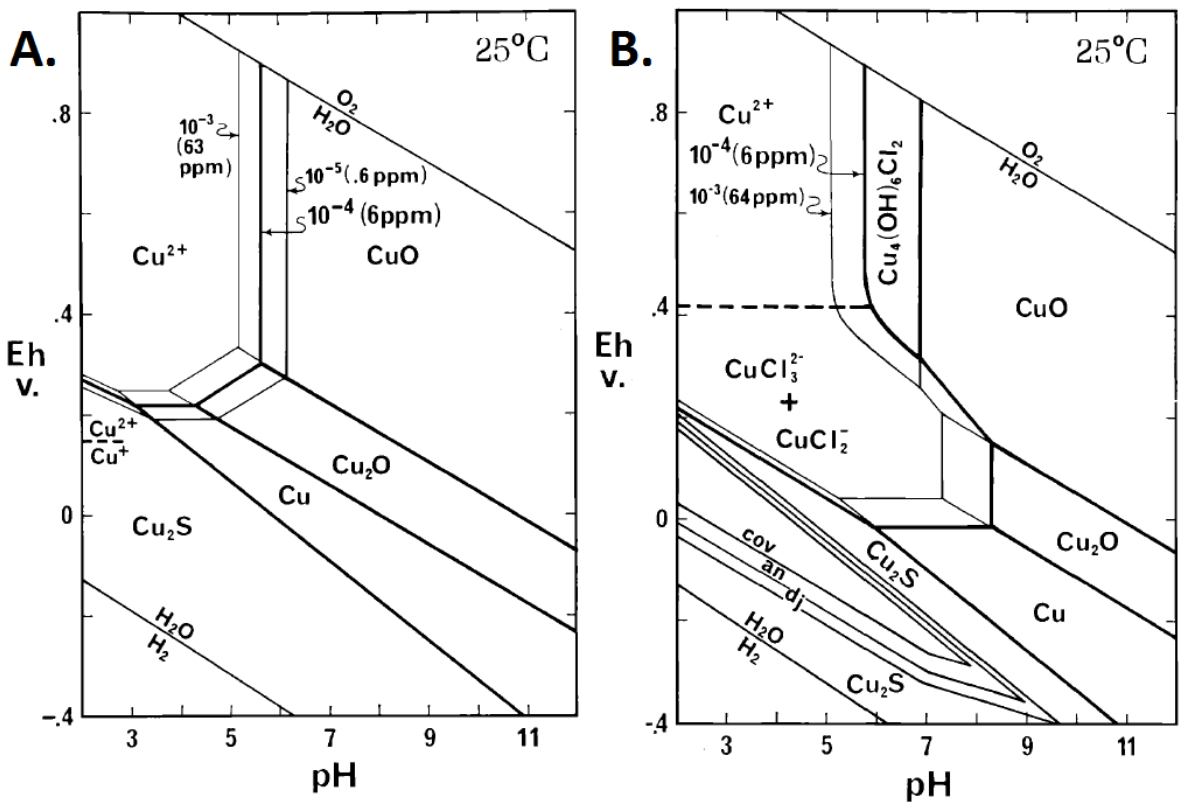

***Figure 2.3**: Eh-pH stability field diagrams for **A**.: the Cu-O-H-S system at 25°C, ΣS=10^{-4} and for **B**: the Cu-O-H-S-Cl system at 25°C, ΣS=10^{-4} and Cl^-=0.5m as NaCl. In the saline system **B**., copper is stable in the soluble, transportable forms of $CuCl_3^{2-}$ and $CuCl_2^-$ ions at near neutral pH's and only mildly oxidising Eh's. This is in contrast to the non-saline system **A**., where copper is stable only as soluble, transportable Cu^{2+} at low, acidic pH and in oxidising Eh conditions.*

After leaching, the resultant saline, oxidising, near neutral pH, low-temperature, mineralising fluids would be likely to contain anything between 1 and 150ppm Cu based on their calculated Cu concentrations at other S.S.C. deposits (White, 1968; White, 1971; Cathles *et al.*, 1993) depending on the period in which the fluids spent circulating through the source rocks. Leaching of a pre-mineralised basement (e.g. Dejonghe and Ngoyi, 1995; Sillitoe *et al.*, 2015) would likely produce fluids in which copper was even more highly concentrated.

There are two likely mechanisms for the initiation of fluid flow in the Katangan basin, both of which may have prevailed at different times and within different sub-basins. First, within hydrologically closed basins, the geothermal gradient would have created convection cells where fluids heated at depth would be pushed higher through the rock column, before cooling or meeting a hydrologically impermeable boundary and sinking again in a circulatory manner. Where no such impermeable boundary was encountered, the mineralising fluids could be expelled to higher stratigraphic units (Hitzman *et al.*, 2010). The second model for a fluid transport mechanism is gravity-driven, topographically-recharged flow, where meteoric groundwater rained onto the highlands flows hydrologically downhill, into the redbeds at the centre of the basin, and flows up into the higher stratigraphy by the pressure of the 'hydraulic head' (Brown, 2009; Brown, 2014). Hitzman *et al.* (2010) and Hitzman (2015b) consider the former mechanism of convective circulation to have more capacity at a basin-to-sub-basin scale to form larger, higher grade deposits, as the convective circulation of Cl^--bearing fluids can more efficiently strip Cu and Co from source rocks than the 'single pass' approach of the gravity-driven flow model.

Being driven by either geothermal convection, or by gravity, the metalliferous fluids likely exploited extensional basin faults as transport conduits to the higher, receptive stratigraphies (Unrug, 1988; Hitzman *et al.*, 2012), resulting in mineralisation being controlled to a certain extent by basin architecture and fault positioning (Selley *et al.*,

2010a; Bull *et al.*, 2011). Fluid flow along these faults may also have introduced some stratabound Cu-Co mineralisation that appears contemporaneous to stratiform mineralisation (Hitzman *et al.*, 2012). A conceptual model for the metal source, fluid source, flow mechanism and transport conduits implicated in stratiform mineralisation is given as Figure 2.4**.** An alternative, but not necessarily competing model for the transport of metalliferous fluids is that of Fay and Barton (2012) who postulate that, at Tenke-Fungurume (location shown in Figure 1.1), the Upper and Lower Orebodies are distributed either side of the R.S.C. because that unit was responsible for major lateral transport of copper-bearing fluids. They envisage post-silicification, pre-mineralisation dissolution of dolomite which made the R.S.C. much more permeable than the surrounding units, causing fluid to be preferentially transported through it. When the fluids encountered the less permeable, more reducing lithologies of the S.D.B. and R.S.F. above and below the R.S.C., respectively, the Upper and Lower Orebodies were precipitated. The Fay and Barton (2012) model of fluid transport is summarised in Figure 2.5.

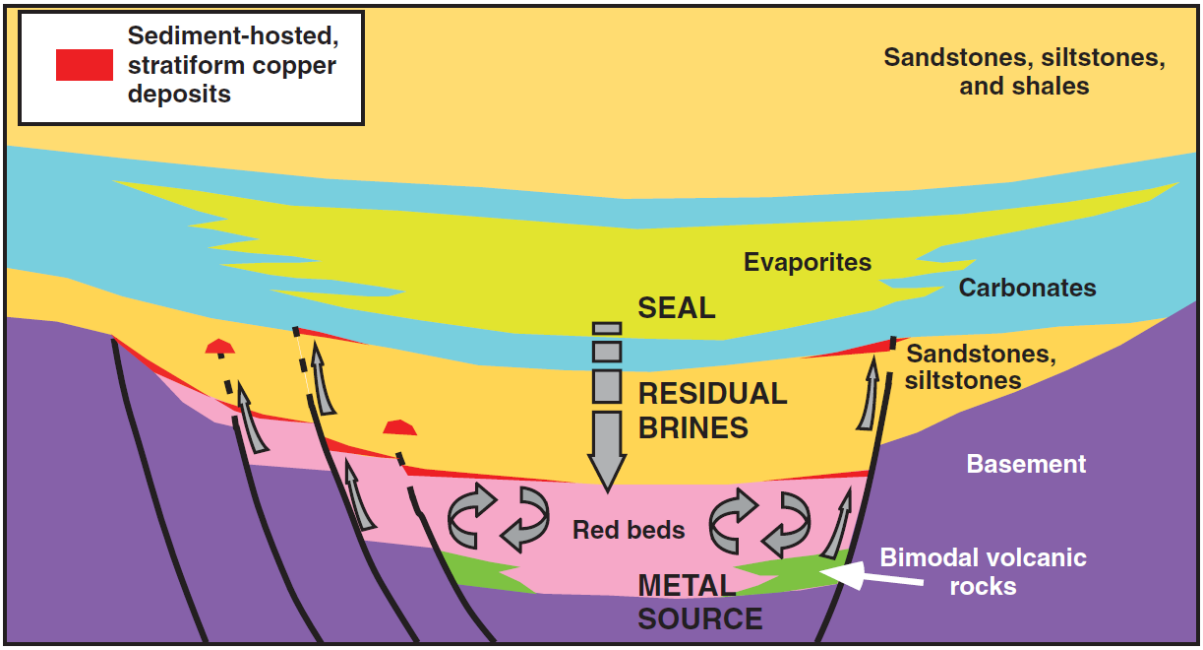

Figure 2.4*.: Generalised model for the generation and transport of copper-rich fluids responsible for forming S.S.C. deposits. Evaporitic, Cl^--bearing fluids descend into redbeds where they circulate in a closed system and strip copper from labile minerals. In the Copperbelt, circulation of these fluids within the basement as well as the redbeds is thought to have been important in mobilising the quantities of copper observed in the stratiform deposits. From Hitzman et al. (2010).*

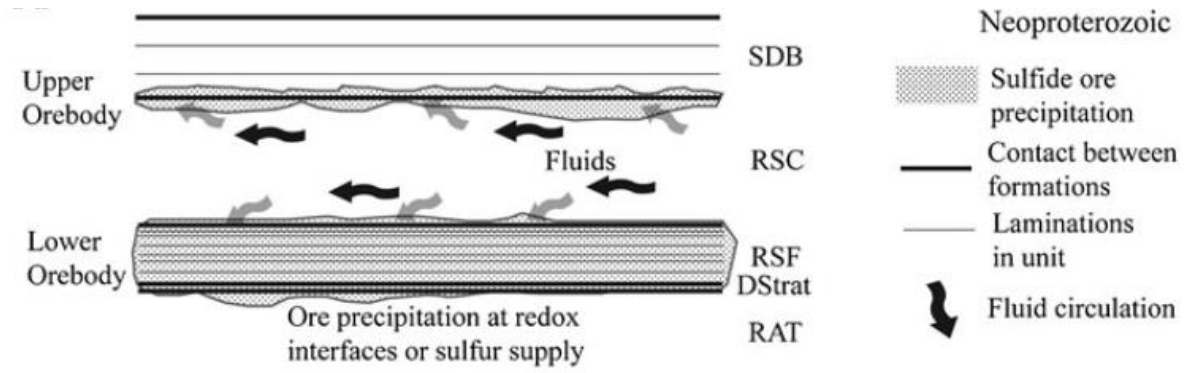

***Figure 2.5**.: Model for the lateral transport of primary ore fluids through the R.S.C. and deposition of the Upper and Lower Orebodies above and below this unit. From: Fay and Barton (2012).*

Precipitation of sulphides from these metal-ion bearing ore solutions required two things. First, a source of sulphur and secondly, a change in redox conditions. Early diagenetic pyrite, precipitated before the introduction of ore fluids, has long been recognised in the sequence (e.g. Oosterbosch and Schuiling, 1951; Bartholome, 1958; Bartholome and Katekesha, 1971) and this pyrite is thought to be a major contributor to the sulphur source, with isotope studies showing that the $\delta^{34}S$ values of copper sulphides from the stratiform mineralisation stage match those of the pre-mineralisation diagenetic pyrite (e.g. Jensen and Dechow, 1962; Dechow and Jensen, 1965). Bacterial Sulphate Reduction (B.S.R.) of H_2S within anoxic, pre-lithification sediment is an important process in the formation of this pyrite and, by extension, is a control on the later precipitation of stratiform ore in S.S.C. mineralisation (Brown, 2014). In many cases, this early diagenetic pyrite would have been completely replaced by the later mineralisation-stage Cu-Co sulphides (Bartholome, 1962; 1974; Bartholome *et al.*, 1973). Evaporitic gypsum and anhydrite may also have contributed sulphur to the system. Notably, Muchez *et al.* (2008) have found that stratiform copper sulphides at Kamoto, Musonoi and Luiswishi are actually pseudomorphic to earlier anhydrite nodules.

The second factor necessary for the precipitation of Cu-Co sulphides is a change in the redox conditions. Cu^{2+}, $CuCl_2^-$, $CuCl_3^{2-}$, $CoCl(H_2O)^{5+}$, $CoCl_4^{2-}$ and $CoCl_2(H_2O)_2(aq)$ ions are easily transported by oxidising fluids through the redbeds within which they originated. However, upon meeting some kind of reducing agent the fall in Eh (see Figure 2.3) will cause the precipitation of copper and cobalt sulphides. This reducing agent, in the case of Katangan stratiform mineralisation, usually takes the form of the greybeds of the Mines Subgroup

(Hitzman *et al.*, 2012). Oxidising metalliferous fluids travelling through the R.A.T. Subgroup meet the carbonates, organic carbon, evaporites and pyrite of the Mines Subgroup and are reduced such that copper is no longer stable as soluble ions, combining with locally-sourced sulphur to precipitate copper sulphides. This stratigraphic redox horizon at the base of the Mines Subgroup results in an upwards zonation of sulphides typical of S.S.C. deposits (Rose, 1989; Brown, 2014), with copper rich sulphides (e.g. chalcocite) prevalent proximal to the horizon in the Kamoto Formation and iron rich sulphides (e.g. chalcopyrite, pyrite) distally present in the Kambove Formation. The zonation sequence of chalcocite → bornite → chalcopyrite → pyrite applies throughout the Copperbelt to the stratiform mineralisation stage, and where these phases occur together, iron rich sulphides (e.g. pyrite) precipitated first and copper rich sulphides (e.g. chalcocite) precipitated last (e.g. Oosterbosch and Schuiling, 1951; Bartholomé and Katekesha 1971; Sweeney *et al.*, 1991; Dejonghe and Ngoyi, 1995; Selley *et al.*, 2005; Broughton and Rogers, 2010; Hitzman *et al.*, 2012; Seibel *et al.*, 2013; Schmandt *et al.*, 2013). Pyrite from the stratiform ore stage should not be confused with an earlier phase of diagenetic pyrite (from which sulphur is sourced), which is widely distributed throughout the Mines Subgroup and which has crystals described as 'on the verge of classification as framboids' (Love and Amstutz, 1966). Sometimes, this mineralisation-related phase of pyrite can be seen overgrowing the earlier, 'sub-framboidal' pyrite as a rim containing up to 4% cobalt (Bartholome and Katekesha, 1971). The relationship between stratigraphic redox condition change, mineralisation and sulphide zonation is illustrated in Figure 2.6. In certain examples of stratiform mineralisation, trapped fluid hydrocarbons rather than lithological greybeds are implicated as the reducing agent to mineralising fluids (El Desouky *et al.*, 2007).

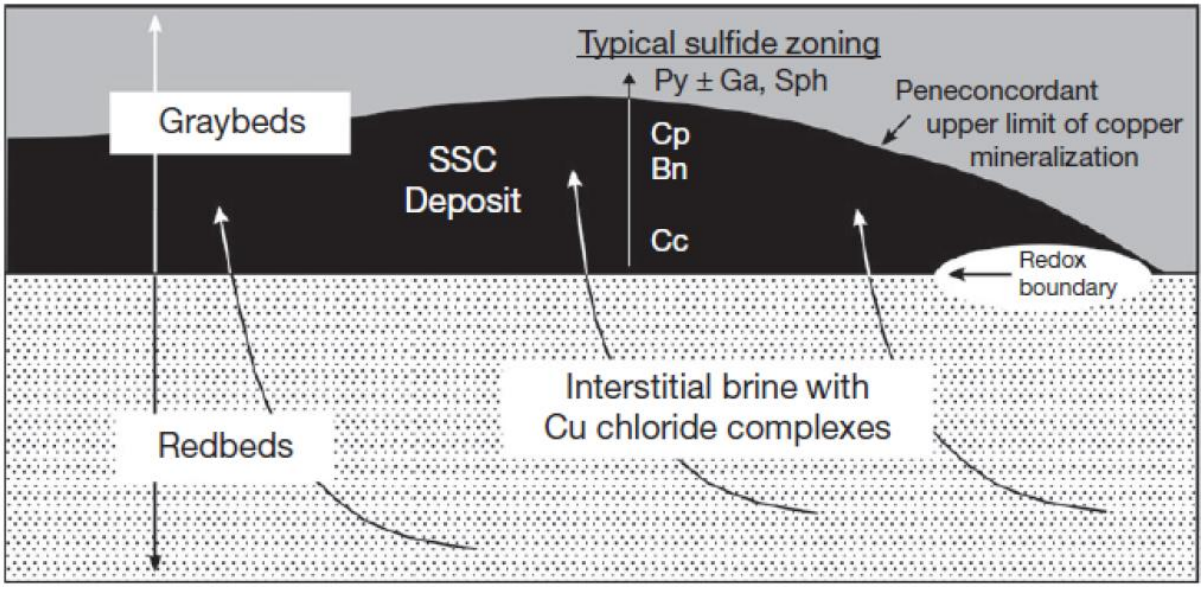

***Figure 2.6**: Conceptual illustration of the relationship between mineralisation, sulphide zonation, and lithological redox horizons in S.S.C. type mineralisation. In the Katangan Copperbelt, the R1 Subgroup serves as the redbeds and the R2 Subgroup serves as the greybeds creating a major regional reduction front.*

This approach to reviewing the Katangan stratiform mineralisation has so far focussed on the formation of copper (and iron) sulphides, which are more typical products of S.S.C. type mineralisation. However, the high quantities of cobalt in the Copperbelt are also accommodated in part by the stratiform mineralisation stage, in the form of the copper-cobalt (± nickel) sulphide, carrollite ($Cu(Co,Ni)_2S_4$). The distribution of stratiform carrollite is not well agreed upon between different deposits but in many Katangan deposits it appears to be more prevalent in the Upper, rather than the Lower Orebody (e.g. Chartrand and Brown, 1984). In the atypical stratiform deposit of Kamoa, where mineralisation is hosted in the Ng1 Grand Conglomerat unit rather than in the Mines Subgroup, a crude metal zonation of Cu → Co → Pb → Zn → Fe sulphides is observed (Broughton and Rogers, 2010). In addition to its predilection for the Upper Orebody, carrollite seems to have a distinct spatial association "adjacent to and within the R.S.C." (Hitzman, 2012), when compared with the other mineralisation phases of the stratiform ore stage. This association would seem to suggest a link to the Fay and Barton (2012) model of fluid transport, rather than the 'bottom up' zonation pattern where each mineralisation phase fits in with zonation from fluids reduced at the R1/R2 redox boundary. Paragenetically, carrollite of the stratiform mineralisation stage is usually precipitated early, with most studies placing it before or

contemporaneous with the deposition of chalcopyrite (e.g. Oosterbosch and Schuiling, 1951; Chartrand and Brown, 1984; Dejonghe and Ngoyi, 1995; van Langendonck *et al.*, 2013) although El Desouky *et al.* (2010) describe a paragenesis for the stratiform ore stage at Luiswishi and Kamoto of (first) chalcopyrite → bornite → carrollite → chalcocite (last). Other than its distribution and rather uncertain paragenetic relationships, stratiform cobalt appears to have many genetic factors in common with stratiform copper and is considered by most authors to be part of the same mineralisation stage.

The common sulphide minerals attributed to the stratiform mineralisation stage are pyrite, chalcopyrite, bornite, chalcocite and carrollite. In addition to these phases, galena, sphalerite and pyrrhotite (Selley *et al.*, 2005; Broughton and Rogers, 2010; Schmandt *et al.*, 2013; Seibel *et al.*, 2013) may also be found in small quantities, commonly at the peripheries of Cu-Co deposits, representing peripheral Pb-Zn-Fe halos which are common features of S.S.C. deposits (Rose, 1989). Where they occur together galena, sphalerite and pyrrhotite are precipitated paragenetically early, before Cu or Co sulphides. Stratiform copper mineralisation seems to have a geochemical association of Cu-As-Ni-V-Mo-Bi ± Pb-Zn-U-Co, most elements of which are hosted as traces within Cu-Co sulphides (McGoldrick *et al.*, 2010), based on the whole rock geochemical studies (e.g. at Kolwezi; Selley *et al.*, 2010b).

With regard to the stratiform deposits of the Mines Subgroup, a great deal of metasomatic alteration has affected the host rocks and in some cases accompanied the mineralisation. According to Hitzman *et al.* (2010b) this process began in the very early stages of diagenesis with the growth of gypsum and the subsequent silicification of much of this gypsum. Stromatolite and algal growth, too, would have contributed to early diagenetic silicification, particularly in stromatolite and algal-mat rich units such as the R.S.F., R.S.C., and parts of the C.M.N.. Stromatolites are known to experience early post-mortem silica fixation and a complicated history of alternating carbonate-and-silica-replacement during diagenesis (Kremer *et al.*, 2012). Within oxidising sediments (siliciclastics) early authigenic, tabular haematite as well as rutile were formed (Dejonghe and Ngoyi, 1995). Early diagenetic framboidal pyrite also grew in the reducing-environment sediments (black shales, carbonates) during this period, some of which recrystallized to more cubic forms over time (Hitzman *et al.*, 2012). Although early diagenetic haematite and pyrite are generally mutually exclusive, being formed in oxidising and reducing conditions respectively, there is some coexistence of these two mineral phases, possibly due to post-burial fluctuation in Eh-

pH conditions within the sediments in which they were deposited (Dejonghe and Ngoyi, 1995).

The first hydrothermal alteration event recognised by Hitzman (2010b) was potassic, involving the growth of potassium feldspar and biotite-phlogopite throughout the entire R1 and R2 sequence, but concentrated in the R.A.T. and the Kamoto Dolomite Formation.

This was followed by a magnesian alteration event involving the growth of talc and chlorite in argillaceous rocks, and magnesite and dolomite in carbonate rocks. Isotopic evidence suggests that the fluid responsible for magnesian alteration is likely to have carried organic carbon (Hitzman, 2010b).

Following potassic and magnesian alteration, there was a period of further microcrystalline silicification; in this case with silica introduced through hydrothermal fluids (Fay and Barton, 2012) and then prismatic, coarse grained recrystallisation of both quartz and dolomite (Hitzman *et al.*, 2012). The last alteration event that occurred during diagenesis was sodic, involving the growth of albite predominantly at the top of the R1 unit (primarily along the R.A.T. Gris unit, contributing to its 'bleached' appearance). The potassic, magnesian and sodic alteration events appear to all have been accompanied by the growth of stratiform Cu-Co sulphides, although the bulk of stratiform mineralisation appears to have occurred during or after magnesian alteration (Hitzman, 2010b; Hitzman *et al.*, 2012). Although magnesian alteration may be temporarily associated with stratiform mineralisation, this alteration type is widespread through many units of the Katangan Supergroup and it is not well spatially associated with deposits. The widespread nature of Mg-alteration makes its presence (or lack thereof) unsuitable for use in exploration as a vector towards deposits, although Oosterbosch and Schuiling (1951) report that chlorite content correlates directly with copper grade at Fungurume (see Figure 1.1 for location).

Dolomite precipitation related to magnesian alteration, in some cases, took the form of syn-extensional veins "formed by fluid overpressure during very early diagenesis" which contain Cu-Co sulphides from the stratiform mineralisation stage (Hitzman *et al.*, 2012). These veins tend to be smaller (usually limited to a few centimetres in length), contain a different mineralogy and are less cross-cutting in nature than vein type mineralisation of Dewaele *et al.* (2006a) (discussed later). The dominant mode of occurrence of mineralisation from the stratiform stage is indeed stratiform-disseminated; but the presence of veins associated with this stage of mineralisation should not be overlooked.

In terms of the timing of mineralisation and metasomatism, early deposit models that espoused a syngenetic timing of mineralisation were all but rejected as early as Oosterbosch and Schuiling (1951) and epigenetic, post-depositional models came into favour. In fact, studies of the Copperbelt have helped inform global scientific opinion on the origin of S.S.C. deposits worldwide, with Katangan studies such as Bartholome, 1958, 1962, 1974; and Bartholome *et al.*, 1973 helping the syn-diagenetic model to become popular (and remain so). Today, the mineralisation process, initiated by the passage of metalliferous fluids, was thought to have begun during early diagenesis of the sedimentary host rocks (see Figure 2.7).

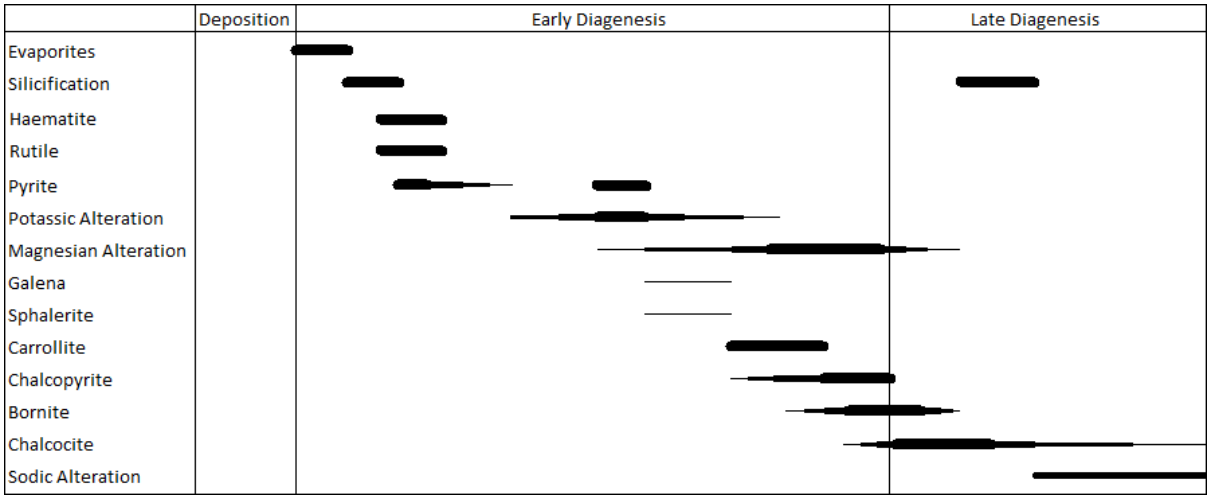

***Figure 2.7**: Generalised paragenesis for sulphides and associated metasomatism related to the stratiform mineralisation stage of the Katangan Copperbelt. Compiled based on information from: Dejonghe and Ngoyi (1995), Dewaele et al. (2006a), El Desouky et al. (2010), Hitzman et al. (2010), Fay and Barton (2012), Hitzman et al. (2012), Schmandt et al. (2013).*

A diagenetic origin for stratiform Cu-Co is supported by diagenetic, authigenic quartz and dolomite mantling some of the ore sulphides (Bartholome *et al.*, 1971; 1973). Stratiform ore may also be observed to have been deformed by later folding events, meaning that it certainly predates Lufilian compression (Bartholome *et al.*, 1971). Low temperatures of mineralising fluids calculated by fluid inclusion thermometry (Muchez *et al.*, 2008; El Desouky *et al.*, 2009; Kampunzu *et al.*, 2009; Schmandt *et al.*, 2013), together with $\delta^{34}S$ values suggesting that at least some sulphur in the ore sulphides was bacteriologically fixed (Jensen and Dechow, 1962; Dechow and Jensen, 1965), contribute towards the early

diagenetic model. Sweeney and Binda (1989) show that at Konkola (a Zambian stratiform deposit), precipitation of carrollite occurred in sediment with a porosity of 60-70%, corresponding to a burial depth of only about 30m and indicating a very early diagenetic, pre-compaction age of carrollite mineralisation (Sweeney *et al.*, 1991). Some authors, however, infer a late diagenetic age for mineralisation (e.g. Unrug, 1988), and it is likely that stratiform Cu-Co mineralisation in the Katangan Basin occurred in a punctuated series of events or semi-continuously over a protracted length of time spanning diagenesis. Due to the remarkable stratigraphic continuity of Congolese stratiform mineralisation, the majority of this mineralisation stage is thought to have occurred prior to significant dismemberment of the R2 Subgroup by tectonic and/or halokinetic and/or olistrosomic processes (Demesmaeker *et al.*, 1963; François, 1973; Cailteux, 1994; Cailteux *et al.*, 2005).

In attempting to establish an absolute date for stratiform mineralisation, a study by Decree *et al.* (2014) found three discreet periods of uranium mobilisation, through inherited U-Pb ages taken from heterogenite, at ~876 Ma, ~823 Ma, and between ~720 to ~670 Ma. These ages are significant because the conditions in which U is soluble and may be transported by hydrothermal fluids are very similar to the conditions necessary for Cu-Co transport (Brown, 2014). Widespread mobilisation of uranium would probably correspond to mobilisation of Cu-Co (and other metals). Stratiform mineralisation in the Katangan could not be older than 883±10 Ma, the maximum age for the host rocks of the Katangan Supergroup according to the dating of detrital zircons found in the Roan Group by Armstrong *et al.* (2005). At Konkola, in Zambia, Barra *et al.* (2004), using Re-Os dating of stratiform sulphides, established a mineralisation age of 816±62 Ma. Stratiform sulphides at the Kamoto deposit in DRC are Re-Os dated to ~800 Ma by Muchez *et al.* (2015) (although later remobilisations are identified at 682±28 and 230±36 Ma). However, the stratiform ore deposit at Kamoa is certainly not older than 765 Ma, which is an upper limit for the age of deposition of the host Grand Conglomerat unit based on U-Pb dating of gabbro clasts included in the unit (Key *et al.*, 2001). This, together with the ages given by Decree *et al.* (2014) for uranium mobilisation in the Katangan Basin (cited above), suggests that the stratiform mineralisation stage took place over a protracted period spanning more than 100 million years, between ~875 and ~765 Ma. However, different parts of the basin may have been mineralised at different times, given the broad range of study areas considered in this review. This long period of mineralisation may in part explain the rich metal endowment of

the Copperbelt. Interestingly, the stratiform ore mineralisation period broadly agrees with the estimate of Muchez *et al.* (2010) for the age of the tectonic Katangan Rifting Stage (~877-750Ma). This leads to speculation that the rifting process may have contributed towards the mineralising system indirectly in some way, through enhanced heat-driven convection, input of Co etc.

2.1.2 'Vein Type' Mineralisation

The second distinction made by Dewaele *et al.* (2006a) of Katangan Cu-Co mineralisation is described as 'vein type' mineralisation, although post-stratiform vein-hosted sulphides have been noted at deposits by numerous authors prior to this study (e.g. Garlick, 1962; Mareé, 1963; Winfield and Robinson, 1963; Bartholome *et al.*, 1973; Bartholome, 1974; Lefebvre, 1976; Hoy and Ohmoto, 1989; Cailteux *et al.*, 1994; Dejonghe, 1997; Cailteux *et al.*, 2005). The 'vein type' mineralisation stage consists of vein-hosted Cu-Co sulphides which cross-cut stratiform mineralisation and metasomatism where the two stages occur together. In Zambia, Selley *et al.* (2005) distinguished two varieties of vein-type mineralisation, the first being "prefolding bedding-parallel veinlets" with "texturally and compositionally comparable disseminated Cu-Co sulphides" to stratiform mineralisation. The second variety of vein-type mineralisation is characterised by post-folding veins with a Cu-U-Mo-(Au) geochemical association, containing chalcopyrite, bornite, molybdenite, uraninite, pitchblende and brannerite. However, this variety of mineralisation is rarely reported in the Congolese portion of the basin. In the case of both pre-folding and post-folding veins, coarse-grained quartz and dolomite are the main gangue minerals present (Muchez *et al.*, 2008; Hitzman *et al.*, 2012). This stage has been shown to be capable of remobilising and redistributing stratiform Cu-Co sulphides, with minor depletion of sulphide stages from this stage concentrated around these veins (Cailteux *et al.*, 2005). Although vein-type mineralisation is a common feature of many Congolese Copperbelt deposits, frequently co-existing with stratiform mineralisation, this stage does not form any significant economically exploitable deposits in the region and is volumetrically minor when compared to the stratiform stage (Sweeney *et al.*, 1991; Sweeney and Binda, 1994; Dewaele *et al.*, 2006a). There are, however, deposits linked to vein-type Cu-Co in Zambia (e.g. Kansanshi, Musoshi). Vein-hosted Cu-Zn deposits (e.g. Kabwe, Kipushi) together with vein-hosted Cu-Zn-Pb-Fe-Ag

deposits in the Lufilian foreland (e.g. Dikulushi, Lufukwe) share features in common with this stage such as a post-diagenetic timing, higher temperatures and salinities of mineralising fluids and a vein-hosted, stratabound mode of distribution (see below).

Isotope studies by El Desouky *et al.* (2010) and van Wilderode *et al.* (2014) point to the diagenetic sulphides of the stratiform mineralisation stage being the primary source of metals for the vein-type mineralisation stage. Although the fluid which created the mineralised veins at Kamoto, Luiswishi, and Kambove may have interacted with the granitic basement, Turlin *et al.* (2015) consider the stratiform mineralisation to be the primary source of copper in the Domes Region. According to van Wilderode *et al.* (2014), "Whether this resulted in a renewed contribution of metals is uncertain."

The fluids which caused this remobilisation of sulphides were derived from metamorphic dewatering of the Katangan Supergroup sediments and the underlying basement (Hitzman *et al.*, 2012) and were higher temperature (200-500°C) and more saline (35-45% NaCl) than those associated with diagenetic stratiform copper (Richards *et al.*, 1988a; el Desouky *et al.*, 2009; Eglinger *et al.*, 2014a; 2014b). This extreme salinity associated with the fluids of the vein-type mineralisation stage is an indication that evaporite concentrations were present within the system and were being dissolved right up until the formation of this stage, rather than having completely left the system during early diapirism. The fluids attained their high temperature through deep migration (El Desouky *et al.*, 2010).

The heat from regional low-grade metamorphism was responsible for the liberation of fluid from hydrous minerals during this period, which was then transported up section and through the Mines Subgroup (the primary source of metals) by compressive seismic pumping (Hitzman *et al.*, 2012; van Langendonck *et al.*, 2013), a well-known mechanism for the remobilisation of metals (Sibson *et al.*, 1988; Pitcairn *et al.*, 2006). In many orogenic systems, these fluids are concentrated along compression-accommodating reverse/thrust faults and funnelled from large, first order fault systems into smaller, second and third order faults where metals carried by the fluid become the most concentrated (e.g. Dewaele *et al.*, 2004; Cox, 2005). El Desouky *et al.* (2010) consider compressional faults and breccia zones to be the main fluid conduit in the vein-type mineralising system; however, van Langendock *et al.* (2013) emphasise the role of the R.S.C. and other permeable stratigraphic horizons in the transport of mineralising fluids for this stage. Both explanations could easily co-exist,

with vertical transport mostly accommodated by faults and lateral transport mostly occurring along these permeable stratigraphic conduits.

Metal and sulphur were both remobilised from the sulphides of the stratiform mineralisation stage by the fluids of the vein-type mineralisation stage, with similar $\delta^{34}S$ values shared by sulphides of both stages (Dechow and Jensen, 1965; El Desouky *et al.*, 2010). There is no published evidence for a renewed external input of sulphur during this stage, with sulphur likely remobilised from sulphides and sulphates native to the host rocks by Thermochemical Sulphate Reduction (TSR) (El Desouky *et al.*, 2010).

Precipitation of sulphides from the mineralising fluids was likely to have been induced by two factors. First a drop in temperature and secondly, a reductant, both encountered by the fluids as they permeated into receptive host rock and fractures surrounding the primary fluid conduits. The reductant would have been carbonaceous material and pre-existing sulphides from greybeds (Hitzman *et al.*, 2005; Hitzman *et al.*, 2012) or hydrocarbons (Annels, 1979; McGowan *et al.*, 2006; Selley *et al.*, 2005; El Desouky *et al.*, 2007) as was also the case for stratiform mineralisation. Because of the limited extent to which vein-type mineralisation occurred, and because sulphide precipitation during this stage was not induced by reduction along a quasi-planar stratigraphic surface, vein-type mineralisation does not clearly exhibit the sulphide zonation found within ore deposits of the stratiform ore stage (Dewaele *et al.*, 2006a). Nevertheless, according to El Desouky *et al.* (2009), the ore mineralogy of the stratiform and vein-type mineralisation stages is very similar. Sulphides of the vein-type stage show a similar paragenetic sequence to the stratiform stage, with a general precipitation order of chalcopyrite → carrollite → bornite → chalcocite observed at Kamoto and Luiswishi (El Desouky *et al.*, 2010). Dewaele *et al.* (2006a) state that digenite and chalcocite are the most common sulphide products at the Kamoto and Musonoi deposits, and van Langendonck *et al.* (2013) add carrollite to these two minerals at Kambove West. Gangue minerals found within the veins are mostly coarse-grained dolomite and quartz (Muchez *et al.*, 2008) and hypogene vein-hosted haematite is occasionally present (Dewaele *et al.*, 2006a). Large *et al.* (2002) find a spatial association between veins of this period and both potassic and sodic alteration. Albite, biotite and muscovite have been found in several deposits in Zambia associated with post-peak-metamorphic Cu-mineralised veins (Darnley *et al.*, 1961; Richards *et al.*, 1988a,b; Hitzman *et al.*, 2012).

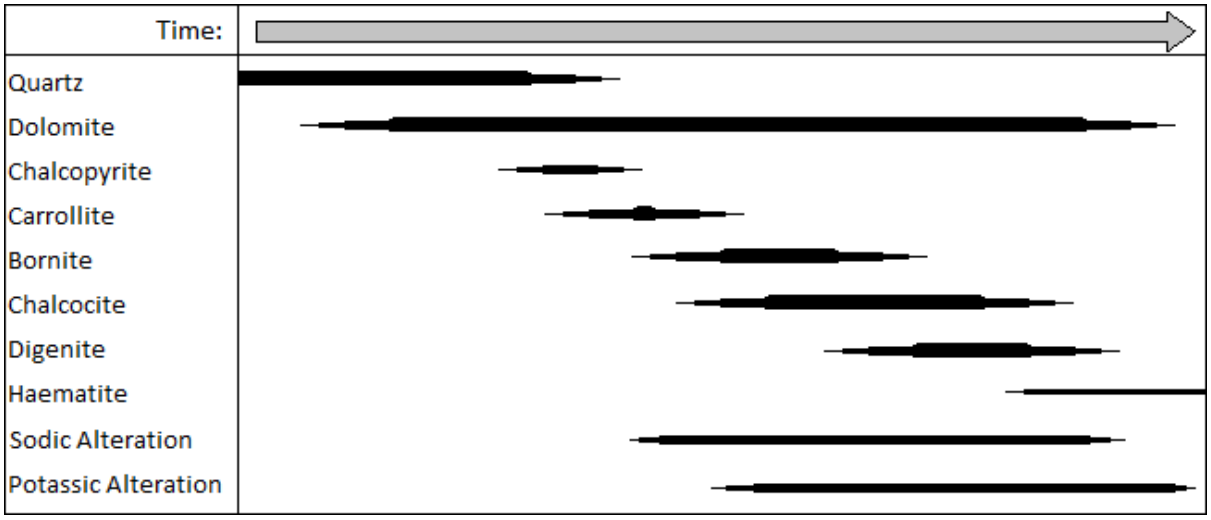

Figure 2.8: *Generalised summary of the paragenesis of 'vein-type' Cu-Co mineralisation from the Katangan Copperbelt described by Dewaele et al. (2006a). A timeline is not included because many vein type Cu-Co mineralising events with a similar paragenetic history appear to have occurred at different periods in the history of the Copperbelt.*

Attempts to date vein-type mineralisation across the Copperbelt have resulted in a wide range of ages which different studies have variously assigned to late-diagenetic, early-metamorphic, syn-orogenic and post-tectonic in origin; it is clear that no single mineralising event was responsible for all the vein-type Cu-Co throughout the region. Dawson (2002) identified five discrete hydrothermal events associated with ore in the Zambian Mufulira, Konkola, Chambishi and Ndola deposits with dates ranging between ~615-470 Ma: showing that fluid flow and ore deposition were episodic and protracted over the course of the Lufilian Orogeny. The mineralisation ages of Dawson (2002) fall just within the estimated time period during which the Katangan Basin was subjected to greenschist-facies regional metamorphism (Mendelsohn, 1961; Cahen and Snelling, 1981). An age of 576 ± 41 Ma is recorded from Re-Os dating of Cu-Co sulphides in Zambia by Selley *et al.* (2005), found within 'pre-folding' veinlets and interpreted as late-diagenetic-to-early-metamorphic/orogenic in origin. El Desouky *et al.* (2009) interpret the vein-type mineralisation at Kamoto and Luiswishi in the D.R.C. to be syn-orogenic. Their study found fluid inclusions from vein-type mineralisation showing high temperatures and salinities. Other studies (e.g. van Wilderode *et al.*, 2014) show that there was no magmatic interaction with the mineralising fluids. Combining these two pieces of evidence strongly suggests that

the salinities and temperatures of these fluids were attained under the kind of deep-burial conditions typical of an orogeny. Syn-orogenic fluids may have also formed the quartz-rutile-biotite-muscovite potassic alteration event described by Richards *et al.* (1988a) and dated at 514 ± 2 Ma, which was responsible for the redistribution and modification of ore. Vein-type Cu-Co found in the Kansanshi-deposit, Zambia, is dated by Torrealday *et al.* (2000) to between 499.3 ± 2.9 Ma and 492.9 ± 2.9 Ma, making it post-orogenic – certainly post-peak-metamorphism. The closely related post-peak-metamorphism Cu-U-Mo-(Au) veins in Zambia, described by Selley *et al.* (2005) give a similar age of around 500 Ma. Eglinger *et al.* (2014b) date two uranium mineralisation events In the Domes Region to ~550-530 Ma and ~510-500 Ma, which likely coincided with periods of Cu mineralisation (Turlin *et al*., 2015). However, Muchez *et al.* (2015) identify hypogene fluid flow events which remobilised stratiform mineralisation as early as 682±28 and as late as 230±36 Ma. Through Re-Os dating of molybdenite across a range of Zambian deposits, Sillitoe *et al.* (2017) claim that both stratiform and vein-type mineralisation were introduced in a '50 Myr Cambrian window' between 540 and 490 Ma. However, this study presents no convincing textural evidence of the studied molybdenite paragenetically co-occurring with or pre-dating the stratiform copper mineralisation. In the author's opinion, Sillitoe *et al.* (2017) record a syn/late-orogenic period of Mo mineralisation in the Zambian Copperbelt which may be coincident with vein-type Cu/Cu-Co mineralisation events (e.g. Selley *et al*., 2005; Torrealday *et al.*, 2000).

Given the broad range of ages exhibited by the 'vein-type' Cu-Co mineralisation of Dewaele *et al.* (2006a) across the Copperbelt, it can be concluded that this mineralisation stage is associated with fluid movement during the Lufilian Orogeny and continued in multiple events over the entire span of the orogeny, from basin inversion through to post-orogenic relaxation.

2.1.3 Supergene Mineralisation

Most primary Cu-Co deposits of both stratiform and vein-type also exhibit secondary supergene alteration (Dewaele *et al.*, 2006a), which frequently results in enrichment to grades higher on average than those attained by primary mineralisation. To date, the majority of mines in the D.R.C. have preferentially exploited high-grade oxide zone

supergene mineralisation (Hitzman *et al.*, 2012). Despite this; there is a paucity of scientific literature which focusses on the supergene mineralisation stage, when compared to research on hypogene mineralisation.

The most common minerals encountered within supergene Cu-Co deposits are malachite, chrysocolla, heterogenite and chalcocite. Other secondary Cu-Co minerals include native copper, cuprite, tenorite, azurite, libethenite, pseudomalachite, kolwezite, spherocobaltite and cobaltoan carbonate (Master, 1991; Gauthier and Deliens, 1999). Supergene alteration and mineralisation is found in some Katangan deposits at depths of >1km (Hitzman *et al.*, 2012), due to a deep weathering profile but also because of permeable lithological conduits which allow the deep infiltration of supergene fluids into the subsurface, such as breccias and the R.S.C. unit (Fay and Barton, 2012). More commonly, economic deposits dominated by supergene mineralisation are found at <100m depth, and display a depth profile zonation typical of supergene deposits (Taylor, 2011). A surficial leached zone, where no appreciable quantities of Cu-Co minerals exist, overlies an oxide-enriched zone usually dominated by malachite in carbonate host rocks and chrysocolla in siliciclastic host rocks (Hitzman *et al.*, 2012). This, in turn, overlies a mixed/transition zone, where supergene oxide and sulphide minerals co-exist, and below this is found a sulphide-enriched zone dominated by a supergene 'chalcocite blanket'. Beneath the sulphide-enriched zone may be found the primary sulphide zone consisting of unaltered hypogene mineralisation. A conceptual illustration of this is given as Figure 2.9.

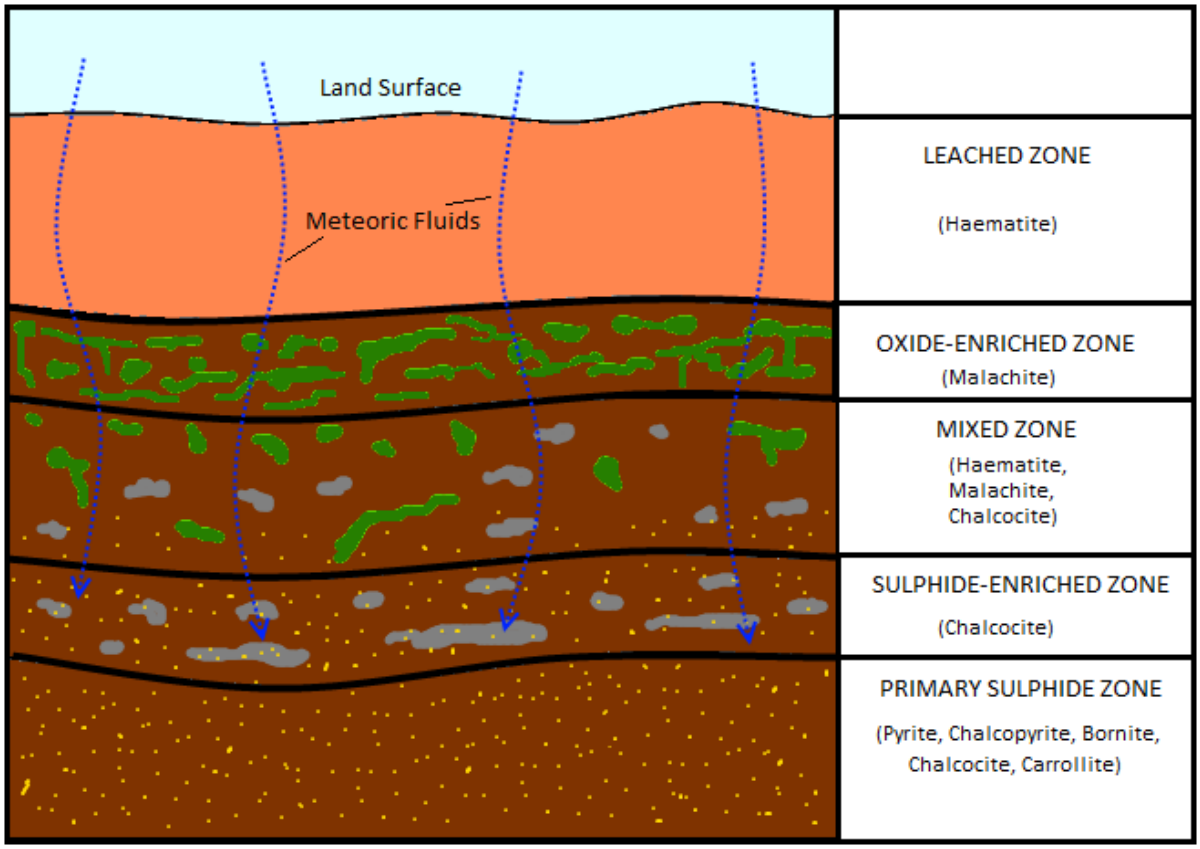

Figure 2.9: *Conceptual illustration of the generalised depth-profile-zonation of supergene alteration in Katanga, showing the various alteration zones together with their dominant ore mineralogy. The depth to the Primary Sulphide Zone, where meteoric fluids have ceased to percolate (or have lost their oxidising potential by the time they arrive) is typically anywhere between 100-200m.*

Copper and cobalt tend to decouple in the supergene environment and cobalt oxides are usually found closer to or at the surface, with copper oxide minerals found below these 'cobalt caps' (Decree *et al.*, 2010). Because of Zambia's tendency to have siliciclastic-hosted, rather than Congolese carbonate-hosted Cu-Co mineralisation, leached zones tend to be more pronounced in Zambia than in Congo, with correspondingly deeper supergene enrichment (Hitzman *et al.*, 2012). This is in part due to the buffering capability of carbonate rocks to neutralise acidic meteoric fluids. Like stratiform and 'vein-type' mineralisation, supergene mineralisation is most frequently hosted in the rocks of the R2 (Mines Subgroup), however an important sub-class of supergene deposits is found within the underlying R.A.T. (R1 Subgroup) (Dewaele *et al.*, 2006a).

The source of metals and sulphur for supergene mineralisation is the primary hypogene stratiform and 'vein-type' mineralisation. A clear progression exists up-section

from primary, unaltered sulphides, to the progressive in-situ replacement of primary sulphides, to complete dissolution of the primary sulphides, with later transport and reprecipitation of the metals as secondary oxides and sulphides. In other supergene copper deposits, progressive copper isotope fractionation (Seo *et al.*, 2007) from primary sulphides, to secondary sulphides/oxides, to residual oxides exists (Mirnejad *et al.*, 2010), unequivocally shows that supergene Cu mineralisation results from the progressive alteration and remobilisation of primary Cu mineralisation.

The primary metals are dissolved and transported by meteoric fluids; essentially rainwater at low temperature (<30°C) with low (acidic) pH, very low salinity, and highly oxygenated. Atmospheric CO_2 dissolves in rainwater to become dilute H_2CO_3, carbonic acid, which attacks Cu-Co sulphides on contact. Dissolution of these sulphides and particularly dissolution of pyrite (FeS_2) creates dilute sulphuric acid (H_2SO_4) which enhances the acidity of the meteoric fluid and gives it the capacity to cause further, powerful supergene alteration (Taylor, 2011). Figure 2.10 shows that primary Cu sulphides are stable only under reducing conditions, if the Eh is raised to the point where oxidising conditions are attained these minerals will dissolve to form Cu^{2+}. Acidic rainfall percolates downwards from the surface through the soil and rock under the influence of gravity. Supergene alteration in the Copperbelt is particularly pronounced because of the region's 'Humid Subtropical' – 'Subtropical Highland' climate classification (Peel *et al.*, 2007), ensuring high average rainfall and temperatures to contribute towards meteoric fluid supply and reaction rates respectively.

The depth and extent to which supergene mineralisation will occur is governed primarily by the permeability of the rock units through which meteoric fluids will be able to percolate. In coarse grained siliciclastic units, such as the R.A.T., supergene alteration may occur at greater depths than in the relatively fine-grained carbonates found in the Mines Subgroup.

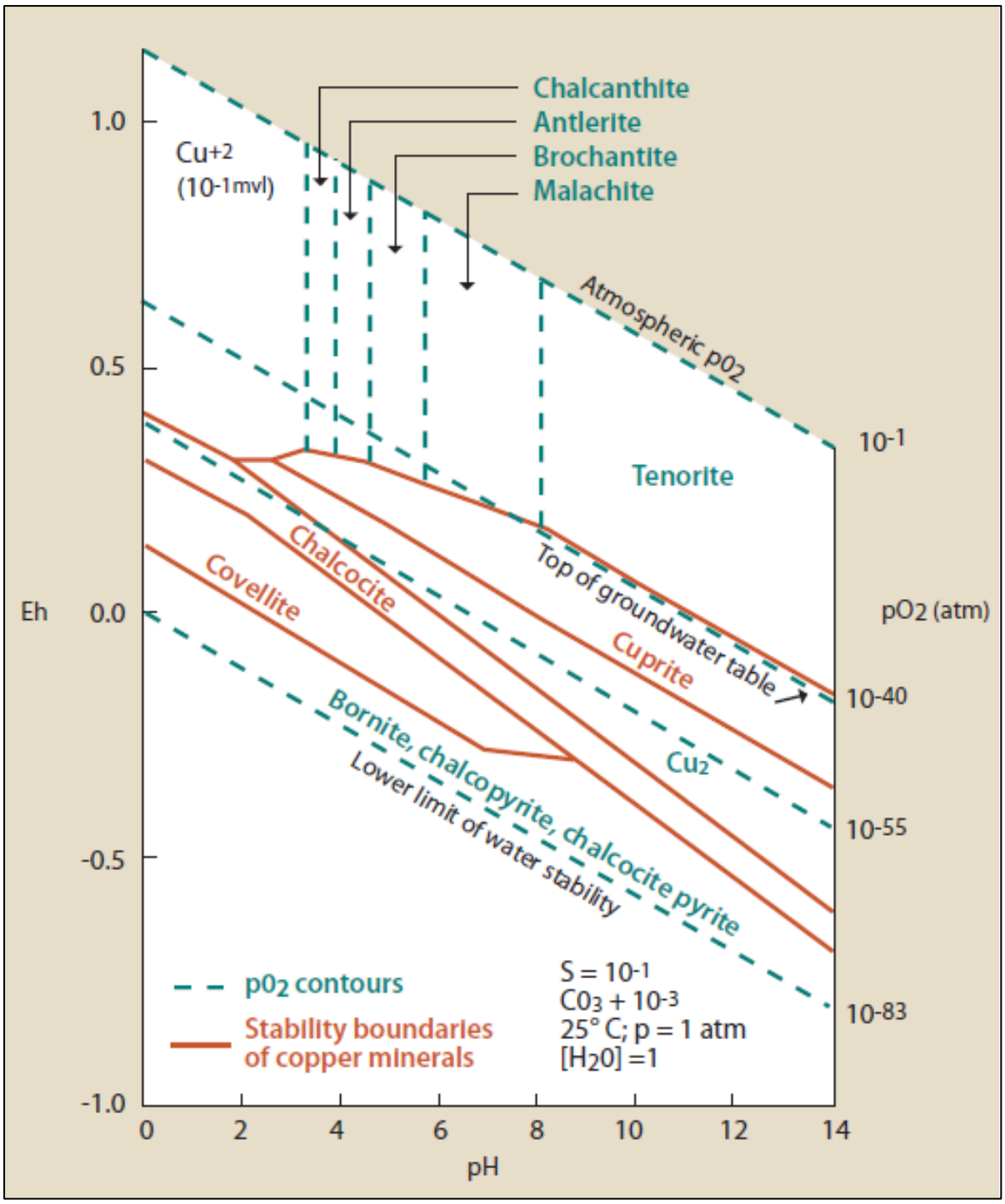

Figure 2.10: *Eh-pH diagram showing copper mineral stability at surface conditions and at low f(CO_2) (from Taylor, 2011; c.f. Anderson, 1982).*

The depth of supergene alteration is also restricted in carbonates by the ability of these rocks to buffer acidic solutions to a small degree, releasing CO_3^{2-} ions as they dissolve and thus bringing the percolating fluids closer to neutral. The best fluid conduits to allow the deep infiltration of meteoric fluids are the R.S.C. unit (Fay and Barton, 2012) and the

multitude of tectonic/halokinetic/olistrosome breccias (Dewaele *et al.*, 2006a) which are found in abundance throughout the region. Supergene mineralisation may be found within, and in proximity to, these units at >1km depth (Hitzman *et al.*, 2012). Within carbonate-dominated host rocks, the development of karstic features in the form of subsurface voids, fractures and caverns are important in the development of oxide-zone mineralisation, allowing meteoric fluids to pool, drain and recharge allowing them to gradually precipitate supergene oxides such as malachite (De Putter *et al.*, 2010).

The precipitation of supergene ore is governed by changes in Eh-pH as described in Figure 2.10. Oxide ore such as malachite and chrysocolla will begin to precipitate with a relatively moderate drop in oxidation potential and an increase in pH (towards neutral), perhaps initiated by prolonged contact with buffering carbonates in karstic voids (De Putter *et al.*, 2010). Precipitation of supergene sulphide ore requires, primarily, a significant drop in Eh, and this usually occurs at the top of the poorly-oxygenated water table. Therefore, the oxide-enriched ore zone tends to occur at the bottom of the vadose (unsaturated) zone while the sulphide-enriched ore zone will occur at the top of the phreatic (saturated) zone, with the mixed/transition ore zone occurring in between where there have been past-fluctuations in the water table (Taylor, 2011). It is important to note that the present-day water table may not correspond with the position of the palaeo-phreatic which prevailed when the supergene orebody was formed.

Co-occurrence of Cu and Co in the hypogene, primary environment is not as pronounced in the supergene environment. Cu and Co decouple from each other as a result of the greater solubility of the former within oxidising, acidic fluids (Katsikopoulos *et al.*, 2008), meaning that Co may be left behind as a residual phase in the near surface, or reprecipitated closer to the surface than copper as the fluid becomes less oxidising and less acidic. This results in the formation of 'cobalt caps' above deposits of supergene copper in Katanga (Decree *et al.* (2010) as illustrated in Figure 2.11). These 'cobalt caps' may produce a significant geochemical anomaly of Co in a soil sampling survey where no Cu anomaly, or a negligible Cu anomaly exists, making Co an important indicator element in the exploration for buried supergene Cu orebodies. Because residual cobalt oxides are less soluble than copper oxides at the surface, they have a higher tendency to be dispersed laterally through physical weathering rather than chemically leached towards depth. Co-oxides may thus be redistributed downriver of Cu-Co deposits, or may accumulate at the base of scree slopes

adjacent to 'inselbergs': topographic features of positive relief formed by the erosion-resistant Mines Subgroup (R2) blocks of Katanga (Decree *et al.*, 2010). Although Cu and Co will decouple in individual leaching events, variations in leaching regime over time mean that there is usually a 'mixed zone' where Cu and Co oxides (commonly malachite and heterogenite) will coexist, with Co-oxides usually precipitating earlier than Cu-oxides on account of the relatively low solubility of Co in supergene fluids (Katsikopoulos *et al.*, 2008).

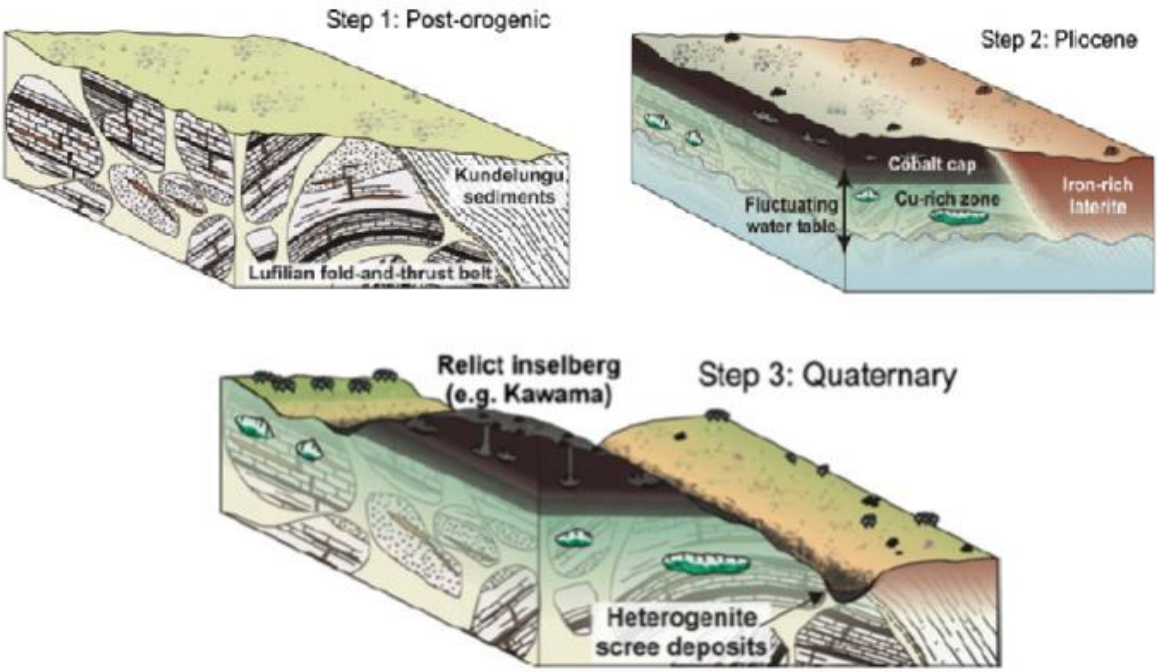

Figure 2.11: *Conceptual illustration of the process of Cu-Co decoupling in the supergene environment, to form 'cobalt caps' over supergene copper deposits. The lateral dispersal of residual cobalt through physical weathering is also illustrated. Modified from Decree et al. (2010).*

The lithologies in which supergene Cu-Co mineralisation may be found are mainly controlled by factors which govern the precipitation of primary hypogene Cu-Co, rather than by the process of supergene enrichment, which is climate controlled and affects the Copperbelt region fairly evenly (Peel *et al.*, 2007). Therefore, supergene mineralisation is most commonly found in the rocks of the Mines (R2) Subgroup, which hosts, volumetrically, the majority of the stratiform and vein-type mineralisation in the Katangan Copperbelt (Oosterbosch and Schuiling, 1951). However, an important sub-class of supergene Cu-Co

deposit exists within the R.A.T. (R1) Subgroup, which could be described as 'para-exotic' in nature. The term 'para-exotic' is used in this thesis to describe supergene deposits which occur some distance away from the hypogene deposits from which they sourced metals. Generally, in Katanga, they occur vertically below, rather than at great lateral distance, from the original position of hypogene mineralisation. These R.A.T. hosted para-exotic supergene deposits form by the same processes described above which usually cause supergene alteration in the Mines Subgroup. They occur where a Mines Subgroup fragment/block, formerly overlying the host R.A.T. unit, has been chemically leached of metals and physically eroded away, leaving the metals to reprecipitate within the R.A.T. at a depth of <50m. These deposits concentrate the entire metal budget of a Mines Subgroup block within a high grade, near surface orebody, and are economically desirable as a result. Mashitu North, adjacent to the Mashitu South study area, is an example of this type of mineralisation (Chimvinga, pers. comm., 2014).

Due to its 'humid subtropical' - 'subtropical highland' climate (Peel *et al.*, 2007), the whole of the Katanga Region is affected by surficial argillic alteration, with the development of 10m of clay, often kaolinite saprolite at the top of the rock profile being typical (Giresse, 2005; Timmermans, 2015). This saprolitic weathering may extend to a depth of 50m in some places, such as at the Safwe North Cu deposit adjacent to the Mashitu South study area (Chimvinga, pers. comm., 2014). Because of the near-surface nature of supergene Cu-Co, the host rocks to these deposits are often affected by chemical weathering. It is likely that H_2SO_4 contribution, made by the dissolution of primary sulphide Cu-Co mineralisation to the low pH, acidic environment required for argillic/advanced-argillic alteration, may enhance argillic alteration and saprolite development associated with supergene Cu-Co, as has been extensively documented in Andean porphyry copper deposits (Sillitoe, 1973). However, the proliferation of saprolite development across the region makes argillic alteration unusable as an indicator for supergene Cu-Co mineralisation. Pyrite (Fe_2S), the main sulphide contributor to H_2SO_4 production and argillic alteration in porphyry systems, is relatively less abundant in most DRC Cu-Co deposits (Hitzman *et al.*, 2012) and therefore the geochemical signature of argillic alteration in proximity to these deposits is correspondingly weaker. Supergene haematite formation also accompanies the development of supergene copper minerals, partially derived from the breakdown of Cu-Fe sulphides (e.g. Haest *et al.*, 2009a; Mirnejad *et al.*, 2010).

The timing of supergene alteration has long been known to have been geologically recent, and clearly postdates all other mineralisation types (e.g. Oosterbosch and Schuiling, 1951). Decree *et al.* (2010) dated supergene heterogenite in the Katangan Copperbelt to two periods of formation: the earlier in the Late Miocene, at or before 10.3 Ma, and the latter in the Pliocene (5.3–2.3 Ma). The first period of supergene ore formation is attributed to regional epeirogenic uplift initiated by the reactivation of the West African tectonic margin in the Miocene (Lavier *et al.*, 2001), increasing the rate of erosion of the sediments above the host rocks to primary Cu-Co and exposing them to meteoric fluids. The second period of supergene ore formation was initiated by a regional Early-Middle Pliocene transition to a more humid climate (Alexandre, 2002; Giresse, 2005; Miller *et al.*, 2010) which increased the supply of fluid and the rates of reaction for supergene alteration processes to occur. Since the formation of these two stages of supergene ore, and beginning in the Late Pliocene at around 2 Ma, more arid conditions have prevailed in Katanga (Gasse, 2006; Miller *et al.*, 2010). An important requirement for the formation of laterites and in-situ supergene metallic deposits is that the rate of chemical weathering outpaces that of physical weathering, ensuring that supergene ore is continuously leached deeper into the rock, rather than being eroded away at the surface, which is what occurs where physical weathering outpaces chemical weathering. Localised near-surface supergene redistribution of copper still occurs in Katanga at present (Figure 2.12). However, because of the prevailing 'humid subtropical' – 'subtropical highland' climate (Peel *et al.*, 2007); which is more arid than the Miocene-Pliocene palaeo-climate classification of tropical rainforest climate (Gasse, 2006; Miller *et al.*, 2010), the current rate of physical weathering outpaces the rate of chemical weathering and economic concentrations of ore minerals are not currently being formed in the region by chemical weathering processes.

As mentioned earlier, the oxide-enriched and sulphide-enriched supergene zones tend to occur either side of the water table from the time that they were formed. It should be noted that fluctuations of the water table, meteoric fluid supply and the temperature over time result in temporal and spatial overlaps in the formation of different supergene ore minerals, making a definitive paragenetic sequence for supergene Cu-Co difficult to assemble (De Putter *et al.*, 2010). This is further complicated by the two distinct periods of supergene alteration identified by Decree *et al.*, 2010. As a general rule, supergene sulphides precipitate before native copper and supergene oxides, which themselves

precipitate before supergene carbonates, hydroxides, silicates and other species, as the fluids from which they precipitate become more oxidising and more acidic (see Figure 2.10) (cf. Dejonghe and Ngoyi, 1995; Dewaele *et al.*, 2006a; El Desouky *et al.*, 2007; 2008a; 2010; Schmandt *et al.*, 2013; van Langendonck *et al.*, 2013).

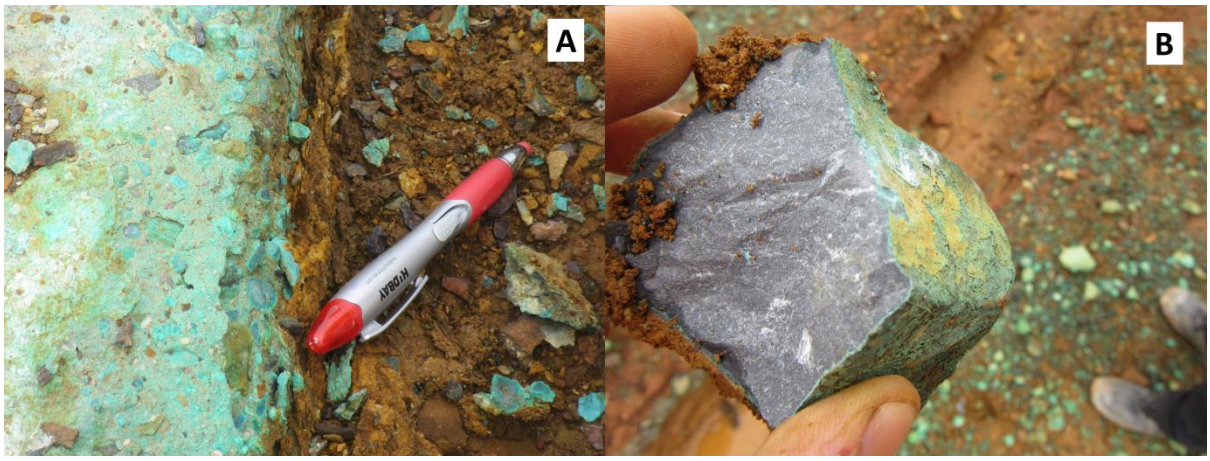

Figure 2.12: *Photographs of anthropogenic supergene copper minerals (some form of verdigris) near a tailings pond for the Kipushi Mine, Katanga, D.R.C.. **A**: anthropogenic construction cement with overgrowth of copper verdigris. Pen for scale. **B**: Cross-sectionally-split dolomite road cobble showing the surficial nature of the copper minerals. Thumb and finger-tips for scale.*

To summarise: Cu-Co mineralisation in the Katangan Copperbelt can be sub-classified into the three broad categories of stratiform, vein-type and supergene mineralisation, according to Dewaele *et al.* (2006a). The stratiform mineralisation stage can be considered the primary Cu-Co mineralising event for the Katangan Basin, while vein-type and supergene mineralisation are both essentially remobilisations and redistributions of metals from the stratiform stage (El Desouky *et al.*, 2010; van Wilderode *et al.*, 2014). These mineralisation types often co-exist and it is rare for a Cu-Co deposit not to contain expressions of all three stages in some form or another (Dewaele *et al.*, 2006a), though it does occur (for example, at Kamoa, where the vein-type stage is mostly lacking: Broughton and Rogers, 2010). Across the Katangan Copperbelt, the stratiform and supergene mineralisation stages are considered the more economically significant over the vein-type stage (Dewaele *et al.*, 2006a; Hitzman *et al.*, 2012).

2.2 Related Deposit Types

Cu-Co mineralisation such as that occurring in the study area at Mashitu South, is considered here to be the most relevant mineralisation type for an introduction to this thesis. However, there are several other types of mineralisation in the Copperbelt which may be considered related to sedimentary-hosted stratiform Cu-Co, either through metallogeny, timing, or processes of formation. This section will briefly describe these related deposit types and discuss their similarities and differences to Cu-Co mineralisation.

2.2.1 'Zambian-Type' Cu

'Zambian-type' Cu is similar in many ways to 'Congolese-type' stratiform Cu-Co, so much so that several Zambian-type deposits are described in the discussion of Congolese-type mineralisation genesis in Section 2.1. Generally, stratiform copper deposits further to the southeast of the Copperbelt exhibit features that are more 'Zambian' and deposits towards the northwest are more 'Congolese', hence the names. However, this is not an absolute rule and there is a continuum of similarities and differences between the two mineralisation types, which can be only broadly be categorised in this geographic manner (Hitzman *et al.,* 2012).

Zambian Cu deposits also exhibit the stratiform, vein-type and supergene distinctions displayed by Congolese Cu-Co, although vein-type deposits are more prevalent within Zambia than in the Congo (Dewaele *et al.*, 2006a). This is perhaps because the Zambian portion of the Katangan Basin reached higher grades of metamorphism during the Lufilian orogeny than in the Congo (Ramsay and Ridgway, 1977), resulting in more early/syn/post-orogenic remobilisation of metals.

Sillitoe *et al*. (2017), through Re-Os dating of molybdenite mineralisation across 15 different Zambian deposits, find no evidence of a syn-diagenetic mineralisation event and contend that all Zambian hypogene Cu-Co mineralisation was emplaced 'syn-orogenically' around ~540–490 Ma. This is, however, refuted in replies by Hitzman and Broughton (2017) and Muchez *et al*. (2017), who point out that the dated molybdenite does not show paragenetic evidence for contemporaneous formation with stratiform Cu-Co sulphide

assemblages at the studied deposits. Instead, it is suggested that the Re-Os ages acquired by Sillitoe *et al*. (2017) simply constrain a syn-orogenic molybdenum mineralisation event.

Supergene deposits in southern Zambia are less developed on account of the slightly more arid climate (Peel *et al.*, 2007). However, because the Zambian stratigraphy is more siliciclastic, with less carbonate host rocks to buffer acidic meteoric fluids, surficial leached caps are more pronounced and supergene alteration often occurs at greater depths in Northern Zambia than in the Congo (Hitzman *et al.*, 2012). Chrysocolla, rather than malachite, is usually dominant in Zambian supergene copper deposits due to the greater availability of silica to the system (Hitzman *et al.*, 2012).

This leads onto another difference between Zambian and Congolese type deposits: the stratigraphy. It is unclear whether Zambia represents an along-strike, shallower and more shoreward continuation of the stratigraphy in the Congo (e.g. Cailteux *et al.*, 1994), whether the Zambian Roan occupies a lower stratigraphic level than the Congolese Roan (Bull *et al.*, 2010; 2011), or whether the two sides formed in separate sub-basins (Selley *et al*., 2005; Hitzman, 2015b). What is known is that stratiform mineralisation in Zambia is primarily hosted in relatively shallow-water-facies siliciclastic sediments (the 'Copperbelt Orebody'), whereas in the Congo it is primarily hosted in deeper-water facies carbonate sediments (the 'Mines Subgroup') (Cailteux *et al.*, 1994).

The Zambian Roan also does not show the same kind of tectonic disruption that the Congolese Roan does, meaning that deposits tend to be more laterally extensive rather than being broken up into separate blocks as is the case in the Congo (Hitzman *et al.*, 2012).

Geochemically, the trace element associations of both Congolese and Zambian hypogene ores seem fairly similar as a result of them both being transported by oxidised, saline fluids (Cooke, 2003); McGoldrick *et al.* (2003) have identified an ore-association of Cu-Co-Ag-Bi-Mo-U-W-(local Au, Pt, Pd) ± Ni-V in several Zambian deposits and Selley *et al.* (2010b) have identified an ore association of Cu-As-Ni-V-Mo-Bi ± Pb-Zn-U-Co at the Kolwezi deposit in Congo. However, although Zambian deposits usually contain trace Co, fewer contain Co in economic quantities than in Congo, with the few that do mostly concentrated in the northwestern portion of Zambia close to the border with Congo (Hitzman *et al.*, 2012). The most likely explanation for the lack of Co in Zambia would be contrasting metal sources; perhaps some abundant source of cobalt in Congolese Copperbelt was not so prevalent in the Zambian Copperbelt. Additionally, potassic alteration in the Zambian

Copperbelt tends to be more pronounced and more closely associated with mineralisation than in the Congo (Large *et al.*, 2003).

Other than the differences in stratigraphy, structure and geochemistry noted above, Zambian-type Cu is very similar to Congolese-type Cu-Co in almost all genetic aspects (Hitzman *et al.*, 2012). Both Zambian and Congolese ores sourced metal primarily from the basement, were transported by oxidised, saline fluids pumped along faults and permeable lithologies, and were deposited in reducing-facies host rocks which also supplied sulphur, with a syn-diagenetic timing. Both deposit styles were affected by syn-orogenic 'vein-type' and Tertiary supergene remobilisation.

2.2.2 Domes Region Cu (± Co, Ni, Au, Mo, U)

The copper deposits of the 'Domes Region' of northwest Zambia are hosted primarily in metasedimentary rocks analogous to the Roan Group sequence in Zambia (Hitzman *et al.*, 2012), which directly overlie a domal, folded terrane of gneissose-schistose Palaeoproterozoic basement rocks. They are, again, part of the broader Katangan Cu-mineralising system together with Congolese and Zambian type deposits, with stratiform, folded chalcopyrite mineralisation at the Kansanshi deposit indicating that the Domes Region experienced the same kind of syn-diagenetic stratiform mineralisation as found in the rest of the Copperbelt (Broughton *et al.*, 2002). However, the vast majority of Cu mineralisation in the Domes Region occurs within late, cross-cutting veins and within shear zones (Hitzman *et al.*, 2012) indicating a similarity to the 'vein-type' mineralisation of the DRC as described by Dewaele *et al.* (2006a).

Although the sediments of the Domes Region are analogous to the Zambian Roan, they (and the underlying basement) are metamorphosed to between greenschist and upper-amphibolite-facies grades and locally contain metamorphic garnet-kyanite-biotite-phlogopite assemblages (Cosi *et al.*, 1992). Based on the metamorphic grade the Domes Region is considered to have been deep within the core of the Lufilian Orogeny (Ramsay and Ridgway, 1977). Kyanite-talc whiteschist assemblages, once thought to be eclogitic and representative of Lufilian subduction (John *et al.*, 2003), are now presumed to have been formed by high temperature, high salinity metasomatism (Hitzman *et al.*, 2012; Wood *et al.*, 2014; Halley *et al.*, 2016) which may or may not have accompanied mineralisation.

Mineralisation in the Domes Region is dominated by vein and shear-zone hosted chalcopyrite, with pyrite, pyrrhotite, molybdenite, uraninite, Ni-Co sulphides and native gold occasionally associated (Torrealday *et al.*, 2000; Broughton *et al.*, 2002). Quartz, dolomite, calcite, phlogopite, talc and kyanite are common gangue phases in vein-hosted mineralisation, which is variously haloed by Na, K, Mg and/or Fe alteration in the schistose host rock (Torrealday *et al.*, 2000). A geochemical association of Cu (± Co, Ni, Au, Mo, U) is described for the regional mineralisation (Halley *et al.*, 2016). At the Enterprise deposit, Ni is hosted in economic quantities in a variety of nickel sulphides (Capistrant *et al.*, 2015) and the Kansanshi deposit contains 0.17g/t Au together with 1.25% Cu (Hitzman *et al.*, 2012).

The vein and shear-zone hosted nature of Domes Region mineralisation, association with Au and the occurrence within amphibolite-facies metamorphic rocks draws distinct parallels with vein-type, syn-orogenic mineralisation found in Congolese and Zambian type deposits. This is corroborated by mineralisation ages of 549 ± 8 Ma at the Sentinel deposit (Steven and Armstrong, 2003), 541 ± 2 Ma at the Enterprise deposit (Capistrant *et al.*, 2015) and a cluster of ages between ~ 539 and 497 Ma for deposits around the Mwombhezi Dome (notably Lumwana) (Sillitoe *et al.*, 2015). All these ages are coincident with the ~550-500 Ma progression of the Lufilian Orogeny (peak metamorphism between ~540-535 Ma according to Kroner and Stern (2005)) and suggest a protracted early-syn-late orogenic origin for Domes Region Cu. However, a small portion of the mineralisation pre-dates folding, recorded by folded, stratiform chalcopyrite (Broughton *et al.*, 2002) and peak metamorphism, evident by chalcopyrite inclusions within metamorphic kyanite porphyroblasts (Hitzman *et al.*, 2012). It is possible that the majority of the Domes Region mineralisation is analogous to 'vein-type' remobilisation of earlier stratiform mineralisation, as seen in the Congo (Dewaele *et al.*, 2006a; El Desouky *et al.*, 2010; van Wilderode *et al.*, 2014).

It is from the Domes Region that we find direct evidence for a pre-Katangan stage of mineralisation in the Palaeoproterozoic basement, in the form of basement-hosted molybdenite dated at 1084 to 1059 ± 5 Ma by Sillitoe *et al.* (2015), an age coincident with the earlier Irumide Orogeny. This corroborates speculation by such authors as Wakefield, (1978) and Dejonghe and Ngoyi (1995) that the metallogenic fertility of the Copperbelt could be due to pre-Katangan mineralising events which enriched the underlying basement.

2.2.3 Zn-Pb-Cu Deposits

Considering the oxidising, saline fluids responsible for much of the metallogenesis within the Copperbelt, one might expect sedimentary-exhalative (SedEx) or carbonate-hosted lead-zinc deposits to occur alongside the abundance of sedimentary-hosted stratiform copper, but these deposit types are strangely lacking from the Copperbelt (Cooke, 2003). There are, however, a number of stratabound Zn-Pb-Cu (± Cd, Co, Ge, Ag, Re, As, Mo, Ga, V) deposits, including Kengere, Lombe, Bob Zinc, Lukusashi, Millberg, Mufukushi, Sebembere, Broken Hill and Star Zinc, and the larger deposits of Kipushi (which is more structurally controlled) and Kabwe (Kampunzu *et al.*, 2009).

These deposits are primarily stratabound, fault and/or breccia related, have a strong structural control and mineralisation is expressed as metal sulphides including sphalerite, chalcopyrite, pyrite, bornite, and chalcocite, sometimes with minor galena, arsenopyrite, tennantite, and the unusual copper-zinc-arsenic-germanium-iron sulphide renierite at Kipushi (Intiomale and Oosterbosch, 1974; Kampunzu *et al.*, 2009). These deposits are typically hosted in higher lithologies than the Roan Group, which hosts the majority of other mineralisation types in the region. The Kipushi deposit is hosted in dolomites and carbonaceous shales of the Nguba Group adjacent to a major reverse fault along which megabreccia is found (De Magnee and François, 1988). According to De Magnee and François (1988), the generation of the megabreccia and the associated pipe-like sulphide orebody is directly related to the development, upwards migration and dissolution of a salt diapir along the fault. Oxidising, metal-bearing fluids migrated along this structural conduit, encountering H_2S derived from thermochemical reduction of sulphate found in the adjacent host rocks and precipitating sulphides as the Eh of the fluids was lowered (Heijlen *et al.*, 2008). Most other Zn-Cu-Pb deposits in the Copperbelt exhibit similar genetic features to Kipushi, sharing a similar mineralogy, being structurally controlled and having an association with faults and megabreccia (Kampunzu *et al.*, 2009). However, a number of genetic interpretations for these deposits other than diapiric-related have been proposed: magmatic-hydrothermal (e.g. Taylor, 1954), basin dewatering (Kortman, 1972), metamorphic dewatering (Unrug, 1988) and pre-orogenic karstification-related mineralisation (Chabu, 1990), including a reinterpretation of the Kipushi deposit as

developed along a syn-depositional carbonate reef edifice rather than along a fault or diapir structure (Turner *et al.*, 2018).

The two largest deposits which have been dated, Kabwe (~680Ma) and Kipushi (~450Ma) indicate ages coincident with very early basin inversion and post-orogenic processes (orogenic relaxation) respectively (Kampunzu *et al.*, 2009). Other than Kipushi and Kabwe, Zn-Pb-Cu deposits in the Copperbelt tend to be fairly small and are not widely exploited.

2.2.4 Cu-Ag (± Zn, Pb, As) deposits in the Lufilian Foreland

So far this chapter has focussed on mineralisation styles existing in 'Zone 4 – The External Fold-and-Thrust Belt' (and 'Zone 3 – the Domes Region) of the Lufilian tectonic domains described by Kampunzu and Cailteux (1999). However, a number of copper deposits exist within the 'Lufilian Foreland', the most distal tectonic domain to the Lufilian Orogeny, situated towards the northeast of what is traditionally considered the Copperbelt in the D.R.C. (see Figure 1.7). The Dikulushi, Mwitapile and Kinkumbe deposits are all examples of typical 'Lufilian Foreland style' mineralisation.

The Dikulushi deposit is hosted within various lithologies of the Kalule and Kiubo Subgroups of the Kundelungu Group (Lepersonne, 1974), deformed into a series of anticlines and locally brecciated. There are two main stages of mineralisation (Dewaele *et al.*, 2006b). The first is a polymicitic-breccia-hosted Zn–Pb–Fe–Cu–As assemblage of arsenopyrite, tetrahedrite, pyrite, chalcopyrite, sphalerite, chalcocite, digenite, bornite and galena with gangue dolomite. This stage is formed from a high salinity, (20-25 wt.% CaCl2 equiv.) moderate temperature (90-140°C) fluid. Because of its association with breccia and relation to Lufilian-age folding it is classified as syn-orogenic (~520 Ma) in timing (Haest *et al.*, 2009b). The second mineralisation stage is hosted in a series of thin quartz-calcite-chalcedony-dolomite-barite veins which can be seen to cross-cut the first breccia-hosted mineralisation stage. These veins are associated with a massive chalcocite and minor haematite assemblage which makes up the orebody at Dikulushi. The chalcocite from this stage contains, on average, 2500ppm Ag and is responsible for the considerable silver content of the ore (Dewale *et al.*, 2006b). According to Haest *et al.* (2009b) the second mineralisation stage was formed by a low temperature (~65°C) saline (≥ 19 wt.% NaCl

equiv.) fluid, which mixed with a low salinity fluid (≤ 3 wt.% NaCl equiv.) and precipitated ore as late as ~100 Ma.

The Mwitapile and Kinkumbe deposits are both sandstone-hosted sulphide deposits found in the Kundelungu and Nguba Groups respectively, containing hypogene ore-stage pyrite, chalcopyrite, bornite and chalcocite in stratiform-disseminated, occasionally nodular or banded form (El Desouky *et al.*, 2007; El Desouky *et al.*, 2008a; 2008b). Like the Dikulushi deposit, they both occur in proximity to domal anticlines (El Desouky *et al.*, 2008b). The mineralising fluids were of varying temperatures (120 to 280 °C) and salinities (2.4 to 19.8 wt.% NaCl equiv.), with El Desouky *et al.* (2008b) suggesting that ore precipitation occurred when higher temperature, more saline fluids carrying Cu and Ag mixed with lower temperature, less saline fluids. Sandstone permeability, as a function of feldspar dissolution and porosity, is an important control on the grade of ore (El Desouky *et al.*, 2008a). Based on the relationship of mineralisation to stratigraphy and faulting, El Desouky *et al.* (2008a; 2008b) infer a post-orogenic, <512 Ma timing for hypogene mineralisation at these deposits.

Supergene alteration often occurred to hypogene ore, like almost all mineralisation types in the Congo, on account of the region's 'humid subtropical' to 'subtropical highland' climate (Peel *et al.*, 2007). Abundant supergene sulphide mineralisation occurs within Lufilian Foreland deposits in the form of digenite and covellite, but native copper, cuprite, azurite, malachite, chrysocolla and haematite are also common alteration products (El Desouky *et al.*, 2007; 2008a; 2008b).

Although there are notable differences in mineralisation between copper deposits in the Lufilian foreland, they all share a post-orogenic timing, with the exception of the first syn-orogenic, breccia-hosted mineralisation stage at Dikulushi. They have a Cu-Ag geochemical signature, are precipitated when a moderate temperature, saline fluid mixes with a low temperature, low salinity fluid and are hosted primarily in sandstones of the Nguba and Kundelungu groups in proximity to domal anticlines.

2.2.5 Copperbelt Uranium Deposits

The Congolese Copperbelt, Zambian Copperbelt and the Domes Region are host to a number of uranium deposits and uranium is a common geochemical associate of copper mineralisation throughout the Central African Copperbelt (Meneghel, 1981; Unrug 1988;

Torrealday *et al.*, 2000; McGoldrick *et al.*, 2003; Selley *et al.*, 2010b; Decree *et al* 2011; 2014; Turlin *et al.,* 2015). The most famous example of Copperbelt U mineralisation would probably be the Shinkolobwe deposit, the source of uranium for the World War 2 Manhattan Project. The genesis of Congolese Copperbelt U deposits will be discussed briefly here.

Uranium, like copper, is highly mobile in oxidising, saline fluids resulting in its common mode of occurrence in roll-front type deposits (Brown, 2014). Uranium present in the basement to the Katangan Supergroup (Cailteux *et al.*, 1994, van Wilderode *et al.*, 2014) was mobilised by the same fluids which transported copper, precipitating as U-oxides such as uraninite upon reduction of the fluids by a lithological or chemical redox front. This leads to a close correspondence in the distribution of uranium and copper-cobalt ores (Loris *et al.*, 2003) and uranium mineralisation, along with stratiform Cu-Co, has long been assumed to have begun at an early diagenetic stage (Cailteux *et al.*, 1983). U minerals are often found within Cu-Co deposits and vice-versa. Decree *et al.* (2014) find evidence for this early diagenetic uranium mineralisation with U-Pb ages of ~876 Ma and ~823 Ma from two Shinkolobwe uraninite samples. However, it is clear that uranium, like copper, was also remobilised by later hydrothermal events: Decree *et al.* (2011) and Decree *et al.* (2014) also find evidence for uranium concentration in the periods between ~720 to ~670 Ma and another stage at ~530 Ma, based on uraninite samples from the Shinkolobwe, Kambove, Luishia, Swambo, Kalongwe, Kamoto, Kolwezi, Luiswishi, Musoshi and Nkana deposits. Hypogene uranium therefore seems to have formed in three stages. The first stage (~876 Ma to ~823 Ma) is syn-diagenetic, together with stratiform Cu-Co. The second stage (~720 to ~670 Ma) is contemporaneous with late Nguba proto-oceanic rifting and Decree *et al.* (2014) relate its formation either to remobilisation from fluid circulation initiated by rift-magmatism and an enhanced geotherm, or to very early orogenic faulting and fluid migration. The third stage of hypogene uranium (~530 Ma), which encompasses vein-hosted U concentrations such as those at Lumwana and Kansanshi, appears to have been mobilised by syn-orogenic fluids (Decree *et al.*, 2014). Eglinger *et al.* (2013), Eglinger *et al.* (2014a; 2014b) and Turlin *et al.* (2015) also date uranium mineralisation episodes in the Domes Region to a period of between ~550-500 Ma.

Supergene remobilisation of uranium is common, with a plethora of secondary uranium minerals present both in U deposits and Cu-Co deposits, including β-uranophane,

carnotite, becquerelite, studtite, curite, schoepite and oursinite. Like secondary Cu-Co minerals, they form in the uppermost, surficial portions of hypogene U deposits, and due to a very high mobility in supergene fluids they also have a propensity to occur at depth within the R.S.C. unit or within other permeable fluid conduits (Loris *et al.*, 2003). The timing for mineralisation is likely to be similar for that of supergene Cu-Co, dated by Decree *et al.* (2010) to two periods: in the Late Miocene, at or before 10.3 Ma, and in the Pliocene (5.3–2.3 Ma).

2.3 Synthesis

Mineralisation in and around the Central African Copperbelt is complex, multistage, and polymetallic with economic concentrations of Cu, Co, Ni, Zn, Pb, Ag, Au, Ge and U together with sub-economic As, V, Mo, Bi, Ga, Pt, Pd and Re variously developed at different deposits. Sub-classifications of mineralisation can be made, including Congolese-type Cu-Co, Zambian-type Cu, Domes Region Cu, Kipushi-type Zn-Cu-Pb, Lufilian Foreland Cu-Ag, and Copperbelt uranium. A pre-mineralised, metallogenically-fertile basement (Sillitoe *et al.,* 2015) as well as voluminous redbeds at the base of the stratigraphic sequence (Cailteux *et al*., 1994) are likely to have contributed a rich metal endowment to hydrothermal deposits hosted within sediments of the upper Katangan Supergroup. The first mineralisation event was syn-diagenetic, with metals transported by oxidising, moderate salinity, low temperature fluids, and ore subsequently precipitated along or above redox boundaries. Remobilisations of these metals occurred via syn-rifting, early-orogenic, syn-orogenic, post-orogenic and supergene fluid events, with many metal deposits containing ore which has been redistributed by more than one of these mineralisation stages. Almost 900 Ma of ore-forming processes have contributed to the modern distribution of ore.

This Chapter, which reviews the available literature on mineralisation in the Copperbelt, forms a background to the original work carried out as part of this thesis on the Mashitu South deposit, placing it within a context of well-described and well-studied deposits as well as existing metallogenic models that have been put forward for mineralisation in the region.

CHAPTER 3: FIELDWORK AND LOGGING AT THE MASHITU COMPLEX

As part of the effort to understand hypogene and supergene mineralisation at the Mashitu South study area, several visits were made to the Copperbelt Region between May-June 2014, August 2014, November-December 2014 and May 2015. Field excursions were made to the nearby deposits of Mashitu North, Mashitu Principal, Safwe North, Pungulume Principal, Anticline, Kalukundi, Kii and Kinshasa. Visits to deposits further away included the Kakanda Group, Kabolela, Mukondo, Kipushi and Frontier. Detailed core logging within the Mashitu Complex and the Pungulume Group was completed, during which a core sampling program was also conducted. This study details the observations and interpretations made during these visits to the D.R.C. between 2014 and 2015.

3.1 Introduction to Mashitu South

Before observations are given, this section will first present and discuss previous work conducted on the Mashitu South deposit.

3.1.1 Geography

The Mashitu South Deposit forms part of the Mashitu Complex (Figure 3.1), a cluster of deposits which comprises the Mashitu North, Mashitu Principal, Mashitu South, Mashitu Northeast, Mashitu East, Safwe North and Safwe South deposits (Figure 3.2). The cluster is situated roughly 40km ENE of the town of Kolwezi in the Katanga Region of D.R.C., just to the east of Lac (Lake) Nzilo (Figure 3.1). It is accessed at the junction of the N39 road to the South of the village of Kisamfu (Figure 3.2). Mashitu South falls under the 'Camrose Concession' (Appendix 1) currently owned by Comide S.P.R.L., a subsidiary company of Eurasian Resources Group (E.R.G.). The Camrose Concession forms the wider study area for which soil geochemical modelling has been conducted (See Chapter 6). It is to the south-west and adjacent to the Africo permit, currently owned by Africo Resources Ltd.

Figure 3.1: *Regional map showing the location of the Mashitu Complex. Imagery from Google Maps: ©2016 CNES/Astrium, Map data ©2016 Google.*

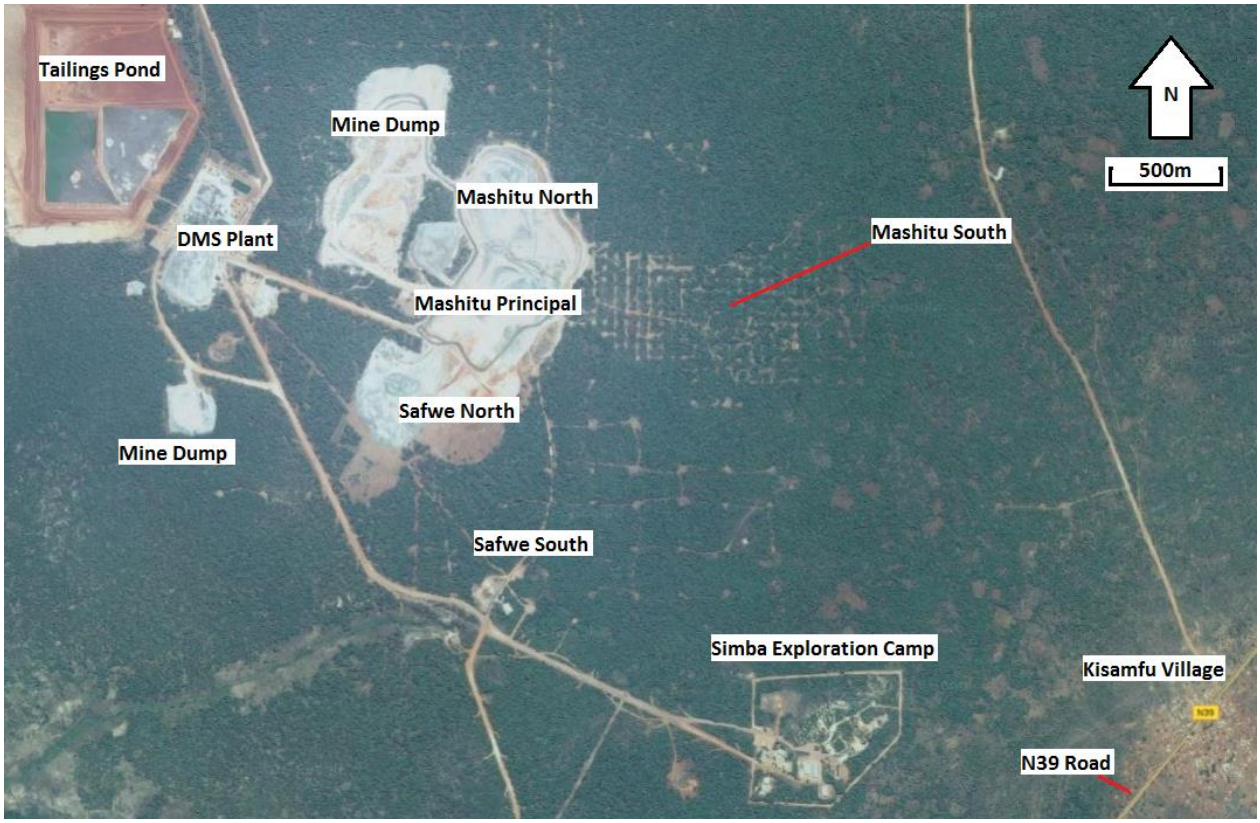

Figure 3.2: *Map showing the location of Mashitu South within the Mashitu Complex and in the context of local infrastructure. ©2016 CNES/Astrium, Map data ©2016 Google.*

The Mashitu South deposit is currently a prospect, identified by Gécamines-era pit-sampling-based mapping (Chimvinga, pers. comm., 2014). It lies on relatively flat terrain with relatively little topographical expression and is covered, like most of the region, by thick tropical-savanna bush. Unlike the adjacent deposits of Mashitu Principal, Mashitu North, and Safwe North it has not yet been mined and as a result there is no surface exposure of rock, the deposit being covered by a thick saprolitic regolith. Because of this, field visits focussed primarily on the adjacent deposits in the Mashitu Group which, through open pit mining, are much better exposed. These deposits made useful analogues to unexposed mineralisation at Mashitu South. The geology of the Mashitu South deposits is known mostly through an extensive drilling program of Diamond and Reverse Circulation (RC) drilling conducted by Comide S.P.R.L. between 2005-2012.

3.1.2 Regional Geology

The Mashitu Complex is a cluster of 'megaclasts' of the R2 'Mines Subgroup' stratigraphic unit situated in a roughly triangular shaped 'matrix' of 'undifferentiated Roan Group rocks' according to a regional pit-sampling-based mapping study conducted by the Gécamines mining company and François (1973). Other 'megaclasts' exist within this 'matrix' including Anticline, Kalukundi, Kii, Kinshasa, Kesho, Golf, C5 Ouest and Nzilo. According to Hitzman (pers. comm., 2015) the undifferentiated Roan Group and the Mines Subgroup fragments which lie in it are part of a 'Kalukundi Diapir' structure and the fragments have been disaggregated by halokinetic processes, from an originally stratigraphically continuous orientation, in pre-Lufilian times. However, it should be noted that, due to poor exposure, the nature of the 'undifferentiated Roan' which 'surrounds' fragments of Mines Subgroup is not well constrained, mapping having been conducted by the identification of rocks in shallow pits by Gécamines workers in the 1960s-1970s. Due to finds of the R.A.T. and R.G.S. stratigraphic units around the peripheries of deposits, much of the enigmatic 'undifferentiated Roan' is assumed to be brecciated R.A.T. and R.G.S. (Chimvinga, pers. comm., 2014). Regionally, the Roan Group exists as erratically distributed inliers to the surrounding, younger Nguba and Kundelungu Groups, which are relatively intact, stratigraphically speaking, exhibiting gentle folding with wavelengths generally ranging from 3-10km. A regional geological map of the Camrose Concession is presented as Figure 3.3.

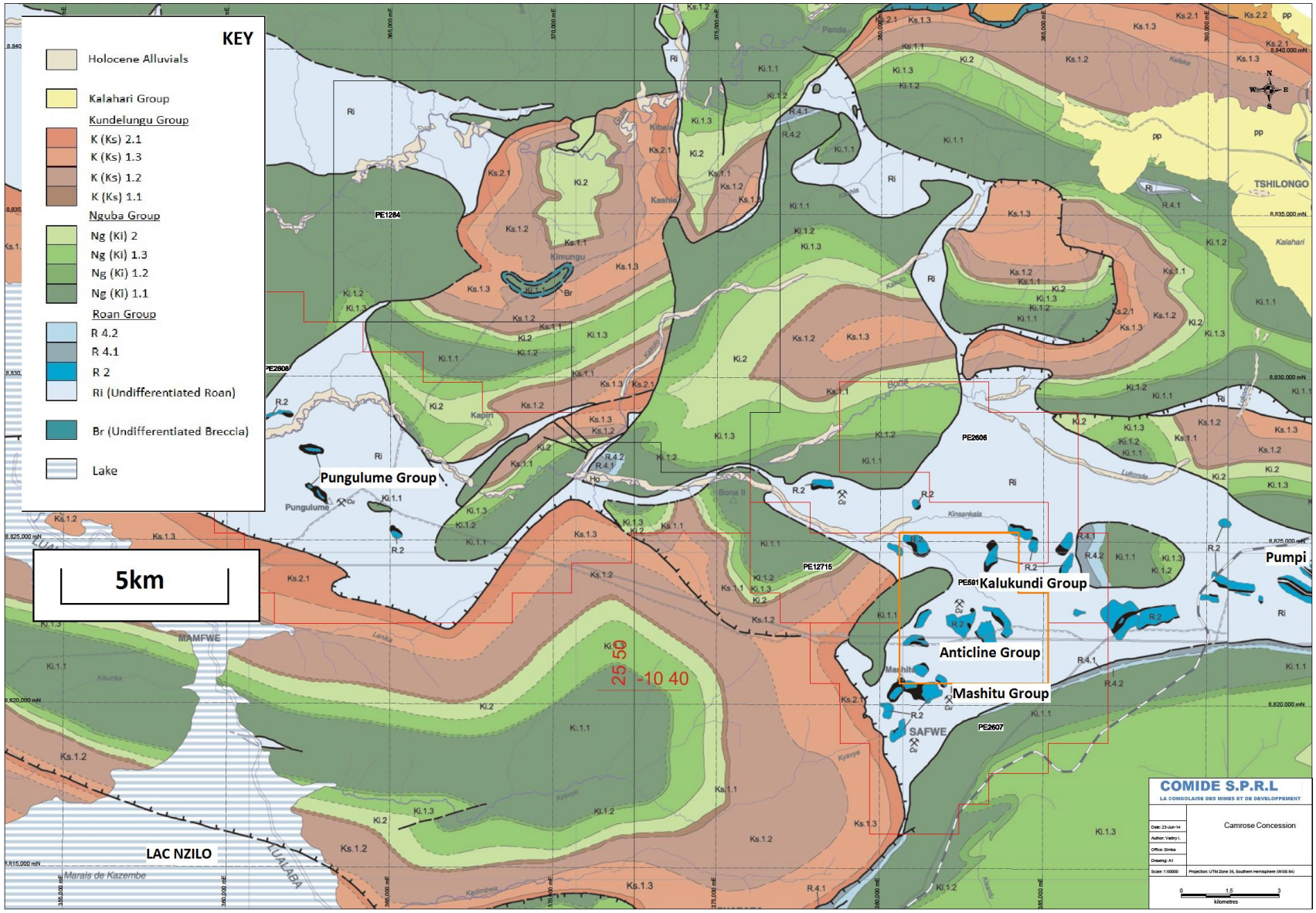

Figure 3.3: *Regional Geology Map of the Camrose Concession. Map supplied by Comide S.P.R.L. after François (1973).*

3.1.3 Structure of the Mashitu Complex

Due to a lack of orientated drill-holes and no surface exposure (Chimvinga, pers. comm., 2014), no detailed structural study of the Mashitu South deposit yet exists. The adjacent Mashitu North and Principal deposits, however, having been mined via open-pit methods, are well exposed and are the subject of several fieldwork studies, e.g. Cheshire, (2014); mapping by P. Cheshire (2014); an MSc thesis by Byrne (2017), as well as mapping conducted by Comide S.P.R.L.. A geological map of the Mashitu Complex is given as Figure 3.4.

The surface geology of the Mashitu Complex is dominated by two 'fragments' of Mines Subgroup, which make up the deposits of Mashitu South and Mashitu Principal. The two fragments are separated by breccia, which also surrounds the Mashitu North fragment. Mashitu South does not appear to be surrounded by breccia in the same way but this could be due to the lack of exposure and less drilling coverage at the peripheries. Beyond this the deposits are surrounded by the R.A.T. unit, making them either structural outliers, or 'megaclasts' in the wider 'Mashitu Diapir' structure (Hitzman, 2015, pers. comm.; Byrne, 2017).

Both Mashitu South and North exhibit local and deposit-scale folding. However, there does not appear to be any structural fabric within the constituent rocks that is associated with this folding event. On a deposit scale, the Mashitu South fragment exhibits two perpendicular anticlines, the first axial trace of which strikes roughly ESE-WNW and the second strikes NNE-SSW, creating a domal structure. The ESE-WNW anticline, together with the stratigraphy, appears to plunge towards the east, given the asymmetrical outcrop either side of the NNE-SSW anticline. The Mashitu Principal fragment, by contrast, exhibits two perpendicular synclines striking NE-SW and NW-SE, turning it into a basinal structure. The two fragments are separated by a breccia, but the stratigraphy can be traced across this breccia.

Mashitu North is a supergene R.A.T. hosted deposit which is believed to have been overlain by a fragment of Mines Subgroup, since leached of metals and eroded (Chimvinga, pers. comm., 2014). Safwe North is another supergene deposit provisionally mapped as occurring within the C.M.N. unit but the deeply weathered nature of the stratigraphy makes its provenance uncertain (Robertson, pers. comm., 2014).

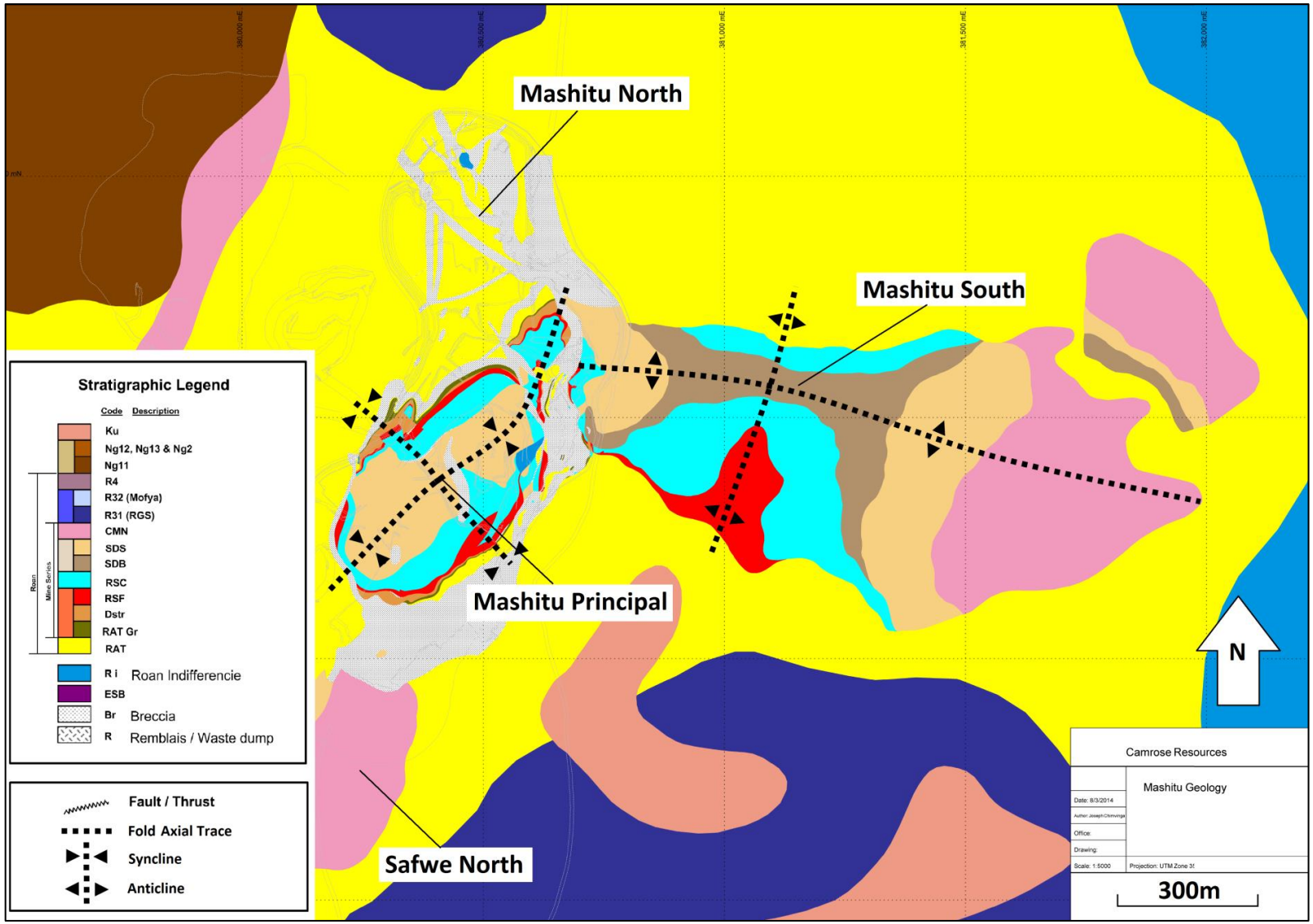

Figure 3.4: *Local geology of the Mashitu Complex. Map supplied by Comide S.P.R.L. and based on work by P. Cheshire (2014). Structural interpretations of fold axes creating a dome-and-basin architecture are modifications made by the author. See Appendix 2 for a descriptive summary of the stratigraphy.*

As well as the surface geology, a more complicated structure of the Mashitu Complex is apparent at depth. An apparent repetition of the stratigraphy underneath the eastern margin of the Mashitu South deposit, combined with local brecciation, suggests that the 'surface block' is faulted or otherwise juxtaposed over another underlying block of Mines Subgroup (See Figure 3.5). This repetition may also occur under the adjacent Mashitu Principal deposit, under which are enigmatic rocks of uncertain provenance which may even be part of the Dipeta (R3) Subgroup, though this interpretation is uncertain (Robertson, pers. comm., 2014). The R.A.T. (R1) unit is found beneath the upper and lower Mines Subgroup Blocks in different locations, but Comide (S.P.R.L.) drilling usually stops a few metres into the R.A.T. and so far no lithology has been discovered which lies stratigraphically below this unit.

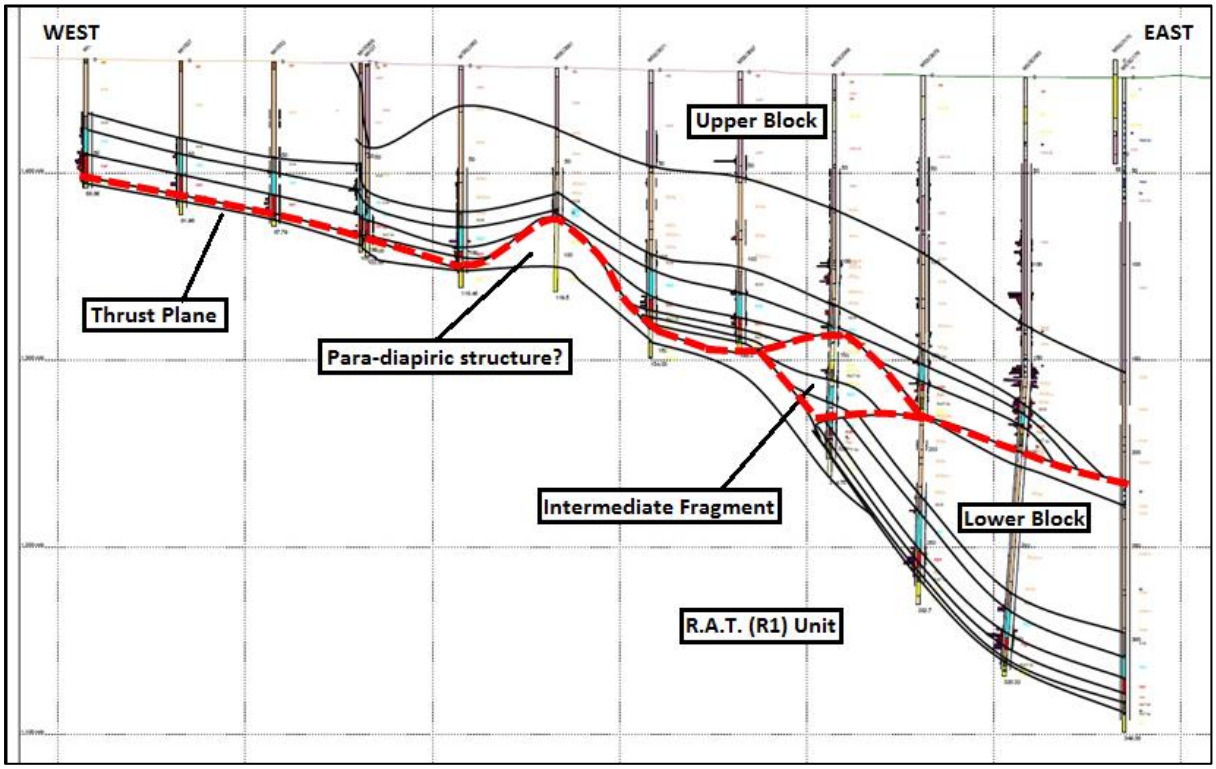

Figure 3.5: *East-west cross section through the eastern margin of the Mashitu South Deposit, showing an Upper Block of Mines Subgroup juxtaposed over a Lower Block of Mines Subgroup, along what appears to be a thrust-fault plane of dislocation. A breccia of irregular thickness, found along this plane of dislocation, may be related to rheid flow processes caused by evaporite mobilisation along the fault plane, with local diapirism occurring where evaporites became concentrated enough. The stratigraphic boundaries (black lines), position of the fault and 'para-diapiric structure' have been interpreted during the present study, while the cross section has been supplied by Comide.*

3.1.3.1 Brecciation at Mashitu North and the other deposits of the Complex

Mashitu North is a 'para-exotic' supergene Cu-Co deposit (deposited beneath hypogene mineralisation) hosted in the R.A.T. (R1) Subgroup (Figure 1.4). Copper and cobalt are thought to have been leached from an overlying fragment of Mines Subgroup (R2), which has since been eroded away, apart from a small inlier of lower R2 that was mined out early in the development of the Mashitu North open pit (Chimvinga, pers. comm., 2014). The pit offers a deep cross section through the R1 stratigraphy, which is seemingly broken up by a series of cross-cutting breccias.

Cheshire (2014) categorises these breccias into two groups.

- 'Protocataclasite-Breccias': "Fractured and clast supported brecciated rock with angular to subangular monomict medium to large (decimetre) fragments derived from local sidewall lithologies. Limited fragment rotation and displacement, occasionally bedding can be traced across adjacent fragments."
- 'Cataclasite-Breccias': "Matrix supported breccia rock, rounded, subrounded to subangular polymict or monomict generally pebble sized fragments. Fine grain zones also present grading to ultracataclasite-breccias".

The brecciation is extremely heterogeneous, with many generations of breccia apparent but difficult to discern from one another. Cheshire (2014) considers the cataclasite breccias to be sites either of tectonic or rheid dislocation between two blocks of contiguous R.A.T., or to be injection sites where a fluidised, brecciated mass of rock has squeezed between two blocks of R.A.T. The protocataclasite breccias are then considered to be 'damage zones' surrounding these dislocation sites where shear stress and hydraulic pressure have caused fracturing of the rock and infiltration of vein-forming fluids with little, if any, displacement. Although they are best exposed in Mashitu North, these breccias can also be found cutting the stratigraphy of the Mines Subgroup fragments at Mashitu Principal and Mashitu South where they can occur as cross-cutting planar/tabular, pipe-like or totally irregular bodies.

These observations are broadly in line with those of Cailteux *et al*. (2018) who describe similar features from Luiswishi, pointing to them as evidence of fluidisation brecciation during compression tectonics (rather than diapiric breccias generated during halokinetic extension tectonics).

3.1.4 Stratigraphy of Mashitu South

Comide (S.P.R.L.) logging has identified the Mashitu South Fragment as a typical block of Mines Subgroup stratigraphy. The Kambove, Dolomitic Shales and Kamoto Formations are present, with the C.M.N., S.D.S., S.D.B., R.S.C., R.S.F., and D.Strat units (see Figure 1.4) being the terminology used by Comide. Notably, the Dolomitic Shales Formation (the S.D.) is divided by Comide workers into the S.D.1a, 1b, 2a, 2b, 2c, 2d, 3a and 3b according to the Gecamines terminology. A stratigraphic column displaying the terminology used by Comide is presented as Appendix 2. These units are underlain stratigraphically by the R.A.T. (R1) Subgroup, which is divided by Comide logging into the R.A.T. Gris and the R.A.T. Rouge, the former only being a few metres thick and the latter of unknown (but probably great) thickness. The highest stratigraphic unit identified at Mashitu South is the C.M.N. (Calcaire et Mineraux Noire). All units at Mashitu South show marked similarity in many respects to Mines Subgroup stratigraphy across the Congolese Copperbelt and have been correlated as such.

3.1.5 Mineralisation, Metasomatism and Mineralogy at Mashitu South

The Mashitu South deposit has an inferred resource of 4.7Mt of ore running at 1.7% Cu and 0.2% Co. The adjoining Mashitu Principal and Safwe North deposits contain a combined resource of 16.6Mt ore at 2.1% Cu and 0.2% Co (Yeldar, 2012).

Mashitu South is known to be a combined hypogene-supergene orebody, also incorporating the transition zone between hypogene and supergene mineralisation. This is partly why it was chosen for the present study which aims to investigate hypogene and supergene mineralisation and the geochemical and mineralogical transition between the two types. Hypogene mineralisation is primarily hosted as Cu-Co sulphides at a depth of >100m, within in the R.S.F. unit, analogous to the 'lower orebody' of Hitzman *et al.* (2012). Hypogene mineralisation can be observed more readily in the deeper portions of the deposit towards the east, and in the underlying Mines Subgroup fragment (Chimvinga, pers. comm., 2014). Supergene mineralisation is abundant at Mashitu South, existing primarily in the top 100m, with a distinct oxide mineralised zone at around 30m depth corresponding to the position of the water table (Robertson, pers. comm., 2014). Supergene mineralisation is

more common in the shallower, more westward part of the deposit where it is sometimes found within the R.A.T. unit at high grades.

According to a mineralogical study by S.G.S. South Africa (Pty) Ltd. (Ellerbeck, 2011), the major rock-forming minerals identified from five samples examined from the Mashitu South deposit were dolomite, quartz, chlorite and mica. Other minerals found in lower abundances were magnetite, K-feldspar, talc, serpentine, clays, apatite and Fe-Ti oxides/hydroxides. The five samples analysed were classified petrographically by McLaren (2011) as a siliciclastic dolosparite, two argillaceous silicate mudstones, and two siliciclastic dolomicrosparite/-sparites. Malachite, pseudomalachite, heterogenite, pyrite, chalcocite, covellite, carrollite, chalcopyrite, chrysocolla, kolwezite, bornite, cobaltoan dolomite and haematite were identified by Ellerbeck (2011) and McLaren (2011) as directly related to supergene and hypogene mineralisation in the Mashitu South samples. Figure 3.6 shows some ore-assemblages from the deposit.

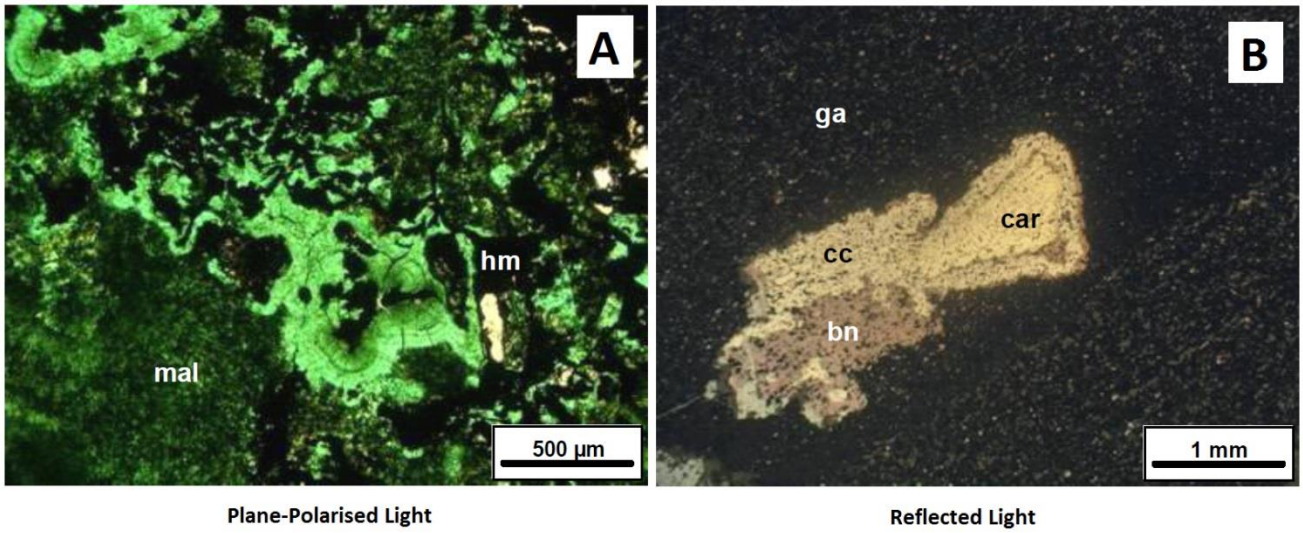

Figure 3.6: *Ore assemblages from the Mashitu South deposit. Mal=malachite, hm=haematite, ga=gangue, cc=chalcocite, car=carrollite, bn=bornite.* ***A****: Malachite-haematite ore from a supergene vein in an argillaceous silicate mudstone.* ***B****: Carrollite-bornite-chalcocite stratiform-disseminated hypogene ore from an argillaceous silicate mudstone. Images and interpretations taken from McLaren (2011).*

3.1.6 Objectives of Fieldwork and Core Logging

The fieldwork and core logging conducted at the Mashitu Complex was primarily intended to familiarise the author with the local stratigraphy, structure, alteration and mineralisation, and also to select samples for mineralogical and petrographic analysis (see Chapter 4). Secondary objectives were the provision of more detailed logging on selected boreholes than that already available and using this to ground-truth more extensive, less detailed logging conducted by Comide S.P.R.L. across the Mashitu South deposit. This was also used to provide an analogy to data in the extensive Comide geological logging database, the analysis of which is described in Chapter 5.

3.2 Methods

3.2.1 Field Excursions

During the 2014-2015 period several field excursions were made to deposits near Mashitu South (the locations of which are detailed in Figure 3.7) with the author often accompanied by local geologists, Comide S.P.R.L. employees and fellow researchers. Field visits were also made to the more distant Kakanda Group, Kabolela, Mukondo, Kipushi and Frontier deposits. These visits were not intended to be systematically descriptive but rather to provide conceptual analogies for the study object of the Mashitu South deposit, which, because of lack of surface exposure, could not be mapped or otherwise directly analysed from the surface. Observations and interpretations which are relevant to the study of Mashitu South will be detailed in the later sections 3.3. Results and 3.4. Discussion.

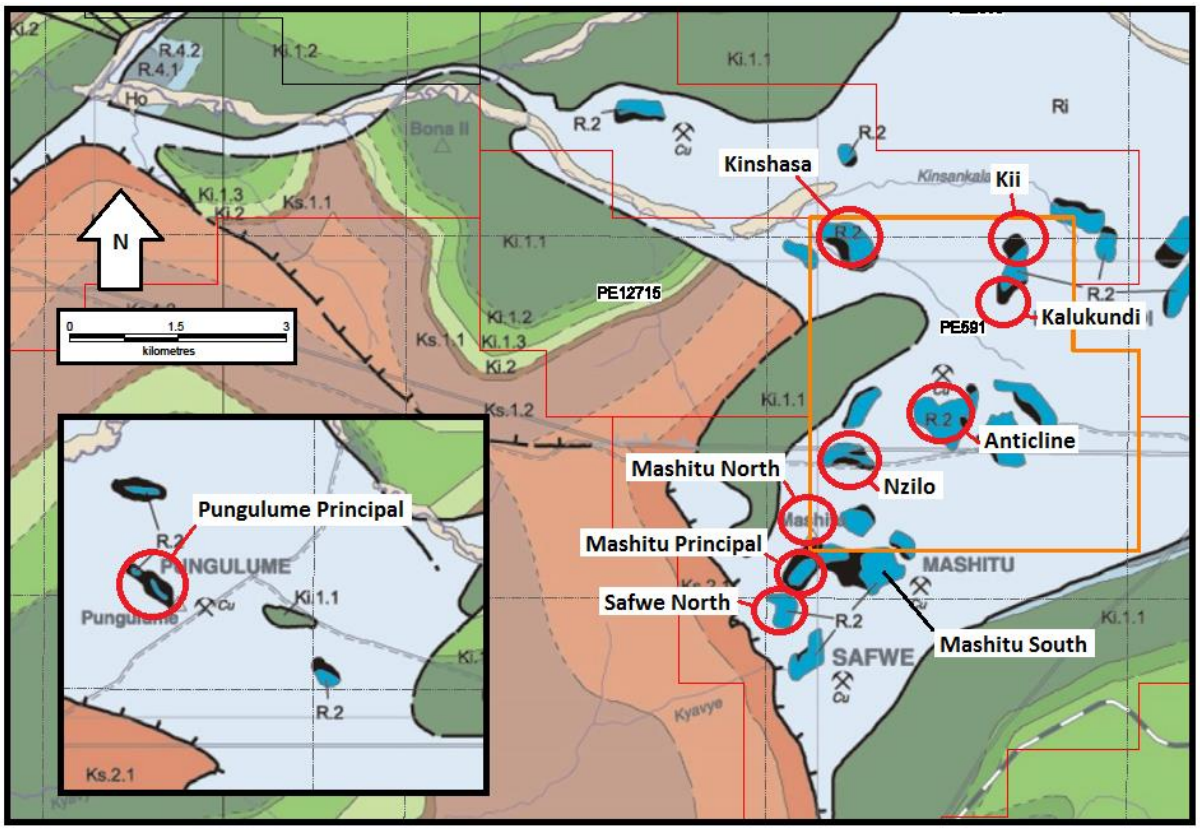

Figure 3.7: *Red-circled locations of field visits to various deposits in the area of Mashitu South. For a key to the geology and the location of the Pungulume Principal deposit (shown on the inlay), refer to Figure 3.3. Map provided by Comide S.P.R.L. after François (1973) and modified in this study.*

3.2.2 Core Logging

Diamond-drill core from selected boreholes held by Comide S.P.R.L. from the Mashitu South, Mashitu Principal, and Pungulume East deposits was systematically logged in detail during the May-June 2014 period. This accompanied less detailed logging already conducted by employees of Comide S.P.R.L.. The focus of this logging was on identifying and classifying mineralisation, as well as ascertaining its relation to stratigraphy, structure and alteration at Mashitu South. Holes from Mashitu Principal and Pungulume East were logged to give a broader understanding of mineralisation in the region. In total, 10 holes were logged: four from Mashitu South, two from Mashitu Principal, and four from Pungulume East. Each hole was chosen because it contained significant hypogene, supergene, or, importantly, a mixture of and transition between the two types of mineralisation. However, this section will focus on the logging from Mashitu South, as this deposit is the core of this thesis.

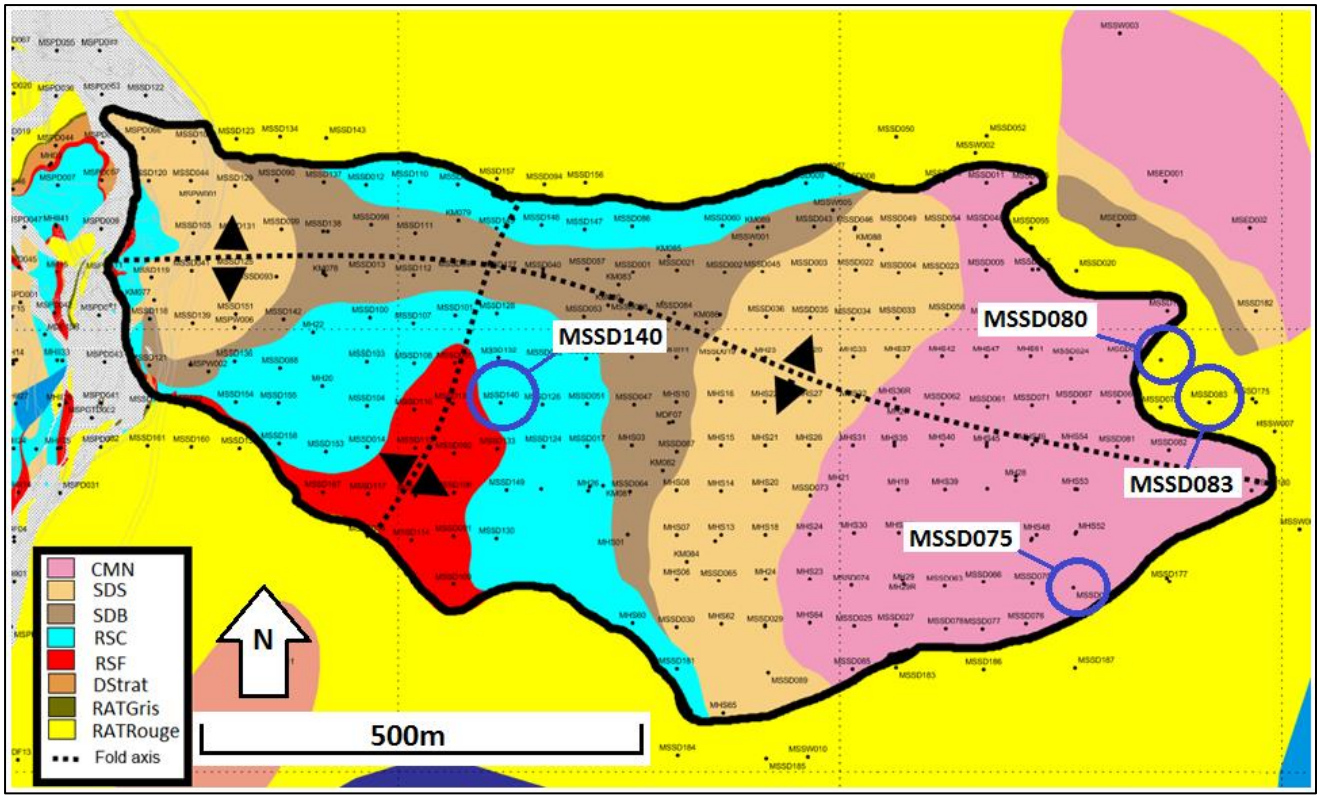

Figure 3.8: *Geological Map of the Mashitu South Mines Subgroup fragment (outlined in thick black). The locations of the four holes which were logged as part of this study (MSSD075, MSSD080, MSSD083, and MSSD140) are indicated and circled in dark blue.*

The four holes logged from Mashitu South were: MSSD075, MSSD080, MSSD083 and MSSD140. MSSD075, 080 and 083 are all deep holes (>200m depth) found along the eastern flank of the deposit which intersect significant hypogene mineralisation, as well as supergene mineralisation at shallower depths. All three collar in the upper Mines Subgroup (C.M.N.) and end a few metres into the R.A.T. MSSD083 also intersects the lower fragment of Mines Subgroup which underlies the 'surface fragment' at Mashitu South. This lower fragment is also host to hypogene and supergene mineralisation. MSSD140 is a shallower hole (~106m) found near the centre of the Mashitu South fragment. It collars in the R.S.C. or R.S.F. and extends for almost 100m into the R.A.T. It intersects exclusively supergene mineralisation which is thought to have been leached from eroded Mines Subgroup rocks which would have originally overlain it. It was therefore chosen to be a good comparison to hypogene mineralisation, such as that found in MSSD075, 080 and 083, for the purpose of studying the transition between the two mineralisation types. Figure 3.8 is a geological map of the Mashitu South Deposit with the locations of the four logged holes marked.

Each hole was systematically logged using a standardised template logging sheet. Geological intervals were selected based on lithological changes, and given two abbreviated lithological designations to describe the lithology (e.g. Lith1: Dol, Lith2: Arg to describe a Dolomitic Argillite. The lithology was then represented graphically according to its grain/clast size with any minor variations in this also represented. Mineralisation was logged and described in parallel, independent of lithology. Each geological interval would then be described according to lithology, structure, alteration and mineralisation, and the unit would be representatively illustrated, with colour, on the graphic log. Figure 3.9 is an example of the logging template used.

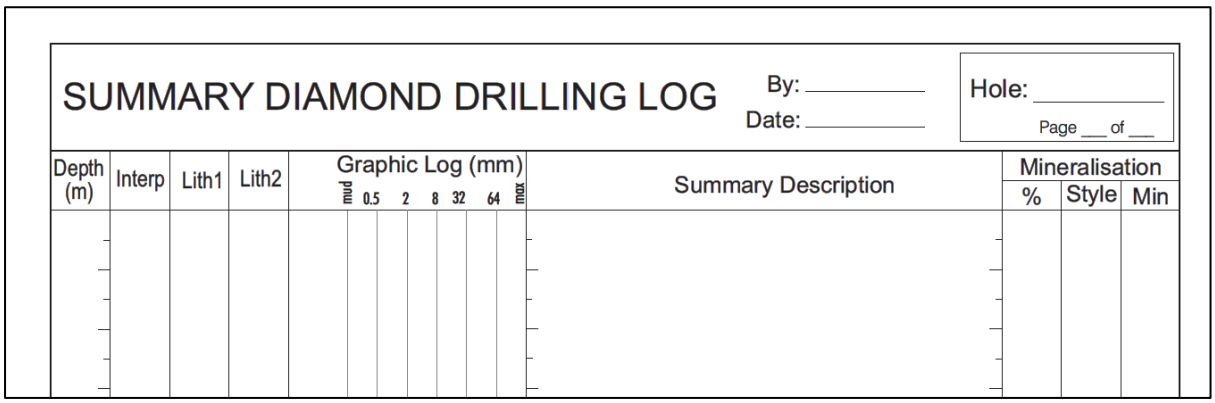

Figure 3.9: *Logging template used in the present study to log MSSD075, 080, 083 and MSSD140.*

3.3 Results

3.3.1 Field Excursions

Due to the qualitative and highly interpretive nature of observations made in the field, these observations and the evidence for them will be presented and discussed in section 3.4: Discussion.

3.3.2 Core Logging

The original hand-drawn logs for the 4 boreholes logged in detail by the author from Mashitu South: MSSD075, 080, 083 and 140, were scanned and are presented as Appendix 3. A summary of the results of the logging are given in this section, focussing on lithology,

alteration, mineralisation and structure. Many lithologies in MSSD075, 080 and 083 were found to be essentially the same and were correlated between the different holes. However, there is a stratigraphic repetition below the first lithological package in MSSD083 (see Appendix 3c). The lithology, alteration and mineralisation in MSSD140 is rather different and will be considered separately.

3.3.2.1 MSSD075, MSSD080 and MSSD083

The base of all three of these holes is marked by a monomictic, protobrecciated reddish sandy siltstone with angular clasts supported by a matrix of white carbonate veins (Figure 3.10). In MSSD075 (but not 080 or 083), there is a transition to a polymictic, poorly sorted, matrix supported breccia with rounded clasts of gravel to pebble size (Figure 3.11). Over these basal breccias, both holes exhibit several metres of reddish sandy siltstone, locally containing orange-to-whitish blotches, cut by white carbonate veins and similar in appearance to the clasts of the basal monomictic breccia (Figure 3.12). This sandy siltstone is transitional to a mottled red-to-greeny-grey colour for several more metres which is occasionally host to wavy, possibly enterolithic white dolomite veins (Figure 3.13).

Figure 3.10: *Photo of monomictic dolomite-vein-supported protobreccia. H.Q. core size for scale.*

Figure 3.11: *Polymictic, matrix-supported breccia. H.Q. core size for scale.*

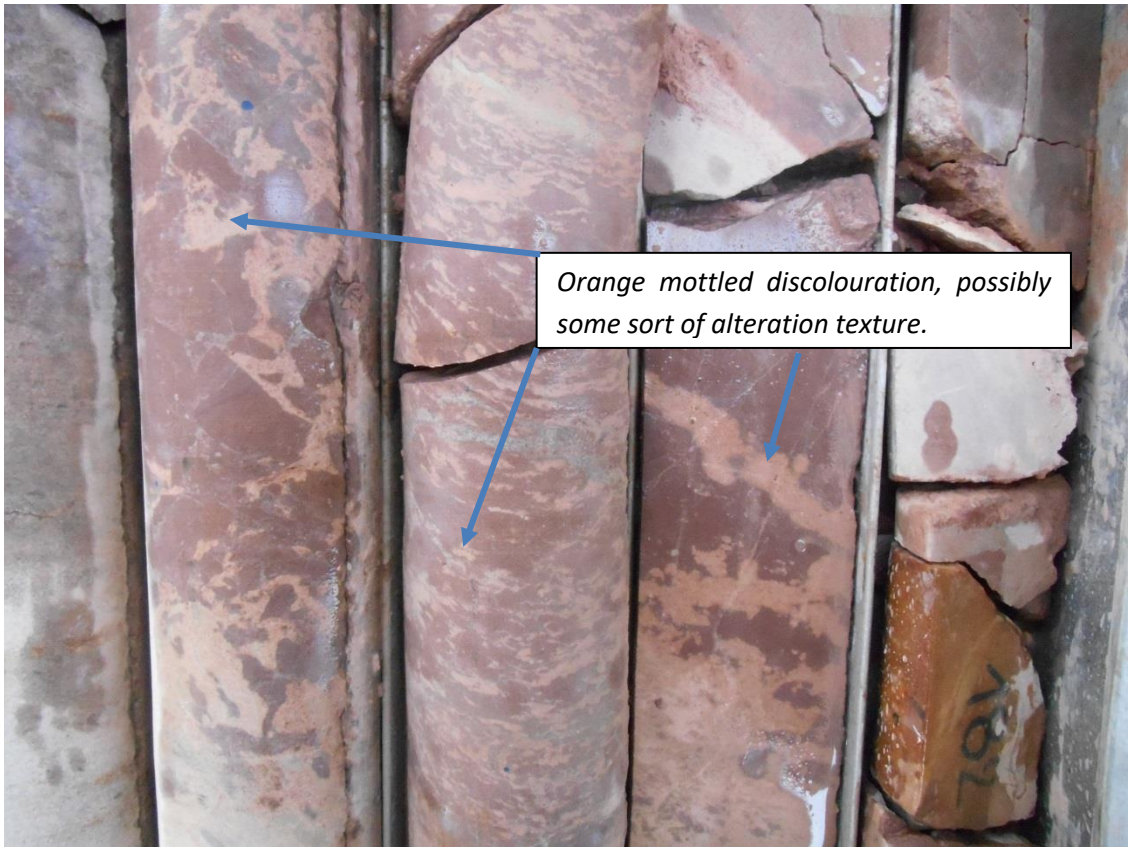

Figure 3.12: *Reddish sandy siltstone. H.Q. core size for scale.*

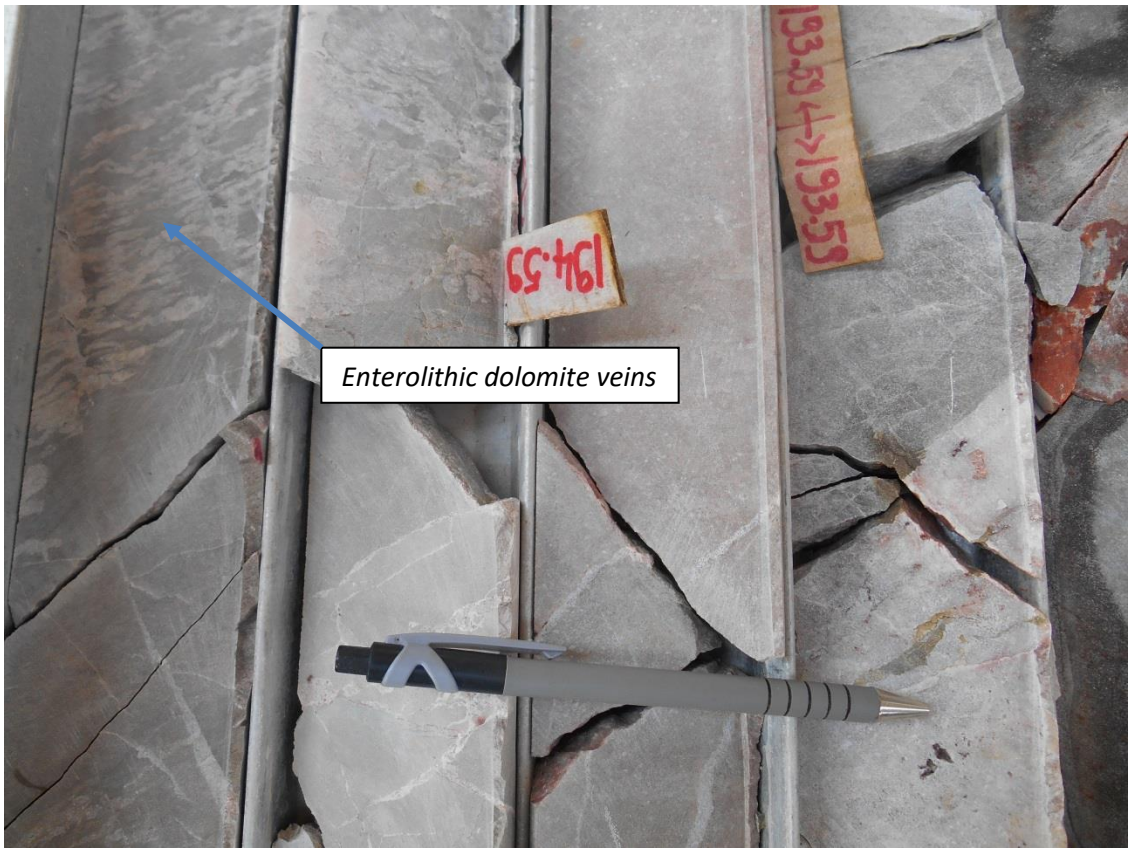

Figure 3.13: *Greenish sandy siltstone with enterolithic dolomite (top left). H.Q. core size for scale.*

Above these siliciclastic and brecciated units there is a bedded, grey, micritic dolomite often with strange, nodular-or-layered chert lenses which are elongated parallel to bedding, giving the appearance of boudinage (Figure 3.14). Upwards, there is a slightly thicker, laminated, micritic/silicic dolomite, with intense silicification along alternating, locally wavy but mostly planar laminae. The laminae alternate between white, grey and blueish in colour (Figure 3.15). The total thickness of these two units does not exceed ~15m. Next, above this laminated dolomite, comes a ~12m thick unit of intensely silicified crystalline rock composed of >50% microcrystalline silica. The remaining composition of the rock is mostly coarse crystalline dolomite and the unit is locally vuggy, probably due to the dissolution of dolomite in preference to silica. There is no bedding evident, rather the silica and dolomite vary along irregularly wavy, non-planar laminae which locally show growth features suggestive of stromatolites. The colour of this unit, as with the texture, is highly variable, commonly ranging from blue to orange to red to white to grey with the more silicic portions tending to be white, grey or orange (Figure 3.16).

Figure 3.14: *Bedded micritic dolomite with cherty layers. H.Q. core size for scale.*

Figure 3.15: *Wavy-laminated silicified micritic dolomite. H.Q. core size for scale.*

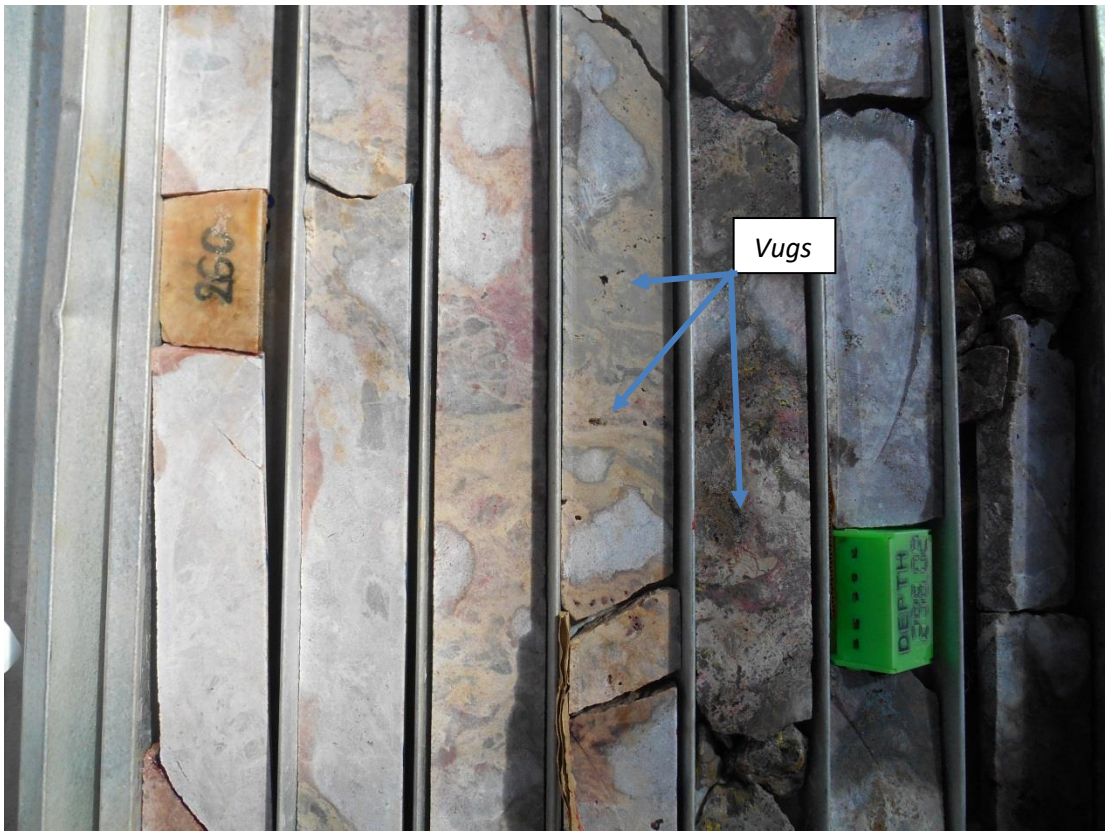

Figure 3.16: *Stromatolitic, silicic, vuggy crystalline dolomite. N.Q. core size for scale.*

Above this sequence of dolomites is a fairly monotonous dolomitic argillite unit with a thickness of ~30-40m. It is variously a mudstone, shale or micritic dolomite, with varying carbonate content according to acid-testing, although it is generally dolomitic. It is usually distinctively blotchy in colour, varying from red-to-green (Figure 3.17). Red coloration may be blotchy and random but it also occurs in stratiform, bedding parallel fashion and in proximity to dolomite veins which cross-cut the host rock. The bedding in this unit is fine and shaly towards the bottom, but bed size generally increases in width upwards in the section. At the top of this unit there is a ~5m thick, very fine grained, finely laminated fissile shale. In MSSD080 and 083 this shale is black and carbonaceous (Figure 3.18), with abundant fine grained stratiform-disseminated pyrite. However, in MSSD075 the shale is yellow and locally reddish. Because this unit is significantly deeper in MSSD080 and 083, the yellow colour of the shale in MSSD075 is attributed to weathering, which is supported by the presence of green supergene Cu-oxide veins which only occur in MSSD075. Above this black/yellow shale is another dolomitic argillite, ~30m thick in MSSD075, ~40m thick in MSSD083, but ~80m thick in MSSD080. This argillite is very similar in nature to the unit below the black/yellow shale with some indication that bedding width may continue to increase upwards towards the top of the unit (Figure 3.19). In MSSD080, this unit is brecciated between 184 and 191m into a monomictic, dolomite-vein-supported protobreccia. In MSSD083 the top of this unit is marked by a ~4m thick unit of breccia grading from rounded and matrix supported at the centre to more angular and clast supported, and at the sides a dolomite-vein-supported protobreccia is found before the transition to contiguous rock. Above these breccias, a stratigraphic repetition occurs in MSSD083 (see Appendix 3c).

Figure 3.17: *Lower mottled red-green dolomitic argillite. H.Q. core size for scale.*

Figure 3.18: *Black carbonaceous shale, cross-cut by veins of dolomite. H.Q. core size for scale.*

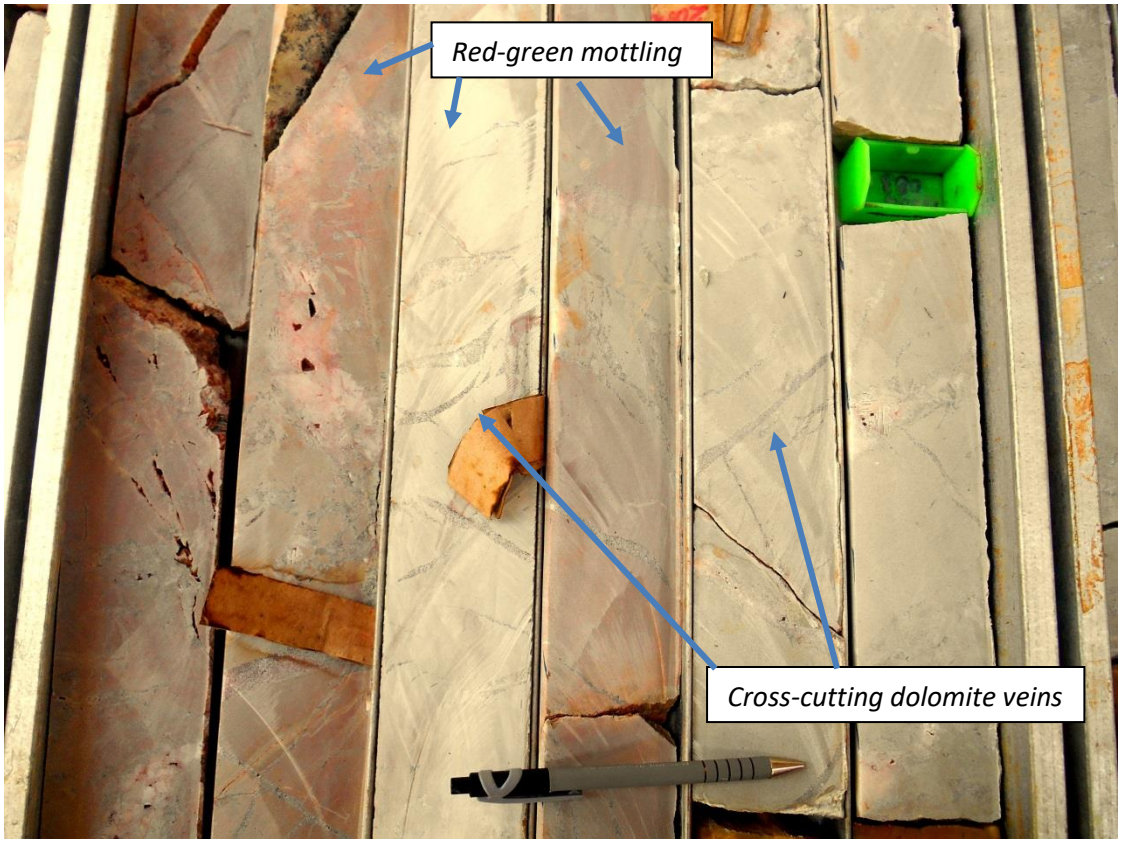

Figure 3.19: *Upper mottled red-green dolomitic argillite, cross-cut by a wide variety of orientations of dolomite veins. H.Q. core size for scale.*

The transition from this argillite to the calcareous unit above occurs gradually. The underlying red-green bedded dolomitic argillite becomes interbedded with blue-grey-black micritic carbonaceous dolomite. This transition may occur over ~20m with micritic dolomite slowly becoming dominant over dolomitic argillite. In MSSD075 and 083 the micritic dolomite unit above is finely bedded, contains wavy laminations in places, and heavily carbonaceous, with locally-developed layers of white, coarsely crystalline dolomite. By contrast MSSD080, above the transition zone, contains a unit of coarsely crystalline blue-grey-white dolomite which is almost 20m thick before the unit transitions to a monomictic, dolomite-vein-supported protobreccia. Despite this disparity, however, after 25-30m of variation immediately above the red-green dolomitic argillite, all three holes contain a 6-7m thick unit of highly silicic rock very similar to the unit immediately below the red-green dolomitic argillite. Again a >50% microcrystalline silica, minor dolomite with vugs composition is apparent, with irregular, wavy, non-planar possibly stromatolitic laminae, and colour ranging from blue to orange to red to white to grey (Figure 3.20). Above this unit,

the micritic dolomite of MSSD075 and 083 goes through a 50m sequence of micrite which is mostly grey, carbonaceous, and thinly laminated (Figure 3.21). As well as this dominant lithology, there are a number of intervals where the micrite gives way variously and seemingly without pattern, to: 1. blue, partially crystalline (fine-medium grain size) dolomite, generally <1m in width (Figure 3.22). 2. wavy-laminated, occasionally silicified micrite with growth structures that could be stromatolites or algal mats, these point up-hole, indicating that the section is the right way up (Figure 3.23); 3. cryptic, <1m wide white-nodule-rich layers; the nodules in which are soft, clay and/or carbonate rich, elongated along bedding planes and have a broken, cauliflower-like shape somewhat reminiscent of 'chicken-wire textures', common in evaporite nodules (Figure 3.24); 4. <1m wide cryptic layers of micrite, rich in sand-gravel-sized irregularly shaped dark clasts, perhaps sedimentary intraclasts?; and 5.; <1m wide layers of pervasively silicified rock, where the original texture is difficult to discern because of the silica, but looks micritic (Figure 3.25). In all of these layers, bedding is often disturbed, very locally, from the horizontal. This deformation could be indicative of sedimentary structures such as cross-bedding, algal processes, flame and load structures, or soft sediment deformation. In MSSD080, this 50m interval shows evidence of these lithologies, with occasional units of grey, laminated, carbonaceous micrite and wavy-laminated silicified micrite. However, these units are separated by numerous cross-cutting breccias, which are mostly polymictic and matrix supported. These breccias are surrounded by argillic alteration, with occasional supergene mineralisation, making the original lithologies difficult to discern. Argillic and advanced-argillic alteration is inferred in the Mashitu South core by the development of fine-grained, powdery material assumed to be clay minerals, pervasively altering and replacing the original fabric of the rock, most prevalent near the surface. Mineralogical inferences from this Chapter are expanded upon in Chapter 4: Petrography and Paragenesis.

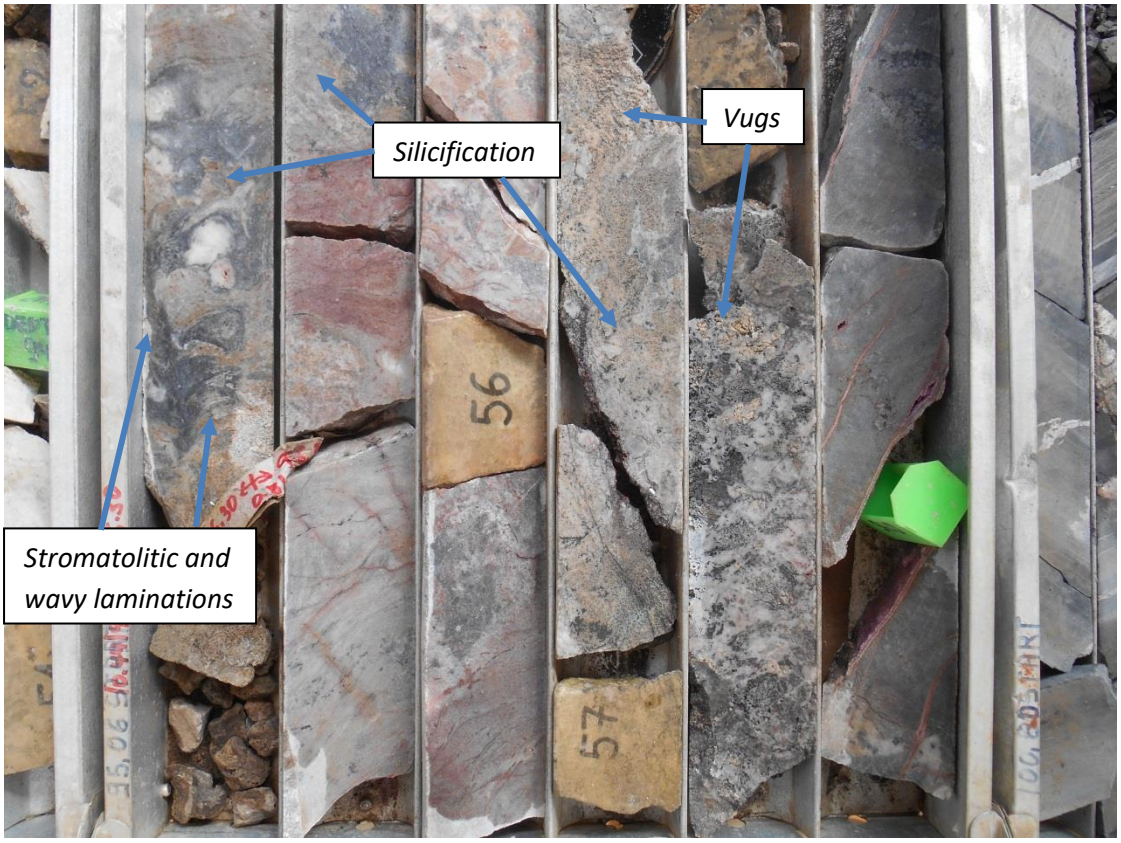

Figure 3.20: *Silicified stromatolitic unit in the upper micritic dolomite. H.Q. core size for scale.*

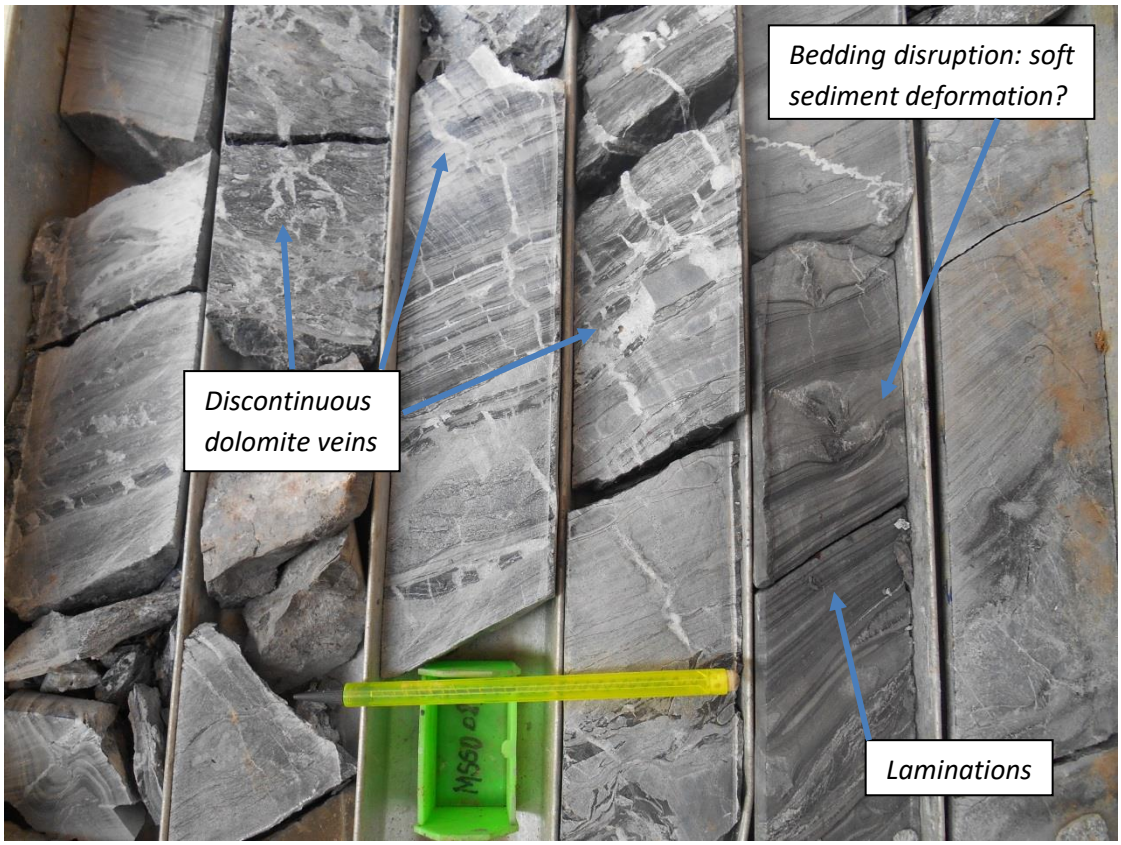

Figure 3.21: *Carbonaceous grey micritic dolomite with laminations. H.Q. core size for scale.*

Figure 3.22: *Fine-medium grained crystalline blue dolomite. H.Q. core size for scale.*

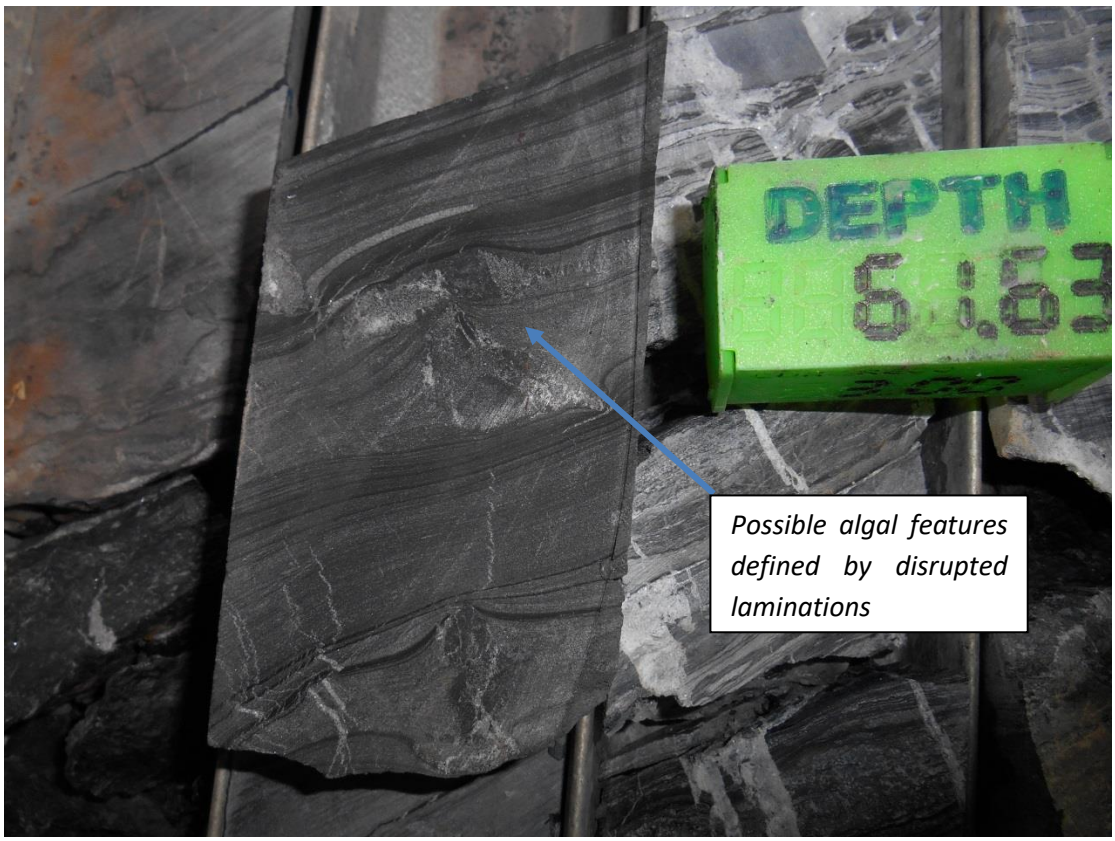

Figure 3.23: *Algal-laminated micritic dolomite . H.Q. core size for scale.*

Figure 3.24: *'Cauliflower shape' elongate dolomite nodules, reminiscent of chicken wire texture. H.Q. core size for scale.*

Figure 3.25: *Silicification overprint to an originally carbonaceous micritic dolomite. H.Q. core size for scale.*

In the near-surface profile of the three holes, the alternating breccia-micrite/argillite in MSSD080 is capped by about a metre of friable black rock containing a high proportion of clay. This rock transitions into a bleached-white clay-stone (Figure 3.26), usually fragmented, occasionally containing laminations which may follow the trace of protolith bedding, at a depth of ~42m. The bleached-white clay-stone continues upwards until ~20m depth, where the clay becomes saprolitic and red-brown (Figure 3.27). The top 2m of the hole consist of this red-brown clay punctuated by plant roots. In MSSD075, an alternating breccia-micrite/argillite sequence affected by significant argillic alteration, similar to that in MSSD080, occurs from the depth in the sequence where rock is easily discernible (~41m) and continues to a depth of ~19m. Unlike in MSSD080, units of unconsolidated, sandy 'grit'

are occasionally present amongst the argillite/micrite. The top ~19m consists of the same red-brown saprolitic clay found in MSSD080, with plant roots in the top 4m of the profile. MSSD083 is similar with the upper ~45m of the core showing advanced-argillic-to-argillic alteration over some sort of argillite/micrite protolith, with red-brown saprolitic clay dominating the top ~12m.

Figure 3.26: *White rock affected by surficial advanced argillic alteration. P.Q. core size for scale.*

Figure 3.27: *Red-brown near-surface saprolite. P.Q. core size for scale.*

The most dominant alteration type affecting MSSD075, 080 and 083 is supergene, taking the form of supergene mineralisation and argillic alteration. Advanced argillic alteration can be found at the tops of both holes with a well-developed saprolite extending to a depth of ~20m (Figures 3.26 and 3.27), and less intense argillic alteration can be found up to a depth of 100m or even more, particularly in proximity to breccias. Haematite development is also common, which may be responsible for the mottled reddening of the two red-green dolomitic argillite units (Figures 3.17 and 3.19), and reddening of other units particularly along fractures and veins. Fe-oxides such as limonite or jarosite may also be responsible for the yellow colour of the 'black shale' in MSSD075.

Silicification is common, affecting most units which display 'stromatolitic' or 'algal' structures, including the bottom-most laminated micritic dolomite, and local algal micrites in the uppermost carbonaceous micritic dolomite unit (see Figures 3.16, 3.20 and 3.25). Silicification is most abundant in the lowest, ~12m thick crystalline unit where microcrystalline silica makes up >50% of the bulk composition of the rock.

Dolomitisation has occurred throughout the sequence with crystalline fine to coarse-grained dolomite found to a greater or lesser degree in all of the carbonate units. There are also two types of primarily dolomite veins developed. The first vein-type (Type 1) does not cross-cut bedding planes very effectively, is usually very irregularly shaped, tends to be thin in width (usually 2-20mm) and often fills space created by very local deformation (thought to be soft-sediment deformation), as shown in Figure 3.28. The second type (Type 2) is cross-cutting, ubiquitous through all lithologies and may reach thicknesses of 5cm (1-2cm is more common though). These veins also form the 'matrix' in the vein-supported protobreccias which are found in some lithologies (Figure 3.29). In some cases the first type appears to be cross-cut by the second type, indicating that the first type formed first. Both vein types may be host to sulphide and oxide mineralisation.

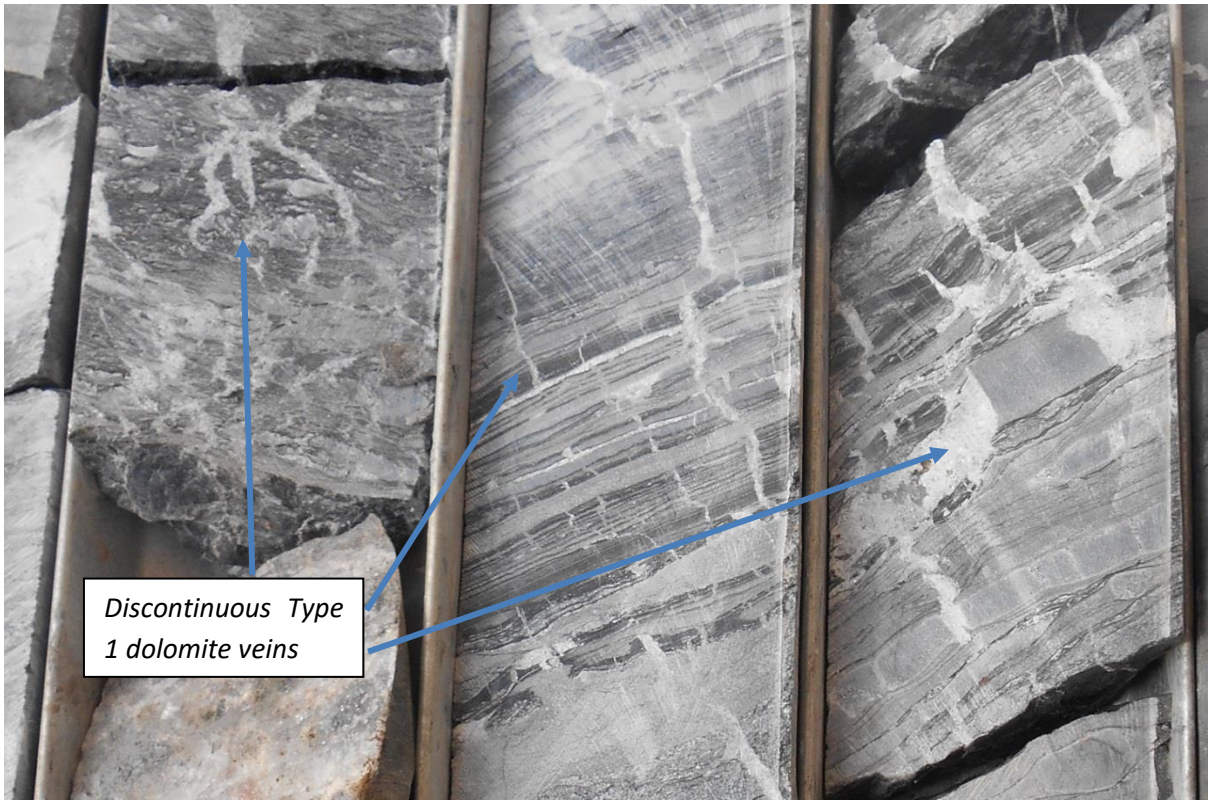

Figure 3.28: *Type 1 dolomite veins cutting through the upper micritic dolomite. H.Q. core size for scale.*

Figure 3.29: *Type 2 dolomite veins cutting through dolomitic argillite. H.Q. core size for scale.*

Another type of alteration in MSSD075 and 080 occurs in the transition between the basal red sandy siltstone and the green sandy siltstone above it (Figures 3.12 and 3.13). Non-planar mottling between green and red suggests that this contact is gradational and alteration-related rather than lithological. Around this transition, white-to-orange blotches can be found in both the green and the red sandy siltstone, which suggest the development of a lighter coloured mineral and are reminiscent of fine-grained albite alteration. Along fracture planes near this transition, there is often a very fine-grained white-to-green mineral developed which has a soapy feel when rubbed between the fingers. This could be clay from the breakdown of feldspar, or talc, suggestive of either magnesian, sodic or potassic alteration. Alteration type and intensity is recorded in the graphic logs in Appendix 3.

Mineralisation is found throughout the entire sequence in MSSD075, 080, and 083 with the exceptions of the basal red sandy siltstone and the breccias underneath it, and the top ~40m or so of the profile. Sulphide mineralisation appears to be most abundant in the lowermost bedded, cherty micritic dolomite, the laminated micritic dolomite above it, and the stromatolitic crystalline silicic-dolomite above that. Sulphide minerals reported from these units include carrollite, chalcocite, bornite, chalcopyrite and pyrite all of which are found in both stratiform-disseminated and vein-hosted modes of occurrence (Figure 3.30). In the red-green dolomitic argillite overlying the crystalline silicic-dolomite, stratiform-disseminated and vein-hosted chalcopyrite and pyrite are the most abundant sulphides, with minor chalcocite found mostly towards the base, near the crystalline silicic-dolomite. Mineralisation is not as well developed in this unit. However, the black/yellow shale which divides the red-green dolomitic argillite in two is well mineralised with stratiform pyrite, chalcopyrite and chalcocite found in the black shale of MSSD080 and 083 (Figure 3.31), and vein-hosted malachite in the yellow shale of MSSD075. Sulphide mineralisation in the upper dolomites is not very well developed and tends to be vein-hosted and independent of lithology, with chalcopyrite, bornite and chalcocite identified and chalcopyrite being the more abundant out of these three minerals. Mineralisation abundance and type throughout the holes is logged graphically together with the stratigraphy, and presented in Appendix 3.

Figure 3.30: *Vein-hosted and stratiform chalcocite-bornite-carrollite in the wavy-laminated silicified micritic dolomite. Chalcocite and bornite are visible as an iridescent blue. N.Q. core size for scale.*

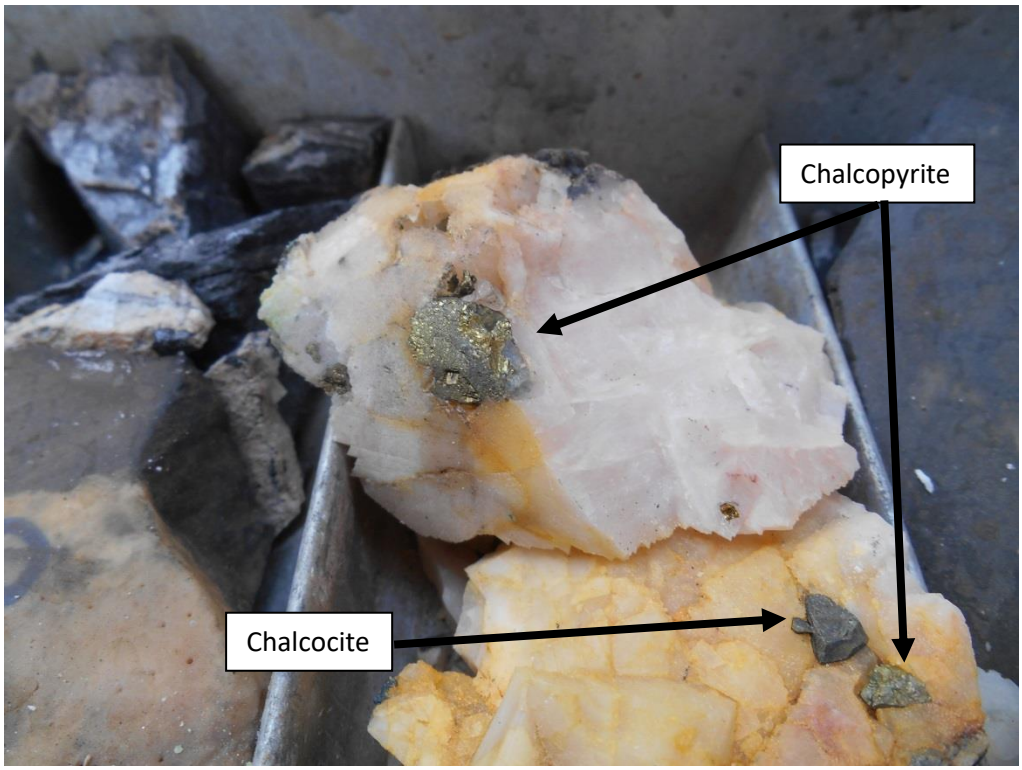

Figure 3.31: *Dolomite vein-hosted chalcopyrite and chalcocite in the black carbonaceous shale. H.Q. core size for scale.*

Oxide mineralisation is particularly concentrated within certain zones in MSSD075, 080 and 083. There is no evidence of Cu-Co oxides in the top ~40m of the profile. However, between 40m and 120m there are various mineralised zones, mostly concentrated around breccia units, which host malachite (Figure 3.32), chrysocolla (Figure 3.33), cobaltoan dolomite (Figure 3.34) and a black, friable mineral with a dull lustre which could be either Mn or Co oxides. These same minerals are found within, and in the immediate vicinity of, the crystalline silicic-dolomite unit, both along veins and disseminated through the stratigraphy, with the extra addition of native copper (Figure 3.35), heterogenite and yellow uranium oxides found within this unit in MSSD080 and 083, coexisting in places with carrollite (Figure 3.36).

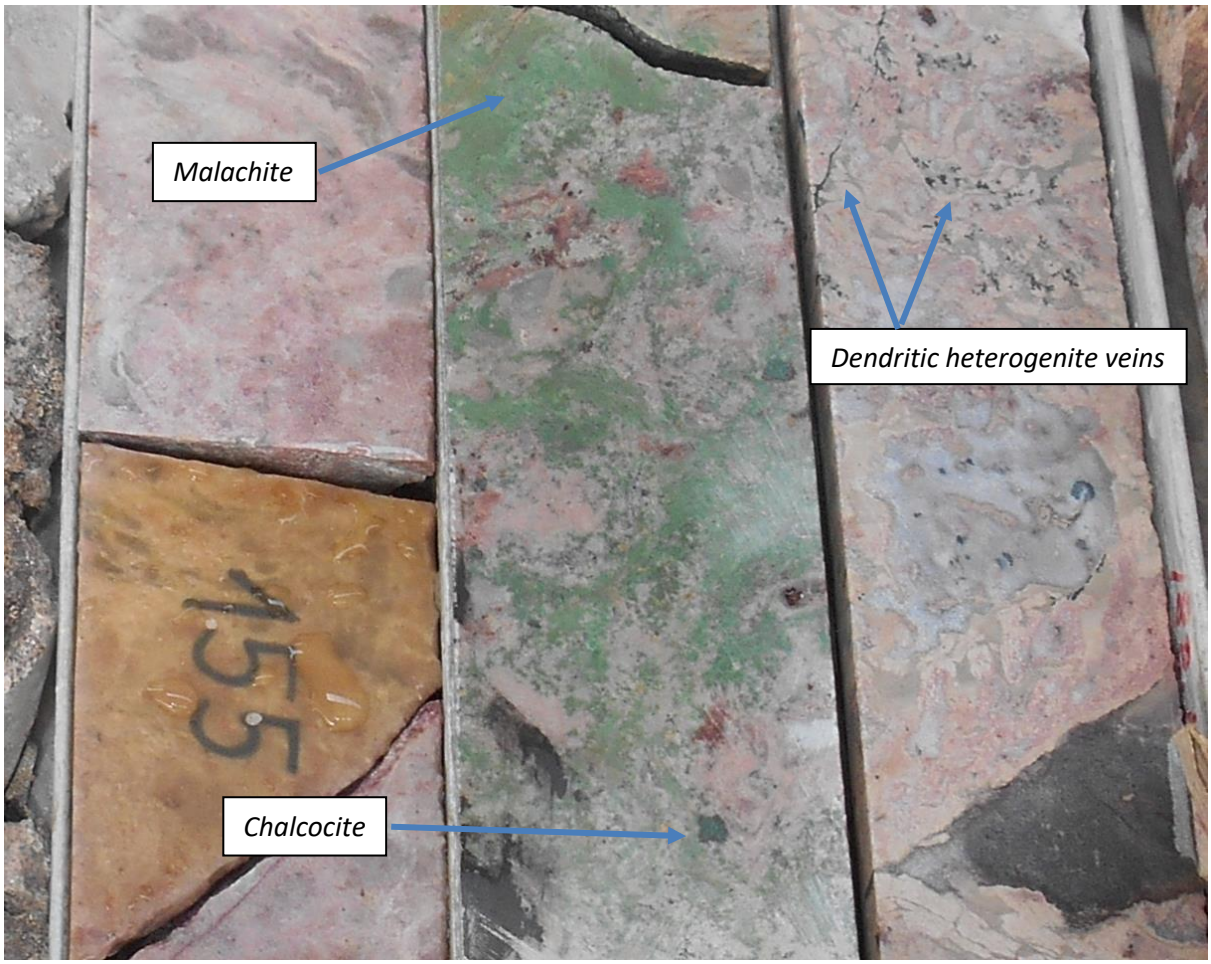

Figure 3.32: *Pervasive green malachite in the lower crystalline silicic dolomite. Small amount of chalcocite and heterogenite are also visible in the picture. H.Q. core size for scale.*

Figure 3.33: *Fracture-filling blue chrysocolla in crystalline blue dolomite. H.Q. core size for scale.*

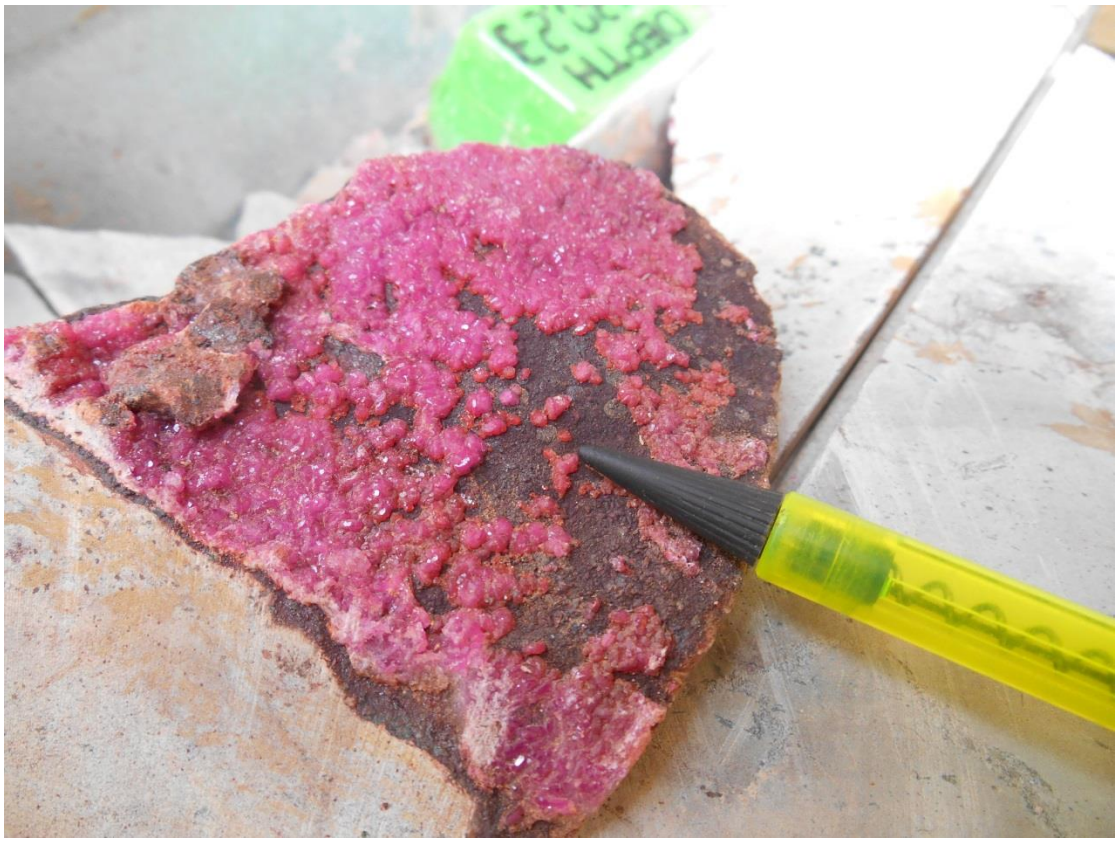

Figure 3.34: *Euhedral fracture-fill cobaltoan dolomite on heterogenite base. H.Q. core size for scale.*

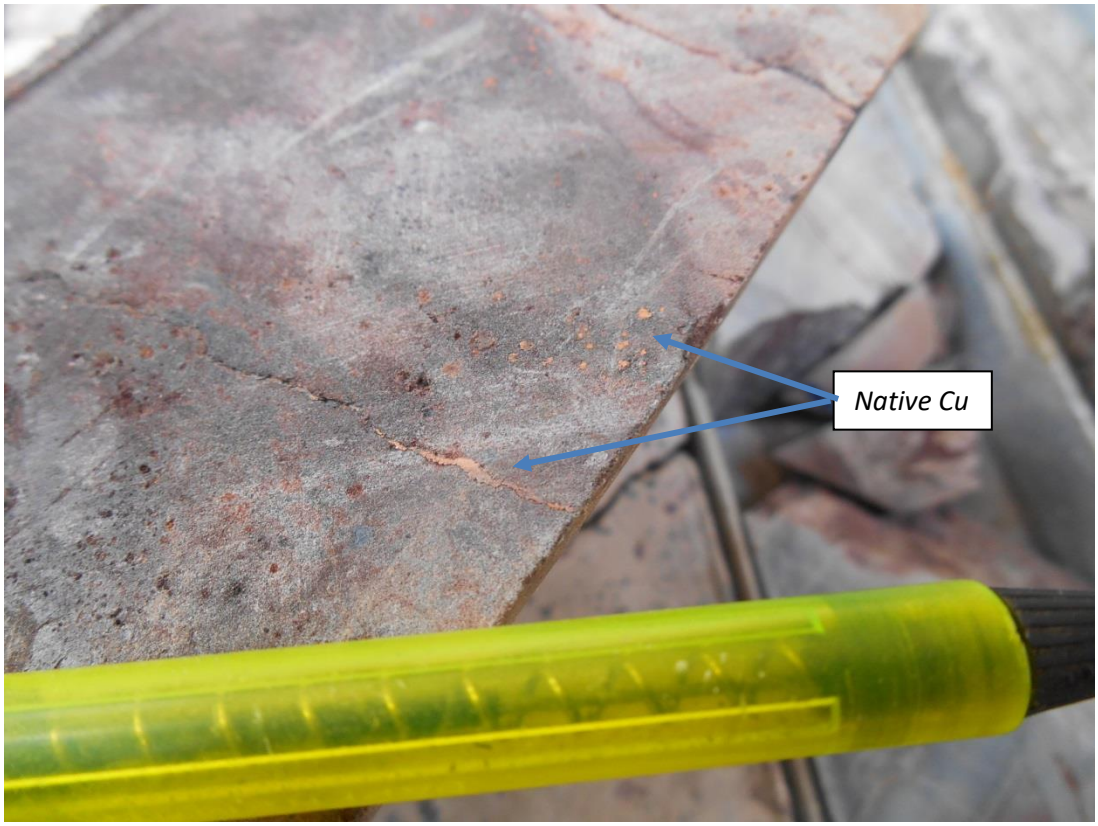

Figure 3.35: *Native copper in the lower crystalline silicic dolomite. N.Q. core size for scale.*

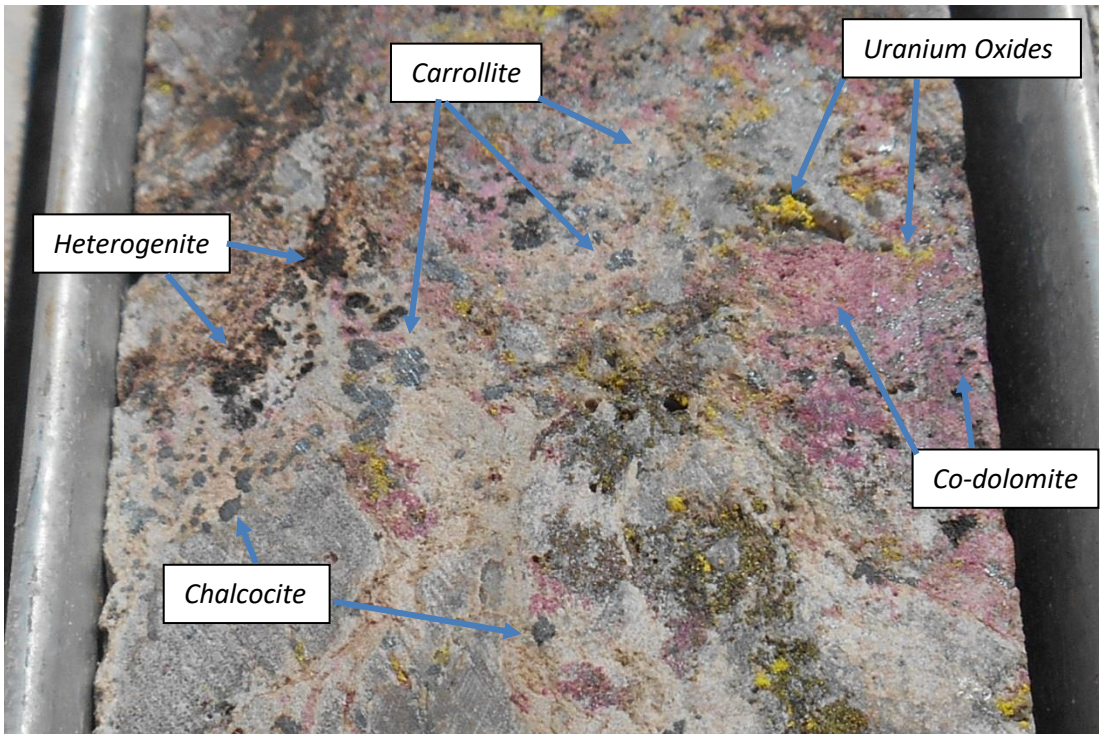

Figure 3.36: *Carrollite (bright-silver), chalcocite (dark-silver-grey), heterogenite (black), cobaltoan dolomite (pink) and uranium-oxide (yellow) in the lower silicic dolomite. N.Q. core size for scale.*

The ‘leached zone’ in MSSD075, 080 and 083 appears to exist down to a depth of ~40-45m. There is an ‘oxide zone’ at a depth between ~40m and 100m in MSSD080 and a small, poorly developed oxide zone exists between ~40m and 50m in MSSD075. From here, oxide and sulphide mineralisation appear to coexist right to the bottom of the three holes (See Figure 3.36), making the deepest portions part of the ‘transition zone’ of oxide-sulphide weathering. Hypogene mineralisation, although clearly present, is not expressed in a discrete hypogene zone (where, by definition, only hypogene mineralisation exists) at the depths drilled to in these three holes.

Structurally, there is no clearly developed foliation which postdates bedding in any lithology from any of the holes. Deformation is largely limited to local variations and disturbances in bedding which cannot be traced with any sort of continuity, which are probably caused by syn-sedimentary processes and soft-sediment deformation. However, the apparent elongation of chert lenses in the basal bedded micritic dolomite and cauliflower-shaped ‘chicken-wire’ textures in the upper carbonaceous micritic dolomite suggest that the rocks have undergone post-lithification extension. The most likely evidence for the accommodation of structural deformation found within the two holes is the abundance of monomictic, vein-supported breccias (Figure 3.10) and also a polymictic, rounded clast, matrix supported breccia found towards the base of MSSD075 (Figure 3.11).

3.3.2.2. MSSD140

MSSD140 is distinct from the other three holes in terms of lithology, alteration and mineralisation. From the surface downwards, the hole begins with less than 2m of red-brown saprolite, in contrast to the 10-20m found in the other three holes. Immediately below this there is almost 5m of a resistant, contiguous rock unit. This rock appears to be primarily laminated microcrystalline silica with some clay, it is highly fractured and contains many small, rounded vugs. Clay-rich laminae alternate with siliceous laminae, and the vugs are primarily found in the clay-rich laminae (Figure 3.37). Immediately below this is less than two metres of rubbly, friable highly weathered clay-rich argillite, with surficial and fracture-hosted black, sooty material abundant within it. A further 25 metres below this consists of highly weathered clay and argillite, sometimes brecciated, with the intensity of weathering strong enough to make the protoliths very difficult to discern.

Relatively fresh rock is found at a depth of ~33m. This rock is a sequence of primarily red sandy siltstone which varies locally between sandstone, siltstone and mudstone, very similar to the 'basal red sandy siltstone' found at the bottom of MSSD075, 080 and 083 (Figure 3.38). The colour varies with lighter, white-ish and more orange blotches frequent which may represent some sort of alteration mineral. The sandy siltstone is ubiquitously cross cut by thick Type 2 dolomite veins, the frequency of which sometimes increases to the point where the veins effectively brecciate the rock in situ. Specular haematite is found both disseminated in the rock, hosted within the dolomite veins, and occasionally forming layer sub-parallel veins of its own (Figure 3.39), and a series of 2-10mm diameter white carbonate nodules occur at intervals mostly in the finer-grained mudstone. This sequence continues down to a depth of ~96m.

Beneath this there is ~8m of a light grey, shaly, dolomitic argillite, which contains a significant amount of carbonate on testing with acid (Figure 3.40). Whether this carbonate is primary or whether it represents a dolomitisation event is unknown. This unit gradually transitions from red mudstone at the base of the previous unit. It is locally vuggy and cut by Type 2 dolomite veins but otherwise is relatively homogeneous throughout. There is then a gradual transition to a red mudstone at the base of the grey, shaly unit, before interbedding of red mudstone and grey shale. The hole finishes in red mudstone.

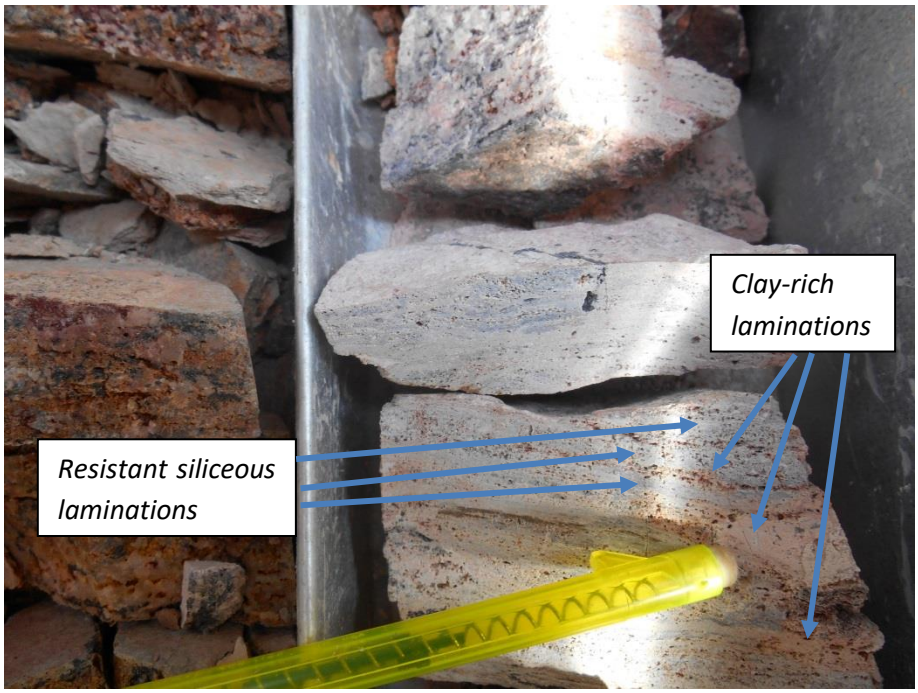

Figure 3.37: *Resistant, weathered, laminated silica-and-clay rock. P.Q. core size for scale.*

Figure 3.38: *Red sandy siltstone. H.Q. core size for scale.*

Figure 3.39: *Layer sub-parallel vein of specular haematite (top left) and monomictic dolomite-vein-supported in-situ protobrecciation of the red sandy siltstone (centre right). P.Q. core size for scale.*

Figure 3.40: *Grey, shaly argillite. H.Q. core size for scale.*

There are several types of alteration in MSSD140. First, an event which resulted in the development of specular haematite, the timing of which is difficult to ascertain but it may be early in the development of the rock, on account of the specular haematite veins being layer sub-parallel rather than cross-cutting (although there could be multiple haematisation events).

Secondly, dolomitisation has occurred, in the form of the cross-cutting Type 2 veins. This event took place post-lithification, evidenced by the in-situ brecciation of angular fragments of the red sandy siltstone which appear to have fractured in a brittle manner. Individual clasts of rock can be matched up to other clasts across the vein matrix (Figure 3.39). Whether dolomitisation in a more pervasive manner has occurred to the grey, shaly, dolomitic argillite, or whether this unit is a primary carbonate, is uncertain.

Silicification has affected the wavy laminated, resistant silica-clay rock found near the top of the hole (Figure 3.37). Due to the amount of weathering the rock has experienced, the microcrystalline silica laminations are almost all that remains of this rock.

The orange and white blotches found in the red sandy siltstone are thought to represent metasomatic alteration: perhaps potassic or sodic alteration events, however the

exact mineralogy within the 'blotches' was unclear during logging so this can only be inferred.

Lastly, surficial argillic alteration affects the top of the profile, similarly to MSSD075, 080 and 083, weathering the rock to almost unrecognisable levels down to about ~33m.

Mineralisation in MSSD140 is represented by a richly endowed supergene oxide zone beginning just where the rock becomes fresh and little affected by argillic alteration at ~33m, and continuing to a depth of ~46m. This ore is high-grade, with botryoidal malachite hosted within fractures in the red sandy siltstone particularly abundant where the rock forms a protobreccia (Figure 3.41). The botryoidal nature of the malachite suggests that it filled open space during its growth. This, together with the abundance of dolomite veins below the mineralised zone, suggests that malachite perhaps filled cavities in the rock left by the dissolution of the dolomite veins by meteoric fluids.

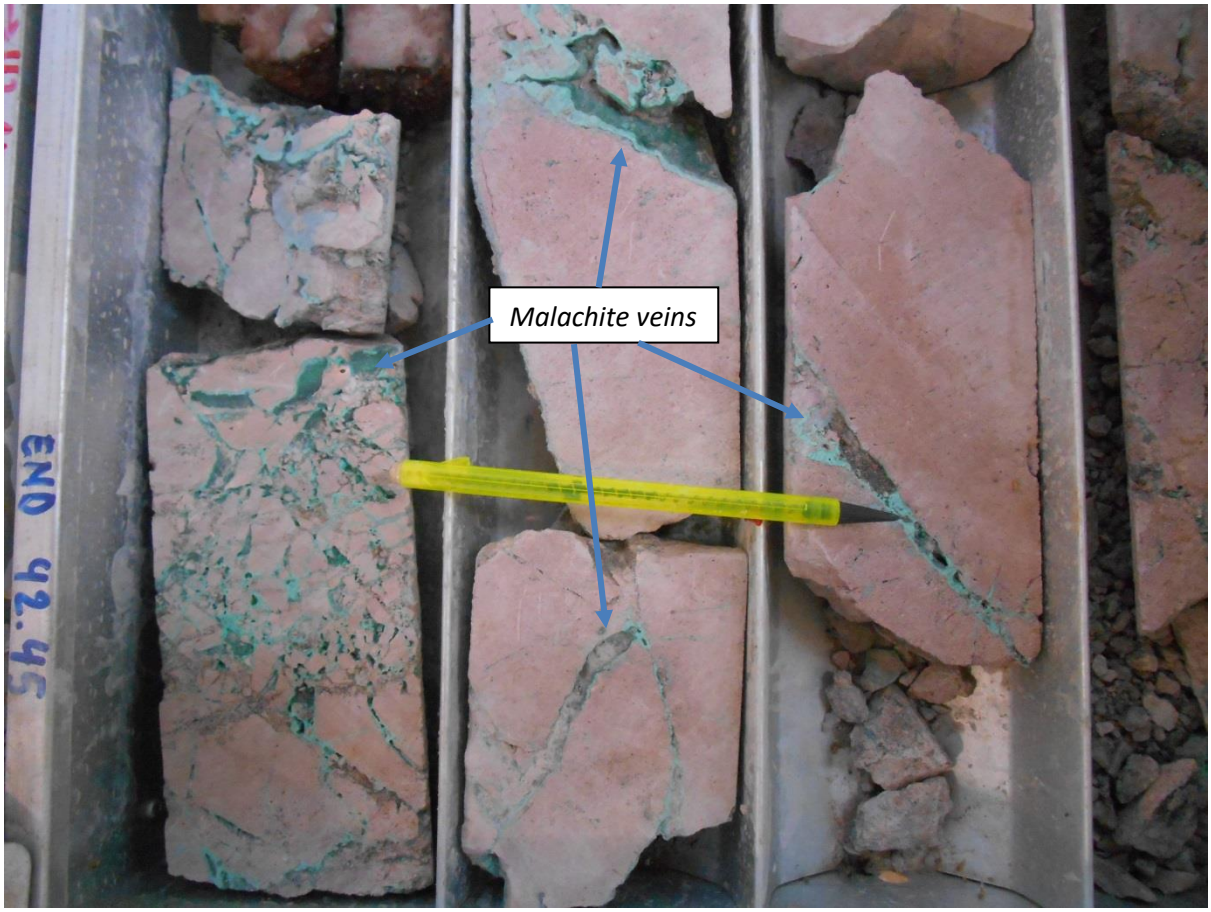

Figure 3.41: *Fracture-hosted botryoidal malachite in the red sandy siltstone. P.Q. core size for scale.*

As well as fracture-hosted malachite in the supergene oxide zone, dark, sooty, friable material found just below the wavy-laminated silica-clay rock near the top of the profile (~7m depth) may be very fine grained Co and/or Mn oxides.

MSSD140 contains a leached zone (<~33m), and a supergene oxide zone (~33m-~46m), but there does not appear to be any supergene sulphide zone, transition zone, or hypogene zone, suggesting that the mineralisation here represents the furthest end-member of supergene mineralisation.

No structural features other than bedding-foliation and localised in-situ protobrecciation were observed in MSSD140.

3.4 Discussion

This section will examine and synthesise observations from fieldwork and core logging and attempt to relate them to geological processes and the established literature.

3.4.1 Stratigraphy

Through the logging of holes MSSD075, 080, 083 and 140, it appears that the stratigraphy is in agreement with the interpretations of workers from Comide S.P.R.L., that the Mashitu South deposit is a fragment of Mines Subgroup stratigraphy. One of the early descriptions of the Mines Subgroup stratigraphy (Oosterbosch and Schuiling, 1951) in the nearby area of Fungurume, corresponds very well to the lithological sequence observed during logging. From top to bottom in MSSD075, 080 and 083: the upper, carbonaceous micritic dolomite is equated to the C.M.N. unit, the mottled red-green dolomitic argillite and intervening black shale with the S.D., the stromatolitic, siliceous crystalline dolomite with the R.SC., the wavy laminated, siliceous dolomite with the R.S.F., the bedded, micritic dolomite with cherty layers to the D.Strat, the green sandy siltstone to the R.A.T. Gris, and the red sandy siltstone to the R.A.T. Rouge (see Appendices 3a, 3b and 3c). In MSSD140 the hole appears to collar in R.S.F. that has been highly weathered, leaving nothing behind but the silica laminations and clay, before descending into the R.A.T (Appendix 3d).

The lithological sequence observed in the four holes also corresponds with more recent systematic descriptions of the Mines Subgroup (R1) and R.A.T. (R2) stratigraphy in the region (e.g. Cailteux *et al.*, 2007; Woodhead, 2013; Broughton, 2014). In these recent descriptions of Mines Subgroup terminology, the D.Strat, R.S.F. and R.S.C. make up the Kamoto Dolomite Formation, the S.D. comprises the Dolomitic Shales Formation, and the C.M.N. is equivalent to the Kambove Formation.

An interpretation of the correlations of the Mines Subgroup stratigraphy in holes MSSD075, 080 and 083 is shown in Figure 3.42. MSSD140 is not included in this correlation as the hole intersects only the lowest units of the Mines Subgroup and the underlying RAT. The stratigraphy of the upper fragment of Mines Subgroup in MSSD083 seems greatly condensed in thickness, perhaps owing to its location in proximity to the NW-SE-running fold axis of an anticline which folds the upper fragment at Mashitu South. This anticline could have caused MSSD075 and 080 to intersect the units at a higher angle and could have exaggerated their thickness. MSSD083 hole also intersects a lower fragment of Mines Subgroup, which the upper fragment is believed to have been thrust over the top of.

The only deviation made from the Comide (S.P.R.L.) logging in the interpretation of the stratigraphy is in the assignment of the S.D.1a, 1b, 2a, 2b, 2c, 2d, 3a and 3b units to the Dolomitic Shales Formation/ S.D. unit. The only true continuity in the lithologies of the S.D. logged between MSSD075, 080 and 083 was the 'black shale' unit, appearing in all three holes roughly equidistantly in the middle of the S.D. All other 'marker horizons' could not be traced with any continuity between different holes. Comparison to Comide logging identifies this black shale unit as the S.D.2.d. Three 'sub-units' of the Dolomitic Shales Formation/S.D. are therefore distinguished, which are used in all further descriptions and analysis of the geology of Mashitu South in this thesis. The rocks above this black shale are designated the S.D.S., the intervening black shale unit is assigned to the S.D.2d. and the lithologies below are designated the S.D.B. These terms are borrowed from the somewhat outdated Gecamines terminology of the Schistes Dolomitique Superieur (S.D.S.) and Schistes Dolomitique du Base (S.D.B.) units, but they are the most descriptive for the Dolomitic Shales Formation at Mashitu South and there appears to be little stratigraphic justification to separate these units further into S.D.1a, 1b, 2a, 2b, 2c, 2d, 3a and 3b units.

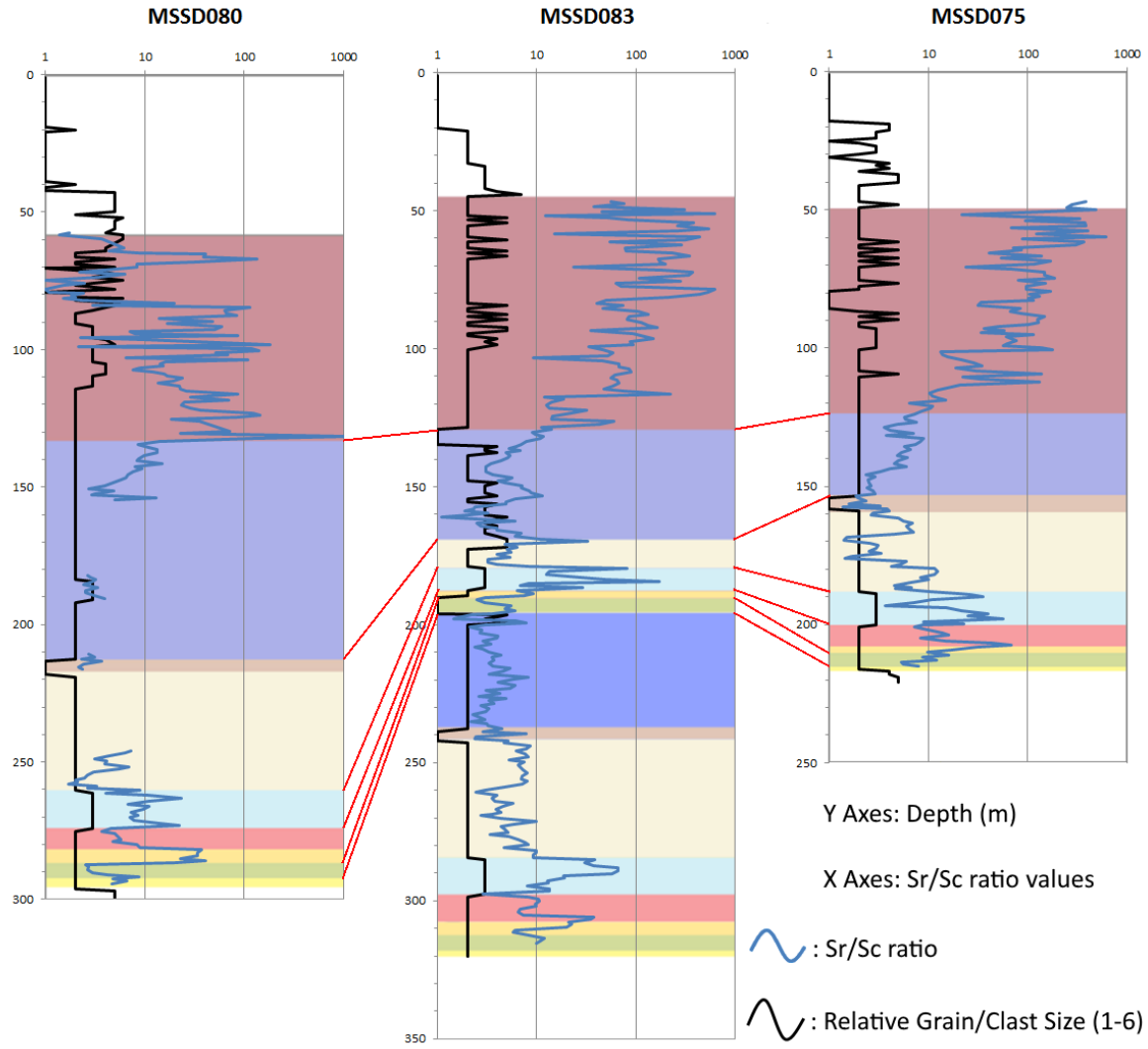

Figure 3.42: *Interpreted correlation of Mines Subgroup stratigraphy between the MSSD075, MSSD080 and MSSD083 drill-holes arranged in order (left to right, SSE to NNW) of their collar position on the Mashitu South Mines Subgroup fragment. Collar locations of these holes are given in Figure 3.8. This interpretation is based on logs of these holes presented in Appendix 3, using lithological similarities, the Sr:Sc ratio (see Chapter 5) and clast/grain size of the rock units. Red lines indicate correlation between different stratigraphic units across the holes, the blue line indicates Sr:Sc ratio of samples taken from the drill core, which was found to be a useful tool for correlating stratigraphy (see Chapter 5) and the black line represents grain/clast size. The blue line is broken in MSSD080 at intervals where the core was not sampled. Stratigraphic units are represented by colours on the graph: see Figures 1.4 and 3.4 for a key. These units are, from bottom to top, the RAT Rouge (yellow), the RAT Gris (green), the DStrat (orange), the RSF (red), the RSC (pale blue), the SDB (beige), the SD2d (brown), the SDS (dark blue) and the CMN (maroon). Note that a repetition of the stratigraphy in MSSD083 exists, probably induced by tectonic stacking, that cuts out the CMN unit from the lower stratigraphic fragment.*

The interpretation of Broughton (2014) that the R.A.T. Gris does not represent a separate lithological unit to the R.A.T. Rouge and is instead, a simple change of colour induced by metasomatism and varying redox conditions, is agreed with. This conclusion is made on the basis that the mineralogy and lithology of both units is essentially the same, and because the transition between the units is always gradational and never sharp, with irregular red-green mottling found in both the R.A.T. Gris and Rouge. However, for logging purposes, the author supports the logging of the R.A.T. Gris as separate to the R.A.T. Rouge because, despite the gradational contact, there is always 'R.A.T. Gris' below the Mines Subgroup, and it is occasionally host to hypogene sulphide mineralisation. Hypogene sulphide mineralisation was not found in any intersection of the R.A.T. Rouge.

When considering a sedimentological environment of deposition for the sequence, the correlation of the lithologies of the four holes with the R.A.T. and Mines Subgroup Subgroups suggests that the interpreted regional environment of deposition for these units is applicable (see section 1.3.2: The Roan Group). The R.A.T. is interpreted to have been deposited as a lowstand systems tract (Bull *et al.*, 2010) in a continental, siliciclastic red-bed environment, perhaps sabkha-dominated, with some development of evaporites (Hitzman, 2015b) evidenced at Mashitu South by enterolithic textures within the R.A.T. Gris (Figure 3.13). A sea-level transgression event caused the deposition of the Kamoto Formation, transitioning from a shore-face intertidal environment to a back-reef lagoonal environment in the D.Strat and R.S.F. units, with the R.S.C. recording the reef environment itself (Bull *et al.*, 2010). The Dolomitic Shales Formation represents further transgression and water deepening from the calcareous Kamoto Formation, into a continental slope environment. The S.D.2d. black shale unit records deep, anoxic water conditions and is considered to be a maximum flooding surface by Bull *et al.* (2010) with the remainder of the S.D.S. therefore deposited in a highstand systems tract. The Kambove Formation records a sea-level regression from the highstand systems tract of the S.D.S. into a sequence of deep and then supra-tidal carbonates. According to Bull *et al.* (2010) there is a minor transgression which deposited sub-tidal carbonates in the middle of the Kambove/C.M.N., followed by a regression and a return to supra-tidal carbonates in the upper C.M.N. The wild variations in the lithologies of the C.M.N. logged at Mashitu South certainly record a turbulent depositional history.

The logging of MSSD075, 080 and 083 also confirms the interpretation of Comide S.P.R.L. that the eastern end of the deposit is underlain by another fragment of Mines Subgroup, tectonically repeated (Chimvinga, pers. comm., 2014). Similarities between the stratigraphy in the two hypothesised 'blocks' are obvious (see Appendix 3c) and the nature of the breccia between them is highly suggestive of a faulted contact being responsible for the repetition. The hypothesis that one fragment or another is actually a mimetic stratigraphic sequence conformably overlying or underlying the Mines Subgroup is rejected, as neither the overlying Dipeta (R3) or the underlying R.A.T. (R1) are anywhere reported to contain a stratigraphic sequence that so closely resembles the Mines Subgroup (R2) (Cailteux *et al.*, 2007) and this, together with the intervening breccia unit, suggests a tectonic repetition.

3.4.2 Structure: Nature of the Mashitu Complex Breccias

The total lack of pervasive tectonic fabric, in the form of any tectonic foliation within the rocks at Mashitu South, suggests that the breccias which are assumed to surround fragments of Mines Subgroup accommodated the vast majority of deformation within the Mashitu Complex and probably within the entire Roan Group during the Lufilian orogeny. The less competent breccias were likely to have behaved more fluidly than the more competent Mines Subgroup, preventing the accumulation of stress necessary to cause tectonic foliation expected in the standard course of events during an orogeny. Whether these breccias were formed before or during the orogeny will be discussed briefly here.

Several types of breccia were distinguished by fieldwork at Mashitu North and core logging at Mashitu South. First, the proto-cataclasites, cataclasites and ultra-cataclasites as described by Cheshire (2014) within the Mashitu North and Principal pits are recognised. However, these terms are abandoned in descriptions used in this thesis as the cataclasite terminology was deemed to imply too much genetic relation to pure tectonic faulting, while the formational processes of these breccias are still poorly understood. The focus of this thesis was not on categorising and understanding brecciation, but the following breccia types were observed:

1. Clast-supported monomictic protobreccia, equivalent to the proto-cataclasites of Cheshire (2014). This breccia type is assumed to be formed in the 'damage envelope' in

the vicinity of a fault surface or breccia conduit. The rock is fractured but very little movement has occurred (Cheshire, 2014; Cheshire pers. comm., 2014).

2. Dolomite-vein-supported monomictic protobreccia (see Figure 3.10): this breccia type may form in similar circumstances to its clast-supported equivalent, described above, but, additionally, hydraulic fracture of the rocks by a pressurised fluid may also have been implicated in its genesis. Essentially this rock is thought to be a crackle-breccia, with the fluids precipitating dolomite within the cavities left by hydraulic fracture (Woodcock and Mort, 2008). The dolomite veins supporting the clasts of this breccia type appear similar in form to Type 2 dolomite veins (Figure 3.29). The change from a high density of Type 2 dolomite veining and a vein-supported protobreccia is gradational (Figures 3.38 and 3.39), suggesting that Type 2 dolomite veins and these protobreccias may be genetically related.

3. Clast-supported polymictic breccia (see Figure 3.43): this breccia type is inferred to occur along the margins of movement zones, where the larger clasts, which are less susceptible to transport, accumulate.

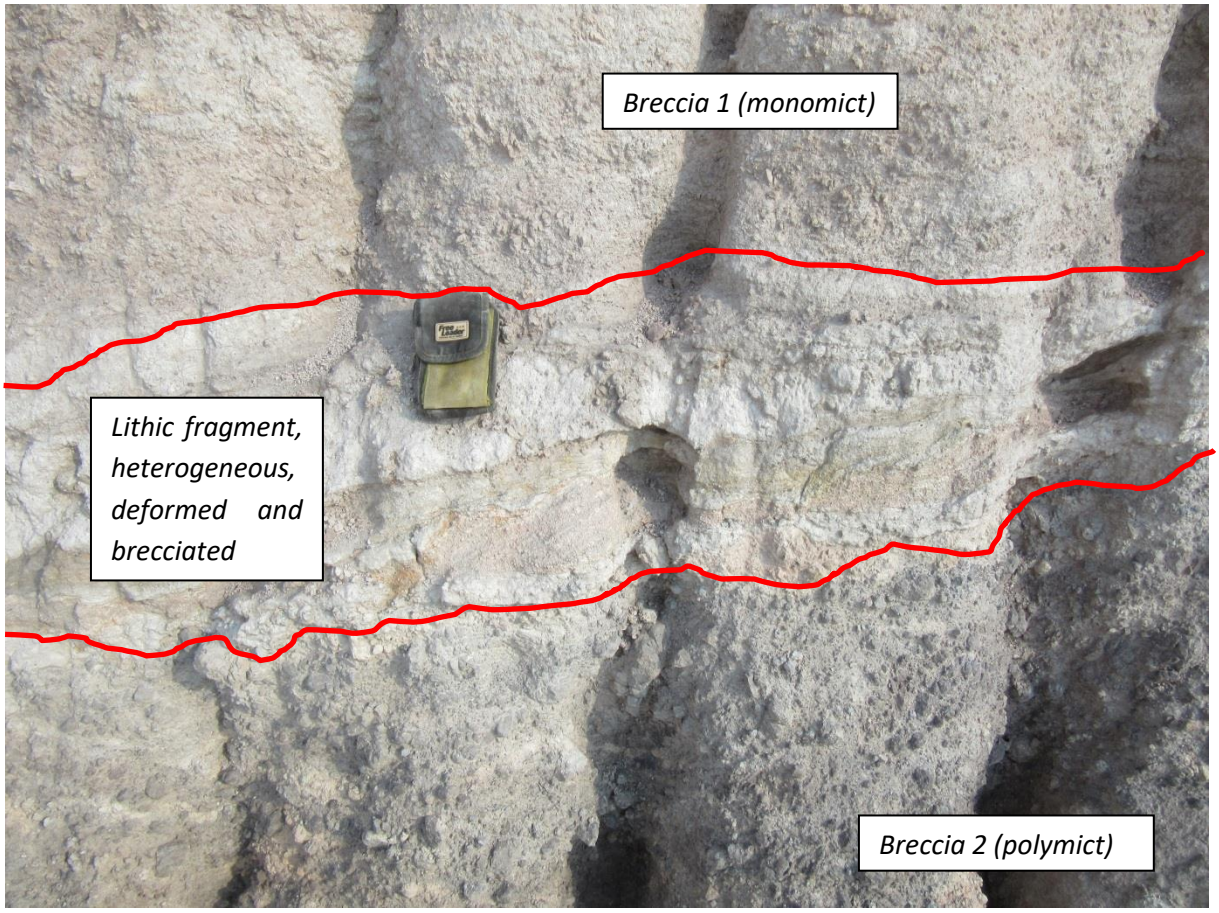

Figure 3.43: *A rock face on the north side of Mashitu Principal pit showing multiple generations of breccia. There is a clast supported monomictic breccia (top) above a deformed lithic fragment (middle) and a clast-supported polymictic breccia (bottom). Camera case for scale.*

4. Matrix-supported polymictic breccia (Figures 3.11 and 3.44): equivalent to the 'ultra-cataclasite' of Cheshire (2014), this breccia type is thought to form in the central portions of movement zones, where transport and grinding processes are stronger and finer-grained particles are more common as a result. Rounding of larger clasts is common in this type of breccia.

Figure 3.44: *A rock face on the north side of Mashitu Principal pit showing a large unit of polymictic, matrix-supported breccia. Hammer for scale.*

These four breccia types have complex inter-relations, cross-cutting and incorporating clasts of previous breccias within each other and having no consistent order of formation between the breccia types (Figure 3.45). These complex breccia histories are suggestive of progressive slip along movement planes, with alternating kinetic and hydraulic brecciation events over time, creating a complex series of breccias-within-breccias. This sequence is similar to interpretations of 'palaeoseismites' made elsewhere in the Copperbelt (Master, 2003; Master, pers. comm., 2014).

A more comprehensive study on breccia types, brecciation fabrics, their possible genetic origins and their relation to mineralisation, written on the adjacent Mashitu North and Mashitu Principal deposits, can be found in Byrne (2017), who interprets many of the features observed in this study as the result of halokinetic, diapiric processes.

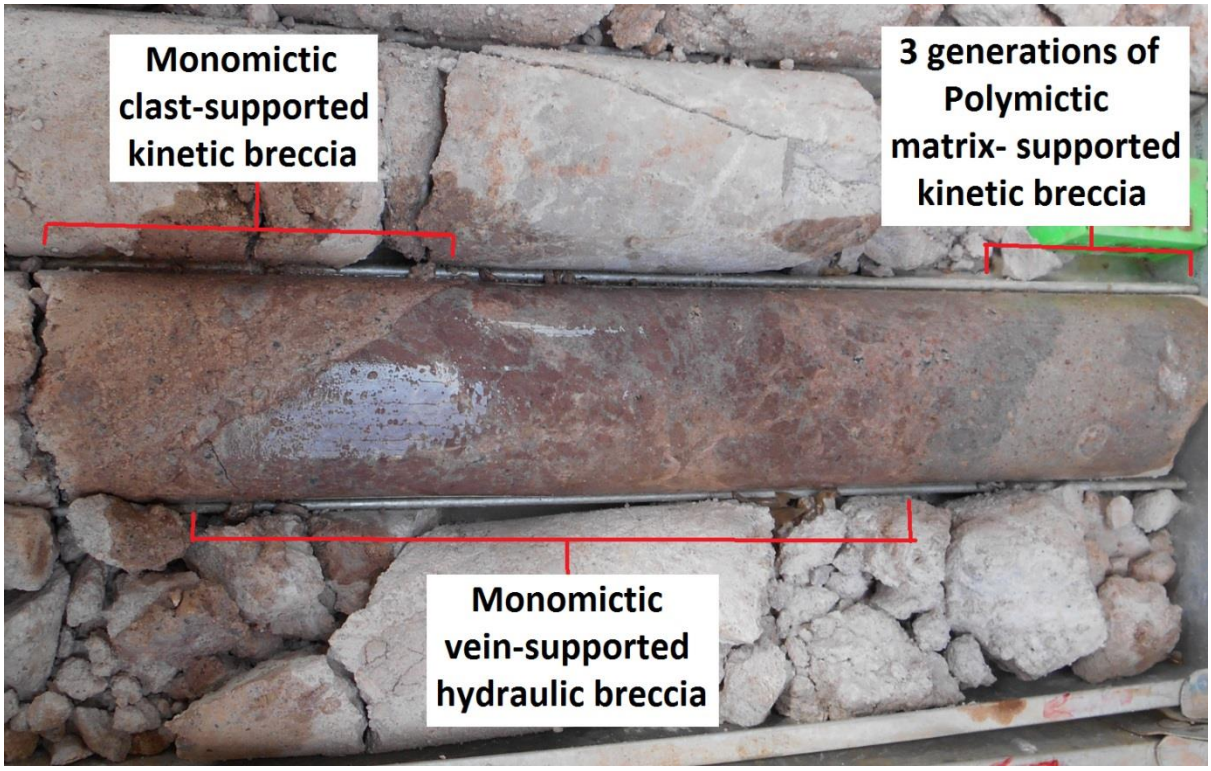

Figure 3.45: *Multiple generations and types of breccia from a hole from Mashitu North. Complex cross-cutting relations are observable, and different generations of breccia are included as clasts within other breccia generations. H.Q. sized core for scale.*

It should be noted that some workers give sedimentary, rather than tectonic or halokinetic interpretations for genesis of some of the polymictic, matrix-supported breccias in the Mashitu Complex, particularly where foliations within the breccias are apparent. For example, Master (pers. comm., 2014) and Dalton (pers. comm., 2015) interpret the breccia pictured in Figure 3.44 as foreset beds of a turbidite.

A definitive genetic origin for the breccias would be presumptuous to conclude based on the limited amount of work done on them as part of this thesis. However, some evidence for the timing of brecciation relative to tectonic deformation is found by examining the geological map of the Mashitu Complex (Figure 3.4). These two fragments are separated by a breccia but, the stratigraphy can be traced across this breccia. This suggests that although displacement between the two has occurred, there has not been a huge dislocation and the two fragments remain almost in-situ relative to each other. This interpretation, together with an eastward plunging fold axis, would fit with the ESE-WNW anticline at Mashitu South curving towards the northwest at the western end of the deposit and continuing through

Mashitu North, accommodating the hypothesised eroded Mines Subgroup fragment that overlay the R.A.T. there (Chimvinga, pers. comm., 2014).

Given that the Mashitu South Dome and the Mashitu Principal basin structures are both cross-cut and separated from each other by breccia, it is assumed that folding occurred prior to brecciation. It would follow that whatever caused the 'megabrecciation event', be it halokinesis, cataclastic tectonics, or olistostrome processes, occurred post-folding. Whether this perpendicular folding was formed by two separate deformation phases or, perhaps more likely, by the constrictional D2 deformation phase of Kampunzu and Cailteux (1999), is unknown (see Figure 1.9). This interpretation is not in agreement with the Jackson *et al.* (2003) diapiric model for megabrecciation, where diapirism occurred during the sedimentation of the Nguba and Kundelungu Groups between ~730 Ma (Kampunzu *et al.*, 2009) and ~573 Ma (Masters *et al.*, 2005), given the ~550-500 Ma age for the progression of the Lufilian orogeny (Kroner and Stern, 2005). Alternative explanations for the brecciation could be:

1. That diapirism and megabrecciation occurred during the Lufilian orogeny, post D2.
2. Megabrecciation was facilitated by tectonic processes during the Lufilian orogeny, post-D2, with faulting and perhaps rheid flow of breccia assisted by evaporites along decollement planes, such as in the Alpine orogeny (Malavieille and Ritz, 1989).
3. That dome-and-basin folding of the Mines Subgroup was somehow caused by diapirism. Structural 'domes' such as Mashitu South were created above ascending diapirs, with basins such as Mashitu Principal formed in between ascending diapirs, and brecciation events somehow occurred late in the mobilisation of diapirs.
4. That local breccias cross cutting the folding structures are not formed contemporaneously to the large scale 'megabrecciation' observed throughout the 'Mashitu Diapir'.

The most plausible genetic explanation for the formation of the Roan megabreccias in the Mashitu Complex appears to lie in between a mixed halokinetic and 'traditional tectonic' theory. Syn-orogenic thrust faulting along decollement planes centred on interbedded evaporite units which may have existed in the R.A.T. (R1) and Dipeta (R2), as well as local diapirism of the evaporites within these units where they concentrated, would explain the breccia features observed during fieldwork and logging (Figure 3.46). Pre-Lufilian diapirism

of speculative thick units of evaporite (>100m thick) (Jackson *et al.*, 2003; Hitzman *et al.*, 2012; Hitzman, 2015b) is rejected as a hypothesis, as is breccia formation by 'dry' fold-and-thrust tectonics (e.g. François, 1973).

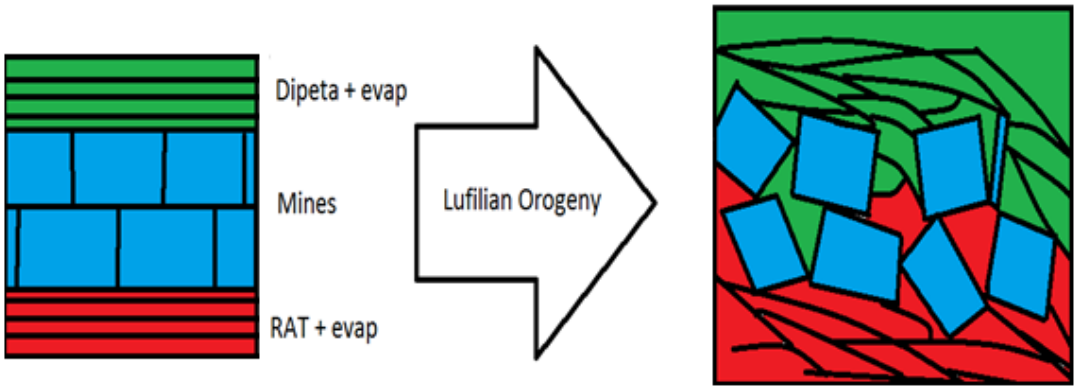

Figure 3.46: *Conceptual illustration for the origin of the Roan megabreccias at the Mashitu Complex. Strain is concentrated in the less-competent, evaporite-interbedded units of the Dipeta and the R.AT. during orogenesis, causing the brittle fragmentation and dislocation of the more competent Mines Subgroup in between.*

3.4.3 Alteration

Several alteration types were identified during fieldwork and core logging, including silicification, dolomitisation, haematisation, and surface-related argillic alteration. Potassic and sodic alteration were inferred based on variations of colour in the R.A.T., however these remain speculative and are investigated further in Chapters 4 and 5. Coincidental links between metasomatism and mineralisation exist. For example, supergene mineralisation is linked to argillic alteration, the two being formed by the same process (Brown, 2014) and the supergene oxide zone in MSSD140 is found at the margin of relatively fresh rock and rock that has undergone advanced argillic alteration. The majority of hypogene mineralisation in MSSD075, 080 and 083 is found in proximity to the intense silicification of dolomites in the Kamoto Formation. Also, sulphides are commonly hosted by dolomite veins. However, argillic, silicic and dolomitic alteration types are all too ubiquitous within the target stratigraphy in the region to be used as vectors towards ore.

3.4.4 Mineralisation

3.4.4.1 Hypogene mineralisation: distribution and zonation

Hypogene mineralisation was not observed during any field visit to the pits of the Mashitu Complex, or any other pit in the area, attesting to the strength and depth of weathering which affects the region.

There appears to be two modes of occurrence of hypogene mineralisation in MSSD075, 080 and 083. The first mode is stratiform-disseminated and hosted within Type 1 dolomite veins. Type 1 veins are usually associated with local, probably syn-sedimentary/diagenetic soft-sediment deformation of bedding and have a complex relationship with stratiform mineralisation. These veins cross-cut stratiform mineralisation in some occurrences, but elsewhere appear to grade into stratiform mineralisation which the sediments adjacent to them. Based on this, it appears that Type 1 veins formed contemporaneously to stratiform mineralisation, while the sediments were still unconsolidated. Stratiform-disseminated sulphides and those hosted within Type 1 veins include pyrite, chalcopyrite, bornite, chalcocite and carrollite, all of which are usually very fine-grained. Stratiform sulphides are best developed in the D.Strat, R.S.F. and the base of the S.D.B. units, where chalcocite and carrollite are dominant and relatively abundant (see Figure 3.47). Upwards into the S.D., chalcopyrite and pyrite become the more prevalent sulphides and stratiform mineralisation is less abundant, occurring only in more localised, apparently carbonaceous horizons. The S.D.2d is somewhat of an exception within the S.D., being fairly rich in stratiform pyrite and chalcopyrite. Stratiform carrollite, chalcocite and bornite are found in limited quantities and in the lower C.M.N. unit, usually in proximity to silicified dolomite horizons. However, out of the stratiform sulphides, pyrite and chalcopyrite are more dominant in that unit. It should be noted that carrollite is the only definitively hypogene sulphide encountered in the R.S.C. unit, which is otherwise devoid of sulphides (chalcocite is found rimming carrollite in the R.S.C. of MSSD083 but its origin could be supergene, see Figure 3.36). The preferential distribution of chalcocite within the Kamoto Dolomites and pyrite-chalcopyrite within the overlying Dolomitic Shales and Kambove Formation is somewhat indicative of the 'bottom-upwards' zonation of Cc → Bn → Cpy → Py from a redox horizon, in this case the R.A.T. Gris-R.A.T. Rouge transition, which would be expected in an S.S.C. type deposit (Brown, 2014; see Figure 2.6). The distribution of

carrollite, however, in particular its association with the R.S.C., R.S.F. and silicified horizons within the C.M.N. unit, is more indicative of a Fay and Barton (2012) type model of distribution (Figure 2.5) where mineralising fluids are transported along the R.S.C.. This model is adapted well by van Langendonck *et al.* (2013) to account for the mineralisation in the lower C.M.N. at the Kambove West deposit (Figure 3.48).

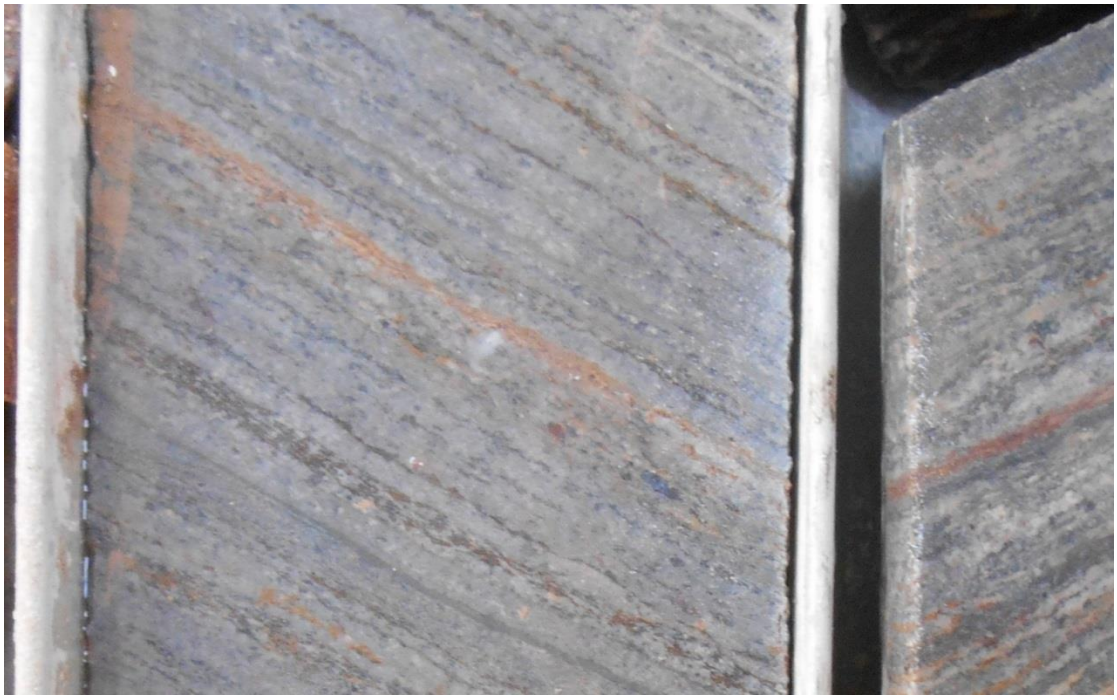

Figure 3.47: *Stratiform mineralisation in the R.S.F. unit in MSSD075. Disseminated chalcocite is visible with a metallic lustre and dark-blue-to-violet sheen. H.Q. core size for scale.*

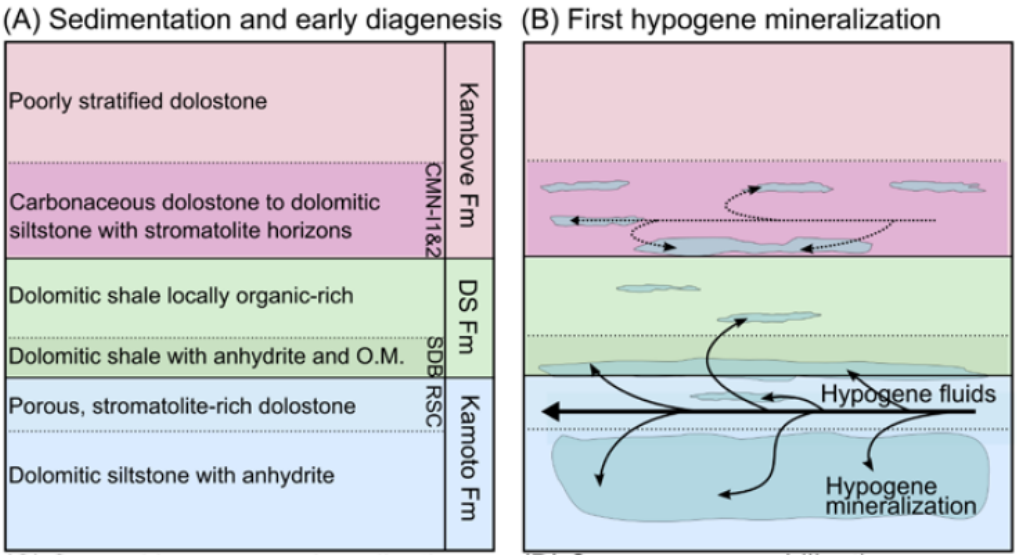

Figure 3.48: *Stratiform mineralisation model for Kambove West from van Langendonck et al. (2013) This model fits the distribution of carrollite at Mashitu South well (but not other Cu sulphides).*

In general, the stratiform mineralisation appears to share many characteristics with the first stage of hypogene mineralisation identified by workers in the region (Dewaele *et al.*, 2006a; Muchez *et al.*, 2008; El Desouky *et al.*, 2009). However, stratiform carrollite, with its distinct association with silicic rocks and non-conformance to the distal-to-redox-horizon distribution expected of Co-sulphides in a stratiform mineralising system (Broughton and Rogers, 2010), does not fit in well. It is possible that stratiform carrollite has a slightly different mode of distribution and perhaps genetic origin to other stratiform Cu-sulphides.

The second mode of occurrence of sulphides occurs within Type 2 dolomite veins. As described earlier, Type 2 veins are generally wider and more extensively cross-cut the stratigraphy than Type 1 veins. They also cross cut stratiform mineralisation (see Figure 3.49). Mineralogically the veins may contain pyrite, chalcopyrite, bornite, chalcocite and carrollite, with gangue dolomite and minor quartz. At the core-logging scale, there is no real zonation of these sulphides and no apparent stratigraphic preference for the distribution of Type 2 veins, which cross-cut the Mines Subgroup stratigraphy fairly indiscriminately. The Type 2 veins which cut the R.A.T. Rouge, however, do not contain sulphides (though they may contain specular haematite, it is uncertain whether this haematite is of hypogene or supergene origin). The sulphides hosted by Type 2 veins appear to be volumetrically minor in comparison to those related to stratiform mineralisation. Clear cross-cutting relationships between Type 2 veins and stratiform (or Type 1 vein-hosted) mineralisation suggests that this stage of mineralisation occurred later than the stratiform stage. It is therefore equated with the 'vein-type' mineralisation described by Dewaele *et al.* (2006a).

Fine-grained stratiform-disseminated pyrite, hosted predominantly within the S.D. and D.Strat units and not always associated with mineralisation (Figure 3.50), could be an early diagenetic, pre-stratiform Cu-Co phase. According to Annels (1974) several horizons in the Mines Subgroup contain such a phase, which is implicated by later studies (e.g. El Desouky *et al.*, 2009) as being the sulphur source for the mineralising fluids which formed later stratiform Cu-Co. This hypothesis is investigated further in Chapter 4.

It should be noted that chalcocite is known to be formed by either hypogene or supergene processes and at the core-logging scale there is no way to definitively conclude one origin or the other. Inference of a supergene origin can be made based on weathering indicators, such as haematitic or argillic alteration in close proximity to the chalcocite.

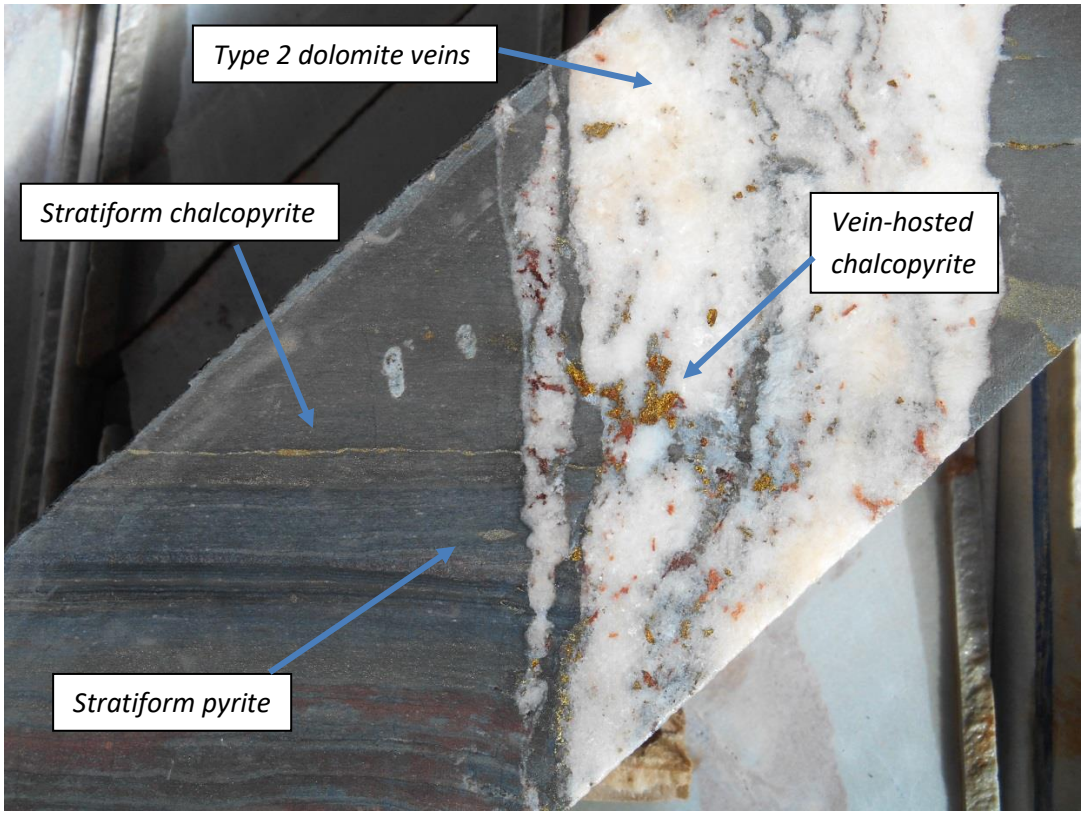

Figure 3.49: *Stratiform-disseminated pyrite and chalcopyrite cross-cut by Type 2 dolomite veins which host chalcopyrite and possibly carrollite, within the S.D.B. of MSSD080. H.Q. core size for scale.*

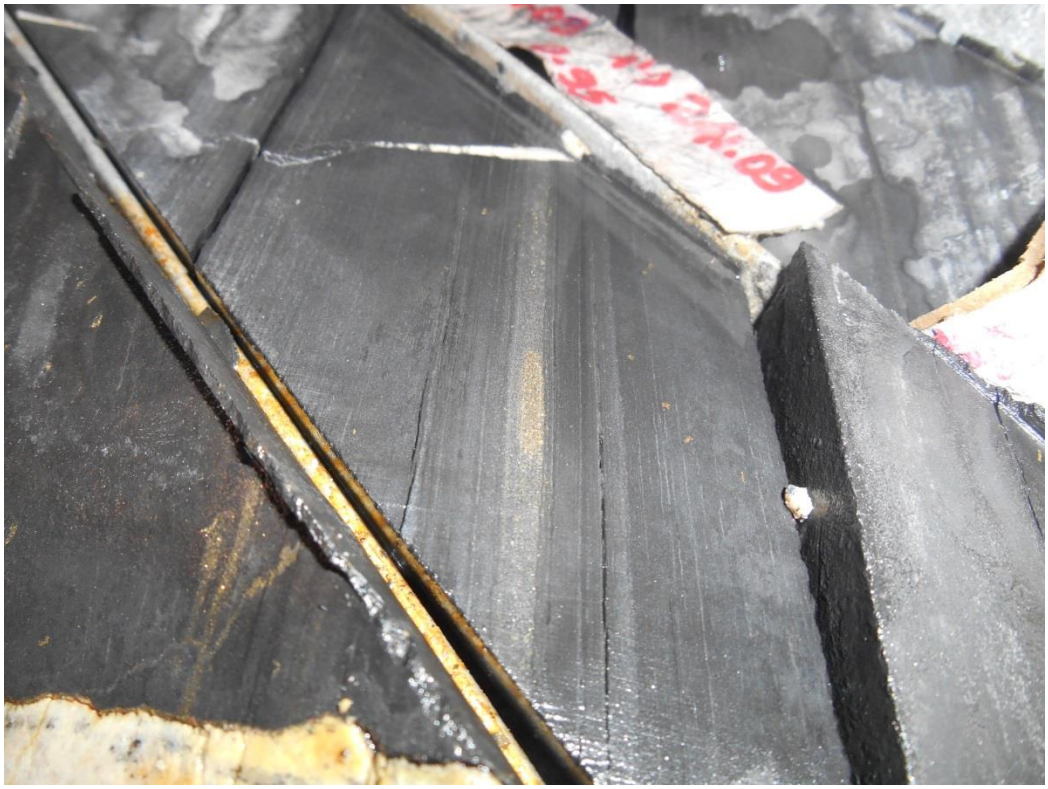

Figure 3.50: *Stratiform-disseminated pyrite in the SD2d of MSSD083. Note the bedding-sub-parallel type 1 veinlets in the bottom left-hand corner.*

3.4.4.2 Supergene mineralisation: distribution and zonation

Supergene mineralisation was found to be abundant both in field visits made to deposits in the area, and in the logging of core from MSSD075, 080, 083 and 140. Malachite (Figure 3.51), heterogenite (Figure 3.52), chrysocolla (Figure 3.53), azurite (Figure 3.54), kolwezite (Figure 3.55), libethenite (Figure 3.56), and pseudomalachite (Figure 3.57) were all identified at or near the surface (in pits) during field visits, while cobaltoan carbonate/spherocobaltite (Figure 3.34), native copper (Figure 3.35) and uranium oxides (Figure 3.36) were found deeper, within drill core. All of these minerals tend to fill vugs, fractures and other voids in their host rock, or they are pervasively disseminated, or they form rims to earlier metal sulphides or oxides, occasionally replacing them in situ. Some of the chalcocite within drill core may be of supergene origin, but it is difficult to be certain without petrographic investigation (see Chapter 4).

Figure 3.51: *Speleothems of breccia-hosted malachite in the Mashitu Principal pit. Pencil for scale.*

Figure 3.52: *Sub-botryoidal heterogenite in the Mashitu Principal pit. Hammer for scale.*

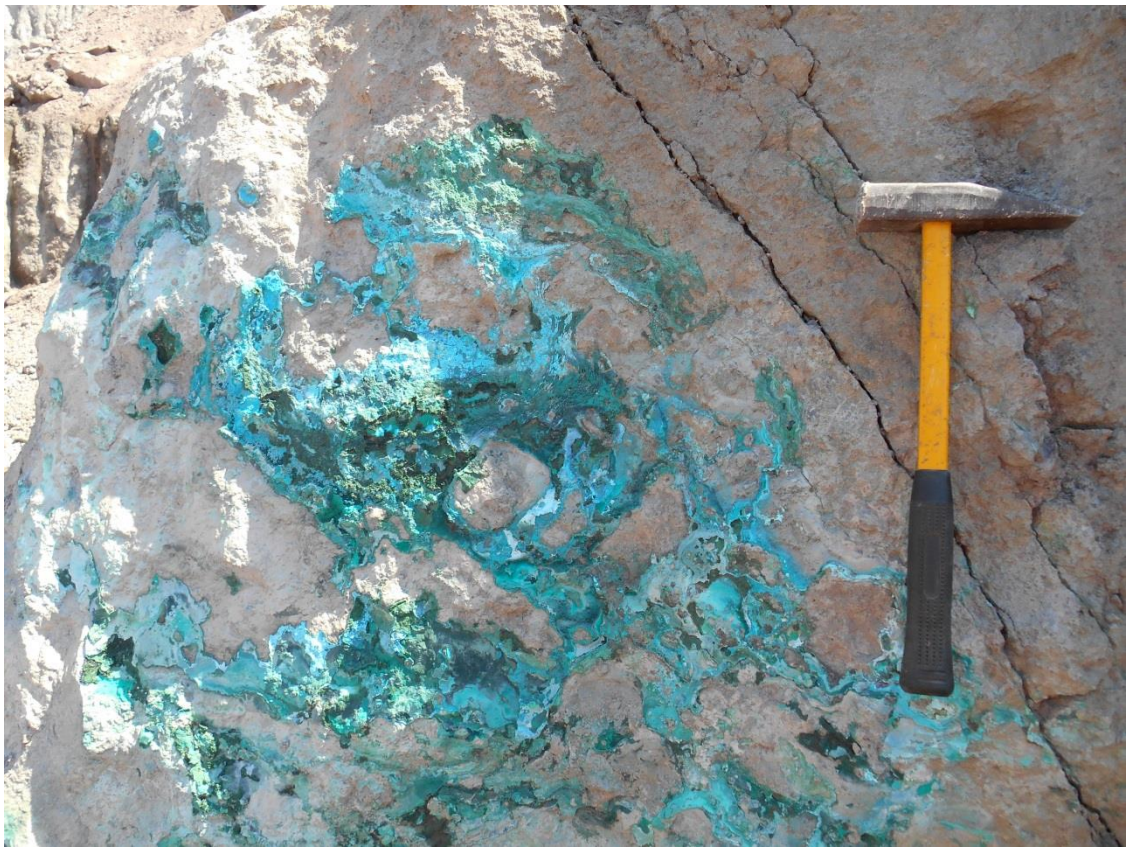

Figure 3.53: *Fracture-hosted malachite and chrysocolla in the Mashitu North pit. Hammer for scale.*

Figure 3.54: *Black-shale hosted azurite in the Kabolela pit. Hammer for scale.*

Figure 3.55: *Kolwezite (green) and heterogenite (black) in the RSF unit at the Anticline deposit, near the Mashitu Complex. Pen for scale. Photo courtesy of Joseph Chimvinga.*

Figure 3.56: *Libethenite from the Mashitu North pit. Fingers for scale.*

Figure 3.57: *Pseudomalachite and malachite from the Kakanda North pit. Fingers for scale.*

There appear to be two main controls on the distribution of supergene mineralisation in the region. First, permeability plays an important role. The highest intensity of supergene alteration and mineralisation can be found in breccias and within the R.S.C. unit. Dissolution of coarse crystalline dolomite within the R.S.C. by supergene (or hypogene) fluids, leaving just the vuggy, silica framework, creates a unit which is extremely permeable to meteoric fluids, to the extent that the unit is locally used as an aquifer (Robertson, pers. comm., 2014). Similarly, the large clast size, abundance of fracturing, lack of cementation, or cementation of the unit by easily-dissolved minerals like carbonates, makes many breccia units very permeable. This conclusion is echoed by Byrne (2017) at the adjacent Mashitu North and Principal deposits. This results in supergene mineralisation within, and in proximity to, these lithologies at greater depths than would otherwise be achieved through less permeable rocks. A model for distribution of supergene ore along the R.S.C. unit was given by Fay and Barton (2012) and presented as Figure 3.58. This model is equally applicable for breccia-related supergene mineralisation. According to De Putter *et al.* (2010), karstification is an important process in the development of permeability, however logging and fieldwork has not revealed any link between carbonate rocks and the development of mineralisation.

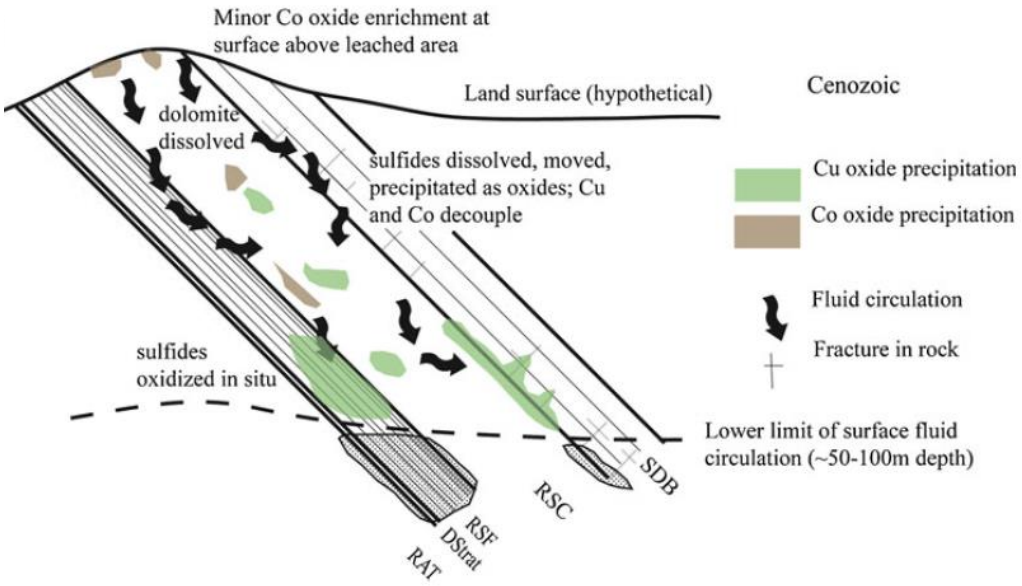

Figure 3.58: *Model for the distribution of supergene mineralisation in and around the R.S.C. stratigraphic unit at Tenke-Fungurume. This model can be applied equally to other permeable lithological units, such as permeable breccias. From Fay and Barton (2012).*

The second major control on supergene ore formation is the availability of metals. In holes MSSD075, 080 and 083, supergene ore is not as well developed as within MSSD140 where a continuous orebody of concentrated, fracture-hosted malachite exists between a depth of ~33m and ~46m. The orebody in MSSD140 is hosted in the R.A.T. Rouge, not ordinarily a host of Cu-Co mineralisation. However, it is hypothesised that metals have been leached from above, from Mines Subgroup which originally overlaid MSSD140 but has since been eroded away (refer to the geological map in Figure 3.8). The wavy-laminated silica-and-clay rock found near the top of MSSD140 appears to be a highly weathered version of the wavy-laminated silicified dolomite of the R.S.F. unit found in MSSD075, 080 and 083 (compare Figures 3.15 and 3.37). After leaching, metals travelled downwards through permeable strata until their transporting fluids were reduced and neutralised to the point where they precipitated as oxides (see Figure 2.10), probably at and below the water table. This leaching process was probably gradual and progressive, but must have outpaced physical erosion of the overlying rocks in order for the mineralisation not to be transported away and scattered by surface processes. Mineralisation beneath this central part of the Mashitu South domal fragment is therefore thought to be analogous to the para-exotic supergene mineralisation at Mashitu North.

By contrast, supergene mineralisation is perhaps not as well developed in MSSD075, 080 and 083 because of their relative lack of availability of metals. MSSD140 has had a whole sequence of Mines Subgroup above it exposed to near surface processes and leached, whereas in MSSD075, 080 and 083, the Mines Subgroup is present at depth and was likely not to have been affected by the same intensity of supergene alteration. Less metal is thus available for supergene fluids to leach and reprecipitate in the eastern, deeper portion of the Mashitu South deposit. One would therefore not expect to find any great supergene orebody similar to the one intersected in MSSD140 here, nor in the R.A.T. below MSSD075, 080 and 083. Although these para-exotic supergene deposits are not well developed in the Mines Subgroup, in-situ supergene alteration of hypogene orebodies, such as the one in the Kamoto Dolomite, is common. Figures 3.59 and 3.60 show the in-situ development of supergene oxide ore in the D.Strat and R.S.C. units, at the expense of all hypogene mineralisation.

Figure 3.59: *Nodular D.Strat with in-situ malachite from the Nzilo deposit. Hammer for scale.*

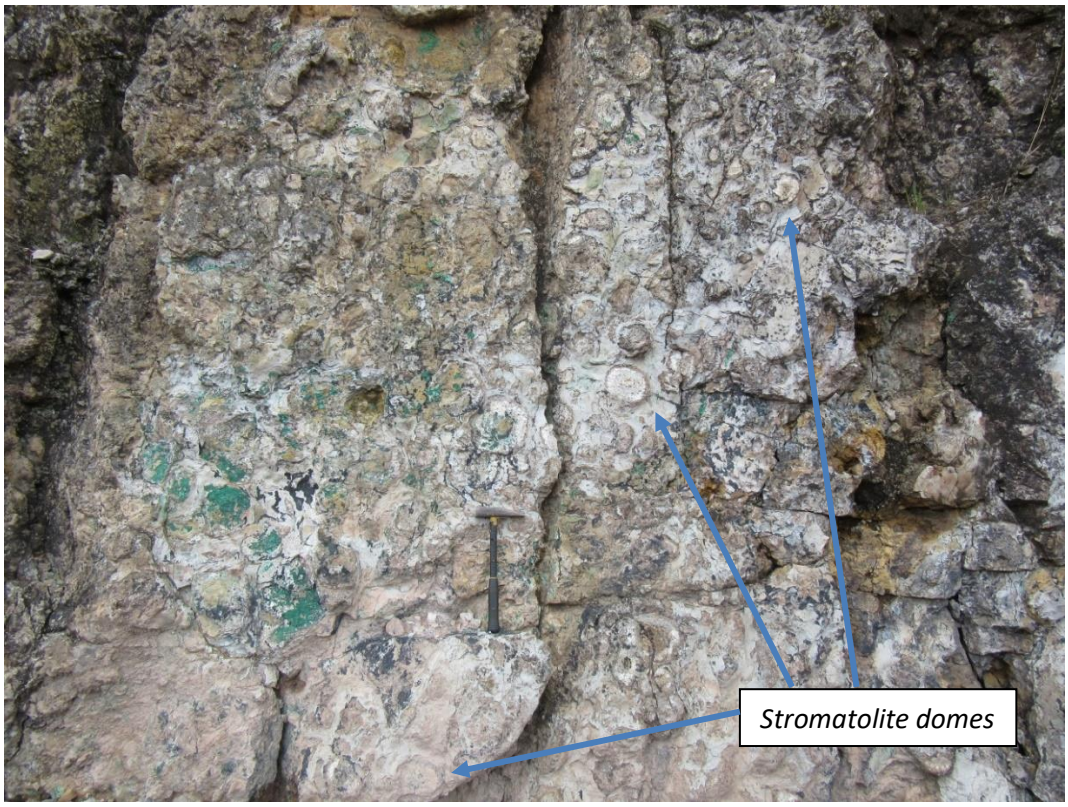

Figure 3.60: *In-situ malachite and heterogenite mineralisation in stromatolitic R.S.C. from the Kii deposit. This photo is taken perpendicular to an exposed bedding surface, showing the domal tops of fossilised stromatolite mounds. Hammer for scale.*

3.4.4.3 The transition from hypogene to supergene mineralisation

Decree *et al.* (2010) describe how the lower solubility in meteoric fluids of cobalt, compared to copper, creates decoupling of Cu-Co when hypogene Cu-Co sulphides are exposed to supergene alteration and leaching. Depending on the intensity of leaching, this may result in a residual cap of cobalt-bearing rocks, or the reprecipitation of cobalt oxides higher in the strata (in more oxidising conditions, due to low Co solubility) than copper oxide orebodies. A zonation of Cu and Co is thus expected based on the distance of transport of supergene fluids with proximal precipitation of Co oxides and distal precipitation of Cu oxides.

Evidence for this process was witnessed in the western wall of the Kakanda pit, where a polymictic, matrix-supported 'ultra-breccia' appears to have acted as a conduit for downward-percolating meteoric fluids, which have infiltrated the footwall of the breccia and precipitated out zoned Cu (distal) and Co (proximal) oxides (Figure 3.61).

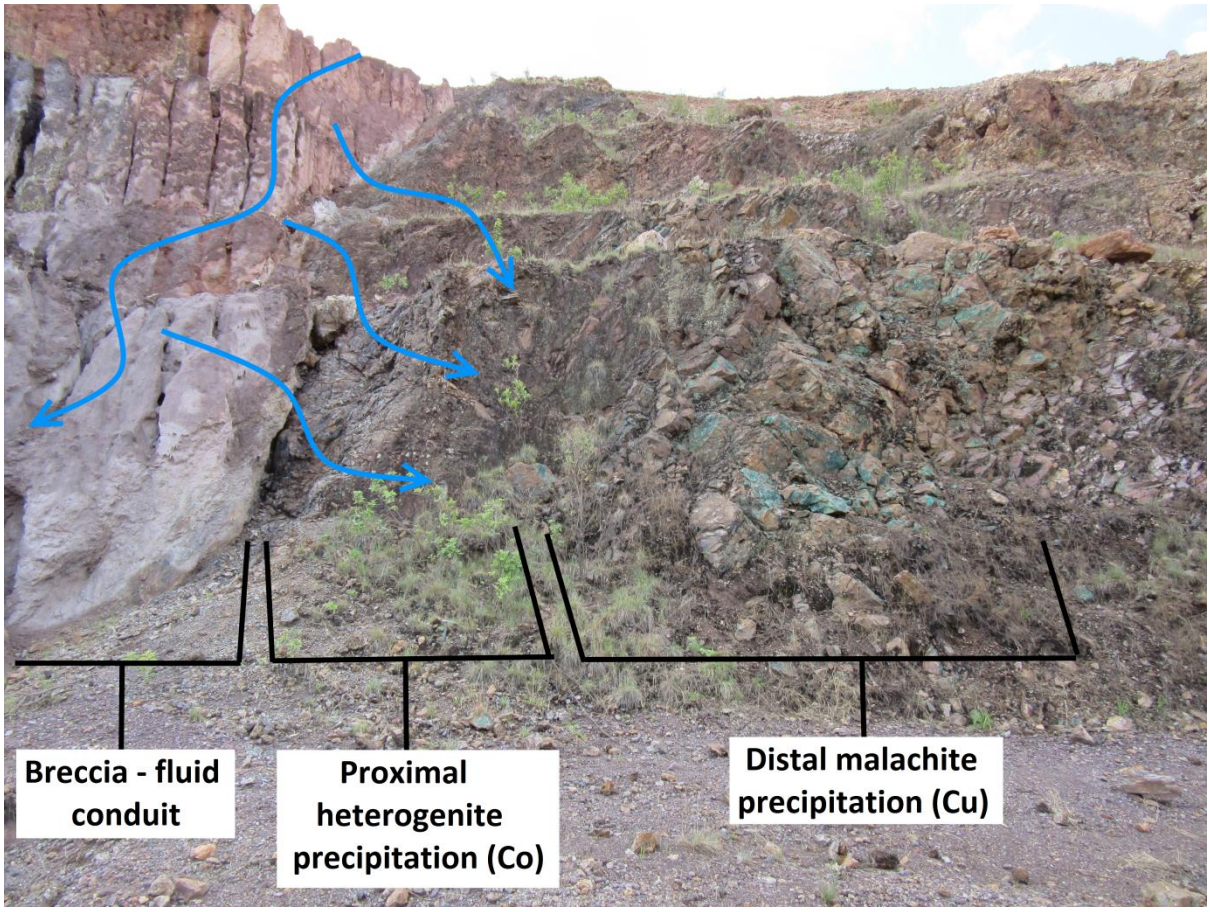

Figure 3.61: *Cu-Co zoning in the supergene environment in the western face of Kakanda North pit. Fluids, travelling down a south-dipping breccia, have infiltrated the country rock, precipitating heterogenite in proximity to the breccia and malachite further away. Benches are 3m high for scale.*

There is a suggestion of 'cobalt caps' occurring within the boreholes of MSSD075, 080, 083 and 140, with all four of these holes displaying cryptic horizons of dark, sometimes friable clay-like material which could be Co oxides near the surface, and significantly above Cu oxide mineralisation. However, these horizons were not mineralogically or spectrographically analysed, meaning that they could not be confirmed as Co-bearing.

The study of Decree *et al.* (2010) focussed on the vertical decoupling of Cu and Co, but it is important to remember that, because of transport of supergene fluids along permeable lithological conduits, supergene decoupling and zonation of Cu and Co will not only be vertical in nature. Inclined dips of such permeable conduits will result in angular and partially lateral zonation as the supergene metal-bearing fluids flow down-dip and infiltrate the surrounding rock. This is also an important consideration with regards to the potential (hypogene) source of metals for supergene mineralisation. For example, given the eastwards dip-direction of the Mines Subgroup on the eastern flank of the Mashitu South deposit (see Figure 3.5), supergene mineralisation in and around the R.S.C. in holes MSSD075, 080 and 083 can be assumed to have sourced and leached metals primarily up-dip from the position of supergene enrichment, from towards the west.

3.5 Conclusions from Fieldwork and Logging

1. The Mashitu South deposit is confirmed as a domal fragment of Mines Subgroup (R2), overlying another, deeper Mines Subgroup fragment on the eastern flank of the deposit.
2. The Mashitu South structural dome and the Mashitu Principal structural basin are likely to have been formed in the D2 constrictional deformation event of Kampunzu and Cailteux (1999) during the Lufilian orogeny. These structures are cross-cut by breccias in the Mashitu Complex, and likely pre-date these breccias. This would argue against an early diapiric, pre-Lufilian model for this brecciation such as that of Jackson *et al.* (2003).

3. Silicification, dolomitisation and argillic alteration are spatially associated with different types of mineralisation, however their ubiquitous nature makes them unreliable as vectors towards mineralisation.
4. Stratiform and vein-type hypogene mineralisation is identified and equated to the classification of Dewaele *et al.* (2006a) of these mineralisation types.
5. The two most important controlling factors on the distribution of supergene mineralisation are metal availability and rock permeability. Breccias, the R.S.C. unit and the R.A.T. (where it was overlain by leached and eroded Mines Subgroup) are identified as good fluid conduits and hosts for supergene mineralisation.
6. Supergene processes have been observed to dissociate metallic components of hypogene ore assemblages, in the form of decoupling of Cu and Co. These metals become vertically (and laterally) zoned as they reprecipitated hydrologically downhill within the supergene environment.

CHAPTER 4: PETROGRAPHY AND PARAGENESIS

STATEMENT: Elements of the work in this chapter contribute to a manuscript in preparation by M. Sośnicka et al. and planned for publication in the journal 'Mineralium Deposita', entitled: "Mineralizing fluids in the supergene-enriched Cu-Co Mashitu South deposit, Katanga Copperbelt, DRC". The work presented in this chapter itself is conducted in its entirety by the author of this thesis.

4.1 Introduction – Aims and Objectives

During logging of holes MSSD075, 080, 083 and 140, quarter-core samples were taken of the diamond drill core and transported to the University of the Witwatersrand for petrographic and sulphur isotope analysis. The primary aim of this exercise was to investigate the mineralogical accommodation of Cu-Co mineralisation in both the hypogene and supergene environments, with particular attention to the paragenetic transition between the two mineralisation types. This deposit paragenesis was used to correlate mineralisation at Mashitu South with regional mineralisation events described in the literature. A secondary, but integrated aim was to investigate gangue phases in these samples, in order to relate mineralisation to alteration events, sedimentary patterns and structural trends.

Many previous petrographic studies have been conducted on Cu-Co deposits in the Congolese Copperbelt, the most noteworthy of which are referenced in Chapter 2. Only one previous petrographic study on the Mashitu South deposit exists, conducted by S.G.S. South Africa (Pty) Ltd. (Ellerbeck, 2011; McLaren, 2011). The results of this study are summarised in section 3.1.5. However, the scope of this study was purely descriptive and limited in extent, and the present study aims to give a more comprehensive and integrated picture of Cu-Co mineralogy at Mashitu South.

4.2 Methods

In total, 105 samples were taken from intervals in MSSD075, 080, 083 and 140, which are summarised in Appendix 8. These were quarter-core samples ranging from 10-20cm in length. Sample selection criteria was aimed at taking samples of visible Cu-Co mineralisation, or interesting alteration, as well as taking samples of visibly unmineralised, little altered rock for comparative purposes. At least one sample, judged to be

representative of the unit, was taken from each logged lithological interval. Each sample was photographed and given a brief description. Representative polished thin sections of each of these samples were made by technicians at the University of the Witwatersrand to prepare them for petrographic analysis. A photo-scan of all of the thin sections prepared for this study is given as Appendix 9.

4.2.1 Optical Microscopy

Using the Olympus BX41 binocular microscopes available at the School of Geosciences, University of the Witwatersrand, descriptions of all of the polished thin sections presented in Appendix 9 were made using both transmitted and reflected light techniques. Each sample was described and interpreted using the principles of transmitted and reflected optical mineralogy outlined in texts including Gribble and Hall (1992), Pracejus (2008), Craig and Vaughan (1994) and Spry and Gedlinske (1987). Photomicrographs of all relevant textures and ore phases that were described were taken using an attached Olympus DP26 5-megapixel digital microscope camera, the most relevant of which are presented in this chapter. As well as describing the phases, textures and relationships of minerals within the samples, optical microscopy was also used to select samples for further analysis using Scanning Electron Microscopy (see section 4.2.2).

4.2.2 Scanning Electron Microscopy (SEM)

Sections of interest identified for SEM analysis were given a 30nm carbon coating in an Emitech K950X TurboEvaporator using a drive current of 200A for 600ms. They were then analysed using the FEICo Quanta 200 ESEM (Environmental Scanning Electron Microscope) with an annular backscatter detector and using high vacuum mode, operated by the Microscopy and Microanalysis Unit (MMU) at the University of the Witwatersrand. BSE (Back-Scattered Electron) images were taken using an acceleration voltage of 30.0 kV at 'spotsize 6' and at a consistent working distance of 10±0.2 mm. The device has an Oxford Instruments liquid nitrogen cooled INCA PentaFETx3 EDS (Energy-Dispersive X-ray Spectroscopy) attachment, operated by INCA software on a secondary computer, which was used to make spot analyses of the section with a beam diameter of ~2µm. A photograph of the SEM setup at the MMU is included as Figure 4.1.

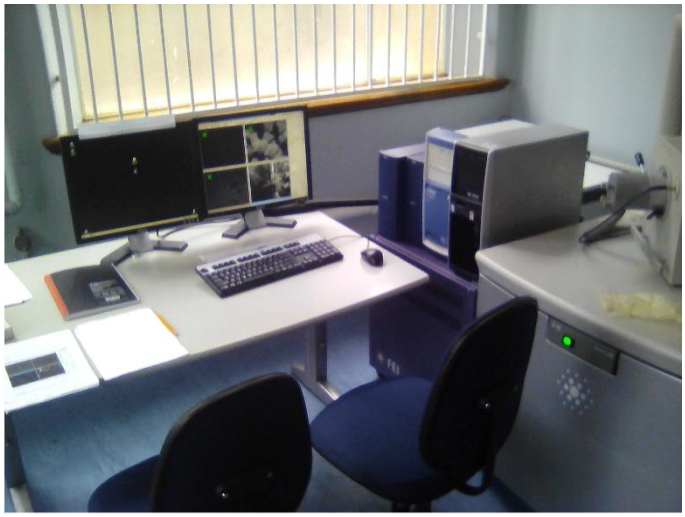

***Figure 4.1**: FEI Quanta 400 FEG-ESEM and EDS setup at the MMU, University of the Witwatersrand.*

4.2.3 Sulphur Isotope Ratio Analysis

Of the 105 core samples taken as part of this study, three were studied further by means of sulphur isotope analysis: MSSD075_19_2, MSSD_083_16_1 and MSSD083_21_4 (see Appendix 8), from which four powder samples were taken, each split into triplicates so that 12 analyses were made. This low number of analyses was originally intended to be part of a smaller, more focussed study on the bacilliforms identified in sample MSSD083_16_1, however the results, though limited in number, were discovered to have more impact on the wider paragenetic study of Mashitu South.

MSSD083_16_1 was selected for analysis because it contained abundant stratiform sulphides, while sulphates or other sulphur-bearing minerals were not detected in the thin section cut from it. Two separate powder samples were collected from this core sample. One powder sample (16_1_D1), from an interval containing only siliciclastic groundmass was chosen because it contained visible groundmass-disseminated sulphides. The powder was collected by using a rock-saw to cut out a ~5cm^3 section of the rock, and crushing it with an agate pestle and mortar to create a whole-rock sample. The second powder sample (16_1_E1) was collected from a band of apparently massive stratiform pyrite which was later discovered to be para-framboidal, though containing <5% minerals other than pyrite by area, so the sample can be assumed to be essentially mono-minerallic. This sample was

collected using a Dremel 4000 rotary tool, with a tungsten carbide drill-bit for precision drilling. This tool powdered the sample in-situ which was then collected into a sample bag by means of a fine paintbrush. The third and fourth powder samples are from core samples MSSD075_19_2 and MSSD083_21_4. These samples were collected using the Dremel precision drilling method from coarse grained sulphides hosted in thick, crosscutting dolomite veins attributed to Vein Type 2 (see section 3.3.2: Core Logging). Coarse-grained chalcocite (19_2_A1) and chalcopyrite (21_4_A1) from these veins were sampled, to compare their δ^{34}S values to those of the stratiform pyrite (16_1_E1) and groundmass-disseminated sulphides (16_1_D1). Each of the four samples were triplicated to check the precision of the methods used, providing roughly 0.1g of material for 12 analyses in total. The sample material is summarised in Figure 4.2.

Powder Sample Name	Parent Core Sample	Sample Type	Method of sampling	Description
16_1_D1	MSSD083_16_1	Whole-rock	Agate pestle and mortar crushing	Whole-rock sample from an interval of groundmass-disseminated mineralisation
16_1_D2	MSSD083_16_1	Whole-rock	Agate pestle and mortar crushing	Triplicate of '16_1_D1'
16_1_D3	MSSD083_16_1	Whole-rock	Agate pestle and mortar crushing	Triplicate of '16_1_D1'
16_1_E1	MSSD083_16_1	Single-sulphide - Pyrite	Precision drilling	Pyrite from a stratiform pyrite band ~3cm above 16_1_D1 interval
16_1_E2	MSSD083_16_1	Single-sulphide - Pyrite	Precision drilling	Triplicate of '16_1_E1'
16_1_E3	MSSD083_16_1	Single-sulphide - Pyrite	Precision drilling	Triplicate of '16_1_E1'
19_2_A1	MSSD_075_19_2	Single-sulphide - Chalcocite	Precision drilling	Type 2 dolomite-vein-hosted chalcocite
19_2_A2	MSSD_075_19_2	Single-sulphide - Chalcocite	Precision drilling	Triplicate of '19_2_A1'
19_2_A3	MSSD_075_19_2	Single-sulphide - Chalcocite	Precision drilling	Triplicate of '19_2_A1'
21_4_A1	MSSD083_21_4	Single-sulphide - Chalcopyrite	Precision drilling	Type 2 dolomite-vein-hosted chalcopyrite
21_4_A2	MSSD083_21_4	Single-sulphide - Chalcopyrite	Precision drilling	Triplicate of '21_4_A1'
21_4_A3	MSSD083_21_4	Single-sulphide - Chalcopyrite	Precision drilling	Triplicate of '21_4_A1'

***Figure 4.2**: Summary of sample material subjected to sulphur isotope ratio analysis.*

Inspection by optical microscopy of polished thin sections from the sampled intervals confirmed their identified mineralogy, and identified chalcocite, carrollite and pyrite as the groundmass-disseminated sulphides in the interval of sample 16_1_D1.

The sulphur isotope analyses were conducted at the Environmental Isotope Laboratory of the iThemba Laboratories at the University of the Witwatersrand, South Africa. To convert the sulphide samples into gaseous SO_2 for analysis, the samples were oxidized using V_2O_5, as per the method of Ricke (1964). Powdered sulphide samples were packed into tin capsules with a small amount of V_2O_5. The analyses were performed using a Flash elemental analyser, and the isotope ratio mass spectrometer used was a Thermo Scientific DELTA V Plus with a universal triple collector. The system is set up for triple N, C and S analysis, so a single reactor filled with WO_3 and electrolytic copper wires is used. Magnesium perchlorate is used to remove water produced during combustion. See section 4.3.4 for the results of these analyses.

4.3 Results

4.3.1 Ore Mineral Paragenesis

Mineralisation-related phases, including all Cu or Co bearing minerals but also pyrite and haematite, were identified by optical microscopy in the relevant thin sections, given an order of paragenesis and collated into a 'paragenesis matrix' in which all phases thought to be equivalent to one another were correlated. Only a single sample from MSSD140: 140_07_1, was found to contain mineralisation and therefore samples from MSSD140 are left out of the paragenesis matrix, which comprises samples from MSSD075, 080 and 083. Samples which did not contain mineralisation-related phases were omitted from the matrix, which was refined by phase confirmation during SEM analysis and is presented as Appendix 10. During the compilation of this paragenesis matrix, 33 different mineralisation-related phases were distinguished, which are described here in the order of their occurrence. Some of these phases are hosted in Type 1 and/or Type 2 veins, which were distinguished during logging and are described in Chapter 3. A further description of these two different types of vein based on petrographic analysis is given in section 4.3.3.1.

1. Pyrite 1 (Py1): Pyrite 1 is the earliest ore phase of the deposit, consisting of clusters of fine grained (<0.1mm) subhedral pyrite disseminated throughout the rock groundmass. These clusters are sometimes concentrically arranged in 'para-framboidal' shapes (Figure 4.3). The phase is found through most of the stratigraphy, although the para-(resembling)-framboidal clusters are best developed in the D.Strat unit.

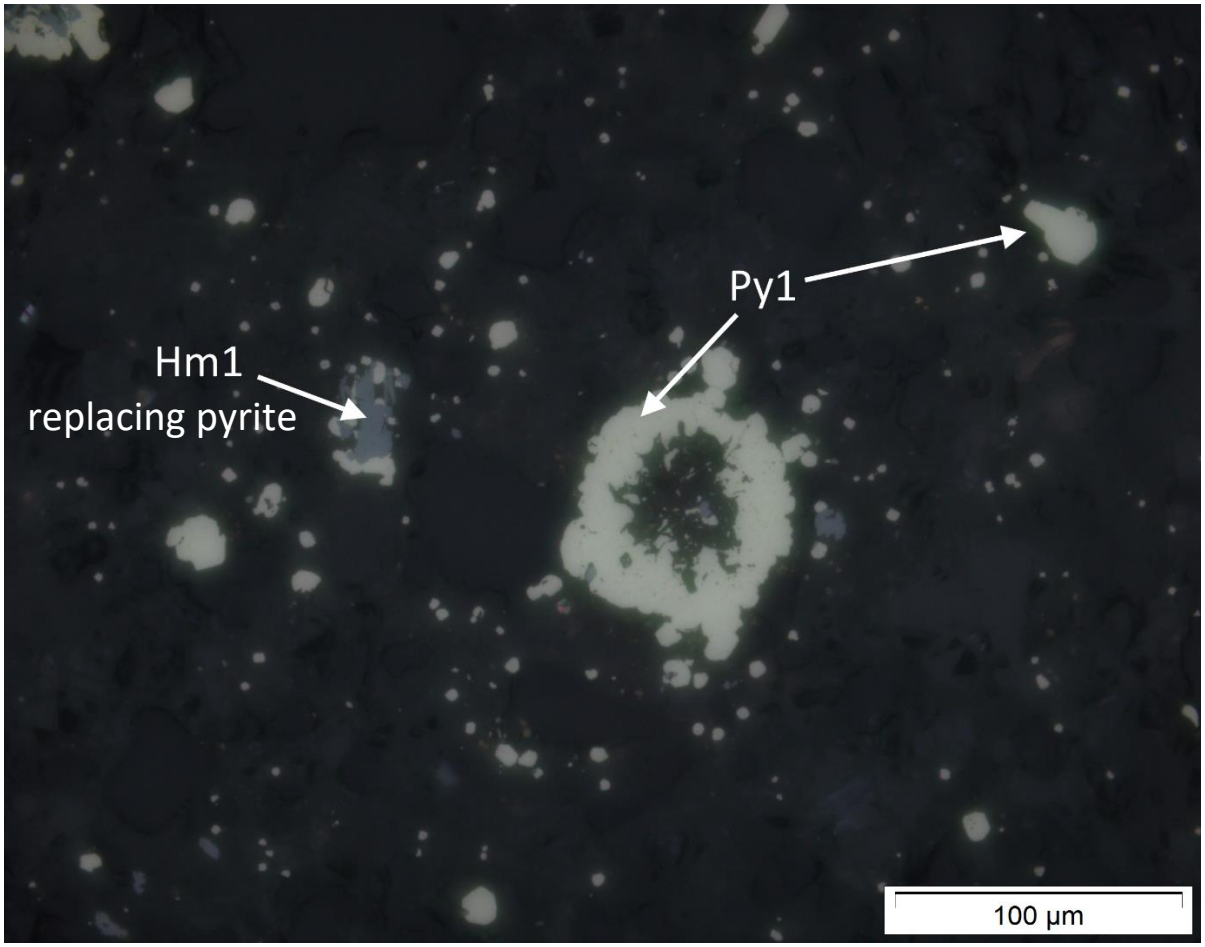

***Figure 4.3**: 'Para-framboidal' clusters of pyrite 1 (Py1) disseminated through the groundmass. Some replacement of pyrite 1 by grey haematite 1 (Hm1) has taken place. Optical image taken in reflected PPL from sample MSSD080_21_1.*

2. Haematite 1 (Hm1): Haematite 1 follows this phase as equally fine grained (<0.1mm) euhedral laths of haematite (Figure 4.4) which sometimes abut and terminate against pyrite 1 crystals and sometimes appear to replace them (Figure 4.3). Under reflected light these crystals usually have a reddish or grey colour, setting them apart

from later phases of haematite which usually display a blue or green tint. Hm1 is restricted in distribution to siliciclastic units, being sparsely disseminated throughout the sediments of the RAT Rouge and Gris as well as the Schistes Dolomitique (S.D.) unit.

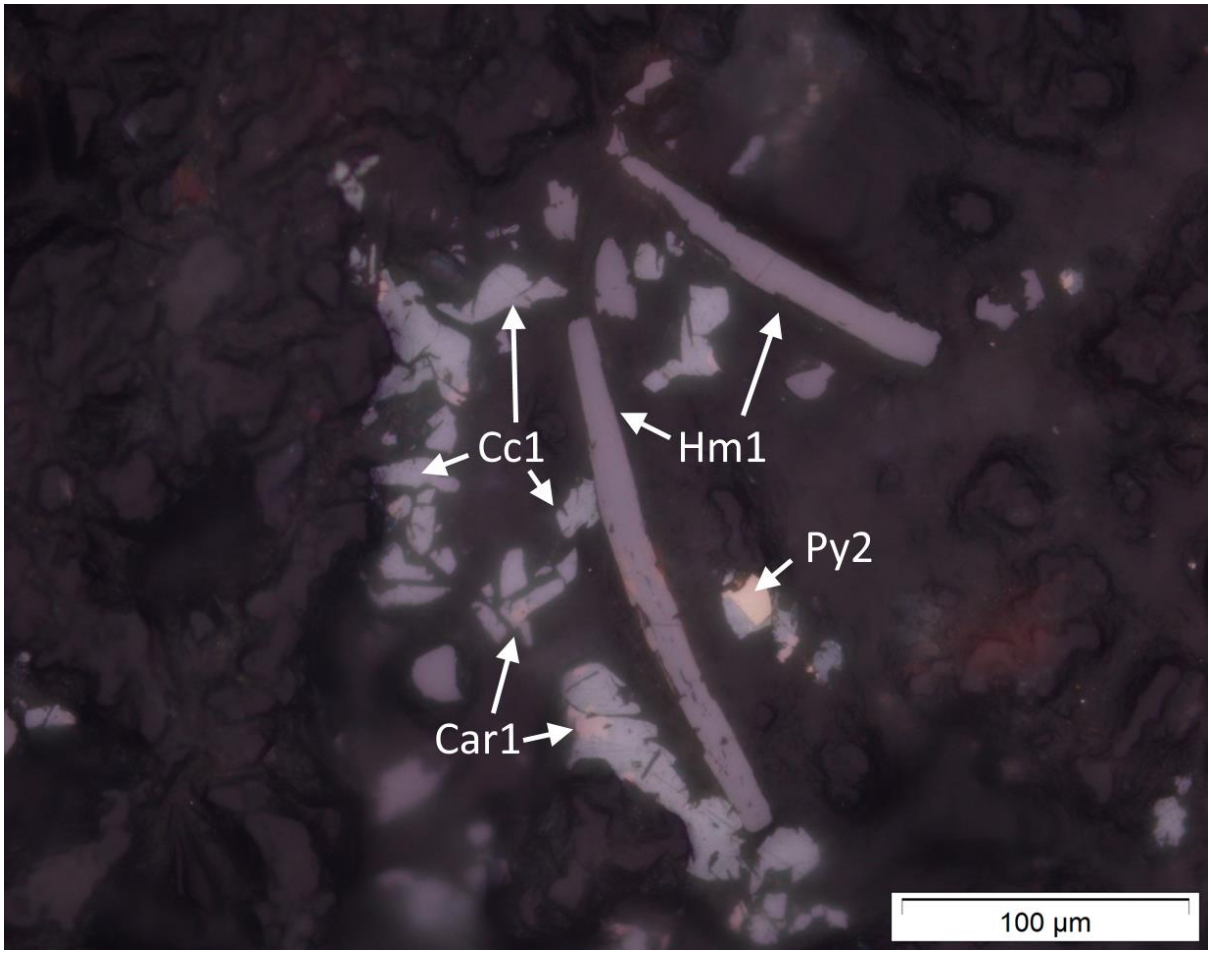

Figure 4.4*: Euhedral laths of disseminated, reddish haematite 1 (Hm1) surrounded by later ore phases. Note the abutment of the chalcocite 1 phase against haematite 1. Optical image taken in reflected PPL of sample MSSD083_16_1.*

3. Pyrite 2 (Py2): Pyrite 2 is a continuous recrystallisation of the earlier pyrite 1 phase, reflecting the transition of pyrite from subhedral clusters to euhedral cubic shapes (Figure 4.5) during diagenesis. It is distinguished temporally from pyrite 1 in showing textures which place it paragenetically later than haematite 1 (see Figure 4.6), however a continuum of early pyrite and haematite crystallisation is likely to have occurred. Like the pyrite 1 from which it has recrystallised, it is stratigraphically widespread.

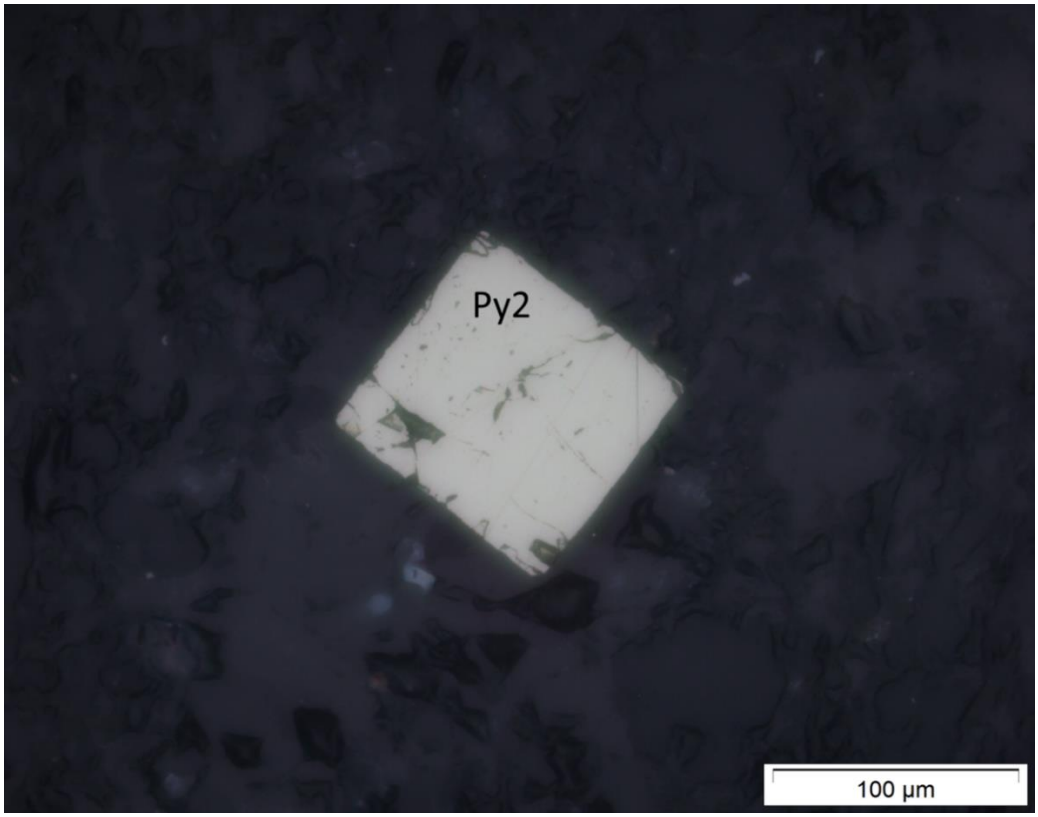

Figure 4.5*: Euhedral, cubic, disseminated pyrite 2 crystal. Optical image taken in reflected PPL of sample MSSD083_23_3.*

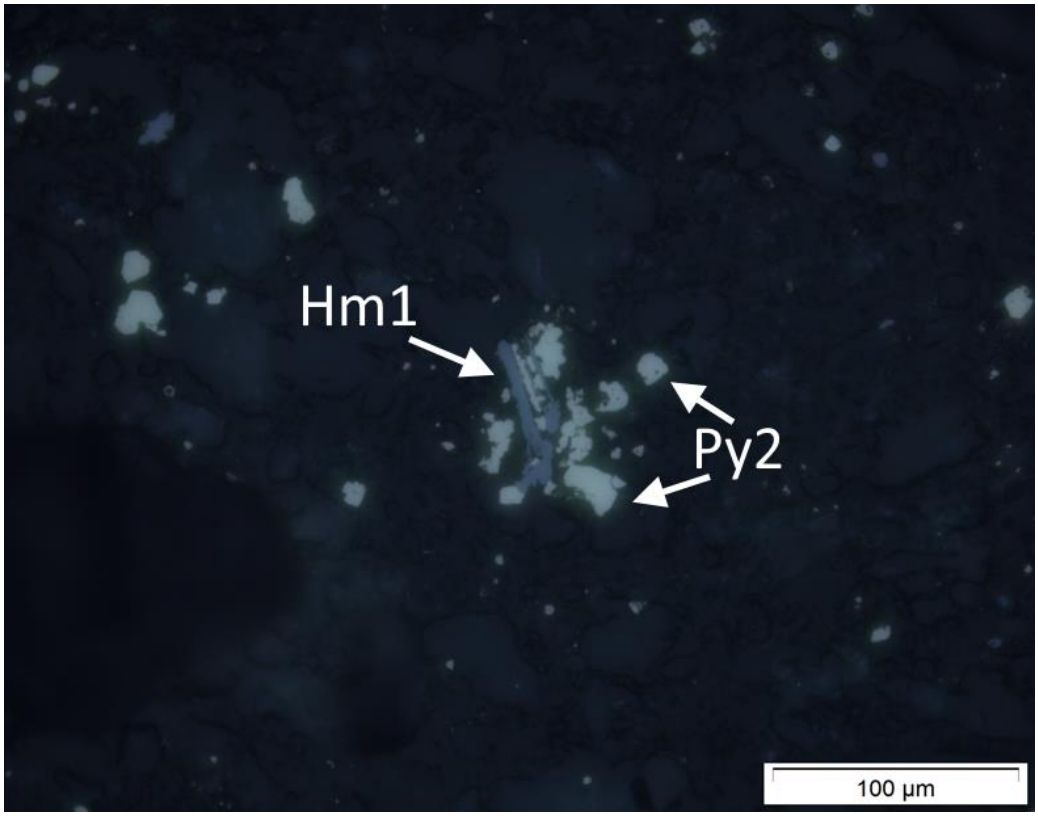

Figure 4.6*: Pyrite 2 crystals around earlier-formed Hm1 laths. Optical image taken in reflected PPL of sample MSSD083_22_2.*

4. Pyrite 3 (Py3): Pyrite 3 is distinguished from earlier pyrite 1 and pyrite 2 by its tendency to be coarser-grained, with crystals commonly over 1mm. It is usually subhedral although anhedral and euhedral examples exist. This phase is primarily groundmass-hosted although occurrence in Type 1 veins is not uncommon, where it is usually distributed towards the vein margins, in association with early quartz. It may also occur in quartz-carbonate nodules or boudins which are found in the Dolomite Stratifee unit (DStrat) and Schistes Dolomitique du Base unit (SDB) (Figure 4.7). It can be seen in some cases abutting against or replacing earlier pyrite and haematite phases. Geochemically, EDS mapping shows that pyrite 3 appears to contain trace amounts of Co (Figure 4.8), whereas this metal is not found in levels detectable by EDS in the earlier pyrite 1 and pyrite 2 phases.

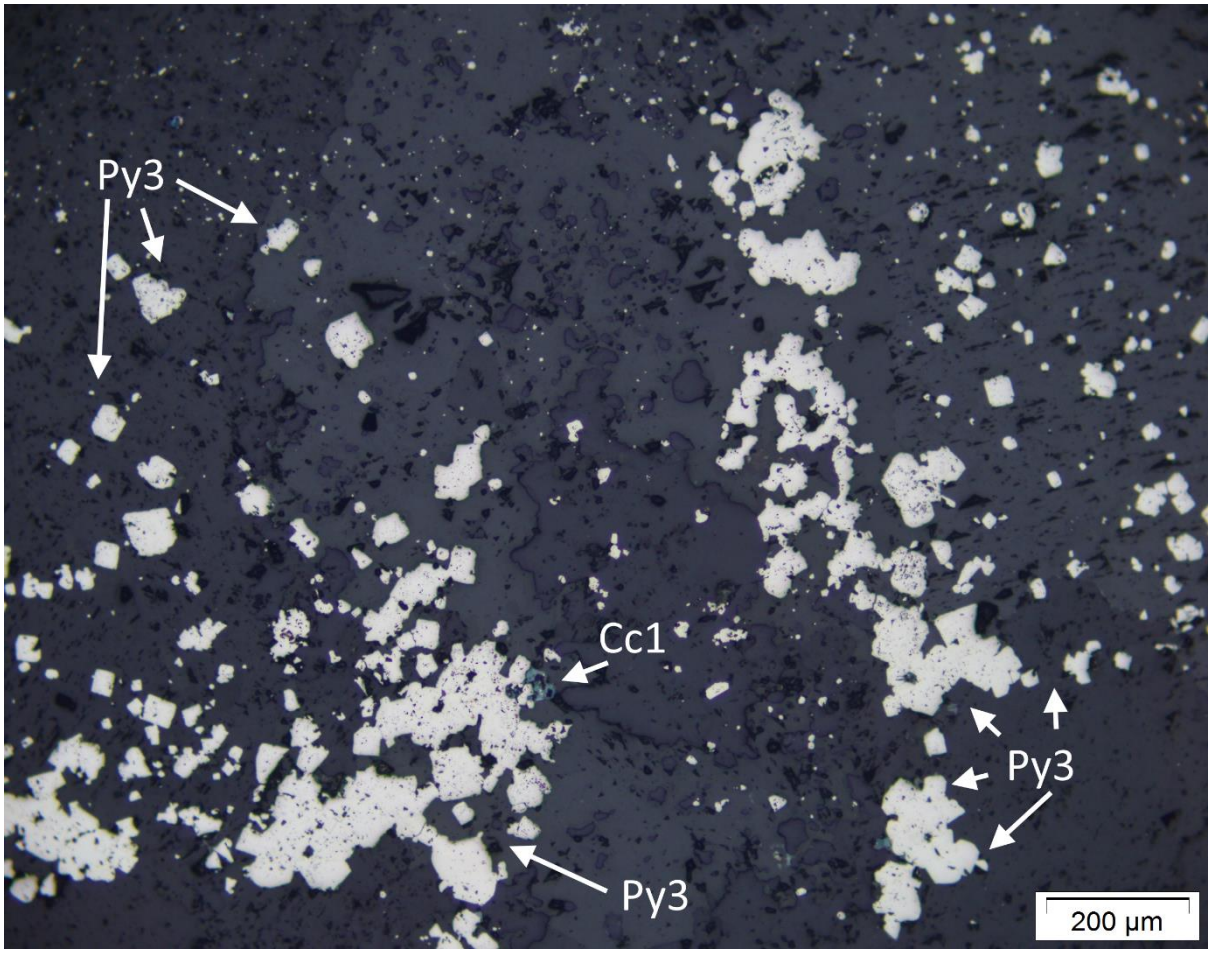

Figure 4.7*: Pyrite 3 crystals associated with Type 1 quartz-carbonate veins, with minor rimming by chalcocite 1, in proximity to nodules/boudins within the DStrat unit. Optical image taken in reflected PPL from sample MSSD080_20_2.*

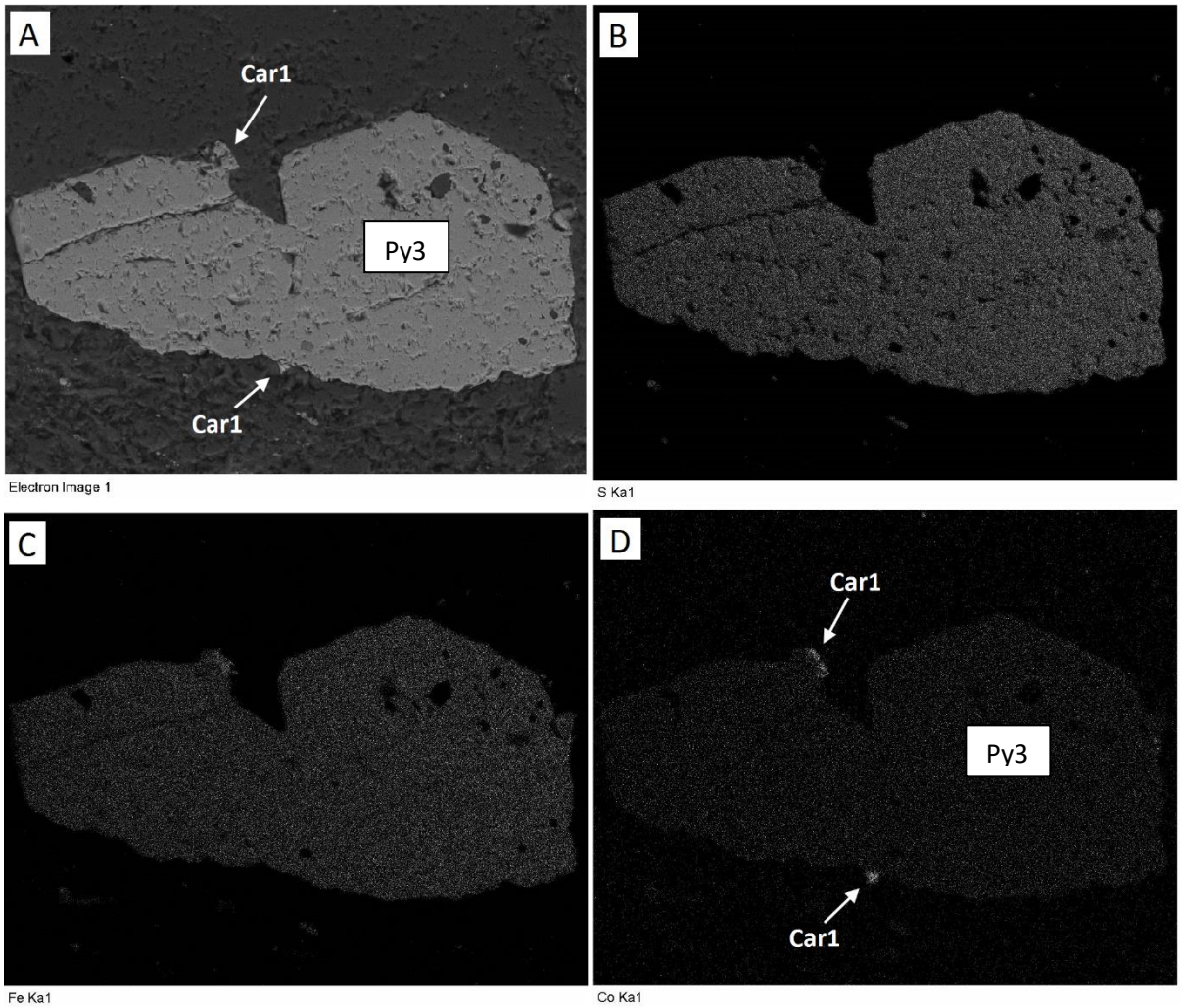

Figure 4.8*: SEM-EDS element mapping images of a pyrite 3 crystal, which is roughly 600 µm in length, at the edge of a quartz-carbonate nodule.* ***A****: SEM image of site.* ***B****: Site map of S concentration.* ***C****: Site map of Fe concentration.* ***D****: Site map of Co concentration. Fe and S are concentrated, as would be expected, within pyrite (FeS_2). As shown by (****D****), Co is concentrated as a trace element in pyrite 3, with the Co element map faintly mirroring the shape of the pyrite crystal. Additionally, the element map reveals the presence of two Cu-Co sulphide crystals rimming the pyrite 3 crystal, which were confirmed as carrollite (Car1) by spot analysis. Sample MSSD083_23_4. Cobaltoan pyrite from the Copperbelt is described by Bartholomé (1971).*

5. Sphalerite 1 (Sph1): Only three small (<10µm) crystals of sphalerite 1 were identified in this study by SEM analysis, all of which were anhedral inclusions in masses of Type 1 vein-hosted (see Section 4.3.3.1) later chalcopyrite 1 and bornite 1 (Figure 4.9).

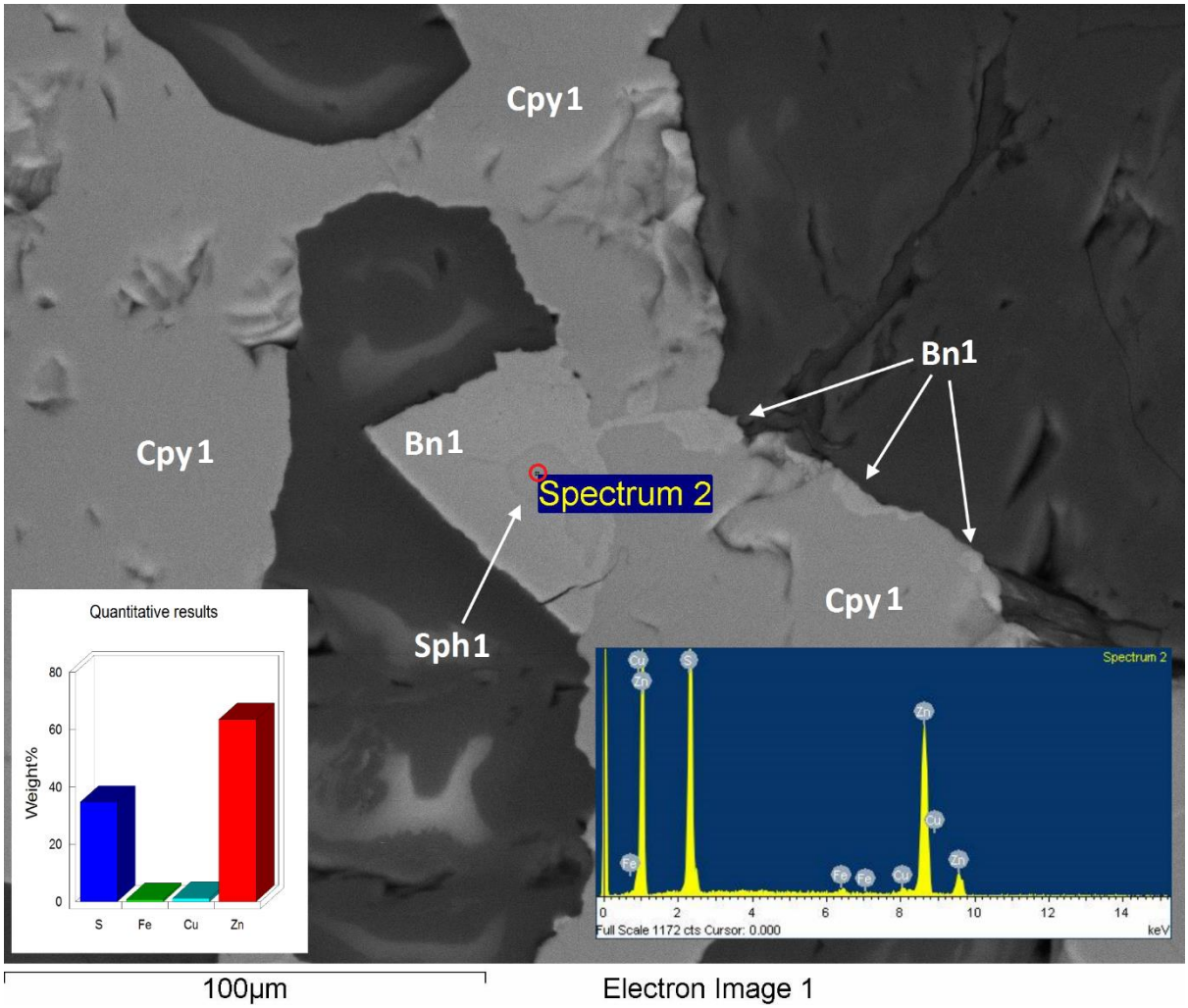

***Figure 4.9**: SEM image of a Type 1 vein-hosted (see Section 4.3.3.1) sulphide assemblage. A large bleb of chalcopyrite (Cpy1) is rimmed and replaced by bornite (Bn1). Sphalerite (Sph1) is the pale, dull grey phase mantled by the slightly lighter bornite. The results of an EDS spot analysis (Spectrum 2) confirm the identity of the crystal as sphalerite. Sample MSSD083_21_4.*

6. Chalcopyrite 1 (Cpy1): Chalcopyrite 1 is found disseminated as anhedral masses within the groundmass (Figure 4.10) or as tiny inclusions within fine-grained, intergranular, crystalline quartz in the groundmass. However, it is also found hosted within Type 1 veins. It frequently rims or includes earlier pyrite and haematite (Figure 4.11).

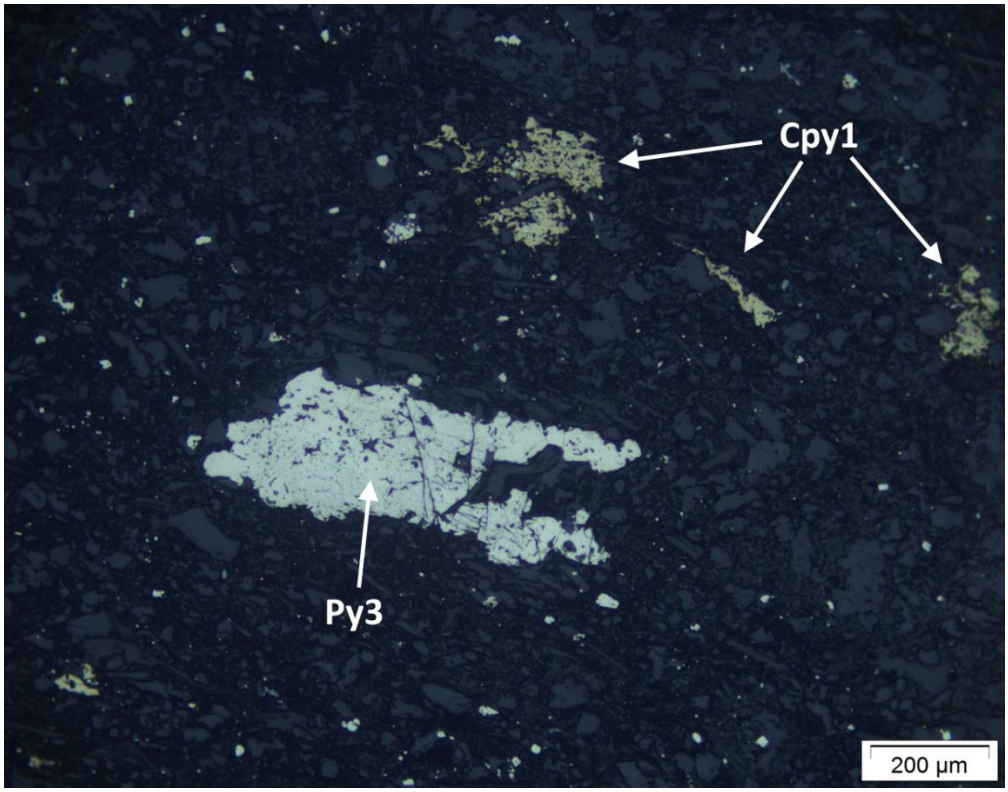

Figure 4.10*: Stratiform, disseminated pyrite 3 and chalcopyrite 1 masses within the siliciclastic groundmass of the SD2d. Optical image taken in reflected PPL of sample MSSD083_22_2.*

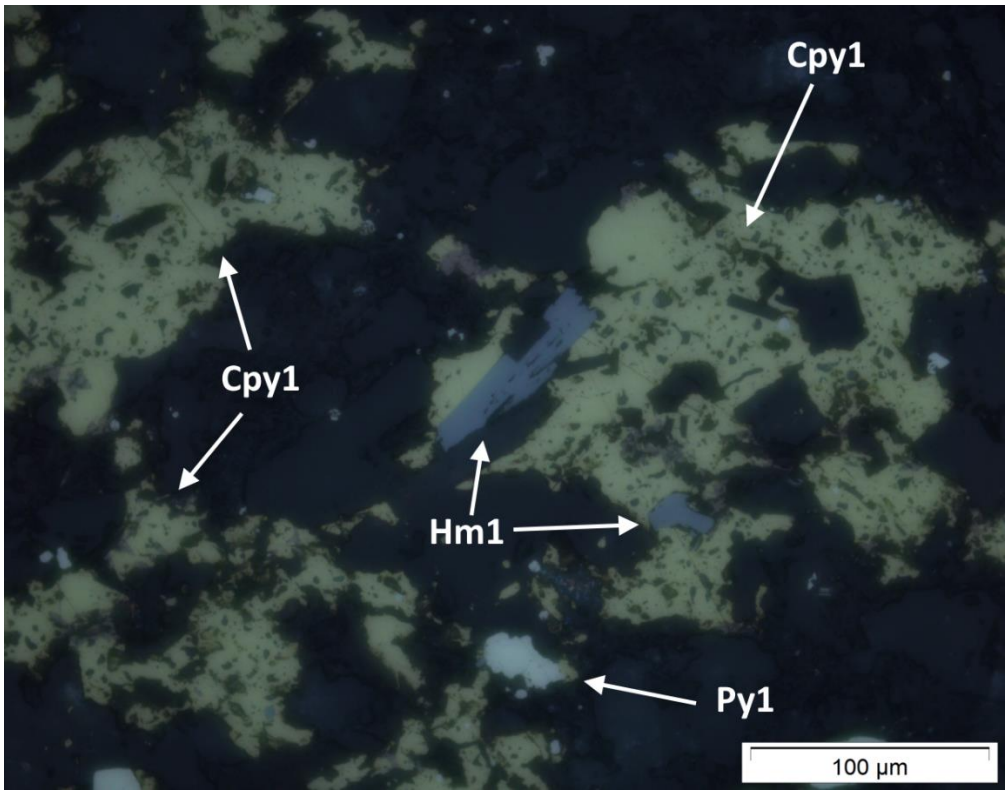

Figure 4.11*: A disseminated mass of chalcopyrite 1 surrounding earlier pyrite (Py1) and haematite (Hm1) phases. Optical image taken in reflected PPL of sample MSSD083_22_2.*

7. Bornite 1 (Bn1): The bornite1 phase is usually found as anhedral, space filling masses rimming and replacing earlier chalcopyrite 1 in the groundmass. It also occurs as rims to Type 1 vein-hosted chalcopyrite (Figure 4.12).
8. Digenite 1 (Dg1): Digenite 1 is only found co-occurring with and as exsolution lamellae within bornite 1 (Figure 4.12).

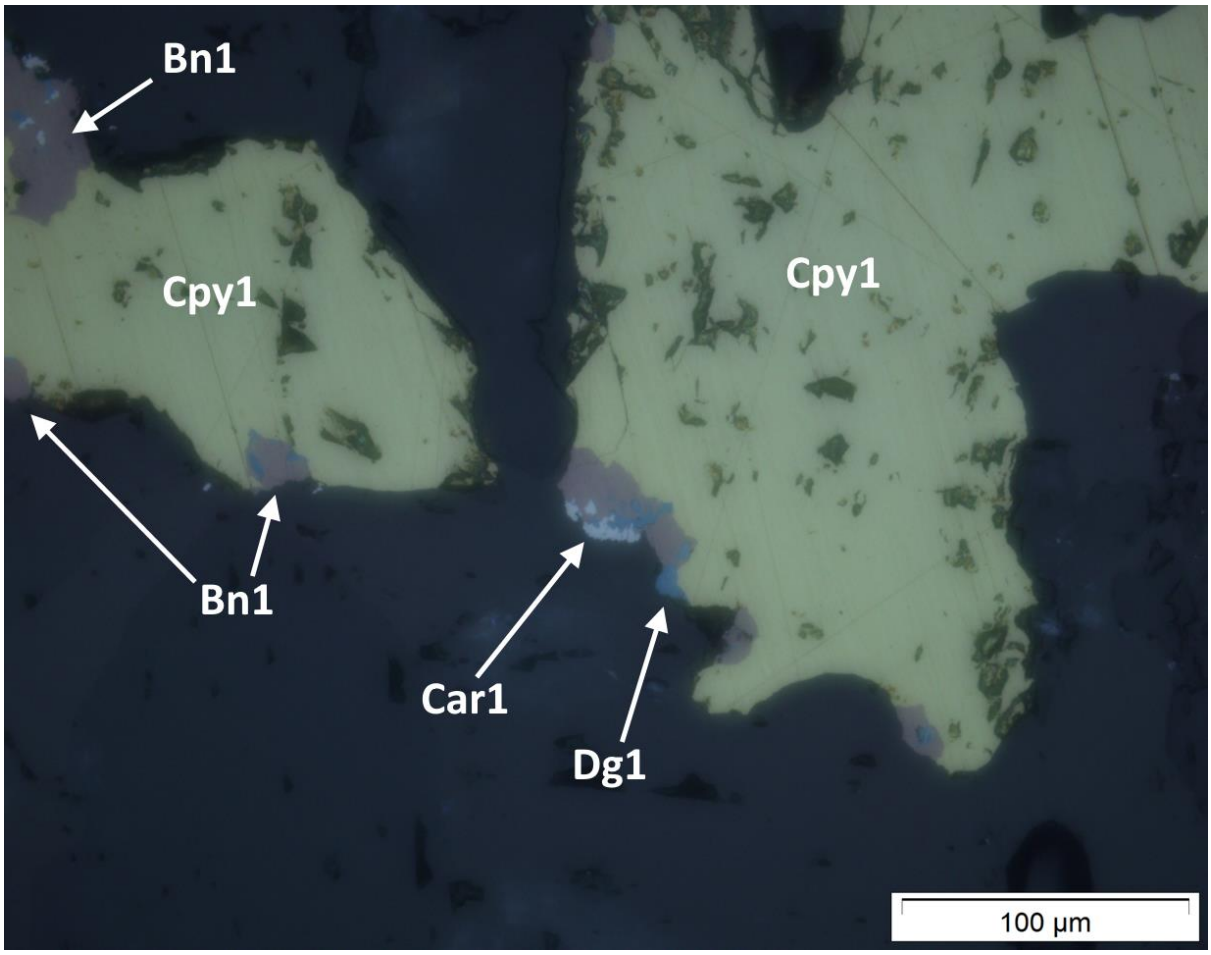

Figure 4.12*: Type 1 vein-hosted chalcopyrite 1 rimmed by bornite (purple, Bn1). Digenite (Dg1, deep blue) forms exsolution textures within the bornite. The Bn1-Dg1 is itself rimmed by carrollite 1 (grey-white). Optical image taken in reflected PPL of sample MSSD083_21_4.*

9. Chalcocite 1 (Cc1) is observed as disseminated, anhedral, intergranular masses (Figures 4.13 and 4.14) and is the most stratiform of the earlier sulphide phases with occasional stratiform layers at the thin-section scale. It appears to be associated with more dolomitic, more carbonaceous bedding or laminations where it occurs.

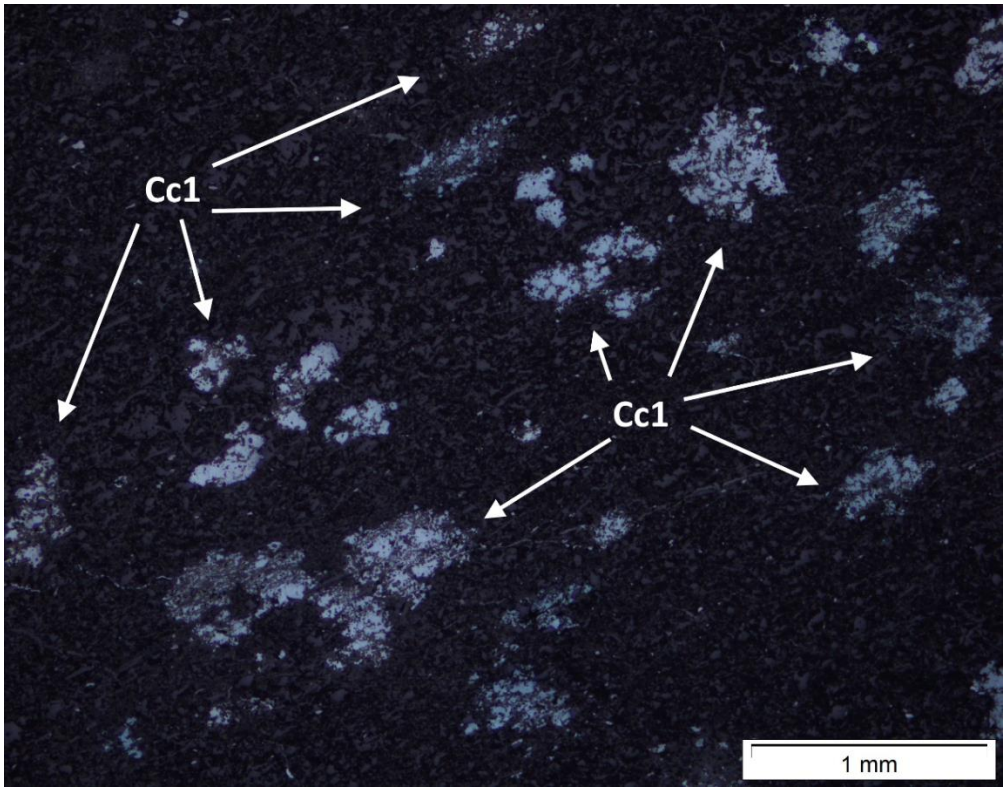

Figure 4.13*: Stratiform disseminated chalcocite 1 masses. Optical image taken in reflected PPL of sample MSSD075_16_3.*

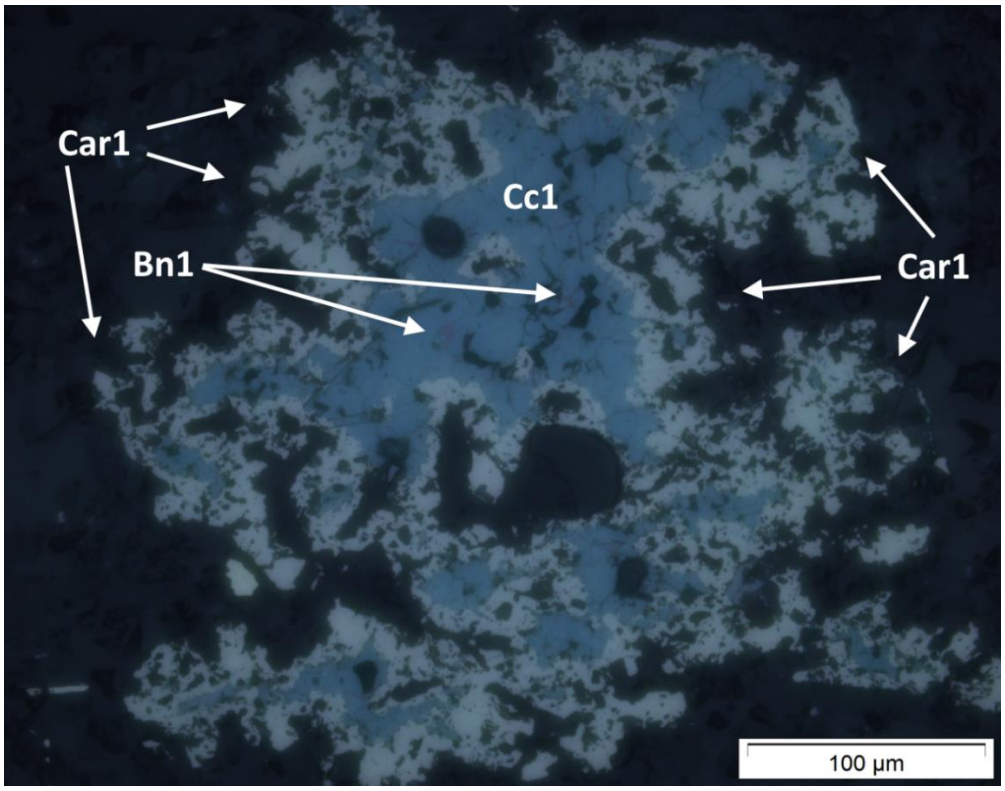

Figure 4.14*: Disseminated chalcocite 1 mass mantled by carrollite1. Bornite 1 is barely visible as purple remnants within the replacing mass of blue Cc1. Optical image taken in reflected PPL of sample MSSD083_23_2.*

10. Carrollite 1 (Car1): This phase is primarily groundmass-disseminated, occurring as anhedral, intergranular masses, however it also occurs in Type 1 veins. In a few of these Type 1 vein occurrences, the veins appear to be antitaxial (Figure 4.15). carrollite 1 is placed late in the order of paragenesis of the early sulphides by its occurrence as a rim to earlier blebs of chalcopyrite 1, bornite 1-digenite 1 and chalcocite 1 (Figures 4.16 and 4.17). This phase is inferred to be associated with a phase of 'cobaltoan pyrite' (CoPy1) which was identified by the EDS in one sample (080_13_2) and found to be distributed as a progressive replacement phase, rimming cores of chalcopyrite 1 (Figure 4.18). It homogeneously contains ~ 5 wt.% Co (see Figure 4.19). No paragenetic relationship was found between CoPy1 and Car1, so CoPy1 is grouped together with the Car1 phase in terms of paragenetic timing, based on its paragenetic relationships with other sulphides and Co content.

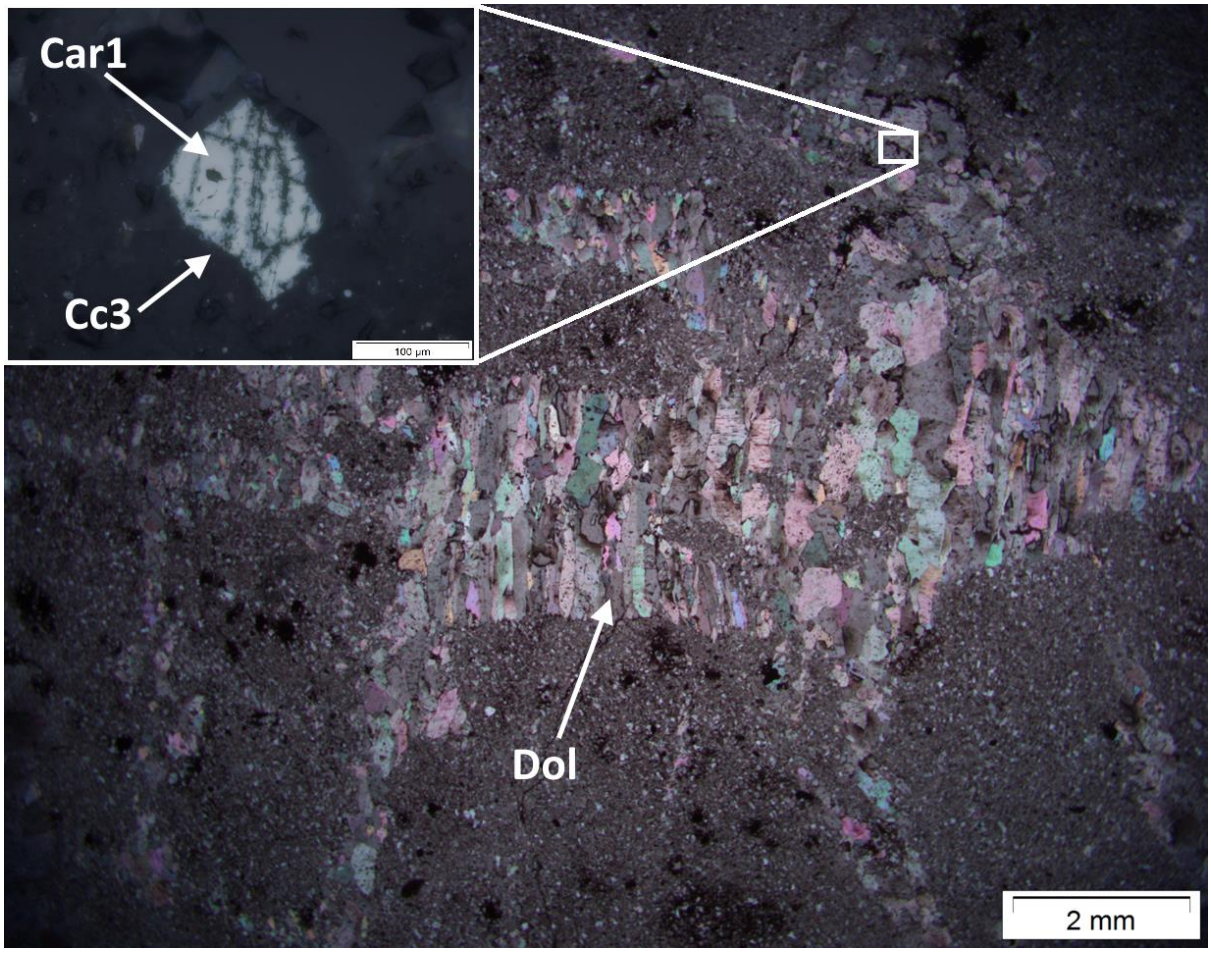

Figure 4.15*: Carrollite (Car1) rimmed and replaced by chalcocite (Cc3) within a Type 1 antitaxial dolomite vein. Main optical image is taken in transmitted XPL, inset image is taken in reflected PPL, from sample MSSD083_20_1.*

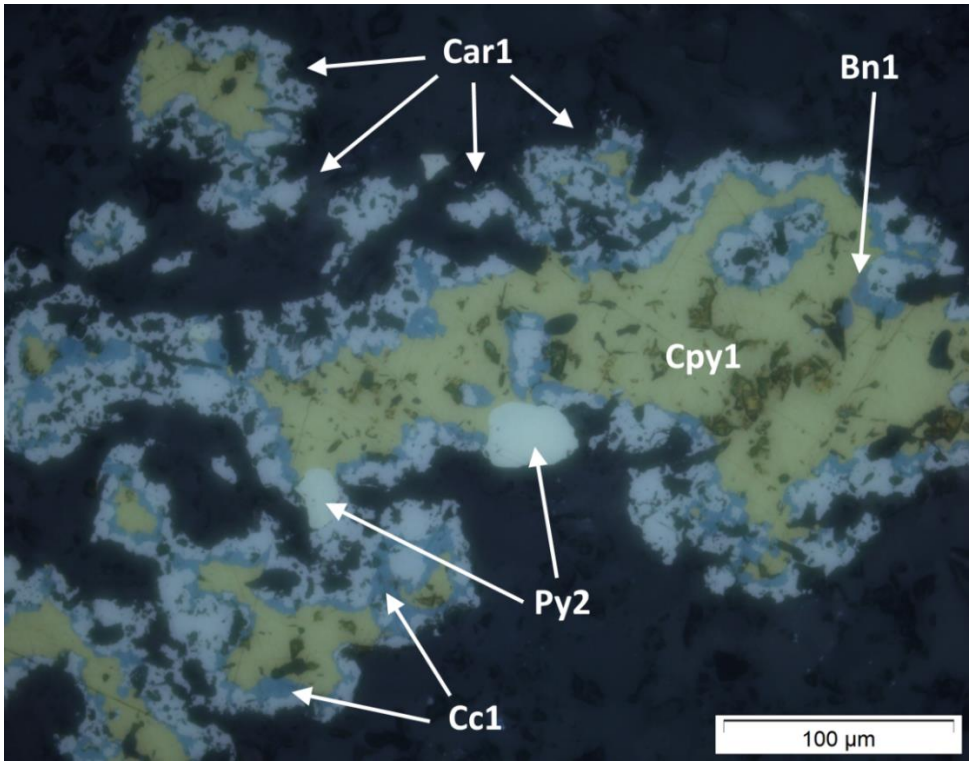

Figure 4.16*: Carrollite 1 as a mantling, replacing phase to an earlier chalcopyrite-bornite-chalcocite disseminated sulphide bleb (bornite, Bn1, is barely visible as purple remnants within chalcocite 1). Note that carrollite 1 does not appear to be replacing pyrite 2. Optical image taken in reflected PPL of sample MSSD083_23_2.*

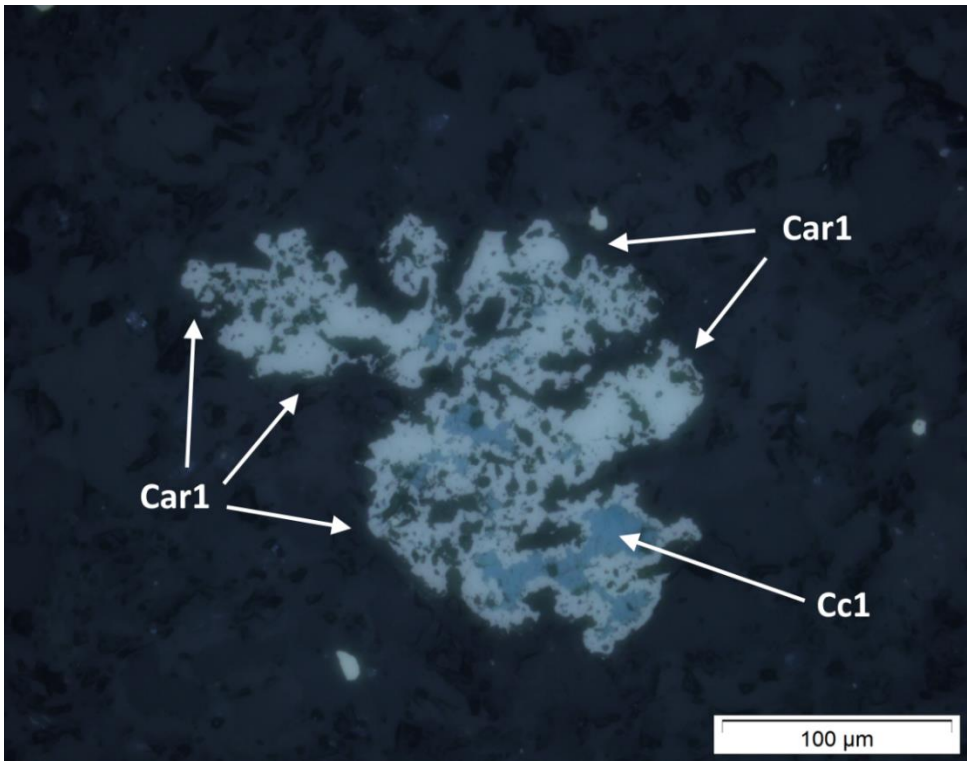

Figure 4.17*: Near total replacement of a sulphide bleb such as the one in Figure 4.16, progressively by chalcocite 1 and then by carrollite 1. Optical image, reflected PPL of sample MSSD083_23_2.*

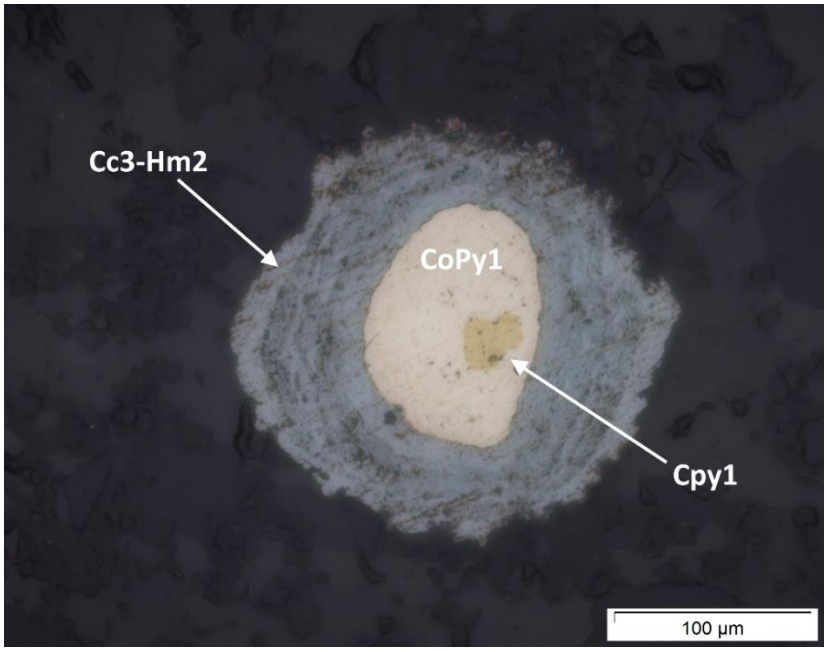

***Figure 4.18**: Replacement of chalcopyrite 1 by a crystal of CoPy1 (cobaltoan pyrite), itself replaced by concentrically banded chalcocite 3 and haematite 2. Optical image taken in reflected PPL of sample MSSD080_13_2.*

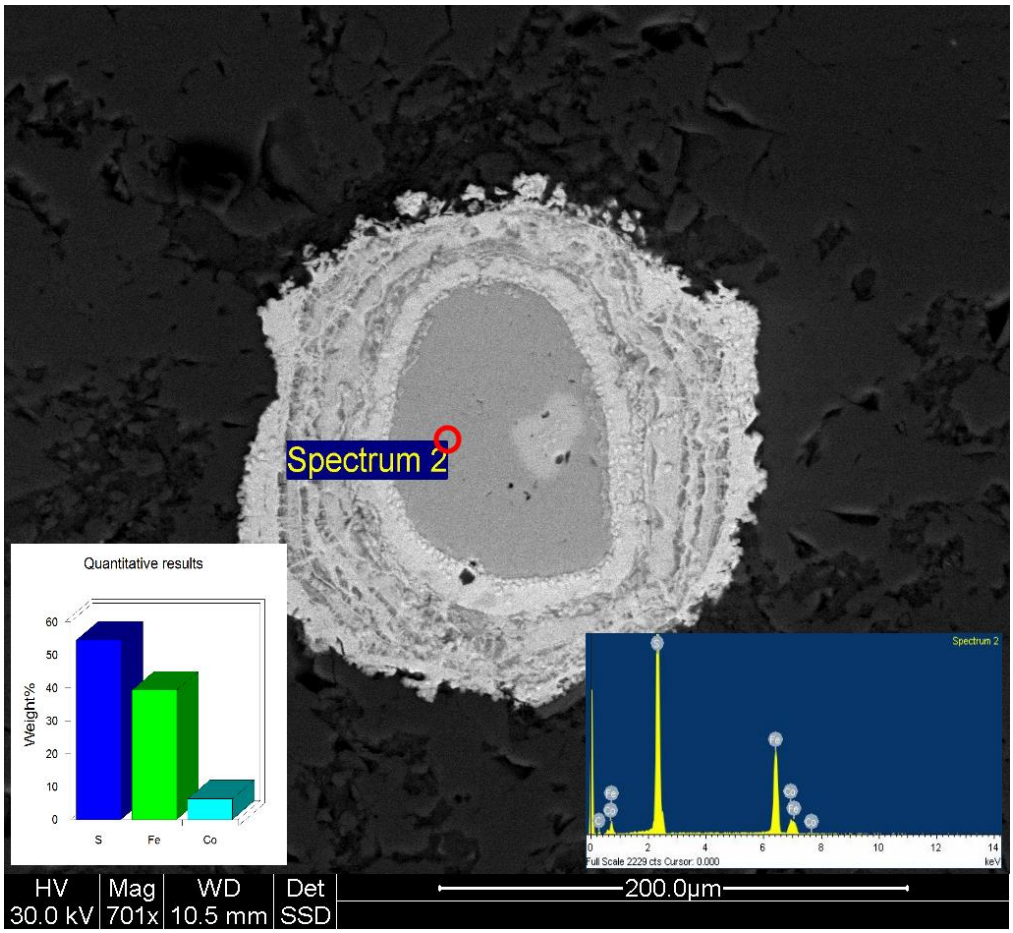

***Figure 4.19**: SEM image of the sulphide bleb in Figure 4.18, showing an EDS spot analysis of the cobaltoan pyrite (CoPy1). The crystal is primarily Fe and S but contains ~5 wt.% Co.*

11. Carrollite 2 (Car2): Description of the carrollite 2 phase is based on collaborative work on the Mashitu South deposit by M. Sośnicka (pers. comm., 2016). It is primarily Type 2 vein-hosted (Figure 4.20) and subhedral-euhedral in habit. No direct paragenetic relationship between carrollite 1 and carrollite 2 has been observed, but carrollite 2 is inferred to have formed later, based on its presence in Type 2 veins which cross-cut stratiform-disseminated mineralisation.

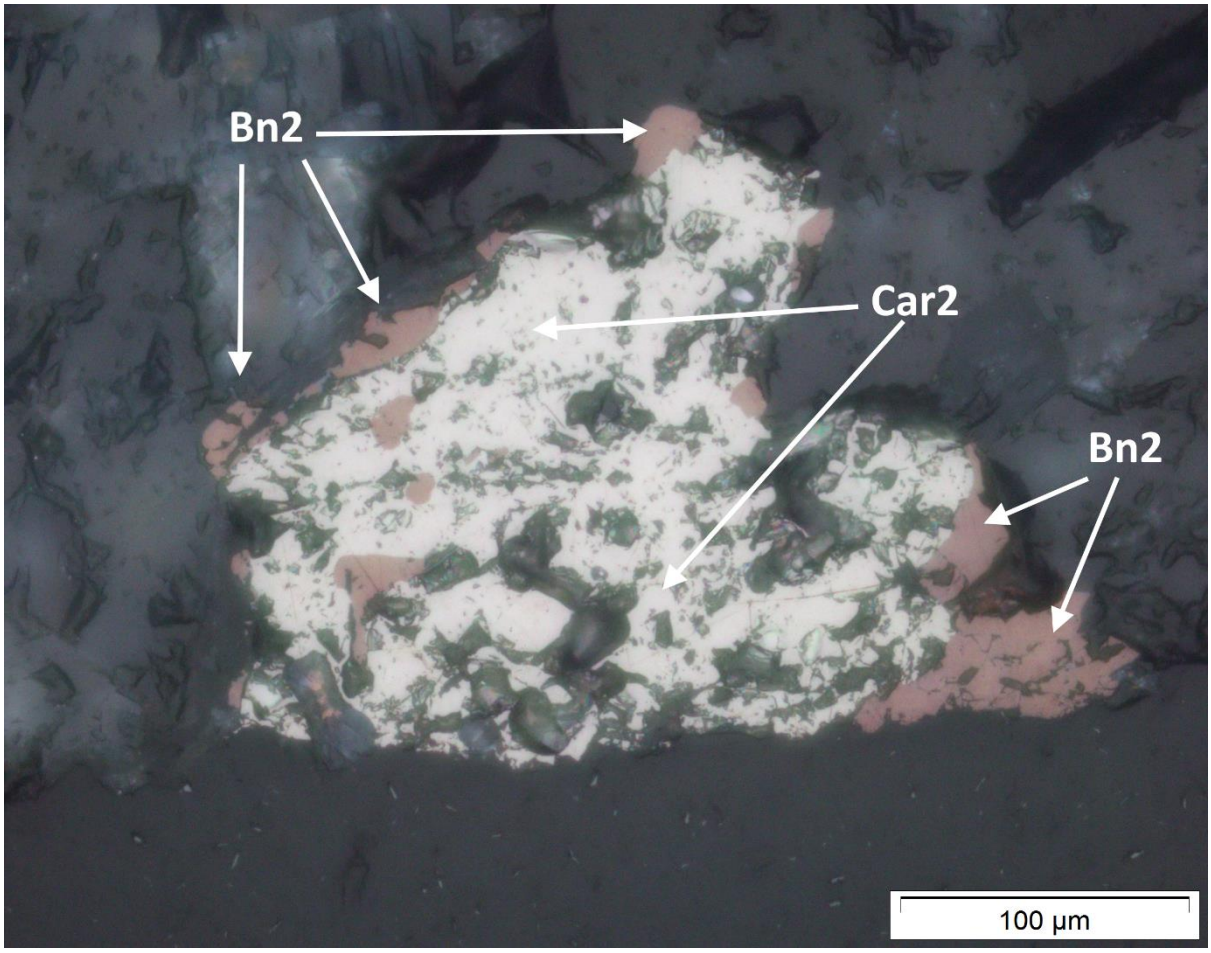

Figure 4.20*: Type 2 vein-hosted carrollite 2, mantled and replaced by bornite 2. Optical image taken in reflected PPL from sample MSSD083_06_5.*

12. Chalcopyrite 2 (Cpy2): Chalcopyrite 2 is a scarce phase usually encountered as small (<0.1mm), anhedral blebs, found as inclusions in dolomite or quartz crystals within Type 2 veins, or as inclusions in later sulphide phases. Later sulphides often form textures that suggest they are replacing this phase.

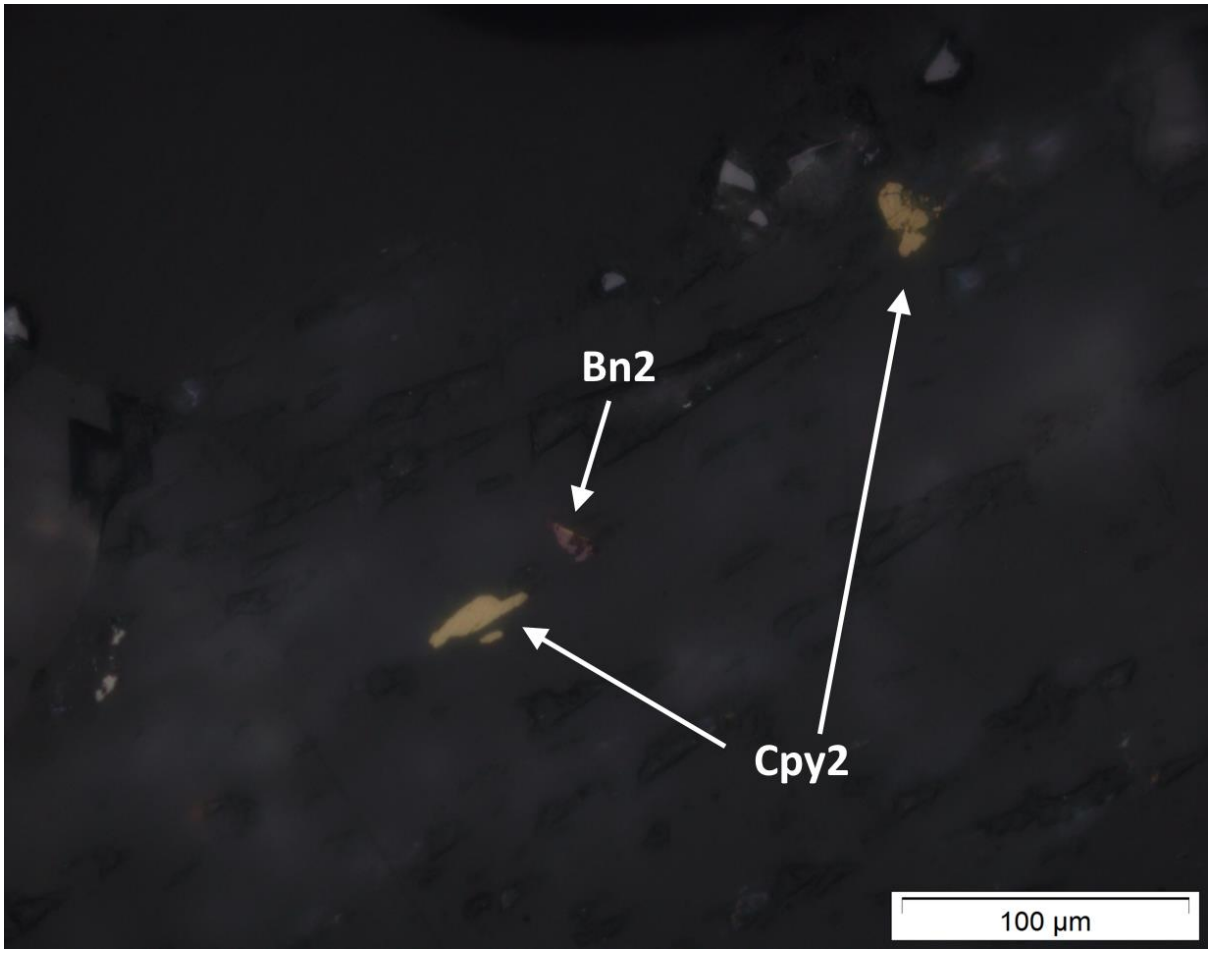

Figure 4.21*: Tiny crystals of type 2 vein-hosted chalcopyrite 2; one crystal is mostly replaced by bornite 2. Optical image taken in reflected PPL from MSSD083_26_2.*

13. Bornite 2 (Bn2): Bornite 2 forms anhedral rims to earlier sulphide phases or, less frequently, isolated interstitial blebs where chalcocite 2 (Figure 4.22) and digenite 2 often form replacement rims or exsolution lamellae. It is always hosted in Type 2 veins.
14. Chalcocite 2 (Cc2): Chalcocite 2 frequently forms anhedral vein-hosted masses or rims and replacement textures to earlier sulphides (Figure 4.22), but also occurs as isolated subhedral blebs within Type 2 veins (Figure 4.23). Figure 4.24 shows an example of Type 2 vein-hosted chalcocite 2 cutting stratiform-disseminated chalcocite 1.

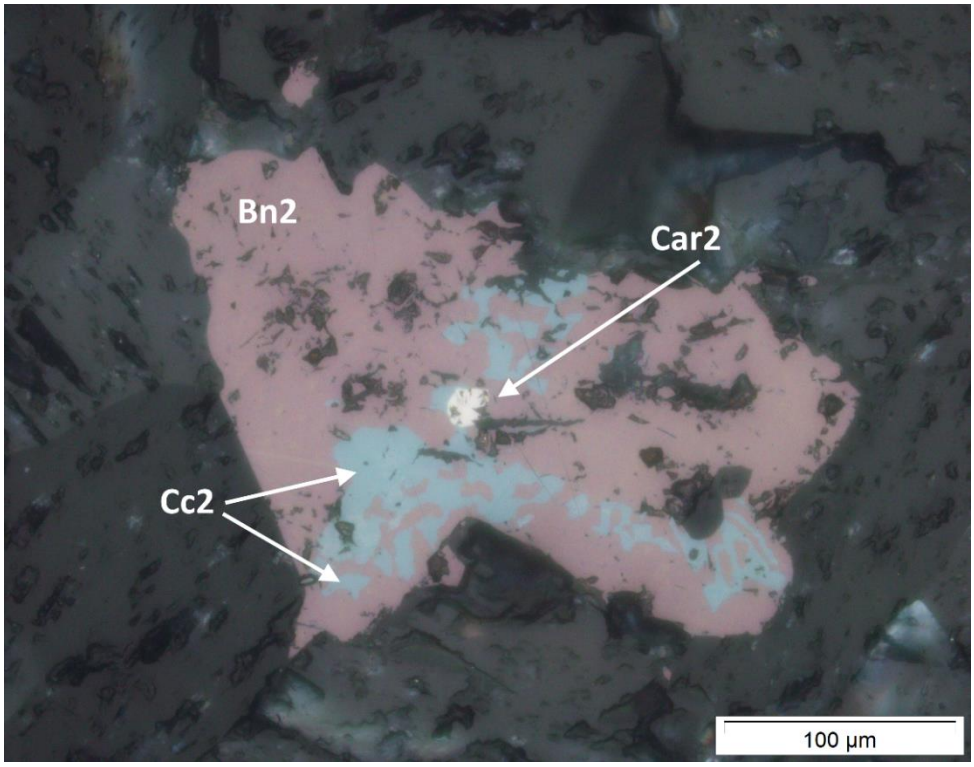

Figure 4.22*: Type 2 vein-hosted sulphide bleb of bornite 2 mantling a small remnant of carrollite 2, with chalcocite 2 apparently exsolving from bornite 2. Optical image taken in reflected PPL from sample MSSD083_06_5.*

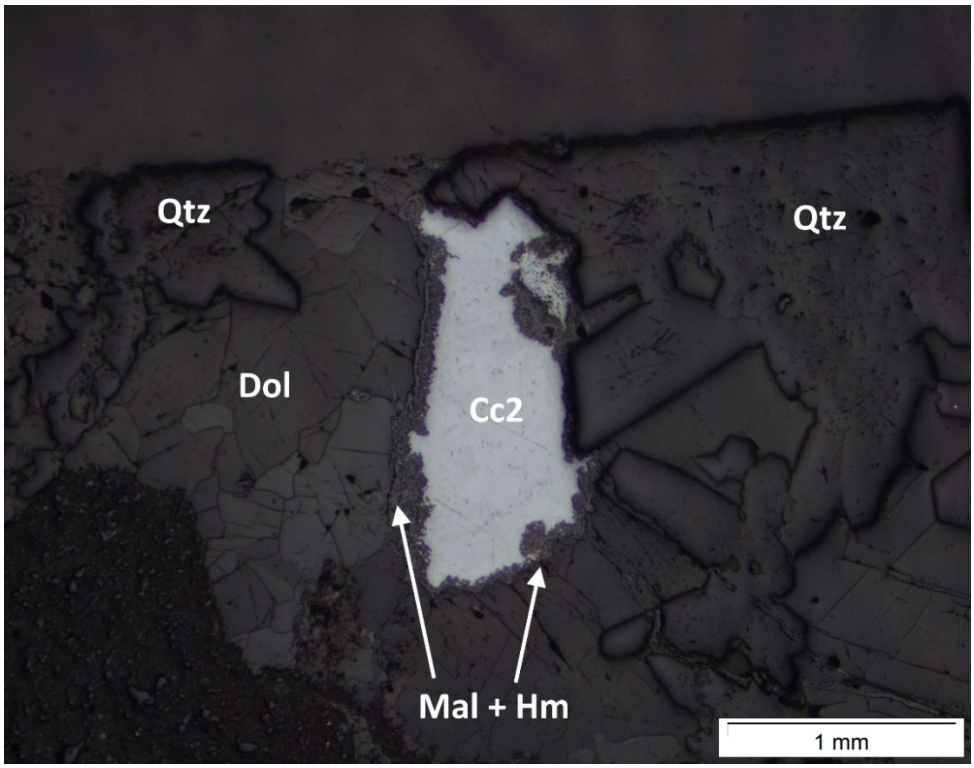

Figure 4.23*: Type 2 vein-hosted bleb of chalcocite 2, which is replaced around the rims by closely-intergrown mixture of malachite and haematite (Mal and Hm). Optical image taken in reflected PPL from sample MSSD080_14_1.*

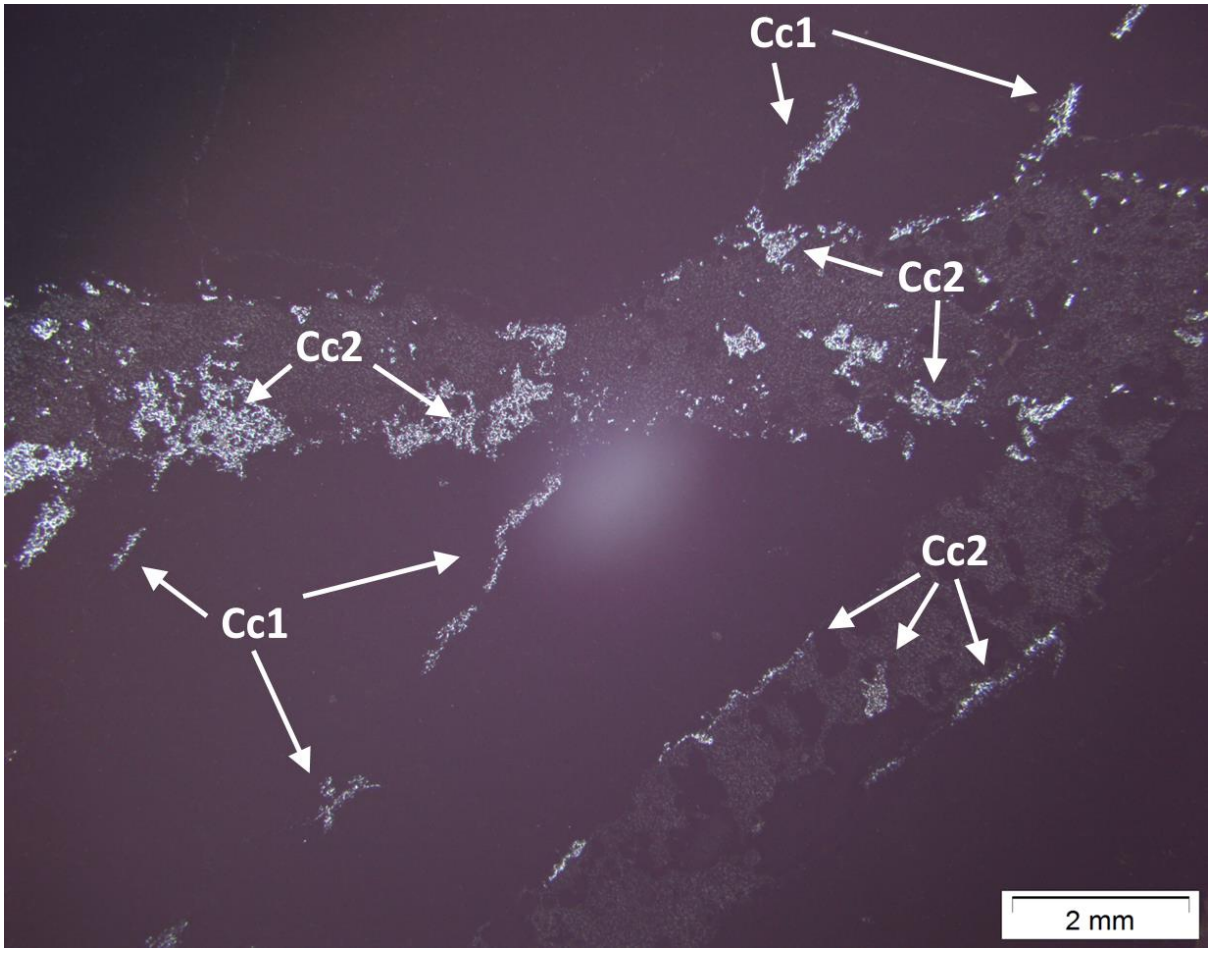

Figure 4.24*: Type 2 vein-hosted chalcocite 2 cross-cutting stratiform-disseminated chalcocite 1. Optical image taken in reflected PPL from sample MSSD083_14_1_M.*

15. Digenite 2 (Dg2): Digenite 2 only occurs as exsolution lamellae, skeletal textures or replacement rims to earlier chalcopyrite 2, bornite 2 or chalcocite 2 within Type 2 veins (Figure 4.25).

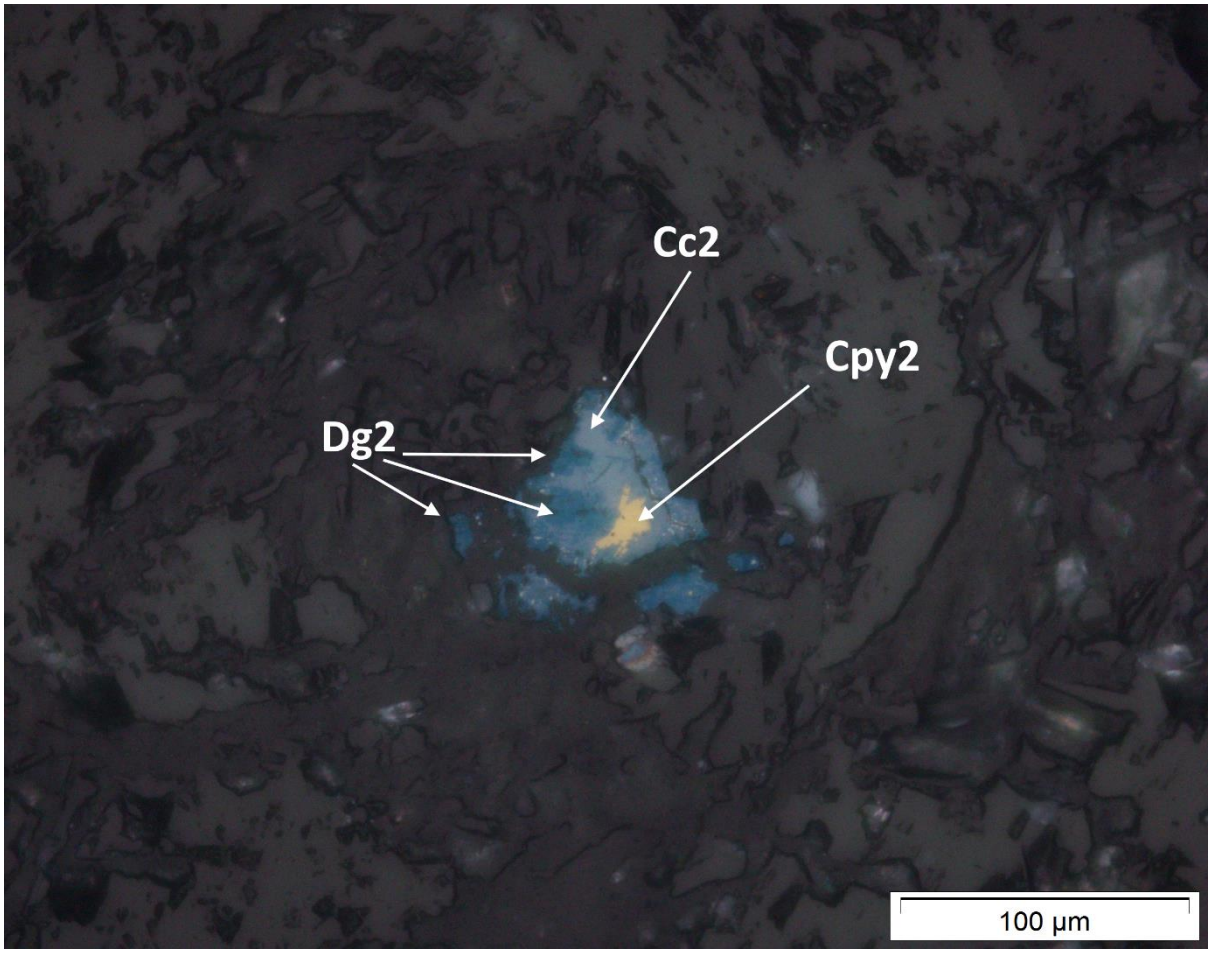

Figure 4.25*: Chalcopyrite 2 being progressively replaced by chalcocite 2 and then digenite 2 within a Type 2 dolomite vein. Optical image taken in reflected PPL from sample MSSD083_06_1.*

16. Native Copper 1 (Cu1): This phase forms amorphous, space filling vein-like masses which are frequently rimmed by cuprite 1 and tenorite 1, or sometimes by chalcocite 3 (Figure 4.26). Native copper 1, cuprite 1 and tenorite 1 are frequently found together, sometimes with azurite 1, malachite 1 and chrysocolla 1. It is only encountered within the RSC unit.

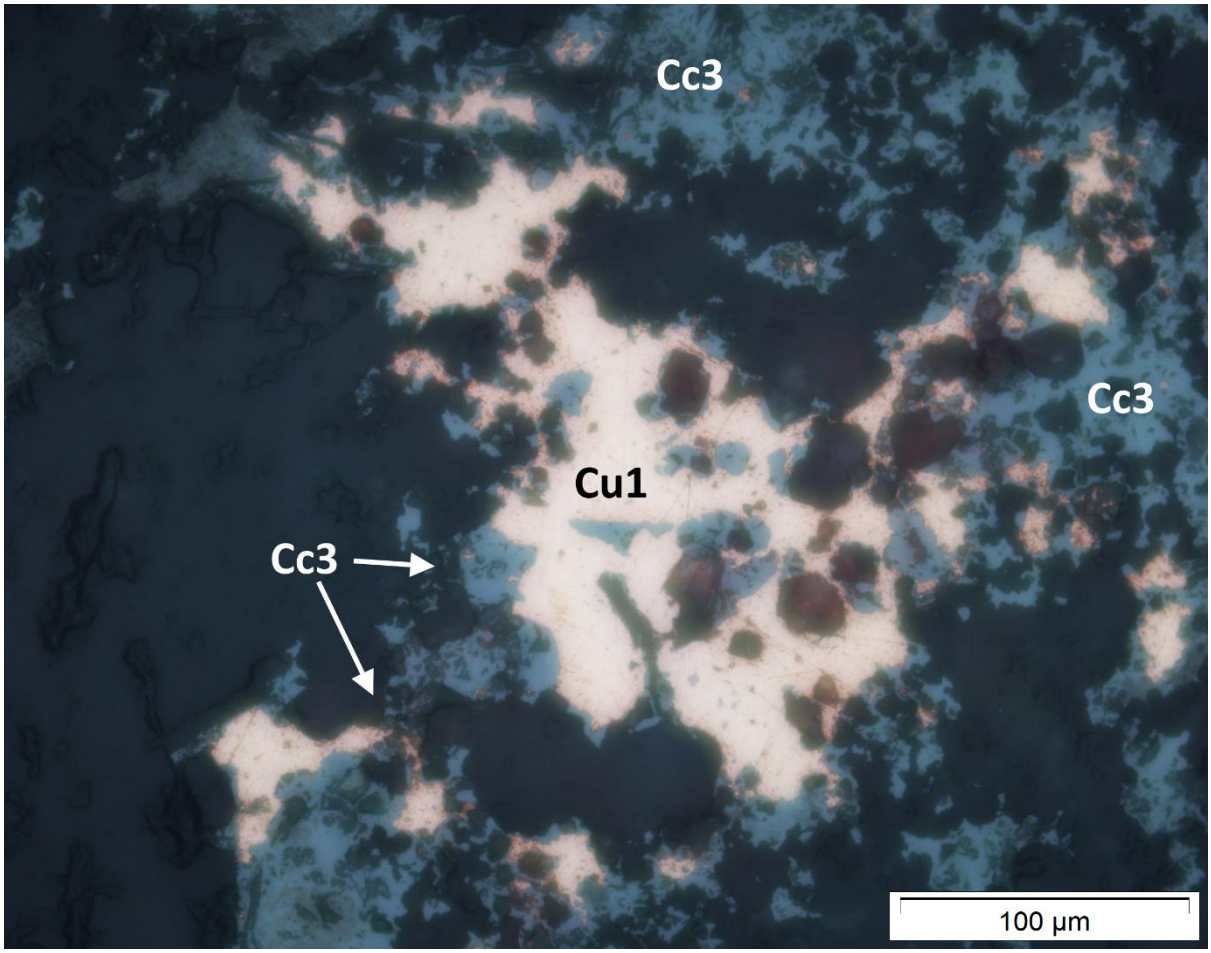

Figure 4.26*: Mass of native copper 1 mantled by chalcocite 3. Optical image taken in reflected PPL from sample MSSD080_18_1.*

17. Cuprite 1 (Cup1): Distributed in amorphous, space filling vein-like masses, and frequently forms a replacement rim to earlier native copper 1 (Figure 4.27). It occasionally forms very fine euhedral crystals but is not easily optically identified.
18. Tenorite 1 (Ten1): Distributed in amorphous, space filling vein-like masses, and frequently forms a replacement rim to earlier native copper 1 and cuprite 1 (Figure 4.27).

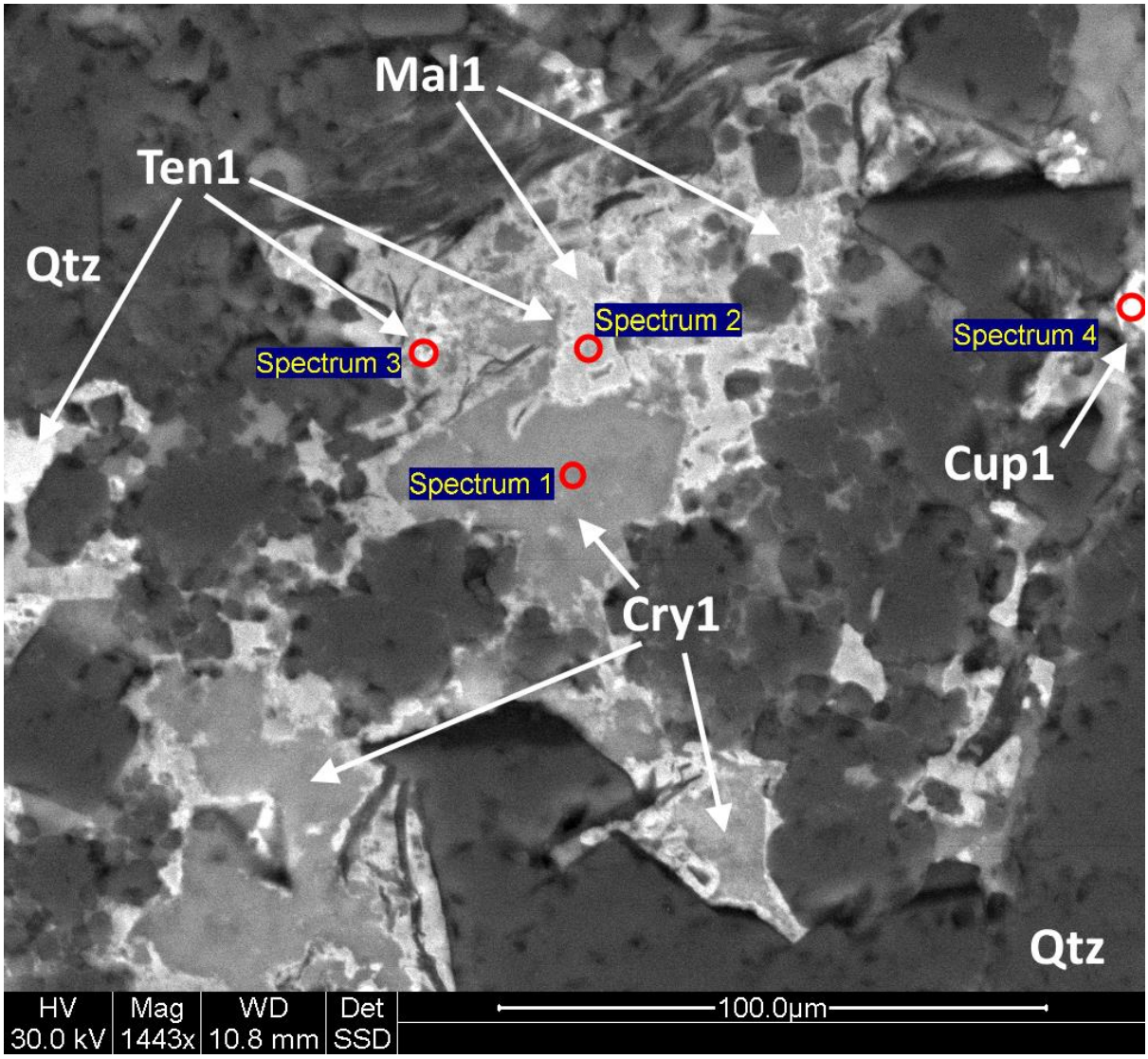

***Figure 4.27A**: SEM image showing the locations of EDS spot analyses. Spectra, shown in Figure 4.27B, indicate that spectrum 1 = chrysocolla 1, spectrum 2 = malachite 1, spectrum 3 = tenorite 1 and spectrum 4 = cuprite 1. These phases occur in the paragenetic order of cuprite 1, tenorite 1, malachite 1 and finally chrysocolla 1, generally appearing to fill voids in the rock from the outside inwards, with chrysocolla 1 filling the last remaining space during crystallisation. Sample MSSD080_18_1.*

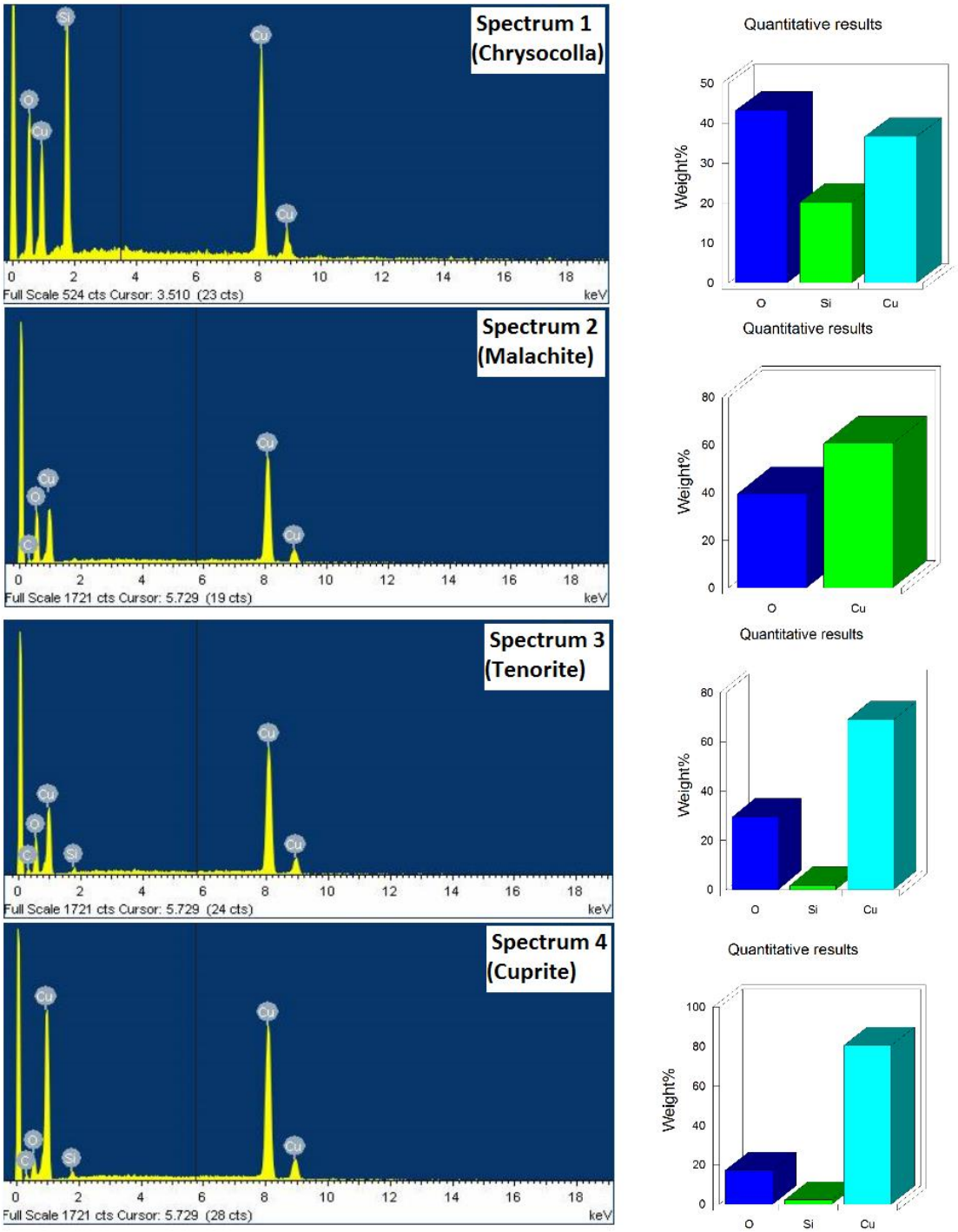

***Figure 4.27B**: Results of EDS spot analyses conducted on Spectra 1-4 as shown in Figure 4.27A. Spectrum 1 represents chrysocolla. Spectrum 2 represents malachite. Note that carbon in the malachite chemical formula ($Cu_2CO_3(OH)_2$) is not represented in the quantitative analysis of malachite, due to the carbon coating of the sample. Spectrum 3 represents tenorite. Spectrum 4 represents cuprite, which contains less oxygen by proportion than tenorite and is also brighter in the SEM image (Figure 4.27A). Si is included in the results for cuprite and tenorite, due to overlapping analysis of nearby chrysocolla within the area of electron-gathering during EDS spot analyses.*

19. Chalcocite 3 (Cc3): Chalcocite 3 is usually found as anhedral-to-rounded blebs and replacement rims to earlier sulphides, and occasionally to masses of native copper 1-cuprite 1-tenorite 1 (Figure 4.26). It is distinguished from earlier chalcocite phases by being concentrically banded with (Figure 4.18, 5.19 and 5.28), or containing exsolution lamellae of (Figure 4.29), haematite 2 at a very fine scale (<10µm).

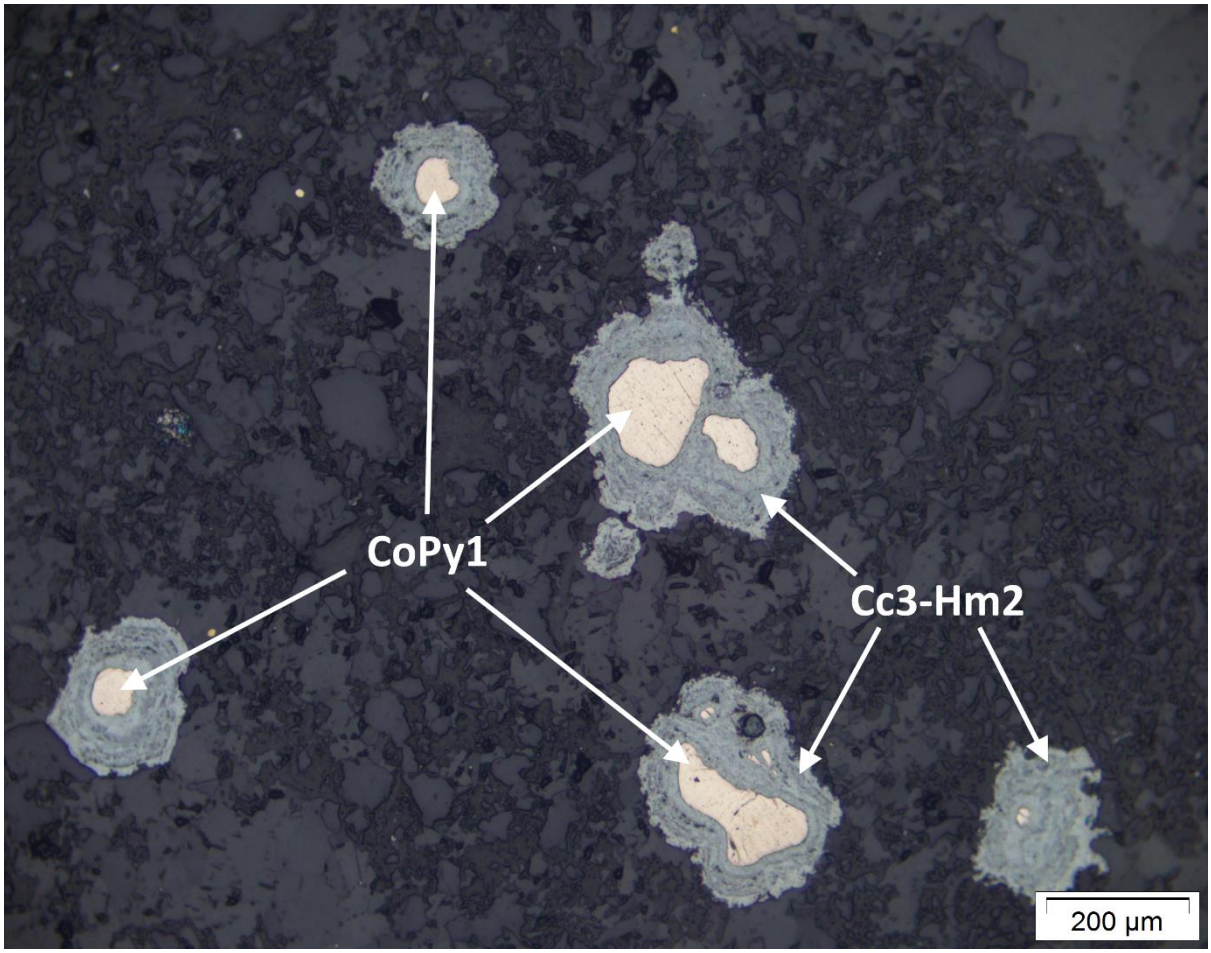

Figure 4.28*: Chalcocite 3, concentrically banded with haematite 2 around cobaltoan pyrite 1, and replacing it. Optical image taken in reflected PPL from MSSD080_13_2.*

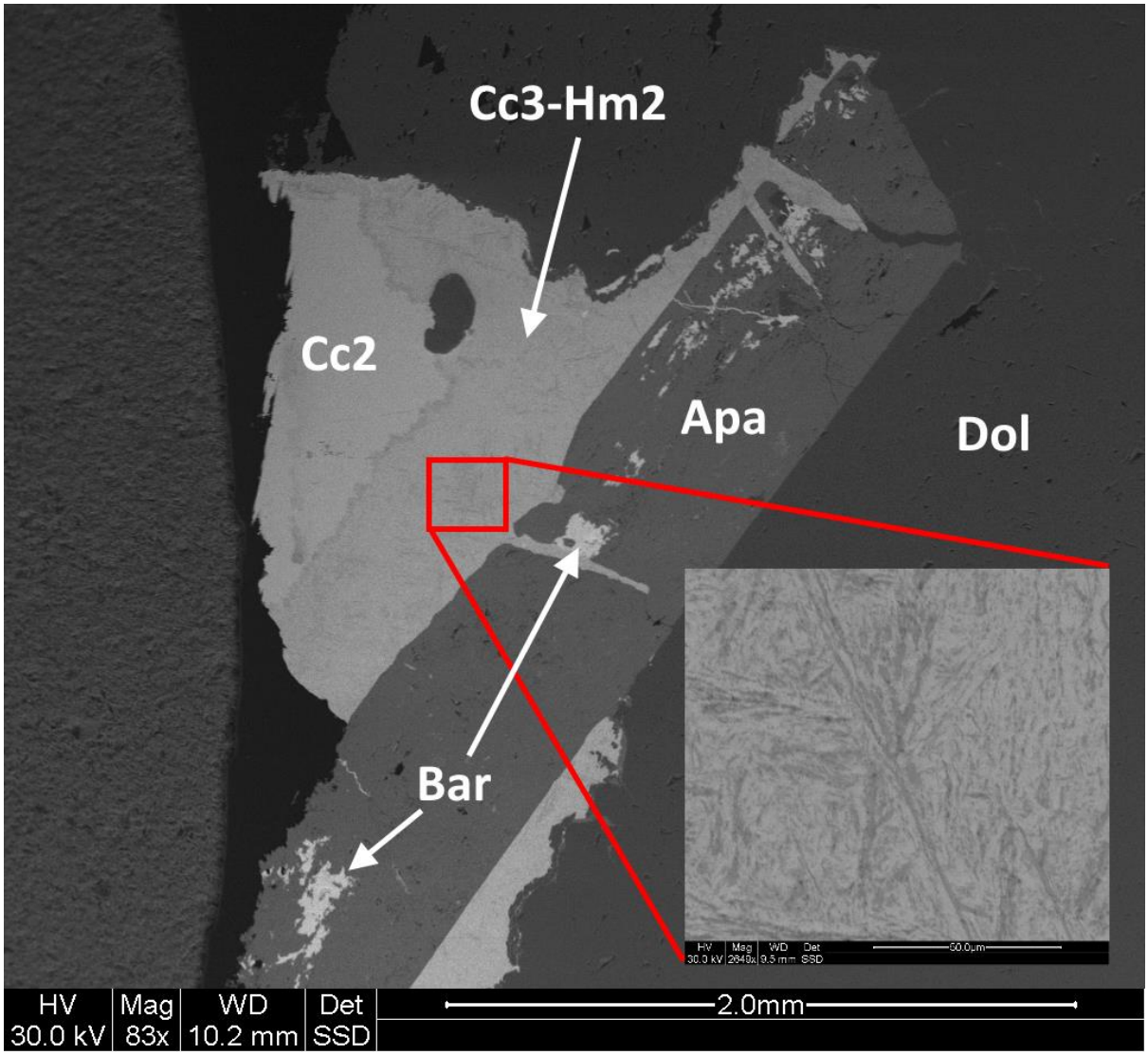

Figure 4.29*: SEM image of chalcocite 3 and haematite 2 intergrown, or forming exsolution textures with each other (see inset – haematite is the darker of the two phases). This mixture appears to be replacing a chalcocite 2 crystal in situ, which is wrapped around a euhedral apatite (Apa) - barite (Bar) crystal within a Type 2 vein. Sample MSSD075_19_2.*

20. Bornite-Digenite-Covellite 3 (Bn-Dg-Cov3): These three phases show intergrowths at a fine scale (<10µm) such that it is difficult to ascertain a paragenetic sequence for these sulphides. They occur almost universally as replacement rims to, or exsolution textures within chalcocite phases (Figure 4.30).

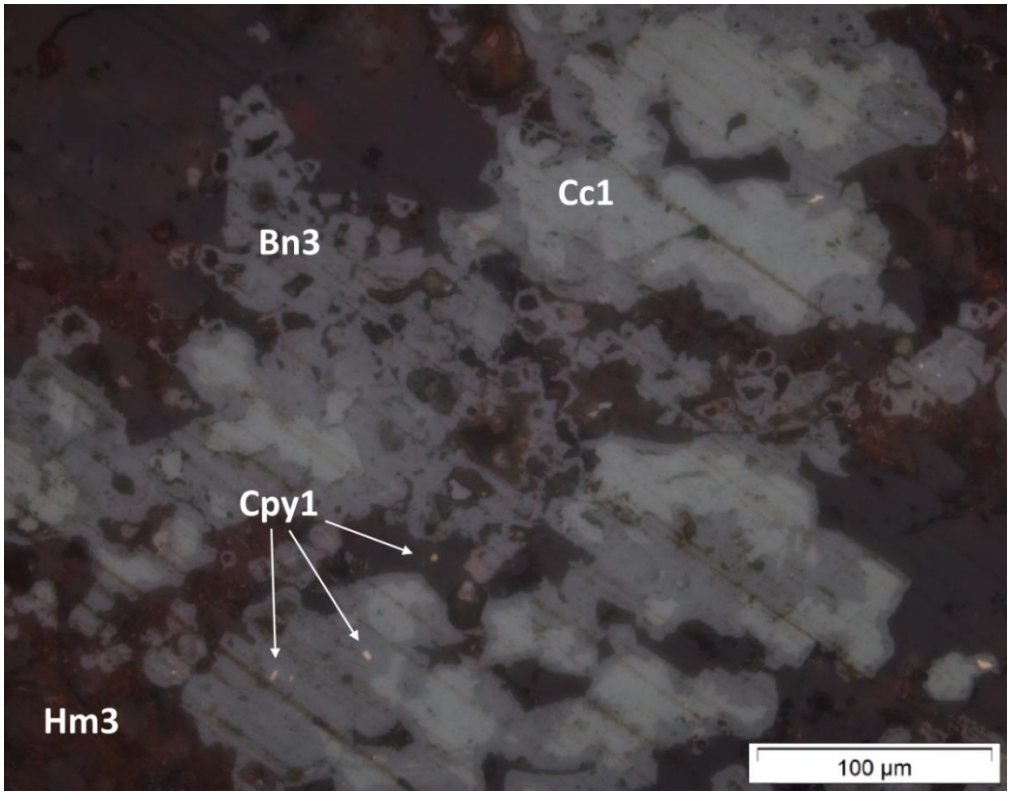

Figure 4.30*: Bornite 3 and haematite 3 rimming and replacing chalcopyrite 1 and chalcocite 1. Optical image taken in reflected PPL of MSSD075_15_1.*

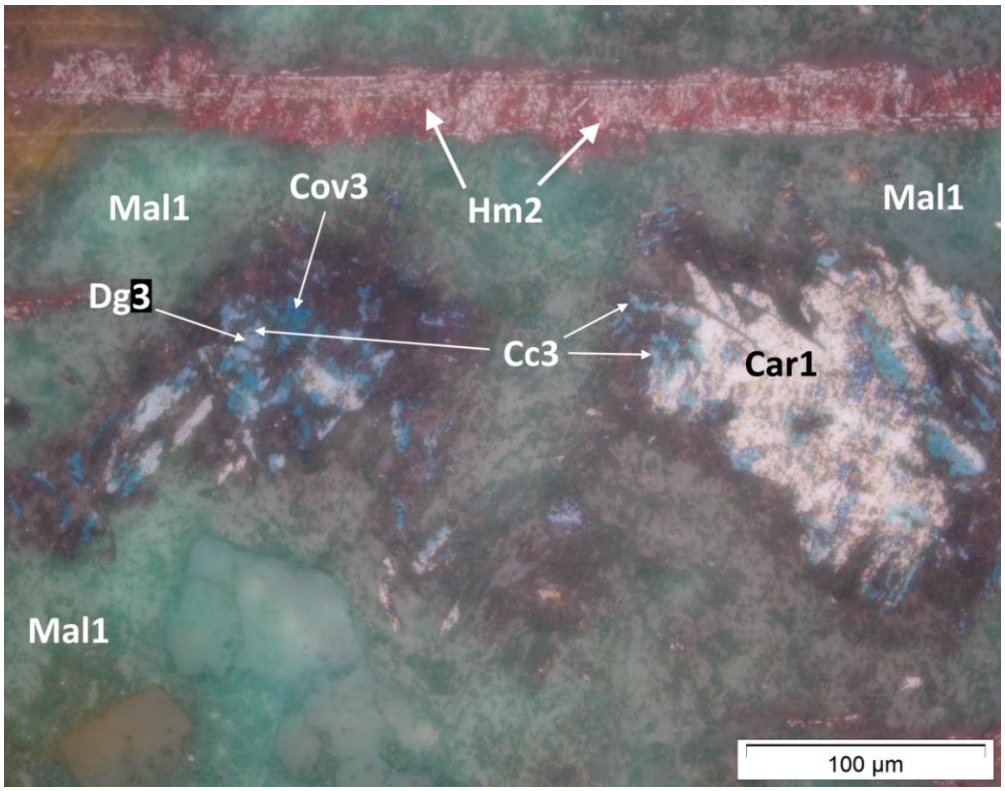

Figure 4.31*: Carrollite replaced by a complicated assemblage of chalcocite 3, digenite 3, and covellite 3, with later haematite 2 and malachite 1. Optical image taken in reflected PPL from sample MSSD080_10_2.*

21. Haematite 2 (Hm2): Haematite 2 forms anhedral replacement rims to earlier sulphide phases (Figures 4.32 and 4.33), although it may also occur as concentric bands within chalcocite 3 crystals (Figures 4.18, 4.19 and 4.28). Occasionally euhedral laths or lattices of haematite 2 may be found growing through and cross-cutting other phases (Figure 4.31). Haematite 2 usually has a blue-green tint in reflected light, in contrast to reddish or grey haematite 1, and is frequently associated with anhedral apatite.

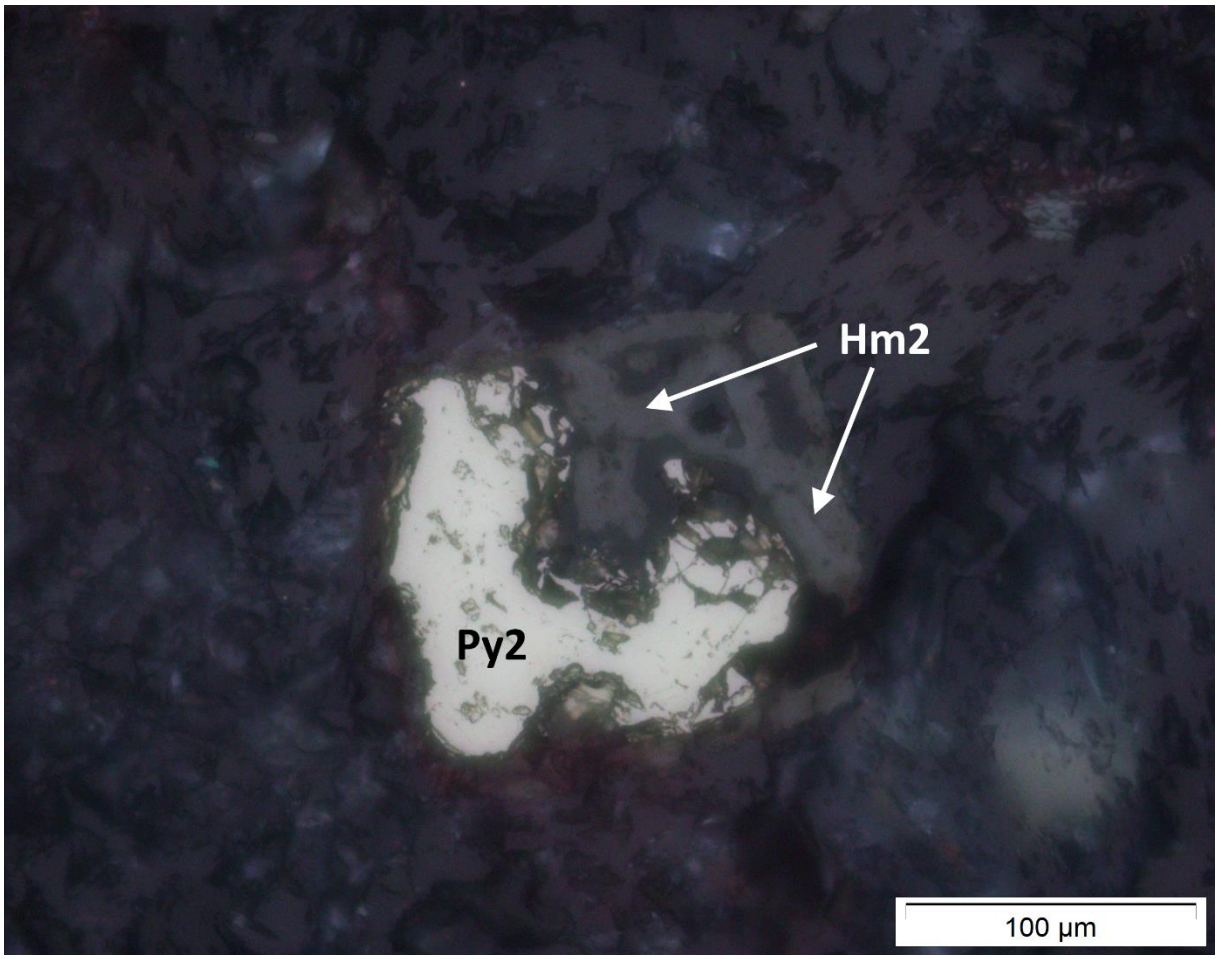

Figure 4.32*: A groundmass-disseminated crystal of pyrite 2 being replaced by haematite 2. Optical image taken in reflected PPL from sample MSSD083_07_2.*

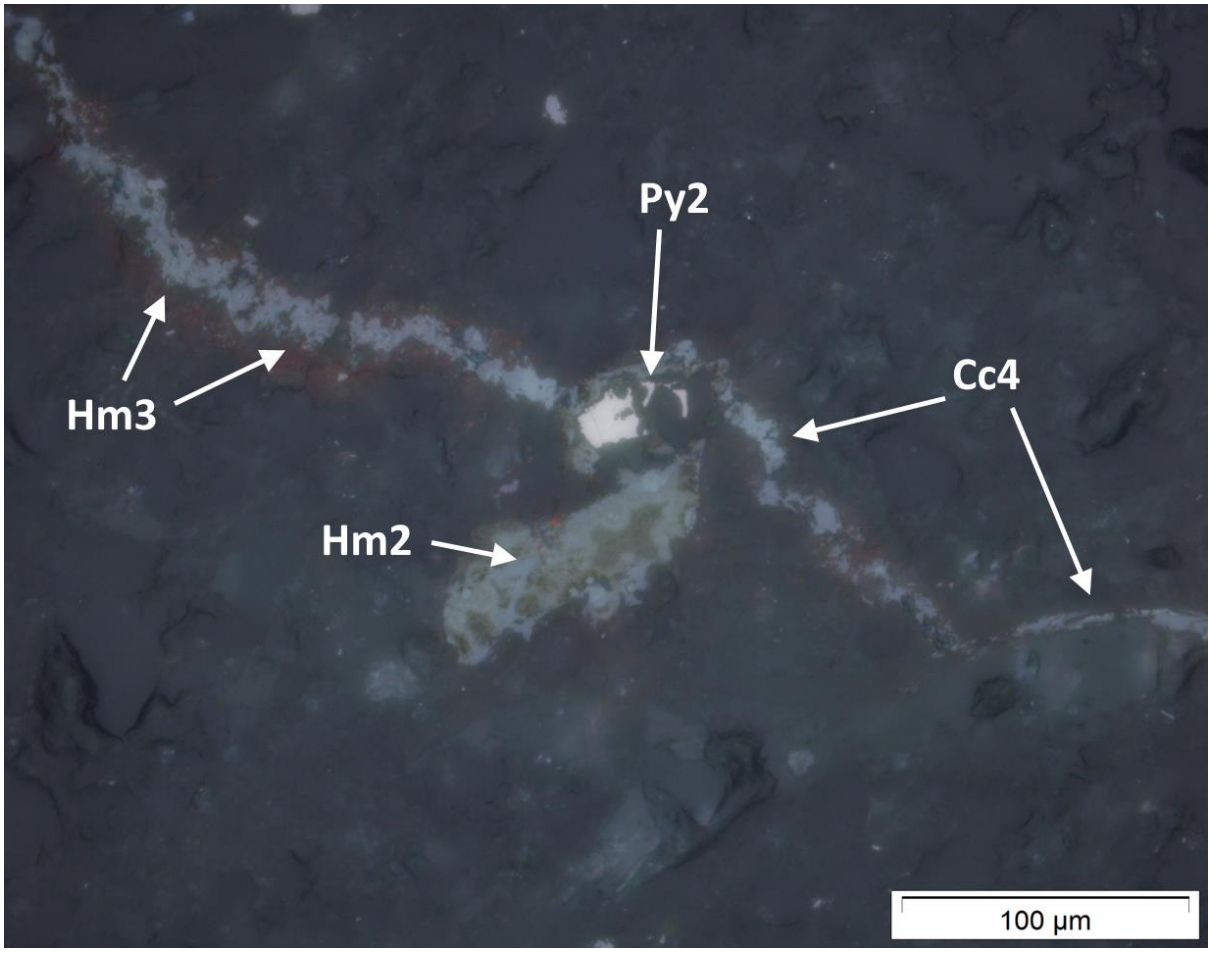

Figure 4.33*: Haematite 2 replacing a crystal of pyrite 2. A vein of later chalcocite 4 and haematite 3 abuts against the rim of haematite 2. Optical image taken in reflected PPL of sample MSSD083_20_1.*

22. Cobaltoan Carbonate 1 (CoCarb1): The Cobaltoan carbonate phase is comprised of spherocobaltite (Sct: $CoCO_3$), cobaltoan magnesite (CoMag: $MgCO_3$ with roughly 10-30 wt.% Co) and cobaltoan dolomite (CoDol: $CaMg(CO_3)_2$ with between 1-35 wt.% Co) usually precipitated in that order of paragenesis, with more cobalt-poor forms precipitated later than more cobalt-rich ones. These three phases, with all the varying Co concentrations, are combined into CoCarb1. Cobaltoan carbonate 1 is frequently found along veins where it appears to pervasively replace earlier dolomite in-situ; it also occurs as concentrically zoned rims to earlier carrollite 1 and blebs of chalcocite 3 and haematite 2 (Figure 4.34 and 5.35).

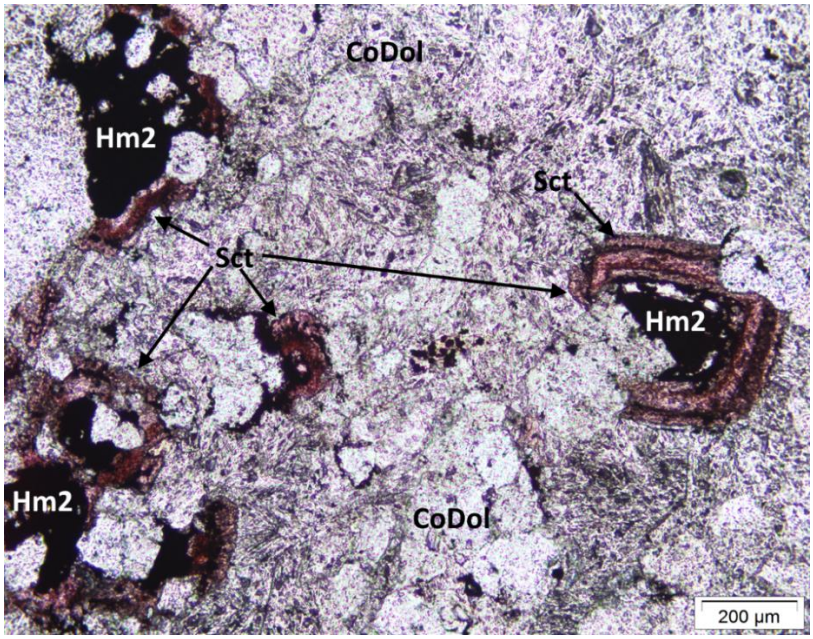

***Figure 4.34**: Haematite 2 crystals in a Type 2 dolomite vein mantled by concentrically zoned spherocobaltite (Sct) and cobaltoan dolomite. The faint pink colour of the vein dolomite belies a slight Co content making it cobaltoan dolomite (CoDol). Optical image taken in transmitted PPL of sample MSSD083_17_1.*

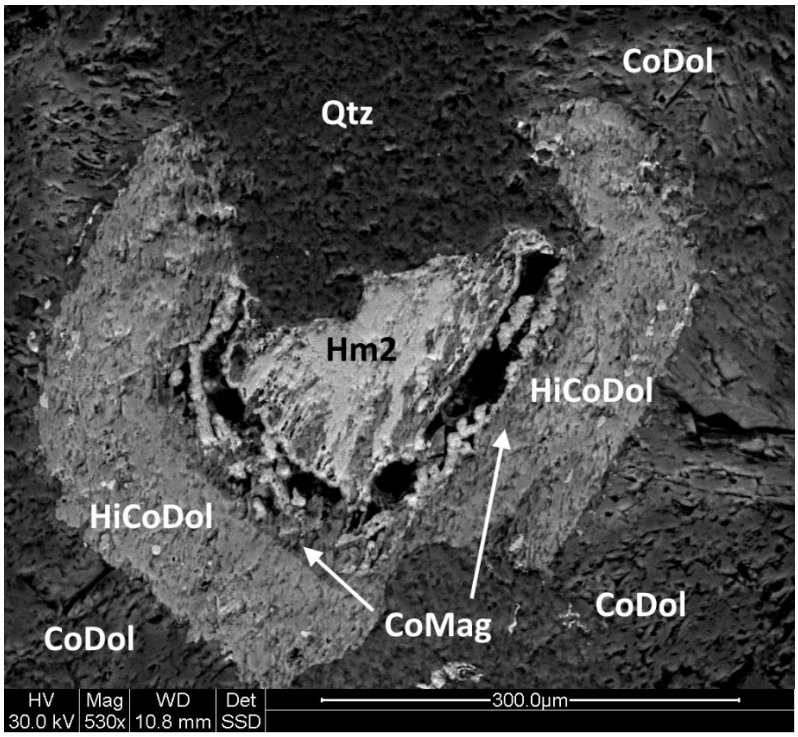

***Figure 4.35**: SEM image of the haematite (Hm2) crystal on the right in Figure 4.34. EDS analyses suggest minute amounts of spherocobaltite in contact with Hm2, mantled by cobaltoan magnesite (CoMag), followed by high-Co cobaltoan dolomite (HiCoDol), and finally low-Co cobaltoan dolomite (CoDol) making up the bulk of the vein. The phases are arranged in order of decreasing-outwards Co-content perhaps suggesting the progressive breakdown and replacement of a central Co mineral.*

23. Heterogenite 1 (Het1): Heterogenite 1 usually occurs as anhedral and space filling masses intergrown with quartz and apatite at a fine scale (<10µm) and containing trace amounts of Cu and Mn. It may also occur as concentric botryoids. See Figure 4.36.

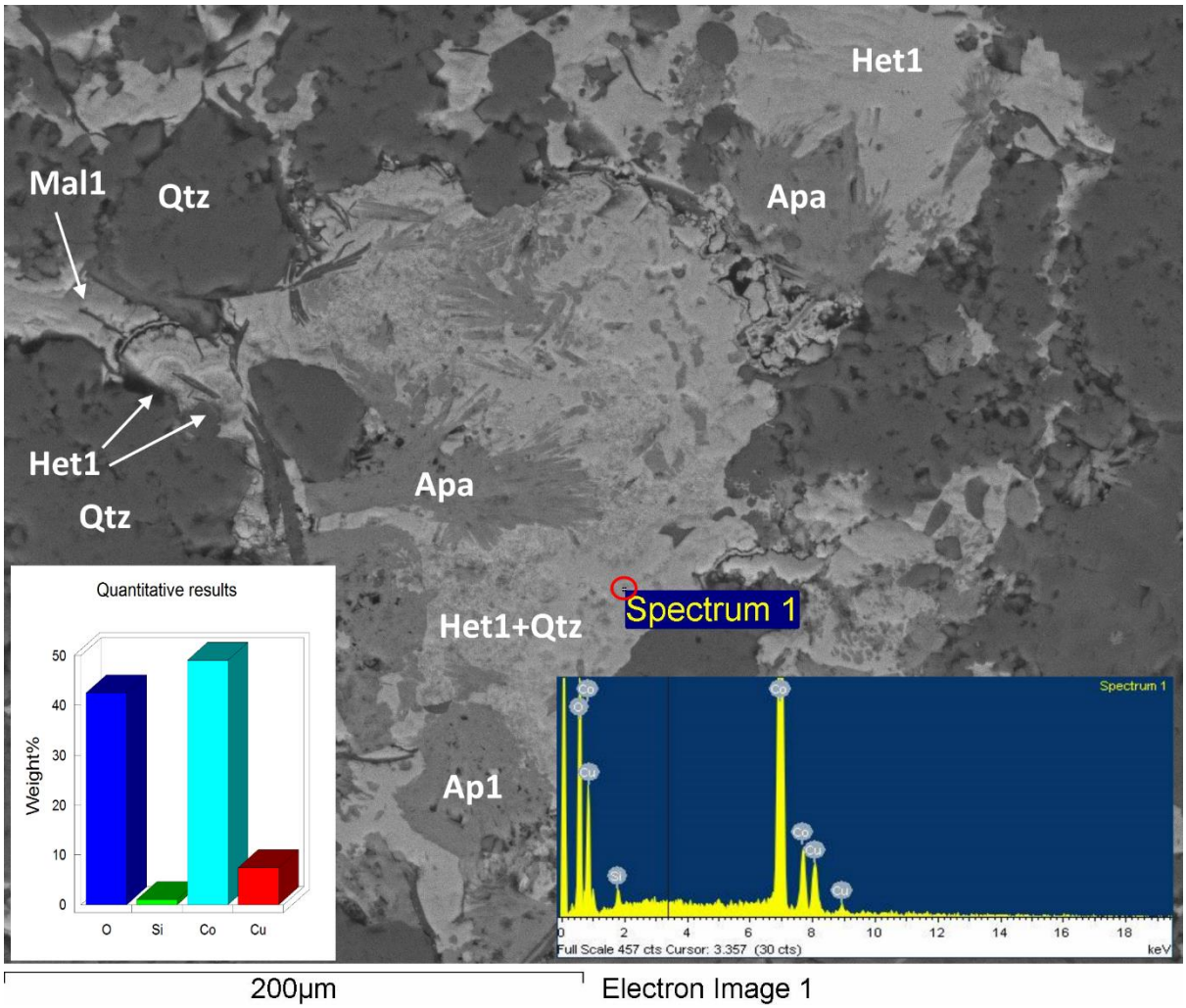

Figure 4.36*: SEM image of heterogenite 1 intergrown with apatite and quartz. EDS analysis of the phase shows that heterogenite 1 contains up to 10 wt.% Cu (Spectrum 1). The Si content of the Spectrum 1 analysis is caused by intergrown quartz. Note the concentrically zoned botryoids of heterogenite 1 towards the upper left of the image. Malachite 1 can be seen abutting against these heterogenite 1 botryoids. Sample MSSD080_18_1.*

24. Azurite 1 (Azu1) occurs as anhedral, space-filling intergranular masses or it is pervasively disseminated throughout the groundmass. It is frequently encountered as a rim to earlier cuprite 1 or tenorite 1 and is associated with chrysocolla 1 (Figure 4.37).

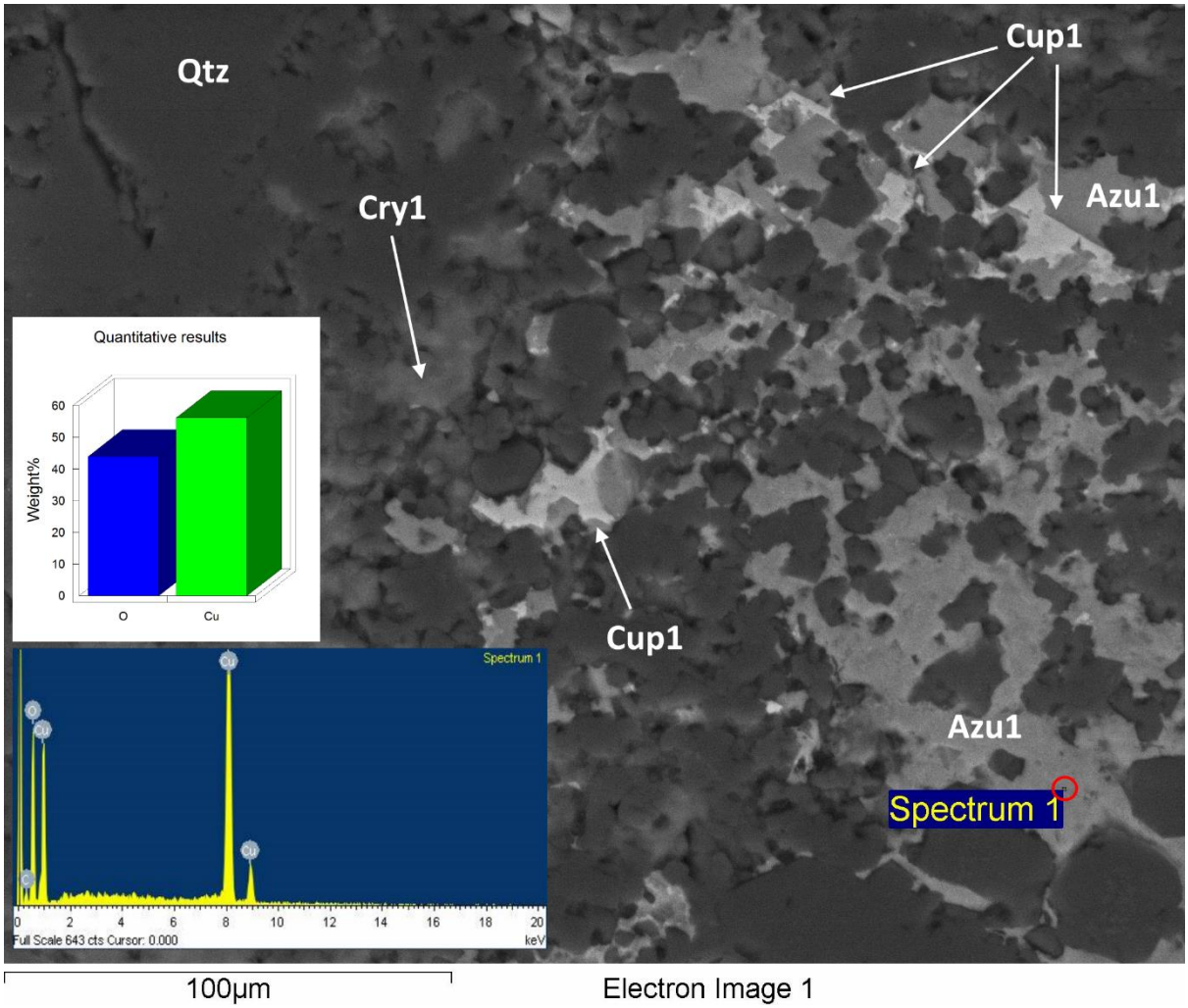

Figure 4.37*: SEM image of azurite 1 rimming and replacing euhedral cuprite 1, while chrysocolla 1 forms rims to azurite 1. Spectrum 1 is the result of an EDS analysis of azurite 1. Note the carbon content of azurite ($Cu_3(CO_3)_2(OH)_2$) is not represented by the analysis, as the sample has been carbon coated. The Cu content of the analysis is too high for the mineral to be malachite, which has a similar signature but contains less wt.% Cu. This is diagnostic of azurite, supported by the deep blue tinge to the portion of the slide from which this image was taken. Sample MSSD080_18_1.*

25. Malachite 1 (Mal1) is a scarcely encountered, anhedral, void-filling phase which takes the form of cross-cutting fracture-fill-veins.
26. Chrysocolla 1 (Cry1): Chrysocolla 1 usually exists as replacement rims to earlier malachite 1, or takes the same form within fracture-fill veins. Figure 4.38 illustrates the contrast between the malachite 1 and chrysocolla 1 phases and the malachite 2 and chrysocolla 2 phases.

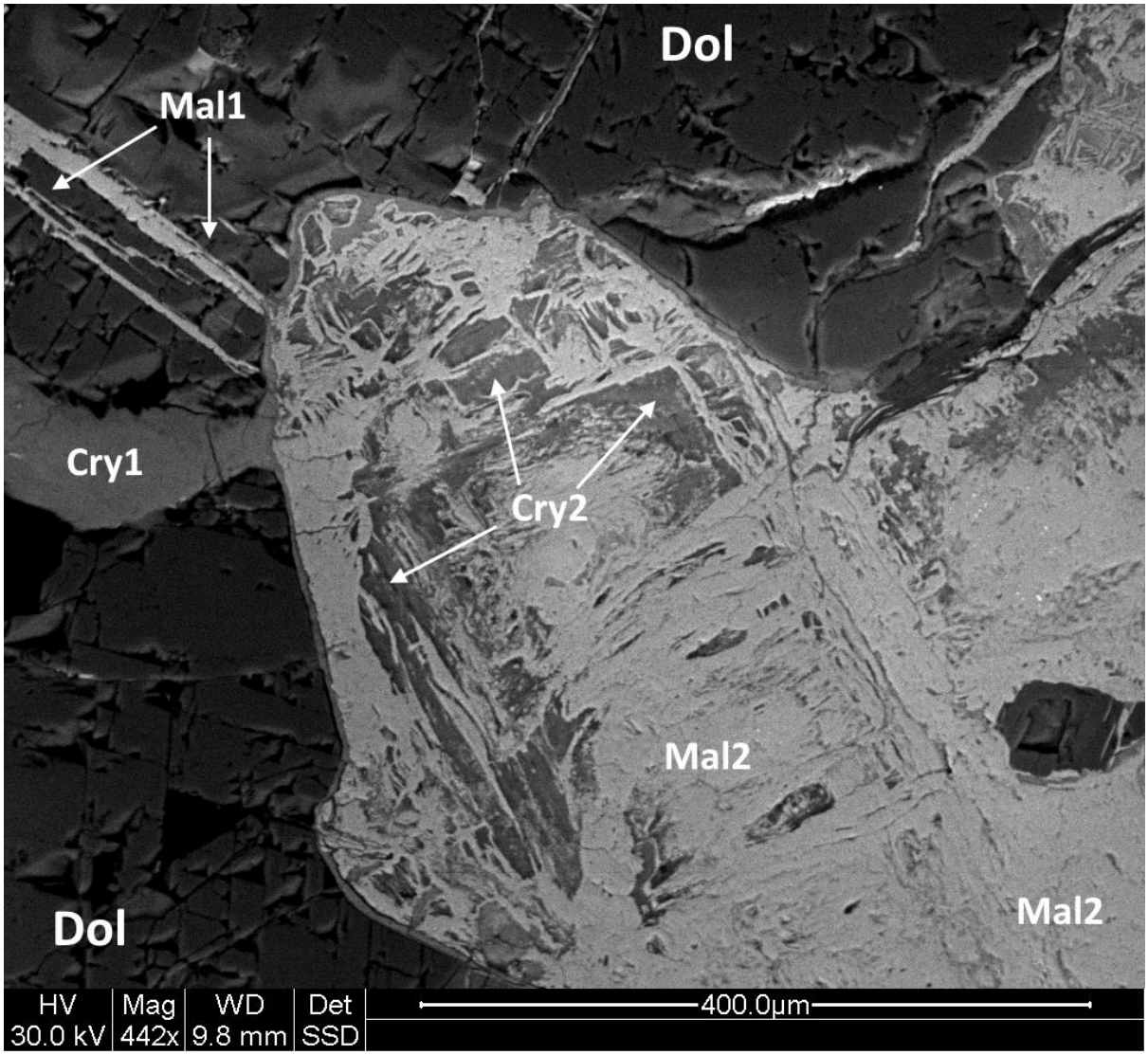

***Figure 4.38**: SEM image of malachite 1, chrysocolla 1, malachite 2 and chrysocolla 2 filling voids in a Type 2 dolomite vein. Malachite 1 and chrysocolla 1 occur as earlier veins which terminate at the void in which malachite 2, followed by chrysocolla 2, grow as outwards-in void fills. Sample MSSD080_10_2.*

27. Chalcocite 4 (Cc4) is an anhedral, void filling phase of chalcocite which tends to occur by itself within the groundmass or interlayered with concentric bands of haematite 3 (Figure 4.39). It may sometimes replace earlier phases of sulphide, including chalcocite 3 (Figure 4.40).
28. Haematite 3 (Hm3): Haematite 3 tends to be more anhedral, pervasive and amorphous than haematite 2, but where it occurs as concentric bands with chalcocite 4 (Figure 4.39), or by itself (Figure 4.41), it again has a blue-green tint in reflected light similar to haematite 2.

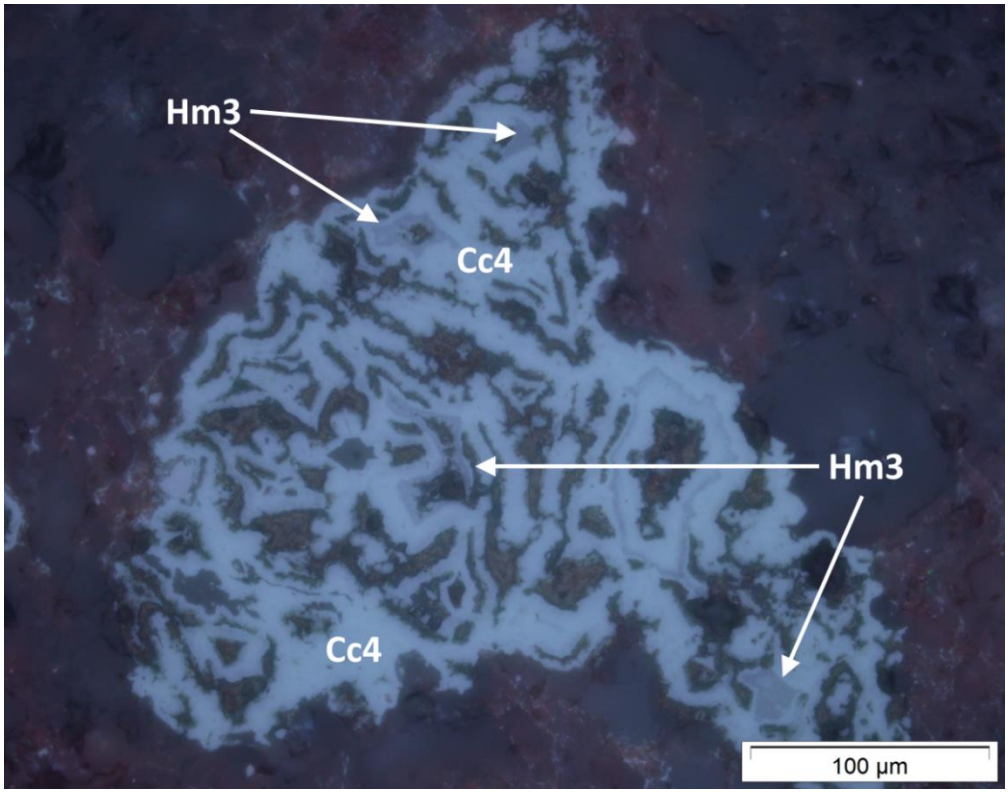

Figure 4.39*: Void filling bands of chalcocite 4 and haematite 3. Optical image taken in reflected PPL from sample MSSD083_20_1.*

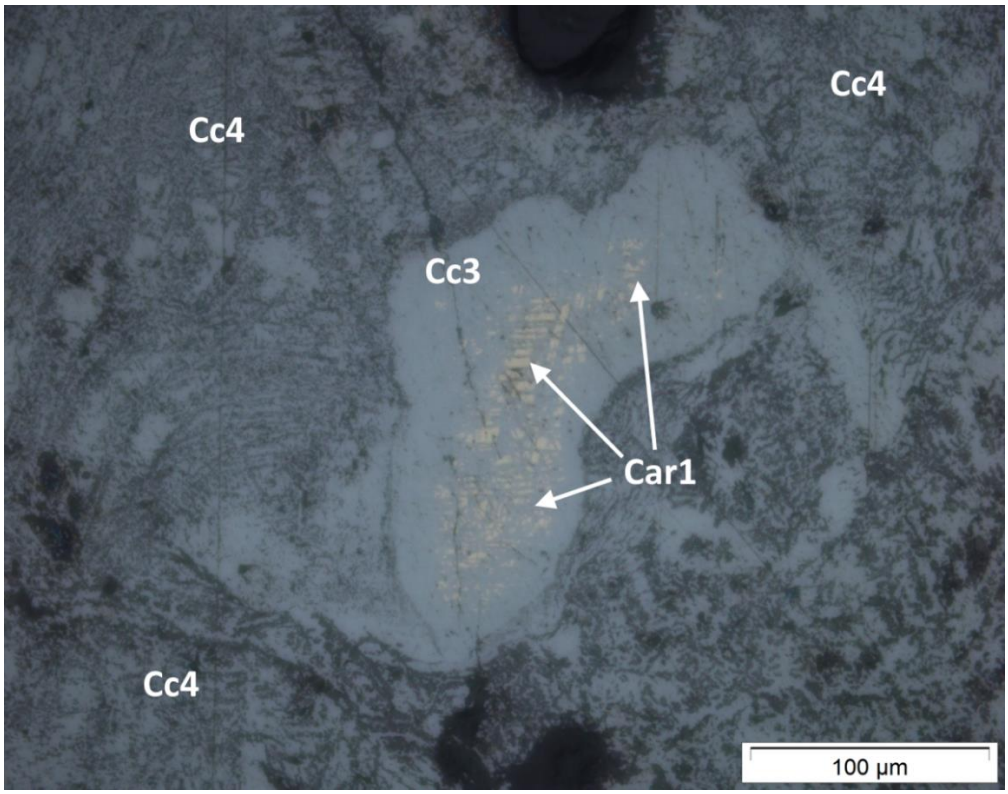

Figure 4.40*: Replacement of a carrollite 1 crystal in two stages: first by chalcocite 3, and then by chalcocite 4 which appears to be intergrown with an unidentified mineral, possibly haematite. Optical image taken in reflected PPL from sample MSSD083_24_2.*

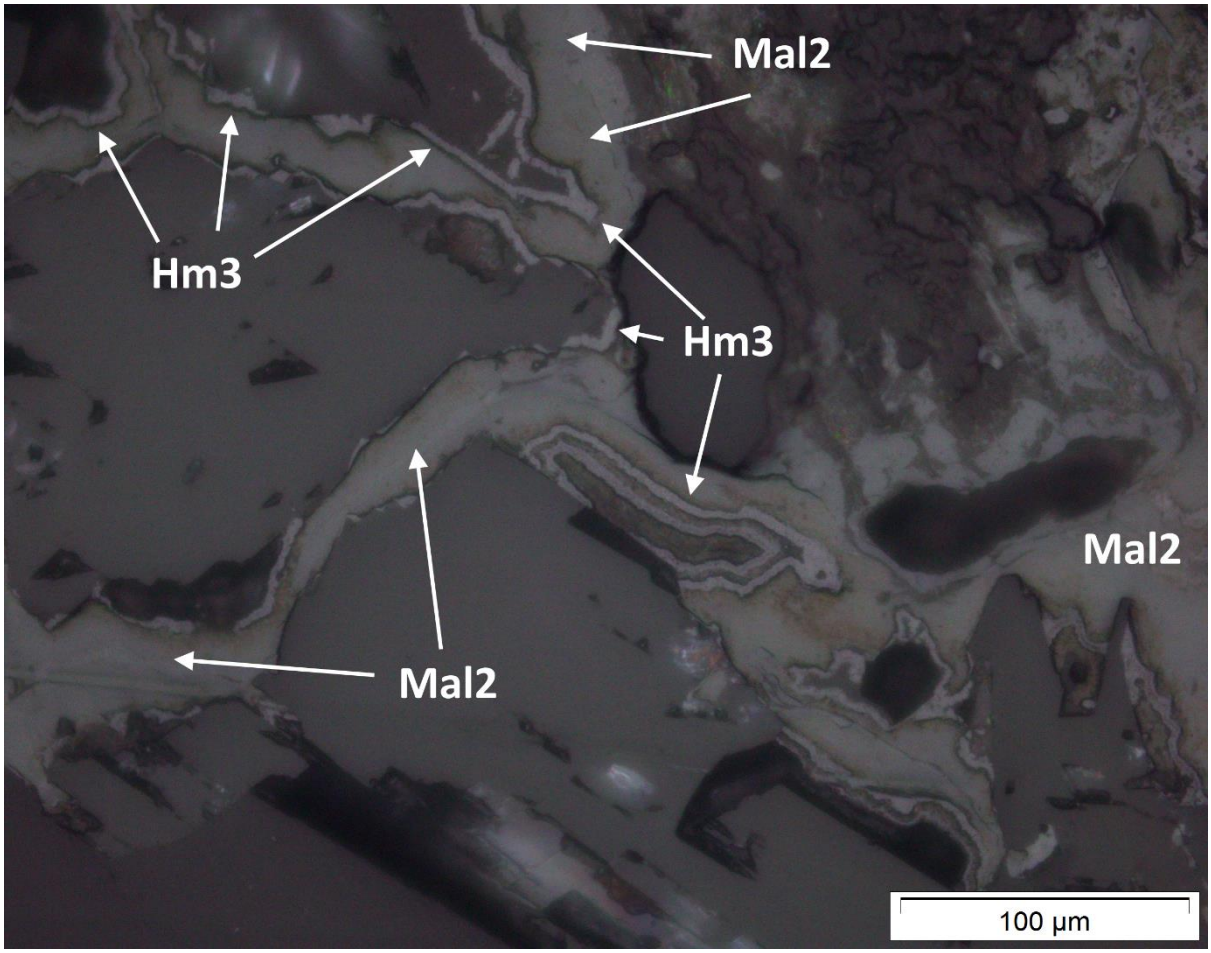

Figure 4.41*: Fracture-fill veins with haematite 3 forming first at the vein margins followed by malachite 2. Optical image taken in reflected PPL from sample MSSD083_07_1.*

29. Cobaltoan Carbonate 2 (CoCarb2): Cobaltoan Carbonate 2 exists primarily as a pervasive replacement phase within earlier dolomite veins (Figure 4.42) and consists of cobaltoan dolomite (no spherocobaltite or cobaltoan magnesite, as in Cobaltoan Carbonate 1).

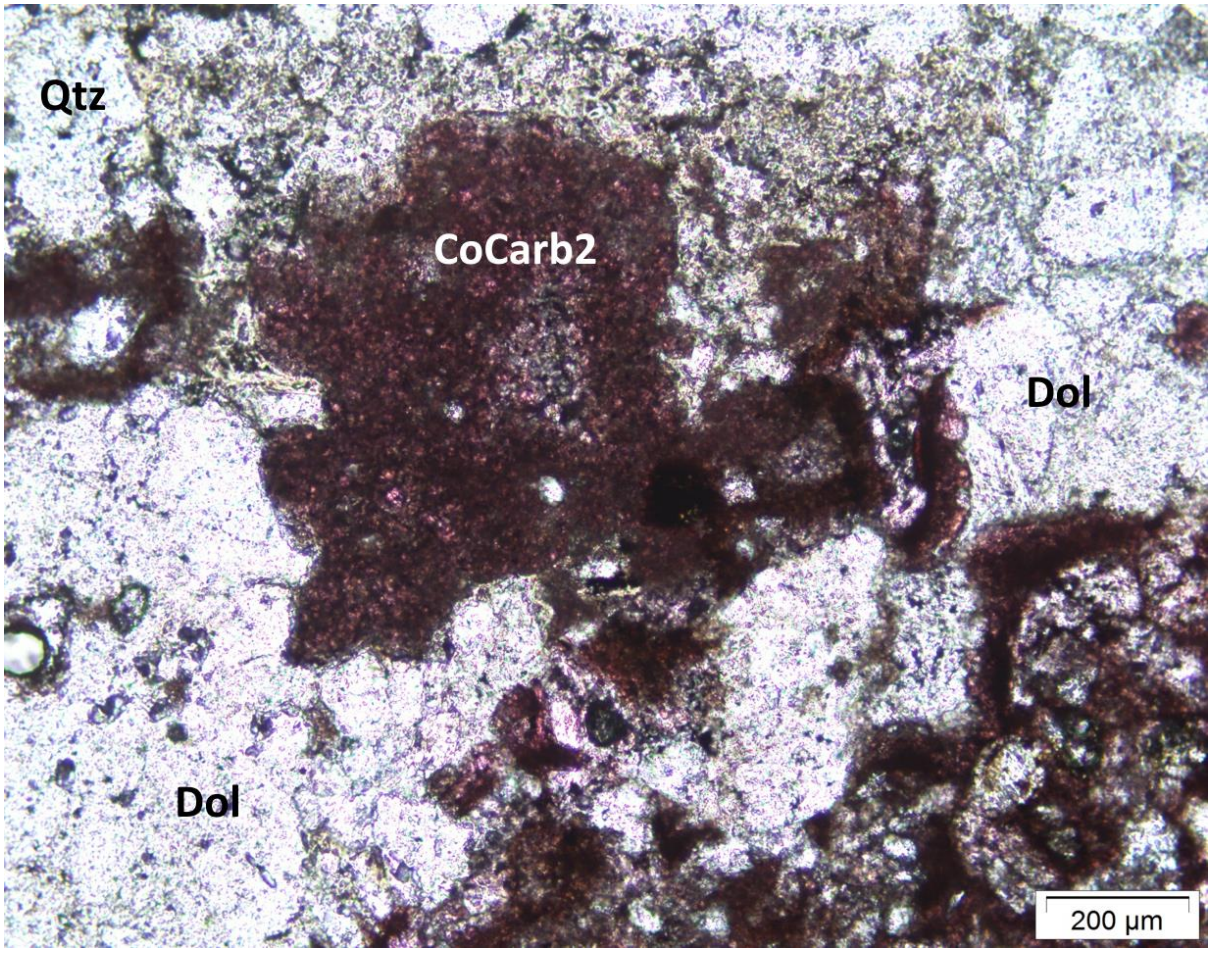

Figure 4.42*: Replacement of dolomite (Dol) along a Type 1 vein by cobaltoan carbonate (CoCarb2). Optical image taken in transmitted PPL of sample MSSD083_17_1.*

30. Heterogenite 2 (Het 2): As with heterogenite 1, the second phase of heterogenite occurs in association with supergene quartz and apatite. It may take the form of amorphous masses (Figure 4.43) or as dendrites (Figure 4.44) disseminated through the sedimentary groundmass. It may also form concentrically zoned botryoids containing varying amounts of Mn and Cu (both between 1 and 10 wt. %). Its textural similarity to heterogenite 1 means that it is best distinguished through paragenetic relationships with other phases.

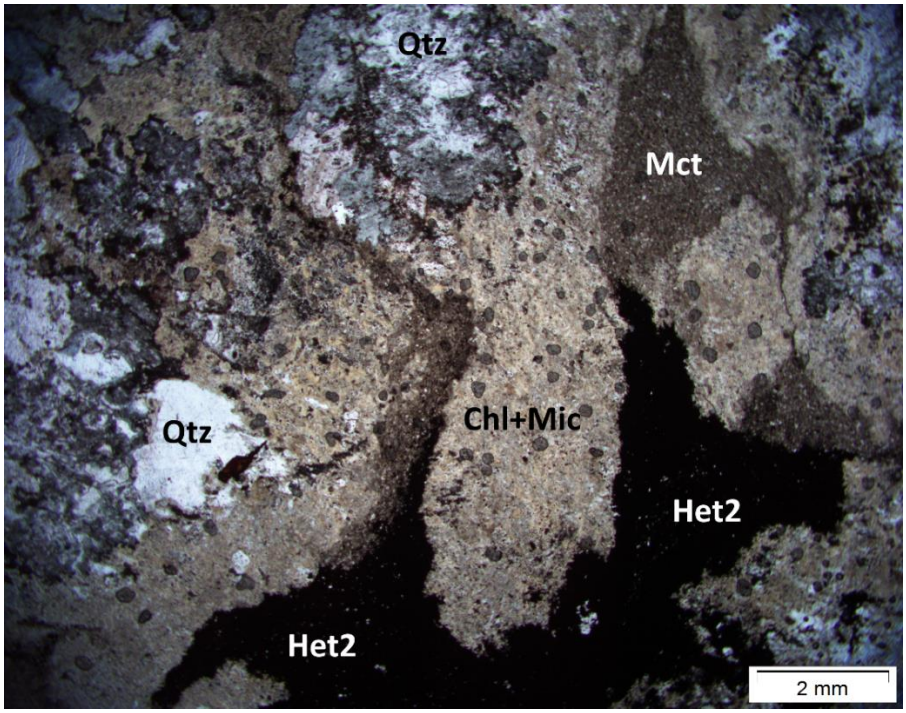

Figure 4.43*: Chaotic distribution of quartz (Qtz), micrite (Mct) and a mixture of chlorite (Chl) and mica (Mic) in the RSC unit. Heterogenite (Het2) occurs pervasively as amorphous masses distributed through the micaceous portion of the rock. Optical image taken in transmitted XPL from sample MSSD075_17_1.*

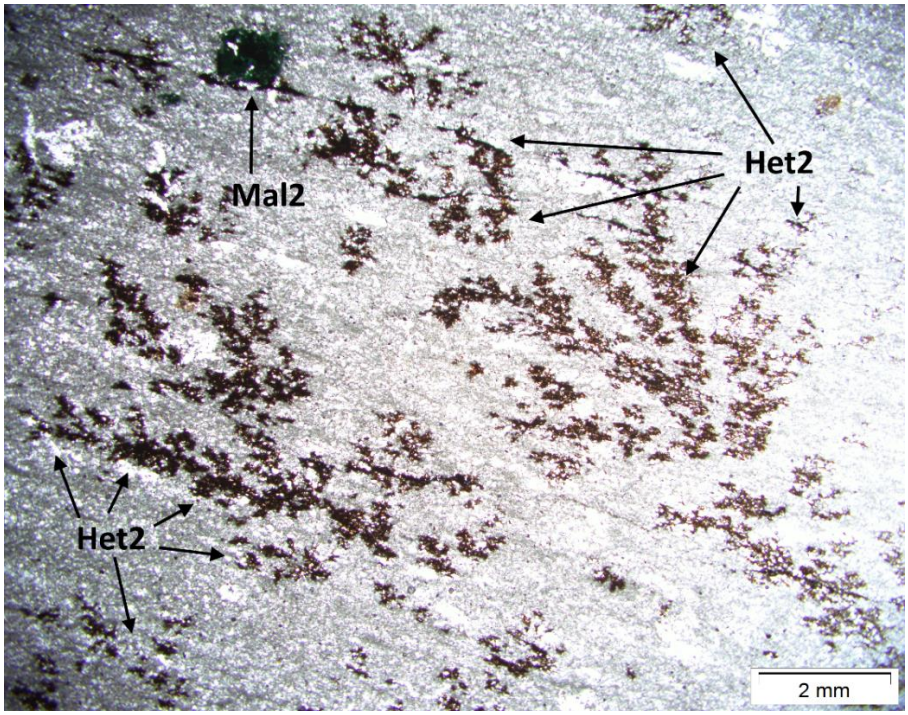

Figure 4.44*: Dendritic heterogenite 2 growing through the groundmass of the Schistes Dolomitique Superieur unit (SDS). EDS analysis shows that heterogenite 2 is intergrown with apatite. Later malachite 2 grows around the Het2 dendrites. Optical image taken in transmitted PPL from sample MSSD080_14_2.*

31. Malachite 2 (Mal2): Malachite 2 is the more abundant of the two malachite phases and is usually void or fracture filling, though it may also be groundmass-disseminated or distributed around the rim of earlier copper-bearing phases. Where it is void filling it often forms botryoids with a radial-fibrous internal structure (Figure 4.45).

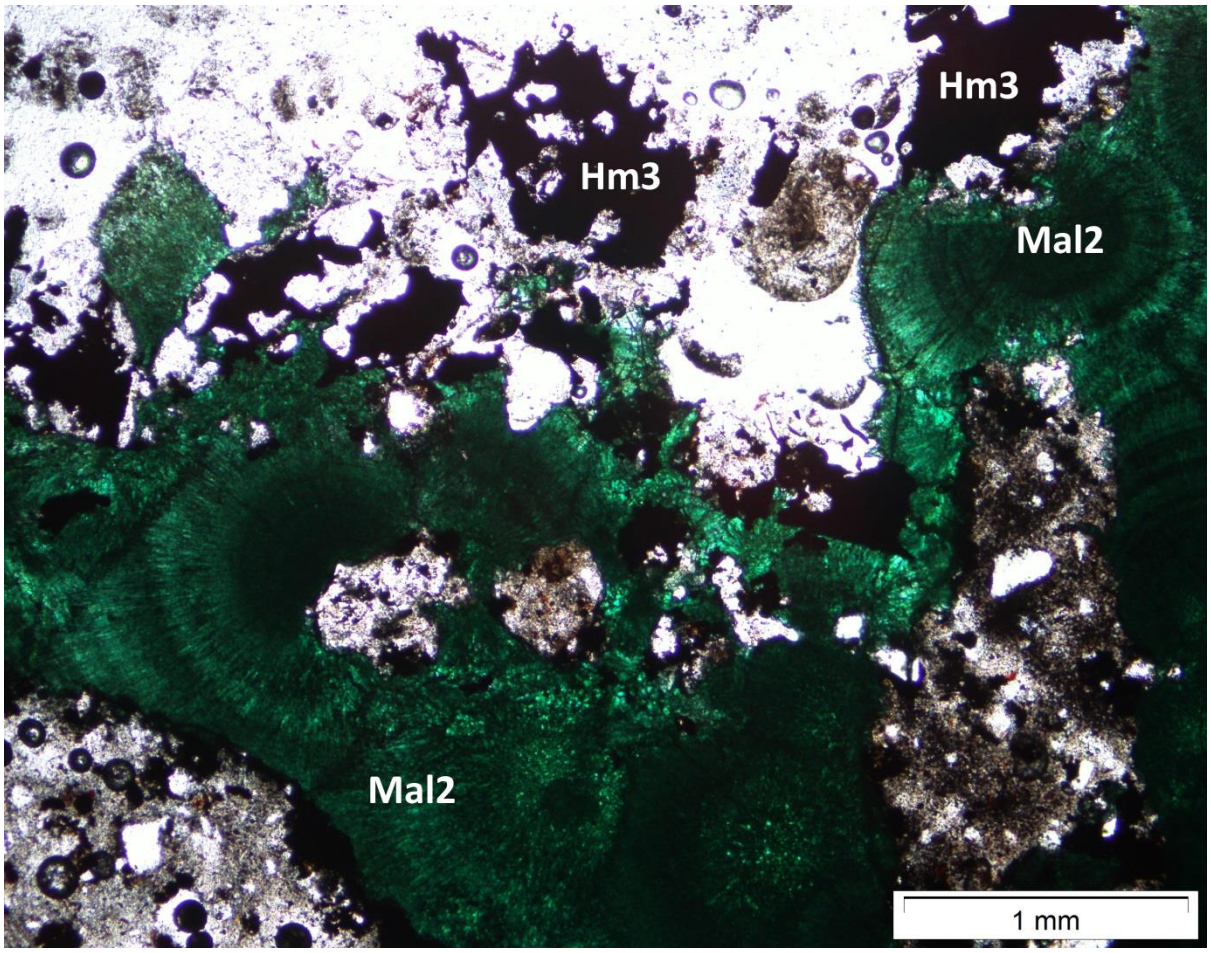

Figure 4.45*: Radial-fibrous malachite 2 within a fracture-fill vein in the RAT Rouge. The earlier haematite 3 phase can be seen around the vein-margins. Optical image taken in transmitted PPL from sample MSSD140_07_1.*

32. Chrysocolla 2 (Cry2): Chrysocolla 2 may be found disseminated within the rock groundmass, as rims to malachite 2, or filling voids within malachite 2 crystals. It is the more abundant of the two chrysocolla phases (Figure 4.46).

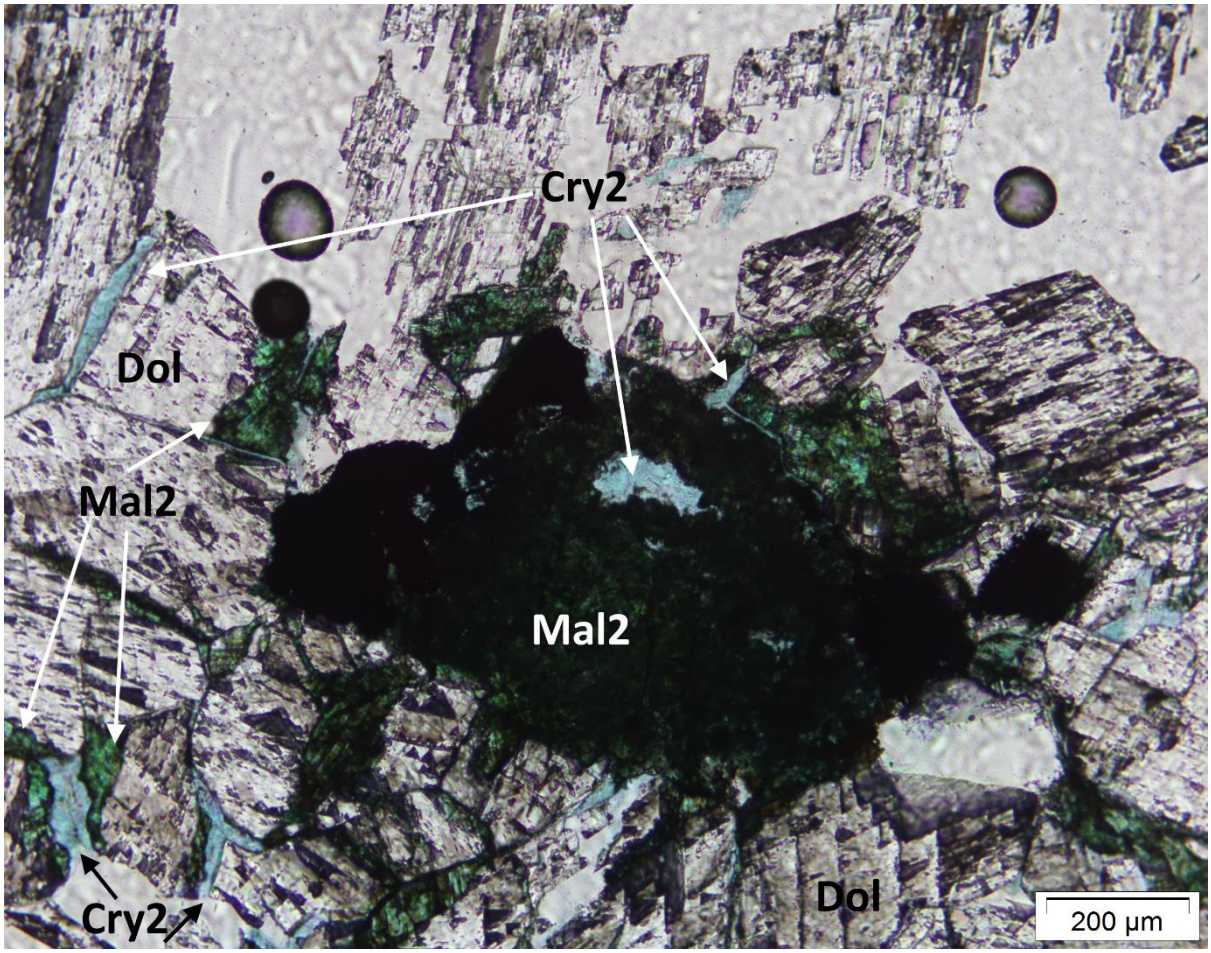

***Figure 4.46**: Anhedral malachite 2 forming in voids and fracture-fill veins, with later-formed chrysocolla 2 forming the centres to these voids and veins. Optical image taken in transmitted PPL from sample MSSD080_10_2.*

33. Pseudomalachite 1 (Psm1): Pseudomalachite 1 fills voids between growing malachite 2 crystals, where it forms spherical, botryoidal masses (Figures 4.47 and 4.48).

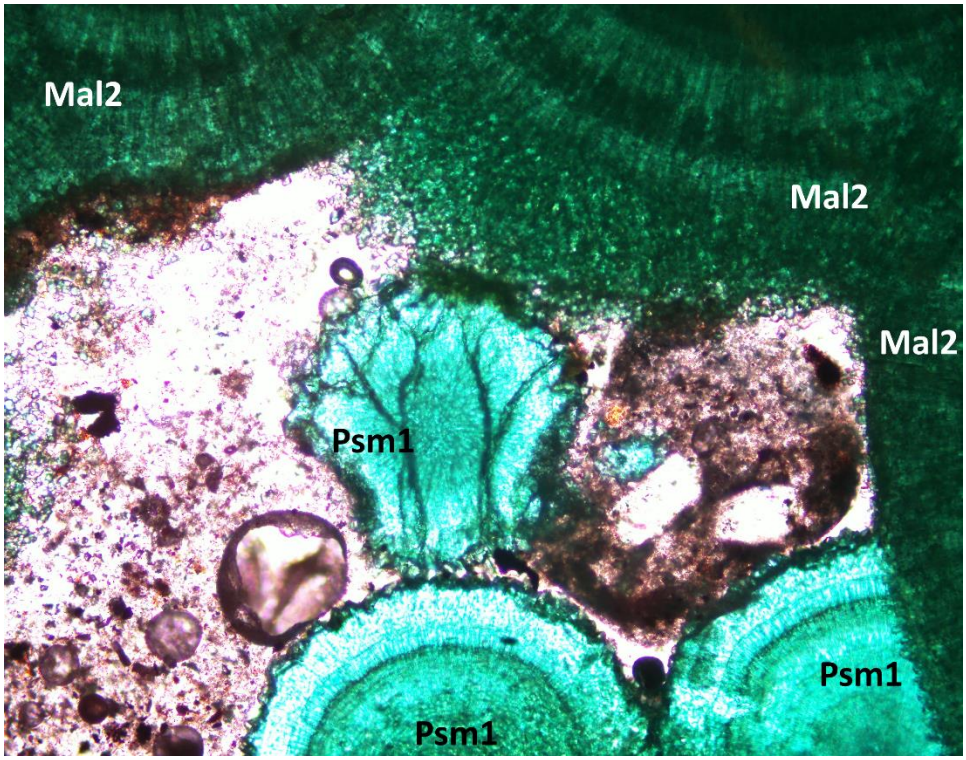

Figure 4.47: *Botryoidal pseudomalachite 1 growing out from earlier-formed botryoids of malachite 2. Optical image taken in transmitted PPL from sample MSSD140_07_1.*

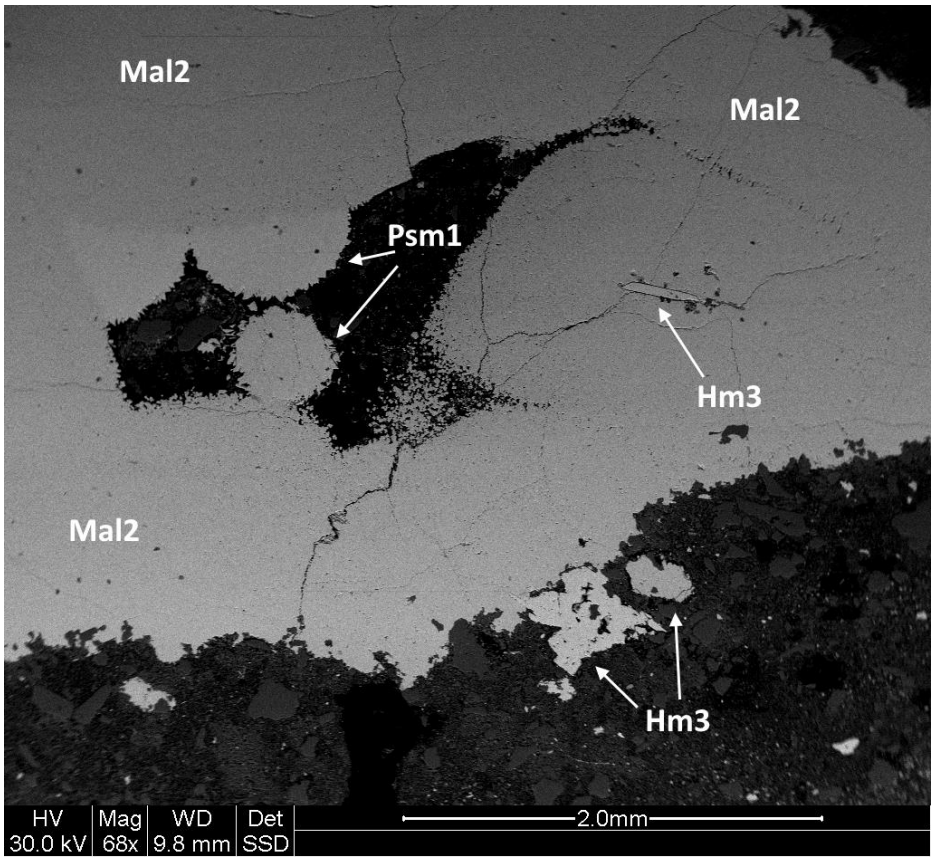

Figure 4.48: *SEM image of an assembly of euhedral laths of haematite 3, radial fibrous malachite 2 and botryoidal pseudomalachite 1, formed in that paragenetic order. Sample MSSD140_07_1.*

4.3.2 Ore Mineral Distribution

The stratigraphic units in which the occurrences of mineralisation-related phases were found were recorded, and the results are presented in Figure 4.49. This figure shows the number of occurrences of different phases identified in each of the stratigraphic units at Mashitu South, but does not represent the absolute abundance of each phase in a particular stratigraphic unit. This is because it does not take into account unit thickness or the number of samples taken from each unit.

4.3.3 Gangue Mineralogy

Investigation of the gangue mineralogy at Mashitu South was not the primary focus of this petrographic study. However, observations on gangue phases that were made, particularly when related to mineralisation, were recorded and are presented in this section.

The siliciclastic nature of rocks from the SD and RAT units was confirmed. In terms of sedimentary minerals, these rocks are primarily composed of detrital, rounded quartz although lesser proportions of micrite and later coarse dolomite cement are also present. Detrital zircons were identified in a few samples (Figure 4.50). In all of the 'calcareous units', from the CMN, RSC, RSF and DStrat stratigraphic units, only a single calcite vein in one sample was identified, cutting a nodule of magnesite (Figure 4.51). Micrite and coarse crystalline carbonate were both found to be primarily composed of dolomite, although a few nodules (Figures 4.51 and 4.52) and vein-hosted (Figure 4.53) occurrences of magnesite were also identified. Chlorite (clinochlore: $Mg_5Al(AlSi_3)O_{10}(OH)_8$, see Figure 4.54), muscovite ($KAl_2(AlSi_3O_{10})(F,OH)_2$, see Figure 4.55) and biotite ($K(Mg,Fe)_3(AlSi_3O_{10})(F,OH)_2$, see Figure 4.56), are commonly developed in both siliciclastic and calcareous units. However, muscovite and biotite are rare in the RAT Rouge, but common in the SD unit. The chlorite and muscovite are often euhedral and sometimes aligned (Figure 4.55), though this alignment can never be traced consistently enough to be called a foliation, other than occasionally where it is parallel to bedding. Chlorite and muscovite usually show textural relationships which suggest that they were formed epigenetically (i.e: were not deposited during sedimentation).

Stage	Pre-Ore Diagenesis			Early Hydrothermal SSC							Late Hydrothermal Cu				
Phase	Py1	Hm1	Py2	Py3	Sph1	Cpy1	Bn1	Dg1	Cc1	Car1	Car2	Cpy2	Bn2	Cc2	Dg2
Stratigraphic Unit: CMN	1		4	1		5			2	6	4	3	1	2	
SDS	1		2							1	1	4	1	2	
SD2d	1	2	1	1	1	3	2	1		2					
SDB		2	2	3		3	2		3	3	3				
RSC									1	2					
RSF				1						5	1			3	
DStrat	2			6		1	1		4	4	1	1	1	2	1
RATGris	1	1	1	1		1	1	1	1	1	3				1
RATRouge		1		1		1				1					
	DIAGENESIS			HYPOGENE											

Stage	Early Supergene											Late Supergene						
Phase	Cu1	Cup1	Ten1	Cc3	Bn-Dg-Cov3	Hm2	CoCarb1	Het1	Azu1	Mal1	Cry1	Cc4	Hem3	CoCarb2	Het2	Mal2	Cry2	Psm1
Stratigraphic Unit: CMN				9	3	5	1			1	2	2	3	1		6	3	1
SDS			1	5	1	4				1		1	2		1	2		
SD2d				1	1							1						
SDB				4	1	1						1	1	1		2	1	
RSC	1	1	1	2		2	2	1	1			1	3	1	2	1	1	
RSF				2										2				
DStrat				1		1												
RATGris				2	1	1						1	1	1				
RATRouge				1		1												
	SUPERGENE																	

***Figure 4.49**: Table showing the distribution of mineralisation-related phases identified in MSSD057, 080 and 083, in each of the stratigraphic units at Mashitu South. The number in each cell shows how many samples from a particular unit carried a particular mineralisation phase. Each cell has a corresponding bar representation, the thickness of which is proportional to the number of samples identified. The 'Stages' into which all the phases are grouped will be discussed in Section 4.4.*

Other minerals in the groundmass of both calcareous and siliciclastic rocks, which appear to have formed epigenetically, include rutile (Figure 4.57), monazite (Figure 4.58), apatite (Figure 4.59), barite (Figure 4.60), and, less commonly: halite (Figure 4.61), gypsum/anhydrite and celestine (Figure 4.62). (It is possible that halite was introduced as a later contaminant during or after sample preparation – see Figure 4.61). These epigenetic minerals have a complex and multistage order of paragenesis, and this order will be discussed where it is relevant to mineralisation in section 4.4: Discussion.

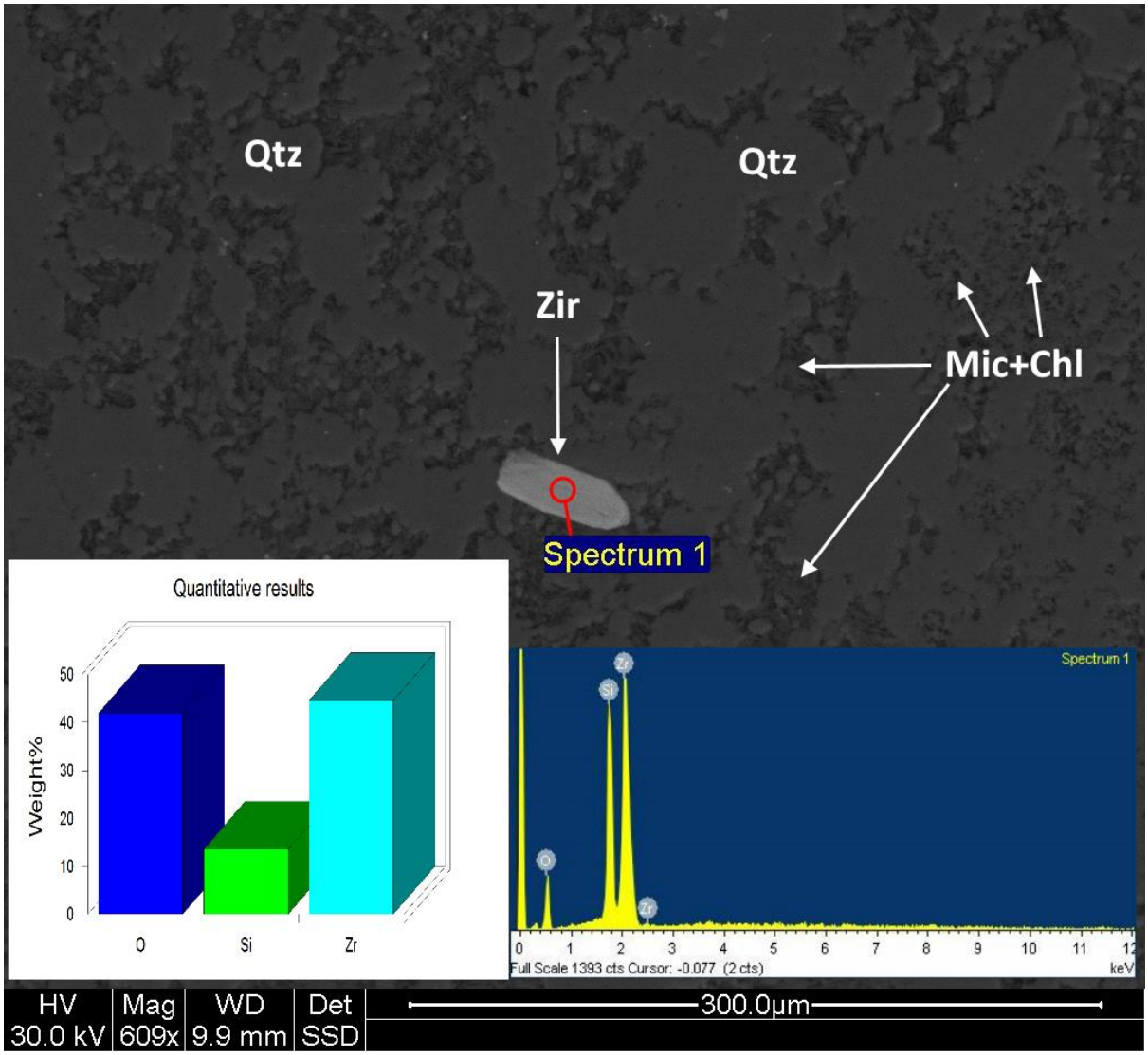

***Figure 4.50**: SEM image of a detrital zircon (Zir) grain within the quartz (Qtz), mica (Mic) and chlorite (Chl) groundmass of the RSC unit, showing EDS spot analysis of the grain (Spectrum 1). Sample MSSD075_17_2.*

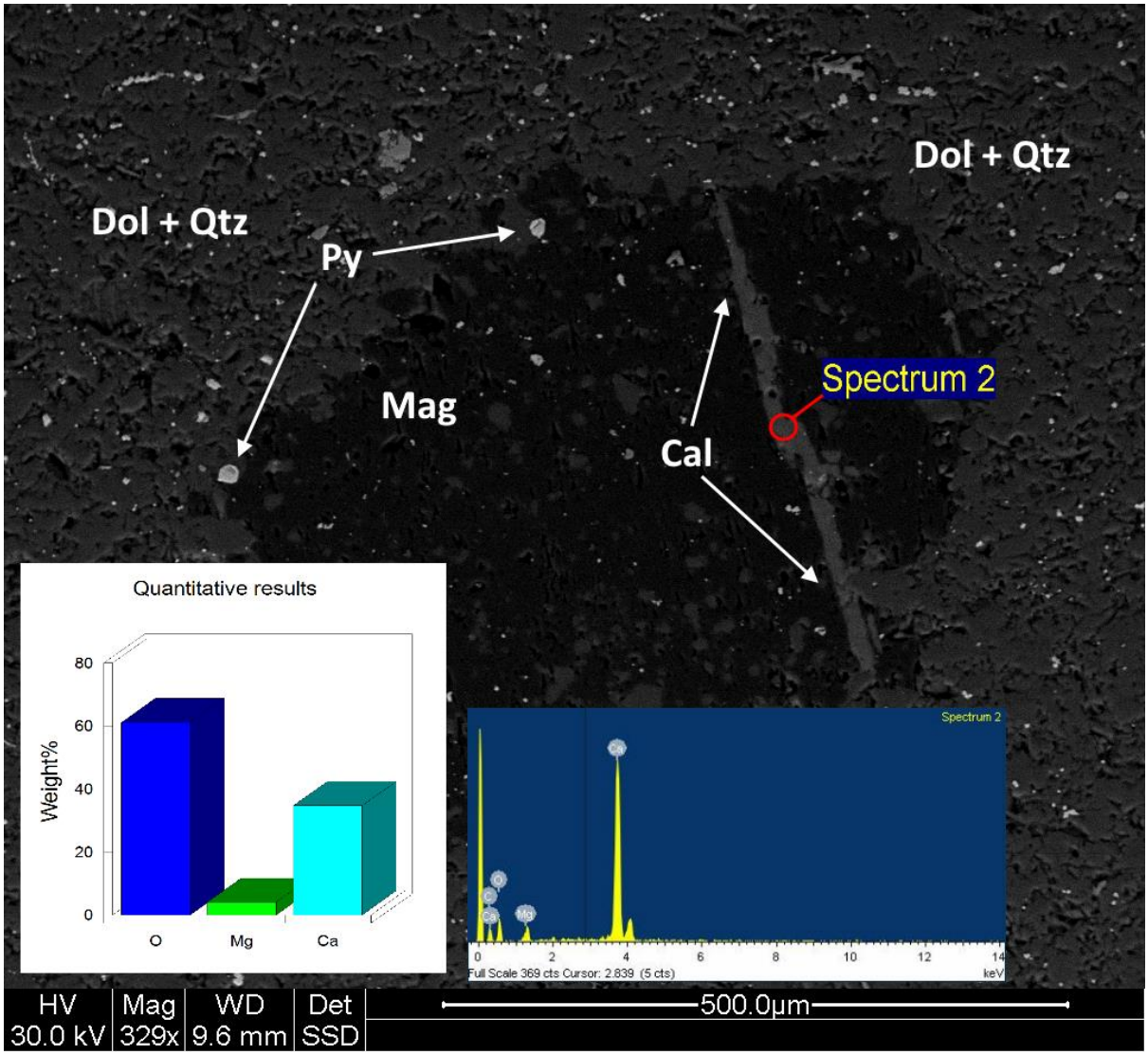

***Figure 4.51**: SEM image of a calcite (Cal) vein cutting through a nodule of magnesite (Mag) within a groundmass of dolomite (Dol) and quartz (Qtz), in the DStrat unit. An EDS spot analysis of the vein shows a high Ca:Mg ratio indicative of calcite (carbon is not represented in the analysis as the sample has been carbon coated). Some, if not all of the Mg indicated by the results may come from overlap of the adjacent magnesite into the analysis. Sample MSSD083_26_1.*

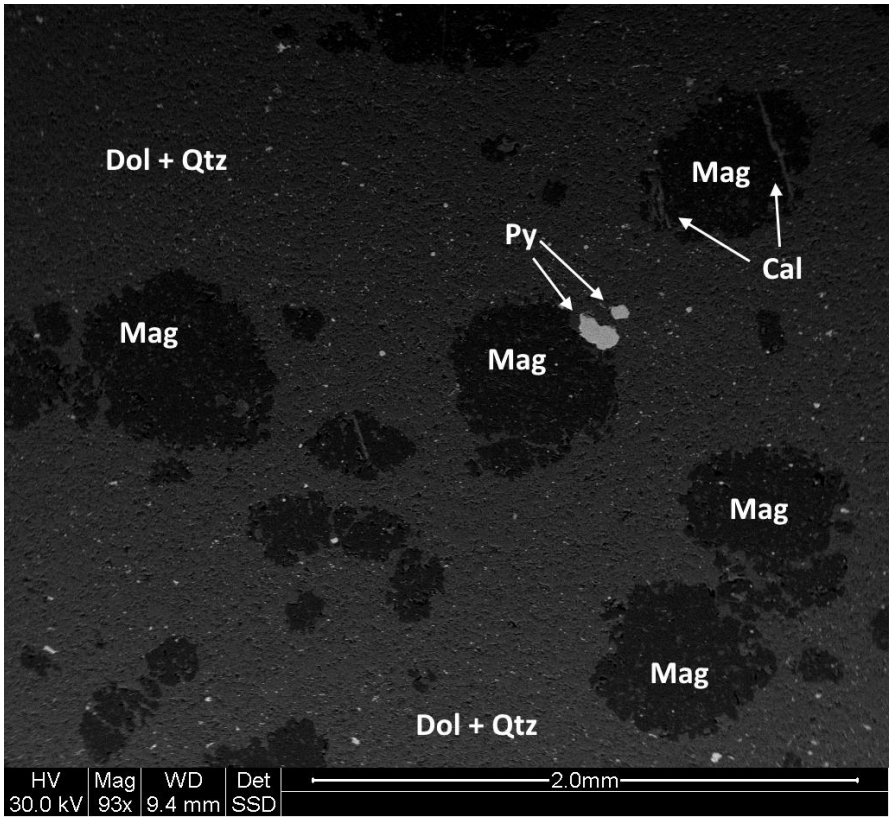

Figure 4.52*: SEM image of magnesite (Mag) nodules within a dolomite (Dol) and quartz (Qtz) groundmass, with disseminated pyrite (Py), in the DStrat unit. Sample MSSD083_26_1.*

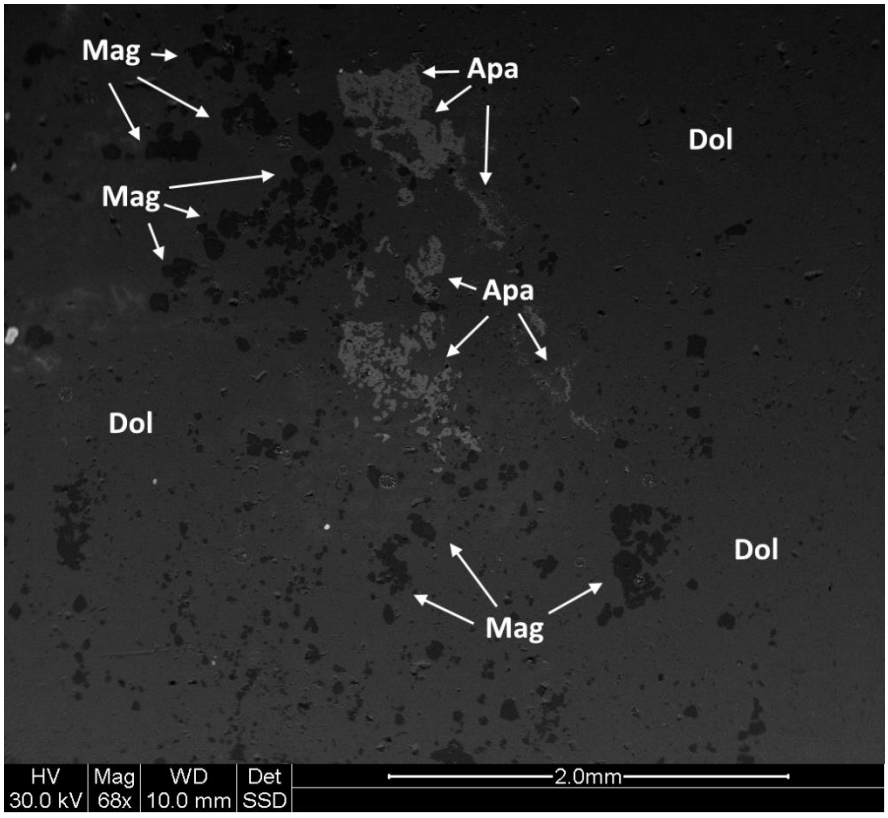

Figure 4.53*: SEM image of magnesite (Mag) and apatite (Apa) in a Type 2 dolomite vein. Sample MSSD080_10_1.*

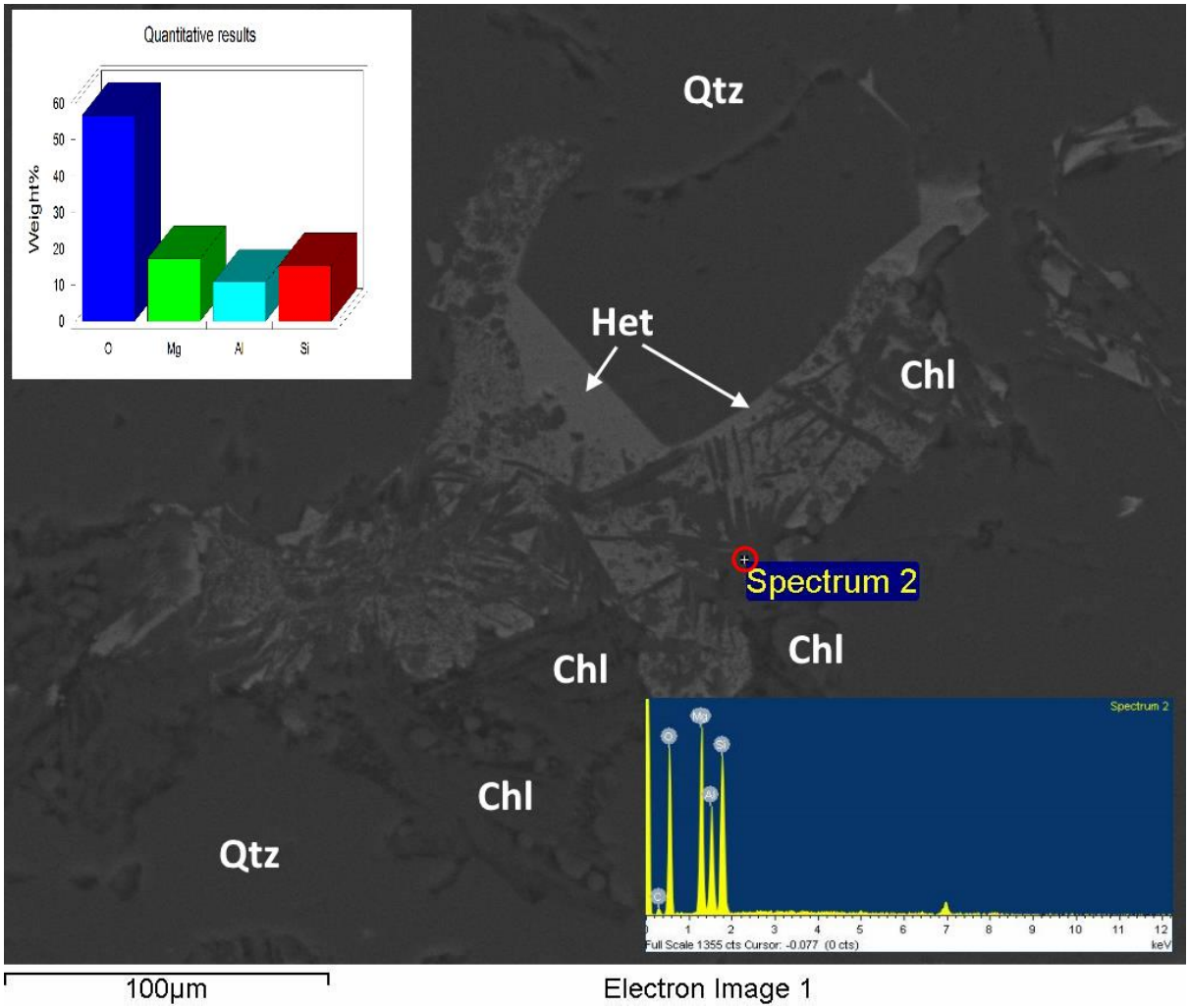

***Figure 4.54**: SEM image of euhedral spars of chlorite (Chl) between crystalline quartz (Qtz). Heterogenite (Het) fills the space between chlorite crystals. Sample MSSD075_17_2.*

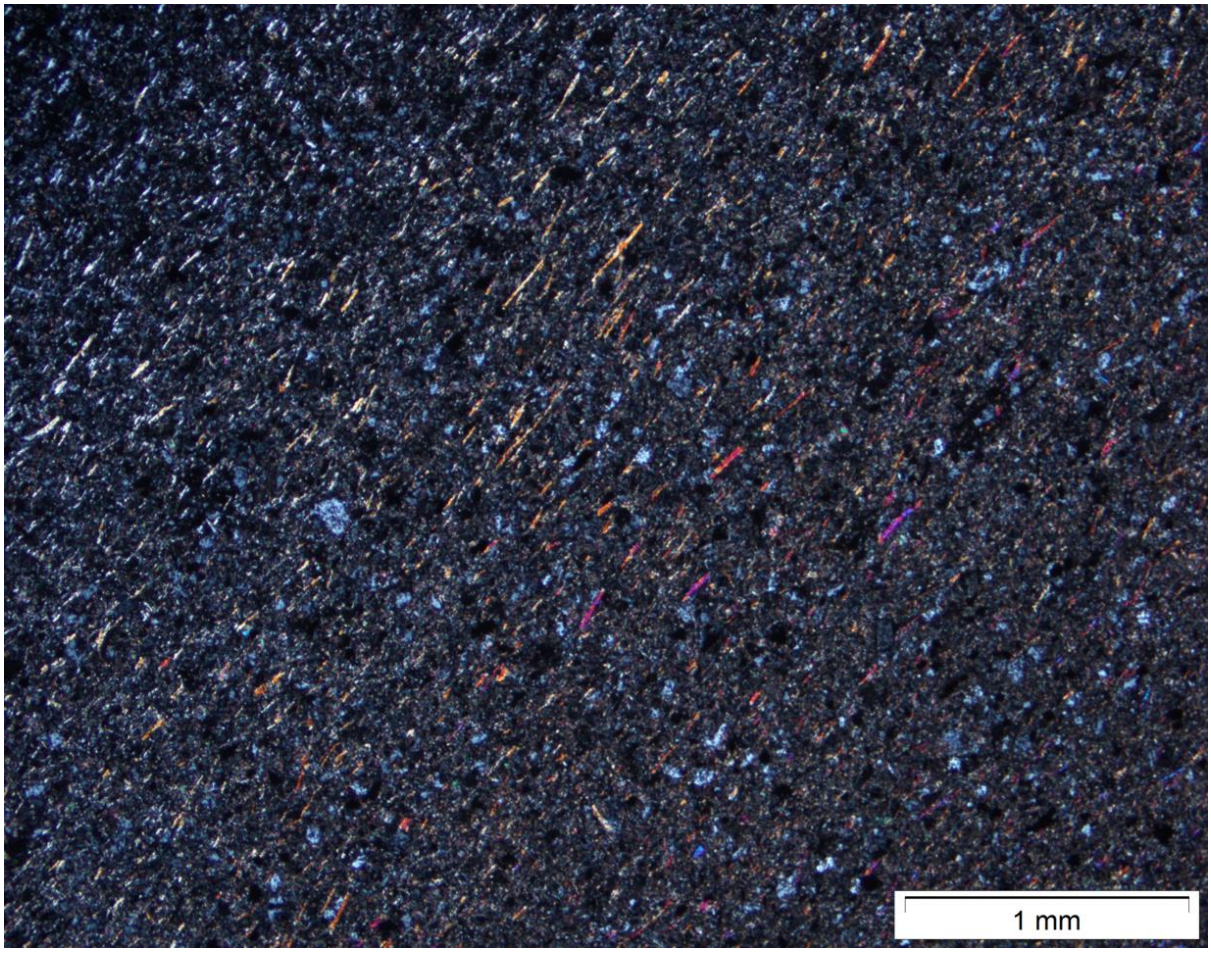

Figure 4.55*: Foliated muscovite mica (elongate crystals and high birefringence colours: purple and orange) within the siliciclastic groundmass of the SD2d black shale stratigraphic unit. Optical image taken in transmitted XPL of MSSD083_21_4.*

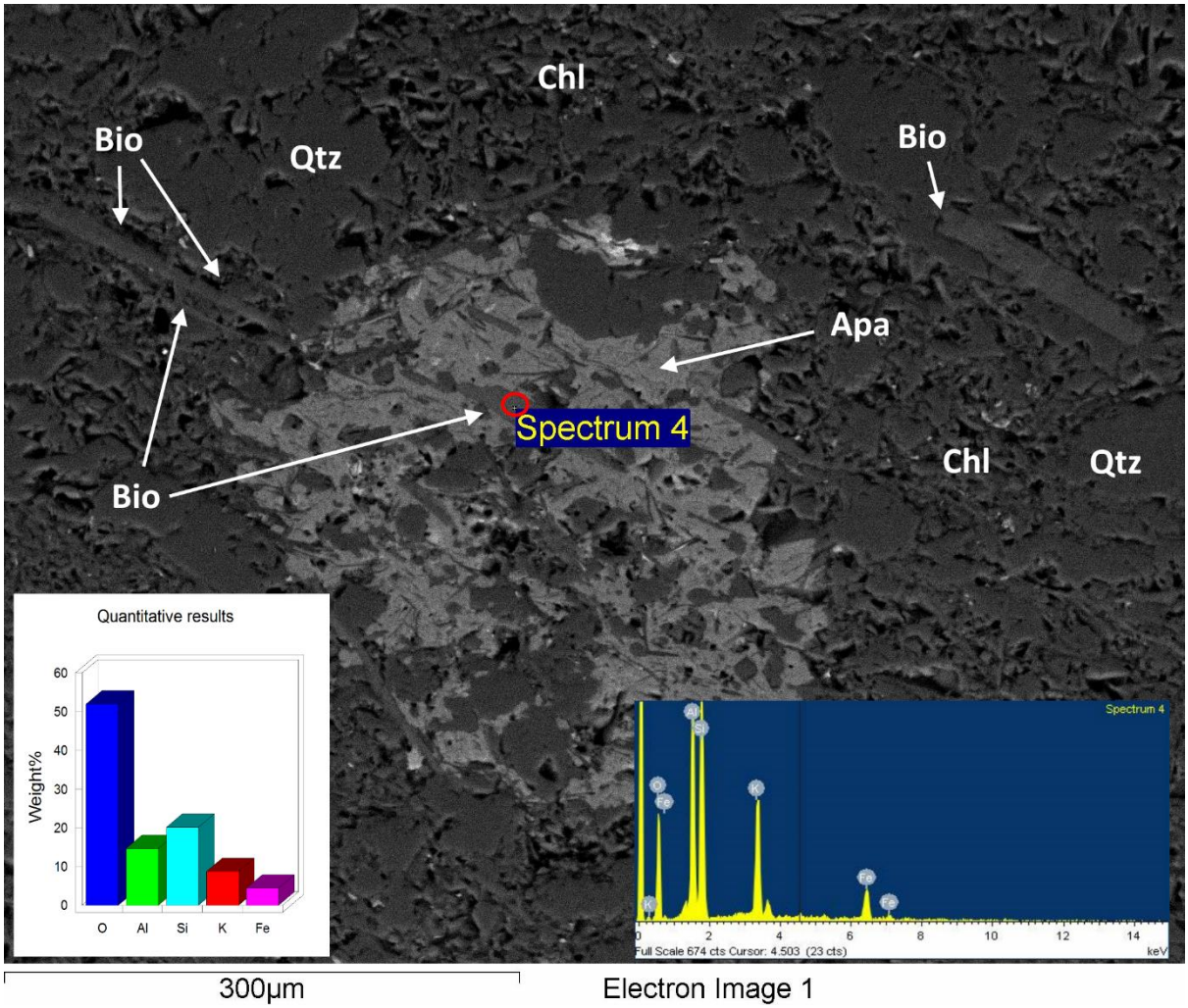

Figure 4.56*: SEM image of laths of iron-rich biotite (Bio) in a siliciclastic quartz (Qtz)-chlorite (Chl) groundmass, with later apatite (Apa). The lack of Mg in the EDS analysis (Spectrum 4) suggests that this crystal is the iron-rich end-member, annite. Sample MSSD080_14_2.*

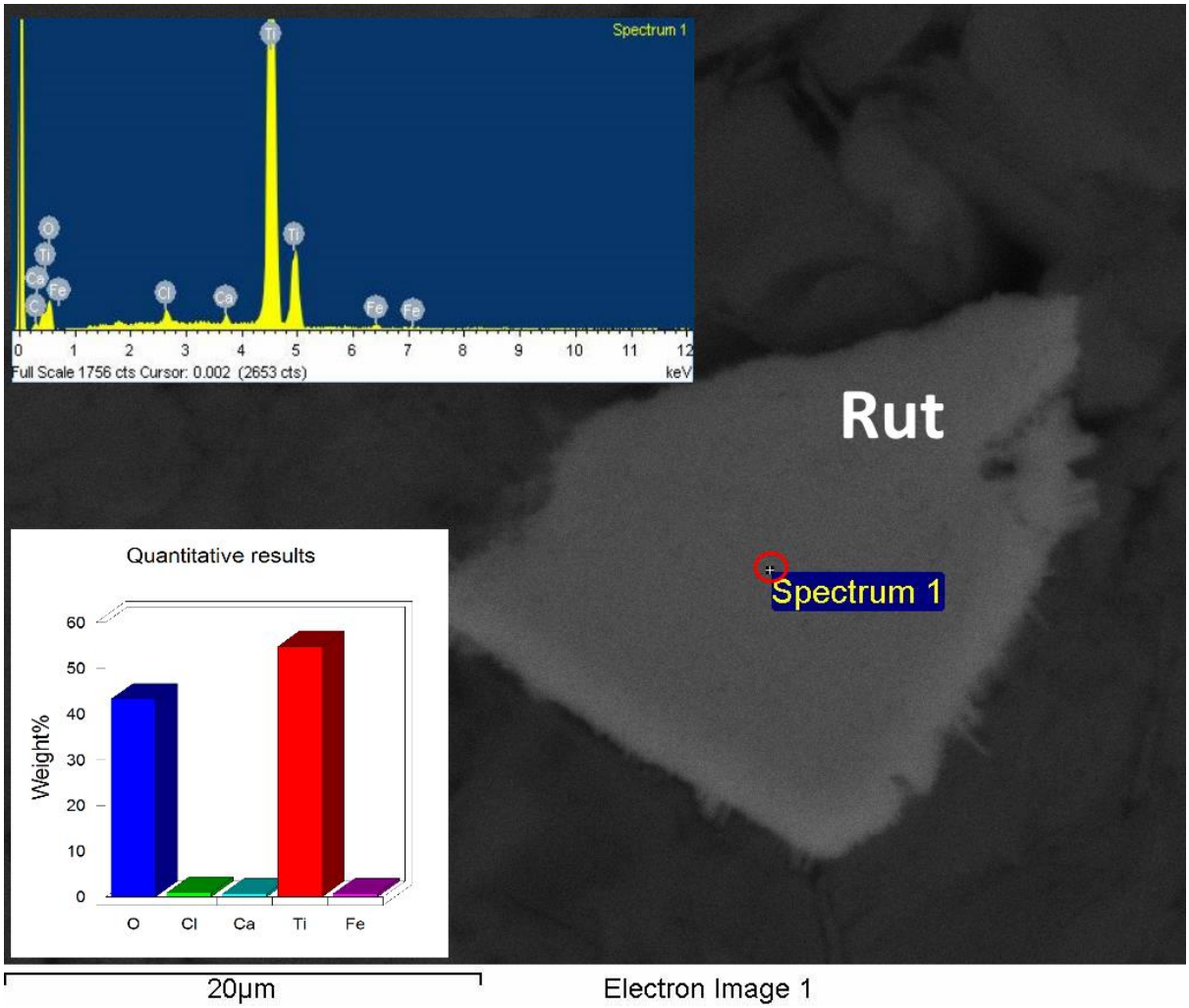

***Figure 4.57**: SEM image and EDS analysis of an authigenic rutile (Rut) crystal. Sample MSSD075_22_2.*

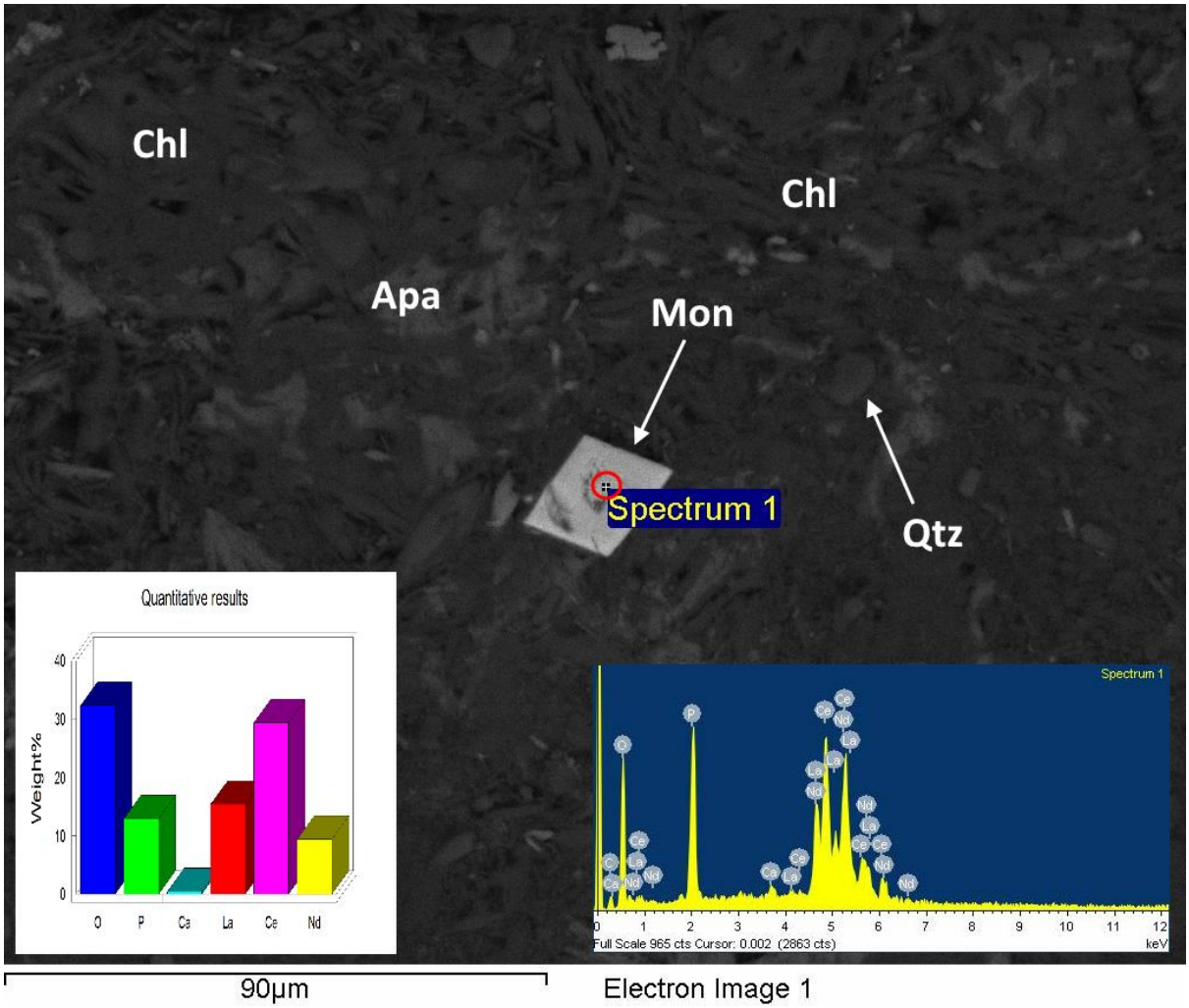

***Figure 4.58**: SEM image and EDS analysis of a euhedral rhombic monazite (Mon) crystal within a chloritic, siliciclastic (Chl+Qtz) groundmass. Sample MSSD075_22_2.*

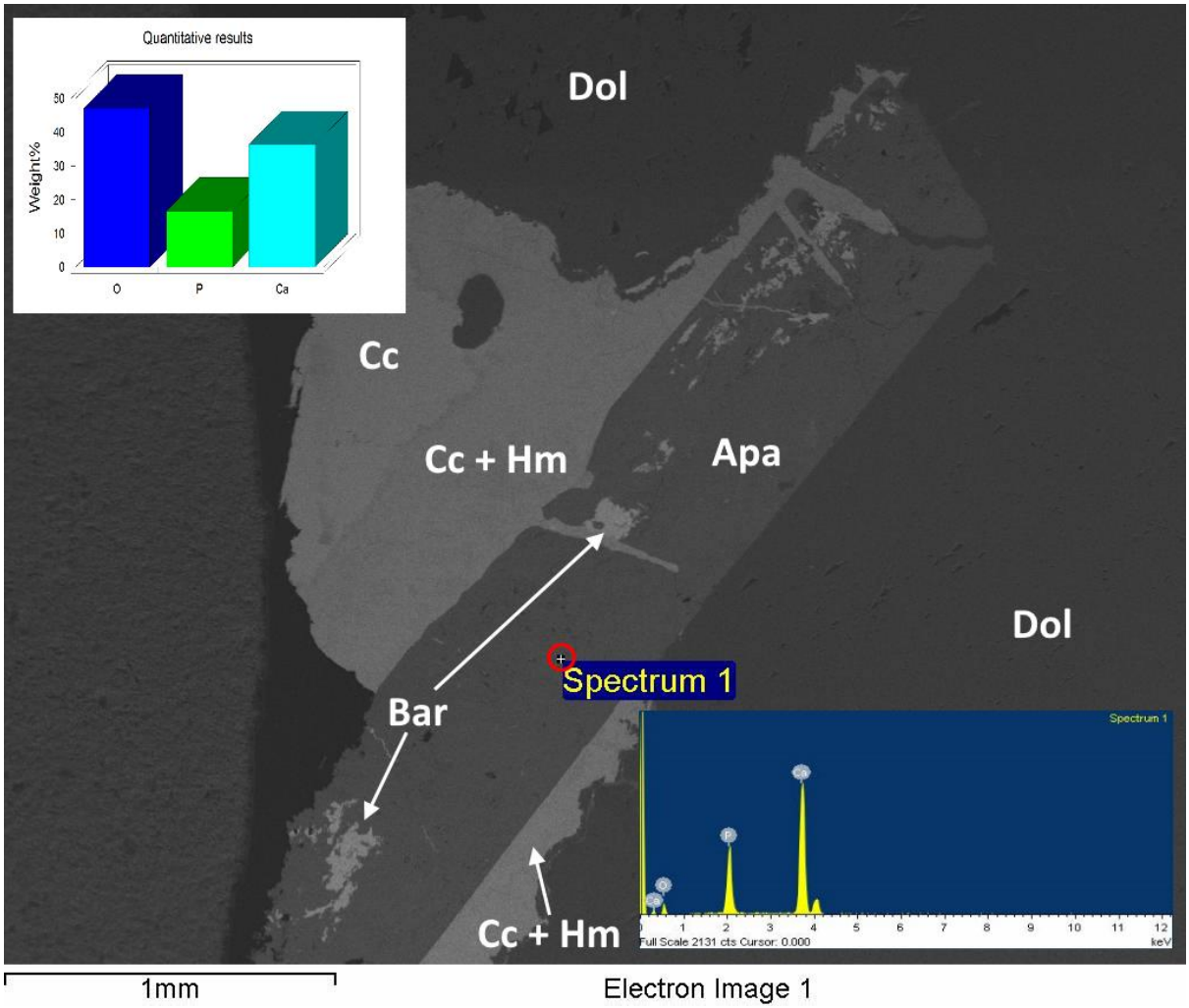

Figure 4.59*: SEM image and EDS analysis of a euhedral lath of apatite (Apa) within a Type 2 dolomite (Dol) vein. The apatite has later barite (Bar) growing within cavities in it, and is mantled and cross-cut by chalcocite (Cc) and haematite (Hm). Sample MSSD075_19_2.*

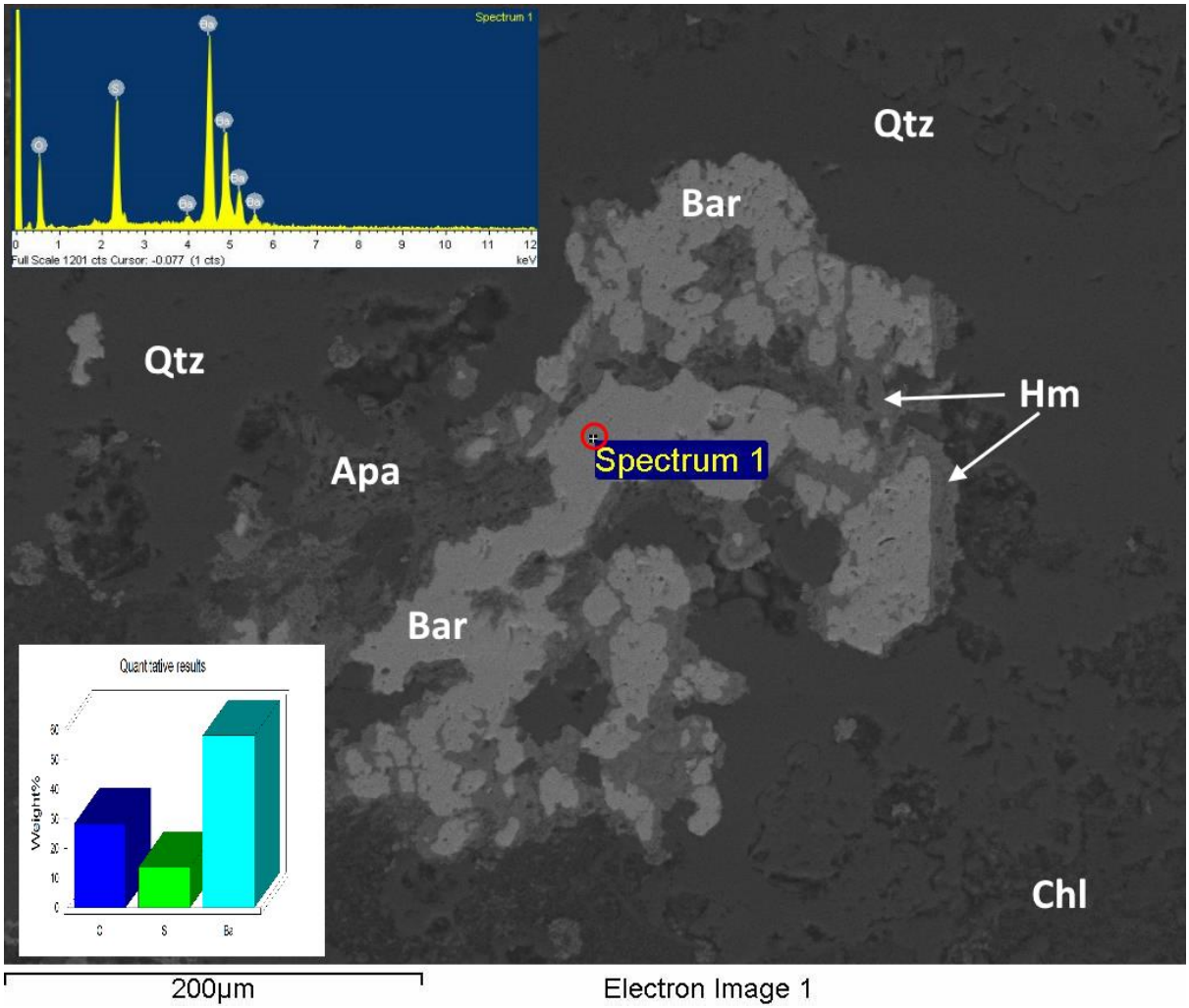

Figure 4.60*: SEM image and EDS analysis of an anhedral mass of barite (Bar), rimmed and replaced by haematite (Hm) and apatite (Apa), in the silicic, chlorite-rich RSC unit. Sample MSSD075_17_2.*

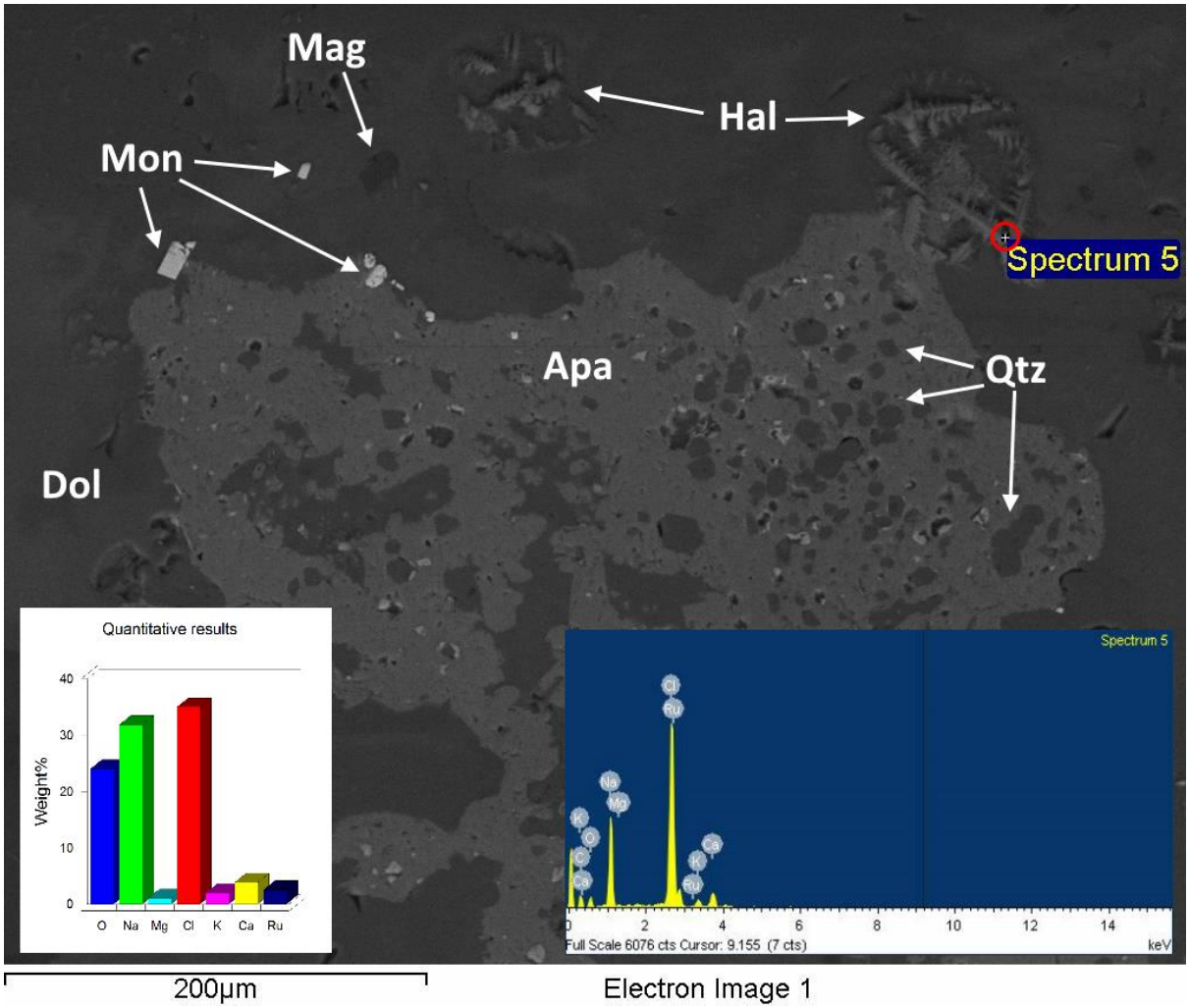

Figure 4.61*: SEM image and EDS analysis of a skeletal halite (Hal) crystal within a Type 2 vein, in proximity to monazite (Mon), apatite (Apa), quartz (Qtz) and magnetite (Mag). The skeletal crystal structure of the halite appears to be in high relief on the sample. This is unusual, as one would not expect halite, with a low hardness, to survive the polishing process in high relief. It is possible that halite crystal growth could have occurred on the surface of the sample sometime after polishing due to contamination. Sample MSSD080_10_1.*

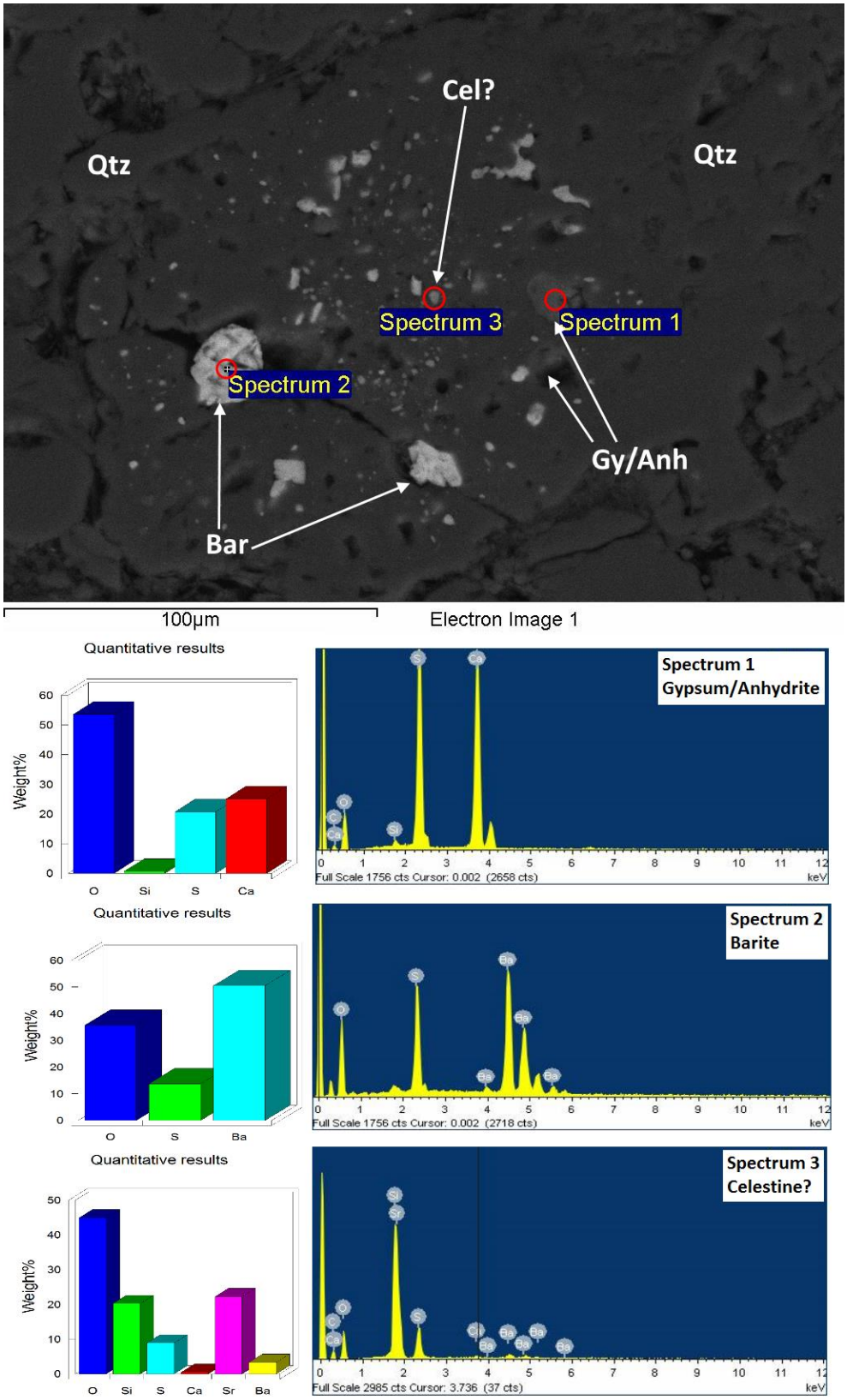

***Figure 4.62**: SEM image and EDS analyses of sulphate phases as inclusions within authigenic quartz. Tiny inclusions of gypsum (Gy) or anhydrite (Anh) and a Sr-bearing mineral that could be celestine (Cel) (Spectrum 3 is mixed and may include analysis of nearby quartz and barite as well as celestine) are replaced along fractures in the quartz (Qtz) by later barite (Bar). Sample MSSD075_22_2.*

4.3.3.1 Type 1 and Type 2 veins

Type 1 and Type 2 veins were described during logging, the results of which are presented in Chapter 3. At this scale, they differ in extent and form, with Type 1 veins consisting of a series of discontinuous, often interconnected veins, some of which terminate at different stratigraphic layers and which may have formed before final diagenesis (Figure 3.28). Importantly, no definitive cross-cutting relationship has been observed between Type 1 veins and stratiform mineralisation. Type 2 veins, by contrast, are more continuous, generally thicker, and their terminations appear to have no stratigraphic control. Rather, they are universally cross-cutting (Figure 3.29). Type 2 veins can be seen to cross-cut Type 1 veins in several places (see Figure 4.63) as well as stratiform mineralisation (Figure 3.49) though the opposite was never observed to occur.

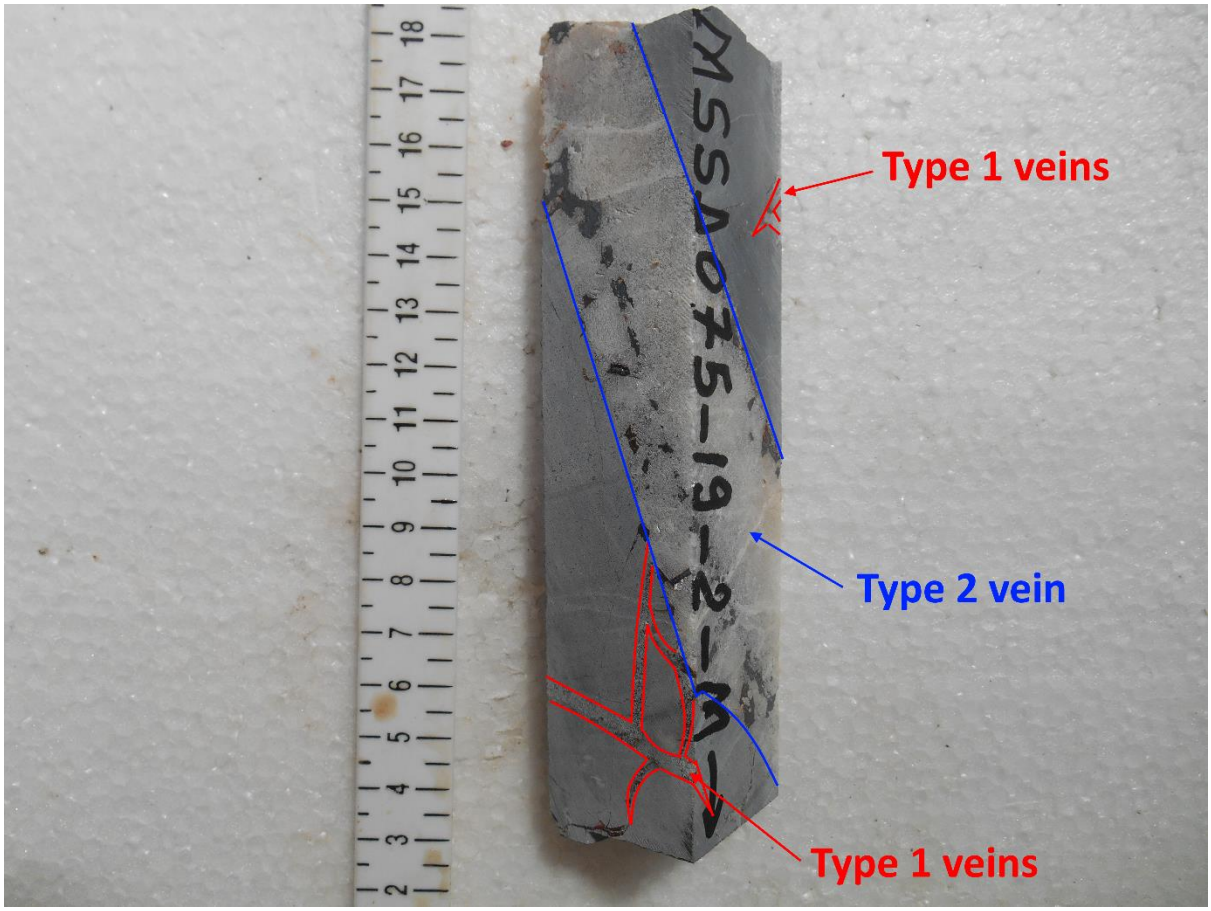

Figure 4.63*: Photograph of a quarter-core sample MSSD075_19_2, from the DStrat. Within this sample a Type 2 dolomite vein, which hosts chalcocite (grey blebs within the vein), can be seen to cross-cut a network of Type 1 dolomite veins. Type 1 and Type 2 veins are outlined in red and blue, respectively. Scale bar at the left of the sample is in centimetres.*

As well as differences in form, petrographic examination reveals there are also mineralogical differences between Type 1 and 2 veins.

Type 1 veins generally consist of a simpler mineralogy than Type 2 veins, containing quartz, apatite, dolomite and sulphides, with dolomite being the most abundant mineral. Sulphides and apatite are not always a feature of Type 1 veins, while quartz is almost always present. Paragenetically, quartz is precipitated first, sometimes as euhedral crystals at the vein margins (Figure 4.64). Apatite is precipitated after quartz, sometimes mantling quartz crystals, and this is followed by dolomite which forms the bulk of the vein mass. The dolomite from these veins can sometimes take on a parallel-elongated antitaxial appearance (Figure 4.15). Sulphides are then precipitated in space between dolomite crystals, replace dolomite along crystal margins, or are precipitated during the last stages of dolomite formation. The typical mineralogy and paragenetic relationships of a Type 1 vein are shown in Figure 4.65.

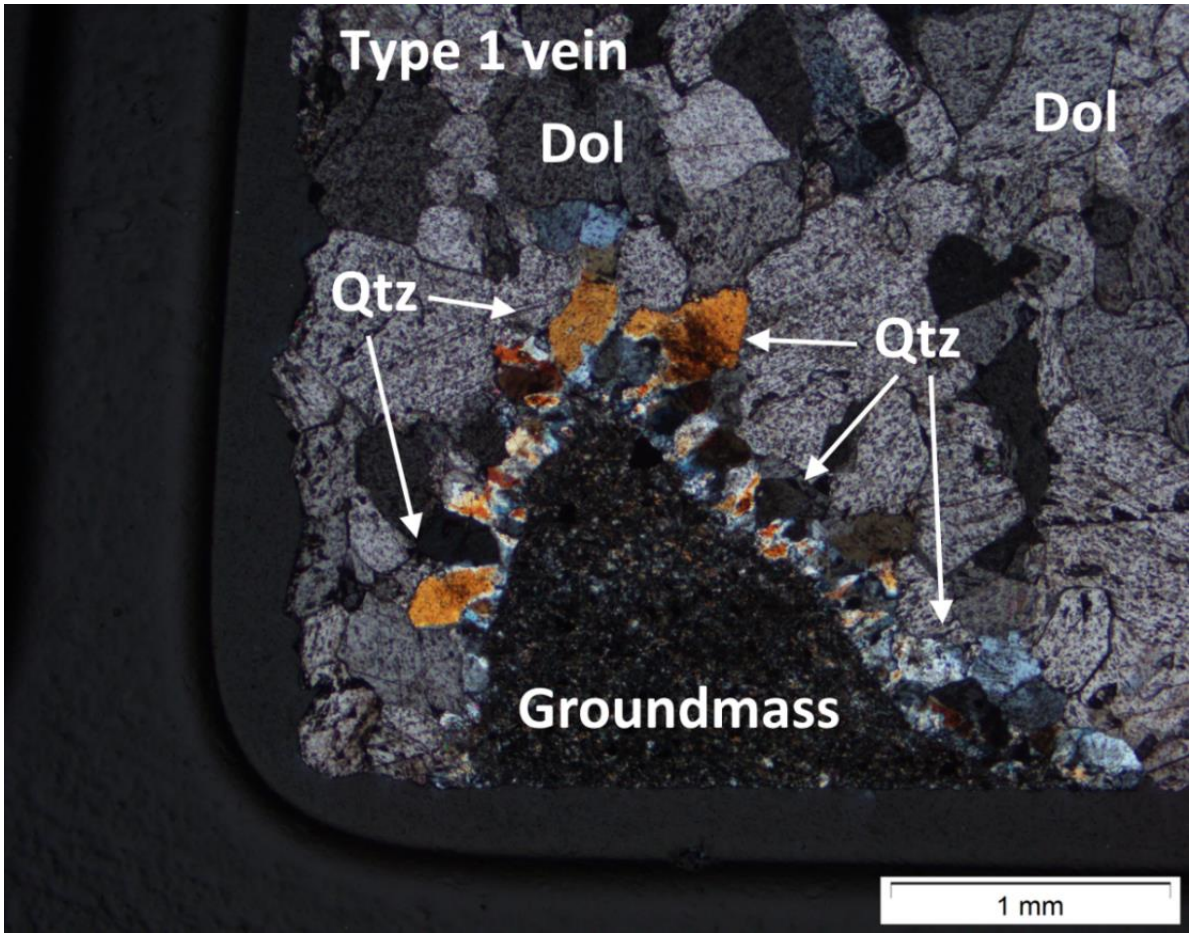

Figure 4.64*: Euhedral quartz (Qtz) at the margin of a Type 1 vein. Optical image taken in transmitted XPL of sample MSSD083_21_3.*

The pyrite 3, sphalerite 1, chalcopyrite 1, bornite 1, digenite 1, chalcocite 1 and carrollite 1 phases have all been identified in Type 1 veins. However, tiny inclusions of pyrite 3 and chalcopyrite 1 have been found within euhedral quartz at the vein margins, indicating that these sulphide phases, at least, began precipitating from the earliest stages of Type 1 vein formation. In terms of distribution, Type 1 veins can be found throughout the stratigraphy, although they are more common in the most calcareous units including the DStrat, RSF and parts of the RSC and CMN.

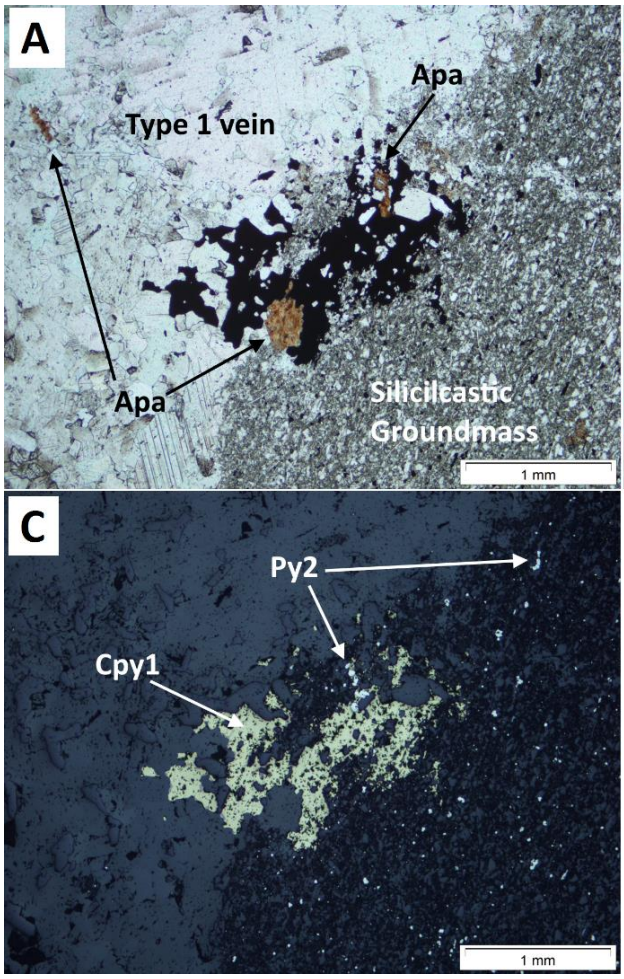

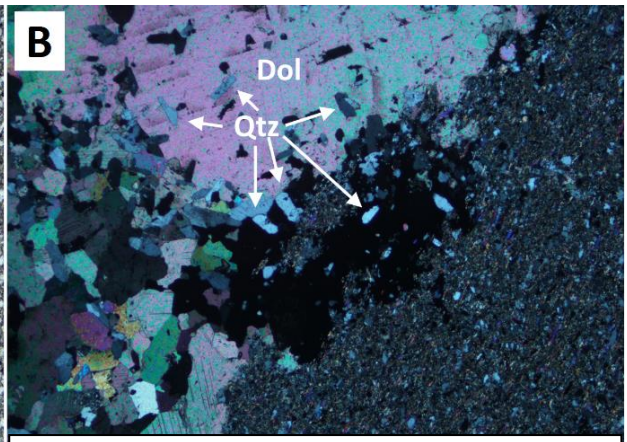

***Figure 4fig.65**: Optical images of various different paragenetic phases of Type 1 veins, taken from the same viewpoint. **A**: subhedral apatite (Apa). Transmitted, PPL. **B**: Euhedral quartz (Qtz) and anhedral dolomite (Dol). Transmitted, XPL. **C**: Anhedral chalcopyrite 1 (Cpy1) which is hosted at the margins of the Type 1 vein, and unrelated pyrite 2 (Py2) which is groundmass-hosted. Reflected, PPL image of*

Type 2 veins are also primarily composed of dolomite. They contain quartz, apatite and sometimes sulphides, like Type 1 veins. Additionally, they frequently contain magnesite, chlorite and barite, may contain monazite, and halite (possibly a later contaminant) was identified in one sample (Figure 4.66). Quartz is less common in these Type 2 veins than in Type 1 veins, but, where present it similarly forms euhedral crystals often at or near the vein

margins. These minerals appear to precipitate in the general paragenetic order of quartz → magnesite → apatite → dolomite → barite → chlorite → sulphides. Chlorite inclusions in Type 2 vein-hosted sulphides are common (Figure 4.67). Sulphide phases identified in Type 2 veins include carrollite 2, chalcopyrite 2, bornite 2, chalcocite 2 and digenite 2. A high concentration of Type 2 veins is found in the SD unit. However, they may be found throughout the stratigraphy. Optical image examples of Type 2 veins are shown by Figures 4.20, 4.21. 4.22, 4.23, 4.24 and 4.25.

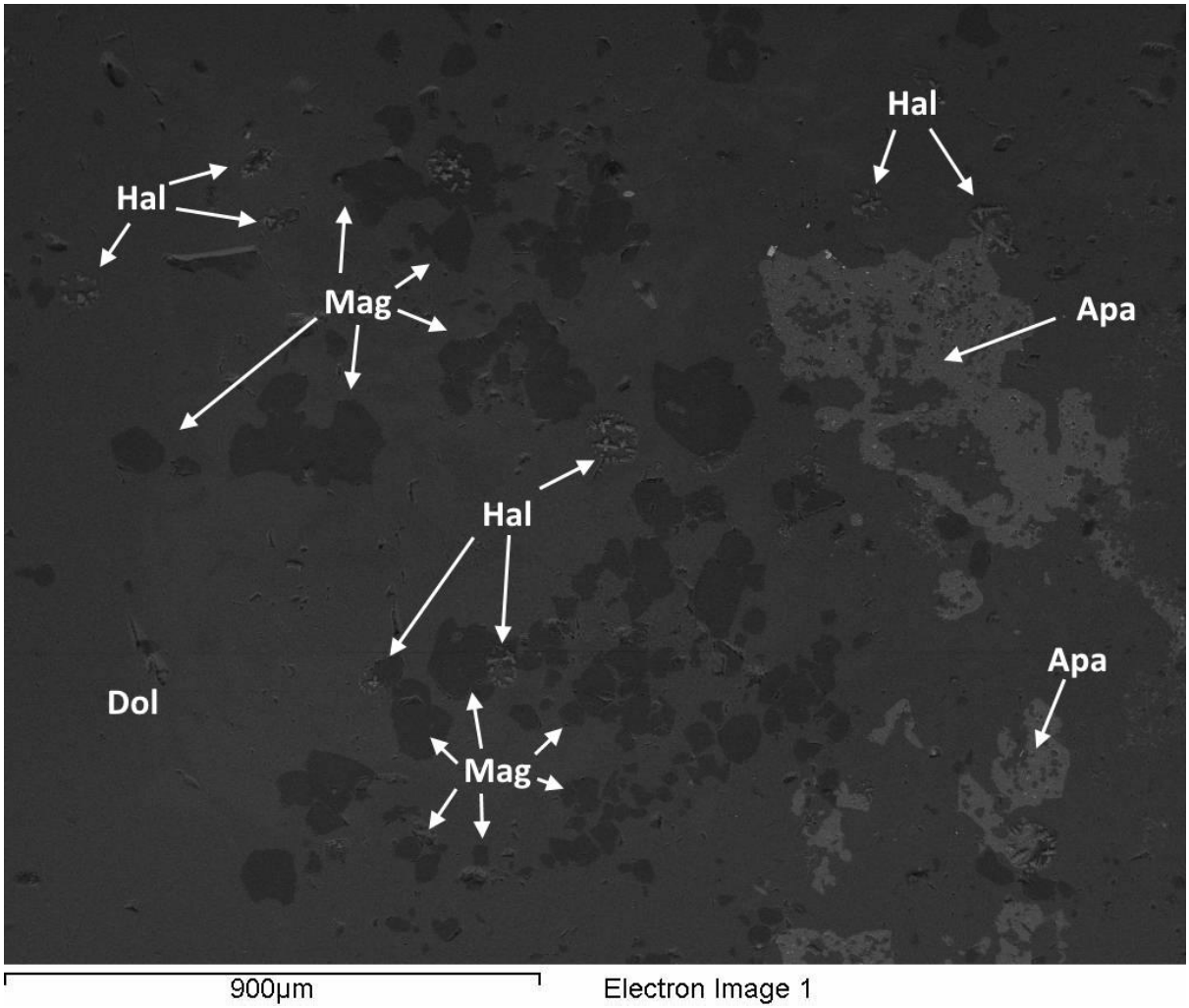

Figure 4.66*: SEM image of a Type 2 dolomite (Dol) vein containing early magnesite (Mag) and later apatite (Apa) and halite (Hal). Sample MSSD080_10_1. (It is possible that halite was introduced as a later contaminant during or after sample preparation – see Figure 4.61).*

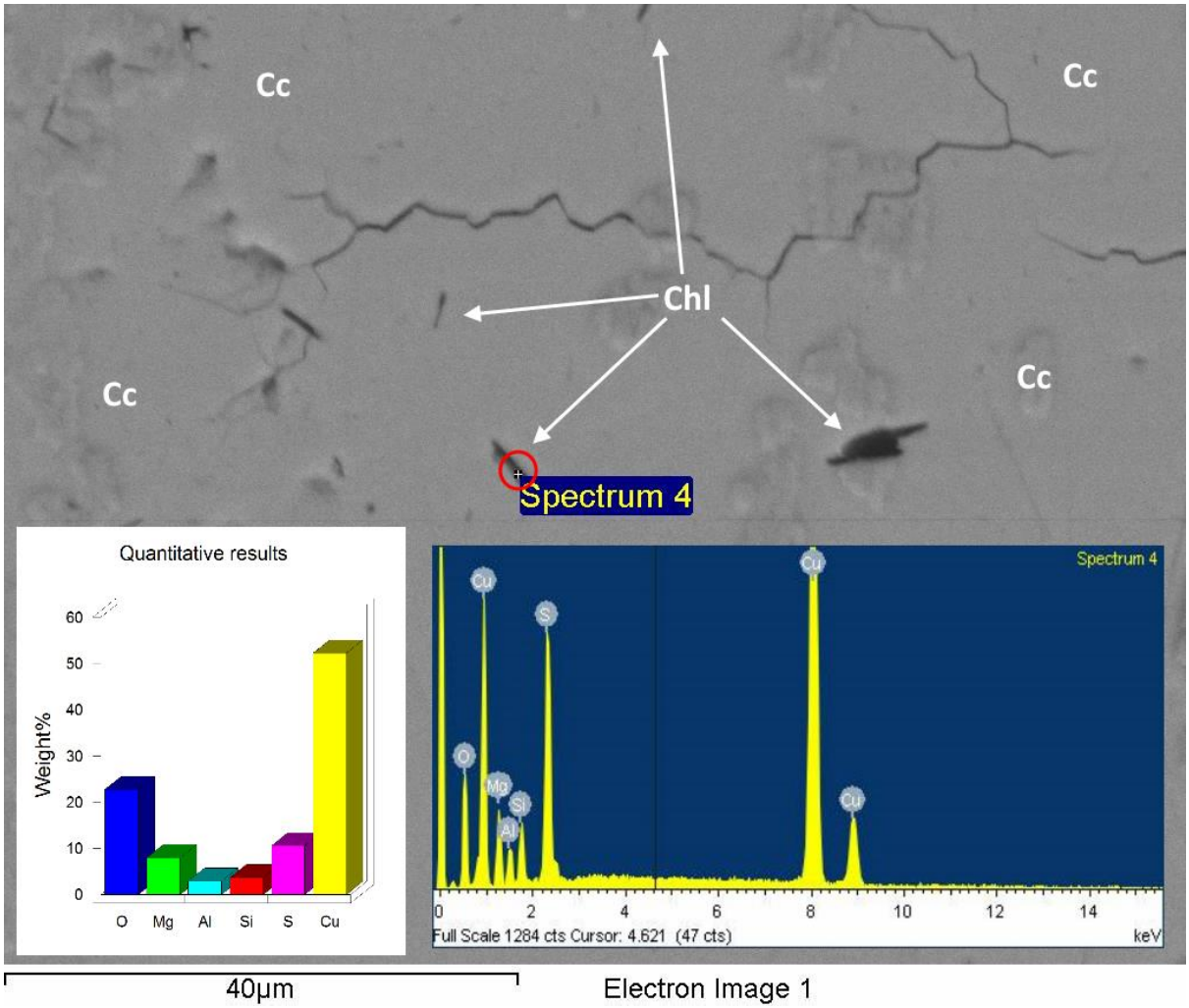

Figure 4.67*: SEM image of tiny inclusions of chlorite (Chl) within Type 2 vein-hosted chalcocite (Cc). The EDS Spectrum 4 presents a mixed analysis which captures some of the chalcocite surrounding the tiny chlorite grains. Sample MSSD080_10_1.*

4.3.4 Sulphur Isotope Ratio Analyses

The results of sulphur isotope analysis are presented in Figure 4.68. The close proximity of values within each set of triplicate analyses attests to the precision of the preparation method. Laboratory precision against standards for $\delta^{34}S$ is stated as ≤0.17 per mille by iThemba Laboratories. Samples from the stratiform sulphide interval (16_1_D) plot in a fairly close group with the Type 2 vein-hosted chalcocite (19_2_A) and chalcopyrite (21_4_A), whereas the massive/framboidal pyrite (16_1_E) has considerably lighter $\delta^{34}S$ values. The significance of this is discussed in section 4.4.6: Sources of Sulphur.

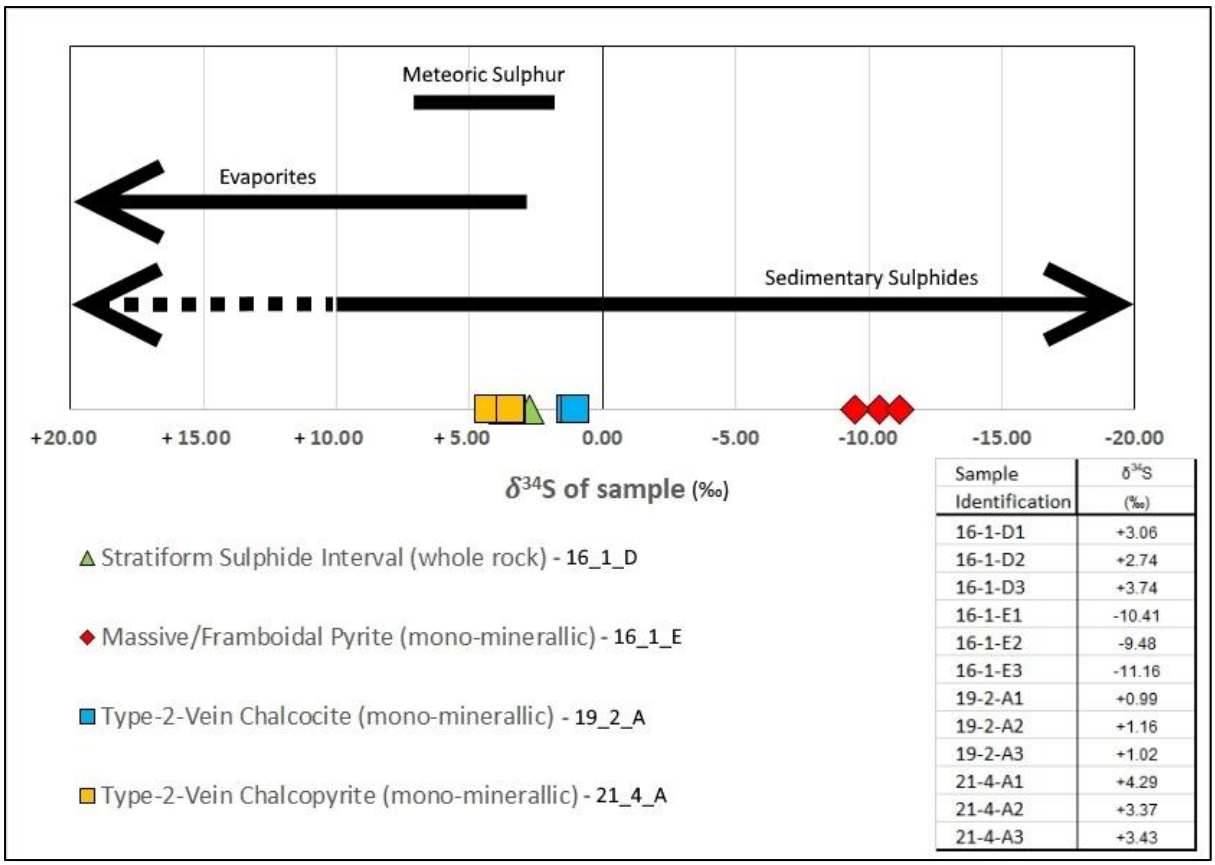

Sample Identification	$\delta^{34}S$ (‰)
16-1-D1	+3.06
16-1-D2	+2.74
16-1-D3	+3.74
16-1-E1	-10.41
16-1-E2	-9.48
16-1-E3	-11.16
19-2-A1	+0.99
19-2-A2	+1.16
19-2-A3	+1.02
21-4-A1	+4.29
21-4-A2	+3.37
21-4-A3	+3.43

***Figure 4.68**: Summary of sulphur isotope results from this study, compared against selected ranges of $\delta^{34}S$ values for different sources of sulphur (Thode, 1991). Meteoric sulphur refers to sulphur dissolved in rain and snow, evaporites refer to evaporitic sulphates such as gypsum and sedimentary sulphides refers to authigenic, diagenetic sulphides such as pyrite. Typical values in this range are represented by a solid black line and uncommon values are represented by a dashed line. Arrows at the margins of the graphs show that the range of $\delta^{34}S$ values for this category extends beyond the area shown by the graph.*

4.4 Discussion - Cu-Co Mineralisation

The 33 mineralisation-related phases have been grouped into 5 different temporal 'stages' of formation, based on comparisons of mineralogy, paragenesis and distribution to other Congolese Copperbelt Cu-Co deposits described in the literature. These stages occurred in the following order, and consist of the following phases:

1. The Pre-Ore Diagenetic Stage: pyrite (Py1), haematite (Hm1) and recrystallised pyrite (Py2)

2. The Early Hydrothermal SSC Stage: pyrite (Py3), sphalerite (Sph1), chalcopyrite (Cpy1), bornite (Bn1), digenite (Dg1), chalcocite (Cc1) and carrollite (Car1)
3. The Late Hydrothermal Ore Stage: carrollite (Car2), chalcopyrite (Cpy2), bornite (Bn2), chalcocite (Cc2) and digenite (Dg2)
4. The Early Supergene Stage: Native copper (Cu1), cuprite (Cup1), tenorite (Ten1), chalcocite (Cc3), bornite-digenite-covellite (Bn-Dg-Cov3), haematite (Hm2), cobaltoan carbonate (CoCarb1), heterogenite (Het1), azurite (Azu1), malachite (Mal1), chrysocolla (Cry1)
5. The Late Supergene Stage: chalcocite (Cc4), haematite (Hm3), cobaltoan carbonate (CoCarb2), heterogenite (Het2), malachite (Mal2), chrysocolla (Cry2), pseudomalachite (Psm1).

4.4.1 The Pre-Ore Diagenetic Stage

The pyrite 1 (Py1), haematite (Hm2) and pyrite (Py2) phases are thought to be formed by very early-diagenetic authigenic iron precipitation, which pre-dates the circulation of Cu-Co-bearing fluids through the groundmass. The sub-framboidal Py1 phase (Figure 4.2) is comparable to similar pyrite described elsewhere in the Central African Copperbelt (Love and Amstutz, 1966; Bartholomé and Katekesha 1971; Dewaele *et al.*, 2006; Annels, 1974; Selley *et al.*, 2005). Certain phases of pyrite at Kamoto are described by Love and Amstutz (1966) as being “on the fringe of classification as framboids”. Studies show that equivalent phases formed by bacterial sulphate reduction (BSR) at low temperatures (<100°C), seawater salinities and under reducing conditions (Jensen and Dechow, 1962; Dechow and Jensen, 1965). The euhedral, cubic Py2 phase (Figure 4.4) is likely to be, primarily, the result of the recrystallisation of earlier-formed, sub-framboidal Py1. Craig *et al*. (1998) show that increased temperatures and pressures associated with progressive diagenesis tend to cause recrystallisation of pre-existing pyrite into a more euhedral-cubic form. However, the possibility of renewed Fe-bearing fluid input during Py2 crystallisation cannot be ruled out. A disseminated, euhedral-cubic pyrite phase at Chambishi, equated to the Py2 phase described here, is shown by Annels (1974) to predate Cu-Co ore-fluid circulation. Both Py1 and its recrystallised Py2 form would have precipitated in reducing sedimentary environments, hence their preferential distribution in calcareous units, and the complete

lack of pyrite in the RAT (Figure 4.49). Muchez and Corbella (2012) propose an alternative explanation for the lack of pyrite in the RAT, in that it was originally present, but was progressively remobilised by mineralising fluids during the formation of Cu-Co sulphides in the Mines Subgroup. However, this model is not universally accepted and is not favoured by this study at Mashitu South due to the lack of positive, direct evidence for the previous existence of pyrite in the RAT Rouge.

Hm1, by contrast, is only found in the RAT and SD units (Figure 4.49), needing an oxidising environment of deposition to form. Hm1 can be found together with Py1 and Py2 (Figures 4.2 and 4.5), indicating that the redox conditions of the environments in which these three phases formed (probably just under the sediment surface, within porous, loose sediment) were prone to change, both temporally and spatially, during early diagenesis. Pyrite would have been precipitated during reducing conditions, and haematite under oxidising conditions. However, the Py1 → Hm1 → Py2 order of paragenesis holds broadly true, where these phases are found together, despite this variation. Tabular, euhedral, early authigenic haematite is reported from other deposits in the Copperbelt (Dejonghe and Ngoyi, 1995; Selley *et al.*, 2005). Although this phase was not responsible for the distribution of any ore itself, the location of reducing horizons and the Py1 and Py2 phases are an important control on the distribution of later sulphide ore, which tends to nucleate around and replace early pyrite (Figure 4.69).The timing of the Pre-Ore Diagenetic Stage is not constrained absolutely by any study in the region but a syn-sedimentary/early-diagenetic origin would bracket it at a maximum age of 883±10 Ma for sedimentation in the Katangan Basin, as dated from detrital zircons thought to be sourced from the Nchanga Granite by Armstrong *et al.* (2005). Given that the stage pre-dates mineralisation (see section 4.4.2) an origin between around 880 and 850 Ma seems likely.

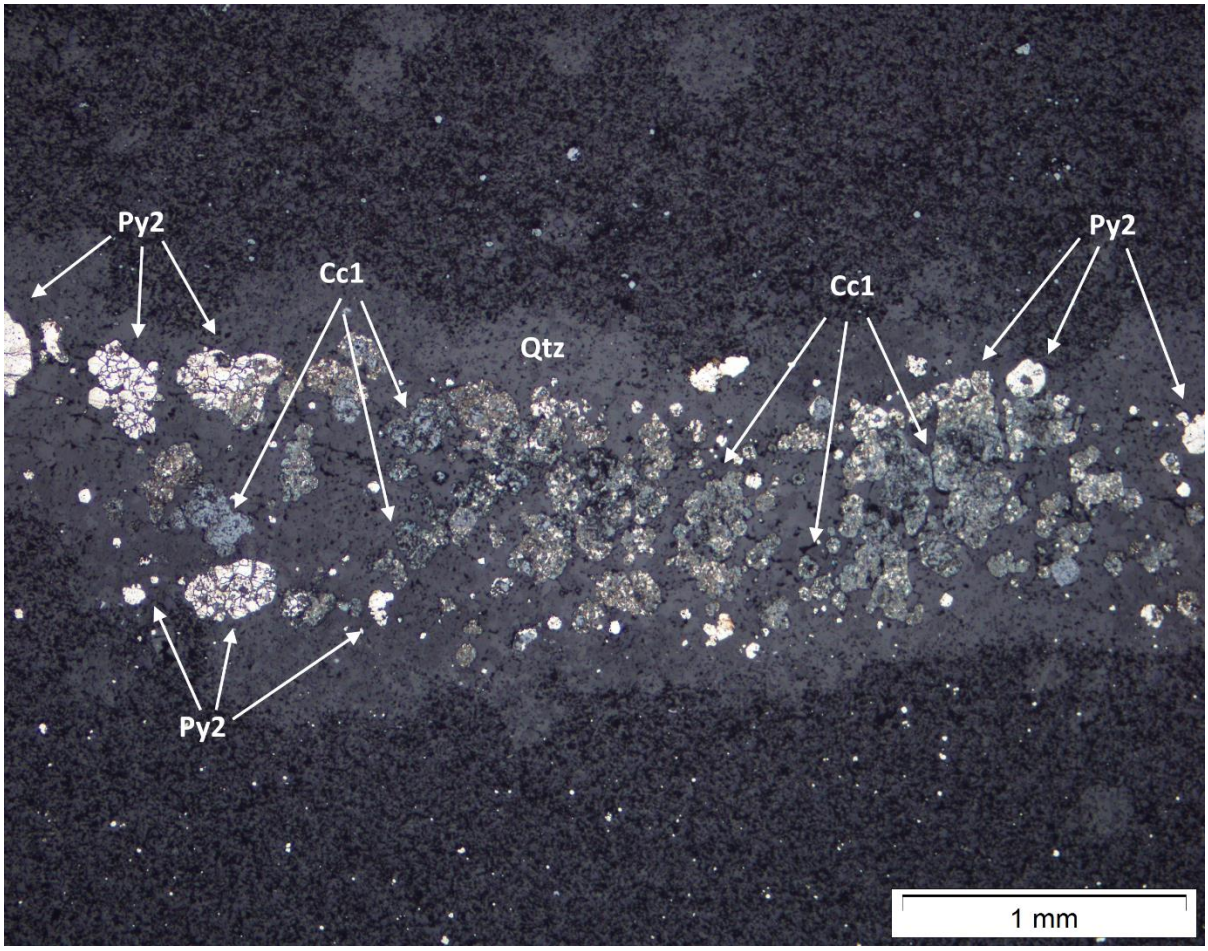

***Figure 4.69**: Pyrite 2 (Py2) being replaced in-situ by chalcocite 1 (Cc1), within a region of microcrystalline quartz silicification in the DStrat. Optical image taken in reflected PPL from sample MSSD075_19_1.*

4.4.2 The Early Hydrothermal SSC Stage

The early hydrothermal SSC stage (Sedimentary Hosted Stratiform Copper) approximately fits the model for sedimentary-hosted stratiform copper mineralisation as described by Brown (2014) and outlined in Chapter 2. It is dominated by stratiform-disseminated sulphides formed in the paragenetic order of pyrite (Py3) → chalcopyrite (Cpy1) → bornite (Bn1) → chalcocite (Cc1). The distribution of the Cpy1, Bn1 and Cc1 phases also fits the stratiform model (Figure 4.49), with chalcopyrite most abundant in the upper (CMN) stratigraphy, bornite most abundant in the middle (SD) stratigraphy and chalcocite most abundant in the lower (Kamoto Formation) stratigraphy. This reflects a chemical zonation pattern with more iron-rich sulphides precipitated distally to the first redox horizon (RAT-

Mines Subgroup transition) and more copper-rich sulphides precipitated proximal to this horizon, as expected for this type of deposit (Brown, 2014) and documented more generally across the Copperbelt (Cailteux *et al*., 2005; Muchez and Corbella, 2012). It also supports the observations made during logging (see Chapter 3) that stratiform chalcopyrite was most abundant in the upper stratigraphy while stratiform chalcocite was only present in the lower stratigraphic units.

The pyrite 3 (Py3) phase is distinct from the pyrite 1 (Py1) and pyrite 2 (Py2) phases in that it contains trace amount of cobalt (Figure 4.8). This is similar to the description of 'cobaltiferous pyrite rims' to earlier, often cubic pyrite (i.e. Py2) at the Kamoto deposit by Bartholome *et al.* (1971). No occurrence where Py3 rims Py1 or Py2 was recognised in this study, though it is possible that more sensitive element mapping targeted at pyrite, such as that conducted by ion microprobe, could reveal such a relationship. According to the SSC model of distribution (Brown, 2014), the upper stratigraphy should host the greatest abundance of Py3, however no such distribution was recognised (Figure 4.49). It is possible that the 'pyrite zone' of mineralisation existed *above* the level of stratigraphy seen at Mashitu South, i.e. the CMN, which appears to be the 'chalcopyrite zone'. Accordingly, the 'pyrite zone', perhaps previously located in the Dipeta Subgroup, could have since been removed from the Mashitu South Mines Subgroup fragment by tectonic or erosive processes.

There are no particularly strong associations between sulphide phases from this stage of mineralisation and gangue phases, although sulphides are frequently accompanied by and included within intergranular, crystalline quartz and dolomite in the groundmass. These authigenic phases could be equivalent to early diagenetic authigenic phases described in the literature (e.g. Bartholome *et al.*, 1971) which adds evidence to the argument that at least some of the mineralisation occurred during early diagenesis. Minerals which could be related to alteration events in the groundmass such as chlorite, muscovite and biotite, were not found to be spatially associated with sulphides at the thin-section level.

A noteworthy relationship exists between early hydrothermal SSC stage mineralisation and Type 1 veins. Some previous Copperbelt authors have interpreted vein-hosted mineralisation by default as late-stage and post-lithification in timing (e.g. Sillitoe *et al.*, 2010). However, according to Hitzman *et al.* (2012) "veins within the Katangan sequence could have been formed due to fluid overpressure during very early diagenesis". This fluid

overpressure, in places, could have been caused by mineralising fluids and Type 1 sulphide-hosting veins frequently show textures which suggest that they are cross-cutting, or are terminated by, layers of pre-lithification sediments (Figure 4.70). Also, the presence of antitaxial textures in certain examples of Type 1 veins (Figure 4.15) indicate that they were formed in an extensional stress-field (Bons and Montenari, 2005), making a pre-orogenic, syn-rifting timing the most obvious candidate for their timing of formation.

No consistent cross-cutting relationships have been observed between Type 1 veins and stratiform-disseminated mineralisation, and in many cases stratiform-disseminated mineralisation appears to grade from the groundmass and into these veins, and vice-versa. Additionally, the sulphide mineralogy and paragenetic sequence observed in these veins is identical to that observed in nearby stratiform-disseminated mineralisation. Type 1 veins do not always host sulphides, and many totally barren examples exist throughout the stratigraphy. Clearly a complicated relationship between stratiform-disseminated and Type 1 vein-hosted mineralisation exists, but for the purposes of this study, both stratiform and vein-hosted mineralisation are considered to be para-contemporaneous, on the broad timescale during which the Early Hydrothermal SSC mineralisation stage is thought to have operated (see below). A parallel is drawn between Type 1 veins at Mashitu South and the "prefolding vein-hosted mineralisation" described by Selley *et al.* (2005) in their review of the Zambian Copperbelt, which is described with regard to stratiform-disseminated mineralisation: "In some cases they appear to be coeval, in other cases they represent distinct mineralisation events." Therefore, it is important to distinguish between Type 1 veins and later-formed Type 2 veins when describing the distribution and form of hypogene sulphide mineralisation.

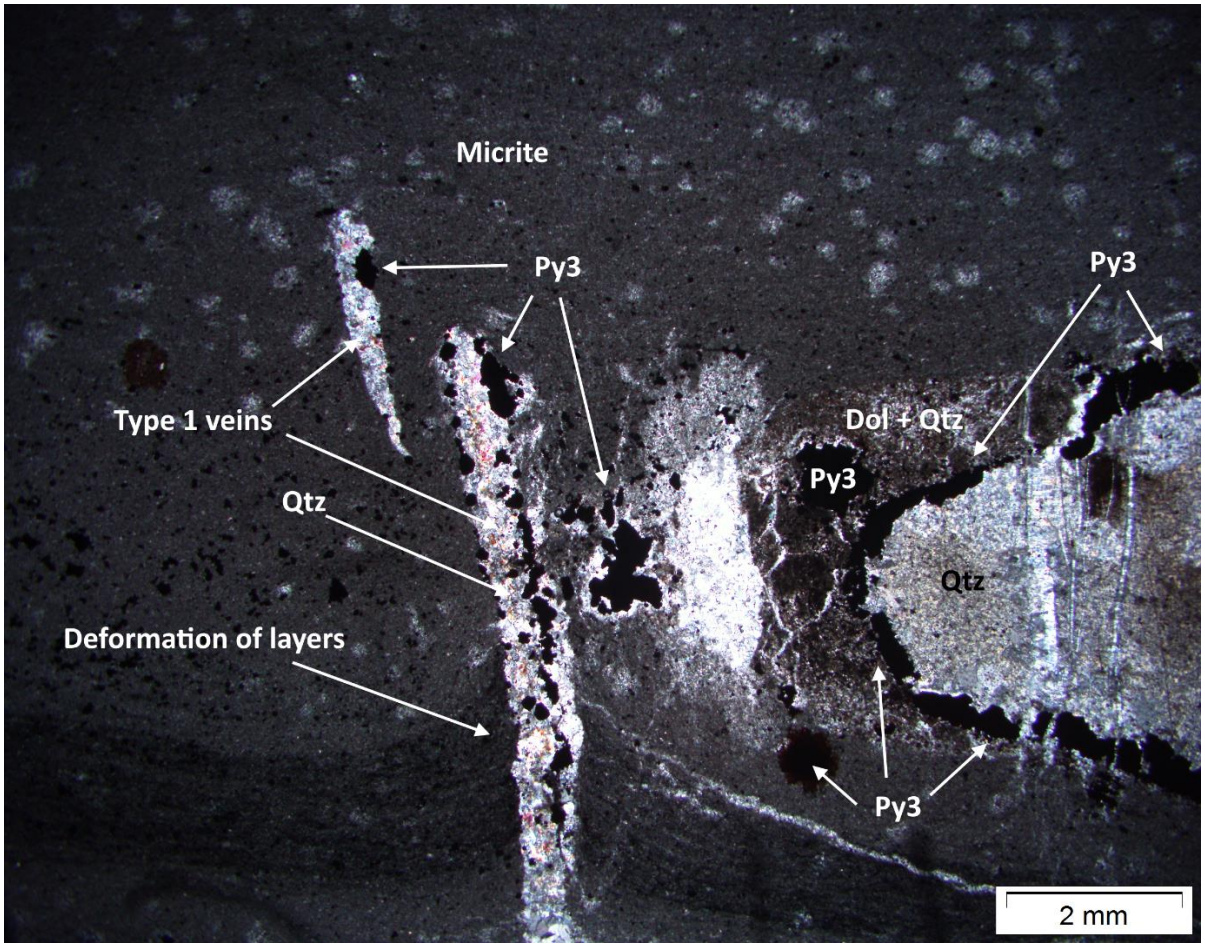

Figure 4.70*: Type 1 veins composed of quartz (Qtz), minor dolomite and pyrite 3 (Py3) 'breaking through' layers of the rock within the micritic groundmass of the DStrat unit. It seems likely that this veining occurred pre-lithification and was caused by fluid overpressure, inducing soft-sediment deformation. Optical image taken in XPL from sample MSSD075_19_1.*

According to the SSC model, saline, low temperature fluids would have likely circulated through oxidised redbeds (the RAT), which, together with the basement (Dejonghe and Ngoyi, 1995; Koziy *et al.*, 2009; van Wilderode *et al.*, 2014), may have acted as the metal source. These oxidised Cu-bearing fluids would then have been transported towards the surface and focussed along extensional faults (Selley *et al.*, 2010) where they hit redox horizons such as the RAT – Mines Subgroup boundary (see Figure 6). At these boundaries, metal ions in solution would be reduced, sourcing sulphur from BSR processes and early diagenetic pyrite and precipitating Cu-sulphides with a syn-diagenetic timing (e.g. Jensen and Dechow, 1962; Dechow and Jensen, 1965; Hitzman *et al.*, 2010; Hitzman *et al.*, 2012). El Desouky *et al.* (2009) analysed fluid inclusions from the Kamoto and Luiswishi deposits to show that this stage of mineralisation was formed by mineralising fluids at a moderate-to-

low temperature (115 to 220 °C or less) and salinity (11.3 to 20.9 wt.% NaCl equiv.). The 'Early Hydrothermal SSC' stage is equated by this study to the regional 'stratiform mineralisation' characterised by Dewaele *et al.* (2006a).

Selley *et al.* (2005) report data from Barra *et al.* (2004), where through Re-Os dating of stratiform sulphides, an age of ~816±62 Ma is determined for early mineralisation at Konkola. Decree *et al.* (2014) find evidence for early diagenetic U mobilisation at Shinkolobwe and Kambove in two periods around ~876 and ~823 Ma; the conditions in which Cu could have circulated would likely have been similar to those which would mobilise U. An age of 846±19 Ma (Kampunzu *et al.*, 1991) is given for the initiation of Katangan-Rift magmatism, probably expediting basin subsidence and instigating the deposition of carbonates (which acted as the redox boundary in the Mines Subgroup). Heat flow from this magmatism may also have increased the circulation of basinal fluids. Therefore, this date (846±19 Ma) is considered a maximum for the deposition of the Early Hydrothermal SSC Stage, and it is likely that this stage of mineralisation took place over a protracted and perhaps punctuated period of time between ~850 and ~760 Ma as the sediments underwent progressive diagenesis. The distribution and paragenesis of the pyrite 3, chalcopyrite 1, bornite 1 and chalcocite 1 phases are typical for stratiform mineralisation and similar findings are reported for equivalent phases from many other Copperbelt deposits (e.g. Oosterbosch and Schuiling, 1951; Bartholomé and Katekesha 1971; Sweeney *et al.*, 1991; Dejonghe and Ngoyi, 1995; Selley *et al.*, 2005; Broughton and Rogers, 2010; Hitzman *et al.*, 2012; Seibel *et al.*, 2013; Schmandt etal., 2013).

The distribution and paragenesis of the carrollite 1 (Car1) phase at Mashitu South is unusual for stratiform carrollite in the Copperbelt, and cannot be explained by the generally accepted regional model. In most deposits, stratiform carrollite is deposited early in the paragenetic sequence, between the deposition of pyrite and chalcopyrite, and is distally distributed with regard to the basal redox horizon between the 'pyrite' and 'chalcopyrite' zones (e.g. Oosterbosch and Schuiling, 1951; Chartrand and Brown, 1984; Dejonghe and Ngoyi, 1995; Broughton and Rogers, 2010; van Langendonck *et al.*, 2013).

At Mashitu South, however, stratiform carrollite (Car1) appears to have a distinct predilection for the RSF unit, is found in significant quantities within the SDB and DStrat, is the only stratiform sulphide present in the RSC unit and is present locally in proximity to

silicified, stromatolitic horizons within the CMN (see Chapter 3 and Figure 4.49). The Car1 phase is also the last to be formed of the stratiform sulphides, displaying textures which show that it precipitated paragenetically later than and replaced stratiform (Figure 4.71) and Type 1 vein-hosted (Figure 4.72) Py3, Cpy1, Bn1, Dg1 and Cc1.

The association of Car1 with stromatolitic, silicified units such as the RSC leads this study to invoke the model of Fay and Barton (2012) for distribution of sulphides (Figure 2.5), which is expanded by van Langendonck *et al.* (2013) to include distribution of ore along horizons in the CMN unit.

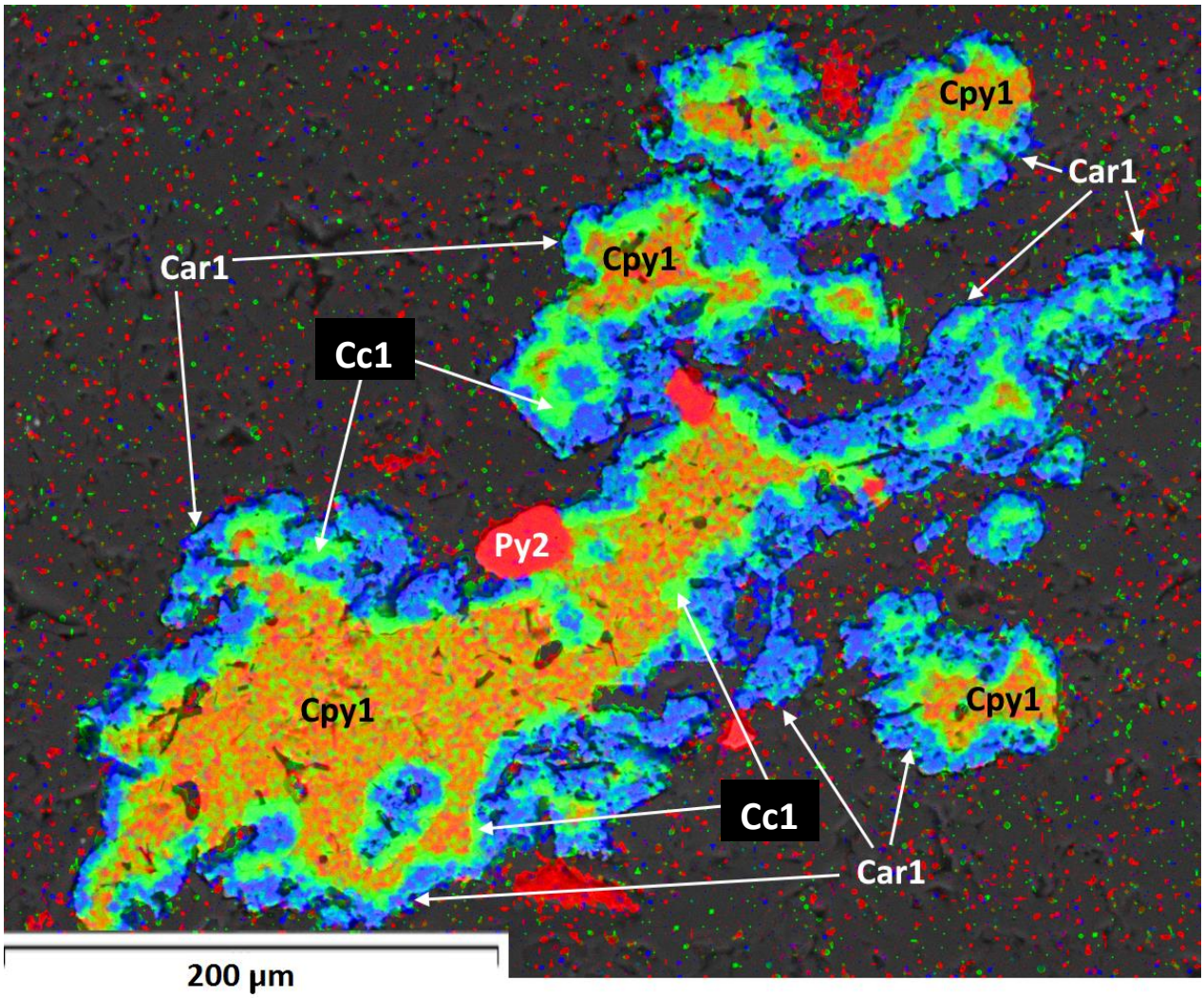

Figure 4.71*: Red-Green-Blue EDS map of a stratiform-disseminated sulphide bleb. Red=Fe, Green=Cu, Blue=Co. Note the blue-green carrollite (Car1) phase rimming all earlier-formed stratiform sulphides, including pyrite (Py2), chalcopyrite (Cpy1) and chalcocite (Cc1). Sample MSSD083_23_2.*

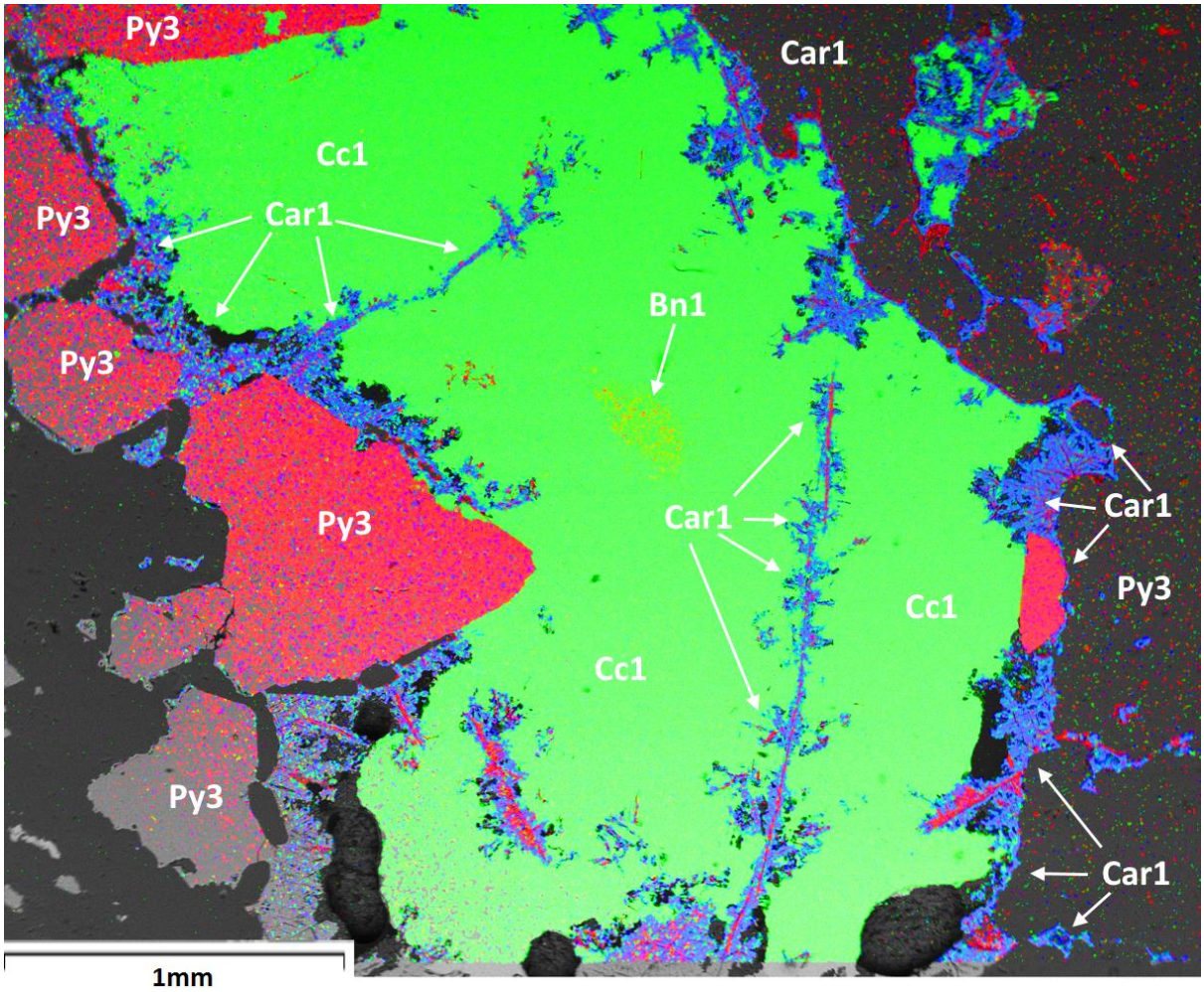

***Figure 4.72**: Red-Green-Blue EDS map of a Type 1 vein-hosted sulphide bleb. Red=Fe, Green=Cu, Blue=Co. Carrollite 1 (Car1) rims chalcocite 1 (Cc1) and in some cases pyrite 3 (Py3), and occurs along grain boundaries and in veins cutting chalcocite 1. A remnant of bornite (Bn1) exists in the middle of the chalcocite. Red streaks within some of the Car1 'veins' are haematite which is thought to have exploited the same fractures in the grains as the Car1 phase, at a later time. Sample MSSD075_16_2.*

In this model, dissolution of dolomite in the stromatolitic silicified units creates a high level of permeability within the unit, which acts as a fluid conduit, allowing mineralising fluids to travel through the unit along strike. As these fluids infiltrate into the less permeable, more calcareous (and thereby more reducing) units above and below these fluid conduits, they precipitate ore. This is exactly the pattern of distribution observed for Car1 at Mashitu South (see Figure 4.49), with the RSC as well as localised silicified, stromatolitic horizons within the lower CMN acting as the fluid conduits, and the RSF, SDB and lower CMN acting as the ore-receptive horizons above and below these conduits.

The question of why the Car1 phase does not fit the model of distribution and paragenesis for the rest of the Cu sulphides remains. Paragenetically, stratiform and Type 1 vein-hosted carrollite is precipitated last of the sulphides of the Early Hydrothermal SSC Stage. It is possible that during the protracted length of time over which the stratiform stage of mineralisation operated (Hitzman *et al.*, 2012), the hydrodynamics of the mineralising system changed towards the end with the precipitation of Car1. This may have happened due to progressive changes to the mineralising fluid chemistry, or due to more abrupt changes to the metal source or fluid transport system.

In terms of a metal source, there is a discrepancy in the Copperbelt metal association of Cu-Co (and sometimes minor Ni), given its designation as an SSC type copper province (Sedimentary-hosted Stratiform Copper), for which a more typical metal association would be Cu-Zn-Pb-Ag or similar (Brown, 2014). The SSC model advocates a metal source of underlying redbeds (i.e. the R1/RAT Subgroup) – the volume of which is insufficient to account for the metal endowments of the Copperbelt deposits (Hitzman 2000; Cailteux *et al.*, 2005) and many authors (e.g. Sweeney *et al.*, 1991; Sweeney and Binda, 1994; Roberts *et al.*, 2009) also infer that the basement could be a potential source of metals. A model where both the R1 redbeds and the pre-Katangan basement contribute to the metal balance seems most likely (van Wilderode *et al.*, 2014). However, this model still does not explain the Co-Ni component of most ores, particularly in the Congolese Copperbelt. A mafic component to the fluid system is thus inferred by many to explain the anomalously high levels of these metals in the copper province (e.g. Annels *et al.*, 1983; Annels & Simmonds, 1984; Unrug, 1988; Annels, 1989; Koziy *et al.*, 2009; Muchez and Corbella, 2012).

Given that the Car1 phase at Mashitu South appears to post-date the other, early diagenetic phases (Sph1, Cpy1, Bn1, Dg1, Cc1), magmatism in the Mwashya or Nguba periods which emplaced gabbroic intrusions and basic volcaniclastics could have not only presented a metal source for mineralising fluids, but also a heat engine to expedite their circulation during the deposition of the Car1 phase, although evidence is lacking to suggest the latter. This study considers the Nguba period rift-associated magmatism, which is by far the more voluminous (Kampunzu *et al.*, 2000; Selley *et al.*, 2005), to be the more likely correlative event. Kampunzu *et al.* (2000) place this magmatism between around 760-720 Ma, and Decree *et al.* (2014) identified a period of U circulation from inherited heterogenite U-Pb ratios soon after this period (between ~720 to ~670 Ma). U and Co are mobile under

similar hydrothermal conditions (Brown, 2014) and therefore, if Nguba magmatism is indeed the metal source for Co and Ni, the ~720 to ~670 Ma age for U circulation would also seem a likely age for the circulation of Cu-Co-Ni rich fluids and the deposition of Car1.

The change of fluid transport system, from fluids travelling upwards from the RAT into the Mines Subgroup, to the Fay and Barton (2012) model of RSC-focussed transport could have been induced by two things. First, dissolution of evaporites, dolomite and other non-silica gangue phases originally present in the rock would have had to occur before the RSC would be permeable enough to act as a fluid conduit. This may not have happened until after the deposition of the Sph1, Cpy1, Bn1, Dg1 and Cc1 phases. Secondly, circulation of fluids containing Cu-Co-Ni through the RSC and similar horizons could have been initiated when Nguba-age igneous intrusions (see above) intersected the Mines Subgroup stratigraphy elsewhere in the basin, connecting the fluid conduits to a metal source. To get significant lateral transport along these units, these events would have had to have happened before the tectonic/halokinetic/olistrosomic dismemberment of the Mines Subgroup.

An alternative distribution and paragenesis to the Car1 phase is significant because Car1 is the second most abundant mineralisation-related phase found in the deposit, with 25 out of the 71 samples included in the paragenesis matrix (see Appendix 10) containing stratiform or Type 1 vein-hosted Car1. This abundance is perhaps responsible for the strong Cu-Co association at Mashitu South (see Chapter 5: Geochemistry). Additionally, Car1 has been found in many samples from which high grades of mineralisation were reported. Figure 4.73 shows the results of the comparison of samples from MSSD075, 080 and 083 that were taken from intervals which assays showed had >1% Cu concentration. Of these samples, 8 out of 14 contained significant quantities of the Car1 phase, all within the 11 highest grade samples (between 2.7 and 8.9% Cu). No other single phase was so common in the highest grade samples. It appears that the Car1 phase makes a significant contribution to the Cu (and Co) grades of hypogene mineralisation.

The transition in the hydrodynamics of the Early Hydrothermal SSC Stage is envisaged as a progressive and gradual process which spanned from early-to-late diagenesis and the majority of the extensional phase of Katangan Basin development. Early sulphide deposition (Sph1, Cpy1, Bn1, Dg1 and Cc1) had a more typical SSC signature and the later Car1 phase was influenced by Nguba magmatism and RSC-focussed transport. The stage

resulted in the para-contemporaneous formation of both stratiform and Type 1 hosted precipitation of all 6 sulphide phases. In total, the Early Hydrothermal SSC stage is likely to have spanned a time period between ~850 and ~670 Ma.

Stratigraphy	Sample Name	Depth Start (m)	Depth End (m)	Closest Grade (<1m) Cu (ppm)	Pre-ore diagenetic			Early hydrothermal SSC							Late hydrothermal ore stage				
					Py1	Hm1	Py2	Py3	Sph1	Cpy1	Bn1	Dg1	Cc1	Car1	Car2	Cpy2	Bn2	Cc2	Dg2
RSC	MSSD083_24_2_M	298	298.15	89200										Car					
SDB	MSSD083_15_1_M	157.5	157.65	55600											Car				
RSF	MSSD083_17_2_M	185.62	185.74	51600										Car				Cc	
RSF	MSSD083_25_1_M	303.92	304.04	45600				Py						Car				Cc	
RSF	MSSD080_19_2_U	279.57	279.72	44100										Car					
RSF	MSSD080_19_1_M	278.51	278.66	43300											Car			Cc	
CMN	MSSD080_13_1_M	110.9	111.05	38500															
SDB	MSSD083_16_1_M	173.83	173.95	35000		Hm		Py					Cc	Car					
RSF	MSSD075_18_1_U	203.63	203.78	31900										Car					
CMN	MSSD083_08_1_M	118.68	118.88	29900									Cc	Car					
SDS	MSSD083_14_1_M	154.68	154.83	27300										Car		Cpy	Bn	Cc	
CMN	MSSD083_07_3_M	116.46	116.66	17650											Car				
SD2d	MSSD075_15_1_U	153.35	153.5	12450						Cpy									
SD2d	MSSD083_22_2_M	240.09	240.24	12450	Py	Hm	Py			Cpy	Bn								

Stratigraphy	Sample Name	Depth Start (m)	Depth End (m)	Closest Grade (<1m) Cu (ppm)	Early Supergene											Late Supergene						
					Cu1	Cup1	Ten1	Cc3	Bn-Dg-Cov 3	Hm2	CoCarb2	Het1	Azu1	Mal1	Cry1	Cc4	Hm3	CoCarb2	Het2	Mal2	Cry2	Psm1
RSC	MSSD083_24_2_M	298	298.15	89200				Cc			CoCarb											
SDB	MSSD083_15_1_M	157.5	157.65	55600				Cc													Cry	
RSF	MSSD083_17_2_M	185.62	185.74	51600																		
RSF	MSSD083_25_1_M	303.92	304.04	45600														CoCarb				
RSF	MSSD080_19_2_U	279.57	279.72	44100				Cc														
RSF	MSSD080_19_1_M	278.51	278.66	43300				Cc										CoCarb				
CMN	MSSD080_13_1_M	110.9	111.05	38500												Cc	Hm					
SDB	MSSD083_16_1_M	173.83	173.95	35000												Cc	Hm					
RSF	MSSD075_18_1_U	203.63	203.78	31900																		
CMN	MSSD083_08_1_M	118.68	118.88	29900																		
SDS	MSSD083_14_1_M	154.68	154.83	27300																		
CMN	MSSD083_07_3_M	116.46	116.66	17650				Cc			CoCarb											
SD2d	MSSD075_15_1_U	153.35	153.5	12450				Cc	Bn													
SD2d	MSSD083_22_2_M	240.09	240.24	12450																		

***Figure 4.73**: Comparison of the paragenetic phases present in all high-grade (>1%/10,000ppm Cu) samples from MSS075, 080 and 083, ranked in order of Cu grade. This figure was compiled by taking the grade of the closest assay interval to the sample. Note that the carrollite 1 (Car1) and chalcocite 3 (Cc3) phases are present in more high grade samples than other phases, and appear to make a significant contribution to Cu grades at Mashitu South.*

4.4.3 The Late Hydrothermal Ore Stage

The carrollite 2 (Car2), chalcopyrite 2 (Cpy2), bornite 2 (Bn2), chalcocite 2 (Cc2) and digenite 2 (Dg2) phases make up the sulphides of the Late Hydrothermal Ore Stage. Unlike the sulphides of the Early Hydrothermal SSC stage which are stratiform-disseminated or Type 1 vein-hosted, this generation of sulphides is found primarily in Type 2 veins, with extremely limited distribution in the groundmass within a few millimetres of Type 2 vein margins. These Type 2 veins appear to have formed after diagenesis (see section 4.3.3.1) and cross cut earlier mineralisation of the Early Hydrothermal SSC Stage (Figures 3.49, 4.24 and 4.63). It should be noted that not all Type 2 veins contain sulphide mineralisation and the majority appear to be barren. Paragenetically, this stage differs from the Early Hydrothermal SSC stage because carrollite (Car2) is precipitated first, rather than last, of all the sulphides.

The distribution of this stage of mineralisation is difficult to interpret. Cc2, the most abundant phase from the stage, is scattered fairly haphazardly throughout all of the units of the Mines Subgroup stratigraphy except for the RSC (Figure 4.49). Dg2 was only identified at the RAT Gris/DStrat transition and Bn2 was found both at this stratigraphic horizon and also in the SDS. Interestingly, all of the sulphides from this stage are found in samples from the SDS, whereas hardly any sulphides from the Early Hydrothermal SSC stage are found in this unit. This is perhaps because mineralising fluids travelling upwards from the base of the Mines Subgroup, and from the RSC (see Section 4.4.2) precipitated the majority of their metal content as sulphides lower in the stratigraphy before encountering the SDS, and because the SDS contains little in terms of carbonaceous or calcareous material to reduce metal ions from solution. The mineralising fluids of the Late Hydrothermal Ore Stage, however, do not appear to have been limited so much by these factors. There is no apparent zonation of sulphides by Cu/Fe ratio in the same way as shown by the Early Hydrothermal SSC stage, at least not at the deposit scale. In summary, it appears that stratigraphy is not a major control on the distribution of ore formed in the Late Hydrothermal Ore Stage.

Although no groundmass-hosted alteration minerals can be linked to this stage, the mineralogy of the Type 2 veins themselves provide some clue as to the chemistry of the mineralising fluids. In contrast to Type 1 veins, which contain dolomite, quartz, apatite and sulphides, Type 2 veins also host magnesite, chlorite, barite, and less commonly, halite.

Magnesite and chlorite are indicative of a high Mg-content to the mineralising fluids, and barite and halite point to a high salinity. The high salinities may have aided in the mobilisation of metals during the period of formation of this stage of mineralisation.

The Late Hydrothermal Ore Stage is equated to the 'Vein-Type' mineralisation of Dewaele *et al.* (2006a) at the Kamoto and Musonoi deposits for being post-lithification-vein hosted, stratabound/cross cutting to earlier mineralisation (Figures 3.49, 4.24 and 4.63) and primarily comprised of chalcocite with minor digenite and bornite (and rare chalcopyrite). A fluid inclusion study by El Desouky *et al.* (2009) shows the mineralising fluids from this stage to be of relatively high salinity and temperature (270 to 385 °C and 35 to 45.5 wt.% NaCl equiv.) compared to mineralising fluids from the stratiform stage at Kamoto and Luiswishi. This agrees with the inference of high salinities of the mineralising fluids of this stage at Mashitu South, based on the presence of barite and halite in Type 2 veins. According to studies by El Desouky *et al.* (2010) and van Wilderode *et al.* (2014), the hydrothermal fluids responsible for vein-type mineralisation were unlikely to have added metals into the system, rather they resulted in remobilisation of metals which were emplaced into the Mines Subgroup by the earlier-occurring Early Hydrothermal SSC Stage. As stated by Dewaele *et al.* (2006a), the location of faults and tectonic breccias is probably the main control on the distribution of the hypogene mineralisation from this stage.

Re-Os dating of sulphides from this stage of mineralisation at the Nkana and Mindola deposits in the Zambian Copperbelt give an age of 576 ± 41 Ma (Selley *et al.*, 2005), corresponding to Katangan Basin inversion and the early stages of the Lufilian orogeny; additionally, El Desouky *et al.* (2007) puts a maximum age to similar mineralisation in the Lufukwe anticline of the Lufilian Foreland of 573 ± 5 Ma – the date given by Master *et al.* (2005) for the end of deposition of the Kundelungu Group, through which faults cut which host the described mineralisation.

Petrographic analysis confirms that, as noted during logging and presented in Chapter 3, Type 2 vein-hosted mineralisation of the Late Hydrothermal Ore Stage does not account for as significant a proportion of hypogene ore at Mashitu South as the Early Hydrothermal SSC Stage. Figure 4.73 shows that only 6 out of 14 of the 'high grade' samples contained one or more phases from the Late Hydrothermal Ore Stage, compared to 10 out of the 14 'high grade' samples containing one or more phases from the Early Hydrothermal SSC Stage. This is in agreement with the study of Dewaele *et al.* (2006a) who observed that,

volumetrically, vein-type mineralisation accounted for a much lower proportion of mineralisation in the Congolese Copperbelt than stratiform mineralisation.

4.4.4 The Early Supergene Stage

The eleven phases of the Early Supergene Stage: native copper 1(Cu1), cuprite 1 (Cup1), tenorite 1 (Ten1), chalcocite 3 (Cc3), bornite-digenite-covellite 3 (Bn-Dg-Cov3), haematite 2 (Hm2), cobaltoan carbonate 1 (CoCarb1), heterogenite 1 (Het1), azurite 1 (Azu1), malachite 1 (Mal1) and chrysocolla (Cry1), are distributed mostly within the CMN and the RSC units (see Figure 4.49). Most of these mineral phases have a distinct association with supergene mineralisation, and therefore the stage is considered to have been formed by supergene processes. The CMN hosts the majority of this stage of mineralisation because in the holes MSSD075, 080 and 083 it is the first stratigraphic unit to be encountered with depth and the closest to the surface, receiving (and reducing) the majority of the oxidising meteoric fluids compared to the rest of the stratigraphy. The RSC and the units immediately next to it also host this phase of mineralisation as its vuggy, void filled nature makes it permeable, allowing meteoric fluids through to a much greater depth than if they had leached through the rest of the stratigraphy directly from the surface. The RSC thus acts as a fluid conduit in a similar manner as towards the end of the Early Hydrothermal SSC stage, as per the model of Fay and Barton (2012) (see Figure 3.58). Permeable tectonic breccias are also likely to have played a role in the distribution of this stage (see Chapters 3 and 4). At thin-section scale, the most abundant mineralisation related to this stage is formed in what appears to be voids in the rock, allowing for the infiltration of supergene fluids.

There does not appear to be an easily discernible zonation of minerals from the Early Supergene Stage with either stratigraphy or depth. There is, however, a tendency for mineralisation within voids and fractures to be zoned, with early-formed phases found at the void margins and later formed phases towards the centre of the voids, sometimes with what appears to be open space in the middle. This relationship is generally the opposite to the paragenetic distribution of hypogene phases, where the first formed phase is usually central, and later phases are deposited as rims to this central phase. This outward-in fill is not usually encountered where mineralisation is not concentrated in voids in the rock, nor where supergene mineralisation is focussed around pre-existing sulphide grains, and care

must be taken when determining a paragenetic order for mineralisation of the Early Supergene Stage.

With regards to paragenesis of Cu-related minerals of this stage, there is an apparent order of the minerals containing the greatest concentration of copper precipitating first (e.g. Cu1, Cup1, Ten1, Cc3) and minerals which contain less copper by wt.% precipitating later (e.g. Azu1, Mal1 and Cry1). This reflects a general trend from more reducing Eh, more alkaline/neutral pH conditions towards more oxidising and acidic Eh/pH conditions during the progression of supergene alteration, which is illustrated as Path 1 in Figure 4.74. A second trend: Path 2, exists, which is also illustrated in Figure 4.74. This path reflects the paragenetic order of the supergene sulphides Cc3 and Bn-Dg-Cov3 which appear to form *after* Cu1. Path 2 appears to be formed by a trend towards more acidic pH conditions, without much corresponding increase in Eh. Both trends indicate that the Early Supergene Stage mineralising fluids increased in acidity and oxidising potential as they evolved towards the end of this mineralisation stage, perhaps due to the gradual onset of climatic conditions favourable to supergene alteration, or ongoing regional uplift (Lavier *et al*., 2001) causing progressively more exhumation and exposure to meteoric fluids.

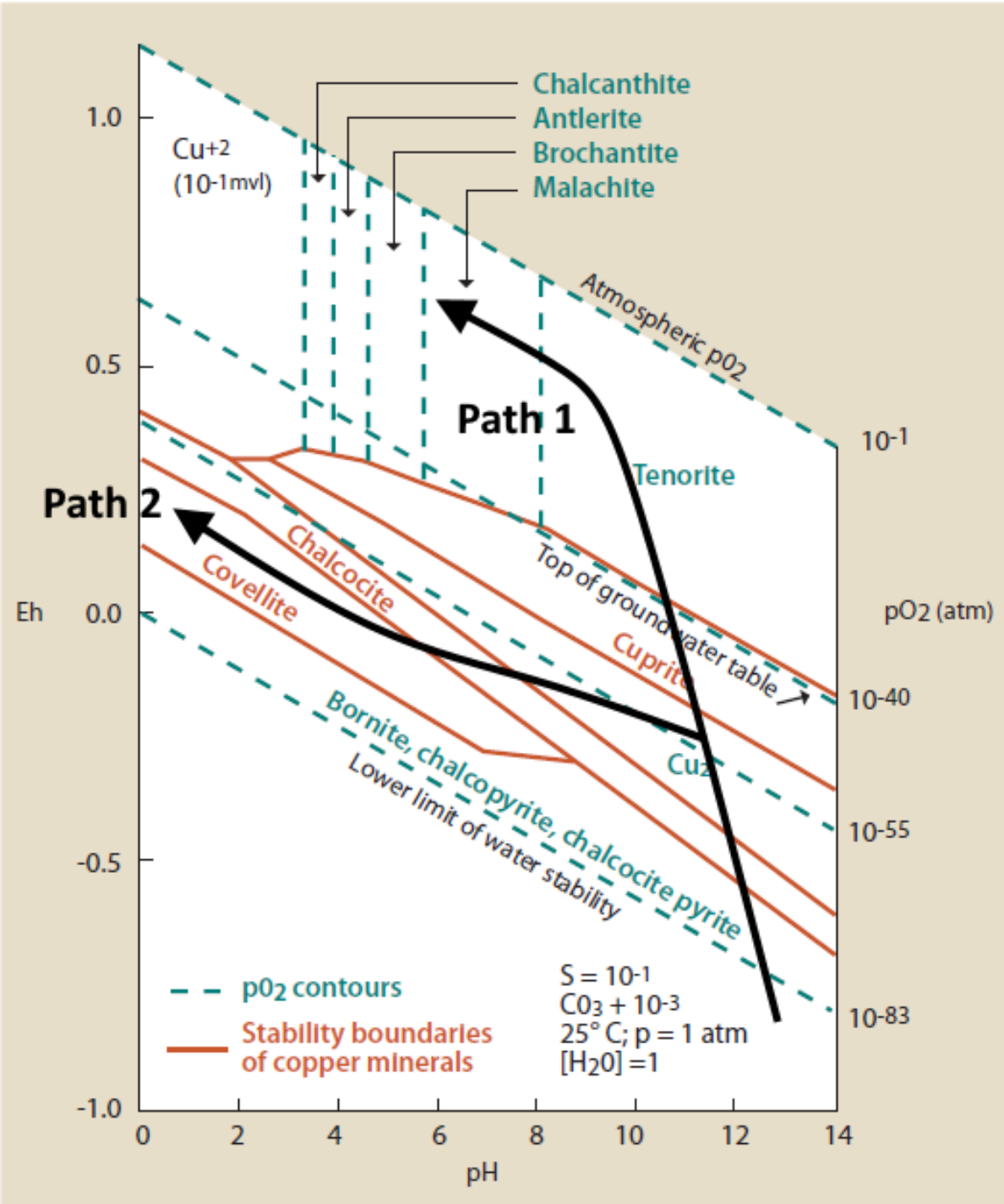

Figure 4.74: *Eh-pH diagram showing copper mineral stability at surface conditions and at low f(CO_2) (modified from Taylor, 2011). Paths 1 and 2 reflect trends of variation in Eh and pH required to form the paragenetic order of mineralisation observed in the Early Supergene Stage at Mashitu South.*

Earlier, more concentrated Cu minerals from this stage are much more abundant than later, less concentrated Cu minerals. Cc3 in particular is far more abundant than any of the other phases of the Early Supergene Stage. It is possible that other phases such as Azu1, Mal1 and

Cry1 were once more abundant from this Stage, but they have since been dissolved, remobilised and reprecipitated as part of the Late Supergene Stage.

Gangue phases which are associated with the Early Supergene Stage include dolomite, quartz, barite and apatite. A mass of supergene barite, apatite and Hm3 occurring in the RSC is shown in Figure 4.60, which appears to have precipitated in the paragenetic order of barite → Hm3 → apatite. The Het1 phase is also associated with supergene quartz and apatite, with which it is commonly intergrown at a very fine scale (see Figure 4.36).

The Early Supergene Stage appears to contribute significantly to ore grades in MSSD075, 080 and 083. As shown in Figure 4.73, 6 out of the 14 'high-grade' ore samples contain the Cc3 phase from this stage. Most of the very highest-grade samples (>4% Cu) contain a combination of the Car1 and Cc3 phases and the Early Supergene Stage appears to be an important upgrader of pre-existing concentrations of sulphides, which probably form the nucleation point for the reprecipitation of Cc3 ore, or are leached of other elements such as sulphur in-situ and altered to Cc3.

The Early Supergene Stage is equated to the first of two stages of supergene heterogenite growth dated by Decree *et al.* (2010) and inferred to be representative of a regional supergene alteration event. This first stage was formed by a period of regional uplift during the Miocene (Lavier *et al.*, 2001), which caused enhanced erosion and exhumation of the rocks of the Katangan Supergroup and exposed hypogene mineralisation such as that found in the Mines Subgroup to meteoric fluids. According to U-Pb dating of heterogenite from this stage by Decree *et al.* (2010), this occurred at or before 10.3 Ma.

4.4.5 The Late Supergene Stage

The Late Supergene Stage is distinguished from the Early Supergene Stage by consisting of a repetition of many of the mineral phases observed in the Early Supergene Stage, namely chalcocite, haematite, cobaltoan carbonate, heterogenite, malachite and chrysocolla. The constituent phases of the Late Supergene Stage are: Cc4, Hm3, CoCarb2, Het2, Mal2, Cry2 and Psm2. These phases show paragenetic relationships with supergene phases from the Early Supergene Stage which identify them as a temporally distinct stage of mineralisation (see Figure 4.38). The abundance of the low-Cu mineral phases such as malachite and chrysocolla is higher in this stage of supergene mineralisation, in contrast to the Early Supergene Stage in which high-Cu mineral phases such as chalcocite are more abundant.

This indicates that during the progression of the Late Supergene Stage, Eh-pH conditions were more likely to follow Path 1 than Path 2 (see Figure 4.75). An additional difference between the stages is that the mineral phases of the Late Supergene Stage are less frequently encountered in proximity to hypogene sulphide mineralisation than mineral phases of the Early Supergene Stage, and it seems that the later stage is characterised more by dissolution, remobilisation and reprecipitation rather than in-situ oxidation.

Other than these two differences, the distribution (see Figure 4.49), textures, gangue-phase relationships, and contribution to high grades of ore (see Figure 4.73) are similar between the Early and Late Supergene Stages in MSSD075, 080 and 083 and it is likely that the two formed under very similar conditions. Both stages are preferentially distributed in the upper stratigraphy, near the top of the holes, and are associated with similar gangue phases.

In terms of contribution to ore, however, it is noteworthy that the para-exotic mineralisation encountered in the RAT Rouge of MSSD140 is considered to be part of the Late Supergene Stage, consisting of the Mal2 and Psm1 phases (see Figures 4.45, 4.47 and 4.48). This RAT-hosted para-exotic supergene mineralisation is high grade, abundant, and of considerable economic importance (Chimvinga, pers. comm., 2014).

The Late Supergene Stage is equated with the second stage of supergene heterogenite growth dated by Decree *et al.* (2010) to the Pliocene at 5.3–2.3 Ma. According to Decree *et al.* (2010), a transition to a warmer, wetter regional climate in Katanga at this time (Alexandre, 2002; Giresse, 2005; Miller *et al.*, 2010) initiated a renewed period of leaching and supergene alteration, which is inferred by this study to have resulted in the creation of the Late Supergene Stage. It should be noted that Caenozoic ages for the Early and Late Supergene stages are inferred from work by Decree *et al.* (2010) on other deposits, and no dating of supergene mineralisation at Mashitu South has been carried out. Hitzman (*pers. comm.,* 2015) points to the possibility of a pre-Karoo (>300 Ma) age for supergene alteration, as has been recorded near Kolwezi, from supergene deposits occurring beneath Karoo Supergroup cover. A summary of all of the key genetic features of each mineralisation stage is given overleaf as Figure 4.75.

	Mineralisation Stage				
	Pre-Ore Diagenetic	**Early Hydrothermal SSC**	**Late Hydrothermal Ore**	**Early Supergene**	**Late Supergene**
Metal association	Fe	Cu + Co + Bi + Ni + V ± Mo ± As ± Fe ± Zn.		Cu + Be + P ± Zn.	
Mode of Distribution	Disseminated	Stratiform-disseminated and Type 1 vein-hosted	Type 2 vein-hosted	Void-filling	Void-filling
Metal Source	Detrital and dissolved sedimentary Fe	Cu from Granitic (pre-mineralised - Rodinian? **(1)**) basement and R1 redbeds, with possible late-stage input of Cu-Co-Ni by Nguba-age mafic igneous bodies.	Hypogene sulphides of the Early Hydrothermal SSC Stage	Hypogene Sulphides	Hypogene Sulphides and earlier supergene oxides
Transporting Fluid	Seawater and early diagenetic fluids (<100°C, 3-4% wt.% NaCl equiv.) **(2)**	Oxidising saline, low temperature diagenetic fluids (115-220 °C; 11.3-20.9 wt.% NaCl equiv.) **(3)**	Oxidising super-saline high temperature (metamorphic?) fluids (270-385 °C; 35-45.5 wt.% NaCl equiv.) **(3)**	Oxidising meteoric low temperature acidic fluids	Oxidising meteoric low temperature acidic fluids
Flow Mechanism	N/A	Topography/highland/ gravity-driven basin-wide flow of meteoric fluids **(4)** and/or burial-heat driven hydrologically closed circulation **(5).** Intrusion related heat may have driven fluids towards the end of this stage.	Compression driven flow/seismic pumping	Gravity driven leaching from surface downwards	Gravity driven leaching from surface downwards
Transport Conduit	N/A	Syn-extensional normal faults, and permeable R1 redbeds **(6).** By the time of Car1 deposition, the RSC and similar units within the CMN had become the primary fluid conduit.	Syn-orogenic/basin inversional reverse faults	Permeable rock units, the RSC, tectonic breccias	Permeable rock units, the RSC, tectonic breccias
Trapping Mechanism	N/A	Mines Series carbonates and black shales with organic carbonaceous material. Reducing agents and lower permeability.	Mines Series carbonates and black shales with organic carbonaceous material. Reducing agents and lower permeability - mostly along structural trap sites	Vadose/Phreatic zone transition (water table) and karstification-formed voids **(7)**	Vadose/Phreatic zone transition (water table) and karstification-formed voids **(7)**
Sulphur Source	BSR (Bacteriogenic Sulphate Reduction) of H_2S in anoxic sediments	Sulphides of the Pre-Ore Diagenetic Stage.	Remobilisation of earlier sulphides	Dissolution of earlier sulphides	Dissolution of earlier sulphides
Timing	<883 ± 10 Ma **(8)**, > Early Hydrothermal SSC	~850 Ma **(9,10,11)** to ~670 Ma **(10)**	~576 ± 41 Ma **(9)**	≥10.3 Ma **(12)**	5.3-2.3 Ma **(12)**

Figure 4.75: *Genetic summary of the 5 mineralisation stages at Mashitu South. Bracketed numbers in bold are references to literature:* ***(1):*** *Sillitoe et al. (2015);* ***(2):*** *Jensen and Dechow (1962);* ***(3):*** *El Desouky et al. (2009);* ***(4):*** *Brown et al. (2014);* ***(5):*** *Hitzman et al. (2010);* ***(6):*** *Selley et al. (2010);* ***(7):*** *De Putter et al. (2010);* ***(8):*** *Armstrong et al. (2005);* ***(9)*** *Selley et al. (2005);* ***(10):*** *Decree et al. (2014);* ***(11):*** *Kampunzu et al. (1991);* ***(12)****: Decree et al. (2010).*

4.4.6 Sources of Sulphur

The limited set of samples subjected to sulphur isotope analysis have $\delta^{34}S$ values in a distinct cluster around +3.00‰ $\delta^{34}S$ (16_1_D, 19_2_A and 21_4_A), while sample 16_1_E exists alone at around -10.00‰ (Figure 4.68). This is significant because the clustered samples represent Cu-Co mineralisation of both the stratiform, groundmass disseminated, Early Hydrothermal SSC Stage (16_1_D – Cc1 and Car1) and the Type-2 vein-hosted, Late Hydrothermal Ore Stage (19_2_A and 21_4_A – Cpy2 and Cc2), whereas sample 16_1_E represents unmineralised pyrite (Py1) of the Pre-Ore Diagenetic Stage. This suggests that, at Mashitu South, the sulphur source for both the early stratiform and late vein-hosted mineralisation was the same, and that sulphides from these mineralisation stages did not source sulphur from early diagenetic, pre-mineralisation pyrite (Py1). This contrasts with S-isotope data from other deposits in the Katangan Copperbelt, which shows matching $\delta^{34}S$ values for Cu-Co mineralisation sulphides and pre-mineralisation, diagenetic pyrite (Jensen and Dechow, 1962; Dechow and Jensen, 1965).

Comparing the $\delta^{34}S$ values to the typical ranges of $\delta^{34}S$ for terrestrial sulphur sources presented by Thode (1991), we see that, predictably, sulphur from Py1 (16_1_E) falls well within the expected range for 'sedimentary sulphides', whereas sulphur from the mineralised samples fits closer toward the range for meteoric sulphur and the lighter end of the range for evaporitic sulphur (Figure 4.68). It should be noted that all of the samples also fit into the ranges presented by Thode (1991) for coal, petroleum, sulphur of volcanic origin and sulphur from igneous rocks, but given the geodynamic setting of the samples these are considered less likely potential sources of sulphur. A primarily evaporitic source of sulphur would agree with the hypotheses of Muchez *et al.* (2008) for the source of sulphur at the Kamoto, Musonoi and Luiswishi deposits. Evaporitic sulphur may have been sourced in-situ from gypsum and other evaporites that existed within the rocks of the Mines Subgroup, the present-day absence of which may be explained by its dissolution within hydrothermal fluids. Alternatively, sulphur may have been sourced from evaporites in other portions of the stratigraphy, which were dissolved and transported by basinal brines, along with metals and the Cl- ion, to the site of metal sulphide deposition.

The sulphur isotope results suggest that the sulphur in the Mashitu South Cu-Co sulphides was sourced from dissolved evaporites, and that either the Early and Late

Hydrothermal Stages of mineralisation shared the same source of sulphur, or that the Late Hydrothermal Ore Stage simply remobilised sulphur from sulphides deposited during the Early Hydrothermal SSC Stage of mineralisation. The latter interpretation would agree with studies of El Desouky *et al.* (2010) and van Wilderode *et al.* (2014) which indicate that there was no new input of metals or sulphur to the system by the late, vein-type mineralisation stage.

A caveat must be taken with conclusions from this sulphur isotope study however, in that they are drawn from a very limited number of samples, with a fairly narrow spatial and mineralogical distribution, and are not necessarily representative of the deposit as a whole. Additionally, some process of sulphur isotope fractionation could exist between the Cu-Co sulphides and the early Fe sulphides on a purely mineralogical basis, which could account for the variation in $\delta^{34}S$ values between the two. It is recommended that a larger sulphur isotope study, including samples from a wider geographic area and a greater variety of mineral phase types, be conducted at the Mashitu South deposit to affirm the source of sulphur for hypogene mineralisation.

4.5 Conclusions from Petrography and Paragenesis

1. There are 33 different mineralisation-related phases at Mashitu South, consisting of different generations of pyrite, haematite, chalcopyrite, bornite, digenite, chalcocite, carrollite, native copper, cuprite, tenorite, covellite, cobaltoan carbonates, heterogenite, azurite, malachite, chrysocolla and pseudomalachite. These phases can be grouped into 5 stages: Pre-Ore Diagenetic, Early Hydrothermal SSC, Late Hydrothermal Ore, Early Supergene and Late Supergene, all of which formed over a punctuated, protracted time period between ~850 Ma and ~2.3 Ma.
2. The Early Hydrothermal SSC Stage is the most economically important stage for hypogene mineralisation at Mashitu South. Ore minerals from this stage include stratiform-disseminated and Type 1 vein-hosted chalcocite (Cc1), bornite (Bn1) and chalcopyrite (Cpy1), which are zoned upwards from the base of the Mines Subgroup such that chalcocite is most abundant in the Kamoto Formation, bornite is most

abundant in the Dolomitic Shales Formation and chalcopyrite is most abundant in the Kambove Formation.

3. Stratiform-disseminated and Type 1 vein-hosted carrollite (Car1) from the Early Hydrothermal SSC Stage is associated with regions of high-grade mineralisation, and is preferentially distributed above and below the RSC as well as within stromatolitic, silicified horizons within the lower CMN. This carrollite is likely to be a significant component, if not the primary Cu-Co-bearing component of hypogene orebodies.
4. The Late Hydrothermal Ore Stage, consisting of sulphides hosted in Type 2 veins, does not make a significant contribution to ore grades at Mashitu South. It does not share the same deposit-scale zonation of phases with the Early Hydrothermal SSC Stage and cross cuts stratiform mineralisation, indicating that it is a discrete, later, possibly remobilising phase of hypogene mineralisation.
5. The grade of hypogene ore is locally upgraded by the in-situ development of chalcocite from the Early Supergene Stage (Cc3).
6. Para-exotic, RAT-hosted supergene orebodies are primarily composed of malachite (Mal2) and pseudomalachite (Psm1) of the Late Supergene Stage.
7. Gangue mineral phases present at Mashitu South which were confirmed by petrography include (in approximate order of abundance): dolomite, quartz, clay minerals, chlorite, muscovite, apatite, biotite, magnesite, rutile, barite, monazite, zircon, halite, gypsum/anhydrite and celestine.
8. An evaporitic source of sulphur is suggested for the hypogene sulphides at Mashitu South, however it is recommended that a broader sulphur isotope study be conducted to investigate this hypothesis.

CHAPTER 5: GEOCHEMISTRY

STATEMENT: The work discussed in this chapter forms the basis for the development of the Gigler and Kinnaird (2017) paper published in Journal of Geochemical Exploration: 'Element mobility in the weathering environment and surface vectors to mineralisation—A case study from the Mashitu South Cu-Co deposit, Katanga, Democratic Republic of Congo' – see Reference List for full details. This paper has been included with this thesis as Appendix 11.

In addition to data and samples collected during fieldwork and logging, the author was also given access to the entire geological and geochemical assay database for the Mashitu South deposit. Various geochemical and statistical techniques were applied to the database in order to investigate mineralisation processes, giving a more comprehensive picture of the deposit than possible with just the data collected by this study.

5.1 Introduction – Aims and Objectives

The Comide S.P.R.L. database for Mashitu South is split into two parts, geological and geochemical assays. The geological database was created by Comide S.P.R.L. employees during diamond drill core logging. The geochemical assay database is compiled from assay data produced by an external company from selected intervals of core, sampled by Comide S.P.R.L. employees. The author combined the geological and geochemical databases, assigning geochemical sampling intervals to the logged geology, so as to be able to build up a picture of the geochemistry of different geological intervals on a deposit scale. This was done with the following objectives in mind:

1. To investigate geochemical variation by stratigraphy, lithology and depth.
2. To investigate whether any particular stratigraphies, lithologies or depth sections have a propensity for Cu-Co mineralisation.
3. To investigate geochemical alteration within the deposit, and whether any alteration type is particularly associated with mineralisation.
4. To identify geochemical associates to both hypogene and supergene Cu-Co mineralisation, other than Cu and Co.

5. To investigate the geochemical changes involved in the transition from hypogene to supergene ore.

These objectives were set in an effort to fulfil the overarching aim: to develop vectors to Cu-Co mineralisation similar to that observed at Mashitu South.

5.2 Methods

5.2.1 Study of the Whole Mashitu South Deposit: Combining the Databases

Before geochemical and statistical techniques could be applied to the whole deposit, the geological and geochemical databases had to be brought together into a combined database. The geology database from Comide was created by digital logging (Chimvinga, pers. comm., 2014). Each interval showing variation was described based on a number of attributes. However, only three of these attributes were used by the author to create the combined database: 'Lith1', 'Lith2, and 'Strat'; essentially, the lithological and stratigraphic interpretations of the employees who logged the deposit. The other attributes included in the digitised logs, including colour, mineral identification, alteration, weathering intensity, etc. were judged to be too subjective and inconsistent to base further analysis on. 'Lith1' and 'Lith2' were combined in a consistent manner to give an overall lithology for ease of analysis. For example, 'Lith1: Dolomite' and 'Lith2: Argillite' would be combined to give 'Lithology: Dolomitic Argillite'.

The geochemical database consists of sample intervals which were selected from the core by Comide geologists and then sent to an unknown ALS Global laboratory for assay using one or more of several methods. It should be noted that this sampling was not completely systematic and assays were not conducted on the entirety of the drill core. Instead, Comide sampling was focussed on core that was visibly mineralised, in the vicinity of visible mineralisation, or within stratigraphy which is usually mineralised such as the R.S.F. (Chimvinga, pers., comm., 2014; Robertson, pers. comm., 2014). Therefore, the results and interpretations in this chapter can be assumed to have a bias towards well mineralised areas. Of the techniques which were used to assay the samples, only the results from the

‘ME-ICP61’ and ‘OG62-ICP’ techniques were selected for inclusion into the combined database, because the majority of the samples in the geochemical database had been assayed with these techniques. These techniques both use four-acid digestion for solution preparation and Induced Coupled Plasma Atomic Emission Spectroscopy (ICP-AES) to analyse the sample, however the OG62-ICP technique is more suited for analysis of the targeted ore-elements (Cu and Co) and does not have so restrictive an upper limit of detection (ALS Global, 2016). The company and the exact procedure used to assay the samples is unknown to the author, but a brief description of the ME-ICP61 and ME-OG62 techniques is given by ALS Global and included in this thesis as Appendix 4. These techniques are assumed to be equivalent to the ones used by the assay company contracted by Comide S.P.R.L.. OG62-ICP assays for Cu and Co, together with ME-ICP61 assays for Ag, Al, As, Ba, Be, Bi, Ca, Cd, Fe, K, La, Mg, Mn, Mo, Na, Ni, P, Pb, S, Sc, Sr, Ti, U, V, W and Zn were available and were selected to be merged into the combined database, giving 28-element data for each sample. Each assay concentration was converted from % to parts per million (ppm) for continuity, where necessary. The ‘DEPTHFROM’ and ‘DEPTHTO’ attributes, being the upper and lower limits of depth-in-the-hole from which each sample was taken, were averaged to give a ‘Mid-point-depth’ attribute for each sample. Only samples which had data for the entire 28-element suite and depth measurements were included in the combined database, giving a total of 12,058 samples from almost 200 drill-holes.

Because the geological data was categorised by arbitrarily assigned, geologically controlled, irregular intervals, and the geochemical data was categorised by sampling intervals (always of ≤1m), the two datasets had to be processed to be combined. The mid-point-depth for each sample in the geochemical database was matched to a geological interval recorded in the geological database, in order to assign a stratigraphy and lithology to each sample. This was done by means of a series of data-matching-functions on Microsoft Excel. Unfortunately, because sampling for assays was not conducted by geological means, a single assay could theoretically contain several small geological intervals, or span the distance between two geological intervals. Therefore, the stratigraphy and lithology assigned to each sample can be considered an ‘average’ with a resolution to the data equal to the length of the sample, always ≤1m. In the combination of the geochemical and geological datasets a new ‘combined database’ was produced. This database contains 12,058 samples; each with the following 32 attributes (Figure 5.1):

HOLEID	W_ME-ICP61_ppm	As_ME-ICP61_ppm	Mn_ME-ICP61_ppm
DEPTH	Zn_ME-ICP61_ppm	Ba_ME-ICP61_ppm	Mo_ME-ICP61_ppm
Stratigraphy	Co_OG62-ICP_ppm	Be_ME-ICP61_ppm	Na_ME-ICP61_ppm
Lithology	Ca_ME-ICP61_ppm	Bi_ME-ICP61_ppm	P_ME-ICP61_ppm
Cu_OG62-ICP_ppm	Ni_ME-ICP61_ppm	Cd_ME-ICP61_ppm	Pb_ME-ICP61_ppm
Sr_ME-ICP61_ppm	Fe_ME-ICP61_ppm	K_ME-ICP61_ppm	S_ME-ICP61_ppm
Ti_ME-ICP61_ppm	Ag_ME-ICP61_ppm	La_ME-ICP61_ppm	Sc_ME-ICP61_ppm
V_ME-ICP61_ppm	Al_ME-ICP61_ppm	Mg_ME-ICP61_ppm	U_ME-ICP61_ppm

***Figure 5.1**: List of attributes assigned to each sample from the combined database.*

After creating the combined database, the geochemical data was 'cleaned' according to the detection limits for analyses provided by Comide S.P.R.L.. Assay values below the stated lower limit of detection were replaced with half the detection limit, in order to provide a non-zero value for statistical analyses. The detection limits are provided as Figure 5.2.

	Lower Limit of Detection (ppm)	Upper Limit of Detection (ppm)
Ag_ME-ICP61_ppm	0.5	100
Al_ME-ICP61_ppm	100	N/A
As_ME-ICP61_ppm	5	N/A
Ba_ME-ICP61_ppm	10	N/A
Be_ME-ICP61_ppm	0.5	N/A
Bi_ME-ICP61_ppm	2	N/A
Ca_ME-ICP61_ppm	100	N/A
Cd_ME-ICP61_ppm	0.5	N/A
Co_OG62-ICP_ppm	10	N/A
Cu_OG62-ICP_ppm	10	400000
Fe_ME-ICP61_ppm	100	N/A
K_ME-ICP61_ppm	100	N/A
La_ME-ICP61_ppm	10	N/A
Mg_ME-ICP61_ppm	100	N/A
Mn_ME-ICP61_ppm	5	100000
Mo_ME-ICP61_ppm	1	N/A
Na_ME-ICP61_ppm	100	N/A
Ni_ME-ICP61_ppm	1	10000
P_ME-ICP61_ppm	100	N/A
Pb_ME-ICP61_ppm	2	N/A
S_ME-ICP61_ppm	100	100000
Sc_ME-ICP61_ppm	1	N/A
Sr_ME-ICP61_ppm	1	N/A
Ti_ME-ICP61_ppm	100	N/A
U_ME-ICP61_ppm	10	N/A
V_ME-ICP61_ppm	2	N/A
W_ME-ICP61_ppm	10	N/A
Zn_ME-ICP61_ppm	2	N/A

***Figure 5.2**: Detection limits for the various assay techniques, provided by Comide S.P.R.L.*

5.2.2 Study of MSSD075, 080, 083 and MSSD140

In order to ground-truth and provide a tangible reference to the Comide geology database, holes MSSD075, 080, 083 and 140, which were logged and sampled by the author (see Chapter 3), were separated from the main database and similarly analysed. The 718 geochemical samples from these 4 holes were assigned stratigraphy and lithology attributes based on logging by the author, again using the mid-point from each sample giving them a resolution of ≤1m.

5.2.3 Data splitting

In the analysis of the Mashitu South deposit, the combined database was split by three attributes in order to comparatively study the deposit: stratigraphy, lithology and depth, using Microsoft Excel. Splitting the data by other attributes such as Cu and Co grades proved inconclusive. The new datasets were compared to each other using the techniques described below.

5.2.4 Univariate Statistics

The Mean, Standard Deviation, Variance and Skewness of each different element attribute within the main Mashitu South combined database were calculated, and frequency histograms were created using Microsoft Excel for certain elements.

5.2.5 Pearson's Correlation Matrices

To assess geochemical associations within various datasets, the Pearson product-moment correlation coefficient was calculated for each numerical attribute with every other numerical attribute, within every split dataset. Microsoft Excel was used to do this, but the coefficient is calculated by the following equation:

$$\rho_{X,Y} = \frac{\mathrm{cov}(X,Y)}{\sigma_X \sigma_Y}$$

Where '*ρ*' is the Pearson product-moment correlation coefficient, 'cov' is the covariance, 'σ' is the standard deviation, and X and Y represent the two datasets. An alternative expression for is *ρ* is 'R', which will be used in further description of the Pearson product-moment correlation coefficient.

This calculation would be done by Excel for each attribute calculated against every other attribute, producing a correlation matrix which would provide a quick and easy reference for possible geochemical associations. The R-values within the correlation matrix were colour coded using the 'conditional formatting' function of Excel: black for a correlation (R-value) =1 (universally the result of comparing the same dataset against itself within the correlation matrix); red for 1 > R ≥ 0.8; orange for 0.8 > R ≥ 0.6; yellow for 0.6 > R ≥ 0.4, white (no colour) for 0.4 > R > -0.4; light blue for -0.4 ≥ R > -0.6; dark blue for -0.6 ≥ R > -0.8; and indigo for -0.8 ≥ R ≥ -1. The values of significance used in the colour formatting were suggested by Kenyon (pers. comm., 2014) based on the type and size of the original combined database, although they are not an absolute indicator of presence (or lack) of a 'significant' correlation. The attributes within each dataset included in the correlation matrix were the assay values for Ag, Al, As, Ba, Be, Bi, Ca, Cd, Fe, K, La, Mg, Mn, Mo, Na, Ni, P, Pb, S, Sc, Sr, Ti, U, V, W and Zn, as well as the depth values (to assess the variation of each element with regard to depth). Figure 5.3 is an example of the output of part of a correlation matrix completed for one of the datasets:

	Cu	Sr	Ti	V	W	Zn	Co	Ca	Ni
Cu		-0.01679	-0.06216	0.17793	-0.0068	0.162387	0.342778	-0.0925	0.206457
Sr	-0.01679		-0.0307	-0.03977	-0.02981	-0.08746	-0.03315	0.44239	0.009369
Ti	-0.06216	-0.0307		0.398559	-0.05319	0.208216	-0.05514	-0.2292	0.045653
V	0.17793	-0.03977	0.398559		-0.02905	0.122379	0.270702	-0.31406	0.338282
W	-0.0068	-0.02981	-0.05319	-0.02905		0.037557	-0.00815	-0.05284	0.04094
Zn	0.162387	-0.08746	0.208216	0.122379	0.037557		0.067736	-0.24229	0.163219
Co	0.342778	-0.03315	-0.05514	0.270702	-0.00815	0.067736		-0.12369	0.473379
Ca	-0.0925	0.44239	-0.2292	-0.31406	-0.05284	-0.24229	-0.12369		-0.10599
Ni	0.206457	0.009369	0.045653	0.338282	0.04094	0.163219	0.473379	-0.10599	
Fe	0.100175	-0.19221	0.327156	0.242984	0.011298	0.314864	-0.03095	-0.43634	0.082452
Ag	0.009322	-0.00894	-0.01675	-0.01268	0.248942	-0.00017	-0.00565	-0.01396	0.299584
Al	-0.0013	-0.13382	0.799508	0.315841	-0.06304	0.311244	-0.08306	-0.37552	0.07415
As	0.157808	0.012195	0.095799	0.215544	0.00523	0.065023	0.137904	-0.01196	0.075246
Ba	-0.00401	0.369408	0.115309	0.084548	-0.01571	0.006774	0.031347	0.083613	0.09742
Be	0.266854	-0.18432	0.431759	0.323348	0.005157	0.454694	0.131993	-0.45563	0.203026

Figure 5.3*: Example of part of a correlation matrix completed for a geochemical dataset. The colour coding of cells is a result of the conditional formatting described above, it allows for a quick and simple assessment of strong positive (warm colours) and negative (cold colours) correlations. In this example we see that the strongest positive correlation is between Ti and Al, while Ca:Sr, Be:Ti, Be:Zn and Ni:Co also correlate well with each other. Strong negative correlations are observed between Ca:Fe and between Ca:Be. This example is from the whole 12,058 sample combined database.*

The Pearson coefficient was used primarily to highlight attributes which appeared to correlate. These correlations were investigated further by plotting the data for the two attributes against each other on a scatter plot (see Section 5.2.6) to see whether a linear or non-parametric relationship existed between them. Spearman's rank correlation coefficient was also considered as an indicator method for geochemical associations, as it is able to identify non-parametric relationships between datasets by comparing the 'rank' of each data-point in two datasets rather than the value. After use on certain datasets, however, it was found to return too many apparent 'false positives': indications of correlation which did not make sense geochemically and were not supported by the scatter plot for the two attributes. Therefore, Spearman's coefficient was not routinely calculated for each dataset. In cases where a non-parametric relationship was apparent from the scatter plot, the Pearson coefficient was found to identify this relationship adequately by providing a reasonably high R-value, even though the Spearman coefficient might have provided a higher R-value.

Multivariate statistical methods such as Principal Component Analysis were also rejected for routine usage, due to their inability to separate possible causation from correlation, which tended to cause false positive associations. Correlation matrices were found to be easier to interpret possible causation from analysing the various correlations calculated between each variable.

5.2.6 Bivariate Scatter Plots

After a correlation was identified using a Pearson correlation matrix, attributes with high positive or negative R-values would be plotted against each other on scatter plots to investigate the nature of the correlation. The scatter plot could show a linear or non-linear relationship between the variables, which might help in the interpretation of the nature of the association behind the correlation. An example of a scatter plot from the data is given as Figure 5.4.

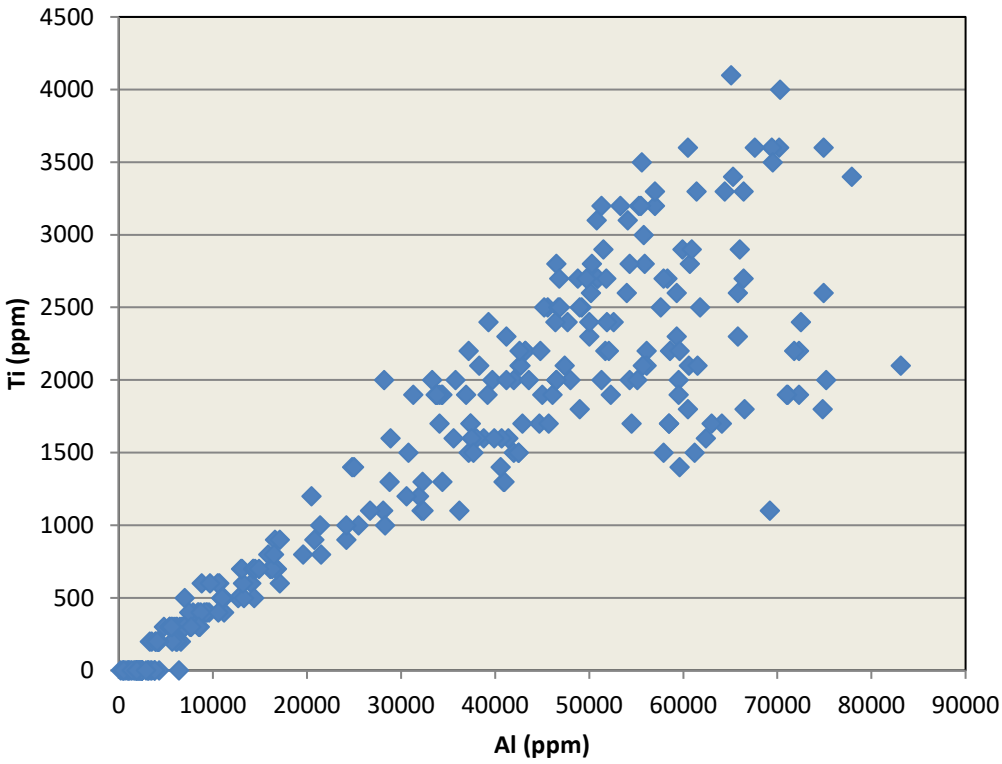

Figure 5.4*: Example of a scatter plot of two attributes created from one of the datasets. This particular example shows a strong positive correlation between titanium and aluminium within all the samples in the core of MSSD083. The R-value for these variables is 0.9096.*

5.2.7 Ternary Plots

The 'ACF' ternary diagram of Eskola (1915) was used in this study to trace metasomatic processes in the rocks of MSSD075, 080, 083 and 140. This approach is more typically used to trace metamorphism (and more rarely metasomatism: El Shazly and Al-Belushi, 2004) in basaltic rocks and its use in discriminating metasomatic processes in sedimentary rocks is not represented in literature sources; nonetheless it was found to be a useful tool by this study for this purpose. The 'AKF' adaptation of this technique was also employed to account for potassic alteration.

The ACF diagram is plotted using a formula which requires the molecular proportions of the oxides of several elements. These first had to first be calculated from the elemental concentration dataset of Al (ppm), Fe (ppm), Na (ppm) K (ppm), Ca (ppm), P (ppm), Mg (ppm) and Mn (ppm), by proportionally scaling up the elemental concentration to account for the oxygen in the oxide. The following atomic and molecular weights were used to do this (Figure 5.5), after the percentage concentration for each element was calculated by dividing the ppm concentration by 10,000:

CaO	Fe_2O_3	Al_2O_3	K_2O	MgO	MnO	Na_2O	P_2O_5
56	159.6	102	94.2	40.3	70.9	39	142

Ca	Fe	Al	K	Mg	Mn	Na	P	O
40	55.8	30	39.1	24.3	54.9	23	31	16

Figure 5.5*: Atomic and molecular weights of the components used to calculate the A, C and F variables, to one decimal point. Atomic weights from Winter (2016).*

The molecular weight was divided by the relevant atomic weight to give the inverse of the weight proportion of the relevant cation in the relevant molecule. This inverse could then be used as a factor to multiply the atomic percentage of the cation, giving the weight percentage of the molecule in the sample in terms of [Al_2O_3], [Fe_2O_3], [Na_2O], [K_2O], [CaO], [P_2O_5], [FeO], [MgO], [MnO], where the bracket symbols indicate the concentrations of the molecular proportions of the oxides.

A sample data point on the ACF graph is made up of three variables, plotted on a triangular diagram. These variables are A, C and F, which are calculated by the following formulae:

$A = [Al_2O_3 + Fe_2O_3] – [Na_2O + K_2O]$
$C = [CaO] - 3.33 [P_2O_5]$
$F = [FeO + MgO + MnO]$

Once these variables have been calculated, they must then be recalculated as percentages to plot them on a triangular diagram. To do this all the other components of the rock, including, SiO_2, are ignored, and the A, C and F components are assumed to represent 100% of the sample. The sum A + C + F is calculated, and each respective value is divided by this sum total and multiplied by 100 to get a percentage proportion between 0 and 100.

The entire process was repeated to give every sample from MSSD075, 080 and 083 an A, C and F value to allow them to be plotted on ternary diagrams. Their location on the diagram tells us about the original sedimentary rock: samples with a higher C value are generally more calcareous, samples with a high A value are usually argillic-siliciclastic and a high F value is typical of basic rocks. A spread of values trending towards a certain point or region on the diagram is often indicative of progressive metasomatism. Figure 5.6 shows fields where different rock types typically plot.

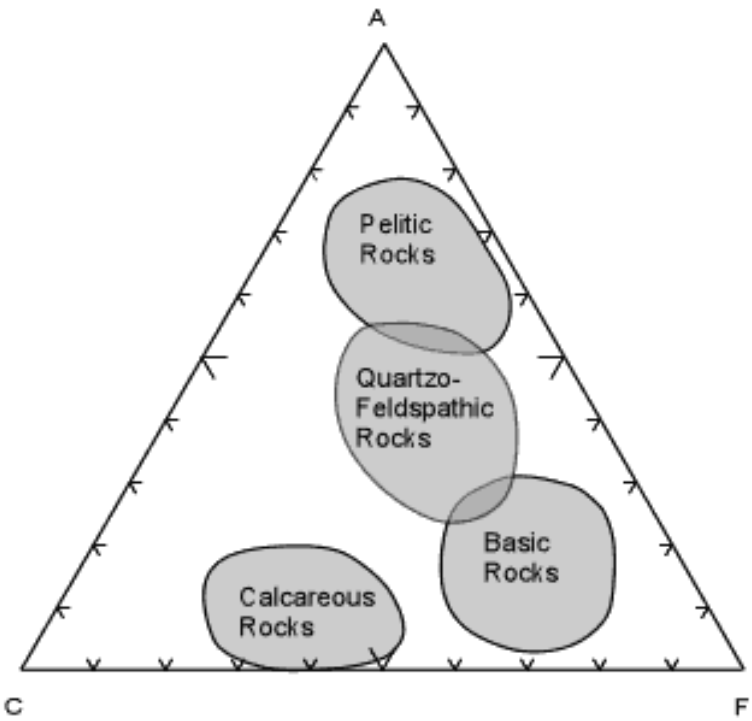

***Figure 5.6**: Triangular ACF diagram showing fields where different rock types typically plot, after Eskola (1915) and taken from Nelson (2011).*

After calculation of the A, C and F values, each sample was plotted using the 'TRI-PLOT' spreadsheet for Excel (Graham and Midgley, 2000). The results were compared to the above diagram (Figure 5.6), then examined based on variation of A, C and F and interpreted.

AKF diagrams are another ternary diagram method of plotting geochemical data, but with a focus on examining the variation of potassium-bearing minerals in each rock sample. The AKF diagram is composed of three components: A, K and F (A and F are not the same components as calculated for the ACF diagram). These components are calculated from the proportional weight of [Al_2O_3], [Fe_2O_3], [Na_2O], [K_2O], [CaO], [P_2O_5], [FeO], [MgO] and [MnO] which are calculated in the same way as for the ACF diagram. However, the formula for calculating A, K and F is different, as follows:

$A = [Al_2O_3 + Fe_2O_3] - [Na_2O + K_2O + CaO]$

$K = [K_2O]$

$F = [FeO + MgO + MnO]$

These results were then converted into percentages, again ignoring the other components of the rock, and plotted onto a ternary diagram using TRI-PLOT, in the same manner as for the ACF diagram. Variations in the 'K' attribute on the AKF diagram are often indicative of potassic alteration.

5.2.8 Data Normalisation

Data normalisation was conceived as a way of assessing the relative concentration of a particular element within a particular dataset, and whether an element's concentration in a particular sample or a dataset is anomalously high or low for the database. Rather than normalising the samples/datasets to chondrite, continental, or primitive mantle values, which the samples would be far removed from anyway, it was decided to normalise them to the Average Concentration of Elements at Mashitu South. ACEMS is a set of normalising factors for each of the 28 element assays which is calculated by taking the mean value for each element from all 12,058 samples in the Mashitu South combined database.

Normalising to ACEMS is a good technique to compare split datasets. To normalise to ACEMS, the mean value for each element in a particular dataset (a particular lithology, stratigraphic unit or depth interval) is calculated and divided by the ACEMS normalising factor. The results are plotted on a spider line diagram with an exponential y-axis consisting of the average values normalised to ACEMS, and the different elements on the x-axis. In a dataset where the composition is relatively close to 'normal' for the Mashitu South deposit, the line will plot as flat and close to the normalising value of '1'. Where certain elements are particularly enriched or depleted relative to normal, these elements will plot above or below the '1' value.

For the purpose of presenting geochemical results relative to ACEMS, an 'anomalously high' mean value for element concentration in a dataset is regarded as any ACEMS-normalised-value which is ≥2 (i.e. twice the average concentration of elements at Mashitu South) and 'anomalously low' values are regarded as ACEMS-normalised-values ≤0.5 (i.e. half the average concentration of elements at Mashitu South). Furthermore, a convention of presenting ACEMS-normalised results was established where each ACEMS-normalised elemental dataset is presented as a row (the elements forming a column). The normalised values are then colour coded such that ACEMS-normalised values ≥10 are

orange; ≥2, <10 are yellow; >0.5, <2 are green; ≤0.5, > 0.1 are blue, and ≤0.1 are purple (Figure 5.7). This is particularly useful for looking at geological datasets where an element is anomalously enriched or depleted, as would be expected for Cu and Co in zones of high grade Cu-Co mineralisation. The ACEMS values are given as Figure 5.8 and an example of normalising by them is given in Figure 5.9.

	Mg	Al	Ca	Fe	Cu	K	Co	Ti	S
(CMN) Sandstone (and)	0.81	0.16	0.39	0.59	0.67	0.02	0.61	0.15	0.10
(CMN) Shale (and)	1.44	0.67	2.32	0.67	0.61	0.95	0.36	0.72	0.94
(CMN) Silicic Rock (and)	0.92	0.15	2.26	0.39	0.35	0.05	0.37	0.12	0.53
(SD2d) Dolomite	0.22	1.79	0.32	0.89	4.79	6.79	0.64	2.40	1.71
(SD2d) Shale and Dolomite	0.58	1.72	0.78	1.11	4.75	5.25	3.69	1.97	12.44
(SD2d) Shale	0.27	1.89	0.41	1.55	3.16	5.81	1.32	2.21	3.02

Figure 5.7*: Example of multiple datasets compared by their ACEMS-normalised-mean-values. Shown here are 6 lithostratigraphically split datasets (left, in rows) and the respective elements by which they are compared (top, in columns). Anomalously high values are in yellow and orange, close-to-average values are in green while anomalously low values are in blue and purple (refer to text).*

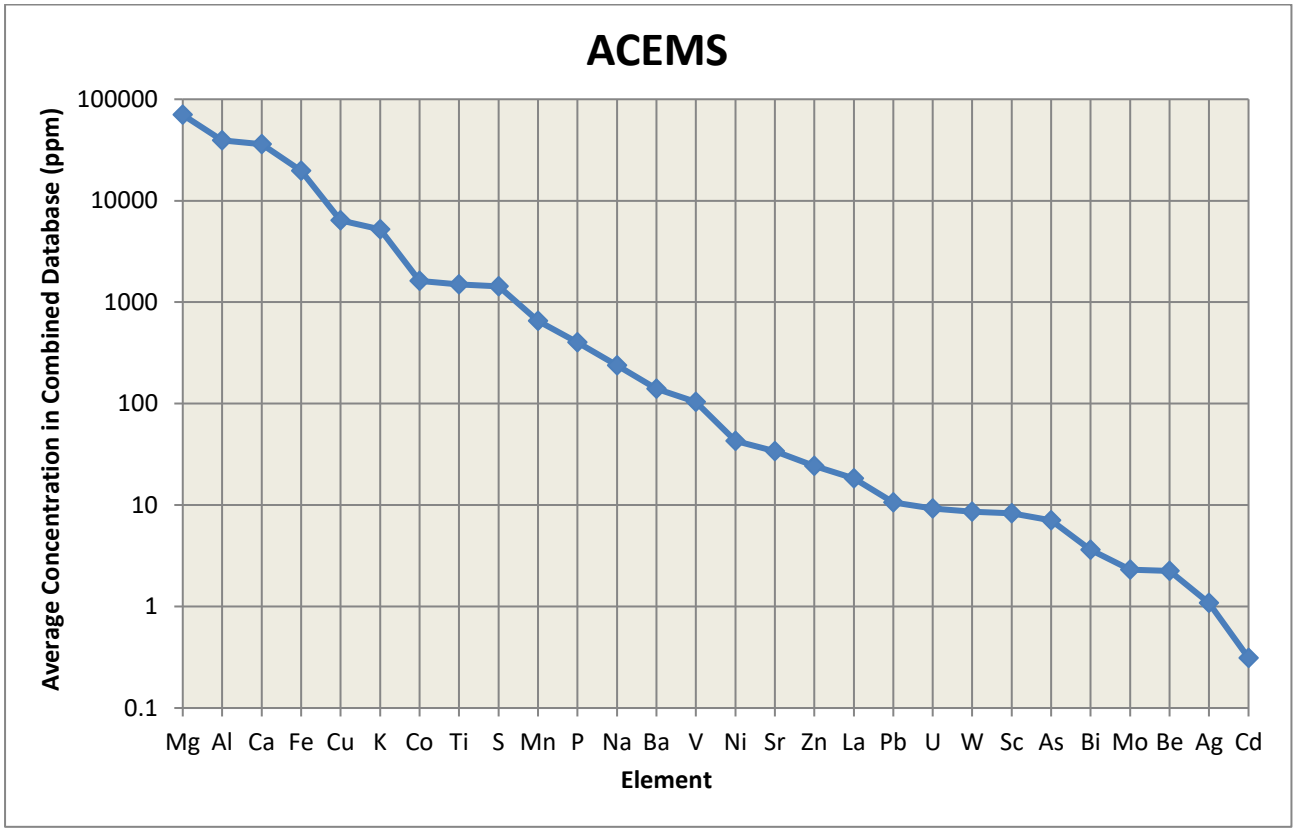

	Mg	Al	Ca	Fe	Cu	K	Co
Mean Value (ACEMS)	70189.53	39312.94	36095.2	19676.71	6388.138	5204.338	1623.426

	Ti	S	Mn	P	Na	Ba	V
Mean Value (ACEMS)	1498.93	1429.813	651.9631	401.6157	238.2931	139.638	103.6417

	Ni	Sr	Zn	La	Pb	U	W
Mean Value (ACEMS)	42.79929	34.0756	24.31384	18.35199	10.58563	9.250228	8.610766

	Sc	As	Bi	Mo	Be	Ag	Cd
Mean Value (ACEMS)	8.305839	7.09028	3.633906	2.307747	2.245957	1.085875	0.311869

Figure 5.8*: Average Concentration of Elements at Mashitu South (ACEMS) normalising values calculated by finding the mean concentration of each element within the entire 12,058 assayed sample combined database.*

Split Dataset: Lithology: Shale and Massive Sulphide (N=3)

A.	**Mg**	**Al**	**Ca**	**Fe**	**Cu**	**K**	**Co**	**Ti**	**S**	**Mn**	**P**	**Na**	**Ba**	**V**	**Ni**	**Sr**	**Zn**	**La**	**Pb**	**U**	**W**	**Sc**	**As**	**Bi**	**Mo**	**Be**	**Ag**	**Cd**
ACEMS (ppm)	**70189.5**	**39312.9**	**36095.2**	**19676.7**	**6388.1**	**5204.3**	**1623.4**	**1498.9**	**1429.8**	**652.0**	**401.6**	**238.3**	**139.6**	**103.6**	**42.8**	**34.1**	**24.3**	**18.4**	**10.6**	**9.3**	**8.6**	**8.3**	**7.1**	**3.6**	**2.3**	**2.2**	**1.1**	**0.3**

B.	Mg	Al	Ca	Fe	Cu	K	Co	Ti	S	Mn	P	Na	Ba	V	Ni	Sr	Zn	La	Pb	U	W	Sc	As	Bi	Mo	Be	Ag	Cd
Mean (ppm)	58866.7	51833.3	77566.7	35833.3	42733.3	23000.0	1593.3	2366.7	29766.7	294.0	453.3	400.0	176.7	213.3	19.5	36.3	222.7	20.0	20.7	5.0	5.0	12.0	11.7	4.3	6.2	1.5	0.4	1.1

C.	Mg	Al	Ca	Fe	Cu	K	Co	Ti	S	Mn	P	Na	Ba	V	Ni	Sr	Zn	La	Pb	U	W	Sc	As	Bi	Mo	Be	Ag	Cd
Norm.	0.84	1.32	2.15	1.82	6.69	4.42	0.98	1.58	20.82	0.45	1.13	1.68	1.27	2.06	0.46	1.07	9.16	1.09	1.95	0.54	0.58	1.44	1.65	1.19	2.67	0.68	0.34	3.53

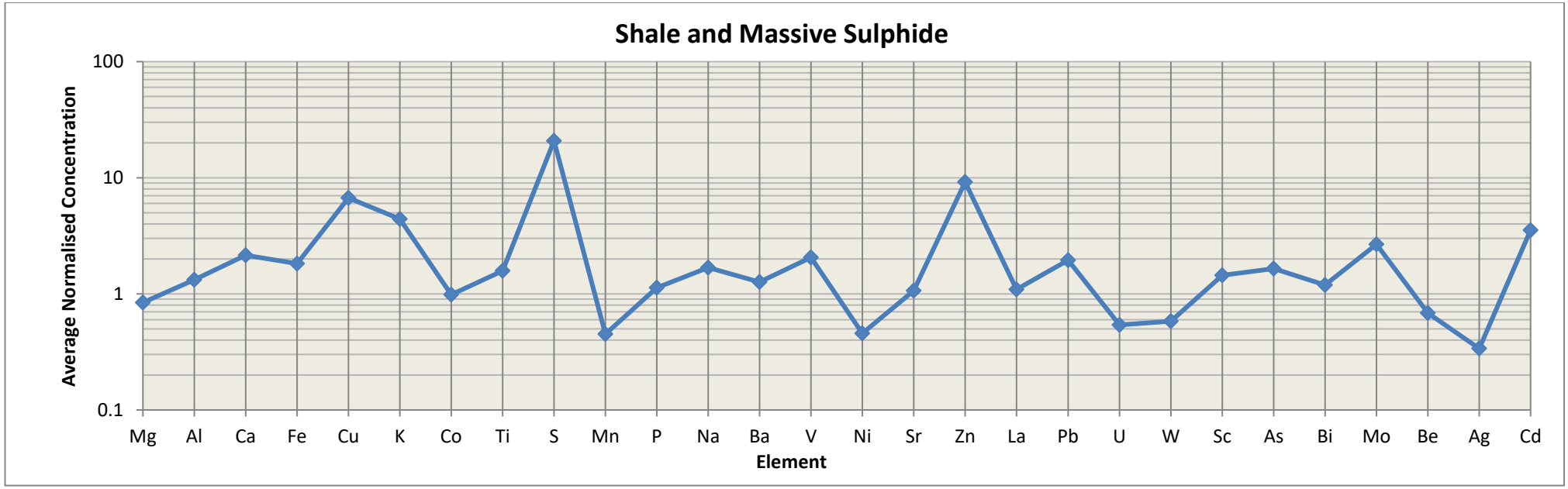

***Figure 5.9**: Example of the application of the normalising-to-ACEMS process. The split dataset comprising the Lithology of 'Shale and Massive Sulphide' is used, a small, 2m interval consisting of 3 samples from hole MSSD182. **Table A**: ACEMS normalising values. **Table B**: Mean concentrations of elements within the dataset. **Table C**: Normalised-to-ACEMS values (Norm.), which are calculated by dividing the values in **B** by the values in **A** and plotted on the multi-element plot below. Values in Table C are colour coded; Orange: Norm. ≥ 10; Yellow: 10 > Norm. ≥ 2; Green: 2 > Norm. ≥ 0.5; Blue: 0.5 > Norm. It is evident by Table C and the spider plot that S, Ca, Cu, K, V, Zn, Mo and Cd are anomalously high in 'Shale and Massive Sulphide', while Mn, Ni and Ag are anomalously low.*

5.2.9 Depth Profiles

Within the holes logged by the author (MSSD075, 080, 083 and 140), the depth profiles of various elements, mostly related to mineralisation, were plotted by creating a line chart of depth vs. concentration of element in Microsoft Excel. The logged lithology or stratigraphy could also be added to this depth profile to show the relationship of different elements with these factors within individual holes. This technique is a visual approach to assessing geochemical associations with lithology, stratigraphy, depth, and other elements, and allows for a spatial, qualitative analysis of relationships that may have been picked up statistically, quantitatively and non-spatially by other techniques.

5.2.10 Other techniques

Many other geochemical and statistical techniques were used to investigate the relationships between elements and lithology, stratigraphy, depth, and other elements. The successful techniques will be detailed below in the 5.3: Results and the 5.4: Discussion sections.

5.3 Results

5.3.1 Overall Geology and Geochemistry of the Mashitu South Deposit

5.3.1.1 Lithology

All of the logged samples within Mashitu South were separated by the attribute of lithology and the results are presented as Figure 5.10. Each lithology name (e.g. sandstone and clay) corresponds to the primary logged lithology code, followed by, if applicable, an ‘and’ and then the secondary logged lithology code. As is apparent, dolomite and shale are by far the most abundant lithologies logged at the deposit, with significant proportions of sandstone, silicic rock, mudstone, clay and siltstone.

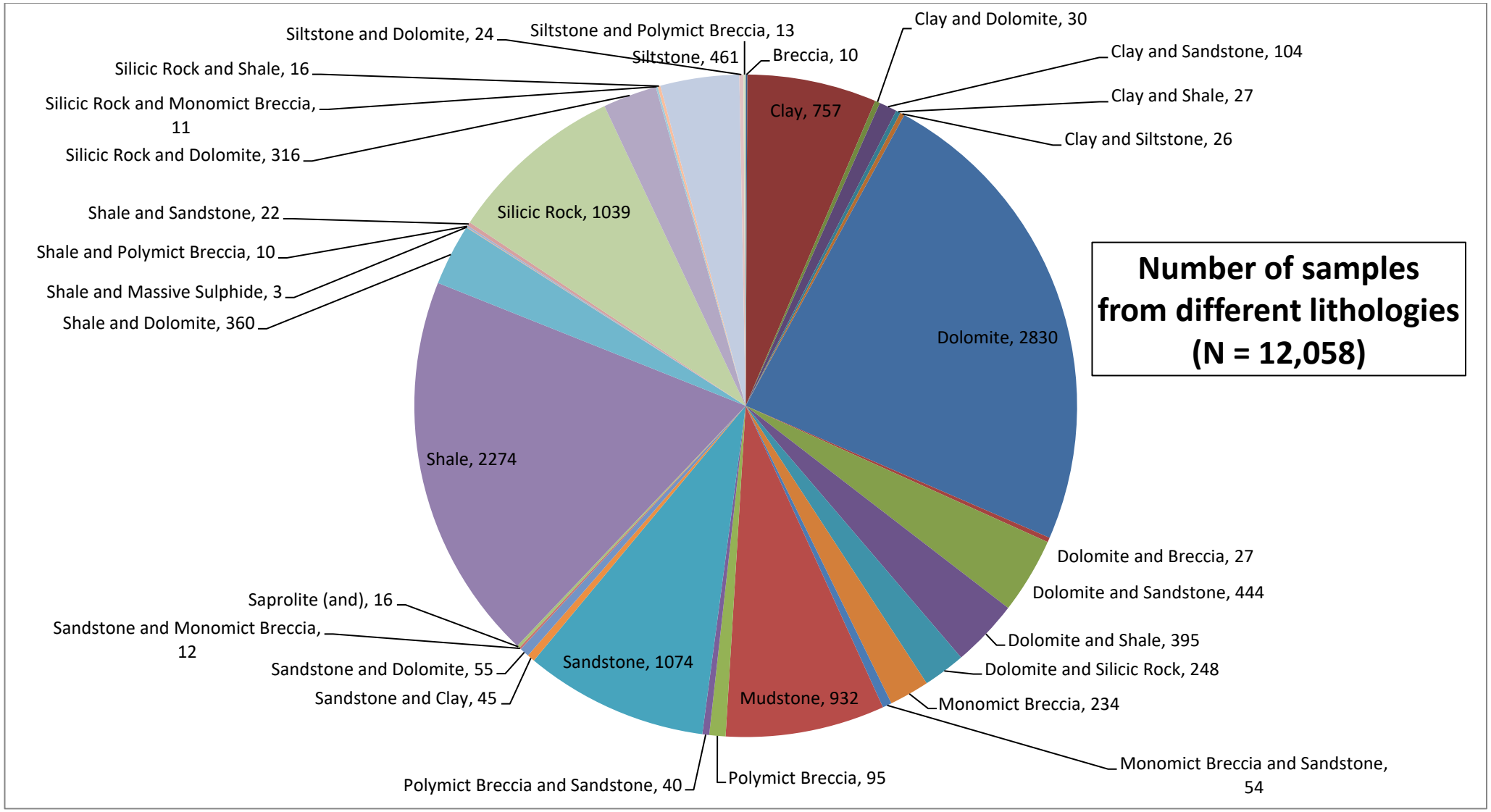

***Figure 5.10**: Pie chart of the various different logged lithologies corresponding to geochemical samples at the Mashitu South deposit, out of a total of 12,058 samples. The number next to each lithology name is the amount of samples which were logged as this lithology.*

5.3.1.2 Stratigraphy

Figure 5.11 is a chart of the number of different samples which corresponded to each stratigraphic unit logged. The units consist of (in order of abundance within the samples): the R.A.T. Rouge, the R.S.C., the S.D.B., the C.M.N., the R.S.F., the S.D.S., the R.A.T. Gris, the D.Strat, the S.D.2d., and 'Undifferentiated Breccia'.

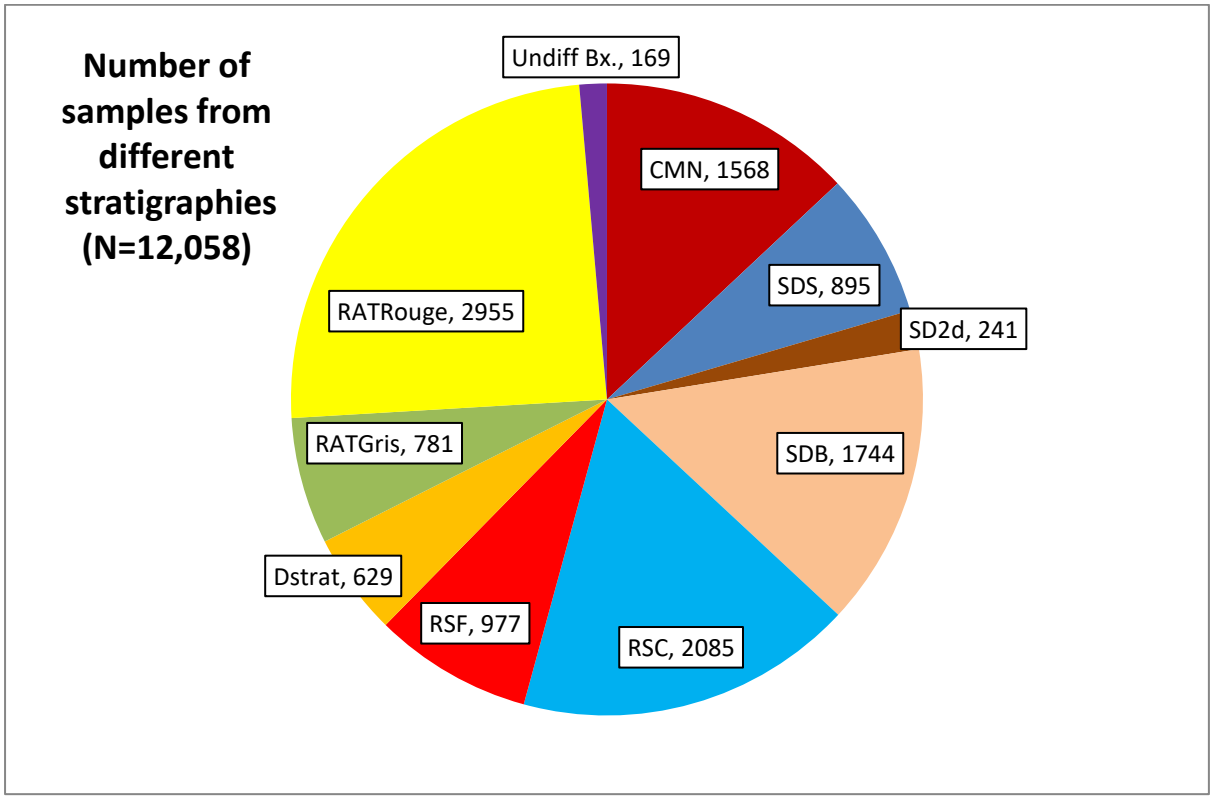

***Figure 5.11**: Pie chart of the various different logged stratigraphies corresponding to geochemical samples at the Mashitu South deposit, out of a total of 12,058 samples. The number next to each stratigraphy name is the amount of samples which were logged as this stratigraphy.*

It should be noted that these numbers of samples for each deposit do not necessarily represent the total abundance of these stratigraphic (or lithological) units over the deposit, because of the bias in Comide sampling towards visible and stratigraphically expected mineralisation (Chimvinga, pers. comm., 2014; Robertson, pers., comm., 2014). The C.M.N. and S.D., for example, are much thicker than the R.S.C., R.S.F. and D.Strat combined, but together the two groups are represented by a similar number of samples each.

5.3.1.3 Geochemistry

The average geochemistry of the Mashitu South deposit, described in Section 5.2.7, is repeated in this section for ease of reference. A line graph showing the composition of ACEMS is given again as Figure 5.12.

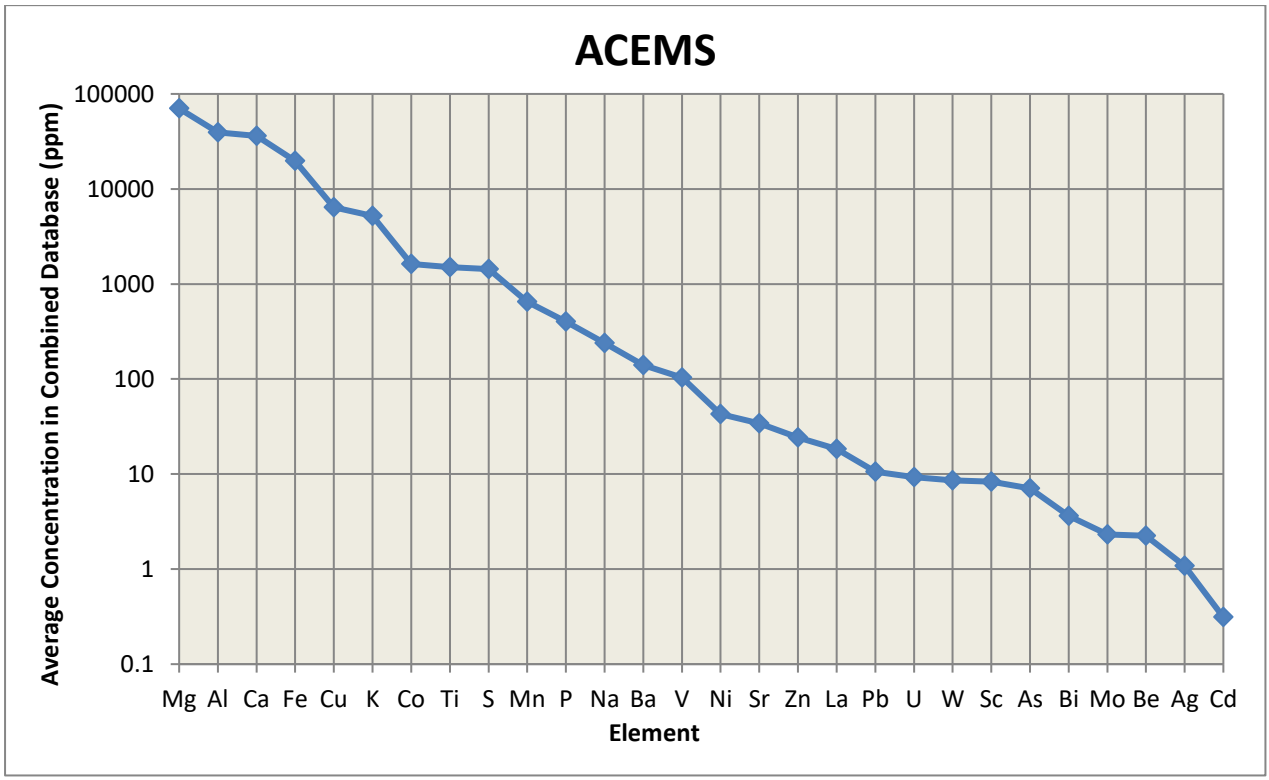

***Figure 5.12**: Logarithmic line chart showing the Average Concentration of Elements at Mashitu South (ACEMS) calculated by taking the mean concentration of each element in all 12,058 geochemical samples from the deposit.*

It should be noted that because only 28 elements were analysed, other elements which are not in the analysis make a significant contribution to samples. In the elemental assays, the total concentration of all the analysed elements did not add up to more than 45% of the rock in any of the samples, with most sample analyses adding up to 10-25% of the total. The remaining mass of the samples is probably mostly accounted for by silicon, oxygen, and perhaps a significant amount of carbon (in the carbonates).

Magnesium, likely hosted by dolomitic rocks and rocks exhibiting magnesian alteration, is the most concentrated element out of the 28 analysed, on average, throughout the deposit. Aluminium, a major component of siliciclastic rocks, comes behind

this, followed by calcium, another significant component of dolomite and calcareous rocks. Iron, probably hosted in ferric silicates, haematite and sulphides, is also common. The frequency distributions of each of these rock forming elements reveals them to have a low skewness, and in some cases, what appears to be a multimodal distribution (Figure 5.13).

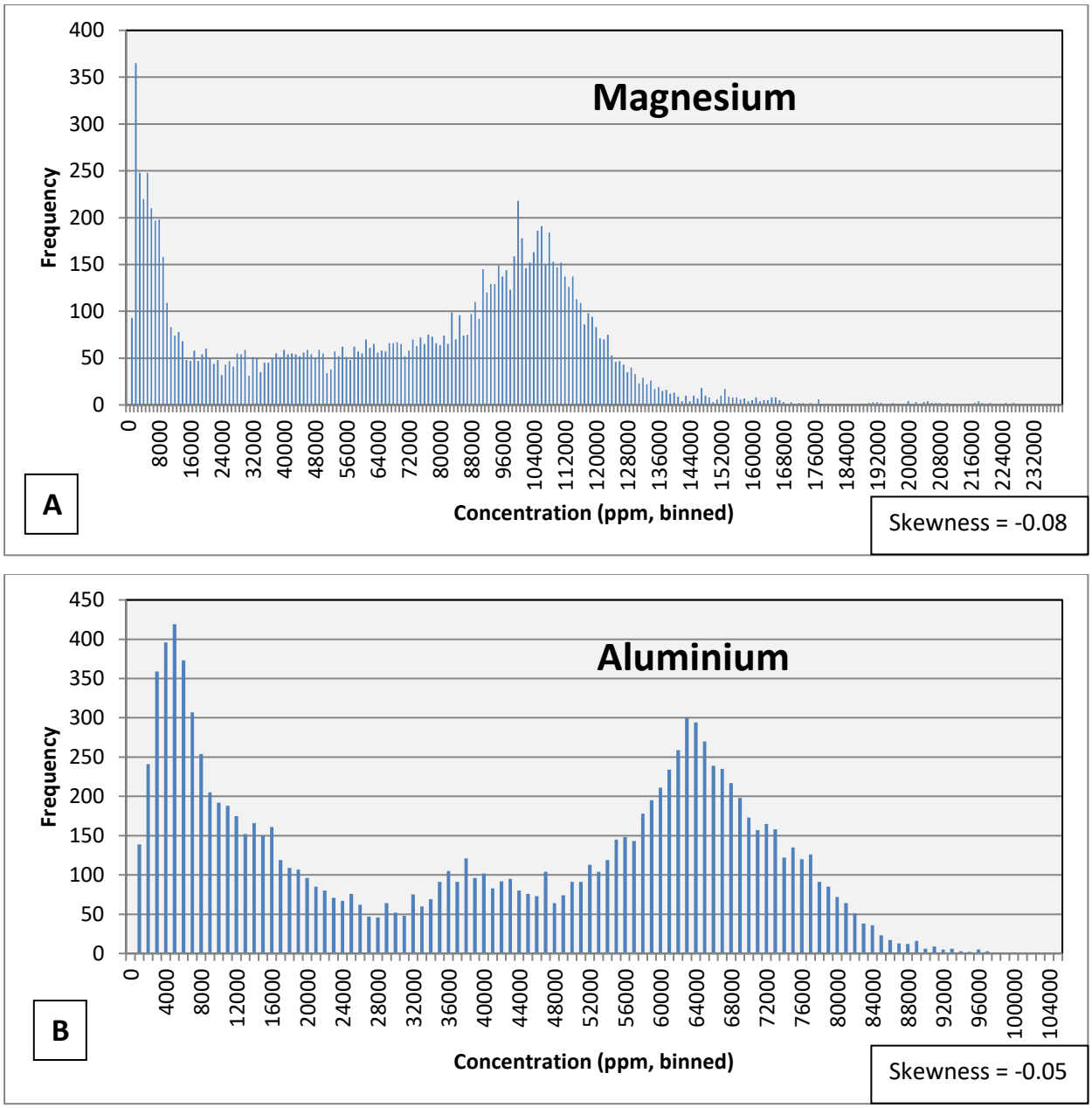

***Figure 5.13**: Frequency distributions for **A**: Magnesium and **B**: Aluminium, the two most abundant elements out of the 28 analysed in the Mashitu South samples. Low skewness in both cases indicates that these are rock-forming elements at the deposit, but both histograms suggest a multi-modal frequency distribution (bimodal for Mg, trimodal for Al) suggesting that both contain multiple populations, some close-to-normally distributed and some with a skewed distribution.*

Multi-modal distributions such as these are indicative of multiple populations of input of these elements. It could also represent different populations of rock samples, each population of which (i.e. siliciclastic vs. argillaceous vs. calcareous) tend to contain a particular concentration of each element.

The two ore metals, Cu and Co, have average concentrations, respectively, of 0.64% and 0.16%, which is relatively high, not even considering a more condensed orebody (or orebodies). However, due to logistical reasons, mining in Katanga is usually only economic at grades upwards of 1% Cu and 0.2% Co (Chimvinga, pers. comm., 2014). Therefore, the orebody at Mashitu South, which is stated as containing 1.7% Cu and 0.2% Co (Yeldar, 2012), must be more condensed than the sum of the sampled drill-core. Looking at the frequency distributions histograms for Cu and Co (Figure 5.14), it can be seen that they are highly skewed, which is typical for ore elements.

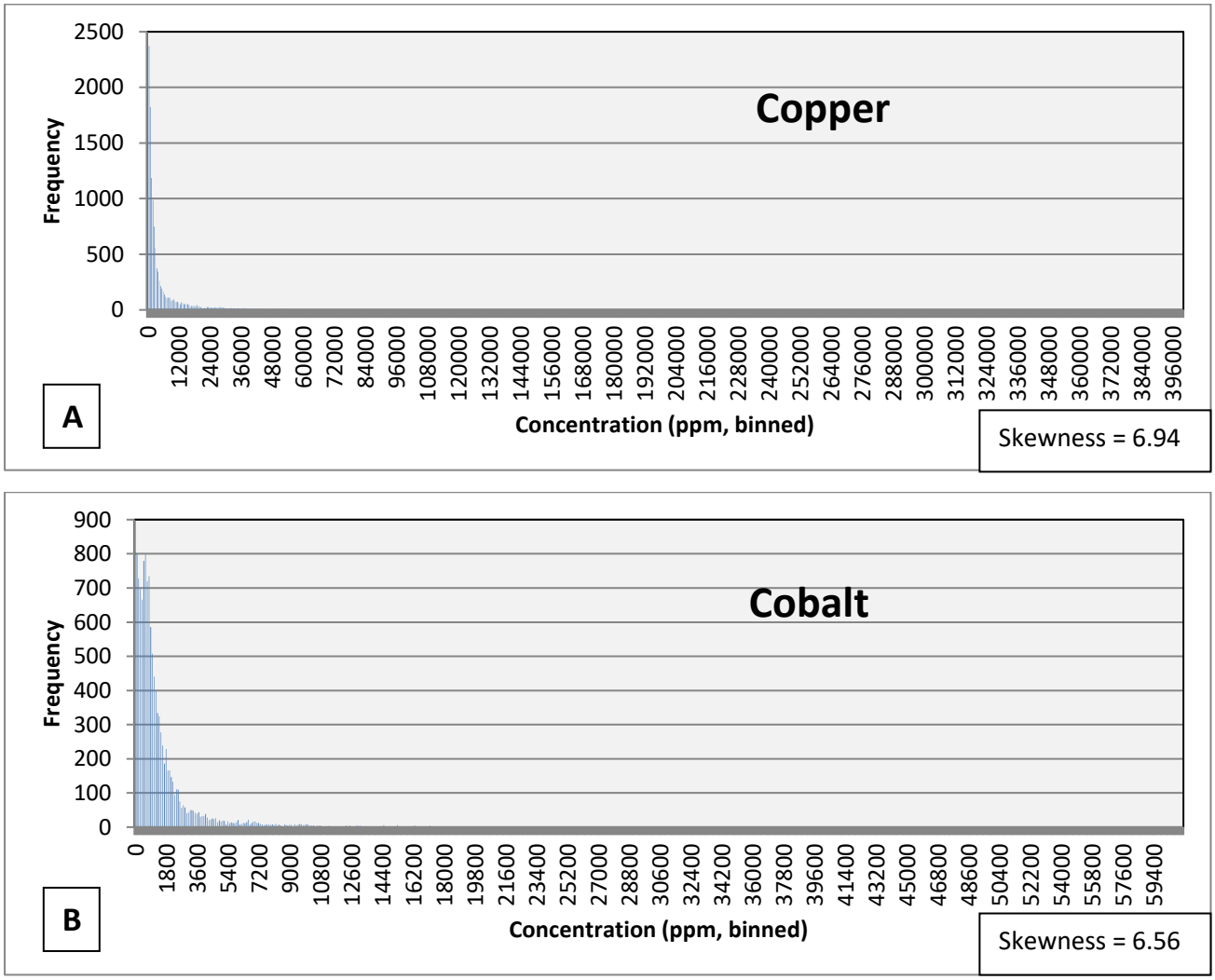

***Figure 5.14**: Frequency distributions for **A**: Copper and **B**: Cobalt. Both distributions appear unimodal and highly positively skewed, typical of ore elements.*

Assessing a chart of skewness for all the elements analysed at Mashitu South (Figure 5.15), there appear to be 6 different population groups of skewness based on the gradient of the line graph connecting them when ranked: **1:** Mg, Al, Sc, Ti, Ca, Fe, K and Be. **2:** V, Bi, S, P, Co, Zn, Cd, Cu and La. **3**: Mn, Ba and Ni. **4:** Sr, W, Na, As and Mo. **5:** U and Pb and **6**: Ag. Interestingly, many of the elements which fall within the same grouping of skewness appear related in some way. Elements which are associated with siliciclastic rocks: Al, Sc, Ti, Be, K and Fe, are found together in group 1, together with the rock forming elements Mg and Ca. Group 2 contains Cu and Co, the ore elements, together with S, which would be present in Cu-Co sulphides. It also contains several other chalcophile elements which one might expect to be associated with Cu mineralisation. Groups 3 and 4 consist of elements which one would expect to be hydrothermally mobile, and group 5 consists only of U and Pb, which could be radiogenically associated. The high skewness of Ag, the only element in group 6, would suggest that silver occurrences at Mashitu South are isolated and highly anomalous.

	Skewness
Mg	-0.08093
Al	-0.05175
Sc	0.511092
Ti	0.905667
Ca	1.070474
Fe	1.415624
K	2.023738
Be	2.082616
V	5.140019
Bi	5.443536
S	5.85274
P	6.376573
Co	6.5577
Zn	6.714221
Cd	6.859734
Cu	6.943531
La	7.667642
Mn	11.11894
Ba	11.67647
Ni	12.98556
Sr	19.67724
W	23.09276
Na	26.52489
As	29.79701
Mo	33.6256
U	48.01876
Pb	51.2495
Ag	107.2155

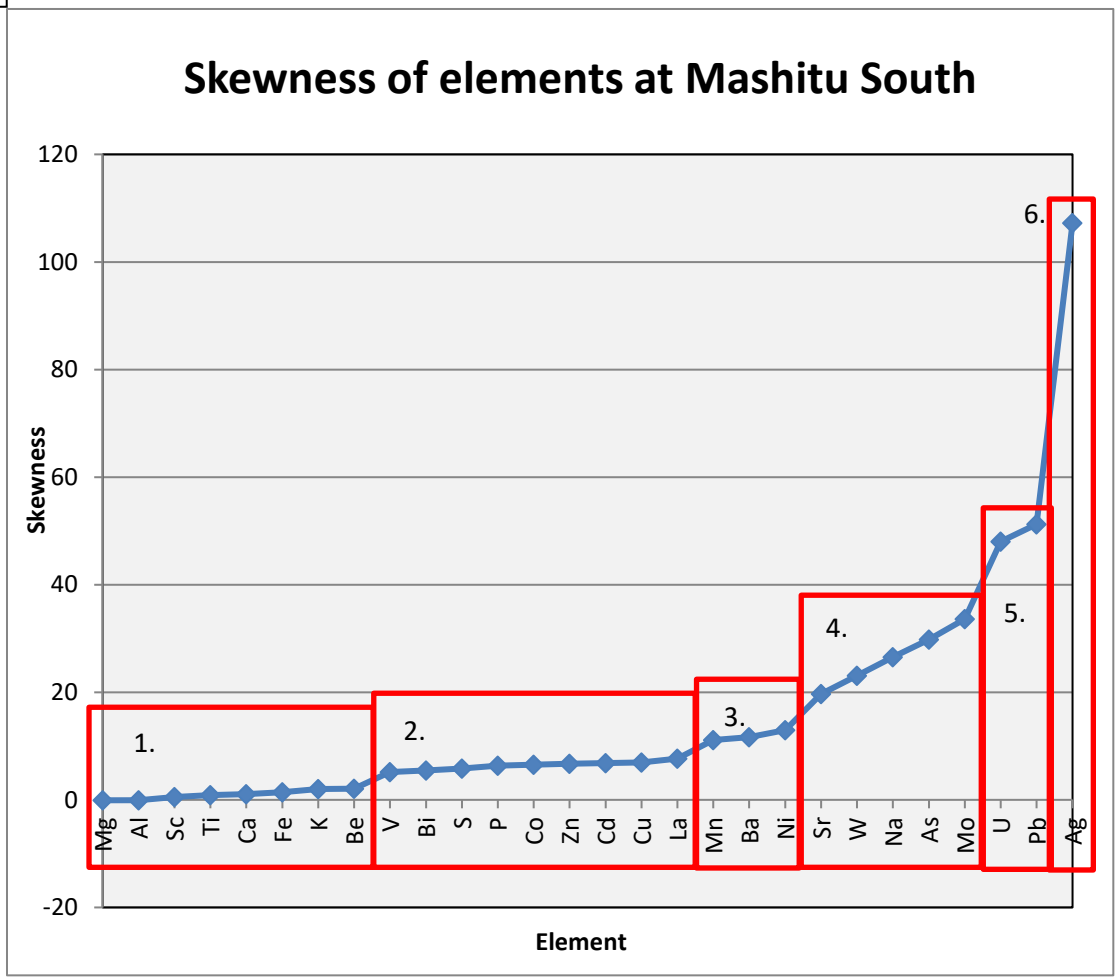

***Figure 5.15**: Ranked skewness of the frequency distributions of elements analysed at Mashitu South.*

The skewness groupings of different elements within the whole combined database begin to suggest geochemical associations. These associations were explored further using other techniques.

Analysis of the element correlation matrix for the total combined dataset (Appendix 5) reveals a number of interesting correlations. First, the correlation between various different elements and depth (Figure 5.16) was examined. A high positive correlation represents an affinity for depth, and a high negative correlation represents an affinity for the surface. A high affinity for depth may represent enhanced mobility in the surface environment (causing leaching) or it may represent an intersection of some lithology in which the element is concentrated only found at depth within the deposit.

Element	R-value correlation with Depth
Fe	-0.2630
Sc	-0.1689
Be	-0.1441
Mn	-0.1423
Al	-0.1326
La	-0.1119
Zn	-0.0829
Bi	-0.0617
V	-0.0502
W	-0.0489
Ti	-0.0119
Pb	-0.0085
Ag	-0.0082
Cd	-0.0023
Mo	-0.0008
Co	0.0143
Cu	0.0284
Na	0.0310
As	0.0491
P	0.0913
U	0.0975
Ni	0.1425
K	0.1513
Ba	0.1568
Mg	0.2217
Sr	0.2842
S	0.3939
Ca	0.5511

Figure 5.16*: Pearson correlations of elements with depth at Mashitu South.*

As can be seen, Ca, S, Sr, Mg and Ba have very high positive correlations with depth, suggesting that they have an affinity for depth. By contrast, Fe, Sc, Be, Mn and Al have high negative correlations with depth, suggesting that they have an affinity for the surface environment.

Interestingly, it is observed that Cu has a slightly higher affinity for/correlation with depth than Co. A scatter graph of Cu and Co against depth shows that there appears to be a zone of enrichment for both metals at a depth between about 150-250m. Both metals have a near-surface zone of enrichment, but this zone appears to be higher for Co (5-30m) than for Cu (30-50m), perhaps accounting in part for the greater affinity for/correlation with depth displayed by Cu (see Figure 5.17).

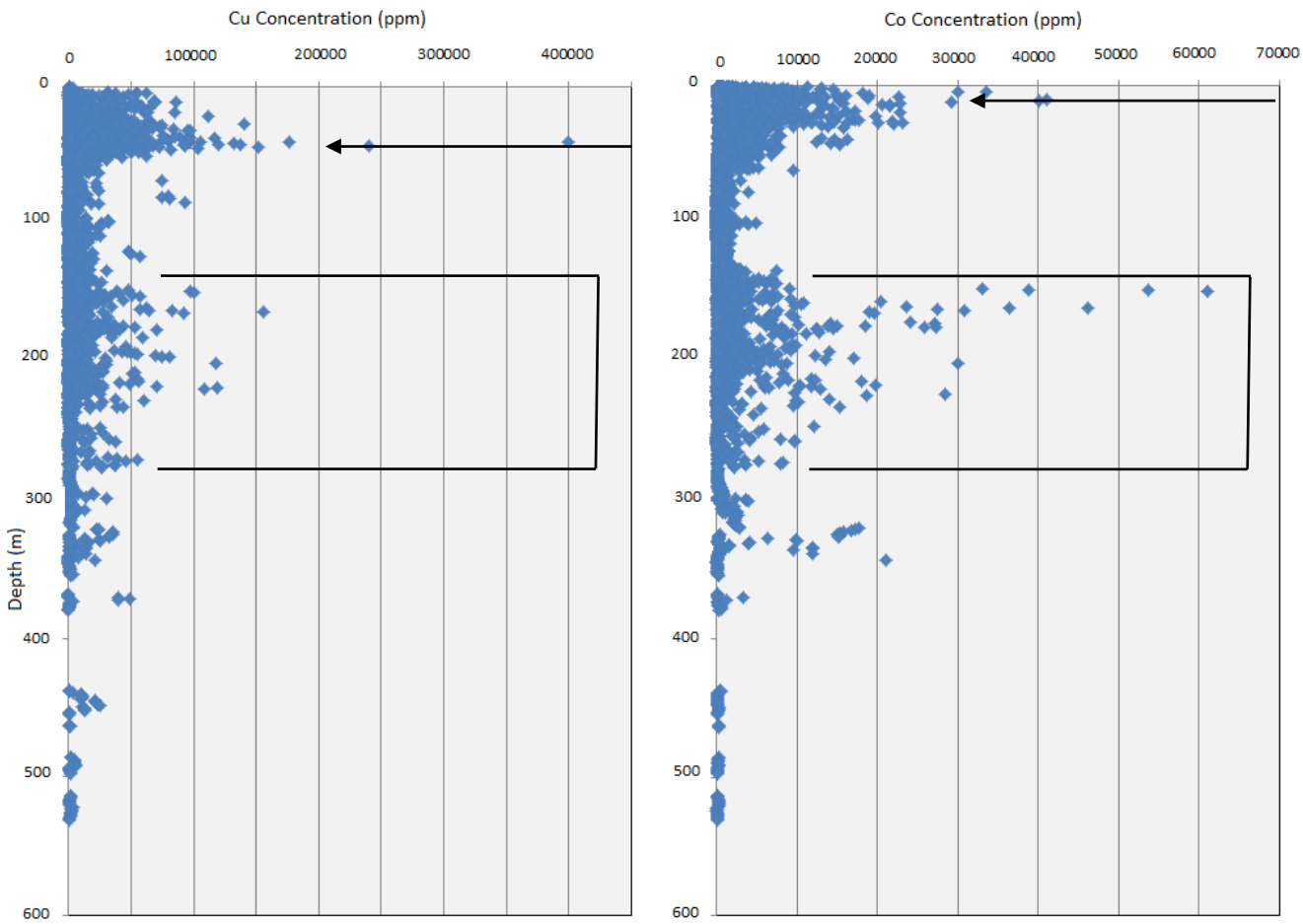

Figure 5.17*: Scatter plot of depth vs. element concentration for Cu and Co in the samples from Mashitu South. There are two zones of enrichment, one at depth (demarcated by brackets) and one near-surface (indicated by arrows). Note that the near-surface zone of enrichment is higher for Co than for Cu.*

This section will briefly describe the correlation of elements with each other. Looking at Appendix 5, the following element groupings appear to have high correlations (R ≥ 0.4) with each other across the combined database:

1. Ca, Mg, Sr
2. Ti, Al, Sc, Fe, K, Be
3. Be, P, Zn
4. Co, Ni

By contrast, strong negative correlations (R ≤ 0.4) are seen between Ca and Fe, Be and Sc. Considering the ore elements Cu and Co, we see that Co correlates fairly strongly with Ni (R=0.47). Cu does not appear to have any correlations above (R = 0.4) with elements in the combined database. If Cu and Co correlations are ranked, however (Figure 5.18), some possible associations are observed. There appears to be a grouping of elements which correlate positively with Cu and Co including Ni, Bi, V, S, As, Zn, P and Be.

Element	R-value with Cu
Cu	
Co	0.343
Bi	0.332
Be	0.267
P	0.266
Ni	0.206
S	0.198
V	0.178
Zn	0.162
As	0.158
Fe	0.100
Sc	0.095
Mo	0.090
La	0.035
U	0.031
Cd	0.028
Pb	0.022
K	0.017
Na	0.015
Ag	0.009
Al	-0.001
Ba	-0.004
W	-0.007
Sr	-0.017
Mn	-0.032
Ti	-0.062
Mg	-0.080
Ca	-0.092

Element	R-value with Co
Co	
Ni	0.473
Cu	0.343
Bi	0.332
V	0.271
S	0.256
As	0.138
Be	0.132
Mn	0.117
U	0.114
Mo	0.109
Zn	0.068
P	0.064
Na	0.045
Ba	0.031
Pb	0.028
Sc	0.027
Cd	-0.001
Ag	-0.006
W	-0.008
Fe	-0.031
Sr	-0.033
La	-0.041
Ti	-0.055
K	-0.068
Al	-0.083
Ca	-0.124
Mg	-0.185

Figure 5.18*: Table of R-values for element vs. element concentration for Cu and Co at Mashitu South.*

5.3.2 Splitting the Data for Mashitu South by Lithostratigraphy

In this section the results of applying statistical methods to datasets split by stratigraphy and lithology are presented. The results will primarily be presented by stratigraphy, with different lithologies considered mainly as data-subsets within each stratigraphy, as logging by the author detailed in Chapter 3 supports the veracity of Comide's stratigraphic interpretations. In many cases lithological subsets within a stratigraphy have been broken down into their primary logged lithology (Lith1) so that datasets were not split so small as to be statistically useless. Where this has occurred, the lithology is denoted in the figure by using its name followed by an '(and)', for example: 'Dolomite (and)'.

Before the presentation of results in this section it should be noted that by comparing the Comide logging to the author's logging in holes MSSD075, 080, 083 and 140, there appear to be many examples where near-surface saprolitic clays have been logged by Comide with a primary lithology of mudstone, siltstone or shale. It can be assumed that this has happened throughout the combined database and that the mudstone, siltstone and shale lithologies are over-represented.

A complete summary of the ACEMS-normalised mean concentrations of elements in each lithology from every stratigraphic unit is given as Appendix 6.

5.3.2.1 C.M.N. Unit

The CMN unit has been primarily logged as the dolomite lithology, with significant proportions of shale and silicic rock (see Figure 5.19). Overall the unit has anomalously high concentrations of Ca, W and Ag. Mg and Sr concentrations are also above-average. The unit is anomalously low in Al, Fe, K, Co, Ti, P, V, Ni, La, Pb, Sc and Be (see Figure 5.20). Lithologically, W and Ag are concentrated in quantities >10x higher than ACEMS in 'Breccia', 'Clay and Saprolite', 'Mudstone', 'Sandstone' and 'Silicic Rock'. Cu is most concentrated (1.25x ACEMS) in 'Clay and Saprolite' (Figure 5.20).

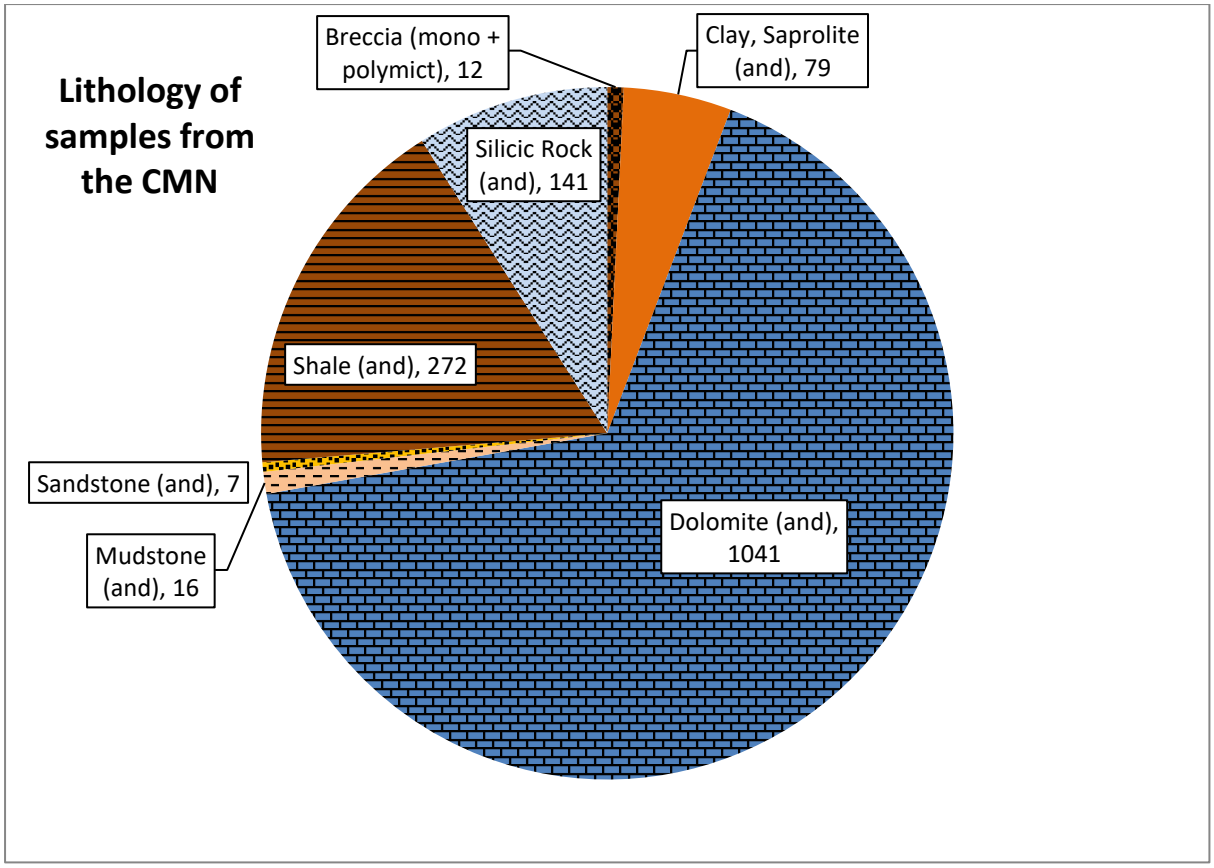

Figure 5.19*: Pie chart showing the lithological composition of the CMN unit.*

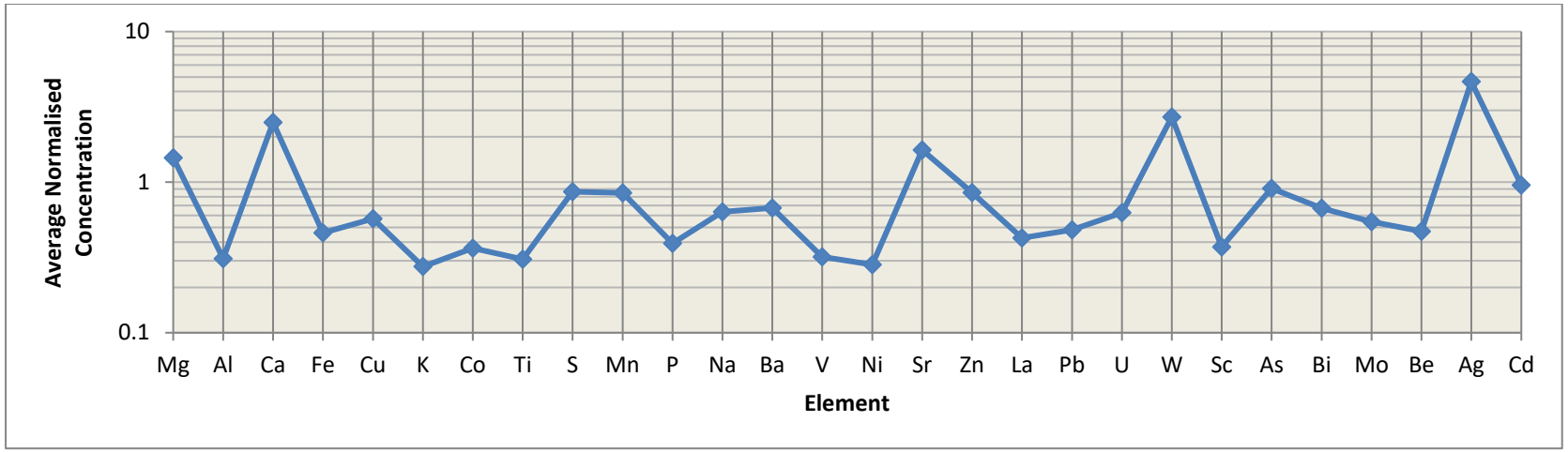

***Figure 5.20**: Spider diagram showing the ACEMS-normalised mean concentrations of different elements in the CMN.*

N	LITHO-STRAT	Mg	Al	Ca	Fe	Cu	K	Co	Ti	S	Mn	P	Na	Ba	V
12	(CMN) Breccia (mono + polymict)	0.81	0.82	0.06	1.17	0.29	0.60	0.62	0.71	0.09	1.17	0.45	1.22	0.42	0.80
79	(CMN) Clay, Saprolite (and)	1.31	0.71	0.08	1.04	1.25	0.27	0.40	0.64	0.05	2.50	0.53	0.75	0.99	0.70
1041	(CMN) Dolomite (and)	1.56	0.20	2.82	0.35	0.55	0.13	0.35	0.19	0.98	0.71	0.33	0.51	0.66	0.21
16	(CMN) Mudstone (and)	0.74	0.47	0.63	1.02	0.28	0.06	0.58	0.47	0.03	1.56	0.34	0.80	0.54	0.56
7	(CMN) Sandstone (and)	0.81	0.16	0.39	0.59	0.67	0.02	0.61	0.15	0.10	1.46	0.21	0.39	0.25	0.30
272	(CMN) Shale (and)	1.44	0.67	2.32	0.67	0.61	0.95	0.36	0.72	0.94	0.93	0.69	1.14	0.77	0.66
141	(CMN) Silicic Rock (and)	0.92	0.15	2.26	0.39	0.35	0.05	0.37	0.12	0.53	0.64	0.19	0.45	0.43	0.18

N	LITHO-STRAT	Ni	Sr	Zn	La	Pb	U	W	Sc	As	Bi	Mo	Be	Ag	Cd
12	(CMN) Breccia (mono + polymict)	0.47	0.60	1.65	0.50	0.54	0.54	10.60	1.15	1.13	0.57	1.73	1.08	17.58	1.04
79	(CMN) Clay, Saprolite (and)	0.58	0.59	1.69	1.09	0.92	0.54	15.66	0.84	1.05	0.65	2.30	1.16	13.66	1.17
1041	(CMN) Dolomite (and)	0.18	1.82	0.68	0.37	0.36	0.62	1.85	0.26	0.90	0.72	0.38	0.37	1.22	0.95
16	(CMN) Mudstone (and)	0.62	0.66	1.61	0.43	0.65	0.54	23.92	0.72	1.00	0.88	1.25	0.90	18.96	1.76
7	(CMN) Sandstone (and)	0.43	0.33	2.16	0.27	0.40	0.54	3.98	0.52	0.66	0.67	0.46	1.18	6.23	1.15
272	(CMN) Shale (and)	0.44	1.66	1.32	0.52	0.95	0.71	0.80	0.68	1.02	0.60	0.63	0.67	0.55	0.89
141	(CMN) Silicic Rock (and)	0.53	1.03	0.51	0.28	0.22	0.54	2.36	0.19	0.70	0.50	0.43	0.29	29.96	0.93

***Figure 5.21**: Summary table showing the ACEMS-normalised mean concentrations of different elements in various lithologies within the CMN.*

5.3.2.2 S.D.S. Unit

The SDS unit is overwhelmingly logged as shale with a significant minority of dolomite and some breccia (see Figure 5.22). The unit has anomalously high concentrations of K and is anomalously low in Ag (see Figure 5.23). When split by lithology, dolomite units within the SDS contain >2x ACEMS values of Ca, K and S, SDS breccia is anomalously high in S and Ba, and SDS shale is anomalously high in K. Cu is most concentrated (1.33x ACEMS) in SDS breccia (Figure 5.24).

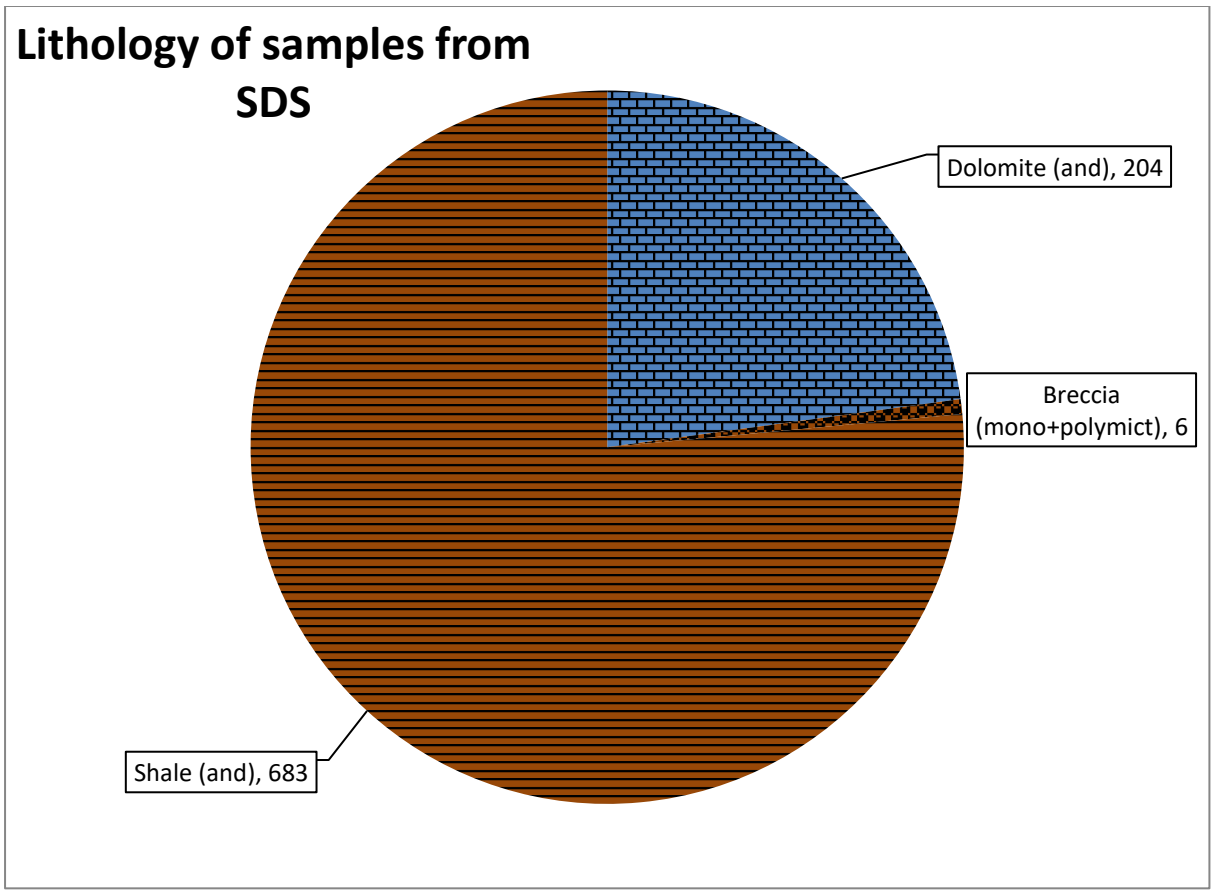

Figure 5.22*: Pie chart showing the lithological composition of the SDS unit.*

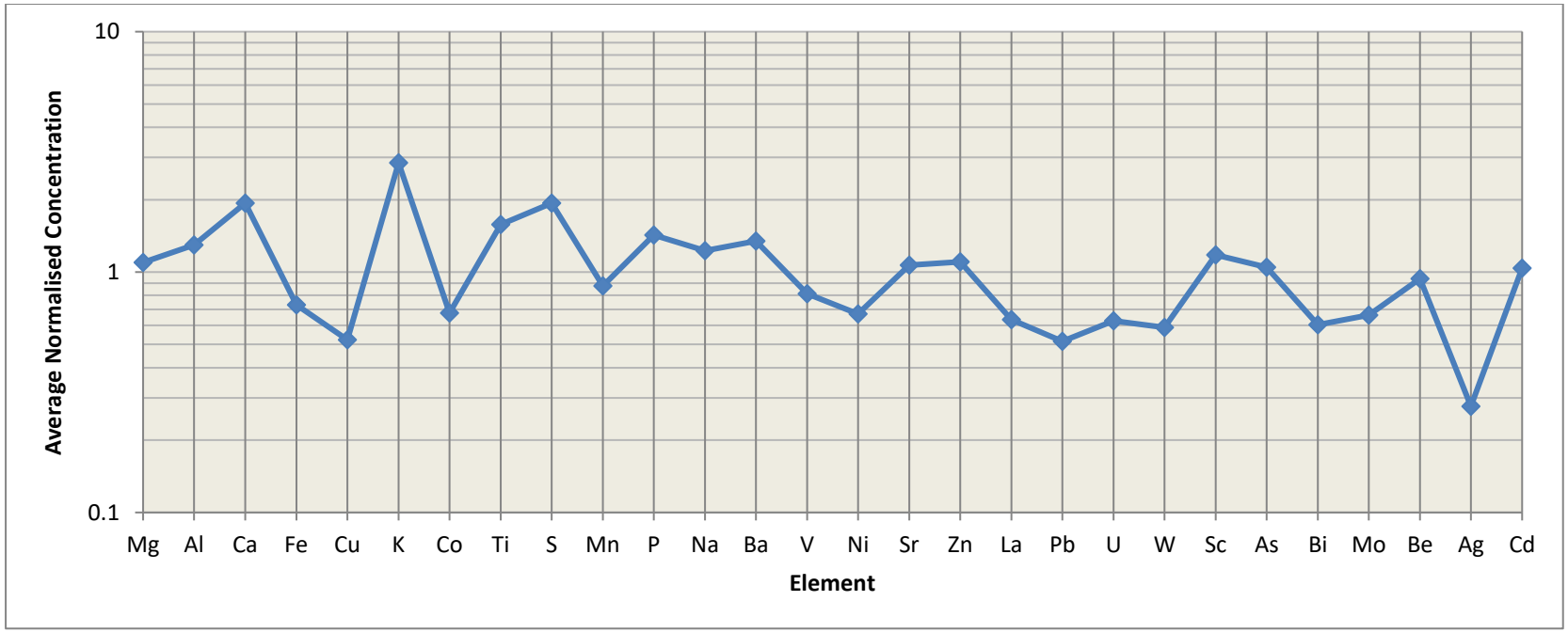

***Figure 5.23**: Spider diagram showing the ACEMS-normalised mean concentrations of different elements in the SDS.*

N	LITHOLOGY	Mg	Al	Ca	Fe	Cu	K	Co	Ti	S	Mn	P	Na	Ba	V
204	Dolomite (and)	1.25	1.15	2.36	0.55	0.82	2.25	1.65	1.29	2.57	0.77	1.24	1.11	1.32	0.66
6	Breccia (mono+polymict)	1.26	1.28	1.56	1.19	1.33	1.42	0.90	1.51	2.75	1.10	1.94	1.05	2.66	1.53
683	Shale (and)	1.05	1.34	1.81	0.78	0.43	3.04	0.39	1.66	1.75	0.90	1.47	1.26	1.34	0.85

N	LITHOLOGY	Ni	Sr	Zn	La	Pb	U	W	Sc	As	Bi	Mo	Be	Ag	Cd
204	Dolomite (and)	0.66	1.23	0.72	0.61	0.39	0.70	0.58	0.98	0.88	0.85	0.70	0.67	0.23	0.85
6	Breccia (mono+polymict)	1.47	1.05	1.38	0.59	0.65	1.71	0.58	1.44	1.69	1.28	1.34	1.50	0.23	1.84
683	Shale (and)	0.67	1.02	1.21	0.64	0.55	0.59	0.59	1.24	1.09	0.53	0.65	1.01	0.29	1.09

***Figure 5.24**: Summary table showing the ACEMS-normalised mean concentrations of different elements in various lithologies within the SDS.*

5.3.2.3 S.D.2d Unit

The SD2d consists of shale, with some of the unit logged as shale and dolomite and a small minority logged as dolomite or dolomite and sandstone (see Figure 5.25). Cu, K, Ti, S, Na, Ba, V, La, As, Bi and Mo are anomalously high throughout the unit (see Figure 5.26). Sulphur is exceptionally high, >10x ACEMS, in the 'Shale and Dolomite' lithology, which perhaps refers to where the unit hosts a high concentration of sulphide-bearing dolomite veins. Mg, Ca, Mn and Ag are anomalously low. Cu is most concentrated (4.79x ACEMS) in dolomite and dolomite and breccia from the SD2d (Figure 5.27), which equates to an average concentration of 3.06% Cu. Cu is exceptionally high throughout the unit, at 2.2% Cu over the whole SD2d stratigraphic interval.

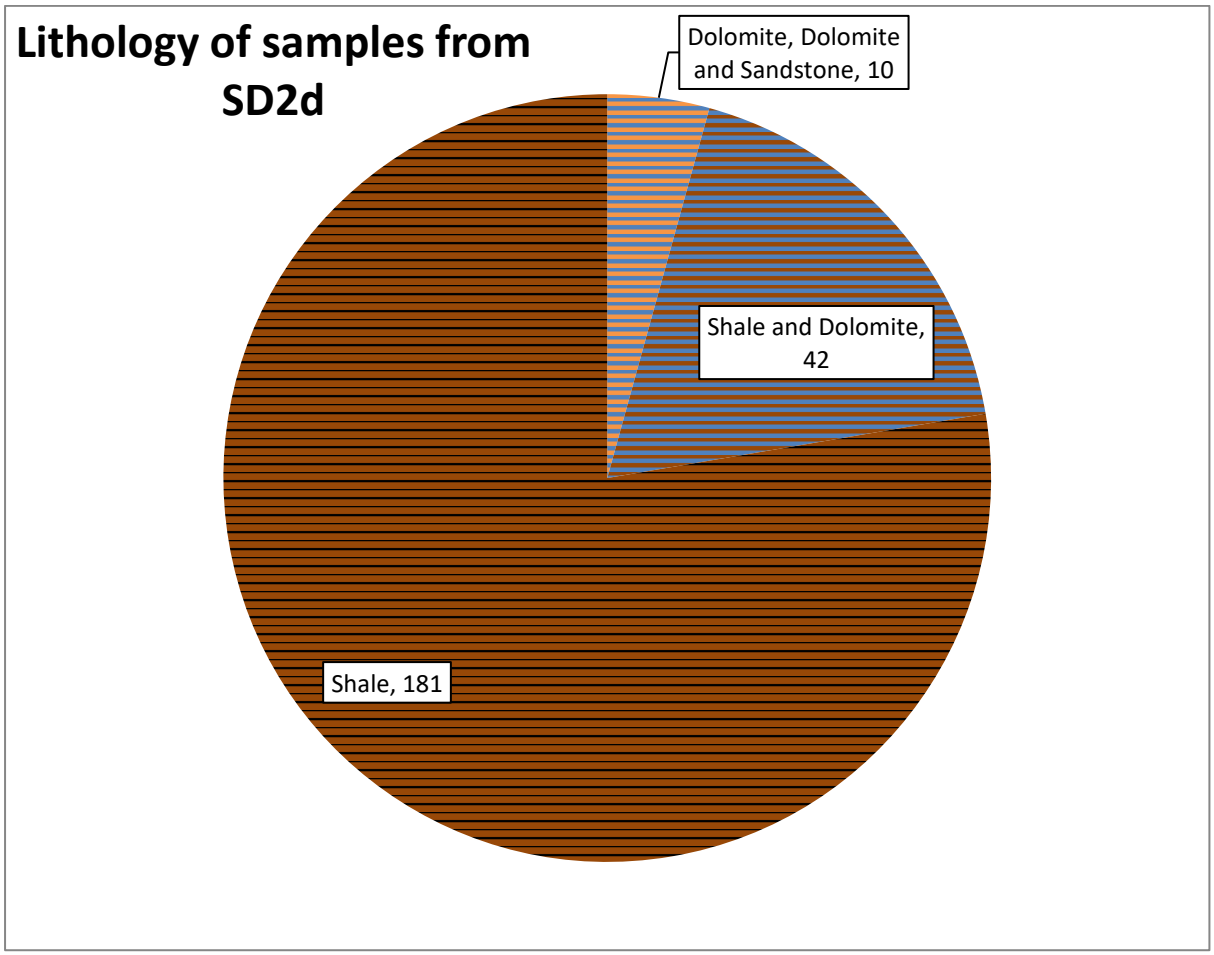

Figure 5.25*: Pie chart showing the lithological composition of the SD2d unit.*

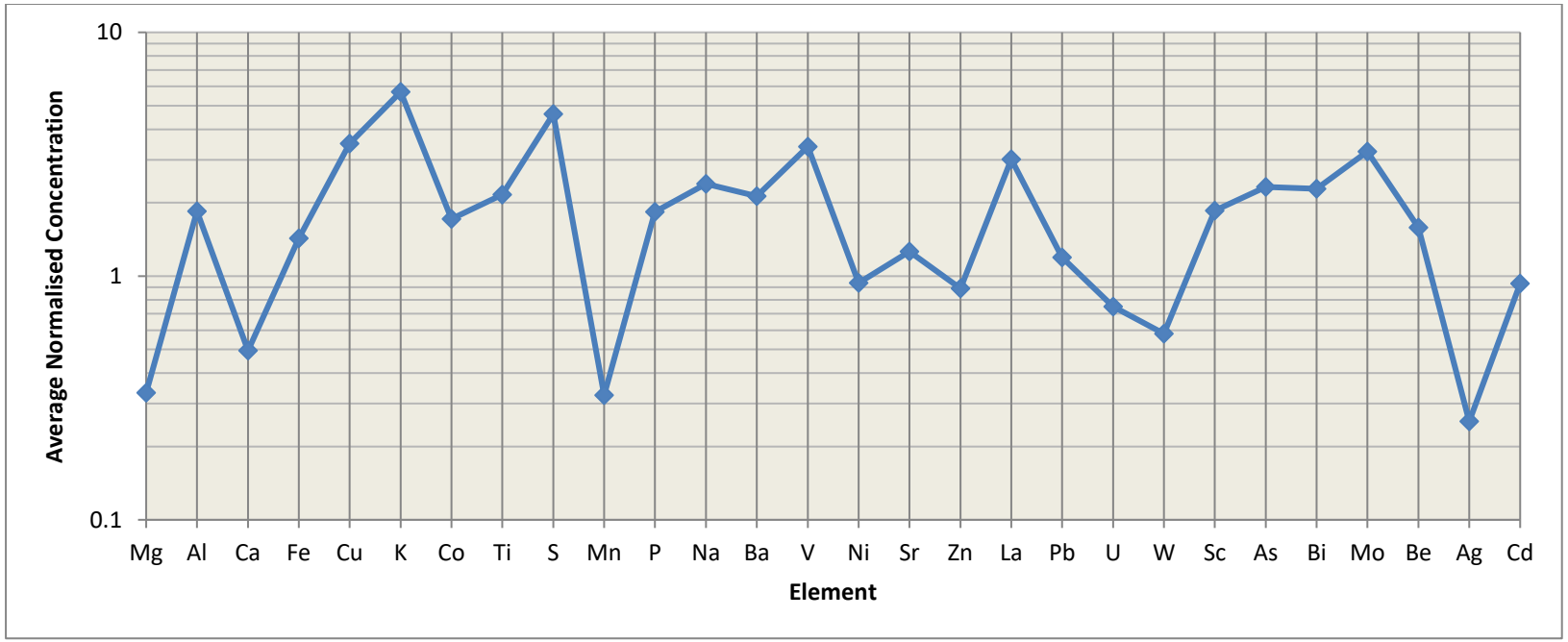

***Figure 5.26**: Spider diagram showing the ACEMS-normalised mean concentrations of different elements in the SD2d.*

N	LITHOLOGY	Mg	Al	Ca	Fe	Cu	K	Co	Ti	S	Mn	P	Na	Ba	V
10	Dolomite, Dolomite and Sandston	0.22	1.79	0.32	0.89	4.79	6.79	0.64	2.40	1.71	0.16	1.63	1.80	1.43	3.83
42	Shale and Dolomite	0.58	1.72	0.78	1.11	4.75	5.25	3.69	1.97	12.44	0.35	1.68	3.04	1.79	2.75
181	Shale	0.27	1.89	0.41	1.55	3.16	5.81	1.32	2.21	3.02	0.32	1.90	2.30	2.22	3.55

N	LITHOLOGY	Ni	Sr	Zn	La	Pb	U	W	Sc	As	Bi	Mo	Be	Ag	Cd
10	Dolomite, Dolomite and Sandston	0.30	0.97	0.74	3.16	0.60	0.86	0.58	1.71	0.78	1.40	3.62	1.38	0.26	0.80
42	Shale and Dolomite	0.92	1.57	0.79	1.31	0.85	0.86	0.58	1.56	1.92	2.66	2.76	1.30	0.25	1.02
181	Shale	0.98	1.20	0.93	3.44	1.30	0.73	0.58	1.94	2.53	2.31	3.36	1.67	0.25	0.92

***Figure 5.27**: Summary table showing the ACEMS-normalised mean concentrations of different elements in various lithologies within the SD2d.*

5.3.2.4 S.D.B. Unit

The SDB is another dominantly shale unit with minor dolomite, siltstone and clay (see Figure 5.28). The unit has anomalously high K and S and anomalously low Ag (see Figure 5.29). Potassium and sulphur are high throughout most of the unit except within clay and siltstone lithologies. Cu is most concentrated (1.50x ACEMS) in SDB siltstone (Figure 5.30).

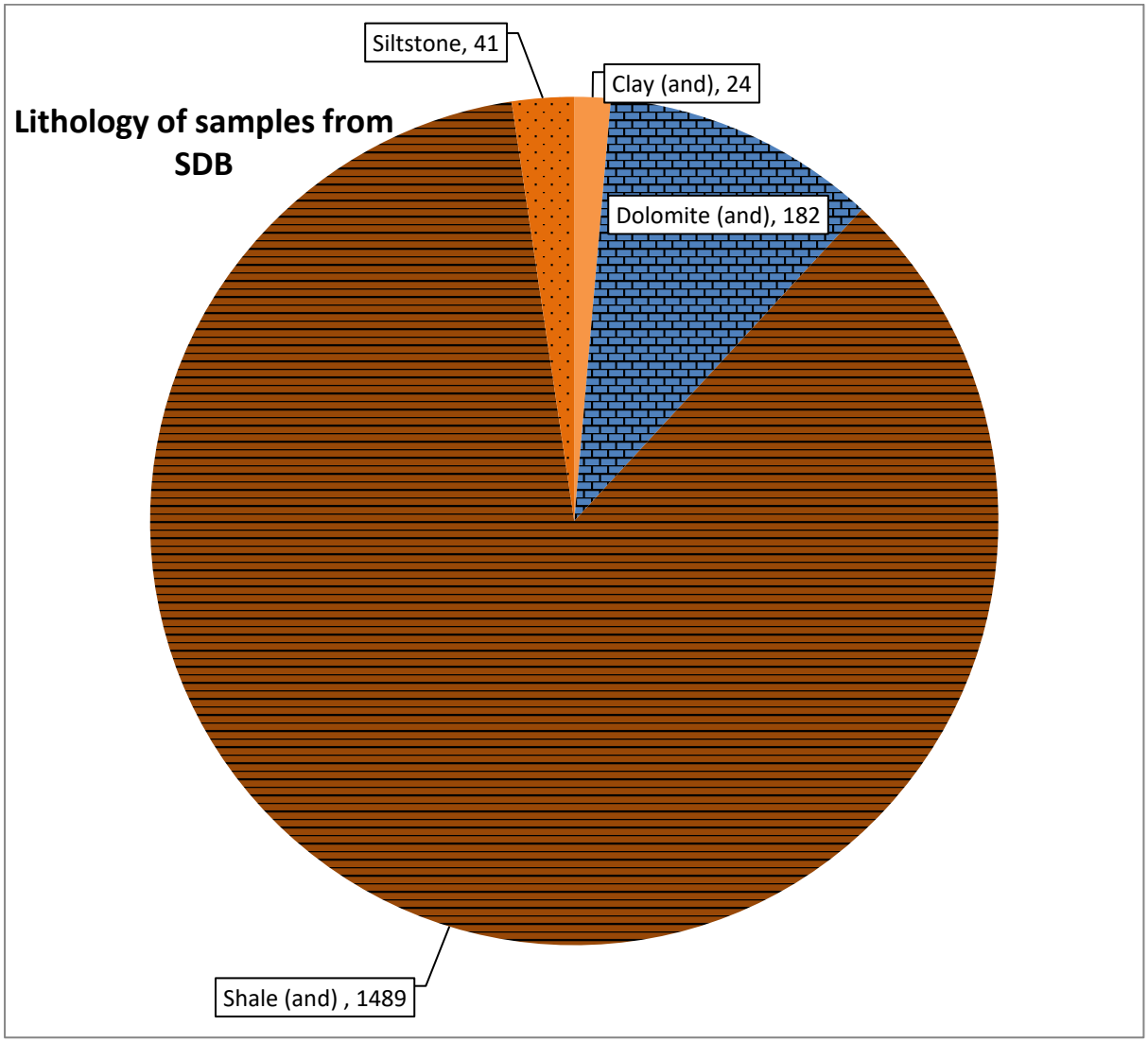

Figure 5.28*: Pie chart showing the lithological composition of the SDB unit.*

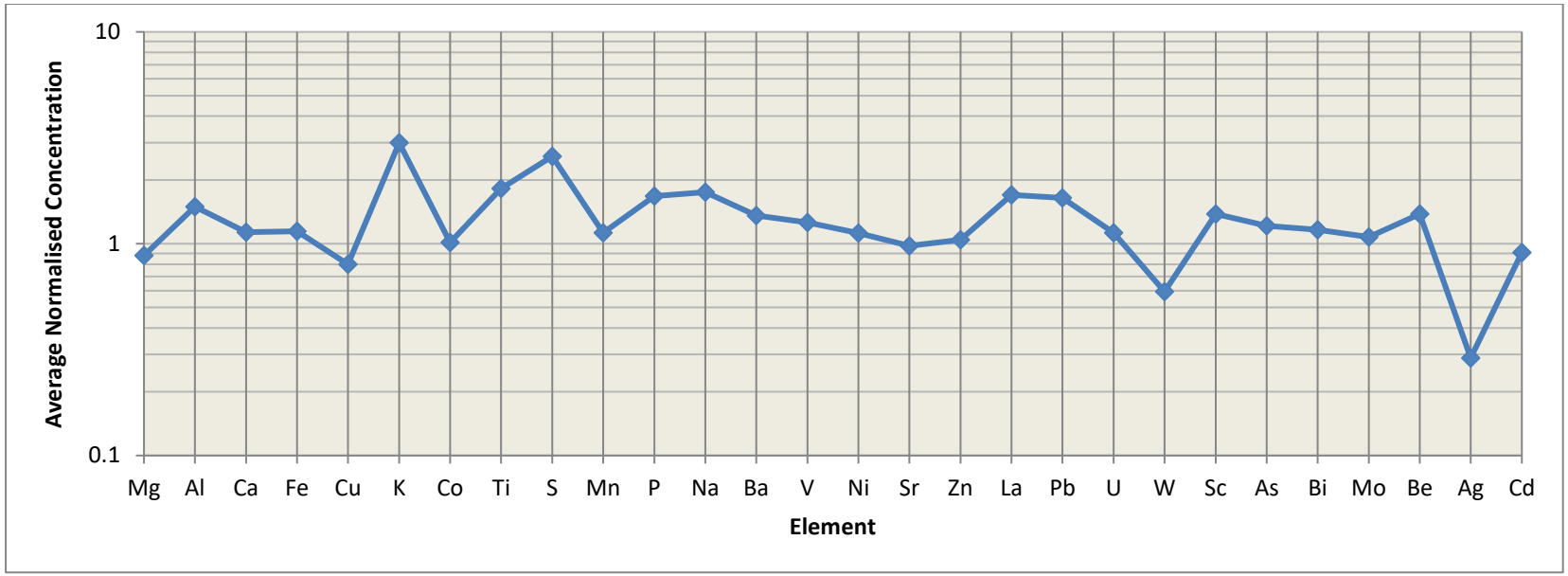

***Figure 5.29**: Spider diagram showing the ACEMS-normalised mean concentrations of different elements in the SDB.*

N	LITHOLOGY	Mg	Al	Ca	Fe	Cu	K	Co	Ti	S	Mn	P	Na	Ba	V
24	Clay (and)	0.53	1.70	0.14	1.68	0.44	4.16	0.44	2.27	0.07	1.02	2.07	1.94	1.38	1.42
182	Dolomite (and)	1.21	1.15	2.42	0.59	0.54	2.36	1.28	1.38	5.13	0.89	1.47	1.16	1.40	0.71
1489	Shale (and)	0.85	1.53	1.00	1.20	0.81	3.04	0.99	1.87	2.39	1.16	1.70	1.81	1.36	1.32
41	Siltstone	0.72	1.59	0.92	0.95	1.50	3.48	0.91	1.81	0.40	0.98	1.87	2.12	1.27	1.32

N	LITHOLOGY	Ni	Sr	Zn	La	Pb	U	W	Sc	As	Bi	Mo	Be	Ag	Cd
24	Clay (and)	0.85	0.73	1.68	1.93	0.68	0.54	0.70	1.56	1.66	0.87	1.05	1.90	0.51	0.80
182	Dolomite (and)	0.95	1.17	0.68	0.67	0.40	1.26	0.58	1.01	0.88	0.50	0.57	0.81	0.23	0.81
1489	Shale (and)	1.15	0.94	1.08	1.77	1.84	1.13	0.59	1.42	1.24	1.24	1.13	1.44	0.29	0.92
41	Siltstone	1.10	1.59	0.85	3.34	0.79	0.65	0.58	1.58	1.20	1.62	0.99	1.40	0.23	0.83

***Figure 5.30**: Summary table showing the ACEMS-normalised mean concentrations of different elements in various lithologies within the SDB.*

5.3.2.5 R.S.C. Unit

Just over half of the RSC samples are logged as mainly silicic rock and just under half are logged as primarily dolomite (see Figure 5.31), with the full lithological descriptions of most of these samples being either 'Silicic rock and dolomite' or 'Dolomite and silicic rock'. There are no anomalously highly concentrated elements out of the 28 assayed for, although Co, Ni, U and Bi are above average. Mg, Al, Fe, K, Ti, S, La and Sc are all found in anomalously low concentrations (see Figure 5.32). Cu is most concentrated (1.35x ACEMS) in SDB 'mudstone' (Figure 5.33).

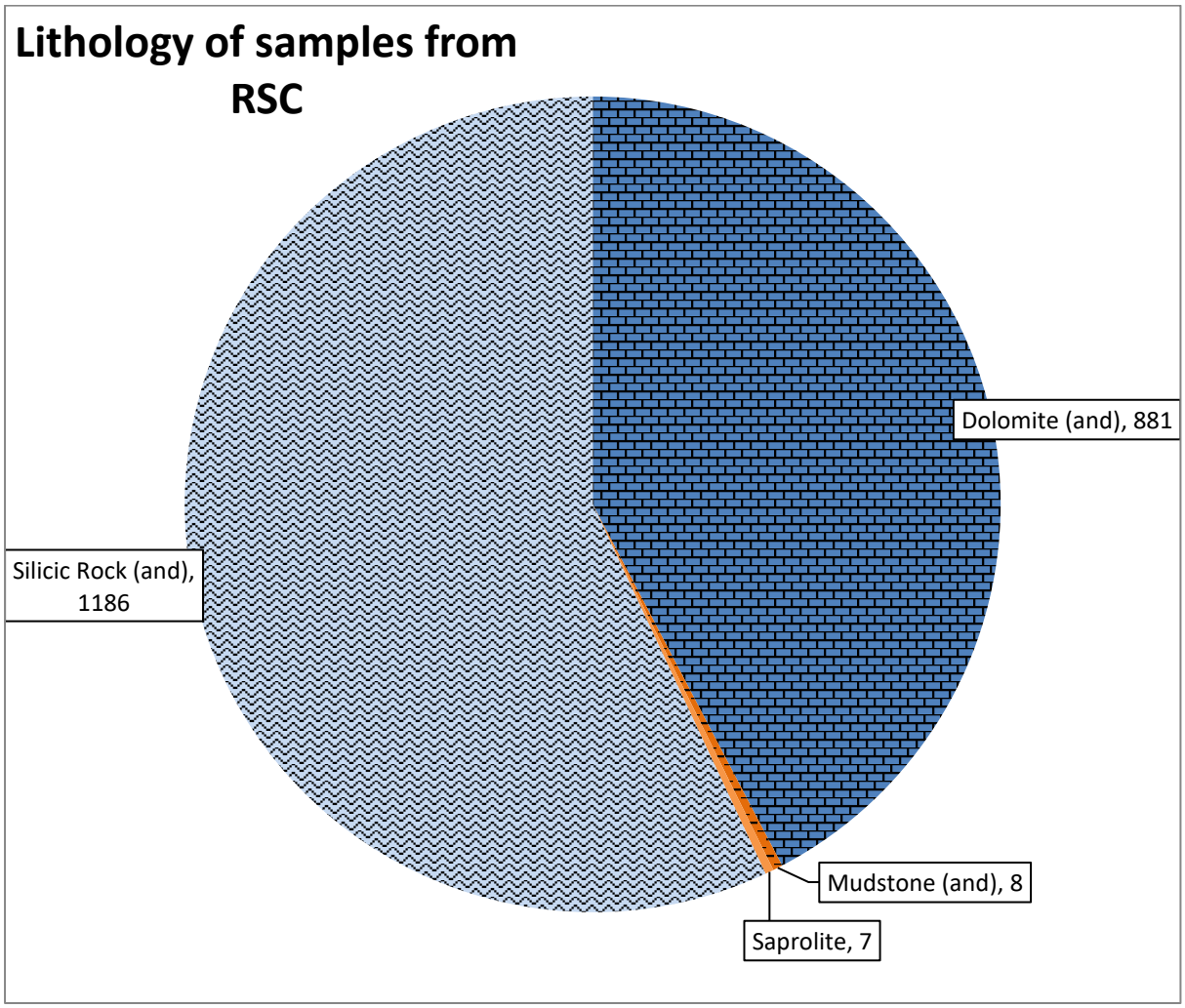

***Figure 5.31**: Pie chart showing the lithological composition of the RSC unit.*

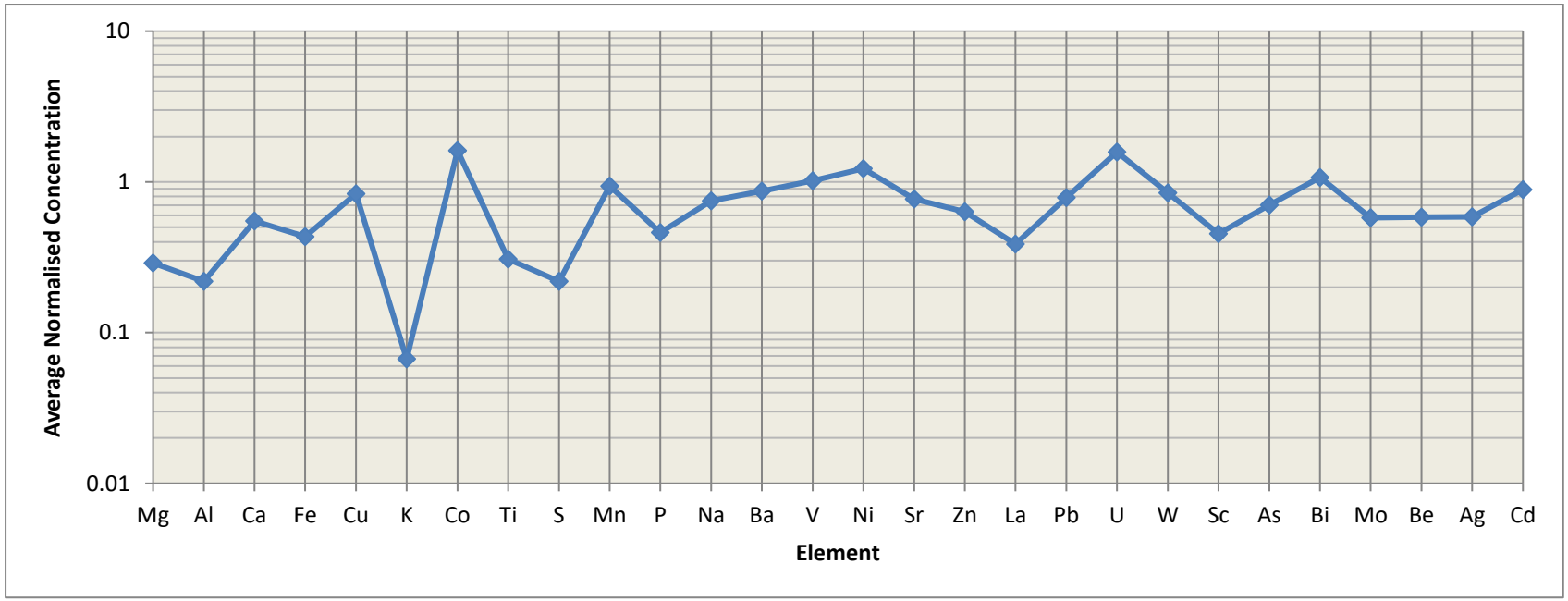

***Figure 5.32**: Spider diagram showing the ACEMS-normalised mean concentrations of different elements in the RSC.*

N	LITHOLOGY	Mg	Al	Ca	Fe	Cu	K	Co	Ti	S	Mn	P	Na	Ba	V
881	Dolomite (and)	0.33	0.22	0.66	0.42	0.73	0.06	1.57	0.31	0.29	0.94	0.46	0.76	1.15	1.10
8	Mudstone (and)	0.33	0.72	0.09	0.62	1.35	0.14	2.18	0.93	0.05	0.84	0.55	1.34	0.20	1.17
7	Saprolite	0.03	0.53	0.01	1.03	0.04	0.19	0.47	0.76	0.03	0.49	0.25	0.81	0.27	1.20
1186	Silicic Rock (and)	0.26	0.21	0.48	0.43	0.91	0.07	1.65	0.30	0.17	0.94	0.46	0.73	0.68	0.96

N	LITHOLOGY	Ni	Sr	Zn	La	Pb	U	W	Sc	As	Bi	Mo	Be	Ag	Cd
881	Dolomite (and)	1.50	0.93	0.63	0.32	1.00	2.97	0.76	0.46	0.71	1.03	0.69	0.63	0.46	0.89
8	Mudstone (and)	0.57	0.50	0.47	5.79	0.71	0.54	6.46	0.66	1.08	3.23	0.30	0.70	3.15	0.80
7	Saprolite	0.34	0.34	0.42	0.58	0.90	0.54	0.58	0.67	1.35	1.89	0.74	0.13	0.23	0.80
1186	Silicic Rock (and)	1.03	0.66	0.64	0.40	0.63	0.56	0.88	0.45	0.69	1.08	0.50	0.55	0.66	0.89

***Figure 5.33**: Summary table showing the ACEMS-normalised mean concentrations of different elements in various lithologies within the RSC.*

5.3.2.6 R.S.F. Unit

Most of the RSF samples are logged as dolomite, with significant minorities of siltstone and silicic rock as well as a few samples of mudstone and shale (see Figure 5.34). Bi is anomalously highly concentrated in the RSF, but it is notable that both Cu and Co are near anomalously high concentrations in the unit on average (1.96x ACEMS and 1.86x ACEMS respectively, see Figure 5.35). In terms of lithology, it appears that Cu and Co are most concentrated in the 'fresh', unweathered lithologies of 'dolomite' and 'silicic rock' (Figure 5.36), as the 'mudstone', 'siltstone' and 'shale' lithological descriptions are often (incorrectly) used to describe saprolite, clay and otherwise weathered rock. The 'dolomite' and 'silicic rock' lithologies have ACEMS-normalised values for Cu respectively of 2.05 and 2.98, which correspond to average Cu grades of 1.31% and 1.90%. The 'siltstone lithology has an ACEMS-normalised value for Cu of 1.61, equating to a respectable average Cu grade of 1.03%.

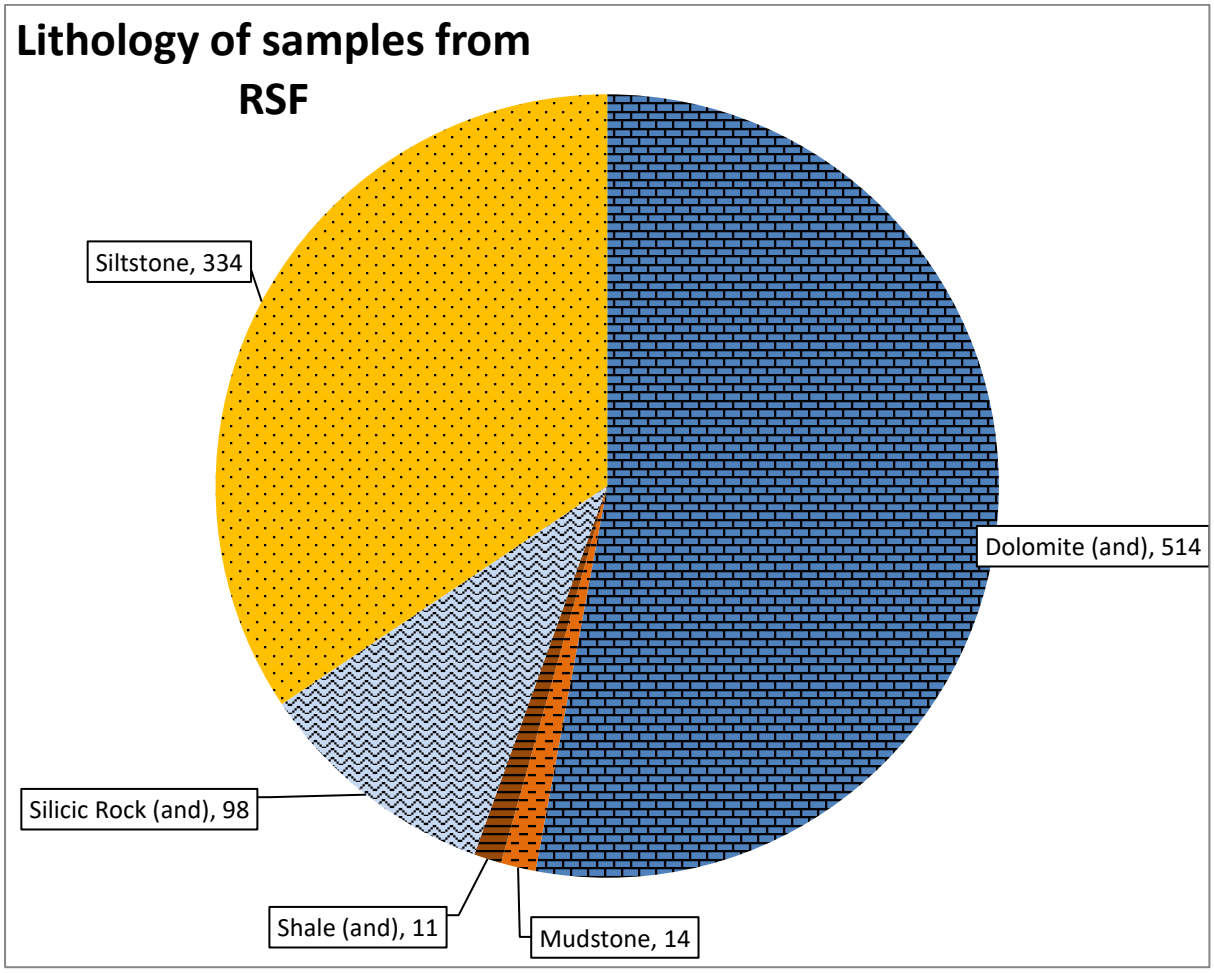

***Figure 5.34**: Pie chart showing the lithological composition of the RSF unit.*

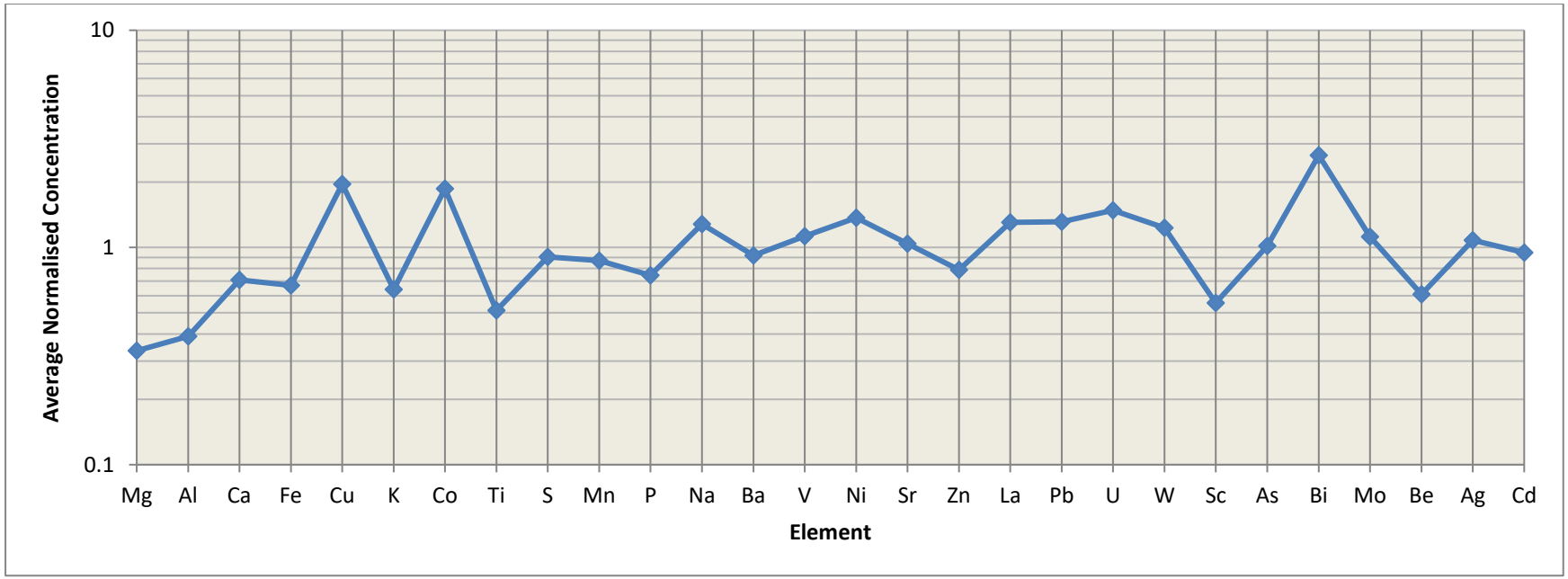

***Figure 5.35**: Spider diagram showing the ACEMS-normalised mean concentrations of different elements in the RSF.*

N	LITHOLOGY	Mg	Al	Ca	Fe	Cu	K	Co	Ti	S	Mn	P	Na	Ba	V
514	Dolomite (and)	0.37	0.39	0.78	0.69	2.05	0.62	1.92	0.50	1.06	0.86	0.82	1.29	1.32	1.19
14	Mudstone	0.02	0.46	0.01	1.20	0.07	0.70	0.64	0.59	0.09	1.21	0.25	1.08	0.30	0.98
11	Shale (and)	0.11	0.34	0.01	0.54	1.08	0.49	1.82	0.50	0.06	1.10	0.65	1.03	0.36	0.92
98	Silicic Rock (and)	0.25	0.35	0.53	0.54	2.98	0.54	2.84	0.48	0.83	1.02	0.56	1.08	0.44	0.96
334	Siltstone	0.32	0.40	0.68	0.65	1.61	0.71	1.56	0.53	0.75	0.82	0.72	1.32	0.48	1.10

N	LITHOLOGY	Ni	Sr	Zn	La	Pb	U	W	Sc	As	Bi	Mo	Be	Ag	Cd
514	Dolomite (and)	1.66	1.06	0.84	1.28	1.53	2.29	0.83	0.54	1.06	2.36	1.18	0.62	0.71	0.91
14	Mudstone	0.57	0.42	0.59	0.95	1.12	0.54	21.98	0.70	0.97	2.14	1.87	0.26	31.44	1.49
11	Shale (and)	0.24	0.38	1.07	1.68	2.22	0.54	0.58	0.61	0.74	2.28	0.97	0.79	0.27	0.80
98	Silicic Rock (and)	1.21	1.28	1.12	1.06	1.40	0.60	0.86	0.56	0.90	3.38	0.62	0.48	0.79	1.14
334	Siltstone	1.05	0.99	0.61	1.43	0.94	0.59	1.04	0.57	0.99	2.93	1.16	0.65	0.39	0.93

***Figure 5.36**: Summary table showing the ACEMS-normalised mean concentrations of different elements in various lithologies within the RSF.*

5.3.2.7 D.Strat Unit

Samples from the DStrat are overwhelmingly logged as dolomite, with a small minority of clay, silicic rock, shale, mudstone, siltstone, and monomict breccia and dolomite samples (see Figure 5.37). As and Mo concentrations in the DStrat are both anomalously high (see Figure 5.38). Both As and Mo are most concentrated in the 'monomict breccia and dolomite' lithology within the DStrat. Anomalously low concentrations of Mg, Ca and S are reported in the 'clay', 'shale', 'mudstone', 'siltstone' and 'silicic rock', however the concentrations of these elements in 'fresh' 'dolomite' is either above average or barely below average (Figure 5.39). Cu is most concentrated in the 3 'silicic rock' samples with a mean of 2.65x ACEMS.

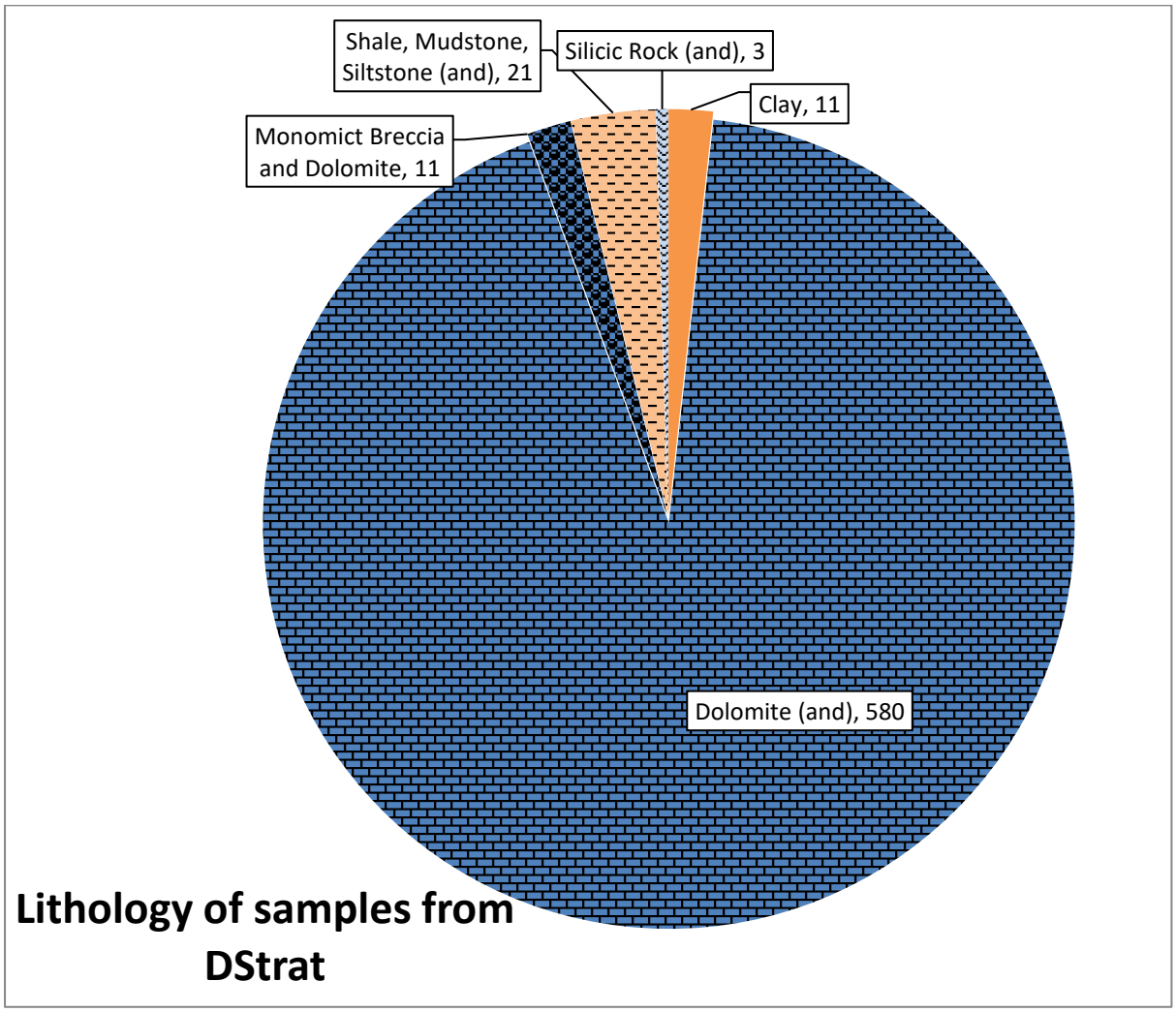

Figure 5.37*: Pie chart showing the lithological composition of the DStrat unit.*

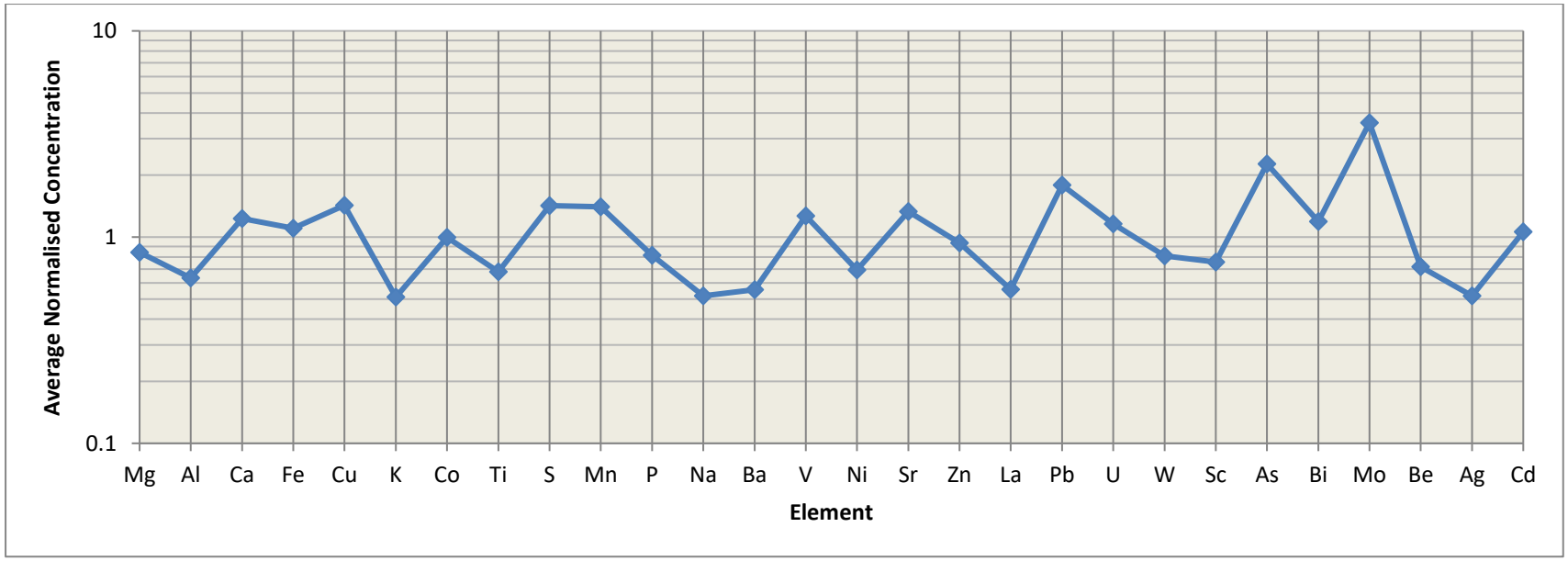

***Figure 5.38**: Spider diagram showing the ACEMS-normalised mean concentrations of different elements in the DStrat.*

N	LITHOLOGY	Mg	Al	Ca	Fe	Cu	K	Co	Ti	S	Mn	P	Na	Ba	V
11	Clay	0.33	0.87	0.02	1.78	0.56	0.12	1.72	1.02	0.05	3.47	0.46	0.46	0.32	2.04
580	Dolomite (and)	0.84	0.63	1.23	1.10	1.43	0.51	1.00	0.68	1.42	1.40	0.82	0.52	0.56	1.27
11	Monomict Breccia and Dolomite	1.12	0.53	1.97	0.95	0.58	0.12	1.26	0.60	0.49	1.76	1.86	0.38	0.58	1.23
21	Shale, Mudstone, Siltstone (and)	0.45	0.81	0.01	1.24	0.95	0.53	1.02	0.99	0.04	1.06	0.34	0.39	0.17	1.60
3	Silicic Rock (and)	0.07	0.56	0.01	1.23	2.65	1.27	0.72	0.76	0.07	1.49	0.22	0.77	0.27	1.23

N	LITHOLOGY	Ni	Sr	Zn	La	Pb	U	W	Sc	As	Bi	Mo	Be	Ag	Cd
11	Clay	1.16	0.28	0.77	0.97	3.50	1.28	2.80	1.54	2.57	2.35	6.34	0.73	2.21	1.06
580	Dolomite (and)	0.69	1.33	0.94	0.56	1.79	1.16	0.81	0.76	2.27	1.19	3.59	0.72	0.52	1.06
11	Monomict Breccia and Dolomite	0.76	0.92	0.82	0.27	2.01	1.13	0.58	0.81	2.67	0.40	13.95	0.99	0.29	1.94
21	Shale, Mudstone, Siltstone (and)	0.53	0.18	0.85	0.62	2.64	0.85	3.46	0.97	2.28	1.18	4.57	0.66	1.19	1.14
3	Silicic Rock (and)	0.26	0.15	0.78	0.27	1.01	0.54	0.58	0.76	1.50	0.46	2.60	0.49	0.34	0.80

***Figure 5.39**: Summary table showing the ACEMS-normalised mean concentrations of different elements in various lithologies within the DStrat.*

5.3.2.8 R.A.T. Gris Unit

The R.A.T. Gris samples are primarily logged as sandstone, though significant minorities of dolomite, clay and siltstone are also logged (see Figure 5.40). It is geochemically distinguished in having anomalously high Ba and Mo, with Ti concentration higher than average. K and Ag are anomalously low (see Figure 5.41). Cu is most concentrated in the 'siltstone' lithology with a mean of 1.16x ACEMS (Figure 5.42).

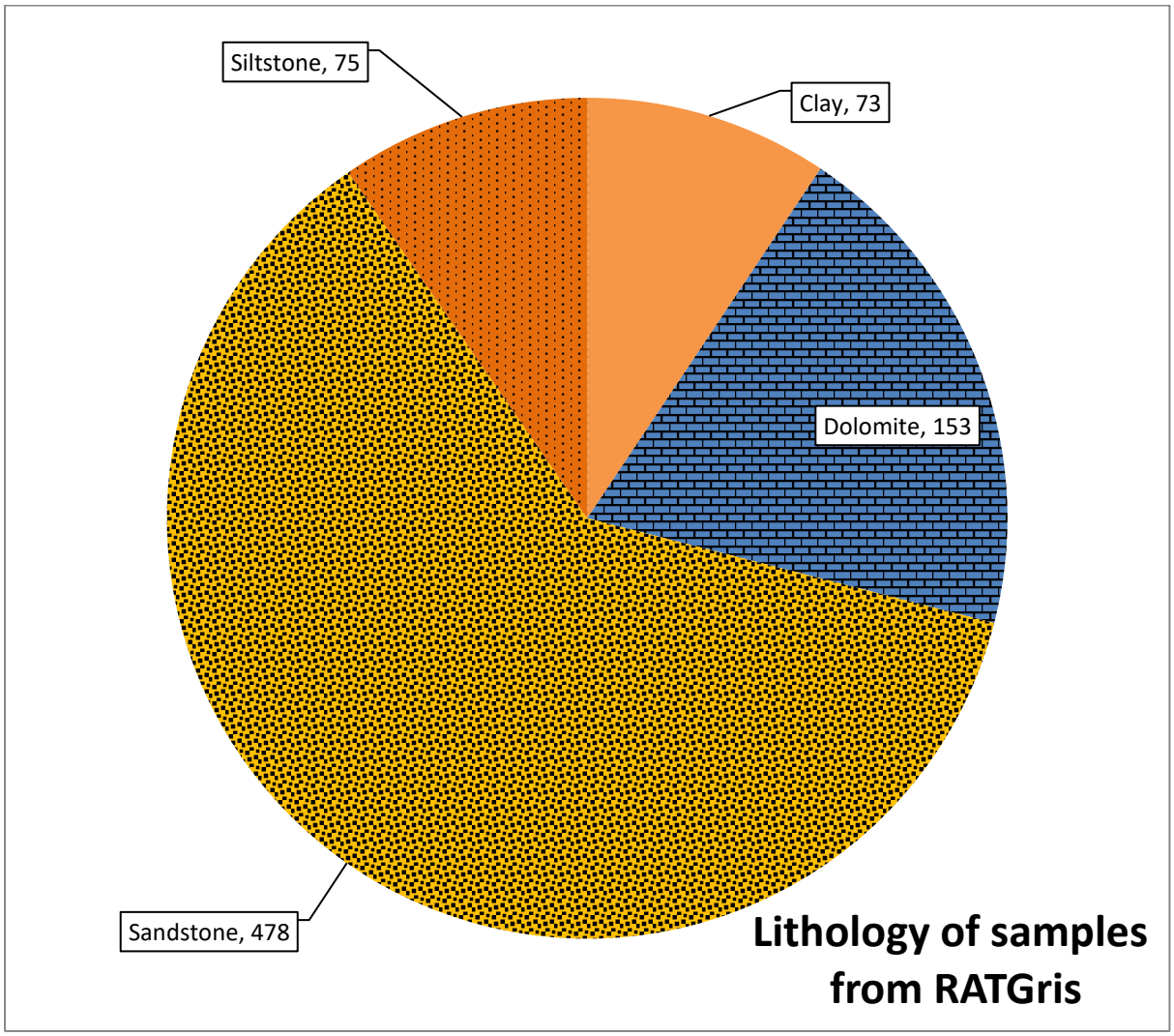

***Figure 5.40**: Pie chart showing the lithological composition of the RAT Gris unit.*

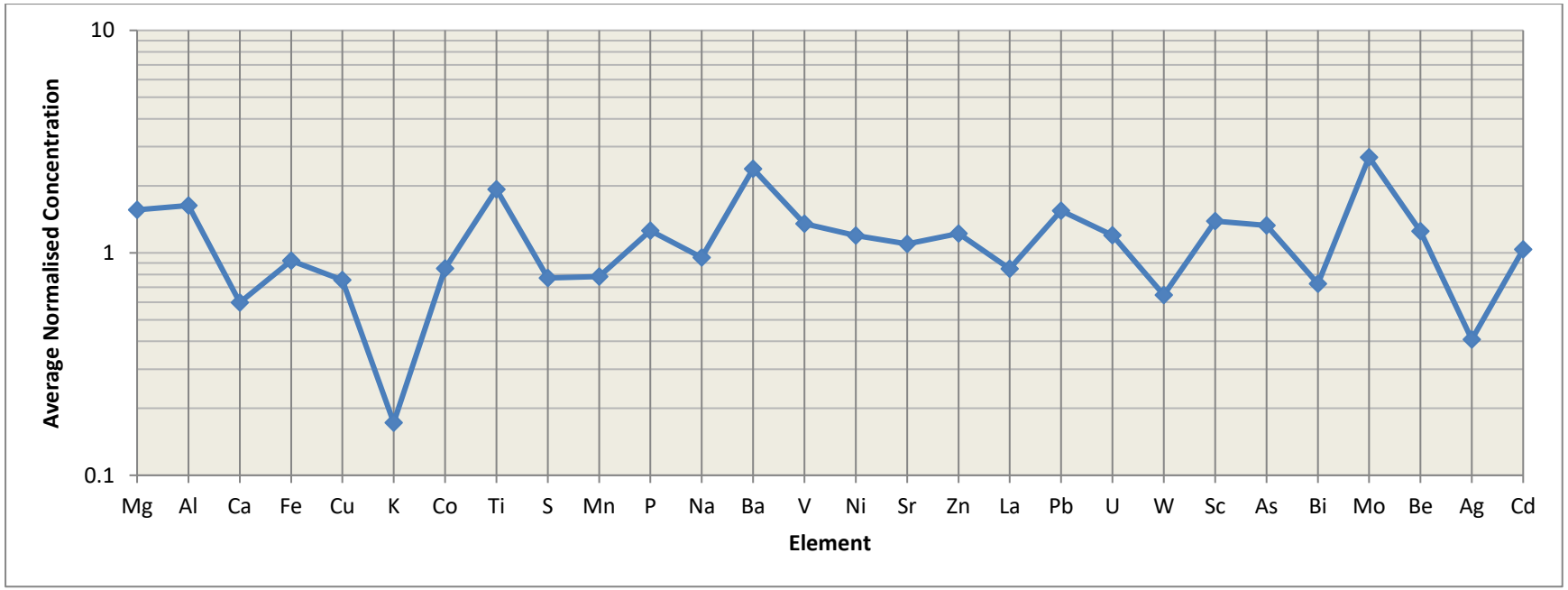

***Figure 5.41**: Spider diagram showing the ACEMS-normalised mean concentrations of different elements in the RAT Gris.*

N	LITHOLOGY	Mg	Al	Ca	Fe	Cu	K	Co	Ti	S	Mn	P	Na	Ba	V
73	Clay	1.44	1.64	0.66	0.89	0.66	0.16	1.08	2.04	1.05	1.16	1.08	0.67	3.31	1.64
153	Dolomite	1.60	1.46	0.93	0.79	0.99	0.11	0.94	1.78	0.95	0.70	1.34	0.80	4.33	1.15
478	Sandstone	1.56	1.69	0.48	0.97	0.63	0.20	0.82	1.97	0.64	0.75	1.23	1.03	1.84	1.39
75	Siltstone	1.62	1.63	0.59	0.91	1.16	0.12	0.64	1.91	0.94	0.74	1.46	1.05	0.79	1.23

N	LITHOLOGY	Ni	Sr	Zn	La	Pb	U	W	Sc	As	Bi	Mo	Be	Ag	Cd
73	Clay	1.37	1.44	1.20	0.93	1.60	1.61	0.77	1.52	1.22	0.75	2.47	1.16	0.76	1.02
153	Dolomite	1.20	1.47	1.18	0.77	1.38	1.79	0.59	1.22	1.42	0.62	1.50	1.20	0.35	1.01
478	Sandstone	1.18	0.98	1.27	0.91	1.67	1.00	0.65	1.43	1.34	0.72	3.35	1.27	0.40	1.06
75	Siltstone	1.16	0.72	1.01	0.52	1.06	0.86	0.63	1.34	1.18	1.01	1.22	1.33	0.26	0.93

***Figure 5.42**: Summary table showing the ACEMS-normalised mean concentrations of different elements in various lithologies within the RAT Gris.*

5.3.2.9 R.A.T. Rouge Unit

The R.A.T. Rouge samples are the most lithologically heterogeneous of all the stratigraphic datasets, with mudstone, sandstone, clay, dolomite, breccia and siltstone samples logged. Mudstone, sandstone and clay are the most abundant, but it should be noted that more breccia samples are assigned to this unit than to any other stratigraphic unit (see Figure 5.43). There appear to be no anomalous enrichments of any element in the R.A.T. Rouge, but Ca, K, S, Mo and Ag concentrations are anomalously low (see Figure 5.44). Cu is most concentrated in the 'breccia' lithology with a mean of 1.39x ACEMS (Figure 5.45).

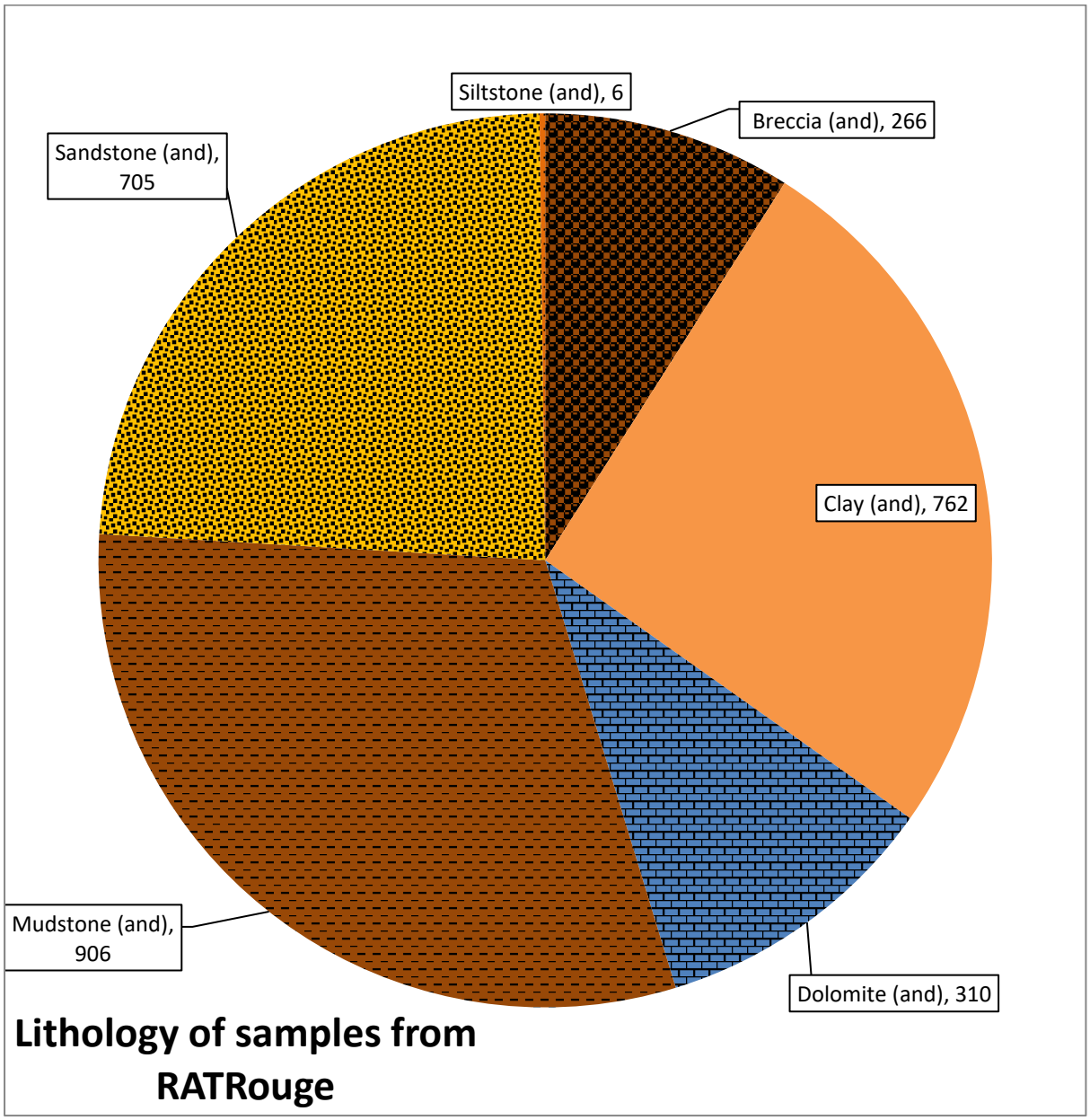

***Figure 5.43**: Pie chart showing the lithological composition of the RAT Rouge unit.*

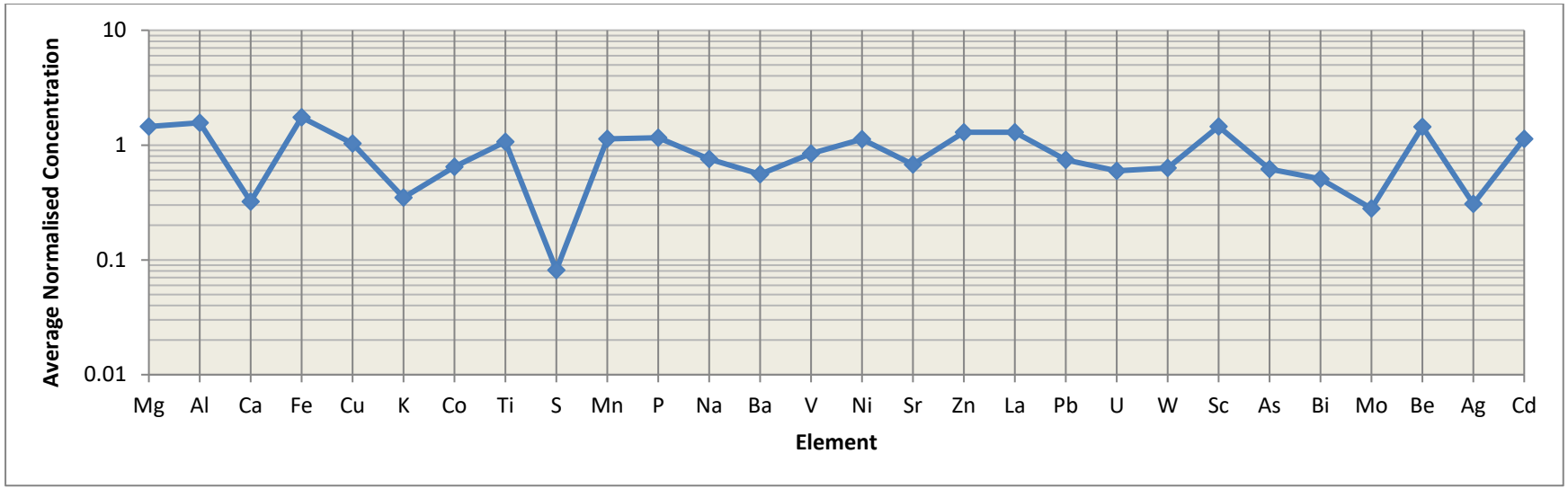

***Figure 5.44**: Spider diagram showing the ACEMS-normalised mean concentrations of different elements in the RAT Rouge.*

N	LITHOLOGY	Mg	Al	Ca	Fe	Cu	K	Co	Ti	S	Mn	P	Na	Ba	V
266	Breccia (and)	1.24	1.43	1.08	1.81	1.39	1.64	0.76	1.18	0.29	1.59	1.13	1.64	1.21	0.81
762	Clay (and)	1.45	1.59	0.22	1.78	0.98	0.26	0.74	1.03	0.05	1.18	1.14	0.65	0.60	0.85
310	Dolomite (and)	1.46	1.36	0.73	1.47	0.75	0.21	0.55	1.12	0.07	0.94	1.08	0.89	0.71	0.79
906	Mudstone (and)	1.48	1.61	0.15	1.79	1.01	0.17	0.56	1.07	0.06	1.05	1.31	0.60	0.39	0.87
705	Sandstone (and)	1.49	1.63	0.19	1.75	1.11	0.25	0.66	1.05	0.06	1.09	1.01	0.65	0.42	0.83
6	Siltstone (and)	1.47	1.83	0.08	1.32	0.37	0.27	0.21	1.57	0.10	0.75	1.58	2.73	0.62	0.85

N	LITHOLOGY	Ni	Sr	Zn	La	Pb	U	W	Sc	As	Bi	Mo	Be	Ag	Cd
266	Breccia (and)	1.06	1.79	1.55	1.65	0.70	0.69	0.69	1.30	0.64	0.50	0.47	1.35	0.37	1.15
762	Clay (and)	1.12	0.55	1.22	1.35	0.42	0.56	0.61	1.49	0.57	0.57	0.25	1.52	0.28	1.08
310	Dolomite (and)	1.07	0.88	1.20	1.02	0.44	0.59	0.60	1.25	0.54	0.39	0.28	1.25	0.34	0.91
906	Mudstone (and)	1.17	0.51	1.23	1.17	0.42	0.58	0.68	1.51	0.64	0.46	0.24	1.52	0.32	1.14
705	Sandstone (and)	1.12	0.52	1.41	1.36	1.66	0.63	0.60	1.47	0.67	0.57	0.30	1.38	0.28	1.25
6	Siltstone (and)	1.10	1.55	0.73	1.73	0.09	0.54	0.58	1.38	1.06	0.28	0.22	1.33	0.23	1.68

***Figure 5.45**: Summary table showing the ACEMS-normalised mean concentrations of different elements in various lithologies within the RAT Rouge.*

5.3.2.10 Undifferentiated Breccias

Undifferentiated breccias are breccia lithologies which have not been assigned to a stratigraphic unit, either because they incorporate clasts from multiple stratigraphic units, or because they cross-cut the unit they are hosted in, or both. Polymict and composite varieties are most commonly logged, although some monomict breccias are also classified as 'Undifferentiated' (Figure 5.46). Ba is anomalously concentrated in these breccias (2.06x ACEMS) and Ca and S are close to anomalously high concentrations (both at 1.95x ACEMS). Ag is found in anomalously low concentrations (0.46x ACEMS) and W concentration is also below average (0.60x ACEMS) which is interesting as both appear to have an affinity for breccias assigned to the CMN unit (Section 5.3.2.1). All other elements analysed for, apart from Ag and W, appear to be enriched to above average levels in Undifferentiated Breccia, however (Figure 5.47). Cu is twice as concentrated in the composite/polymict breccia variety (1.12x ACEMS) than within the monomict breccia variety (0.56x ACEMS) with a mean of 1.39x ACEMS (Figure 5.48).

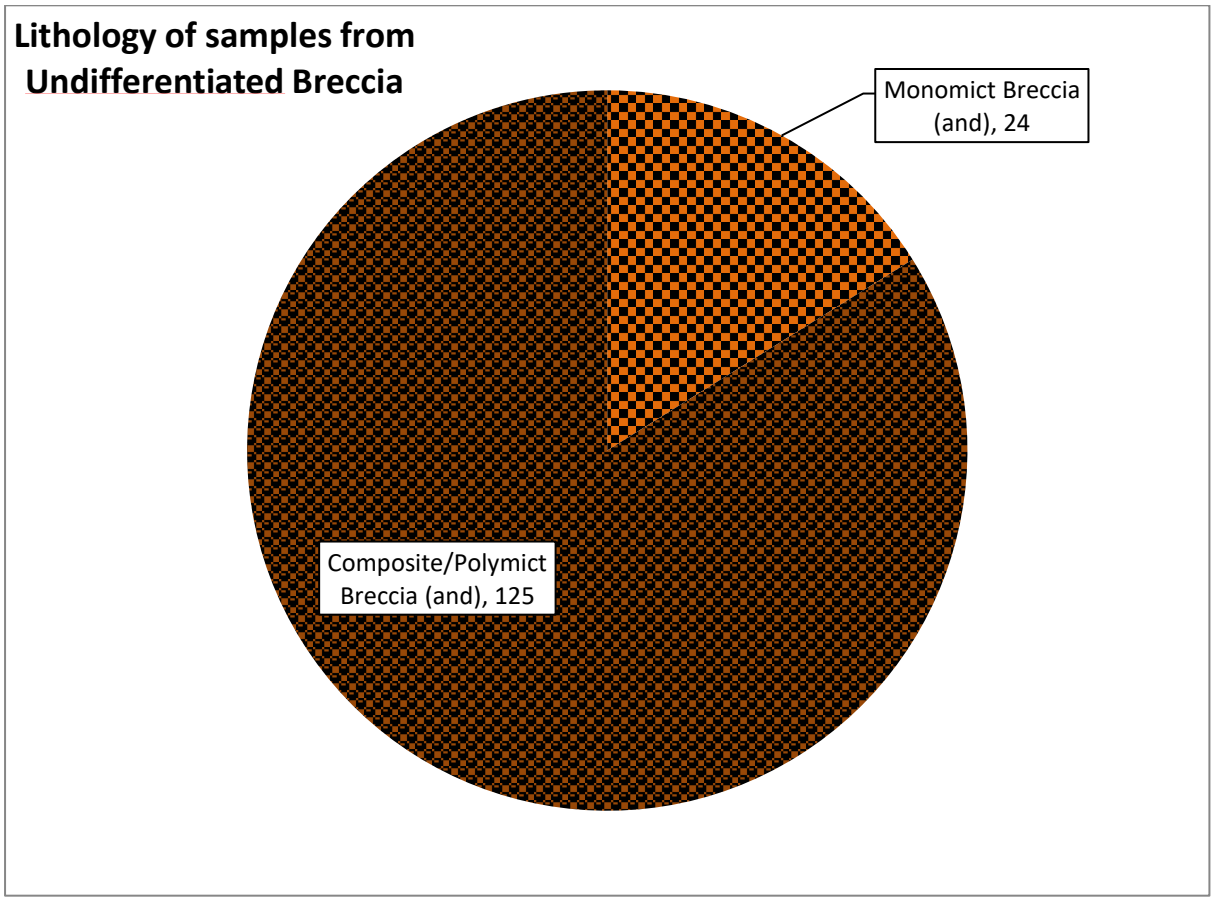

***Figure 5.46**: Pie chart showing the lithological composition of Undifferentiated Breccias.*

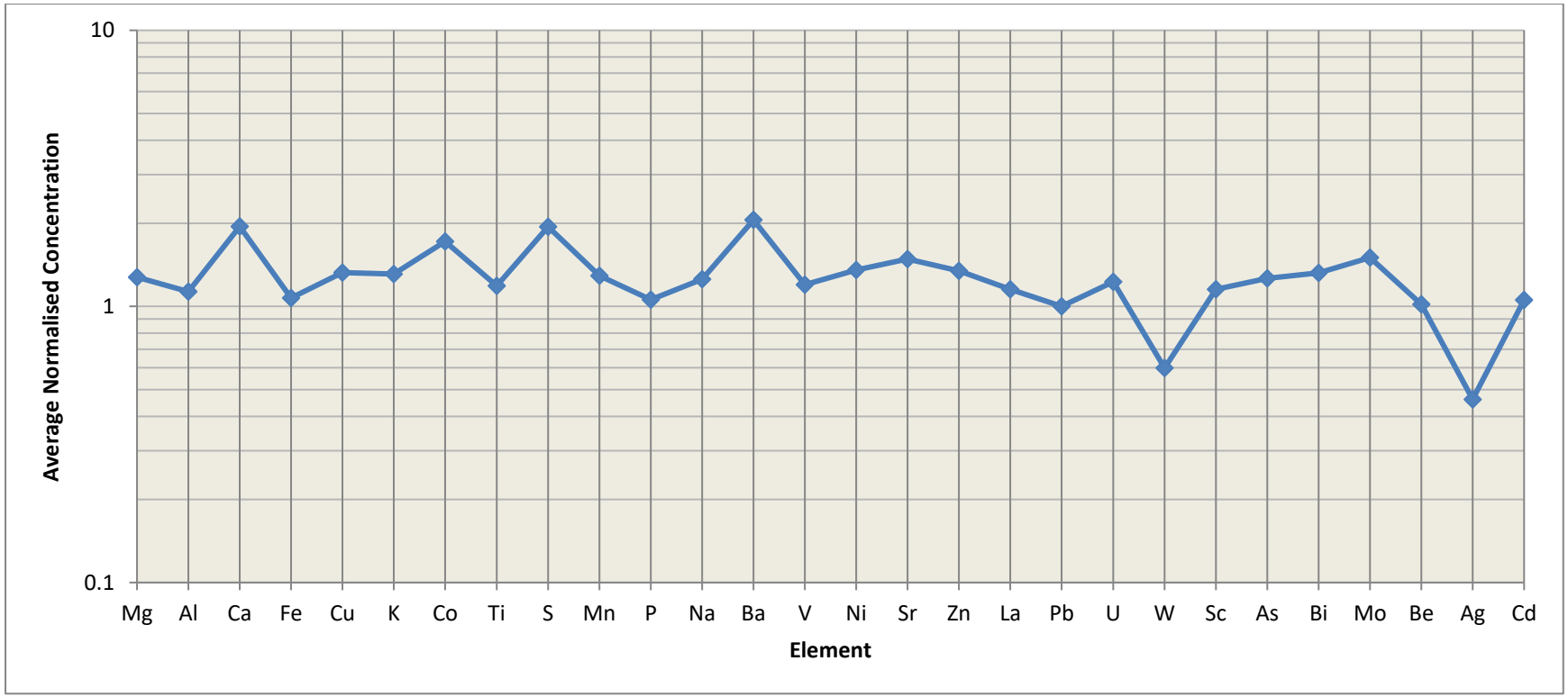

***Figure 5.47**: Spider diagram showing the ACEMS-normalised mean concentrations of different elements in Undifferentiated Breccias.*

N	LITHOLOGY	Mg	Al	Ca	Fe	Cu	K	Co	Ti	S	Mn	P	Na	Ba	V
24	Monomict Breccia (and)	1.32	0.97	2.60	0.84	0.56	1.52	1.29	1.08	1.60	1.08	1.19	1.16	1.01	0.81
125	Composite/Polymict Breccia (and)	1.28	1.19	1.78	1.10	1.12	1.25	1.79	1.24	1.56	1.24	1.02	1.31	2.07	1.27

N	LITHOLOGY	Ni	Sr	Zn	La	Pb	U	W	Sc	As	Bi	Mo	Be	Ag	Cd
24	Monomict Breccia (and)	1.34	1.02	0.99	0.48	0.54	0.79	0.70	0.93	1.30	0.39	1.06	0.95	0.28	1.15
125	Composite/Polymict Breccia (and)	1.39	1.55	1.42	1.36	0.98	1.18	0.58	1.21	1.18	1.40	1.19	1.05	0.50	1.05

***Figure 5.48**: Summary table showing ACEMS-normalised mean concentrations of different elements in various lithologies within Undifferentiated Breccias.*

5.3.3 Splitting the Data for Mashitu South by Depth

This section presents results obtained by splitting the combined database into subsets based on depth, independent of lithology and stratigraphy. This was done to assess the variation in elemental concentrations induced by weathering, leaching and supergene processes, with the assumption that rocks are more affected by these processes at shallower depths (closer to the surface).

5.3.3.1 Variation from depth to surface

To assess the variation in element concentration across the entire range of depths (D), samples from the combined database were split into 5 subsets. These subsets were based on expected intervals of intensity of supergene processes, based on the author's logging (see Chapter 3) or from literature.

1. D <10m: This subset was chosen to represent the greatest extent of supergene processes, where logging shows that weathering has turned the rock almost totally into saprolite, with the exception of the most resistant lithologies such as highly siliceous rock.
2. 10m≥ D <50m: This subset was where the majority of advanced argillic alteration could be found in the holes examined. However, unlike the top 10m, much of the rock in this depth interval was still recognisable and not saprolitic.
3. 50m≥ D <100m: Argillic alteration was still found to occur occasionally within this interval in the logged holes, and Decree *et al.* (2010) states 100m to be roughly the depth limit for the occurrence of supergene mineralisation in Katanga.
4. 100m≥ D <200m: Logging identified occasional supergene mineralisation and argillic alteration in this interval, particularly in proximity to breccias or the RSC, but not restricted to these zones. The vast majority of rock in this interval appears to be unweathered.
5. D > 200m: Minimal evidence of supergene alteration found during logging of this interval, restricted totally to within the proximity of breccias and the RSC.

The mean of the element concentrations from each of these subsets was taken and normalised to ACEMS. The results of this process are given in Figure 5.49 and graphically represented in Figure 5.50.

From analysing these results, we can see that element variation between these datasets may take one of several forms:

1. Progressive depletion with depth: This is observed in a few 'depth-sensitive' elements, where the highest average concentrations are found in the shallowest depth interval, and the lowest concentrations are found in the highest depth interval. Ca, S, Sr and to a lesser extent, Mg, Ba and U display this quality. U is slightly different in that the progressive depletion occurs in the lowest two depth intervals (>100m depth). Above this (<100m), average U concentration seems to stay at the same, low level.
2. Progressive enrichment towards the surface: A few elements show apparent enrichment towards the surface, with lower average values at depth. La, W, Bi, Mo, Co and, to a lesser extent, Ag exhibit this quality.
3. Little variation between depth intervals: Al, Ti, Sc and, to a lesser extent, Mn show little variation in their concentrations between different depth intervals, with no consistent relationship between depth and concentration in what little variation they do show.
4. Inconsistent enrichment/depletion between depth intervals: Certain elements show enrichment/depletion at different depth intervals which shows no consistent relationship with depth. Cu, for example, is most concentrated in the 10-50m depth interval, with moderate values in the intervals deeper than this, and is most depleted in the <10m interval. Be, P, Ni and Fe are similar in that they are neither consistently depleted nor enriched with increasing depth.

If the >200m and <10m depth intervals are compared, it becomes apparent that the following elements are depleted by the weathering process: Mg, Ca, Cu, K, S, P, Ba, Ni, Sr, Zn, U, As, Be and Cd; and the following elements show apparent enrichment: Al, Fe, Co, Ti, Mn, Na, V, La, Pb, W, Sc, Bi, Mo and Ag.

N	DEPTH INTERVAL	Mg	Al	Ca	Fe	Cu	K	Co	Ti	S	Mn	P	Na	Ba	V
1036	<10m	0.28	0.84	0.01	0.93	0.22	1.05	1.28	1.05	0.07	1.22	0.35	1.07	0.54	1.35
4108	10-50m	0.94	1.18	0.11	1.30	1.33	0.59	1.08	1.01	0.09	1.21	0.99	0.87	0.53	1.02
2928	50-100m	1.20	0.98	1.32	1.03	0.74	0.93	0.63	0.92	0.39	0.85	1.02	0.98	0.80	0.83
3047	100-200m	1.06	0.89	1.84	0.70	1.04	1.47	1.14	1.04	2.04	0.84	1.21	1.17	1.76	1.04
938	>200m	1.24	0.83	2.29	0.65	1.09	1.43	1.04	1.01	4.57	0.81	1.03	1.02	1.73	0.91

N	DEPTH INTERVAL	Ni	Sr	Zn	La	Pb	U	W	Sc	As	Bi	Mo	Be	Ag	Cd
1036	<10m	0.52	0.42	0.50	1.29	1.11	0.64	1.54	1.00	1.09	2.05	1.54	0.58	1.39	0.96
4108	10-50m	0.88	0.50	1.16	1.18	1.09	0.59	1.15	1.16	0.97	1.03	1.03	1.26	0.87	1.04
2928	50-100m	0.93	1.15	1.19	0.91	0.90	0.58	1.12	0.97	0.83	0.65	0.67	1.01	1.97	1.00
3047	100-200m	1.32	1.53	0.86	0.83	0.98	1.42	0.63	0.86	1.11	0.97	1.03	0.87	0.34	0.94
938	>200m	1.24	1.64	0.71	0.71	0.85	3.14	0.58	0.83	1.23	0.87	1.18	0.69	0.25	1.08

***Figure 5.49**: Summary of ACEMS-normalised mean element concentration at different depth-intervals.*

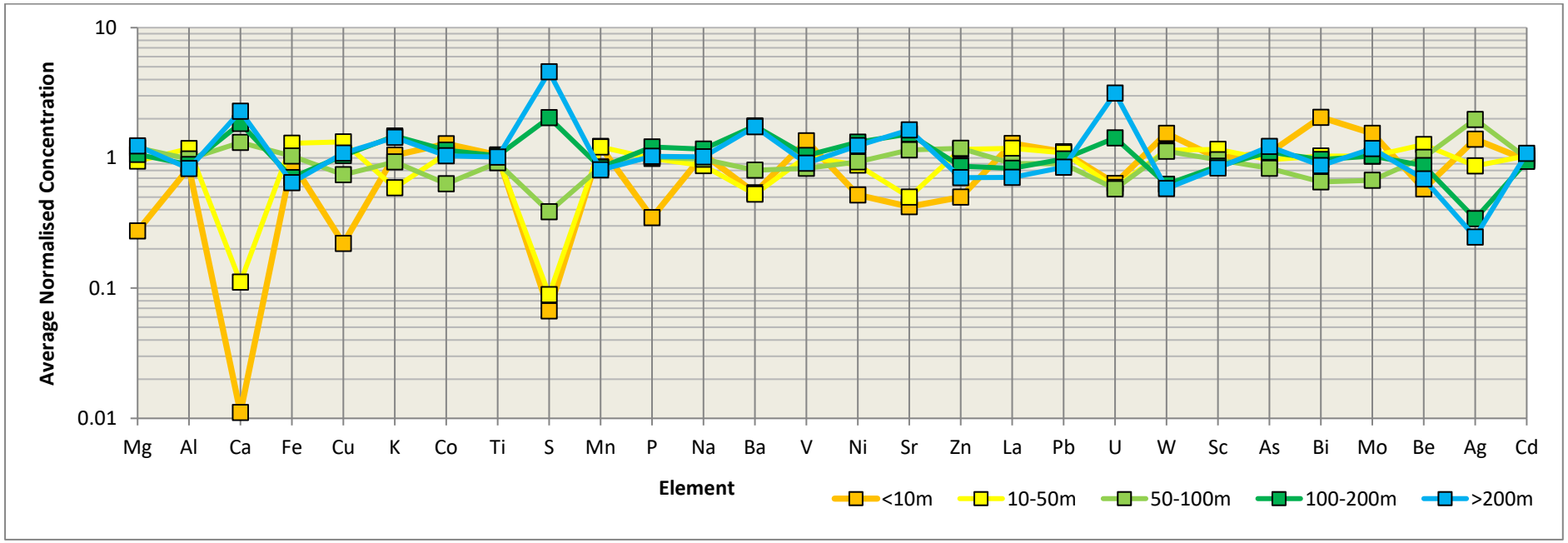

***Figure 5.50**: Spider diagram showing the data presented in Figure 5.49.*

5.3.3.2 Near-surface variation

The effect of supergene processes on the concentration of elements which are more resistant to leaching was hypothesised to be most apparent in the top 10m of the profile. Variation in this subset was also thought to be important in understanding the geochemical changes which occur to turn rock into soil, which would help in the interpretation of soil geochemical data (see Chapter 6). To this end, the 1036 samples from the database from the top 10m were further split into ten 1m depth intervals to understand the near surface geochemical variation at Mashitu South. The results of ACEMS-normalisation for selected elements, which were hypothesised to be potentially related to Cu-Co mineralisation, are presented as Figure 5.51 and graphically represented as Figure 5.52.

N	DEPTH INTERVAL	Fe	Cu	Co	V	Ni	Zn	Pb	U	W	As	Bi	Mo	Ag
41	<1m	1.12	0.08	0.95	1.46	0.42	0.57	1.17	0.65	1.16	1.39	3.11	1.54	1.19
93	1-2m	1.17	0.08	1.22	1.58	0.53	0.50	1.20	0.58	1.39	1.38	2.73	1.33	1.60
96	2-3m	1.02	0.08	1.24	1.41	0.45	0.49	1.46	0.56	0.85	0.94	2.22	1.10	0.99
112	3-4m	0.85	0.12	1.18	1.36	0.46	0.42	0.91	0.54	2.38	0.89	2.08	0.97	1.70
113	4-5m	0.92	0.33	1.41	1.45	0.51	0.43	1.09	0.62	1.81	1.01	2.53	1.37	1.10
116	5-6m	0.91	0.36	1.27	1.29	0.48	0.50	1.02	0.62	1.85	0.98	2.14	1.30	1.66
117	7-8m	0.94	0.19	1.34	1.37	0.55	0.49	1.05	0.70	0.90	1.19	1.80	2.44	0.63
110	8-9m	0.80	0.18	1.39	1.28	0.61	0.56	1.06	0.71	2.04	1.06	1.57	1.83	2.01
122	9-10m	0.83	0.37	1.22	1.20	0.55	0.57	1.08	0.62	1.19	1.12	1.58	1.41	1.40

***Figure 5.51**: Summary of ACEMS-normalised mean element concentrations within 1m depth intervals from the top 10 of core from Mashitu South.*

As we can see from these two figures, certain elements, including, Cu, Ni, Zn and U, are highly depleted throughout the near-surface profile. Cu in particular is progressively depleted from surface, with the lowest values found in the top 3m. Many other elements are enriched in the top 10m, and certain elements show progressive enrichment towards the surface including Bi, Fe and V. Other elements, such as W, appear to show enrichment at some interval below the surface (in this case, between 3 and 9m). Interestingly, Co shows a slight depletion in the top 1m of the profile

Another way this variation can be presented is as a line plot treating each different element as a line series, which was done with selected elements deemed to be associated with hypogene mineralisation, combined with the datasets for element variation below 10m and given as Figure 5.53.

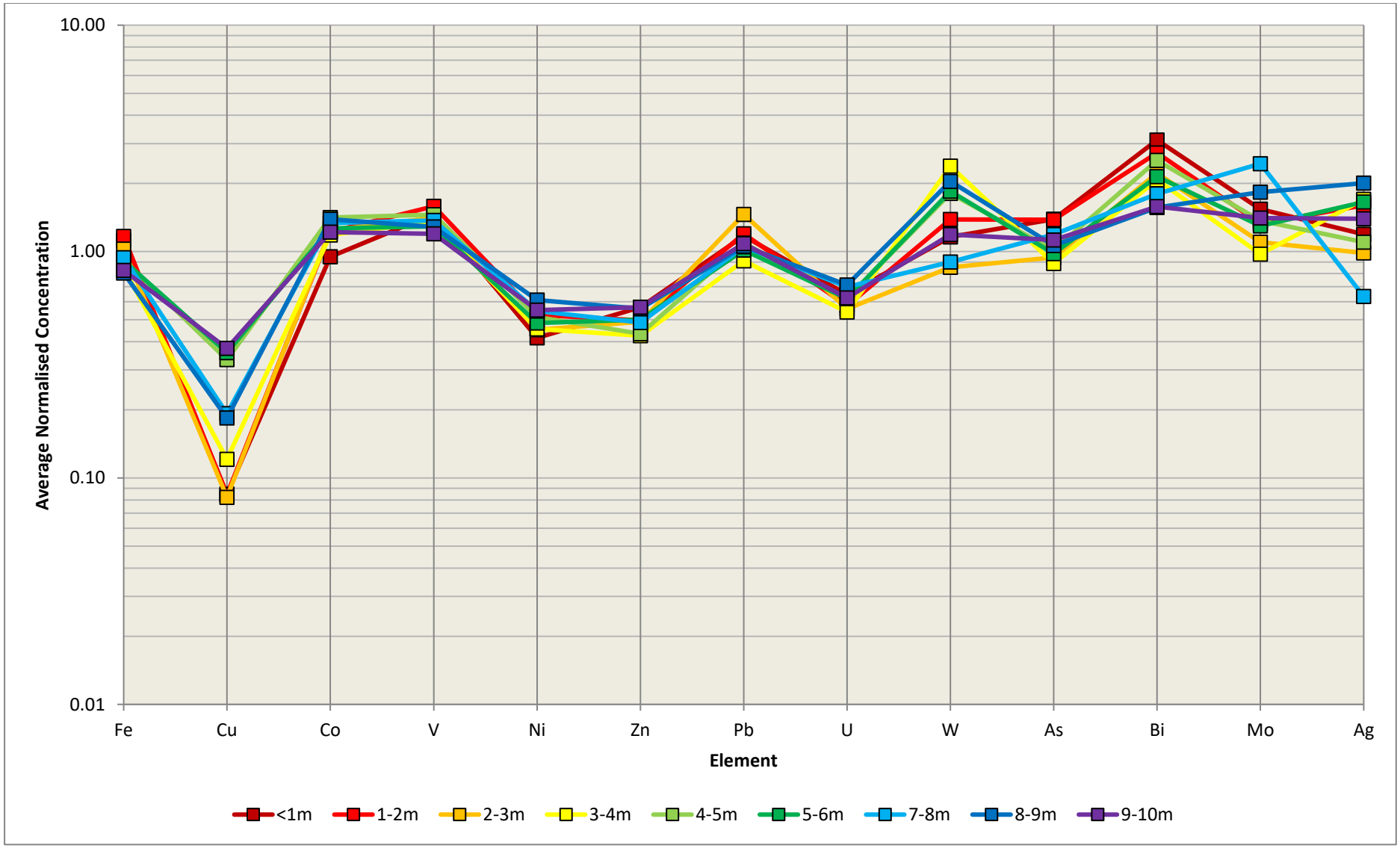

***Figure 5.52**: Spider-graph of ACEMS-normalised concentrations of elements at different depth intervals in the top 10m of drill core at Mashitu South.*

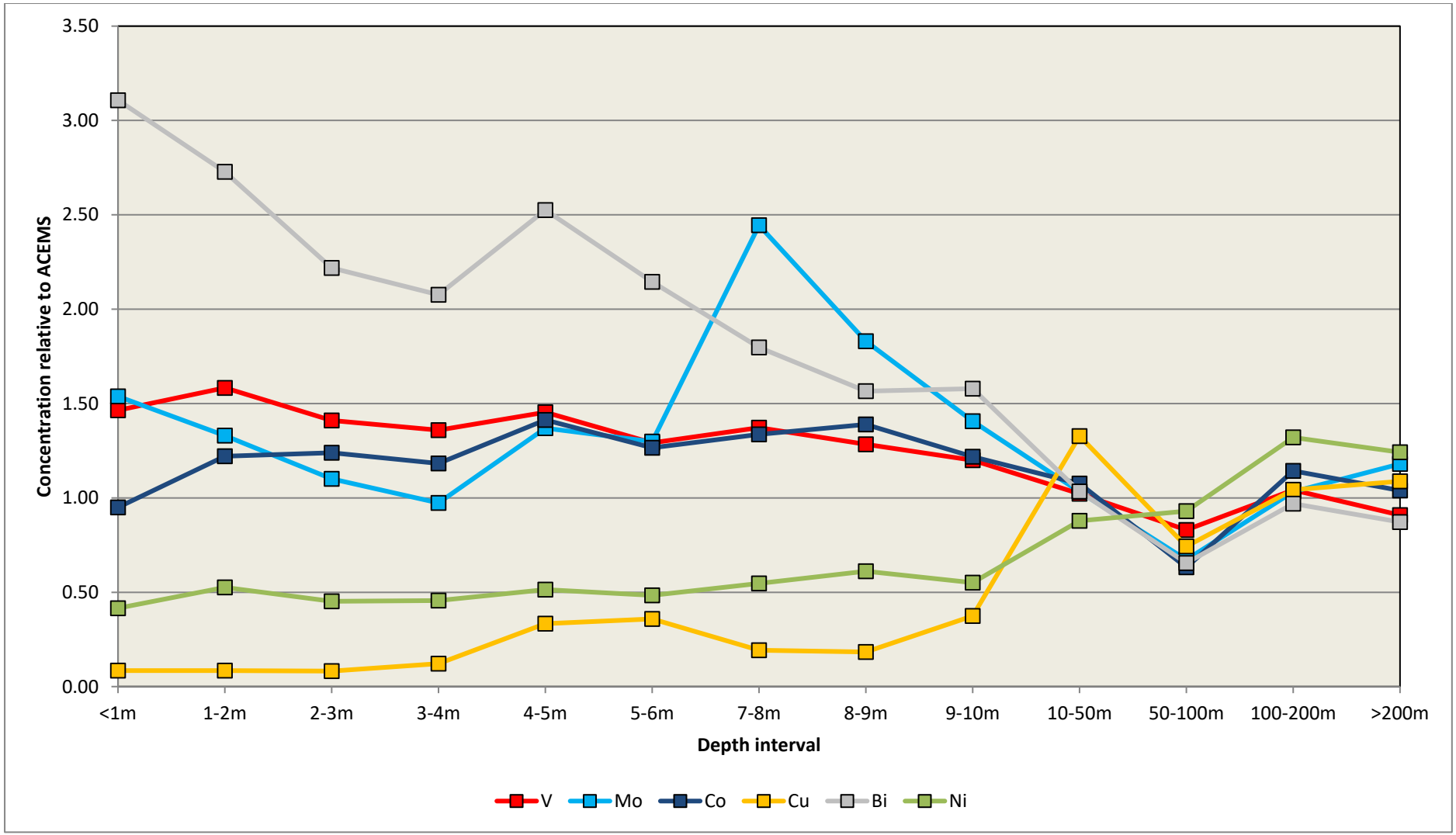

Figure 5.53*: Line graph showing variation of the mean concentrations of selected elements normalised to ACEMS (represented as line series) at different depth intervals.*

Figure 5.53 shows us the progressive depletion of copper in the near surface profile, which continues until the 10-50m dataset, where it is found to be significantly enriched above ACEMS, before returning to fairly average concentrations in datasets below 50m. Cobalt, by contrast, appears to be most enriched between a depth of 1 and 10m, with a very slight depletion relative to ACEMS in samples with a mid-point depth of less than 1m. Mo shows an apparent enrichment in the 7-8m depth interval. Bi shows the highest surface-enrichment of any of the elements analysed, showing a trend of progressive enrichment towards the <1m interval where it is more concentrated than within any other interval in the dataset.

4.3.4 Analysing the four logged holes: MSSD075, 080, 083 and 140

5.3.4.1 Stratigraphy – the Sr : Sc ratio

The stratigraphy of MSSD075, 080, 083 and 140 is already well understood through logging (see Chapter 3). However, attempts to investigate geochemical indicators for different primary lithologies and stratigraphies were made. The most successful of these was an effort to find a method of geochemically distinguishing between primary and secondary (i.e. dolomitised) dolomites. In particular, during logging, the S.D. unit was not well understood to be a primary siliciclastic/argillaceous sequence, having an apparently bulk dolomitic composition on testing with acid (supported by the geochemical assay compositions). After petrographic analysis (see Chapter 4), the primary siliciclastic nature of the S.D. was confirmed. To distinguish between units of primary and secondary dolomite, and therefore the amount of siliciclastic vs. calcareous sedimentary input, several element ratios were considered and tested. Sr:Sc ratios were eventually found to be effective. Strontium is primarily concentrated by chemical sedimentation in calcareous rocks, substituting mainly for Ca in calcite or aragonite (Kulp *et al.*, 1951), whereas scandium concentrates in siliciclastic rocks, where it readily adheres to the surface of clay minerals (Birgul, 1981). Both elements are found in very small quantities at Mashitu South, with ACEMS values of 34ppm (Sr) and 8ppm (Sc).

Sc is mostly immobile in hydrothermal fluids (Iain and Chassé, 2016) and Sr concentration in carbonates is most influenced by conditions during primary carbonate deposition, with the highest Sr concentrations intimately associated with primary

carbonates (Mielke, 1979). Low concentrations of Sr (<~0.1%) tend to be relatively unaltered by the passage of low-temperature hydrothermal fluids, especially where the hydrothermal fluids are evaporitic in nature and contain high concentrations of Sr (Mucci and Morse, 1990) – partly because of the partition coefficient effect – causing instead the preferential mobilisation of calcium from material surrounding Sr-bearing phases (Morse and Bender, 1990). Sr is known to be highly mobile in a surficial weathering environment (Taylor, 1964). However, at Mashitu South, its average relative concentration seems to be much less affected than that of Ca by proximity to surface (Figure 5.50), with the difference in relative concentration enrichment/depletion between all depth intervals for Ca being >3 orders of magnitude, while for Sr this is difference is <1 order of magnitude. Sr and Sc are therefore suggested as being less mobile during secondary alteration events at Mashitu South than other elements indicative of calcareous vs siliciclastic input (such as Ca and Ti), and are used here as a guide to primary sedimentary input and an aid to correlation between stratigraphic units.

Figure 5.54 shows depth profiles of Sr:Sc in holes MSSD075, 080, 083 and 140. Consistent patterns are shown by the Sr:Sc ratios in each hole. A high but extremely variable Sr:Sc characterises the C.M.N., which drops to distinctly low values within the S.D. and is at the lowest within the S.D.2d. In MSSD080, Sr:Sc increases downhole to the bottom of the CMN, in contrast with values in the CMN for MSSD075 and 083, possibly reflecting a higher degree of weathering at this interval in hole 080. Reasonably high Sr:Sc is also seen in the R.S.C. and D.Strat units, with a drop in the R.S.F. in between. The lowest Sr:Sc ratios are observed in the R.A.T., best observed in hole MSSD140. The Sr:Sc ratio corresponds well with the interpreted environments of deposition for each unit in terms of their expected calcareous : siliciclastic sedimentary input (see Chapter 3).

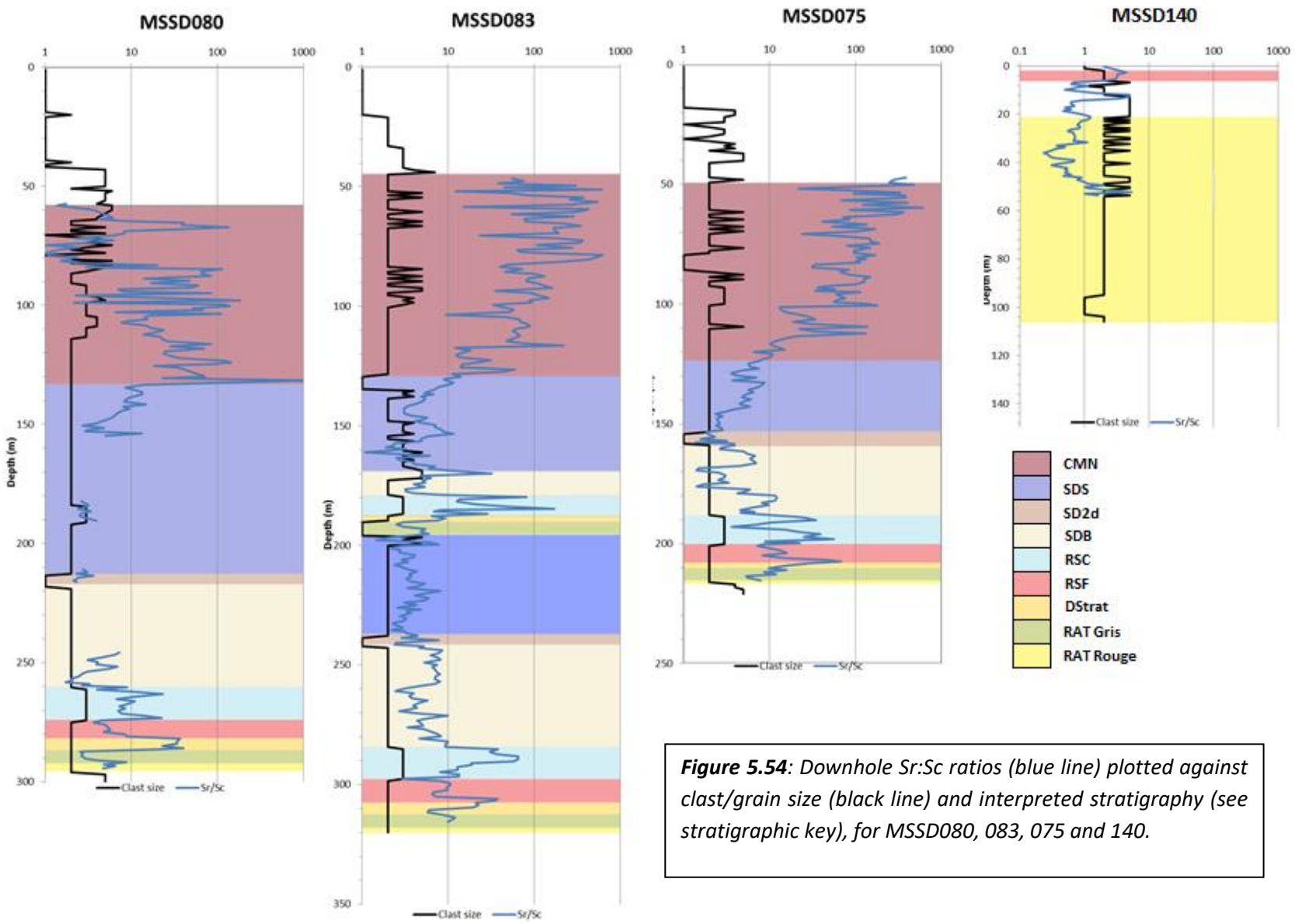

***Figure 5.54**: Downhole Sr:Sc ratios (blue line) plotted against clast/grain size (black line) and interpreted stratigraphy (see stratigraphic key), for MSSD080, 083, 075 and 140.*

5.3.4.2 Alteration

Dolomitisation, silicification, haematisation and argillic alteration were positively identified during core logging. However, studies of the geochemistry of MSSD075, 080, 083 and 140 also revealed that potassic alteration may also be present.

Dolomitisation and magnesian alteration are indicated by several lines of evidence. First, by examination of the ACF ternary diagram for certain stratigraphic intervals (Figure 5.55), it is observed that calcareous lithologies often display a trend from the expected ACF ratios for carbonates towards higher values of F (=[FeO + MgO + MnO]), suggesting input of Mg (or Fe or Mn). Another way of looking at the geochemistry of dolomitisation is through the use of scatter plots. A positive correlation can be seen to occur throughout the data between Ca and Mg. Plotting the two against each other within the CMN (Figure 5.56) reveals several trends. First, a mineralogical limit on the amount of Ca in the system is observed, based on a consistent ratio of about 3:2 Ca:Mg represented by a linear trend in the data, below which there are no samples with a higher Ca:Mg ratio. This 3:2 ratio corresponds to magnesian calcite and may represent the original geochemistry of the calcareous sedimentary rock. Another trend exists in the CMN where the Ca:Mg ratio remains at roughly 1:1, which corresponds to dolomite, possibly an alteration of the primary geochemistry. The third trend corresponds to the existence of high Mg, low Ca samples. Along this trend, Mg and Ca have an apparently negative correlation, and it is possible that this trend represents the growth of magnesium aluminosilicates which do not include calcium, such as chlorite.

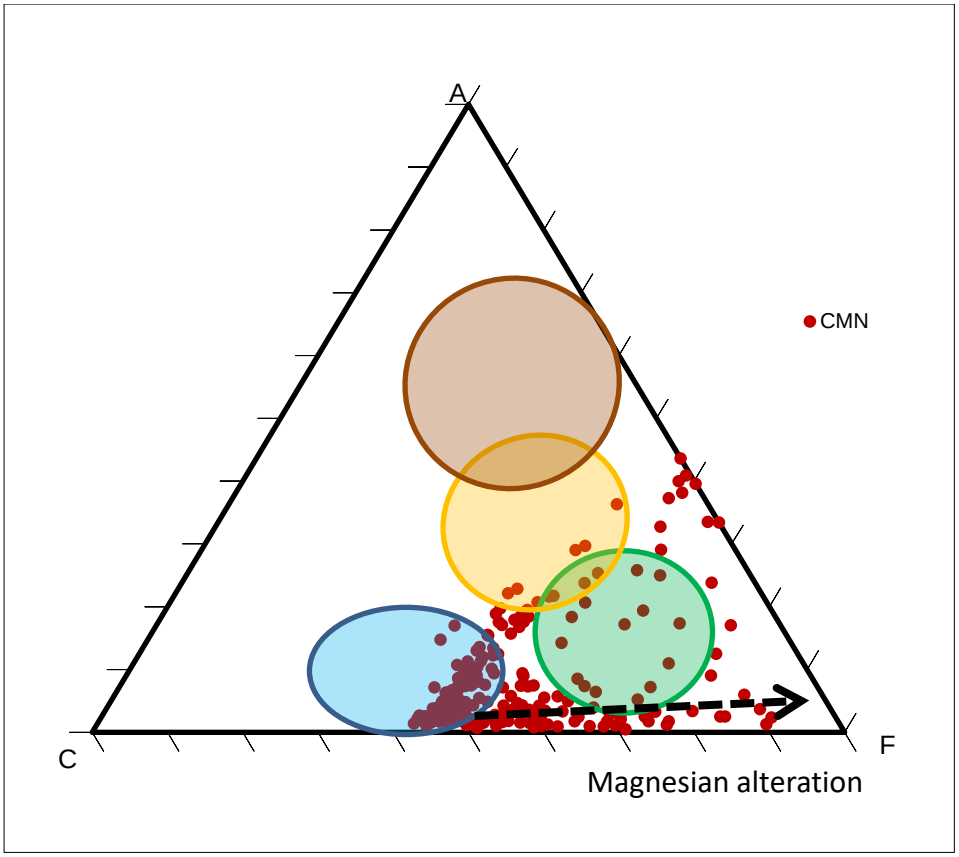

Figure 5.55*: ACF ternary diagram for CMN samples in MSSD075, 080 and 083 showing a trend from originally calcareous rocks towards increasing values of F. Fields in which calcareous rocks (blue), basic rocks (green), quartzo-feldspathic rocks (orange) and pelitic rocks (brown) would be expected to plot are shown on the diagram.*

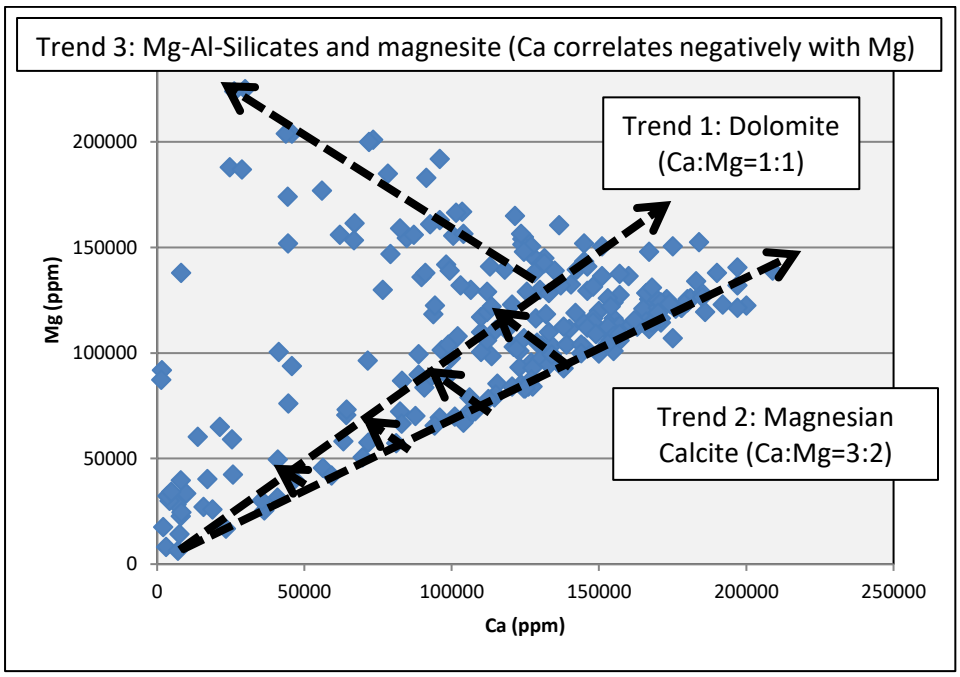

Figure 5.56*: Scatter plot of Mg and Ca concentration in CMN samples in MSSD075, 080 and 083 showing three different trends of Ca and Mg variation. Trends are explained in the text.*

This growth of magnesium-aluminosilicates can also be observed within the SDS, where a scatter plot of Mg vs. Al reveals two separate trends (Figure 5.57). The first trend shows a negative correlation between Mg and Al, which reflects variations in calcareous vs. siliciclastic sedimentary input. The second trend hints at a co-existing positive correlation within the SDS between the two elements, strongly indicative of the growth of Mg-Al-silicates such as chlorite during magnesian alteration.

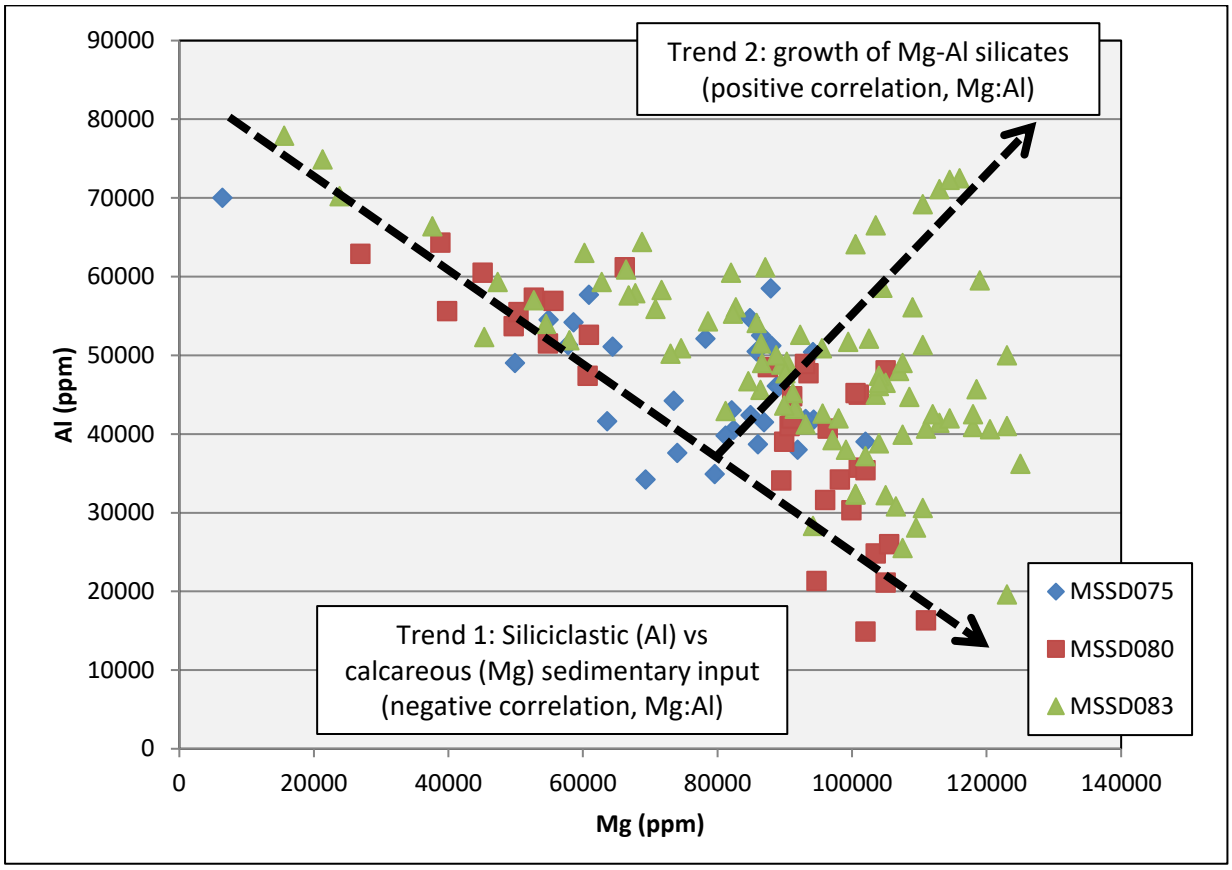

***Figure 5.57**: Scatter plot of Mg and Ca concentration in SDS samples in MSSD075, 080 and 083 showing two different trends of Mg and Al variation.*

Silicification is also apparent within several stratigraphic units in the logging of MSSD075, 080, 083 and 140, notably the RSC, RSF and selected horizons within the CMN. Plotting an ACF ternary diagram for the RSC (Figure 5.58) reveals a trend from an originally calcareous composition, towards a decreasing C value, with no change in the A:F ratio. This would suggest that C (CaO) is being removed without enrichment of any of the elements which make up A and F, and the only major rock component not accounted for by the ACF diagram is SiO_2. Therefore, this trend is probably indicative of silicification.

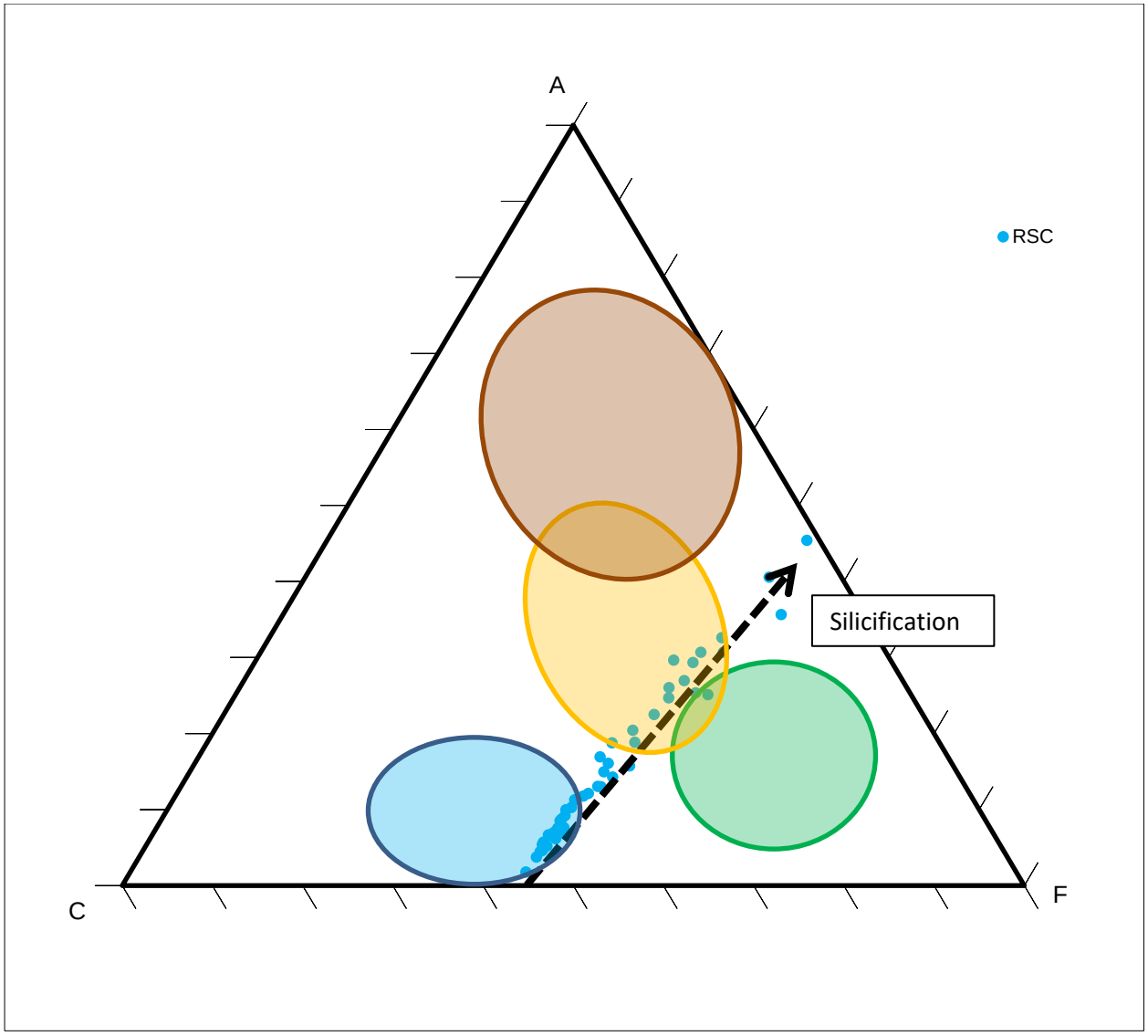

Figure 5.58*: ACF ternary diagram for RSC samples in MSSD075, 080 and 083 showing a trend from originally calcareous rocks towards decreasing values of C, with little change in the F proportions. Fields in which calcareous rocks (blue), basic rocks (green), quartzo-feldspathic rocks (orange) and pelitic rocks (brown) would be expected to plot are shown on the diagram.*

Potassic alteration is inferred from an overwhelming concentration of potassium in the S.D. unit, with the element most concentrated within the S.D.2d. Almost perfect correlations between K and Al with a K=Al 1:1 concentration within certain lithologies (Figure 5.59) suggest the development of K-feldspar ($KAlSi_3O_8$) or biotite ($K(Mg,Fe)_3(AlSi_3O_{10})(F,OH)_2$). It is theoretically possible for the potassium to be sedimentary as part of an arkosic rock, but this would be contradictory to the regionally accepted environment of deposition of the S.D. being a deepening-water shale sequence (Bull *et al.*, 2010; 2011). See Figure 5.59.

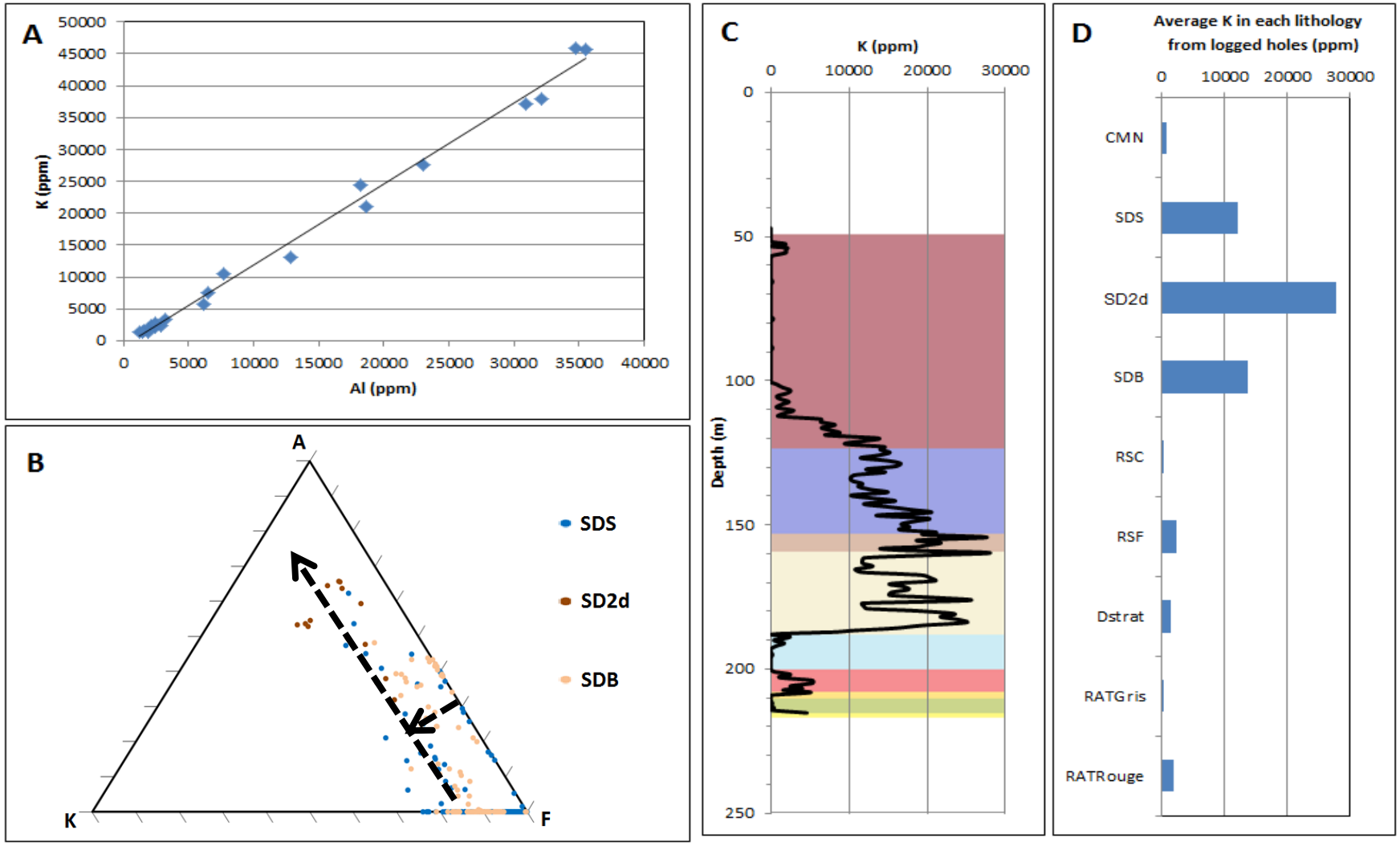

Figure 5.59*: Evidence for potassic alteration in the Mines Subgroup at Mashitu South.* ***A****: high positive correlation between K and Al in hole MNWR016, with nearly a 1:1 relationship between concentrations of the two elements.* ***B****: AKF diagram showing a trend of alteration of S.D. samples towards higher K and A values.* ***C****: depth profile for K with stratigraphy in MSSD075.* ***D****: Average K contents of each stratigraphic unit in MSSD075, 080, 083 and 140.*

The effect of supergene alteration in the samples from MSSD075, 080, 083 and 140 was assessed by comparative study. In hole MSSD140, a very weathered version of the RSF stratigraphic unit was identified right at the top of the profile, between a depth of 1 and 5m. In MSSD075, 080 and 083, however, the RSF is found at a depth of >200m. This disparity in depths made splitting the dataset between these holes and comparing them (MSSD140, and 075, 080 and 083) a good study for assessing the effects of supergene and advanced argillic alteration. The effect of advanced argillic alteration is evident in an ACF diagram of all the samples in these holes (Figure 5.60). The original RSF protolith, thought to be an algal, calcareous limestone of some sort with minor argillic components, has undergone varying degrees of silicification in all of the samples resulting in a drop in the C value. Samples in MSSD140, however, have undergone a subsequent increase in the A:F ratio as a result of leaching.

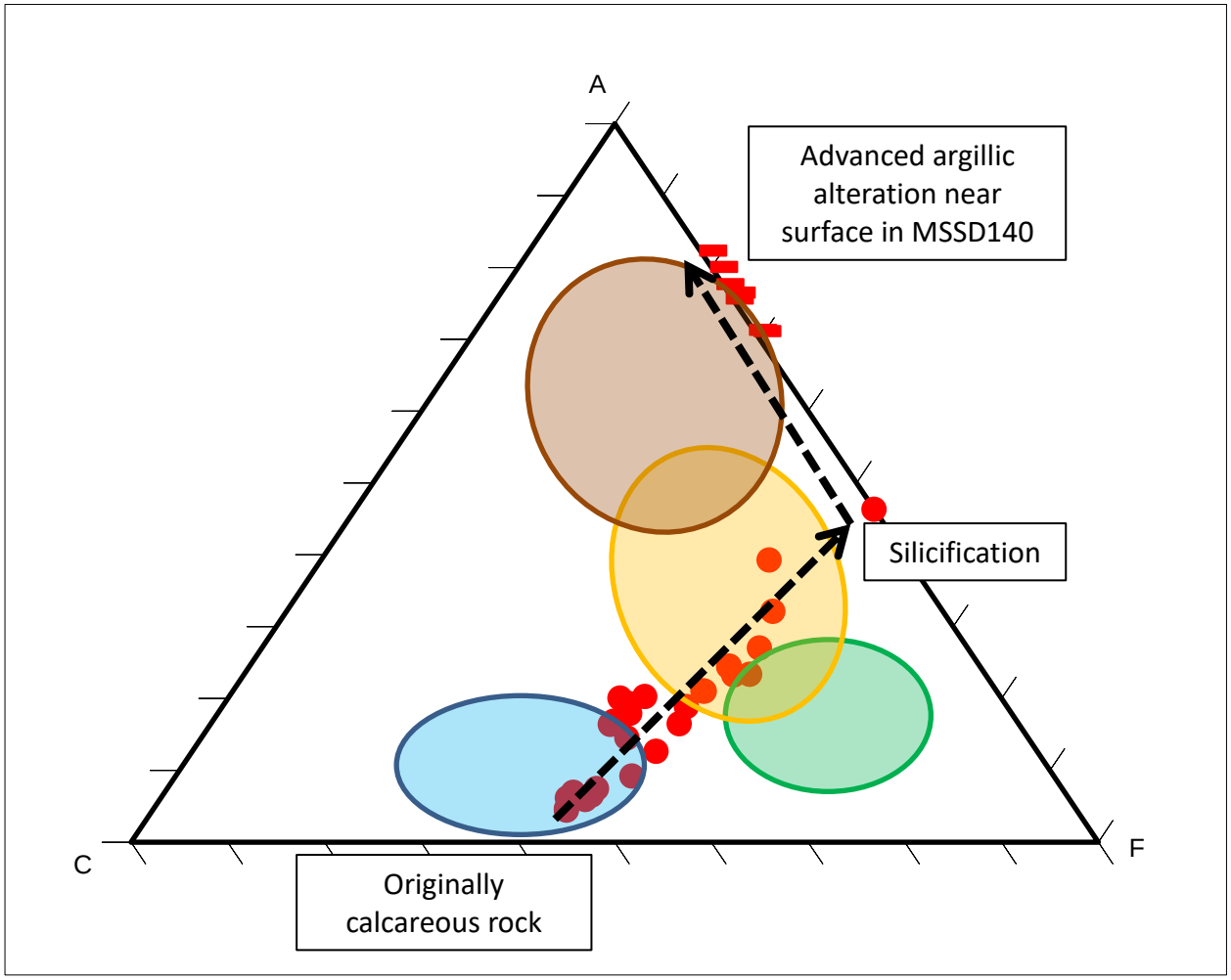

Figure 5.60*: ACF ternary diagram for RSF samples in holes MSSD075, 080 and 083 (symbolised as red dots) and MSSD140 (red bars), showing progressive silicification and subsequent argillic alteration.*

The effects of supergene alteration were also seen when comparing the geochemical datasets for the two groups of RSF samples in a manner similar to the techniques used in Section 5.3.3. Weathered RSF samples in MSSD140 were found to have increased concentrations of Al, K, Ti, Mn, La, Sc and Bi, and decreased concentrations of Mg, Ca, Fe, Cu, S, Co, P, Ba, Na, V, Ni, Sr, Zn, Pb, As, Be and Mo, relative to less-weathered RSF samples from MSSD075, 080 and 083.

5.3.4.3 Cu Mineralisation: geochemical associations

Copper was found to correlate well with several different elements in different stratigraphic units within MSSD075, 080, 083 and 140. To assess the relative strength of these correlations, their R-values within each stratigraphic unit were added up and compared (Figure 5.61). It was found that Co, Bi, Ni, Be, V, S, Fe, Mo, P, As and Zn displayed significant R-values when their Pearson correlation with copper was assessed. However, these correlations indicate elements which are associated with all types of Cu mineralisation, without distinguishing between the stratiform, vein-type and supergene mineralisation distinguished by logging (see Chapter 3). The geochemical distinction between these mineralisation types, or at least hypogene and supergene types is important for exploration and exploitation purposes.

A quick check to compare hypogene and supergene mineralisation processes is to compare correlations between Cu and other elements in the RAT Rouge, where the only mineralisation found to exist by logging was of para-exotic supergene type, and in the units of the Mines Subgroup, where logging found mineralisation to be transitional between hypogene and supergene. Comparing these two stratigraphies in Figure 5.61 shows that out of the 11 associated elements identified over the whole deposit, Be and P show the best correlation with Cu within the RAT Rouge. K also shows a significant correlation with Cu in this column, however it does not correlate well with Cu over the whole database (and is found at extremely low concentrations in the RAT) so it is rejected as a geochemical associate of copper. This would suggest that Cu has a Be-P association in relation to supergene mineralisation, and that Co, Bi, Ni, V, S, Fe, Mo, As and Zn are associated with hypogene mineralisation.

	CMN	SDS	SD2d	SDB	RSC	RSF	DStrat	RATGris	RAT Rouge	Sum of R-values
Al	0.19	0.12	0.03	0.22	0.67	0.61	0.14	-0.42	-0.65	0.90
As	0.11	0.37	0.37	0.14	0.39	0.26	-0.25	0.39	0.23	2.00
Ba	0.01	-0.08	0.13	-0.01	-0.04	0.05	0.31	0.01	-0.26	0.12
Be	0.22	0.46	0.60	0.48	0.49	0.71	0.20	0.08	0.62	3.86
Bi	0.86	0.80	-0.24	0.67	0.57	0.51	-0.15	0.85	0.28	4.15
Ca	-0.22	-0.40	-0.32	-0.60	-0.19	-0.63	-0.01	0.00	-0.27	-2.64
Co	0.42	0.85	0.09	0.68	0.63	0.63	0.35	0.94	-0.09	4.49
Fe	0.44	0.34	0.76	0.11	0.70	0.38	0.27	0.32	-0.28	3.05
K	0.10	-0.18	-0.07	-0.49	0.18	-0.22	-0.18	-0.27	0.53	-0.58
La	-0.07	-0.16	0.17	-0.12	0.14	-0.54	-0.21	-0.29	-0.14	-1.21
Mg	-0.29	-0.07	-0.34	-0.14	0.14	-0.56	-0.22	-0.64	-0.69	-2.82
Mn	0.12	-0.18	-0.33	-0.44	-0.15	-0.43	0.11	0.08	-0.36	-1.58
Mo	0.02	0.30	0.50	0.39	0.43	0.53	-0.11	0.59	-0.10	2.54
Na	0.21	-0.04	-0.09	0.09	0.01	-0.11	0.58	0.16	-0.18	0.64
Ni	0.14	0.68	0.44	0.61	0.43	0.59	0.28	0.91	-0.02	4.05
P	0.08	-0.04	0.44	-0.12	0.48	0.43	0.26	0.15	0.41	2.10
Pb	0.38	-0.08	0.47	0.35	0.10	0.47	-0.07	0.23	-0.46	1.39
S	0.51	0.79	-0.16	0.32	0.82	0.73	0.11	0.54	-0.18	3.48
Sc	0.23	0.08	0.27	-0.13	0.37	0.76	0.28	-0.48	0.11	1.49
Sr	-0.11	-0.19	0.01	-0.07	-0.11	-0.55	0.28	-0.15	-0.34	-1.24
Ti	0.09	-0.08	-0.22	-0.09	0.69	0.67	0.10	-0.54	-0.39	0.22
V	0.40	0.62	0.28	0.63	0.47	0.64	0.24	0.09	0.36	3.73
Zn	0.26	0.08	0.40	0.06	0.37	0.35	0.17	0.20	0.05	1.94

	Sum of R-values, Ranked
Co	4.49
Bi	4.15
Ni	4.05
Be	3.86
V	3.73
S	3.48
Fe	3.05
Mo	2.54
P	2.10
As	2.00
Zn	1.94
Sc	1.49
Pb	1.39
Al	0.90
Na	0.64
Ti	0.22
Ba	0.12
K	-0.58
La	-1.21
Sr	-1.24
Mn	-1.58
Ca	-2.64
Mg	-2.82

Figure 5.61*: Table of correlations between Cu and other elements in the various lithologies of MSSD075, 080, 083 and 140. R-values for the Pearson value for each correlation with Cu are displayed along the rows corresponding to each element. These values are colour coded as explained in Section 5.2.5. The sum of the R-values in each stratigraphic unit are included in the 'Sum of R-values' column, and these are ranked and colour coded separately in the right-most column. It can be observed that Co, Bi, Ni, Be, V, S, Fe, Mo, P, As and Zn correlate significantly over all of the stratigraphic datasets. Assessing the RAT Rouge stratigraphic column, we see that Be, P and K correlate well with Cu. Be and P are inferred to be associated with supergene Cu mineralisation in the RAT, while Co, Bi, Ni, V, S, Fe, Mo, As and Zn are inferred to be associated with hypogene Cu mineralisation in the Mines Subgroup.*

5.3.5. U Mineralisation: Distribution and Geochemical Associations

The presence of oxide minerals of uranium within the RSC of MSSD083 was identified during logging (see Figure 3.36). The extent of this mineralisation was investigated geochemically by searching for samples which contained >0.01% (100ppm) U, judged as a grade of interest for U concentration at U deposits (Douglas *et al.*, 2003). A total of 65 samples containing >100ppm U were identified from 10 holes in the Mashitu South combined database, all of which are on the eastern flank of the Mashitu South Mines Subgroup fragment (see Figure 5.62). These 10 holes are: MSSD072, 075, 079, 080, 082, 083, 174, 176, 179 and 180. Of these samples, 20 meet the requirements for 'low-grade-uranium-ore', containing greater than 500ppm U, and 1 sample containing 5270ppm U would be classified as 'medium-grade-uranium-ore' according to Douglas *et al.* (2003).

All of these samples were taken from within, or within close proximity to the RSC stratigraphic unit, with a significant minority found in the RSF. Indeed, both of these units contain higher than average concentrations of U at a deposit scale (Figures 5.32 and 5.35). The association of uranium with the RSC is most apparent by examination of the depth profile of U in MSSD083 (Figure 5.63). Of the lithological units within the RSC, U is most concentrated within the 'fresh' 'dolomite' lithology (Figures 5.33 and 5.36). The samples were taken at depths ranging from 139m to 343m, from the RSC and surrounds of both the upper and the lower fragments of Mines Subgroup. Figure 5.64 shows that this uranium is concentrated in the lowermost and easternmost portions of the Mashitu South deposit.

Geochemically, U correlates well with Ni and Co at a deposit scale, and to a lesser extent, S, As and V (see Figure 5.65).

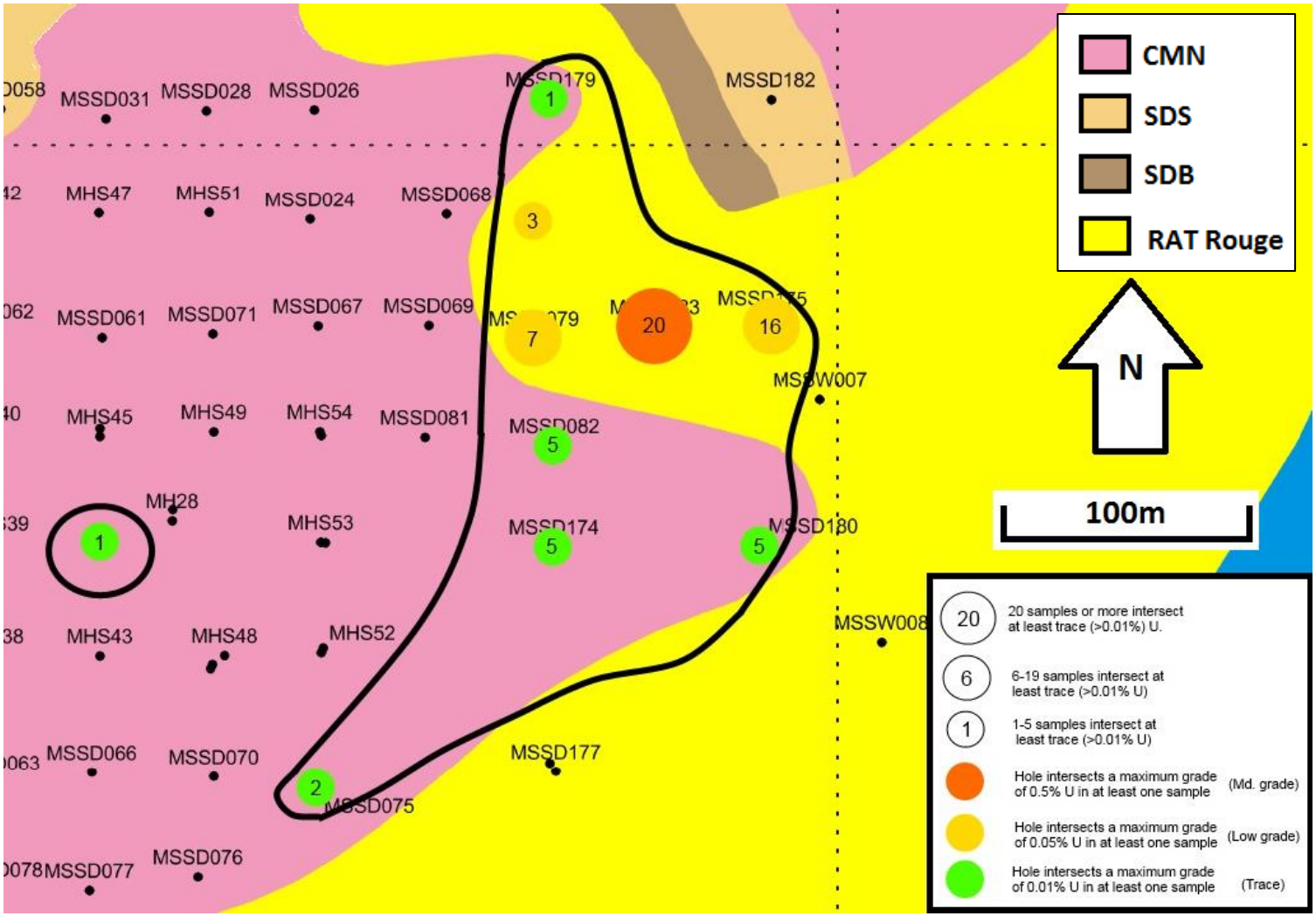

Figure 5.62*: Map of the eastern portion of the Mashitu South deposit (see Figures 3.4 and 3.8) showing the distribution of drill holes from which samples were taken with levels of uranium concentration over 0.01% U. On the circular icons above U-bearing holes, the colours represent the maximum grade of uranium found in a sample and the numbers represent the number of samples in each hole which contain >0.01% U.*

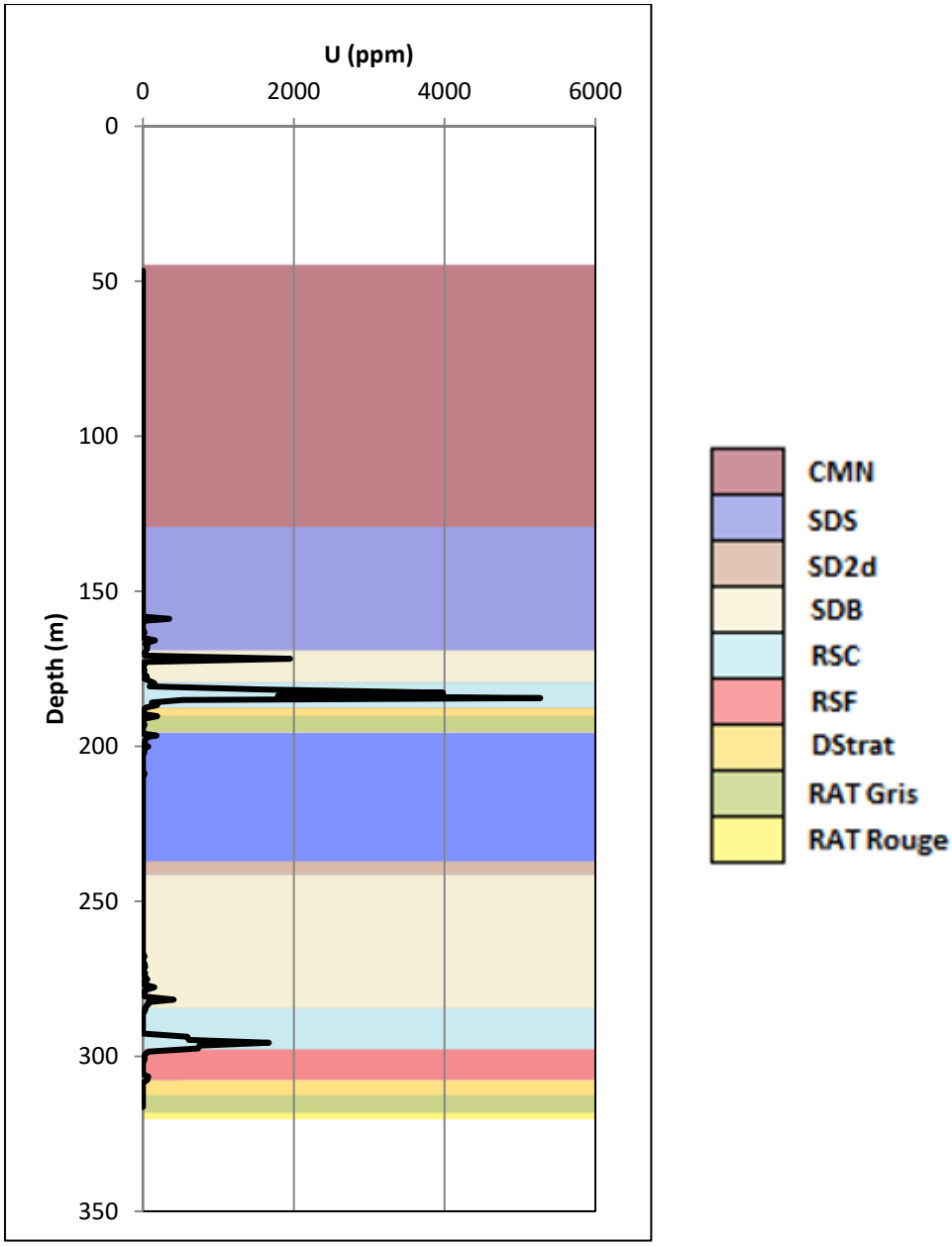

Figure 5.63*: Down-hole profile of uranium concentration in MSSD083 combined with stratigraphy. As we can see, U-grade is particularly pronounced within, or directly adjacent to, the RSC stratigraphic unit.*

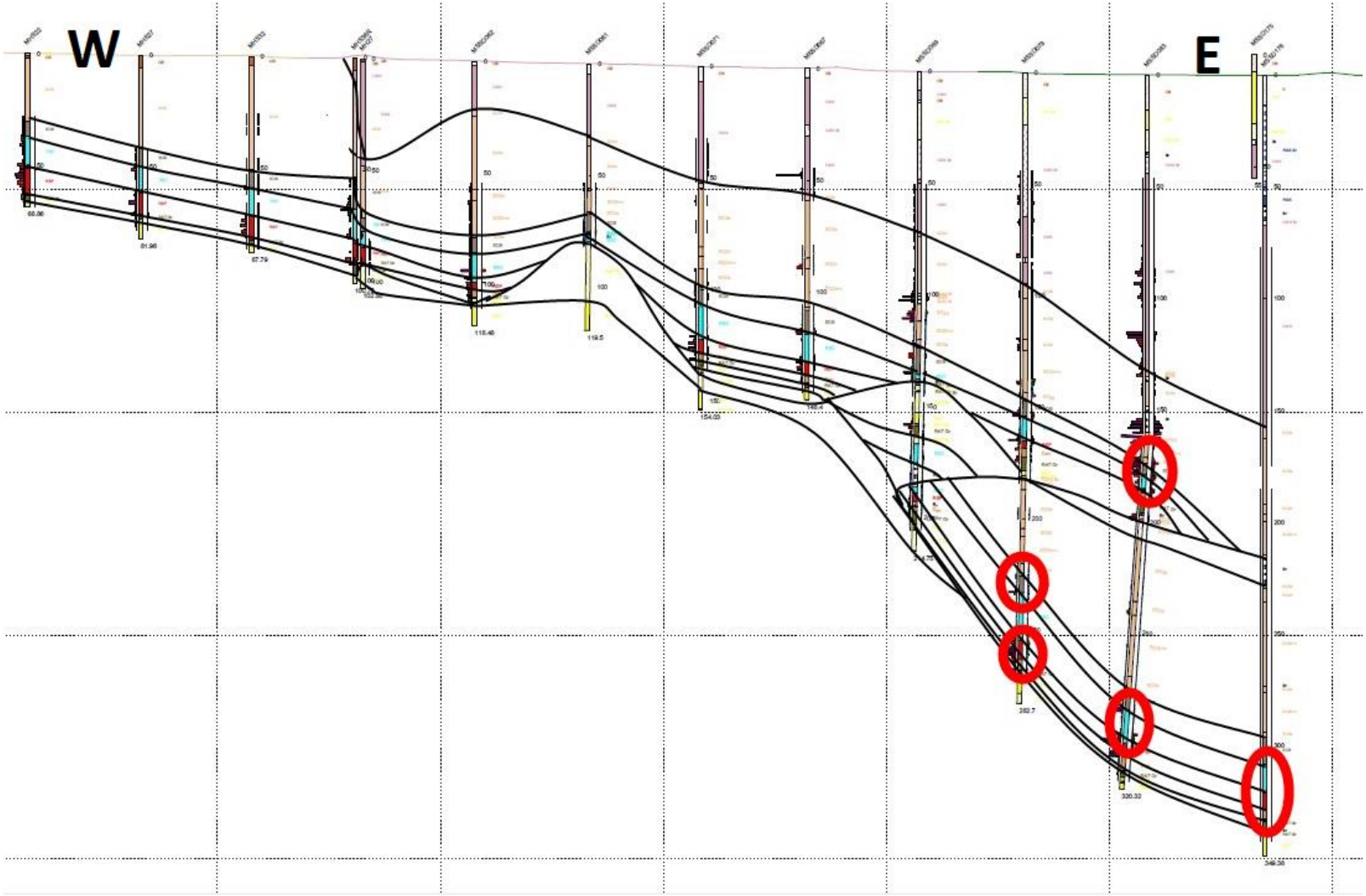

Figure 5.64*: W-E cross section through the eastern flank of the Mashitu South deposit. Intersections with significant grades of U (>100ppm) are circled in red, note that these correspond to the RSC stratigraphic unit. Each square on the grid is 100m x 100m.*

	U
U	
Ni	0.339
Co	0.114
S	0.086
As	0.083
V	0.081
Ba	0.052
Pb	0.046
Cu	0.031
Mo	0.030
Bi	0.023
Sr	0.021
Ca	0.018
Zn	0.014
Be	0.010
Cd	0.003
P	0.000
Ag	0.000
W	-0.004
Na	-0.007
Mg	-0.008
Mn	-0.014
Ti	-0.014
K	-0.015
La	-0.017
Sc	-0.019
Fe	-0.021
Al	-0.027

***Figure 5.65**: Correlations between U and various other elements within the whole Mashitu South combined database. U correlates well with Ni and Co, and less well with S, As and V.*

5.4 Discussion

5.4.1 Lithostratigraphy and Sedimentary Processes

The stratigraphy and constituent lithologies of the Mines Subgroup are well established, and, as shown in Chapter 3, it is apparent that the lithostratigraphy at Mashitu South is fairly typical for the Mines Subgroup of the region. Geochemistry, however, has offered additional insight into the constitution of these units.

Several geochemical distinctions can be made for different lithological and stratigraphic units. The first, and most obvious one is the use of indicators to tell calcareous units apart from siliciclastic ones. Calcareous units such as the CMN (Section 5.3.2.1), RSC (Section 5.3.2.5), RSF (Section 5.3.2.6), and the DStrat (Section 5.3.2.7) typically have high concentrations of the alkali-earth metals: Mg, Ca, Sr and Ba. Mg is generally more abundant in calcareous units at Mashitu South than Ca is and this is likely the result of magnesian alteration (see Section 5.4.2), but whether the rocks were originally a primary limestone (dominated by sedimentary calcite) or a primary dolostone (dominated by sedimentary dolomite) is uncertain. The scatter plot of Mg vs Ca in the CMN of MSSD075, 080 and 083 (Figure 5.56) may offer some evidence towards an answer to this question. Figure 5.56 shows a linear trend along the lower limit of the Mg:Ca ratio within these rocks, at Ca:Mg of 3:2, corresponding to magnesian calcite. It is possible that this 'magnesian calcite' could be remnants of a primary lithology deposited under atmospheric and seawater geochemistry of the Neoproterozoic (Mucci, 1987), but it is also possible that the magnesian calcite represents an alteration phase.

The elements Al, Ti and Sc were found to be elevated relative to ACEMS in the siliciclastic stratigraphic units of the SD (see Sections 5.3.2.2, 5.3.2.3 and 5.3.2.4), the RAT Gris (Section 5.3.2.8) and the RAT Rouge (Section 5.3.2.9). Al and Ti are both likely to have been derived from clastic, detrital aluminosilicates, ilmenite and rutile, while Sc tends to concentrate between phyllosilicate sheets in clay minerals.

The usefulness of the Sr:Sc ratio (Figure 5.54) as a method of determining the primary calcareous vs siliciclastic input to the rock is interesting in that, although Sc would be expected to be relatively immobile during low temperature metasomatism, Sr should theoretically be relatively mobile under these conditions. It can perhaps be explained by the

low concentration of Sr in the rocks, combined with metasomatic fluids which contained a similar or higher concentration of Sr before passing through the Mines Subgroup, thereby creating a partition coefficient for Sr unfavourable for the mobilisation of Sr from the host rocks and into metasomatic fluids which passed through the Mines Subgroup. High strontium concentration in these fluids could have been attained from the dissolution of hypothetical Sr-evaporite minerals such as celestine during passage through the RAT Subgroup, where significant concentrations of evaporites were theorised to have existed (e.g. Jackson *et al.*, 2003). Whatever the reason for the apparent immobility of Sr in metasomatic fluids at Mashitu South, the high correspondence of Sr concentration with calcareous units suggests that this element was indeed relatively immobile during much of the metasomatic history of the deposit. If a low mobility of Sr-in-rock is assumed at Mashitu South, together with the immobility of Sc, it is clear that the Sr:Sc ratio would be a useful indicator of the primary sedimentological nature of the protolith. One would expect that primary calcareous units would have high Sr:Sc values, whereas primary siliciclastic units would have low Sr:Sc values, as is indicated by Figure 5.54. However, it should be noted that Sr shows a relatively high degree of mobility in the supergene environment (though to a lesser degree than Mg or Ca - Figure 5.50) and therefore the ratio would be less reliable in this context when used on highly weathered rocks.

Most of the other geochemical indicators for different units, for example, high K in the S.D. unit, are thought to be derived from alteration, rather than sedimentary processes.

5.4.2 Alteration

Magnesian alteration, silicification, potassic alteration and argillic/supergene alteration are readily discernible within the rocks of Mashitu South through geochemical analysis. An AFC diagram of all the rocks from MSSD075, 080, 083 and 140 (Figure 5.66) displays several different alteration types.

5.4.2.1 Magnesian Alteration

Magnesian alteration can be distinguished by the development of trends in scatter plots towards higher Mg concentrations in both siliciclastic and calcareous rock types (although primary variation in Mg content is also a possibility). These trends may show a positive correlation with Ca and a negative correlation with Al, representing dolomite formation, or a

positive correlation with Al and a negative correlation with Ca, representing the growth of Mg-Al silicates (Figures 5.56 and 5.57). Additionally, this alteration type can be seen in AFC plots for datasets at Mashitu South, associated with trends towards higher proportions of F representing input of Mg (Figure 5.55). Magnesian alteration may be equivalent to the dolomite veining, possible development of talc near the RAT-Mines Subgroup contact, and greenish colouration developed in the SD and RAT Gris stratigraphic units (perhaps indicating the growth of chlorite), all of which were recognised during logging (see Chapter 3). Regionally, Mg-metasomatism is widespread in the RAT (R1) and Mines (R2) Subgroups of the Congolese Copperbelt and is recognised as being temporally, but not spatially, associated with syn-diagenetic stratiform mineralisation (Hitzman *et al.*, 2010b; Hitzman *et al.*, 2012).

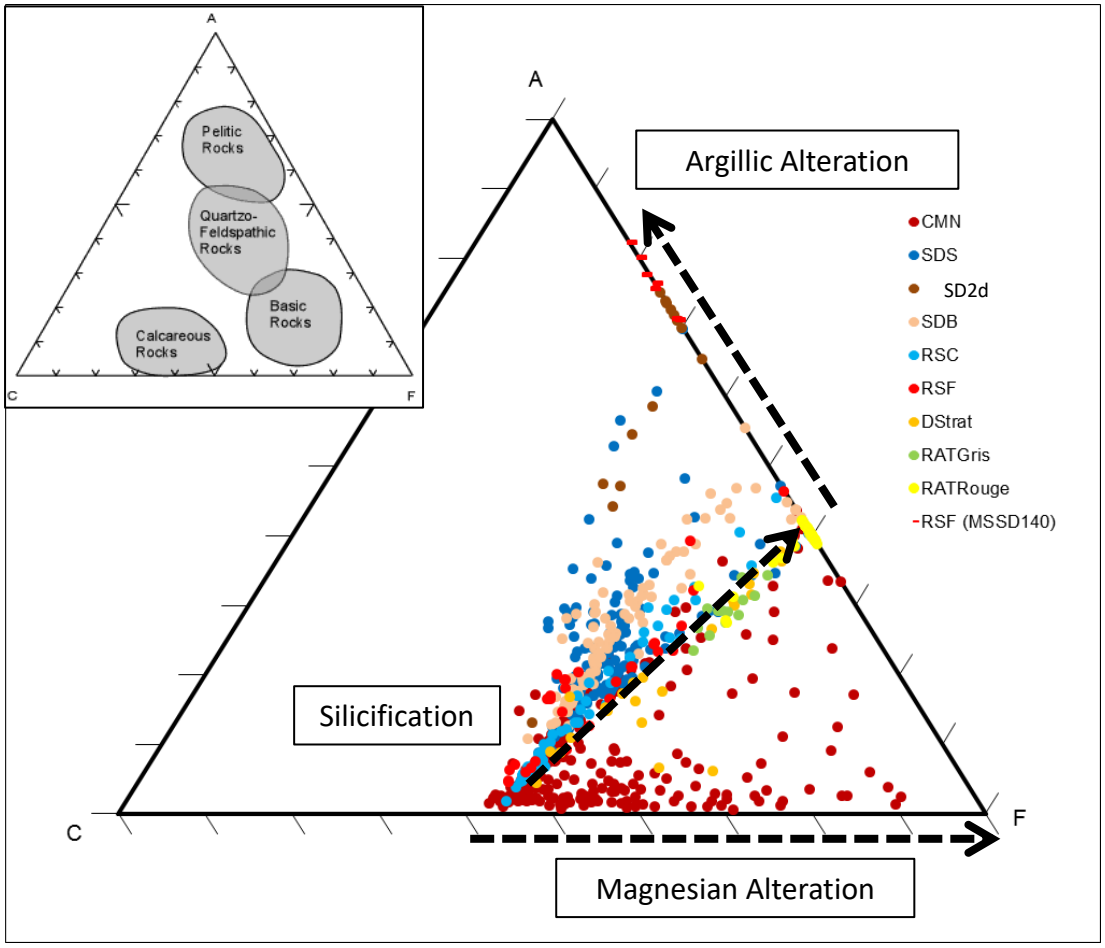

Figure 5.66*: ACF ternary diagram for samples from MSSD075, 080, 083 and 140. Geochemical trends in the samples suggest the presence of a number of different alteration types changing the primary geochemistry of these sedimentary rocks, including magnesian alteration, argillic alteration and silicification.*

5.4.2.2 Silicification

Silicification is most prevalent in the RSC and RSF stratigraphic units, but also occurs in certain horizons towards the base of the CMN (Figures 5.19, 5.31 and 5.34). Silicon was not analysed for in the 28-element geochemical database provided by Comide in this study, however, silicification can be indirectly inferred through trends which exist on AFC diagrams of rocks from MSSD075, 080 and 083. Figure 5.58 shows a trend within samples from the RSC where rocks move away from an originally calcareous composition by a drop in their proportions of C, without a change in the proportions of A and F. This would suggest the addition of some major element not represented by A or F, while the Ca content of the rock drops. The only major element not represented in the dataset is Si, therefore it seems likely that addition of this element is responsible for the trend. This trend away from C, without change in the A:F ratio, is repeated in the data for the RSF (Figure 5.60) and also developed to a more limited extent in the data for other rock units including the CMN and the DStrat. The occurrence of silicification is mostly restricted to units which display wavy algal or stromatolitic laminations, so it is probable that silicification of these units is related to the very early-diagenetic silica-fixing tendencies of cyanobacteria (Hitzman *et al.*, 2010b; Kremer *et al.*, 2012). If this is the case, it is likely that silicification of these units pre-dates early/syn-diagenetic stratiform mineralisation at Mashitu South. However, there are some silicified horizons which do not display wavy algal or stromatolitic laminations, particularly within the CMN (see Chapter 3) and it is possible that these units were affected by a microcrystalline silicification event which post-dated potassic and magnesian alteration, and the bulk of stratiform mineralisation (Fay and Barton, 2012; see Figure 2.7).

5.4.2.3 Potassic alteration

Potassic alteration was not recognised during logging of MSSD075, 080, 083 and 140, but geochemical trends suggest its presence in the Mines Subgroup at Mashitu South. Highly elevated K concentrations and trends towards K on the AFK diagram are found within the rocks of the SD (see Figure 5.59), indicating that this unit, and the SD2d in particular, is the central focus of potassic alteration at Mashitu South. The elevation in K is not thought to be sedimentary, as the RAT, another siliciclastic unit, does not show the same elevation in K – although the low K in the RAT could also be due to a metasomatic depletion of K, or a low

primary (depositional) K content. Additionally, a transgressive, marine environment of deposition for the SD as interpreted by Bull *et al.* (2010) would not be favourable for the survival and sedimentation of K-bearing minerals such as orthoclase, microcline and biotite. Indeed, the RAT unit, some patches of which are almost arkosic in appearance, might be expected to contain high concentrations of potassium, but K is significantly depleted below ACEMS in the RAT Gris and Rouge at Mashitu South (Figures 5.41, 5.42, 5.44 and 5.45). It is possible that K has actually been removed from labile minerals such as K-feldspar within the RAT by metasomatic fluids and redeposited in the SD unit. Similarly, it is also possible that K has been sourced from K-bearing evaporite minerals such as sylvite which once existed in the RAT, and have since been removed from the system (Jackson *et al.*, 2003). If these elevated concentrations of K do indeed represent a metasomatic event, it is perhaps equivalent to the early potassic alteration recognised by Hitzman *et al.* (2010b). This event pre-dated magnesian alteration as well as some of the later stratiform mineralisation, and resulted in the growth of potassium feldspar and biotite-phlogopite throughout the R1 and R2 Subgroups. However, Hitzman *et al.* (2010b) state that this alteration was most concentrated within the RAT Subgroup and Kamoto Dolomite Formation, which is certainly not the case at Mashitu South where elevated K corresponds to the Dolomitic Shales (SD) Formation.

5.4.2.4 Argillic/supergene/surficial alteration

The effects of argillic and supergene alteration on the rocks at Mashitu South has been assessed by the comparison of datasets at different depths, and the comparison of stratigraphic units found close to the surface and clearly affected by advanced argillic alteration to 'fresh' units found at depth. Different elements may show patterns of apparent depletion or enrichment with depth. If the <10m and >200m datasets are compared, it appears that Mg, Ca, Cu, K, S, P, Ba, Ni, Sr, Zn, U, As, Be and Cd are leached from and depleted in the rock by near-surface geochemical processes, whereas Al, Fe, Co, Ti, Mn, Na, V, La, Pb, W, Sc, Bi, Mo and Ag may show apparent enrichment, indicating that they are more resistant to leaching processes (see Section 5.3.3.1). It is important to note that these 'enrichments' are largely apparent or relative enrichments, with the concentration of leaching-resistant elements apparently upgraded by the development of voids within the rock created by the leaching of mobile elements with a corresponding loss of volume in the

analysed rock samples. However, some element enrichment may be caused by the redeposition of elements leached out further up in the profile. Copper is the best example of this, but Be, P, Ni and Fe also show evidence of supergene enrichment at depth as well as depletion towards the surface. This enrichment and depletion zonation is played out for different elements at different scales, with the strongest variation evident in some of the more resistant elements in the top 10m of the profile (Figures 5.51 and 5.52).

Another way of assessing the effect of leaching on element zonation is calculating the correlation of each element with depth value for each sample (Figure 5.15). From this calculation we see that there is an element order of Fe, Sc, Be, Mn, Al, La, Zn, Bi, V, W, Ti, Pb, Ag, Cd, Mo, Co, Cu, Na, As, P, U, Ni, K, Ba, Mg, Sr, S and Ca, representing highest affinity for the near-surface environment (Fe) to lowest affinity (Ca). The change from negative-to-positive correlation occurs between Mo and Co, suggesting that element with R-values more negative than Mo tend to be concentrated near the surface, while elements with R-values more positive than Co tend to be concentrated at depth. Certain elements out of those analysed for, such as Al and Ti, might be expected to have a higher affinity for the near-surface, as they would normally be more resistant to supergene leaching than any of the other elements analysed (Taylor, 2011). It is suspected that Al and Ti do not show such a negative correlation with depth as Fe, Be and Mn because they are resistant enough that they remain at the surface after leaching, and are subsequently eroded and transported away by physical processes. This would be in keeping with the interpretation of Decree *et al.* (2010) that a Quaternary transition to a more arid climate has increased the importance of physical weathering on element redistribution in the Katanga region.

It should be noted that results of both comparison of the at-depth and near-surface datasets, as well as the element-depth correlations, can be skewed by concentration or depletion of elements at a particular depth unrelated to surficial processes. For example, if a particular stratigraphic unit is found at a reasonably consistent depth across the deposit and a particular element is concentrated in this unit before exposure to the surface, this element will appear enriched in the dataset for whatever depth at which this unit occurs, even though its enrichment there has nothing to do with surficial processes. However, due to the domal folding of the Mashitu South Mines Subgroup fragment, all of the stratigraphic units encountered there can be found at a broad range of depths. It is therefore likely that the effect caused by this skewness is present but minimal in the results.

The effects of argillic alteration are evident on the ACF diagram too (Figure 5.60). Rocks affected by near-surface processes trend towards higher values of A and lower values of C, and then F, as argillic alteration intensifies. This trend represents the development of clay mineral aluminosilicates, and leaching of all more mobile elements within minerals.

Near-surface argillic alteration is recognised throughout the Katanga region (Giresse, 2005; Timmermans, 2015), is widely attributed to the prevailing humid subtropical-subtropical highland climate (Peel *et al.*, 2007) and is dated by Decree *et al.* (2010) as occurring in two periods during the Miocene and Pliocene. The intensity of supergene alteration is mostly controlled by the depth, buffering capacity and permeability of the rock, as indicated by the results of logging (see Chapter 3).

5.4.3 Cu-Co Mineralisation

Scatter graphs of Cu concentration vs. the other 27 elements analysed for in the Mashitu South combined database are provided as Appendix 7.

5.4.3.1 Variation by lithostratigraphy

Stratigraphically, copper is most concentrated in the SD2d stratigraphic unit with an average grade of all SD2d samples across the deposit of 2.23% Cu. The RSF is also above the stated grade of the Mashitu South deposit (1.2% Cu; Yeldar, 2012) at 1.25% Cu on average. A list of average copper grade by stratigraphic unit for Mashitu South is given as Figure 5.67.

Comparison of the stratigraphic distribution of Cu with that of Co reveals some disparities between the two elements (Figure 5.68). First, Co is most concentrated in the RSF, rather than in the SD2d, as is the case for Cu. Second, there is a significant concentration of Co in the RSC, whereas this unit is poorly mineralised in Cu. Concentrations of Co that are above the stated orebody grades are found, on average, in the RSF, SD2d, RSC, and within Undifferentiated Breccias.

N	STRATIGRAPHY	Predominant Lithology	Cu relative to ACEMS	Equivalent in %	Primary Correlator
241	SD2d	Shale	3.49	2.23	Bi
977	RSF	Dolomite	1.96	1.25	Mo
629	Dstrat	Dolomite	1.40	0.90	Be
169	Undiff Bx.	Polymict Breccia	1.33	0.85	S
2955	RATRouge	Mudstone	1.03	0.66	Be
2085	RSC	Silicic Rock	0.83	0.53	S
1744	SDB	Shale	0.80	0.51	Co
781	RATGris	Sandstone	0.76	0.48	Be
1568	CMN	Dolomite	0.57	0.36	Bi
895	SDS	Shale	0.52	0.33	Mo

***Figure 5.67**: Table of average copper concentration in the various stratigraphic units of Mashitu South. The 'predominant lithology' column represents the most commonly logged primary lithology of each stratigraphic unit. The 'equivalent in %' column is the result of multiplying the ACEMS value for Cu (0.64%) with the ACEMS-normalised value for each dataset. The 'primary correlator' column represents the element in each dataset which shows the highest Pearson r-value correlation with Cu. The data show that the SD2d and the RSF represent significant stratigraphic orebodies, with Bi and Mo associated with copper in these two units.*

N	STRATIGRAPHY	Predominant Lithology	Co relative to ACEMS	Equivalent in %	Primary Correlator
977	RSF	Dolomite	1.86	0.30	Ni
169	Undiff Bx.	Polymict Breccia	1.72	0.28	Ni
241	SD2d	Shale	1.72	0.28	Ni
2085	RSC	Silicic Rock	1.62	0.26	Ni
629	Dstrat	Dolomite	1.01	0.16	Ni
1744	SDB	Shale	1.01	0.16	Ni
781	RATGris	Sandstone	0.85	0.14	Ni
895	SDS	Shale	0.68	0.11	Mo
2955	RATRouge	Mudstone	0.65	0.11	Be
1568	CMN	Dolomite	0.36	0.06	Be

***Figure 5.68**: Table of average cobalt concentration in the various stratigraphic units of Mashitu South. The 'predominant lithology' column represents the most commonly logged primary lithology of each stratigraphic unit. The 'equivalent in %' column is the result of multiplying the ACEMS value for Co (0.16%) with the ACEMS-normalised value for each dataset. The 'primary correlator' column represents the element in each dataset which shows the highest Pearson r-value correlation with Co. The RSF is the most significant orebody for Co. Ni correlates with Co very consistently in most of the stratigraphic units.*

From the data we can see that Cu-Co mineralisation is most concentrated in the SD2d and RSF stratigraphic units. However, the RSF is the more significant orebody of the two units because it is thicker, more laterally continuous and contains higher Co than the SD2d. This is

in keeping with the long-recognised designation of the RSF as the primary orebody for stratiform Cu-Co within the Mines Subgroup of the Katangan Copperbelt (Oosterbosch and Schuiling, 1951), such that it is called the 'Lower Orebody' by Hitzman *et al.* (2012). The disparity in Cu-Co distribution is suggestive of element zonation or perhaps different modes of distribution for the two elements.

When the datasets are separated by lithology, it becomes obvious that small datasets (N<60) with unusual lithologies dominate the highest-grade lithological units. The only consistent lithological trend is a predisposition for breccias to be well mineralised, with 4 of 6 lithologies which contain the highest average concentrations of Cu being logged as having a primary or secondary lithology of breccia. This would probably be on account of breccias being generally more permeable to mineralising fluids than other rocks. Rocks with the 'silicic rock' lithology also tend to be well mineralised, however the majority of the samples logged as this lithology come from the RSF and RSC stratigraphic units (see Figure 5.69). Note that samples logged as 'saprolite' or with 'clay' as their primary or secondary lithology tend to be extremely poor in Cu: this is probably a reflection of supergene leaching.

N	Lithology	Cu Relative to ACEMS	Equivalent in %
3	Shale and Massive Sulphide	6.69	4.28
13	Siltstone and Polymict Breccia	3.33	2.13
54	Monomict Breccia and Sandstone	2.78	1.78
10	Shale and Polymict Breccia	2.42	1.55
16	Silicic Rock and Shale	2.42	1.55
11	Silicic Rock and Monomict Breccia	1.96	1.26
26	Clay and Siltstone	1.94	1.24
316	Silicic Rock and Dolomite	1.88	1.21
461	Siltstone	1.49	0.96
12	Sandstone and Monomict Breccia	1.43	0.92
95	Polymict Breccia	1.31	0.84
248	Dolomite and Silicic Rock	1.11	0.71
55	Sandstone and Dolomite	1.05	0.67
757	Clay	1.03	0.66
2830	Dolomite	1.03	0.66
444	Dolomite and Sandstone	1.01	0.65
295	Dolomite and Shale	1.01	0.65
234	Monomict Breccia	1.00	0.64
360	Shale and Dolomite	0.98	0.62
932	Mudstone	0.97	0.62
1074	Sandstone	0.94	0.60
27	Dolomite and Breccia	0.88	0.56
2274	Shale	0.85	0.54
1039	Silicic Rock	0.69	0.44
24	Silstone and Dolomite	0.66	0.42
104	Clay and Sandstone	0.49	0.31
45	Sandstone and Clay	0.48	0.31
27	Clay and Shale	0.46	0.30
30	Clay and Dolomite	0.34	0.22
40	Polymict Breccia and Sandstone	0.20	0.13
10	Breccia	0.15	0.10
22	Shale and Sandstone	0.15	0.09
16	Saprolite (and)	0.06	0.04

Figure 5.69*: Table of average copper concentration in the various lithological units of Mashitu South. The 'equivalent in %' column is the result of multiplying the ACEMS value for Cu (0.64%) with the ACEMS-normalised value for each dataset. Cu concentration tends to be high in breccia lithologies and low in 'clay' or 'saprolite' lithologies.*

If the datasets are separated by stratigraphy *and* lithology, similar results are obtained as those presented above. Thus lithologies from the SD2d and RSF are noted to host most of the ore (Figure 5.70). Lithological datasets from the DStrat and SDB also host significant

concentrations of Cu. Interestingly, breccia units are the most mineralised lithologies within the RAT Rouge, reinforcing the observations made during logging in Chapter 3 that these permeable breccia lithologies are the most susceptible to supergene mineralisation.

Altogether it appears that stratigraphic position, rather than lithological composition, plays a more important role in the distribution of mineralisation. However, 'breccia' lithologies tend to be better mineralised than their counterparts regardless of stratigraphic position, and 'clay' or 'saprolite' lithologies tend to be poorly mineralised relative to their counterparts in the same stratigraphic unit. This is broadly in agreement with the importance of stratigraphic control on the distribution of stratiform mineralisation espoused in Brown (2014) and the importance of lithological control in the development of supergene mineralisation (De Putter *et al.*, 2010), both of which have been observed to play a significant role in mineralisation distribution at Mashitu South (see Chapter 3).

It is inferred that the RSF is particularly well mineralised because it represents the first major reducing-front contact for oxidising, metalliferous fluids travelling up through the rock column from the RAT, as is usually the case in the region (Hitzman *et al.*, 2012), and that some distribution of metal may have occurred along the units adjacent to the RSC by both hypogene and supergene fluids (Fay and Barton, 2012). The high average concentration of copper in the SD2d is likely to have occurred because it is the only unit of black shale in the sequence, and is lithologically a strong reducing agent. Any ions which were not reduced while travelling upwards through the RSF would surely have been reduced on contact with the SD2d, and if metal was distributed through the RSC then the SD2d would have been the first major lithological redox front encountered by the transporting fluids in an upwards direction.

It should be noted that lithological variation itself is primarily controlled by stratigraphy and many stratigraphic units in the Mines Subgroup at Mashitu South have only been logged as a single lithological type within each different hole by Comide workers, which may account somewhat for stratigraphic position appearing to be the more important factor over lithology in the development of Cu mineralisation.

N	LITHO-STRATIGRAPHY	Cu relative to ACEMS	Equivalent in %	Primary Cu Correlators
10	(SD2d) Dolomite, Dolomite and Sandstone	4.79	3.06	Sc
42	(SD2d) Shale and Dolomite	4.75	3.03	S
181	(SD2d) Shale	3.16	2.02	Bi
98	(RSF) Silicic Rock (and)	2.98	1.90	Zn
3	(Dstrat) Silicic Rock (and)	2.65	1.69	S
514	(RSF) Dolomite (and)	2.05	1.31	Mo
334	(RSF) Siltstone	1.61	1.03	S
41	(SDB) Siltstone	1.50	0.96	Pb
580	(Dstrat) Dolomite (and)	1.43	0.91	P
266	(RATRouge) Breccia (and)	1.39	0.89	Be
8	(RSC) Mudstone (and)	1.35	0.86	Ca
6	(SDS) Breccia (mono+polymict)	1.33	0.85	Sc
79	(CMN) Clay, Saprolite (and)	1.25	0.80	Bi
75	(RATGris) Siltstone	1.16	0.74	Be
125	(Undiff Bx) Composite/Polymict Breccia (and)	1.12	0.72	K
705	(RATRouge) Sandstone (and)	1.11	0.71	Be
11	(RSF) Shale (and)	1.08	0.69	Mo
906	(RATRouge) Mudstone (and)	1.01	0.64	Be
153	(RATGris) Dolomite	0.99	0.63	Be
762	(RATRouge) Clay (and)	0.98	0.63	Be
21	(Dstrat) Shale, Mudstone, Siltstone (and)	0.95	0.60	Zn
1186	(RSC) Silicic Rock (and)	0.91	0.58	Ni
204	(SDS) Dolomite (and)	0.82	0.53	V
1489	(SDB) Shale (and)	0.81	0.52	Co
310	(RATRouge) Dolomite (and)	0.75	0.48	Be
881	(RSC) Dolomite (and)	0.73	0.46	S
7	(CMN) Sandstone (and)	0.67	0.42	Bi
73	(RATGris) Clay	0.66	0.42	Ni
478	(RATGris) Sandstone	0.63	0.41	Bi
272	(CMN) Shale (and)	0.61	0.39	S
11	(Dstrat) Monomict Breccia and Dolomite	0.58	0.37	P
24	(Undiff Bx) Monomict Breccia (and)	0.56	0.36	S
11	(Dstrat) Clay	0.56	0.35	S
1041	(CMN) Dolomite (and)	0.55	0.35	Bi
182	(SDB) Dolomite (and)	0.54	0.35	Co
24	(SDB) Clay (and)	0.44	0.28	Sr
683	(SDS) Shale (and)	0.43	0.27	Mo
6	(RATRouge) Siltstone (and)	0.37	0.24	Na
141	(CMN) Silicic Rock (and)	0.35	0.22	Fe
12	(CMN) Breccia (mono + polymict)	0.29	0.19	Zn
16	(CMN) Mudstone (and)	0.28	0.18	Be
14	(RSF) Mudstone	0.07	0.04	Mn
7	(RSC) Saprolite	0.04	0.02	Mn

Figure 5.70*: Table of average copper concentration in the various lithostratigraphic units of Mashitu South. The 'equivalent in %' column is the result of multiplying the ACEMS value for Cu (0.64%) with the ACEMS-normalised value for each dataset. The 'primary correlator' column represents the element in each dataset which shows the highest Pearson r-value correlation with Cu. Lithologies from the RSF and SD2d appear to have the highest concentrations of Cu, and 'breccia' lithologies also tend to have high Cu concentrations. 'Saprolite' and 'Clay' lithologies tend to be poor in Cu, by comparison.*

5.4.3.2 Variation by depth

Copper is geochemically associated with a number of different elements in the Mashitu South combined database including Co, Ni, Bi, V, S, As, Zn, P, Mo, Fe and Be, depending on which dataset is analysed (see Figures 5.18 and 5.61). This geochemical association does not distinguish which of these elements are associated with hypogene Cu and which are associated with supergene Cu, however, nor between the stratiform and vein-type hypogene Cu distinguished during logging.

The first method of investigating which elements were associated with supergene and which were associated with hypogene mineralisation involved calculating correlation coefficients for the different elements with Cu in the depth datasets discussed in Section 5.3.3.1. The Masitu South combined database was split into <10m, 10-50m, 50-100m, 100-200m and >200m depth interval datasets. It was found that in each different dataset, different elements showed significantly different correlations with Cu. The elements Co, Bi, Ni, V, S, Mo, As and Fe were found to correlate best with Cu in the 50-100m, 100-200m and in the >200m datasets, where the rock is thought to be relatively fresh and little-affected by supergene remobilisation. By contrast, P and Be were found to correlate best with Cu in the <10m and in the 10-50m datasets, where the bulk of the remobilised supergene Cu mineralisation can be found. Zn has loose correlations to Cu in the <10m, 10-50m and >200m datasets, indicating that its occurrence is loosely associated with Cu at depth and near surface. This data is presented as Figure 5.71.

Be and P correlations appear to weaken with depth, whereas correlations with Co, Bi, Ni, V, S, Mo, As and Fe appear to reduce within shallower datasets and increase within deeper datasets. The change in relationship between Cu and Zn with depth is indistinct, with significant Cu-Zn correlations in both shallow and deep datasets.

To quantify the variation in correlation with Cu between deep and shallow datasets, each depth-interval dataset was given a number by increasing depth, 1-5, with 1 corresponding to the <10m interval and 5 corresponding to the >200m interval (see Figure 5.72). Correlations were then calculated between the R-value correlation coefficients for each element at each depth interval and the 1-5 depth interval classifications, to investigate the 'correlation of: each element-Cu-correlation with depth'. In this way, the elements which have higher R-values with Cu at greater depth in the individual depth interval datasets, will show a higher 'R value between Element Cu correlation R-values and depth

interval designation', putting a single figure on the relative affinity for Cu at depth (positive) or near the surface (negative) of each element. The data shows that out of the ore-associated elements, Co shows the most positive correlation-of-correlation-with-Cu-and-depth (R=0.989), and P shows the most negative correlation-of-correlation-with-Cu-and-depth (R=-0.928). From this calculation (Figure 5.72) the ore associated elements have the following affinity with Cu at depth vs. the surface, with affinity for correlation with Cu at depth first and affinity for correlation with Cu near surface last: Co, Fe, V, Mo, Bi, Ni, As, S, Zn, Be, P.

<10m		10-50m		50-100m		100-200m		>200m	
Element	R-value	Element	R-value	Element	R-value	Element	R-value	Element	R-value
P	0.53	Be	0.36	Bi	0.55	Bi	0.56	Co	0.62
Be	0.37	P	0.36	Co	0.38	Co	0.51	Bi	0.54
S	0.27	Zn	0.24	V	0.33	S	0.34	Ni	0.53
Zn	0.22	Co	0.23	Mo	0.31	V	0.33	V	0.42
Bi	0.21	Bi	0.22	S	0.27	Ni	0.26	S	0.42
Ni	0.21	As	0.17	As	0.25	Mo	0.22	Mo	0.38
Co	0.19	Ni	0.13	U	0.21	As	0.19	Zn	0.26
Na	0.12	S	0.10	Ni	0.18	Fe	0.18	Pb	0.24
Mg	0.12	Fe	0.06	La	0.15	Be	0.15	As	0.23
As	0.09	Sc	0.06	P	0.13	Sc	0.11	W	0.19
Sc	0.09	U	0.05	K	0.13	K	0.06	Sc	0.17
Al	0.07	Cd	0.04	Sc	0.11	Zn	0.05	Be	0.17
Ba	0.06	Mo	0.03	Fe	0.10	Al	0.05	U	0.16
Ti	0.06	V	0.02	Be	0.09	Na	0.05	Fe	0.15
U	0.05	Pb	0.02	Ba	0.05	La	0.04	K	0.10
Cd	0.04	W	-0.01	Na	0.05	U	0.02	Na	0.08
V	0.04	Ag	-0.02	Ag	0.03	Pb	0.02	La	0.07
La	0.04	La	-0.02	Zn	0.02	P	0.02	Cd	0.07
Sr	0.03	Mg	-0.02	Pb	0.02	Cd	0.00	P	0.07
K	0.02	Mn	-0.05	Sr	0.02	Ti	0.00	Sr	0.04
Pb	0.01	Ba	-0.05	W	0.01	Sr	0.00	Ag	0.04
Mo	-0.02	Ca	-0.05	Mn	0.00	Ag	-0.01	Ba	0.02
Ca	-0.03	K	-0.06	Ti	-0.02	Ba	-0.01	Al	0.01
Mn	-0.03	Na	-0.06	Al	-0.04	W	-0.01	Ti	0.00
W	-0.03	Al	-0.06	Cd	-0.04	Mn	-0.06	Mn	-0.14
Ag	-0.03	Sr	-0.09	Ca	-0.07	Mg	-0.19	Ca	-0.28
Fe	-0.04	Ti	-0.15	Mg	-0.24	Ca	-0.19	Mg	-0.34

***Figure 5.71**: Table of Pearson correlation coefficient R-values for each different element, in the 5 designated depth intervals, ranked. The elements Co, Bi, Ni, V, S, Mo, As and Fe, which appear to be associated with copper in deeper datasets, are highlighted in orange, while Be and P, which seem to be associated with copper in shallow datasets, are highlighted dark green. Zn, which shows a loose association with copper in both deep and shallow datasets, is highlighted in yellow. Different elements can be observed to have different correlations with Cu at different depth intervals.*

	R-value between each element and Cu at the indicated depth					R-value between Element-Cu correlation R-values and depth interval designation (1-5)
	1	2	3	4	5	
	<10m	10-50m	50-100m	100-200m	>200m	
Ag	-0.03	-0.02	0.03	-0.01	0.04	0.771
Al	0.07	-0.06	-0.04	0.05	0.01	-0.021
As	0.09	0.17	0.25	0.19	0.23	0.764
Ba	0.06	-0.05	0.05	-0.01	0.02	-0.170
Be	0.37	0.36	0.09	0.15	0.17	-0.750
Bi	0.21	0.22	0.55	0.56	0.54	0.864
Ca	-0.03	-0.05	-0.07	-0.19	-0.28	-0.951
Cd	0.04	0.04	-0.04	0.00	0.07	0.047
Co	0.19	0.23	0.38	0.51	0.62	0.989
Fe	-0.04	0.06	0.10	0.18	0.15	0.920
K	0.02	-0.06	0.13	0.06	0.10	0.613
La	0.04	-0.02	0.15	0.04	0.07	0.360
Mg	0.12	-0.02	-0.24	-0.19	-0.34	-0.944
Mn	-0.03	-0.05	0.00	-0.06	-0.14	-0.714
Mo	-0.02	0.03	0.31	0.22	0.38	0.900
Na	0.12	-0.06	0.05	0.05	0.08	0.047
Ni	0.21	0.13	0.18	0.26	0.53	0.775
P	0.53	0.36	0.13	0.02	0.07	-0.928
Pb	0.01	0.02	0.02	0.02	0.24	0.730
S	0.27	0.10	0.27	0.34	0.42	0.708
Sc	0.09	0.06	0.11	0.11	0.17	0.854
Sr	0.03	-0.09	0.02	0.00	0.04	0.372
Ti	0.06	-0.15	-0.02	0.00	0.00	0.067
U	0.05	0.05	0.21	0.02	0.16	0.365
V	0.04	0.02	0.33	0.33	0.42	0.916
W	-0.03	-0.01	0.01	-0.01	0.19	0.762
Zn	0.22	0.24	0.02	0.05	0.26	-0.151

	R-value between Element-Cu correlation R-values and depth interval designation (1-5), ranked
Co	0.989
Fe	0.920
V	0.916
Mo	0.900
Bi	0.864
Ni	0.775
As	0.764
S	0.708
Zn	-0.151
Be	-0.750
P	-0.928

***Figure 5.72**: Table of Pearson correlation coefficient R-values for each different element in the 5 designated depth intervals, which have been assigned a number 1-5 with increasing depth. The right hand column shows the 'correlation of the correlation of an element with copper, with depth'. These results are summarised in the bottom sub-table. The 'correlation of the correlation of an element with copper, with depth' is most positive in Co, while it is most negative in P, with the order Co, Fe, V, Mo, Bi, Ni, As, S, Zn, Be, and P of affinity with Cu at depth vs. near the surface.*

From Figures 5.71 and 5.72 it can be deduced that Cu is most associated with Co, Fe, V, Mo, Bi, Ni, As and S at depth, which theoretically corresponds to the most unaltered, hypogene environment of Cu mineralisation. Cu is most associated with Be and P near the surface, which theoretically corresponds to the most altered, supergene environment of Cu mineralisation. Zn is associated loosely with Cu in both hypogene and supergene environments. The >200m depth interval is assumed to represent the 'freshest' portion of the deposit, most representative of hypogene mineralisation, and the 10-50m interval is assumed to represent the 'most supergene' portion, as this is the depth at which supergene mineralisation commonly forms malachite orebodies (Robertson, pers. comm., 2014; see Chapter 3). The <10m interval is considered representative of the leached zone of the deposit.

The hypogene correlation of Co, Fe, V, Mo, Bi, Ni, As and S with Cu is also borne out spatially. Figure 5.73 shows the close correspondence of zones of high concentration of Cu, Co, Bi, Ni, V and S in hole MSSD075, all elements which show the strongest statistical correlations with Cu in the deep hypogene environment. These elements are particularly well mineralised together in the RSF and at the base of the SDB, where stratiform, hypogene mineralisation is typically concentrated in the Mines Subgroup (see Section 5.4.3.1).

Therefore, based on the strength of correlation with Cu in these depth interval datasets and the correspondence of these elements in downhole profiles, it is inferred that hypogene mineralisation at Mashitu South has a geochemical association of: Cu + Co + Bi + Ni + V + S ± Mo ± As ± Fe ± Zn.

Supergene Cu mineralisation at Mashitu South is similarly inferred to have a distinct geochemical association of Cu + Be + P ± Zn.

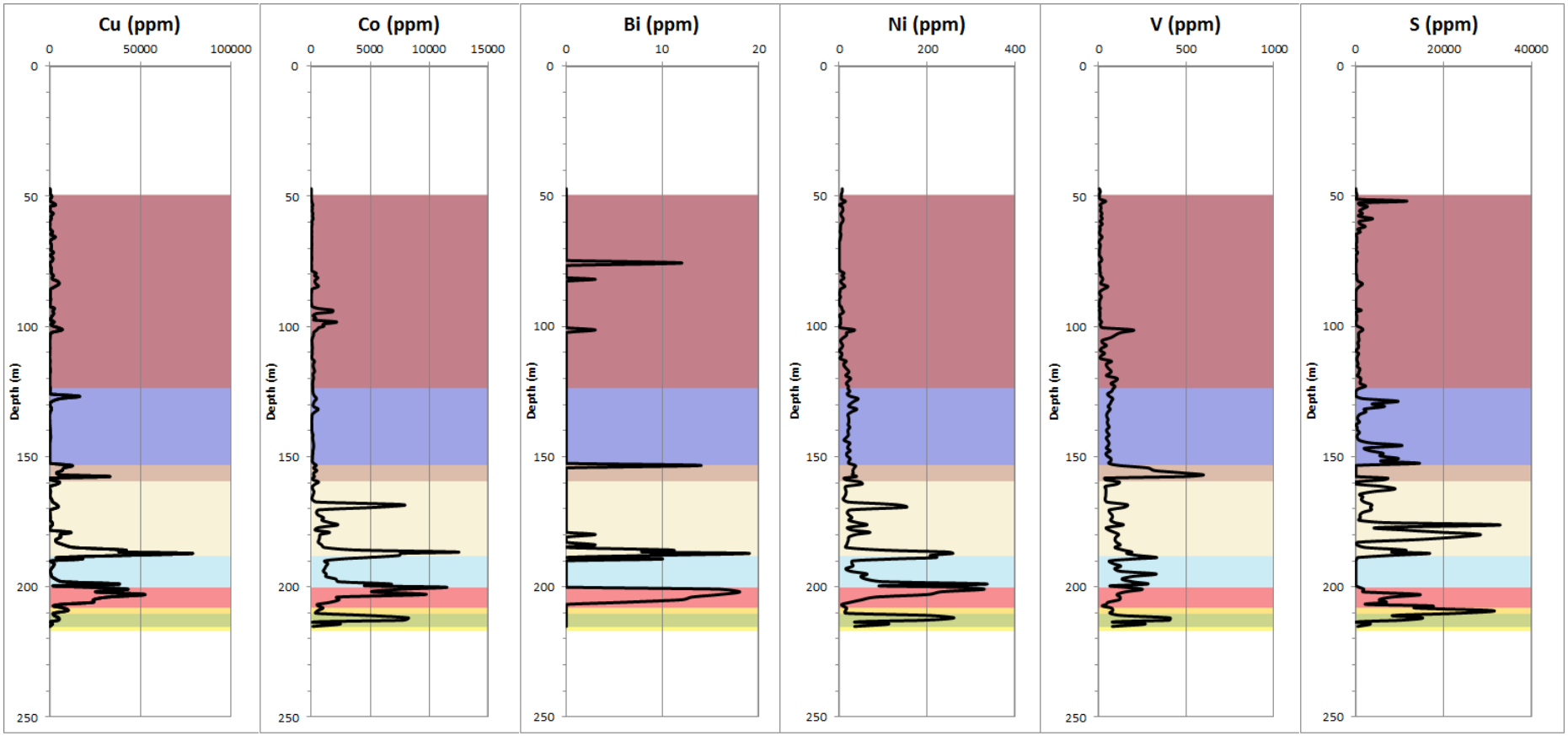

Figure 5.73*: Downhole element plots of Cu, Co, Bi, Ni, V and S within MSSD075. The variation in sample concentration for each element (black line) is shown alongside the logged stratigraphy through each hole, which is represented by shading as follows: CMN: maroon; SDS: dark blue; SD2d: brown; SDB: beige; RSC: light blue; RSF: red; DStrat: orange; RAT Gris: green; RAT Rouge: yellow. Each element shows good spatial correspondence with each other in zones of Cu mineralisation, particularly at depth, and especially within the RSF and SDB stratigraphic units which are known to be regional stratiform Cu-Co orebodies.*

5.4.3.3 The transition from hypogene to supergene mineralisation

Figure 5.71 shows that elements which appear to be have been co-mineralised with Cu in the hypogene environment have apparently dissociated with Cu in the supergene environment. This phenomenon is described by Decree *et al.* (2010), but only in the context of Cu and Co. It is explained by the enhanced mobility of Cu compared to Co in the acidic, oxidising meteoric fluids which cause supergene alteration (Kastikopoulos *et al.*, 2008). The dissociation of Cu and Co in the supergene environment is definitely observed at Mashitu South, but the fates of the other elements which are associated with Cu in the hypogene environment: Bi, Ni, V, S, Mo, As and Fe, when exposed to supergene alteration, are also investigated in this section.

Statistically, the best way of investigating the effect of supergene alteration on these elements is through scrutiny of the dataset when split by depth (Section 5.3.3). As is shown in Figures 5.49, 5.50, 5.51 5.52 and 5.53, copper is highly susceptible to being leached from the surface, where its average concentration in the <10m dataset is depleted to around a 5th of the average concentration of Cu within the >200m dataset (Figure 5.49). The Cu is then reprecipitated deeper within the rock column to form the supergene remobilised orebodies observed in MSSD140 (see Figure 5.75 and Appendix 3d). This process tends to happen at a depth of between 30-50m (Figure 5.75) and the 10-50m dataset shows the greatest average concentration of Cu out of any depth interval, at 1.33x ACEMS (Figure 5.49). The result is the production of high grade, malachite-dominated, permeability-and-metal-availability-controlled supergene orebodies, frequently found in the RAT Rouge unit (see Section 3.4.4.2). These para-exotic, supergene orebodies are highly prospective targets for Cu-Co exploration (Chimvinga, pers. comm., 2014) and represent a significant exception to the generalisation that Cu-Co mineralisation is not found in the RAT Subgroup. This study infers these orebodies to have a geochemical association of Cu-Be-P ± Zn (see Section 5.4.3.2).

Some clue as to the origin of the Cu-P association at least may be found in a scatter plot of Cu vs. P in the Mashitu South combined database (Figure 5.74). This graph reveals, amongst other data trends, a distinct linear trend between the concentration of Cu and that of P, with a ratio of Cu:P of around 5:1. This trend would suggest the growth of a mineral with an elemental Cu:P ratio of 5:1, unfortunately this cannot be explained by pseudomalachite ($Cu_5(PO_4)_2(OH)_4$), which has an elemental Cu:P ratio of 5:2, or libethenite (Cu_2PO_4OH), with a ratio of 2:1. It is possible that the trend could be explained by a

combination of minerals consistently growing together at the same ratio, but the data offers no explanations as to which minerals these might be or how this process might occur.

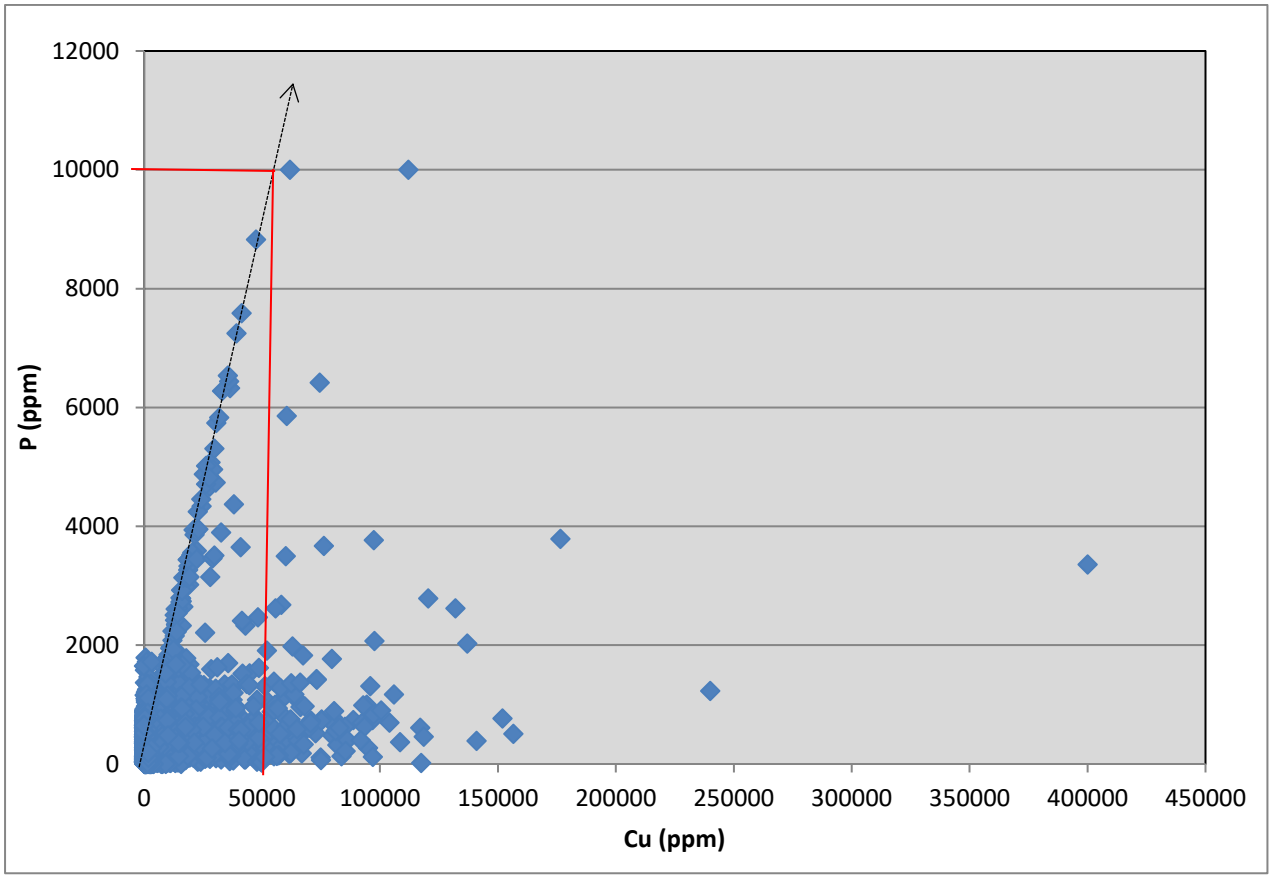

***Figure 5.74**: Scatter plot of Cu vs P in the Mashitu South combined database. Most of the data is relatively scattered, however a very distinct linear trend exists (marked by the dashed black arrow) between the two elements within certain data, with a Cu:P ratio of 5:1 (shown by the red lines). This consistent trend in the data would suggest the growth of a Cu-P mineral with the same elemental ratio of Cu:P.*

Analysing the downhole element profiles for Cu, P and Be in MSSD140 (Figure 5.75) reveals that all three elements occur in greatly elevated concentrations in the 30-50m region, corresponding to a zone of monomict-vein-supported, breccia-hosted remobilised supergene mineralisation, apparently dominated by malachite (see Figure 3.41 and Appendix 3d). Whereas P may be hosted in some sort of Cu-phosphate which is associated with malachite, Be, which is only found in trace concentrations throughout the deposit, is possibly included in malachite or some other secondary Cu mineral as a trace element.

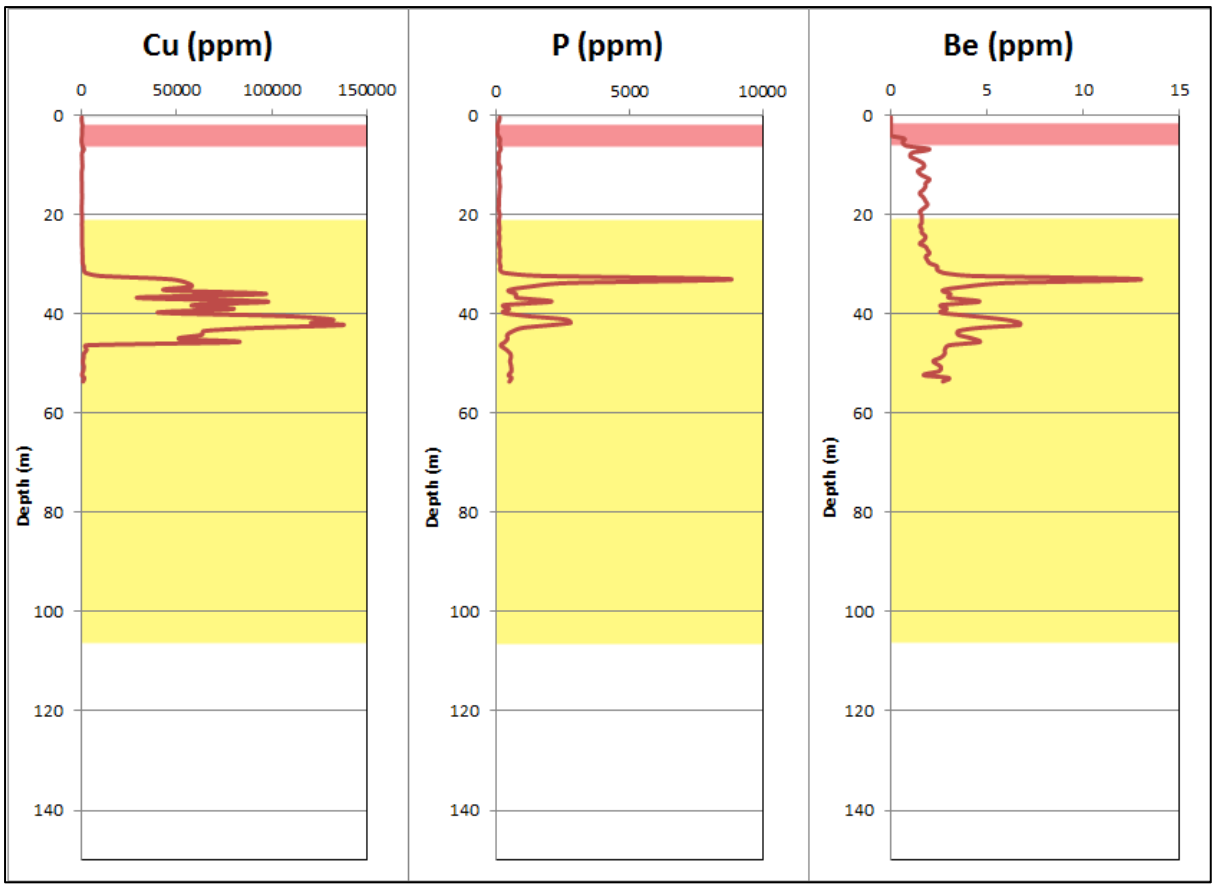

Figure 5.75*: Downhole element plot of Cu, P, and Be in MSSD140. Stratigraphy is represented by the colour shading on the graph: the RAT Rouge is shaded yellow, the RSF is shaded red, and unknown/unassigned stratigraphy is left unshaded. Cu, P and Be all appear in greatly elevated concentrations between a depth of 30-50m, corresponding to a region of breccia-hosted, malachite-dominated supergene remobilised mineralisation.*

5.4.3.4 Surface vectors towards buried Cu-Co mineralisation

The leaching process is extremely effective at removing Cu from the surface environment, such that the average concentration of Cu in the top 1m of the profile is only 0.08x the ACEMS value (see Figure 5.51). The author therefore proposes that Cu concentration in soil may not be the best method of regionally prospecting for supergene remobilised Cu deposits, as the intensity of leaching may reduce the Cu-soil-concentrations to close enough to the detection limits of the prospecting technique to smooth over a geochemical anomaly which may overlie a significant Cu deposit. While this effect may not be so important in larger, closer to the surface, and/or less leached deposits, it may cause the oversight of prospects which are smaller, buried further at depth, more leached by supergene alteration and/or those that are masked by regionally high soil-Cu concentrations. Yet, soil-Cu-

concentration is one of the most widely used methods for Cu-prospecting in the region (Chimvinga, pers. comm., 2014) and the reliance on this method may have left many Cu deposits overlooked. Co in soil has been used by some companies in prospecting for buried Cu to some success, as this element is known to be less mobile in the surface environment (Kastikopoulos *et al.*, 2008), forming 'cobalt caps' over copper deposits in Katanga (Decree *et al.*, 2010). The enabling factor for cobalt to be used in this way is that it is associated with Cu in the hypogene environment, but dissociates from Cu in the supergene environment (Figure 5.71).

Figures 5.52 and 5.53 show that there are some hypogene-Cu-associated elements which have an even higher affinity for the surface than Co, namely Bi, V and Mo. Whereas Co is actually slightly depleted in the top <1m of the profile at 0.95x ACEMS, Bi, V and Mo show enrichment in the top <1m of the profile with average concentrations of 3.11x ACEMS for Bi, 1.46x for V and 1.54x for Mo (Figures 5.51 and 5.52). This is likely to be apparent enrichment caused because these elements are less mobile under the conditions of supergene alteration than Co or Cu. The apparent enrichment of these elements in the top <1m of the profile would make their anomalies in soil geochemistry more pronounced and more focussed than the anomalies for Cu would be, and would make them good vectors towards highly leached supergene Cu mineralisation. Ni could also be used as a vector as it is less depleted than copper in the near surface environment (0.46x ACEMS at <1m) although it would not be expected to be as focussed a vector as Bi, V, Mo and Co. Where broad anomalies of Cu around a deposit are encountered, the elements Bi, V, Mo, Co and Ni might be expected to form a 'bullseye target' type effect closer to the region vertically above a supergene Cu deposit. The principle is demonstrated by Cu and Co soil data presented for the Africo permit, adjacent to the Mashitu Complex (Siebel *et al.*, 2013). Here, a Co anomaly is found closer to and more focussed on the Anticline and Mashitu Mines Subgroup fragments, while Cu is found elevated in a broader, more spread out region around the deposits, and also concentrated heavily along a nearby tributary stream (Figure 5.76). In this case, the Co anomaly appears to have been a better indication of where to drill to intercept mineralisation than the Cu anomaly.

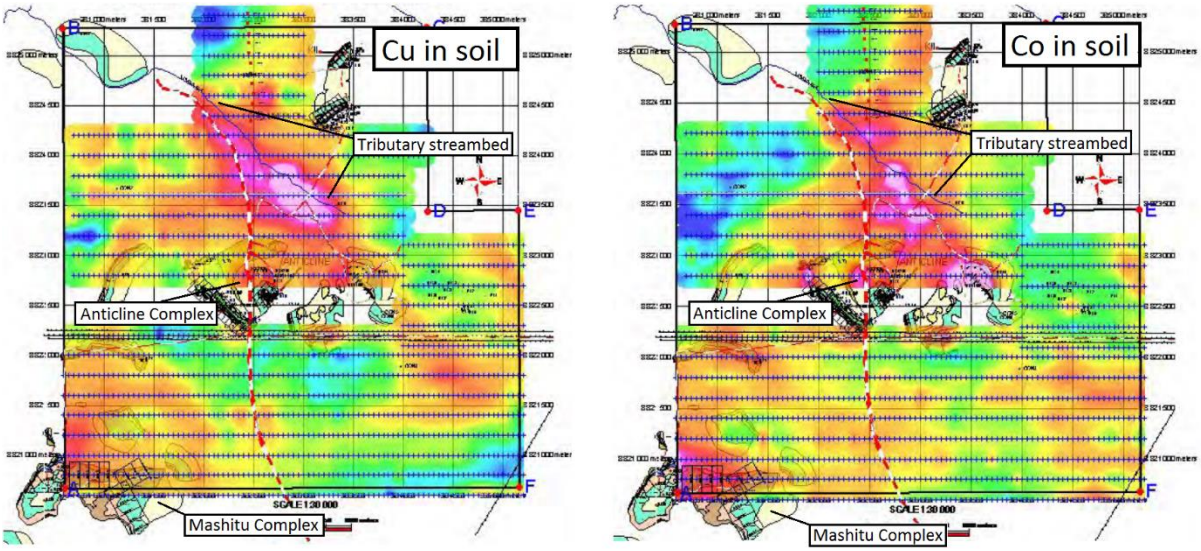

Figure 5.76: *Comparative Cu and Co soil geochemistry maps for the Mashitu and Anticline complexes. At this scale (1:30,000), Co gives a more focussed anomaly, nearer to the mineralised Mines Subgroup fragments than Cu, which is more broadly distributed by comparison. Cu also seems to have concentrated along the bed of a nearby tributary, which Co has not done to such an extent. Modified from Siebel et al. (2013).*

Out of the other hypogene ore-associated elements, Fe and As also show enrichment in the very top of the profile (Figures 5.51 and 5.52), however the association with Cu, Fe and As in the hypogene environment is not pronounced enough (Figure 5.71) that these elements could be recommended as vectors towards ore. Zn is also not associated with hypogene Cu with enough certainty, nor is it particularly enriched in the surface environment, to be recommended as a vector. S is the only element in the hypogene association with Cu which is even more mobile in the surface environment than Cu, showing a pattern of progressive depletion and having concentrations of 0.07x ACEMS in the <10m interval and 0.09x ACEMS in the 10-50m interval. The relative mobility of S in supergene fluids is illustrated by its downhole profile when compared to that of Cu in MSSD075 (Figure 5.73). Peaks of sulphur occur at a greater distance from the RSC than peaks of copper, when the two elements should be co-mineralised in the hypogene environment. This is likely to have been the result of subsequent supergene alteration along the permeable RSC leaching S and redepositing it further away from the RSC contact than the comparatively less mobile Cu. Sulphur, therefore, is also not recommended as a surface vector towards ore.

5.4.3.5 Implications for geochemical exploration

Focussed, positive soil geochemistry anomalies of Co, Bi and V would be expected in proximity to prospective hypogene mineralised units across Katanga such as the RSF, even where these units have been strongly leached by supergene processes. These elements would therefore make powerful surface vectors towards buried, remobilised supergene Cu-Co mineralisation, and would be of particular use as an alternative to Cu where the Cu geochemical anomaly is masked by strong leaching or high background Cu concentration.

Co, Bi and V are identified as surface pathfinders because they show strong spatial correlation with Cu in the deep subsurface hypogene environment, and they are shown to be more refractory with respect to weathering in the near-surface supergene environment. This approach to identifying surface pathfinders can be replicated at any polymetallic deposit type affected by supergene alteration.

Pit sampling or shallow drilling of the pedolith, followed by high-precision 'wet-geochemistry' assay methods are recommended for use in this method of exploration. XRF analysis of soil samples may not be accurate enough to produce conclusive assay results for trace elements present in such low concentrations as Bi and V (see Chapter 6: Soil Geochemistry). In their study of supergene Cu mineralisation at the Mount Isa Inlier, Salama *et al*. (2016a) find that Bi and V are effectively concentrated above Cu-sulphide deposits in ferruginous lag (> 7.6 mm size fraction) and in termitaria. Given a similar weathering regime between the two study areas, these materials are also recommended as sampling media in detecting highly residual surface pathfinders such as Bi and V while exploring for Cu-Co mineralisation in Katanga. Cobalt, which is slightly more mobile in the near-surface than Bi and V (Fig. 5), is enriched in ferruginous duricrusts at the Mount Isa Inlier along with Cu and Ni (Salama *et al*., 2016a), so it is recommended that this medium be used as a sampling material when using these elements as pathfinders. When using Co and even Cu as surface pathfinders, it is recommended to normalise the concentration data against Mn in order to exclude false positives produced by scavenging of these metals by Mn oxides in the near-surface, which has been demonstrated to occur in Cu exploration over the buried Katangan Supergroup of NW Botswana (Salama *et al*., 2016b).

5.4.4 U Mineralisation

U mineralisation at Mashitu South, due to the association of high grades of U with yellow uranium oxides (Figure 3.36), is thought to be secondary and supergene in nature. It is also intimately associated with the RSC (Figures 5.63 and 5.64), suggesting a 'Fay and Barton (2012)' mode of distribution (Figure 3.58) where meteoric fluids use the RSC as a conduit to transport labile metals, which reprecipitated at greater depth as secondary minerals. Uranium may have originally been co-mineralised in the hypogene environment with Cu, as the two are known to occur together in the Copperbelt (Torrealday *et al.*, 2000; McGoldrick *et al.*, 2003; Selley *et al.*, 2010b) and both have a tendency to be mobilised in the same kind of hydrothermal systems (Brown, 2014).

There are two points of significance for U mineralisation with regard to Mashitu South, even though the U mineralisation is insignificant when compared to the volume and grade of Cu-Co. The first is that U mineralisation is only found on the far eastern side of the deposit at great depth. Because the RSC is likely to extend further to the east, dipping in that direction, where there is no coverage of drill holes (Figures 5.62 and 5.64), it is possible that further U mineralisation exists deeper and more eastwards than the previous drilling programs have intercepted.

The second significant point is that U may act as a deleterious element in the mining of the far eastern portion of Mashitu South for Cu-Co, creating health hazards during the blasting and extraction of the ore and necessitating measures of mitigation such as dust-dampening to make mining there feasible from an environmental perspective.

For these two reasons, it is recommended that uranium distribution at the Mashitu South deposit be modelled more fully to ascertain its exact volume and extent.

5.5 Conclusions from Geochemistry

1. The Sr:Sc concentration ratio of a sample dataset can be used as an indicator of calcareous : siliciclastic input in the original depositional environment of sedimentary rocks at Mashitu South. This can be used to discriminate between original vs. dolomitised bulk-composition-carbonate rocks.
2. Each stratigraphic unit appears to have a distinct geochemical signature, which could be used to help identify units where a lithostratigraphic identification is difficult. These geochemical signatures, relative to the Average Concentration of Elements at Mashitu South (ACEMS) are: **CMN**: elevated Ca, W and Ag. **SD**: elevated K. **RSC**: slightly elevated U, depleted in K. **RSF**: elevated Bi. **DStrat**: elevated As and Mo. **RAT Gris**: elevated Ba and Mo. **RAT Rouge:** depleted in S.
3. Geochemical evidence for magnesian, potassic, silicification and argillic alteration exists at Mashitu South, each of which appears to be more prevalent in certain stratigraphic units or lithologies.
4. Hypogene Cu-Co mineralisation appears to be primarily stratiform and is most concentrated in the RSF and SD2d stratigraphic units. It has a geochemical association of: Cu + Co + Bi + Ni + V + S ± Mo ± As ± Fe ± Zn.
5. Supergene Cu distribution is controlled by permeability and is most concentrated in breccia, particularly within the RAT Rouge stratigraphic unit in the form of para-exotic deposits. It has a geochemical association of: Cu + Be + P ± Zn.
6. During the process of leaching and redeposition through which supergene Cu forms from hypogene Cu-Co, the elements Co, Bi, Ni, V and Mo (and possibly Fe, As And Zn) are either left behind within refractory phases or are redeposited closer to the surface in more oxidising, more acidic conditions than where Cu tends to be concentrated. As a result, one would expect these elements to be more highly concentrated in the near-surface environment and to make better surface pathfinders to para-exotic supergene Cu than Cu itself, in the following order of usefulness: Bi → V → Mo → Co → Ni. It is suggested that the concentration in soil of any of these elements, or a multi-element index of Bi-V-Mo-Co-Ni-Cu, would make a good surface vector to buried supergene Cu. These elements could form a 'bullseye'

pattern around supergene Cu mineralisation with Bi at the centre and Cu at the margins.

7. There may be a significant concentration of U around the RSC at depth in the eastern portion of the Mashitu South deposit, which should be investigated and modelled further for economic and mining safety reasons.

CHAPTER 6: SOIL GEOCHEMISTRY

6.1 Introduction – Aims and Objectives

The results of Chapter 5: Geochemistry suggest that elements which are co-mineralised with hypogene Cu-Co are redistributed by supergene processes in a pattern of vertical zonation above deposits. Figures 5.71, 5.72 and 5.73 show that hypogene mineralisation at Mashitu South has an element association of Cu + Co + Bi + Ni + V + S ± Mo ± As ± Fe ± Zn. During supergene alteration, these elements dissociate, and copper recombines with Be and P to form para-exotic (located below the sourcing hypogene mineralisation) supergene mineralisation (see Figures 5.71, 5.72 and 5.73). Sulphur, which is more mobile than Cu in meteoric fluids, has been leached deeper into the rock profile (Figure 5.50) and it is likely that it formed supergene sulphates such as barite and supergene sulphides such as chalcocite (see section 4.4.4 and 4.4.5). However, supergene chalcocite does not appear to be particularly well developed at Mashitu South and the 'chalcocite blanket' observed in some supergene Cu deposits appears to be absent. The remaining metals of the hypogene association are more resistant to leaching than Cu, being more stable in the acidic, oxidising, near surface conditions of supergene alteration, and are thought to be found concentrated above para-exotic supergene Cu mineralisation (Figures 5.49, 5.50. 5.51. 5.52). The 5 metals of Bi, V, Co, Mo and Ni, which are the most closely associated with Cu in the hypogene environment, and were found to have a greater affinity for near-surface conditions than Cu, were thus hypothesised to be surface vectors to ore (see Chapter 5).

Support for this hypothesis is found in Figure 6.1, a depth profile of these 5 elements in MSSD140, showing a spike in their concentration below a depth of 10m, with a 15m thick supergene orebody containing >3% Cu found at a depth roughly 20m below this spike.

The usefulness of Co as a surface vector to hypogene ore is widely recognised. The metal regularly forms 'cobalt caps' over Cu-Co deposits (Decree *et al.*, 2010), first as residual deposits and secondly, as supergene alteration progresses, as remobilised deposits which precipitate out higher in the rock profile than the reprecipitation of Cu (Decree and Pourret, 2013). This resistance to leaching and mobilisation also means that cobalt is less laterally

mobile in supergene conditions. As a result, Co forms smaller, but stronger and more focussed surface anomalies over Cu-Co deposits than Cu does (see Figure 5.76).

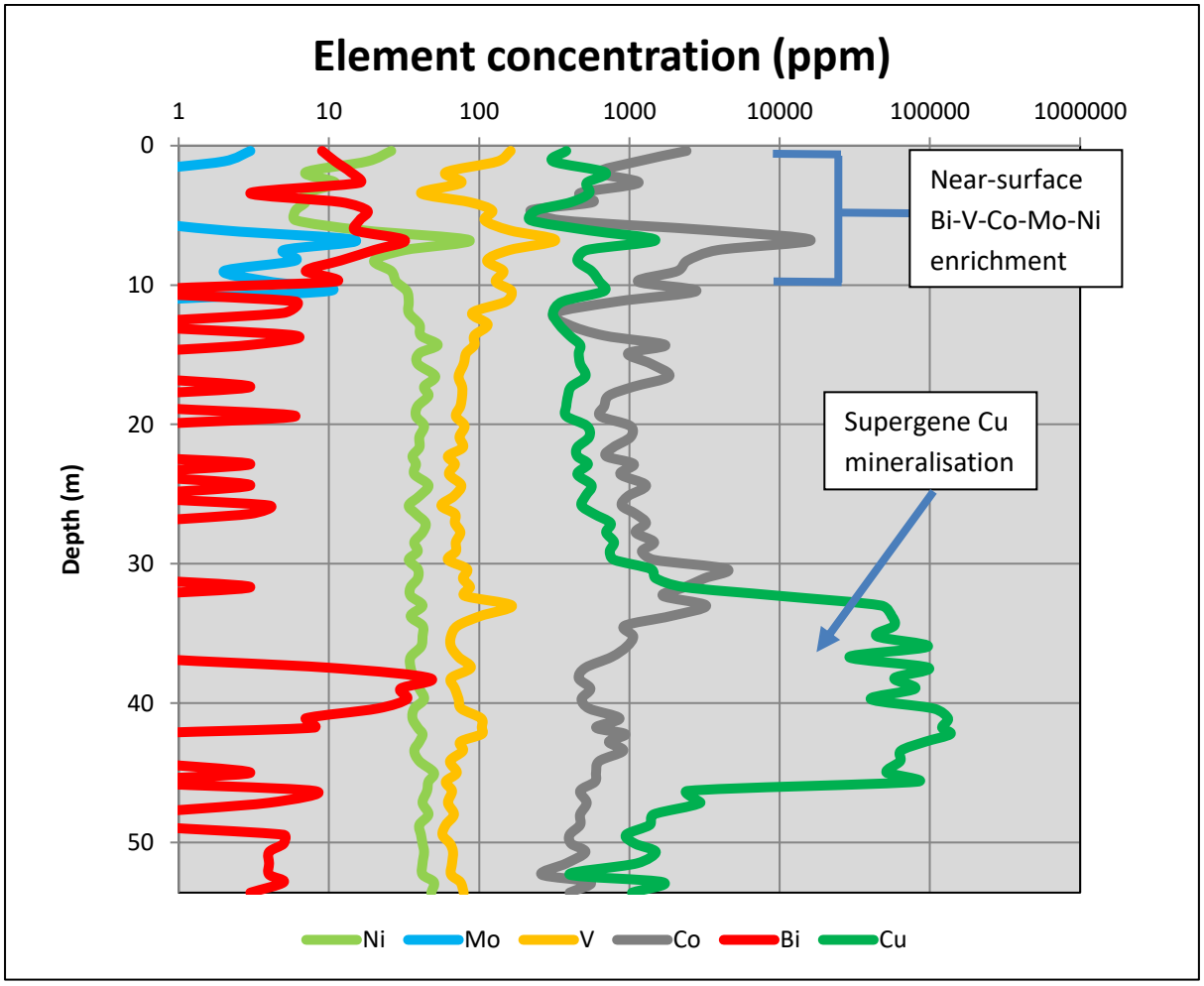

Figure 6.1*: Depth profile for Cu, Bi, Co, V, Mo and Ni concentration in MSSD140. The 30-50m zone of Cu enrichment is overlain by a region in the top 10m where Bi, V, Co, Mo and Ni are enriched.*

It is considered likely that this property will extend to Bi, V, and possibly Mo and Ni, which are shown by Figure 5.53 to have a higher affinity for the surface environment than Cu, together with Co. Therefore, the geochemistry of residual soils above a Cu-Co deposit should be elevated in Bi, V, Co, Mo and Ni, which will all perhaps form more pronounced anomalies over the deposit than Cu itself.

To test this hypothesis, this study will examine soil geochemistry data from Katanga to look for spatial associations between Bi, V, Co, Mo and Ni in areas of known or suspected Cu-Co mineralisation.

6.2 Methods

This study was granted access to the full Comide S.P.R.L. soil geochemistry database, in order to investigate the variation of elements in soil. This database was compiled from XRF analysis of soil samples which were collected from a 50m x 50m grid which spans the entirety of the Camrose concession owned by Comide, the extent of which is shown in Figure 6.2. A total of 27,983 samples were collected and analysed by handheld XRF for their concentration of Cu, Co, S, Cl, K, Ca, Ti, V, Cr, Fe, Ni, Zn, As, Se, Rb, Sr, Zr, Mo, Ag, Cd, Sn, Sb, W, Hg, Pb, Bi, Th and U. The detection limits for this XRF technique provided by Comide indicated that the Lower Limit Of Detection (LLOD) for this technique was 5ppm for all of the elements analysed.

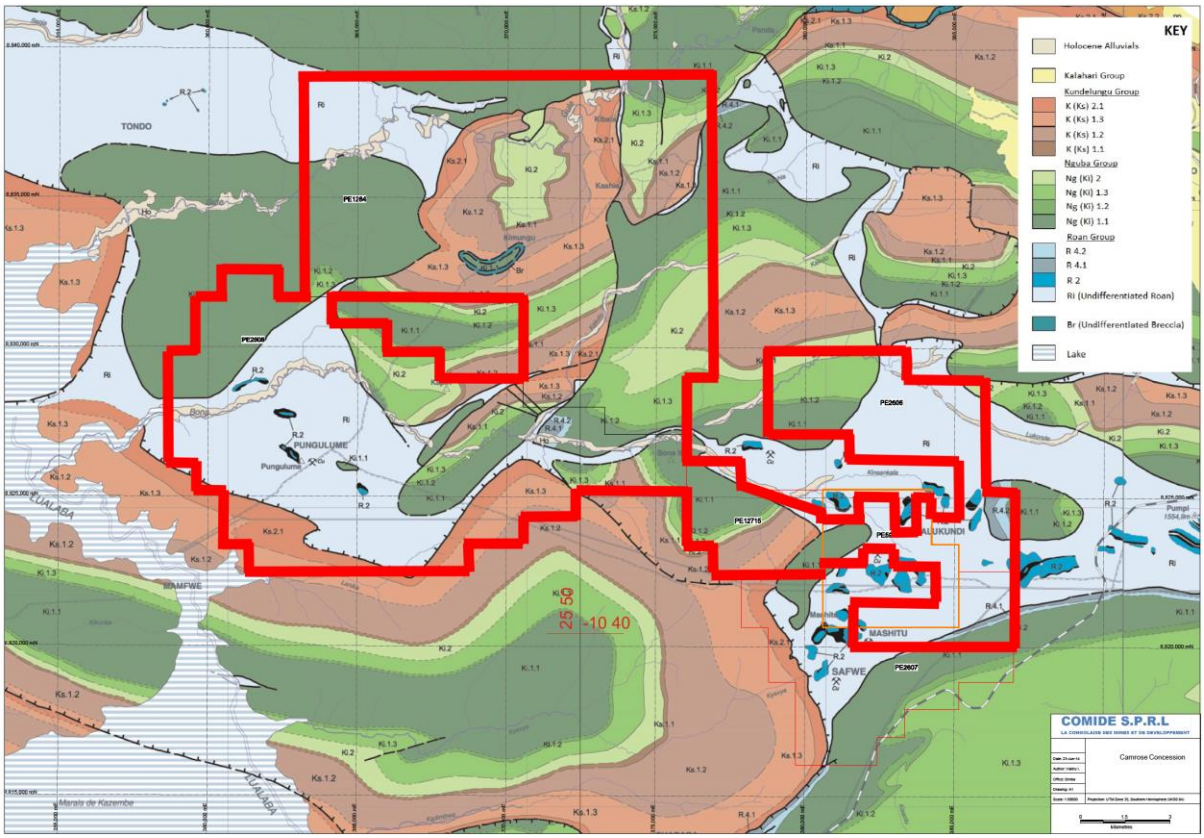

***Figure 6.2**: Map of the extent of the Comide sampling program (outlined in red) overlain on the regional geology, an expanded view of which is shown in Figure 3.3. The grid squares are 5km x 5km for scale.*

The soil database was subjected to basic statistical analysis and in the copy of the database analysed for this, element analyses under the LLOD were replaced by half the LLOD (i.e.

5ppm). Other copies of the database were made for gridding and mapping where element analyses below the LLOD were replaced with 0, so as not to create false concentration values.

In addition to mapping the basic element-soil concentration data, various multiple-element indexes were also created to be mapped, under the premise that hypogene mineralisation would be most certain to exist in proximity to a combined, overlapping anomaly of all of the hypogene-mineralisation-related elements: Cu, Co, Bi, Ni, Mo and V. To create these index values for each sample, the concentration of the various elements in the index were multiplied by the concentrations of all the other elements. Before this was done, the concentration of each element in the sample was normalised against (divided by) the average concentrations of these elements in the entire database, so that naturally more abundant elements (such as Cu) would not have a greater influence on the index value than naturally scarce elements (such as Bi). These normalised values were then multiplied against each other. This would produce an index value that would only be high if a sample contained all of the elements in the index, and would be 0 if any of the element analyses in the sample were 0.

For example, if the index of CuCoNiBiVMo were to be calculated for fictional Sample X, its concentration values for the elements Cu, V, Co, Bi, Ni, Mo would be divided by the average (mean) values for these elements in all of the 27,983 samples of the database to give normalised concentration values for each element. These normalised concentration values would be multiplied by each other ([Cu]x[Co]x[Ni]x[Bi]x[V]x[Mo]) to give the final CuCoNiBiVMo index value (see Figure 6.3).

Average Cu (ppm)	Average V (ppm)	Average Co (ppm)	Average Bi (ppm)	Average Ni (ppm)	Average Mo (ppm)
94.20	106.08	13.22	3.15	2.13	0.29
Cu (ppm)	**V (ppm)**	**Co (ppm)**	**Bi (ppm)**	**Ni (ppm)**	**Mo (ppm)**
215	45	13	7	8	6
Cu (normalised)	**V (normalised)**	**Co (normalised)**	**Bi (normalised)**	**Ni (normalised)**	**Mo (normalised)**
2.28	0.42	0.98	2.22	3.75	20.58
CuCoNiBiVMo index					
163.57					

Figure 6.3*: Exemplary values used for the calculation of the CoCoNiBiVMo index for fictional sample X. See text above for explanation.*

The indexes calculated for this study were: CuCoNiBiVMo, CoNiBiVMo, CoNiBi and CoBi, based on the degree of certainty with which these elements were associated with Cu in the hypogene environment. These indexes, together with the raw concentration values for Cu, Co, Ni, Bi, V, and Mo as well as the concentration values for Ca and Ti (for comparison), were mapped, gridded and contoured using the Surfer 8 contouring software program, by kriging. The contour maps for each element or index were colour coded, overlain on the regional geology with ArcGIS 10.2, using the WGS 84 geographic coordinate system for the 35S UTM zone, and compared to the position of known mineralisation and Mines Subgroup fragments to produce Figures 6.4, 6.5, 6.6, 6.7, 6.8, 6.9, 6.10, 6.11, 6.12, 6.13, 6.14 and 6.15, which are presented in Section 6.3: Results.

Although soil geochemistry from above the Mashitu South deposit was not present in the regional soil geochemical database, ICP-AES borehole data from the 43 samples available with mid-points in the top <1m of the profile at Mashitu South (see Chapter 5) were taken and compared to the XRF data for the regional soil geochemistry. This was done for the purpose of identifying elements which were anomalously concentrated over the Mashitu South Deposit, relative to their background concentration in the region. A discussion of this analysis is presented in section 6.4.4.

6.3 Results

The geology-overlain contour maps for Cu (Figure 6.4), Co (Figure 6.5), Ni (Figure 6.6), Bi (Figure 6.7), V (Figure 6.8), Mo (Figure 6.9), Ca (Figure 6.10), Ti (Figure 6.11) and the CuCoNiBiVMo (Figure 6.12), CoNiBiVMo (Figure 6.13), CoNiBi (Figure 6.14) and CoBi (Figure 6.15) indexes are presented in this section. Large regions of the data for Co were found to be missing and these regions were left out from the map of Co soil geochemistry (Figure 6.5), and for each of the 4 multi-element indexes, which all use Co as one of their constituent elements.

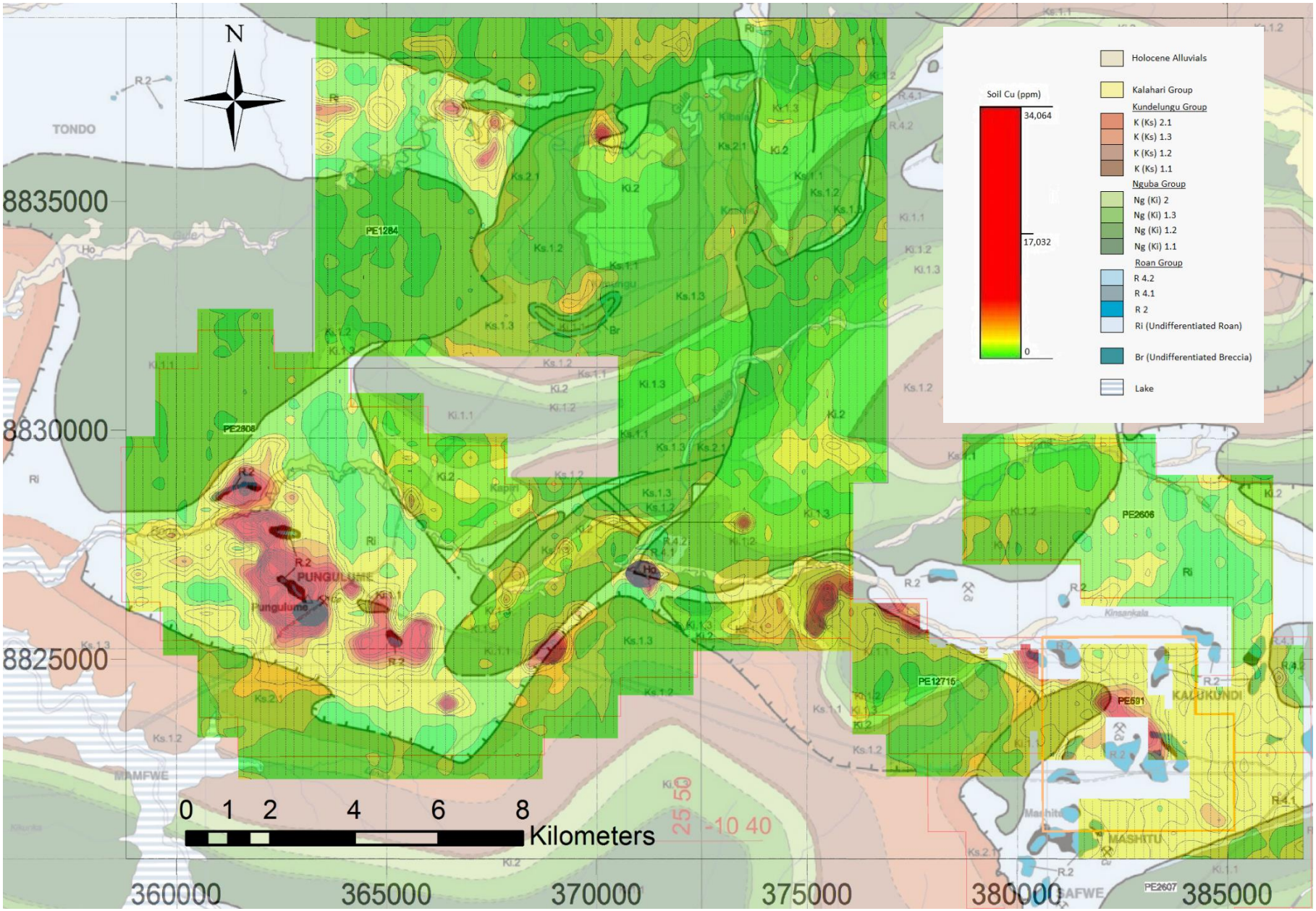

***Figure 6.4**: Soil geochemical contour map for Cu, overlain on regional geology*

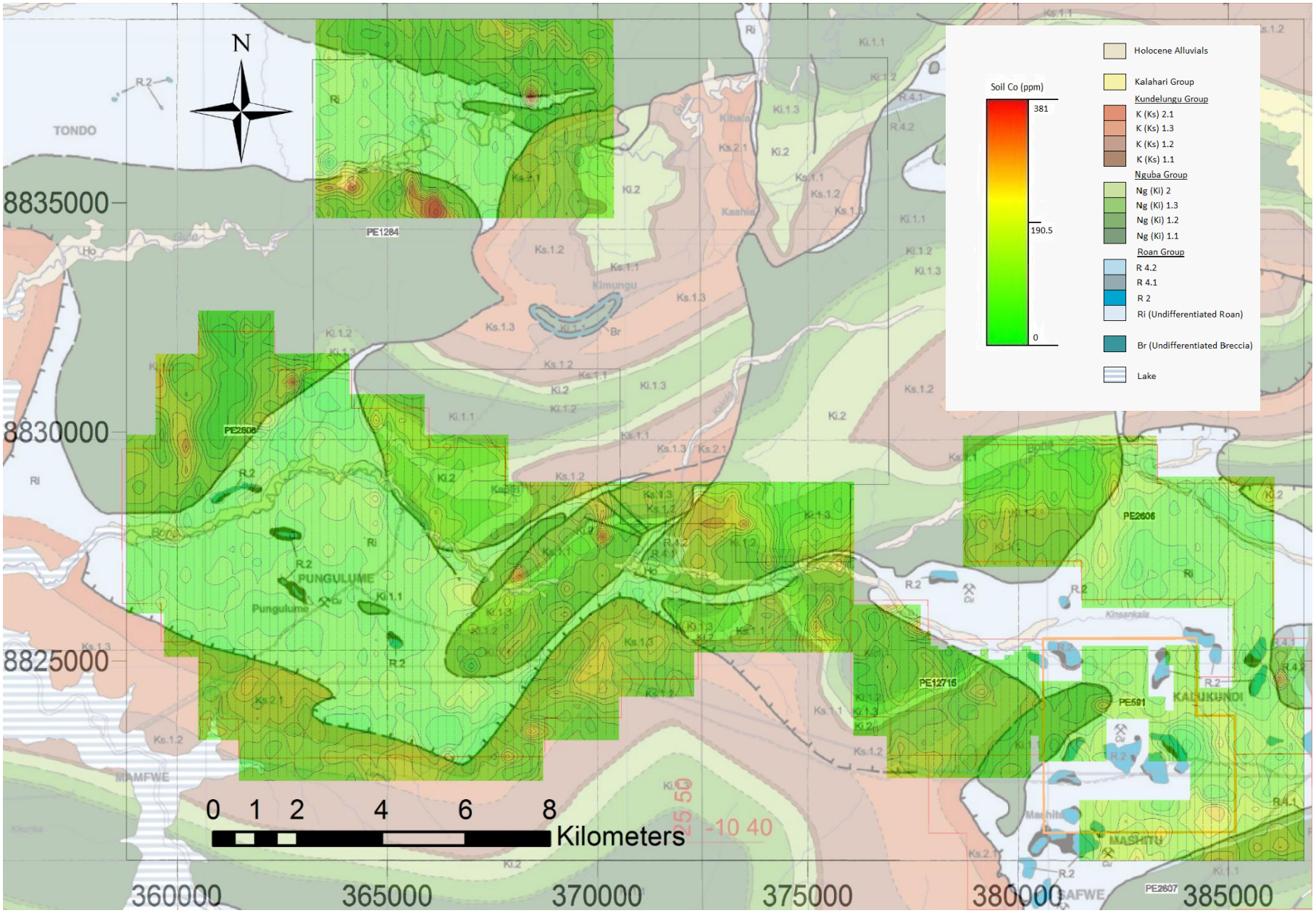

***Figure 6.5**: Soil geochemical contour map for Co, overlain on regional geology*

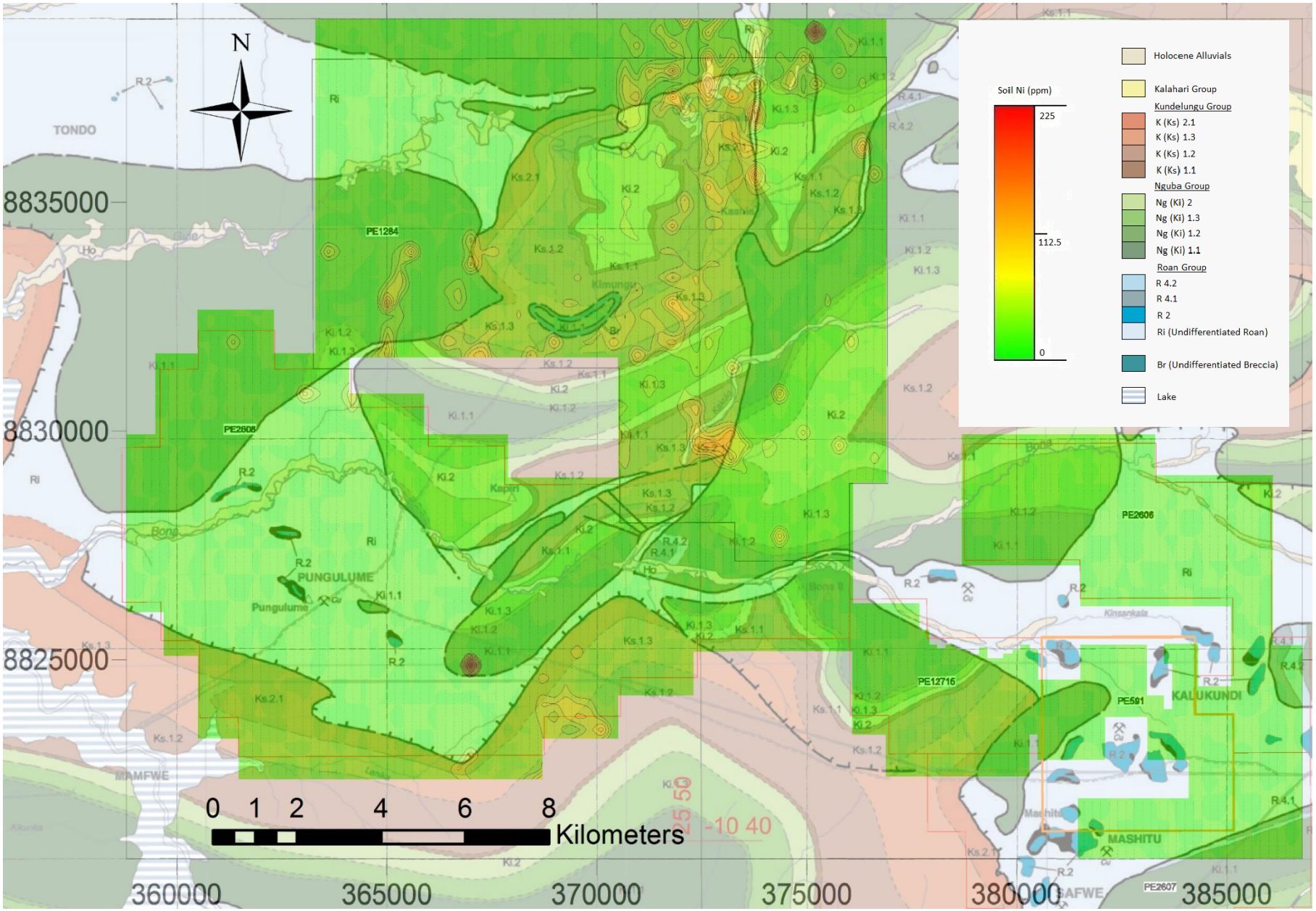

***Figure 6.6**: Soil geochemical contour map for Ni, overlain on regional geology*

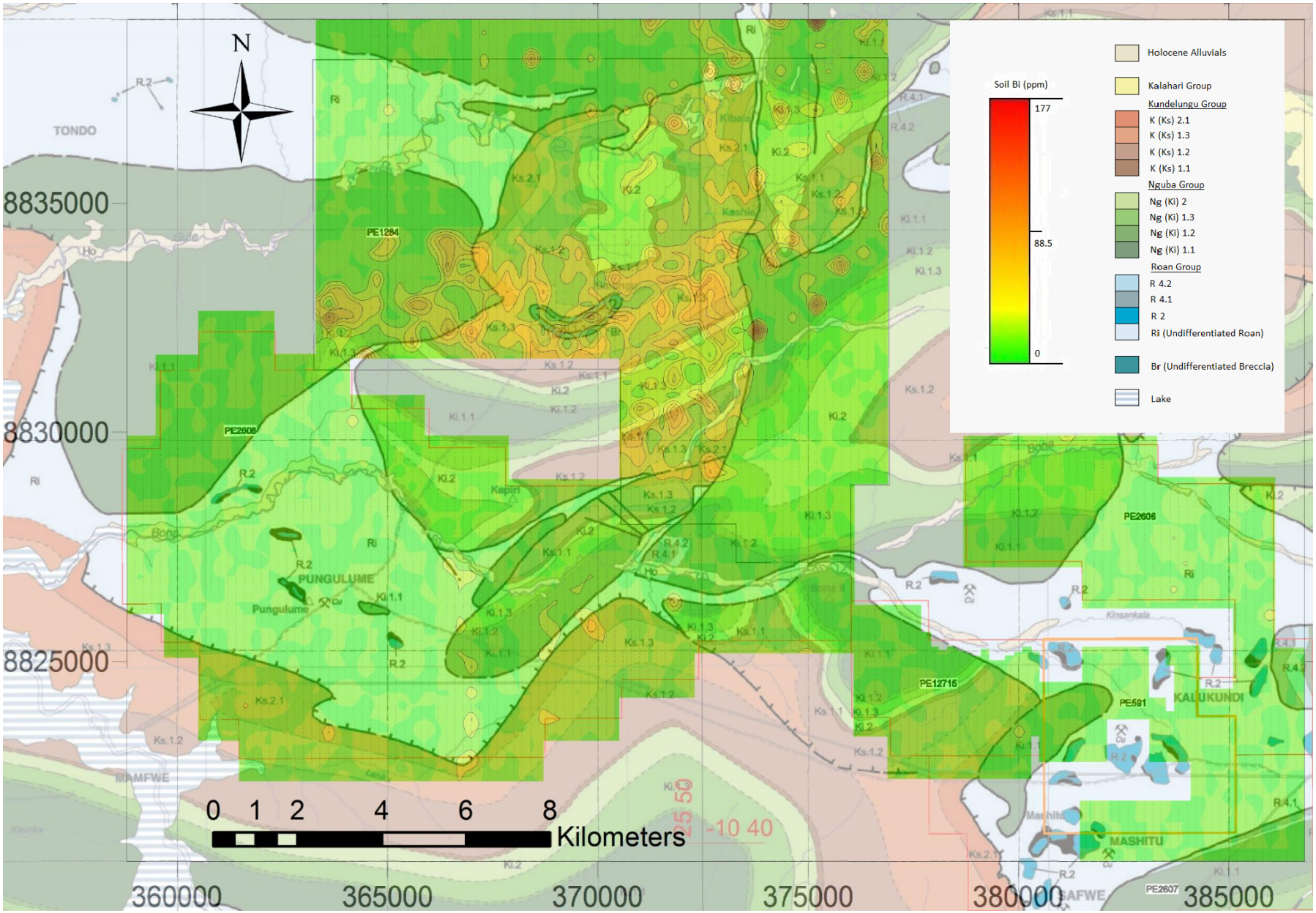

***Figure 6.7**: Soil geochemical contour map for Bi, overlain on regional geology*

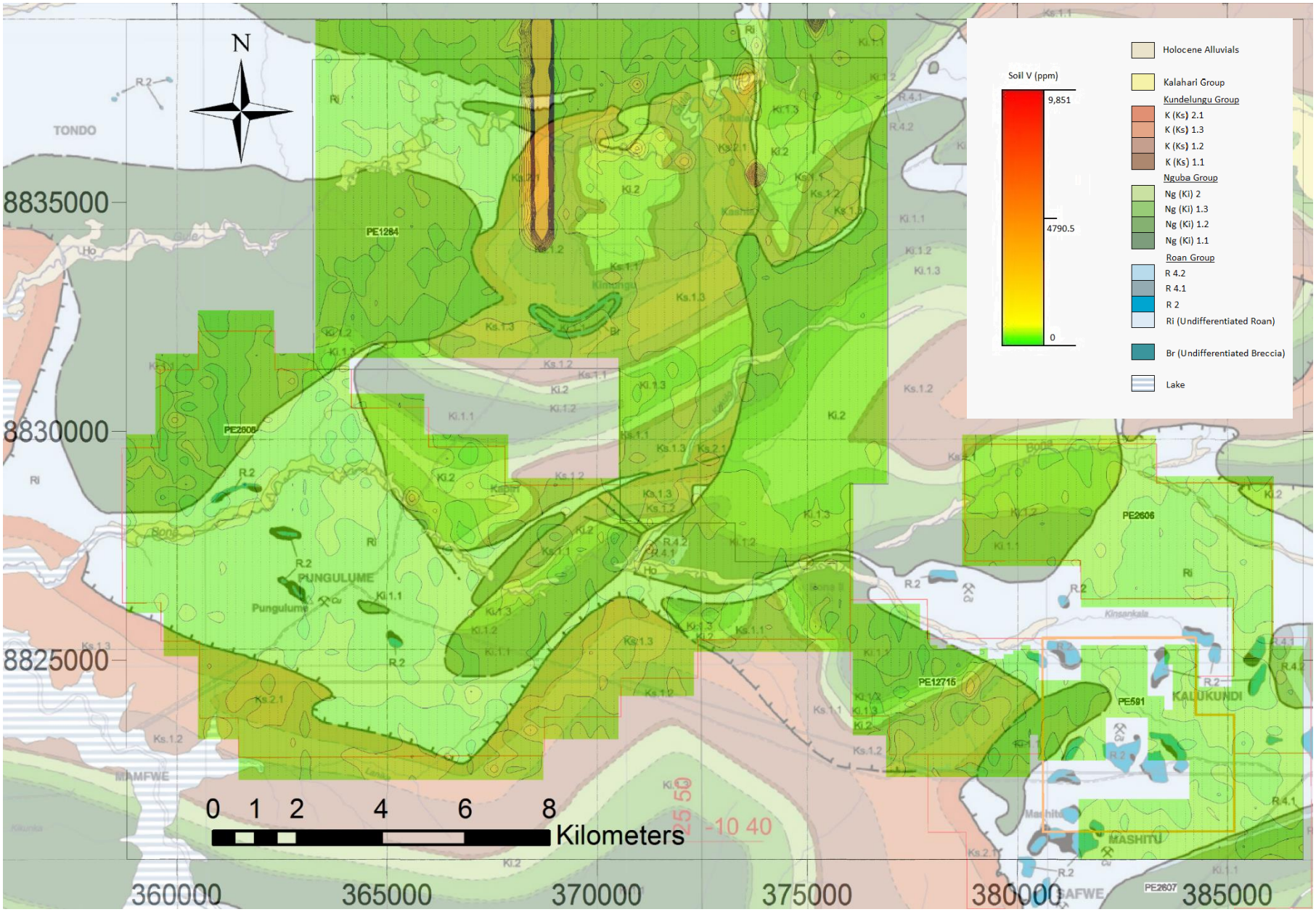

***Figure 6.8**: Soil geochemical contour map for V, overlain on regional geology*

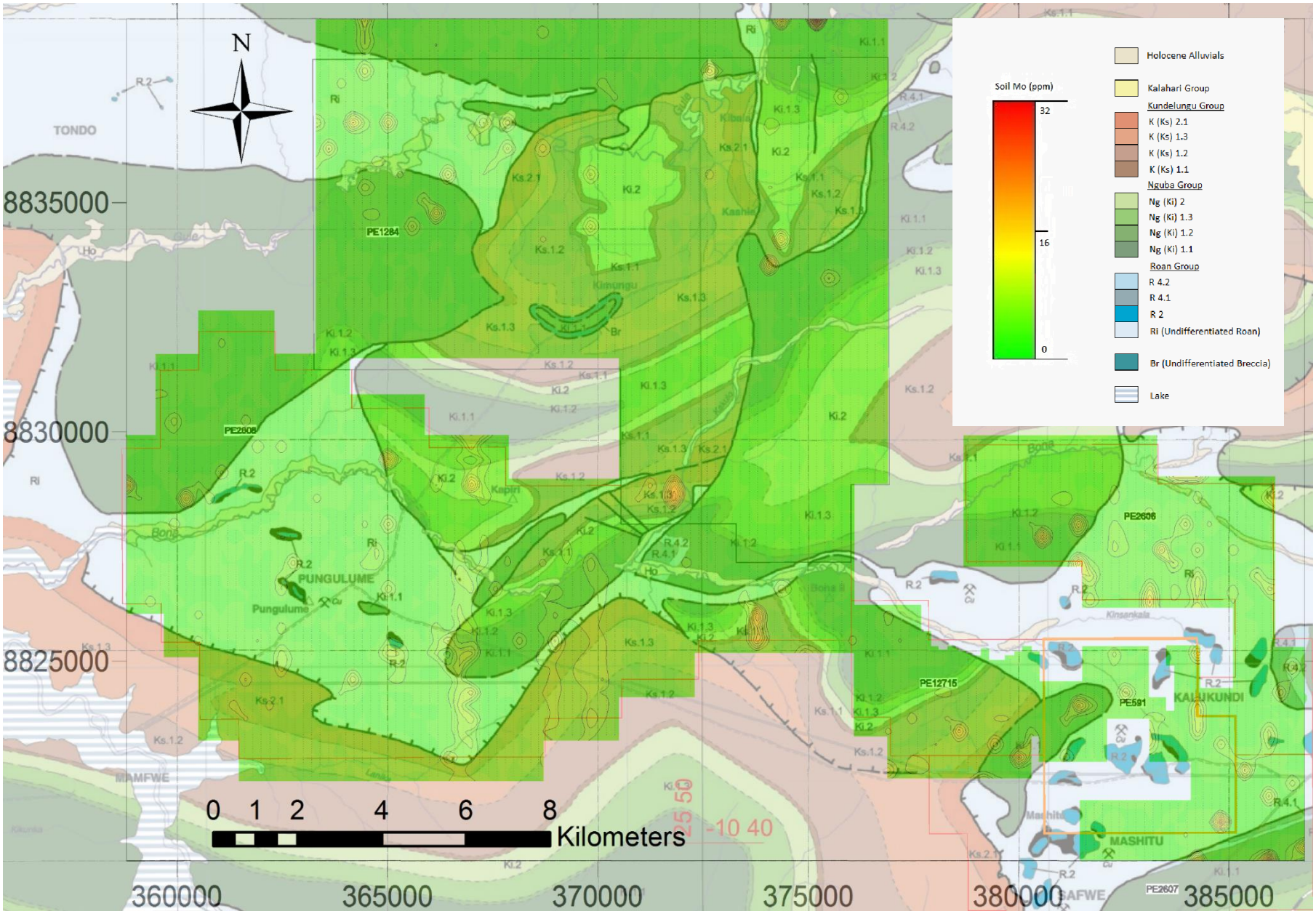

***Figure 6.9**: Soil geochemical contour map for Mo, overlain on regional geology*

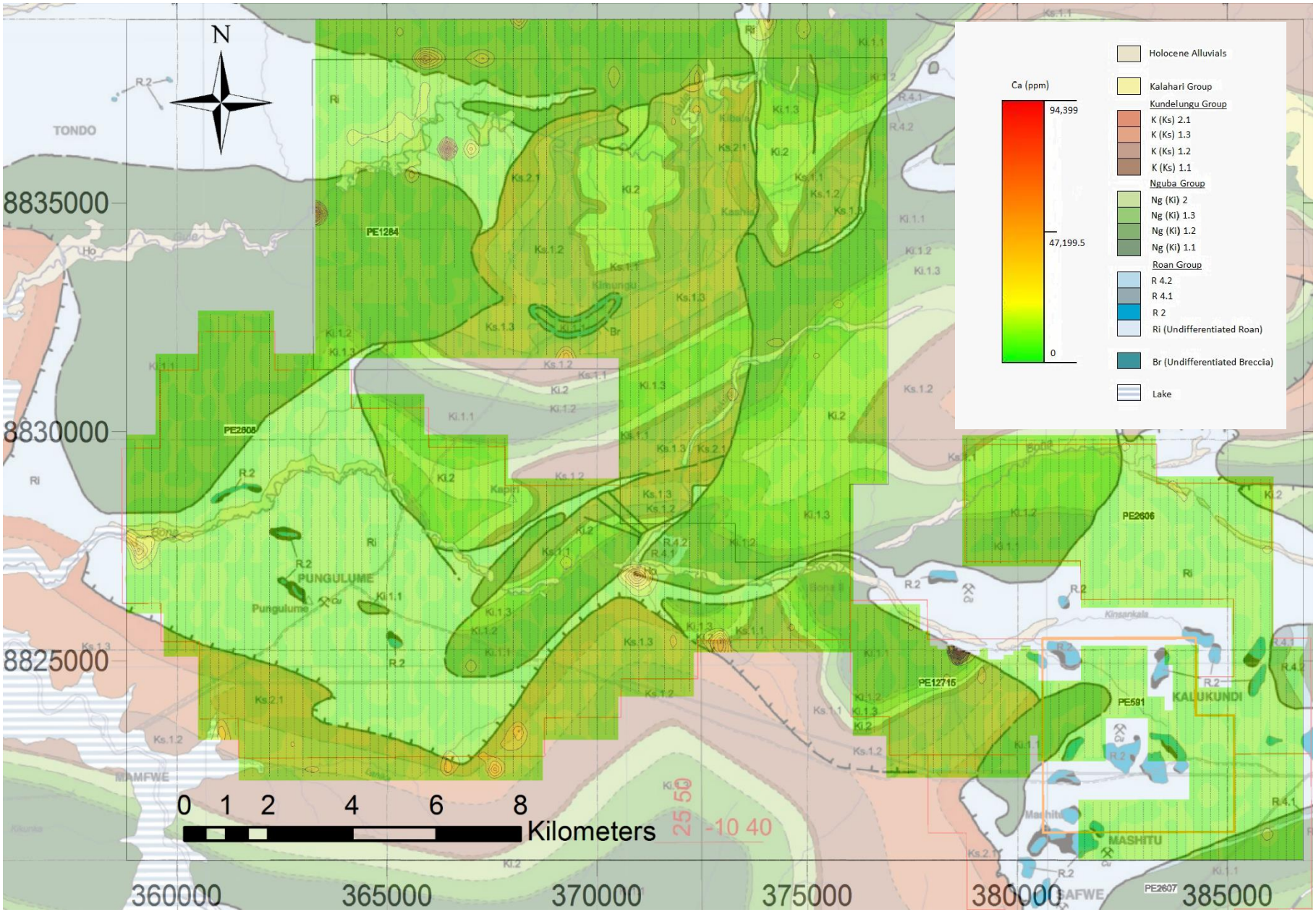

***Figure 6.10**: Soil geochemical contour map for Ca, overlain on regional geology*

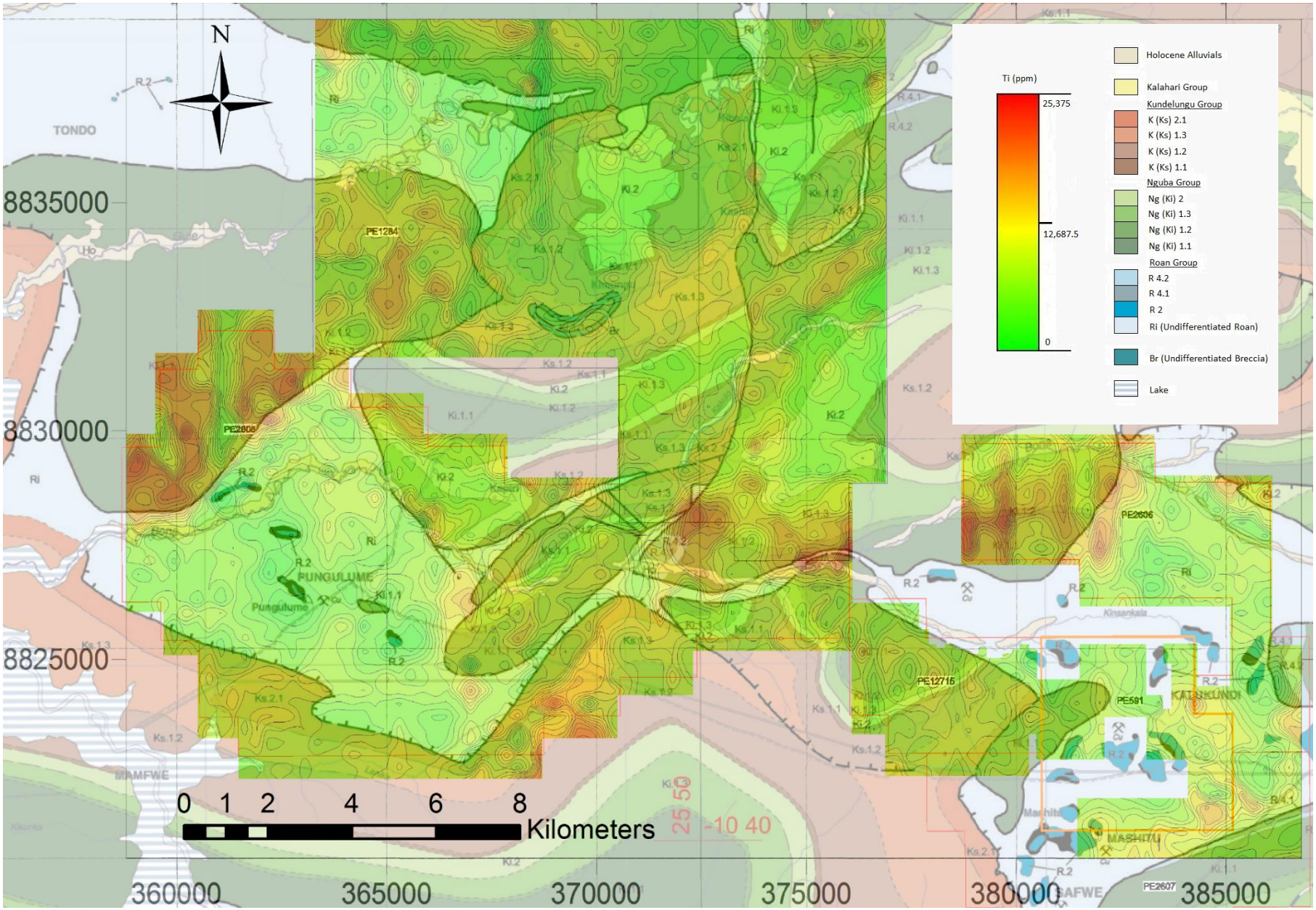

***Figure 6.11**: Soil geochemical contour map for Ti, overlain on regional geology*

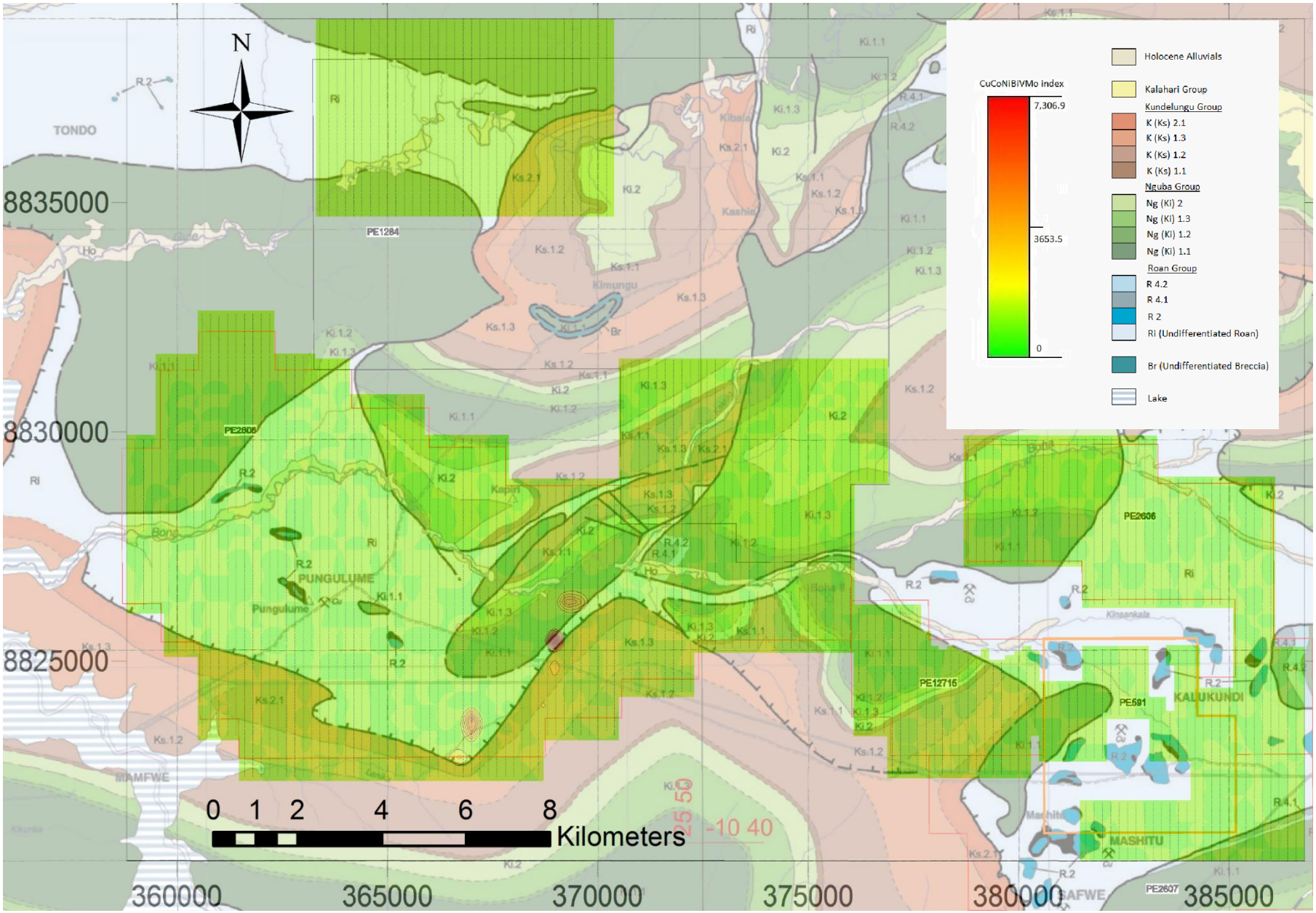

***Figure 6.12**: Soil geochemical contour map for the CuCoNiBiVMo index, overlain on regional geology*

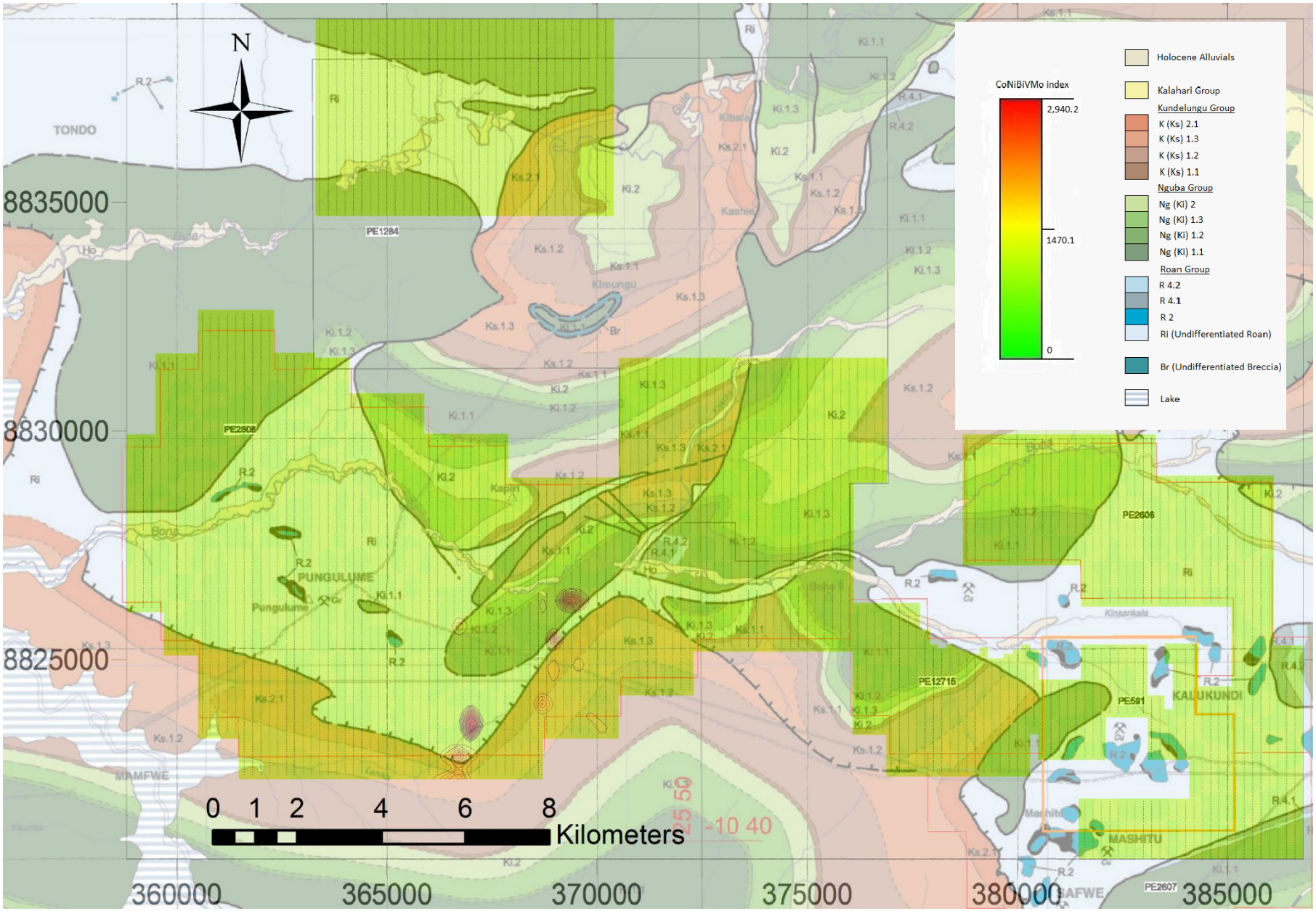

***Figure 6.13**: Soil geochemical contour map for the CoNiBiVMo index, overlain on regional geology*

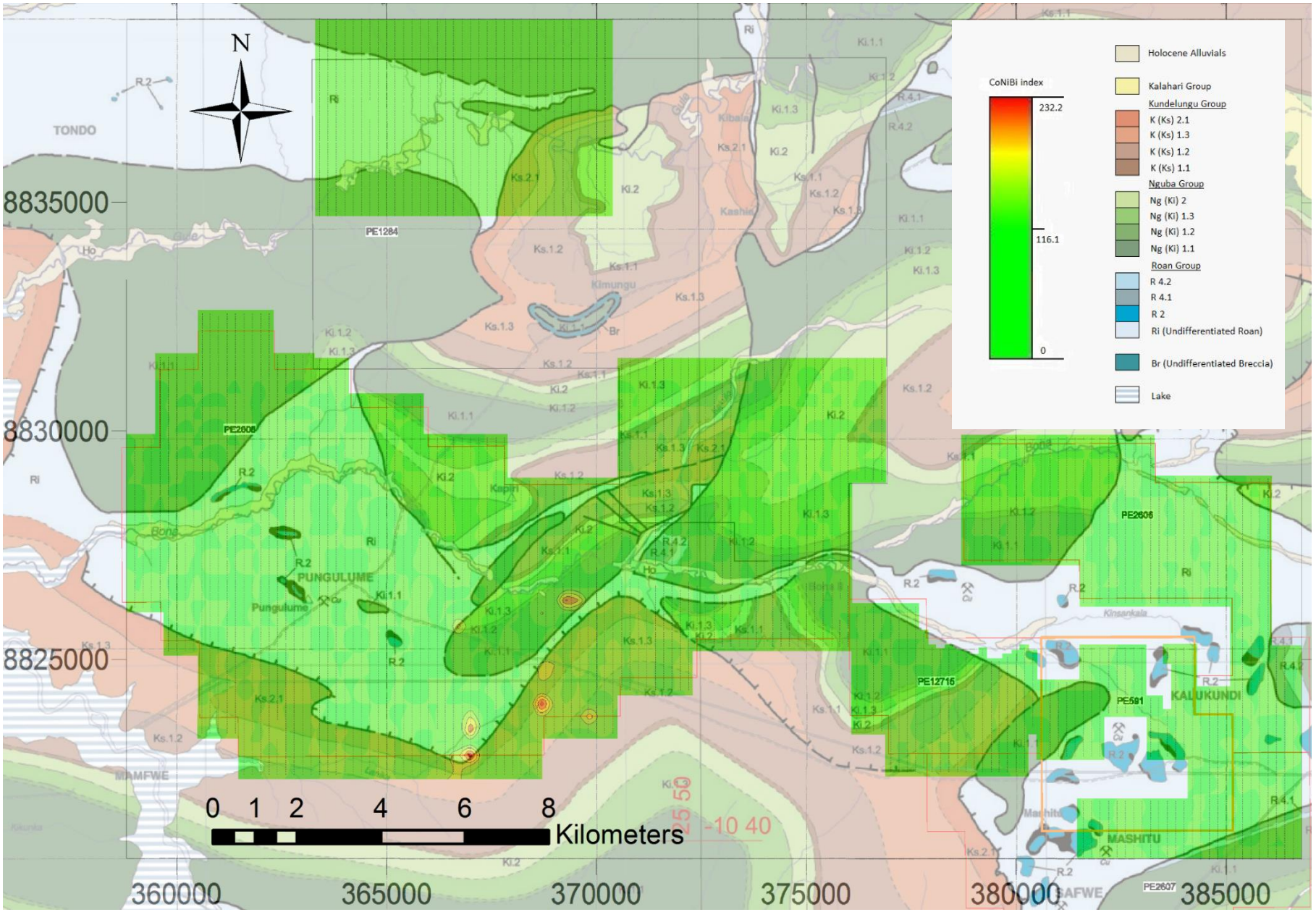

***Figure 6.14**: Soil geochemical contour map for the CoNiBi index, overlain on regional geology*

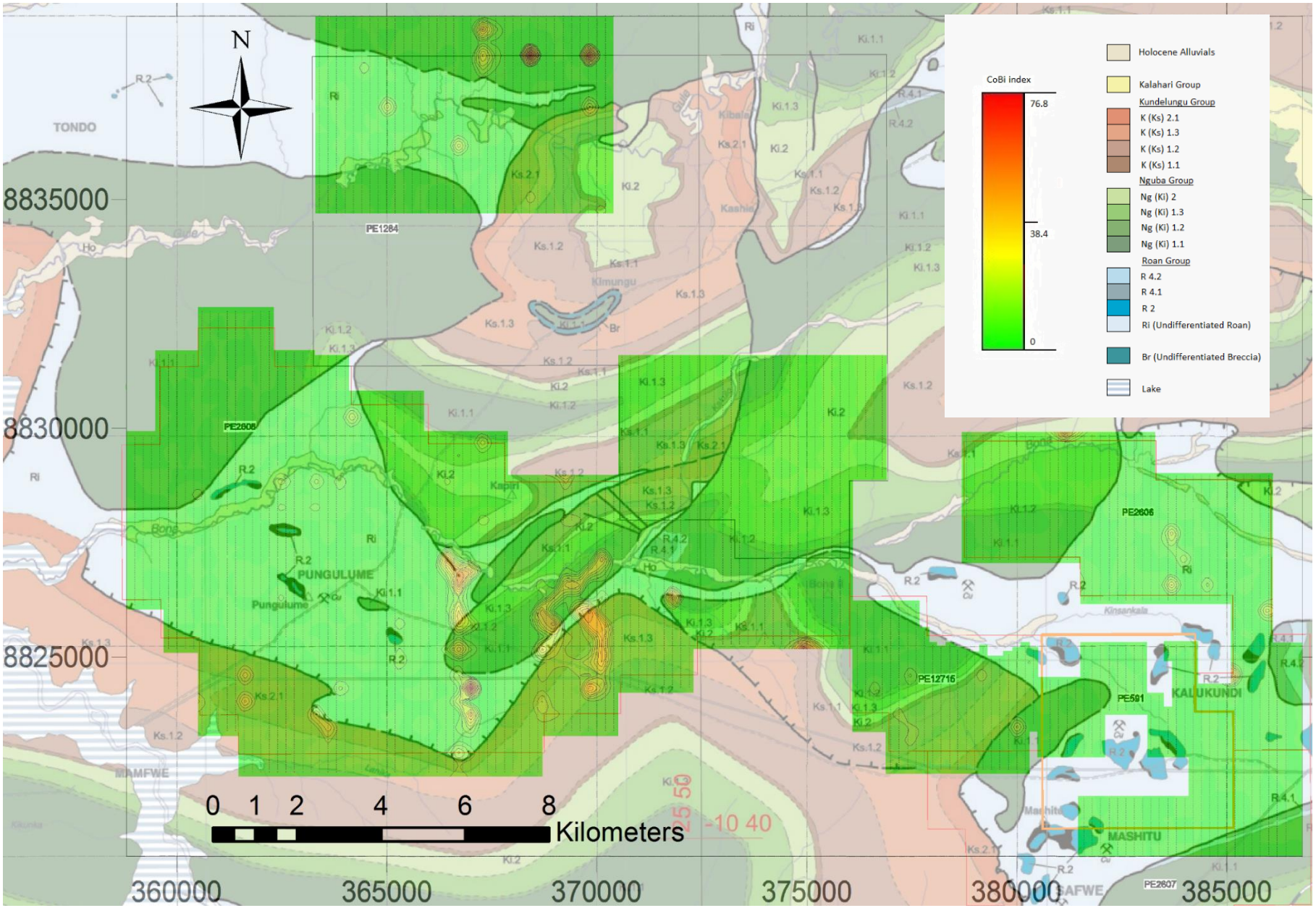

***Figure 6.15**: Soil geochemical contour map for the CoBi index, overlain on regional geology*

6.4 Discussion

Distributions of various elements in the soil geochemical data will be discussed in this section. Some of the elements and indexes contoured for soil geochemistry show useful variation in the dataset, others provided inconclusive results. Aside from limiting factors which were applied to individual element distributions in this study, a limiting factor which applied to all element distributions was the fact that the samples from the Comide dataset were collected and analysed after many of the deposits in the region were put into production, or had been artisanally mined. This made collection of samples from such pit sites unfeasible, and data is absent from the areas immediately above these deposits.

6.4.1 Copper Distribution in Soil

The Cu soil distribution shows anomalies over several important deposits in the region. Although data is absent from the areas above many of these deposits, an anomaly can often be seen in close proximity to them which can be inferred to have been caused as a result of copper concentration at and around these areas of mineralisation. The Anticline and Kinshasa groups of Mines Subgroup fragments both exhibit Cu anomalies in the soil geochemistry around them (Figure 6.16). The anomaly near the Anticline deposit group displays a slightly linear trend away from the deposit, which is shown in a report by Siebel *et al.* (2013) to follow the path of a streambed (see Figure 5.76).

The Kalukundi and Mashitu groups of Mines Subgroup fragments exist within a broader Cu anomaly which covers much of the southern part of the 'Undifferentiated Roan' inlier in which many Mines Subgroup fragments are set (Figure 6.4). However, neither of these deposit groups exhibit a more focussed, appreciable Cu anomaly immediately above them, such that one would be able to target them with drilling, in the way that the Anticline and Kinshasa groups do. The Mashitu South deposit, which is the primary subject of this study, would not have been located by a soil sampling study such as the one conducted by Comide, based only on analysis of the Cu distribution.

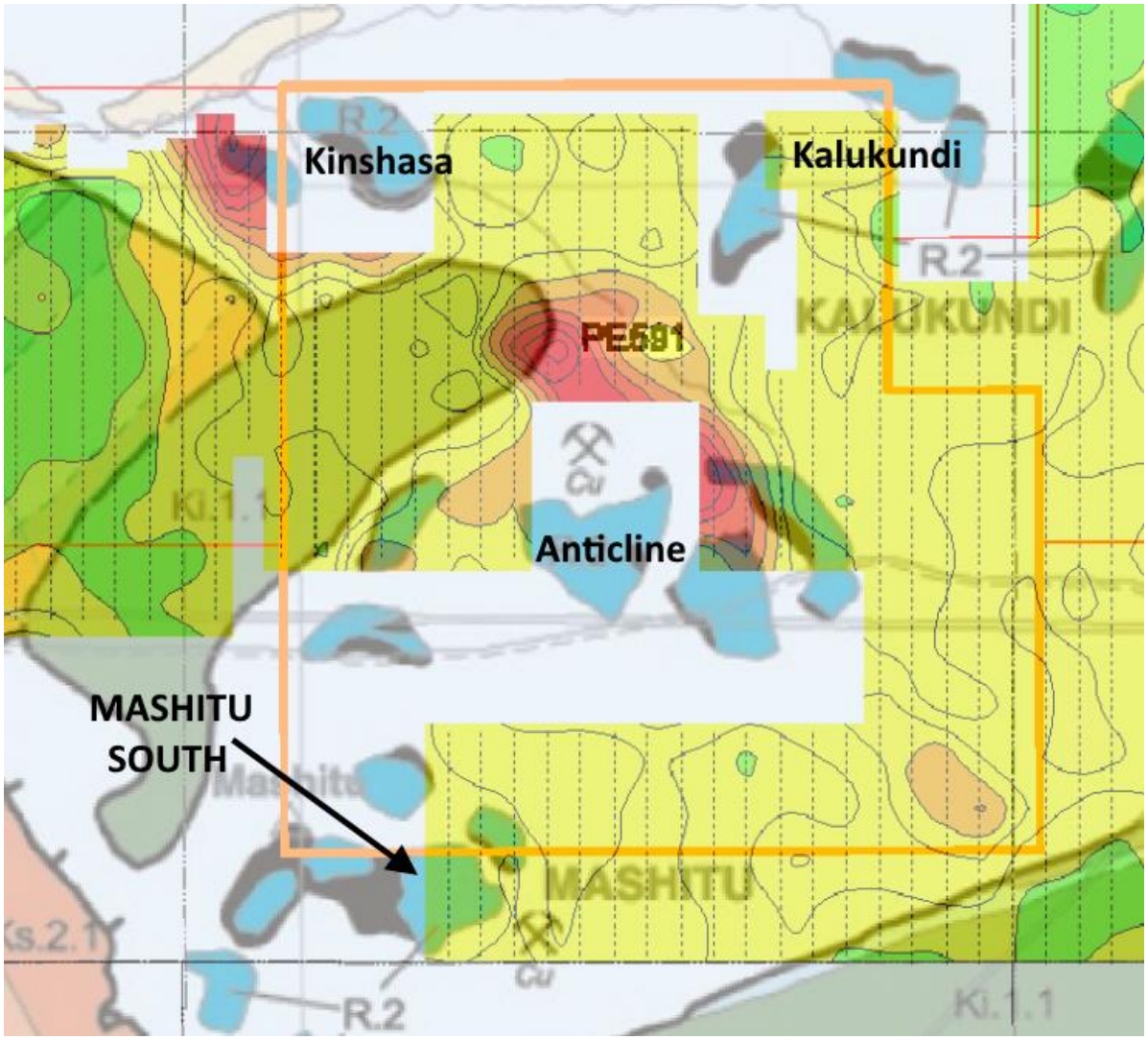

Figure 6.16*: Inflated portion of the SE corner of the Cu soil geochemistry map presented in Figure 6.4, with locations of Cu-Co deposits/Mines Subgroup fragments in the vicinity of Mashitu South. While appreciable Cu anomalies exist over the Kinshasa and Anticline deposit groups, the Mashitu and Kalukundi groups of deposits are not marked by such focussed anomalies. See Figure 6.4 for key.*

Copper-cobalt deposits in the Pungulume region are highlighted well by Cu anomalies. Both the Pungulume Principal and Pungulume East deposits, which are thought to be hosted in the Dipeta Subgroup rather than in the Mines Subgroup (Chimvinga, pers. comm., 2014; Cheshire, pers. comm., 2014) have large Cu anomalies over them and in their immediate vicinities (Figure 6.17). Some of the largest Cu-in-soil values, up to 3 wt.% Cu, are found in this area. The strata of the Pungulume Principal deposit form an isolated area of high topographic relief, and the broad distribution of high-Cu around this deposit may be due to enhanced exposure

to meteoric fluids and enhanced leaching, due to this topography. The Bona South and Bona North deposits are also marked by considerable geochemical anomalies (Figure 6.17).

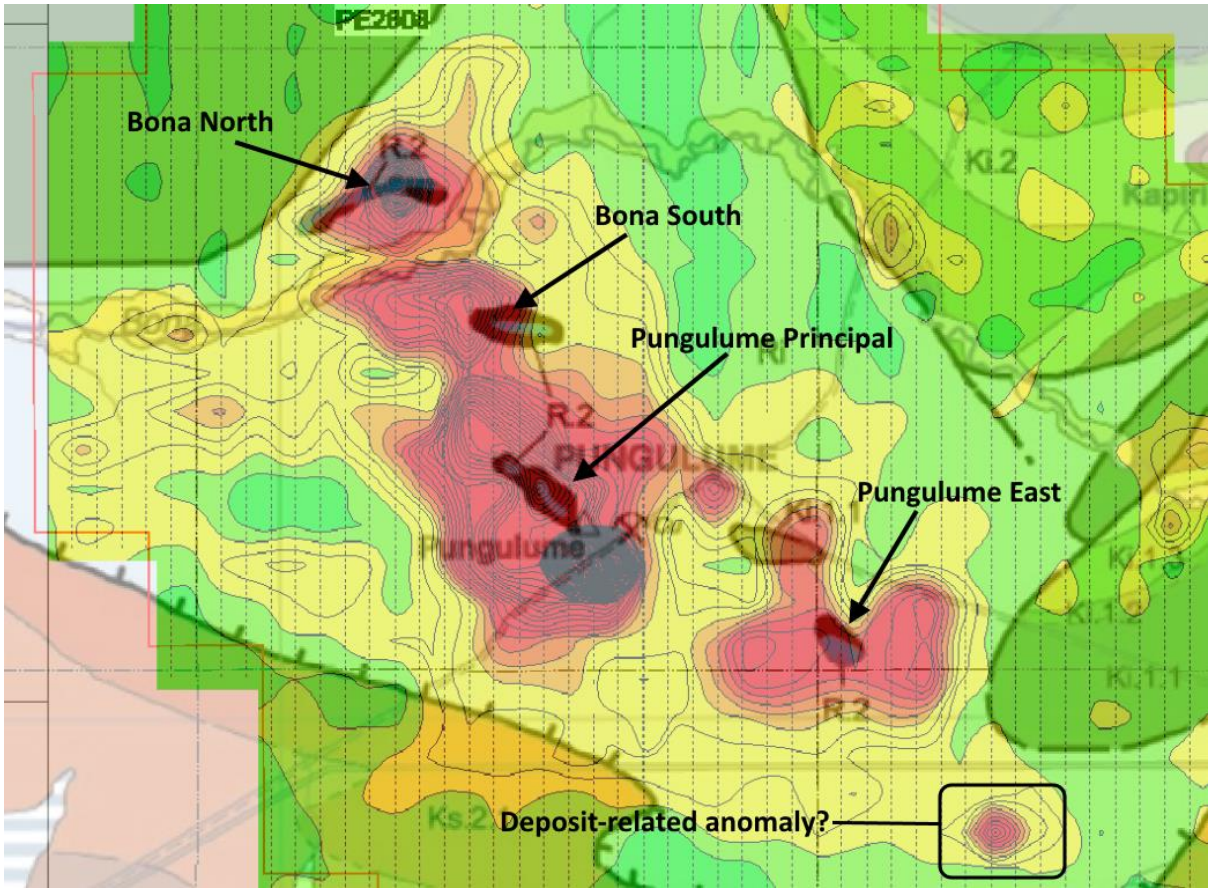

Figure 6.17*: Inflated portion of the SW portion of the Cu soil geochemistry map presented in Figure 6.4, with locations of Cu-Co deposits. Significant Cu anomalies exist over the Pungulume Principal, Pungulume East, Bona North and Bona South deposits. An unidentified, possibly deposit-related anomaly which exists towards the Southeast of this map is indicated. See Figure 6.4 for key.*

6.4.1.1 Cu anomalies which are not found over known Cu deposits

Figure 6.4 exhibits several Cu anomalies which exist over areas where no previously identified deposits of Cu-Co mineralisation are known to exist. These anomalies occur in two broad areas which are shown in Figures 6.18 and 6.19.

The first of these regions (Figure 6.18), to the north of the Pungulume and Bona region mineralisation, shows several small, partially interconnected Cu anomalies. They are distinctly associated with a region which is mapped as 'Undifferentiated Roan (Ri)', and the surrounding Nguba and Kundelungu Group rocks do not exhibit the same pattern of Cu enrichment. It may be that these anomalies represent as-yet undiscovered Mines Series fragments, or that the

Roan Group in general shows a broader degree of Cu enrichment relative to the Nguba and Kundelungu Groups. This broader enrichment could have been concentrated into anomalies by other processes by such as the action of rivers or topography. As well as the group of anomalies found over the Undifferentiated Roan, a smaller, lone Cu anomaly exists at the boundary between the Nguba and Kundelungu Groups, further towards the West. It seems more likely that this anomaly would be associated with Cu concentration by the nearby river than with Cu mineralisation. However, stratiform Cu mineralisation at Kamoa (see Broughton and Rogers, 2010) is hosted at a similar stratigraphic interface, between the Roan and Nguba Groups. Stratabound, vein-type mineralisation described by Dewaele *et al.* (2006) could also be hosted in such a location as there are several faults mapped in the immediate vicinity of the anomaly, although this mineralisation type is not commonly found in Congo.

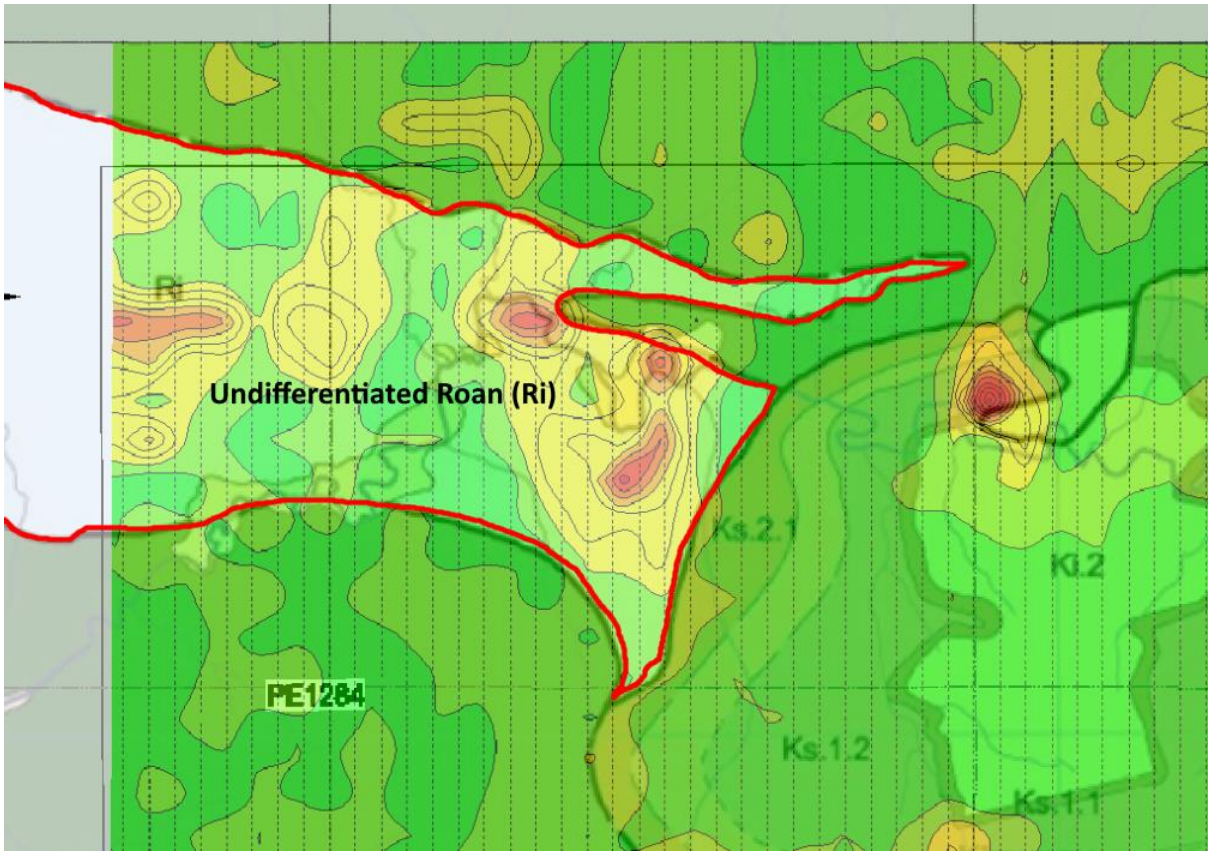

***Figure 6.18**: Inflated portion of the NW portion of the Cu soil geochemistry map presented in Figure 6.4. Several Cu anomalies exist within a region mapped as 'Undifferentiated Roan' (outlined in red). This region is effectively an inlier surrounded by Nguba and Kundelungu Group rocks. An additional, lone anomaly exists further towards the West, at the boundary between the Nguba and Kundelungu Groups. See Figure 6.4 for key.*

The second region which hosts Cu anomalies without the presence of known Cu mineralisation is found in the southern central portion of the Camrose concession, between the Pungulume-Bona and Kinshasa-Anticline-Kalukundi-Mashitu regions of 'Undifferentiated Roan' (Figure 6.19). Here, an elongate series of Cu anomalies may be found in close proximity to a significant riverbed. It is likely that these anomalies were created by detrital and leached Cu travelling downstream from the numerous Cu-Co deposits to the East, towards Lac Nzilo to the West. However, a single anomaly exists which is found in an area mapped as a tight inlier of Roan Group between two faulted Kundelungu Group contacts, and is not in the vicinity of any mapped river. It is possible that this anomaly constitutes some sort of surface expression of an undiscovered Cu deposit, focussed on a Mines Subgroup fragment, or related to the faulted contact between the Roan and Kundelungu Groups.

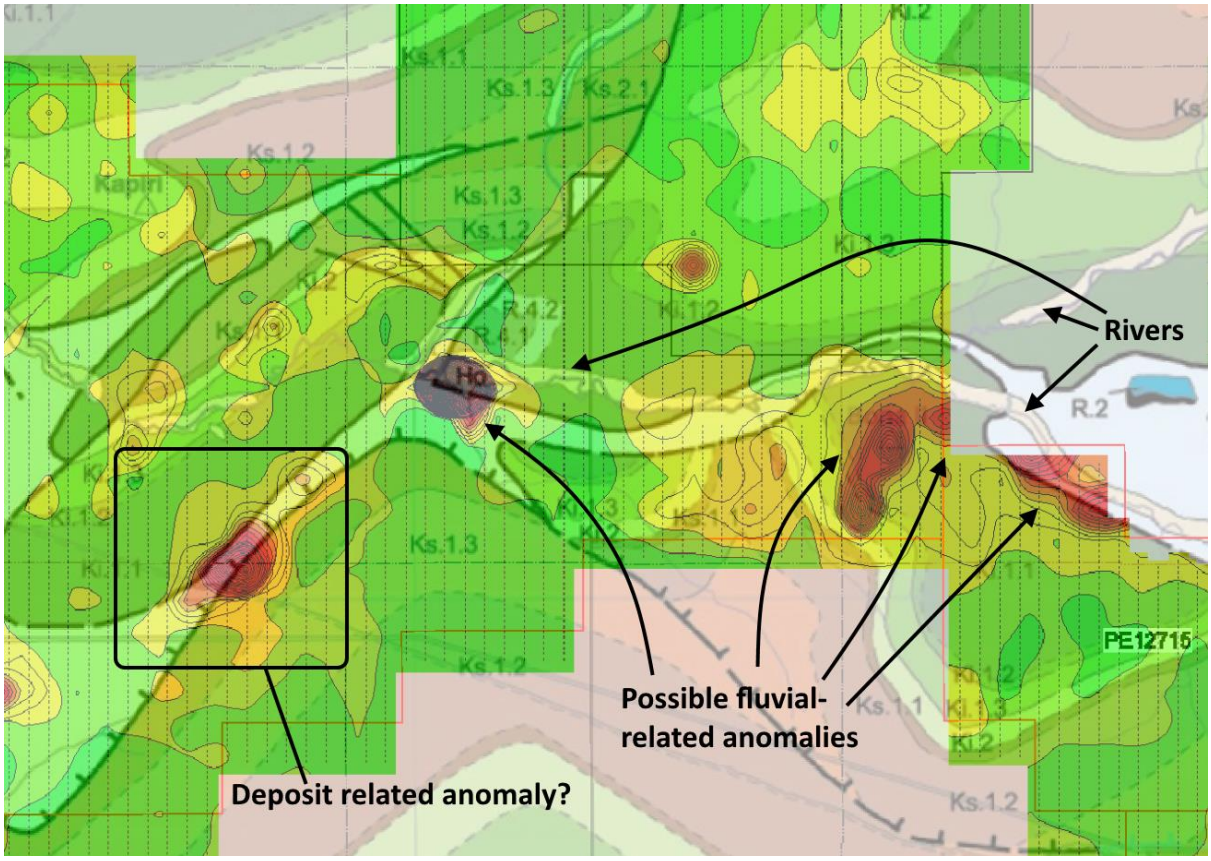

***Figure 6.19**: Inflated portion of the south-central portion of the Cu soil geochemistry map presented in Figure 6.4. A series of indicated Cu anomalies are found in close proximity to a river bed. Another Cu anomaly is indicated over a tight inlier of Roan Group between two faulted contacts with the Kundelungu Group, which could possibly be related to an undiscovered Cu deposit. See Figure 6.4 for key.*

6.4.2 Titanium Distribution in Soil

High values of Ti are not associated with known Cu-Co mineralisation, nor are they associated with Mines Subgroup fragments. However, as Figure 6.20 shows, broad areas of high Ti appear to correspond reasonably well to areas where the Ng1.1 (Grand Conglomerat) stratigraphic unit is mapped as occurring at surface. It is likely that the largely siliciclastic, diamictite Grand-Conglomerat unit is regionally enriched in Ti (perhaps from rutile) relative to other stratigraphic units, and Ti soil concentration could be useful as an indicator of the location of the Ng1.1 unit in regional geological mapping. The Grand Conglomerat - Mwashya Subgroup contact is host to mineralisation at Kamoa (Broughton and Rogers, 2010), and the position of the Grand Conglomerat often delineates the position of the Roan Group, making Ti-in-soil a possible tool for developing regional-scale Cu-Co exploration targets. It may also have use in the compiling and ground-truthing of regional geological maps.

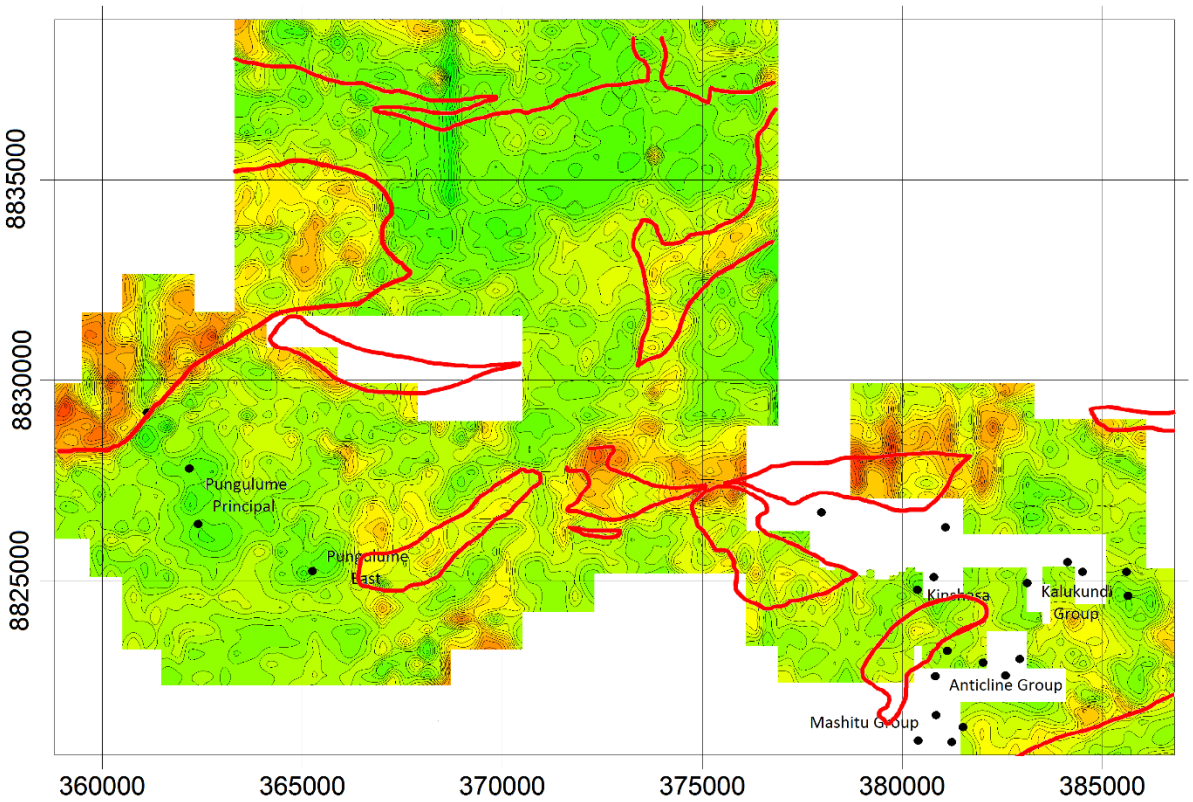

Figure 6.20*: Map of Ti concentration in soil over the Camrose concession. Limits of the Ng1.1 (Grand Conglomerat) stratigraphic unit are outlined in red. The Ng1.1 unit appears to be characterised by broad anomalies of high Ti-in-soil.*

Around the Pungulume and Bona deposits, there are slight negative anomalies of Ti-in-soil (Figure 6.21). They correspond well with positive Cu anomalies (Figure 6.17) and it is possible that Cu enrichment in soil is somehow at the expense of Ti. The host rocks for Cu mineralisation in the region, which are mostly calcareous, may also explain why Ti (generally associated with siliciclastic rocks) appears to be depleted in the vicinity of these deposits.

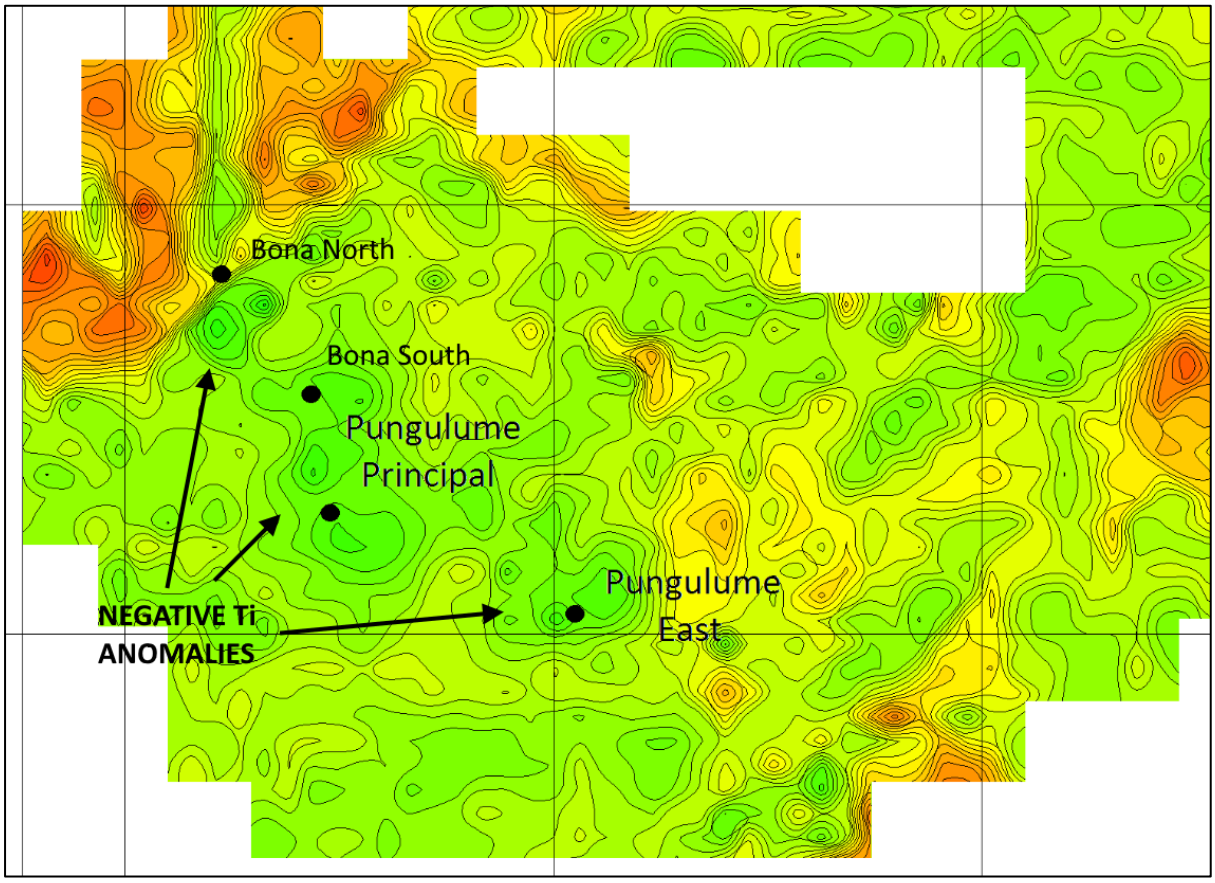

Figure 6.21*: Inflated portion of the map of Ti concentration in soil over the Camrose concession shown in Figure 6.20. Negative Ti anomalies (indicated) surround the Pungulume and Bona deposits.*

6.4.3 Limitations in the Remaining Data

Apart from Cu and Ti, mapping of the remaining elements: Co, Ni, Bi, V, Mo and Ca, and all of the multi-element indexes: CuCoNiBiVMo, CoNiBiVMo, CoNiBi and CoBi, gave inconclusive results (see Figures 6.5, 6.6, 6.7, 6.8, 6.9, 6.10, 6.12, 6.13, 6.14 and 6.15). None of the mineralisation-related elements other than Cu, including Co, were found to produce anomalies over known Cu-Co deposits in the Comide dataset. Calcium was not found in higher concentrations over regions of calcareous rock.

The lack of anomalies of the mineralisation-related elements over known Cu-Co occurrences is unusual, particularly when compared to results from a soil dataset collected in the same area by Africo Resources (Siebel *et al.*, 2013). In the Africo soil data, there is a pronounced soil Co anomaly over the Anticline and Mashitu groups of deposits of up to 800ppm Co, whereas in the Comide soil data, soil Co values never exceed 200ppm in the area of these deposits and no appreciable Co anomaly is found above them (Figure 6.22).

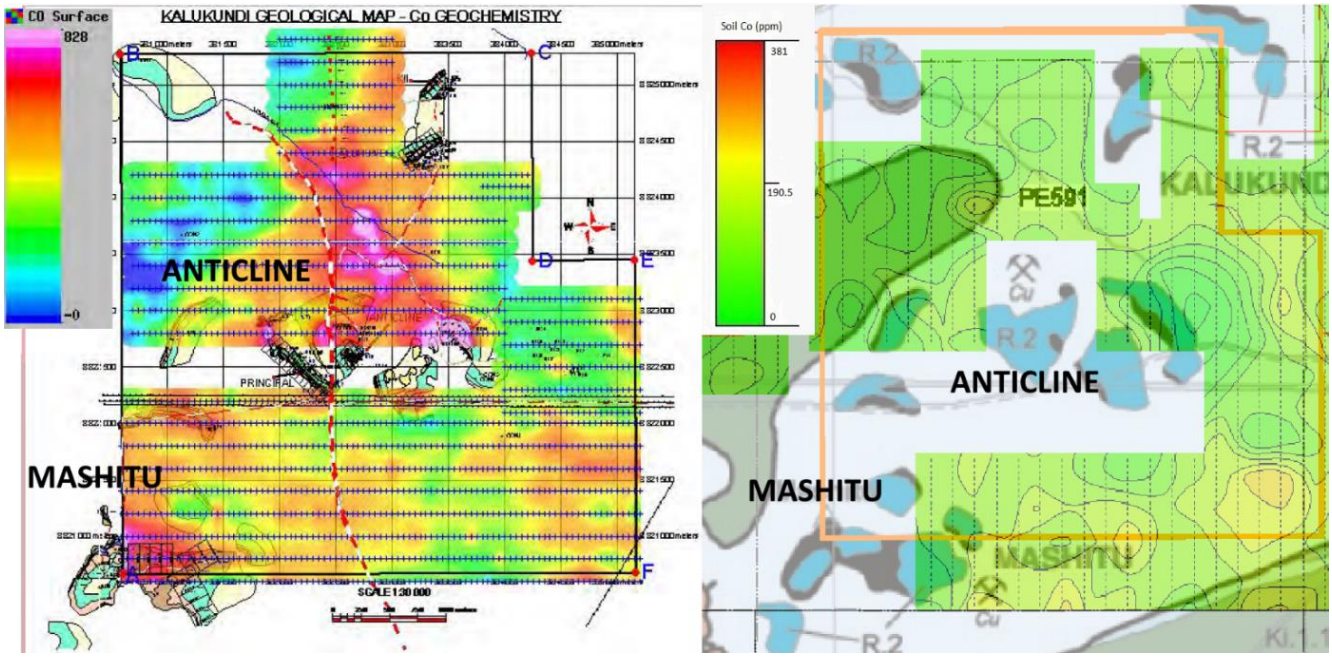

Figure 6.22*: Co concentration in soil maps from the Anticline-Mashitu area. Data collected by Africo Resources is displayed on the left (modified from Siebel et al., 2013) and the Comide dataset is displayed on the right. A pronounced Co anomaly exists over the deposits in the Africo data but not in the Comide data.*

Data for Co, Ni, Bi, V and Mo are relatively free of both positive and negative anomalies, and these datasets are less skewed than might be expected for mineralisation-related elements. Additionally, the largest spatial variation in the data often follows geometric, rather than geological or geographic, patterns. There are large rectangular regions of data which show higher or lower concentrations of elements than the areas around them (Figures 6.23, 6.24 and 6.25), and extremely pronounced linear anomalies which seem geologically implausible (Figure 6.26).

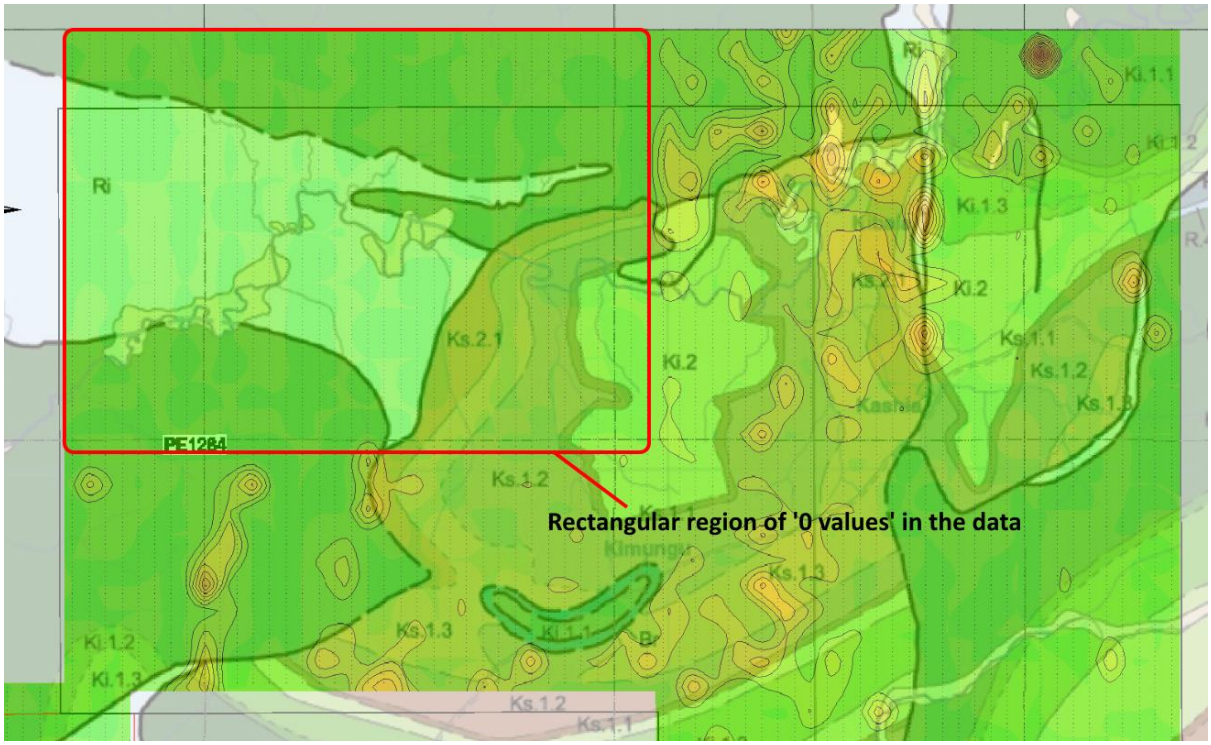

Figure 6.23*: Inflated portion of the Ni concentration in soil map from Figure 6.6, showing a rectangular region where all Ni-in-soil values are 0. See Figure 6.6 for key.*

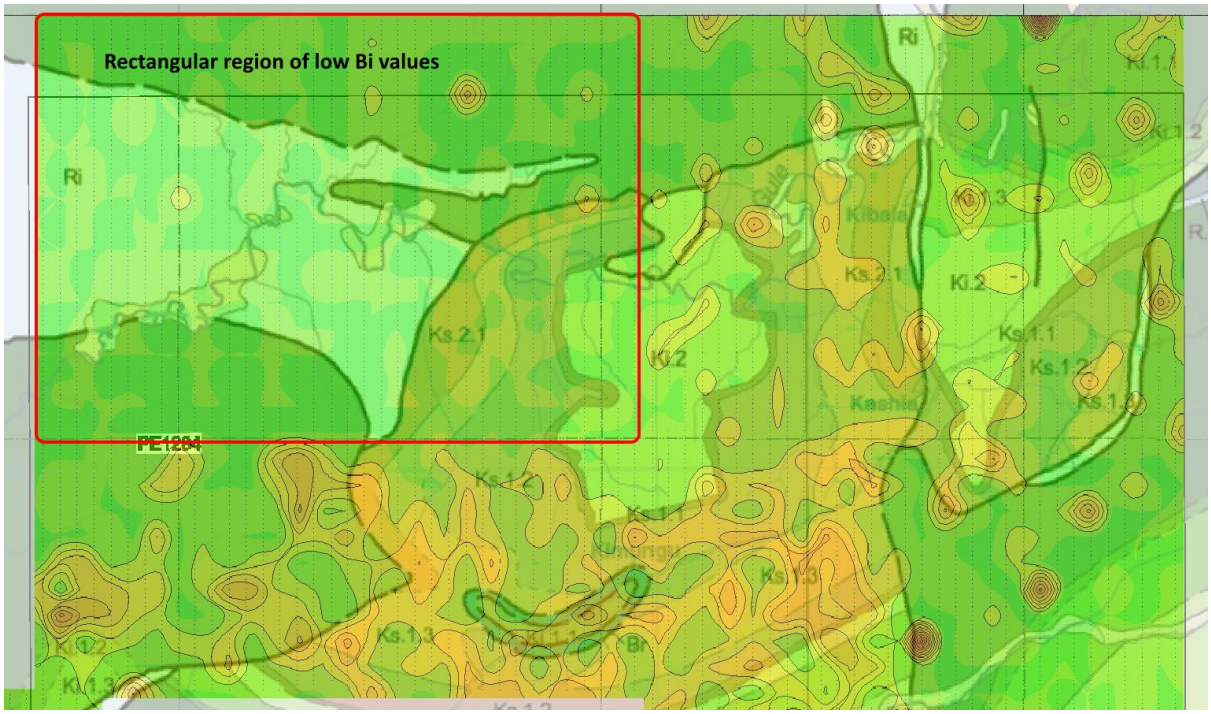

Figure 6.24*: Inflated portion of the Bi concentration in soil map from Figure 6.7, showing a rectangular region where most Bi-in-soil values are 0, with a few isolated exceptions. See Figure 6.7 for key.*

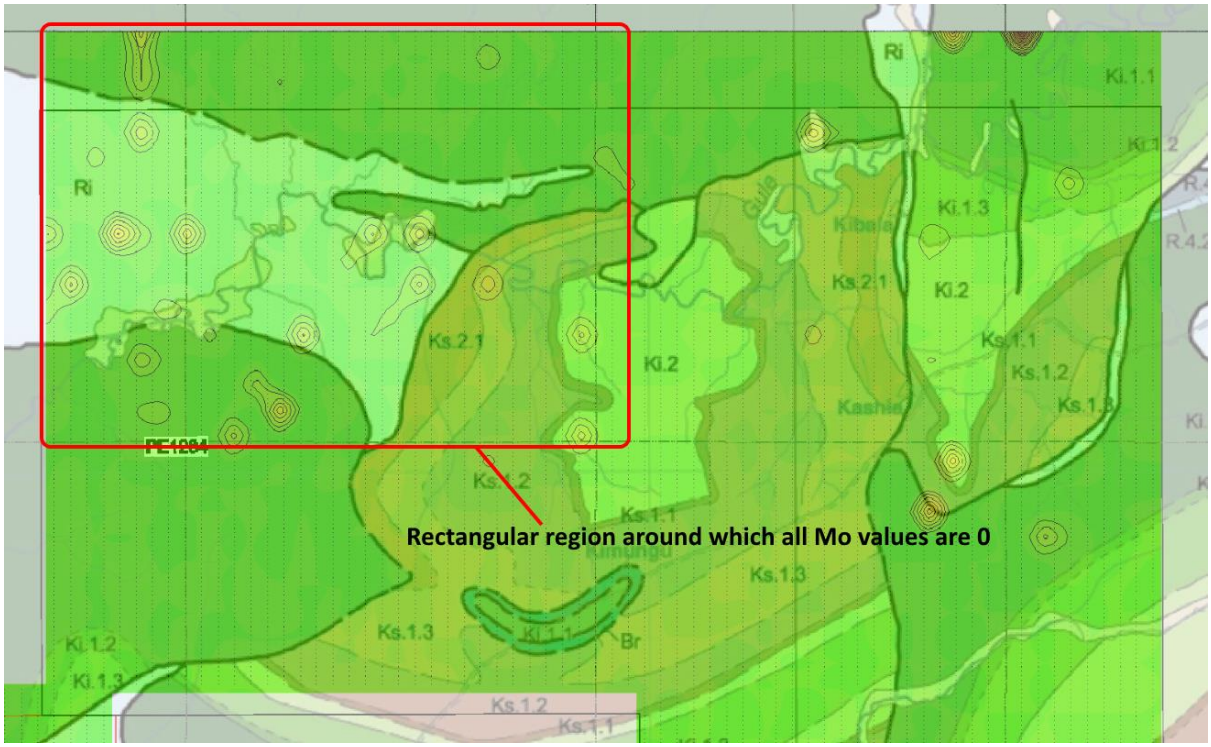

Figure 6.25*: Inflated portion of the Mo concentration in soil map from Figure 6.9, showing a rectangular region outside of which all Mo-in-soil values are 0. See Figure 6.9 for key.*

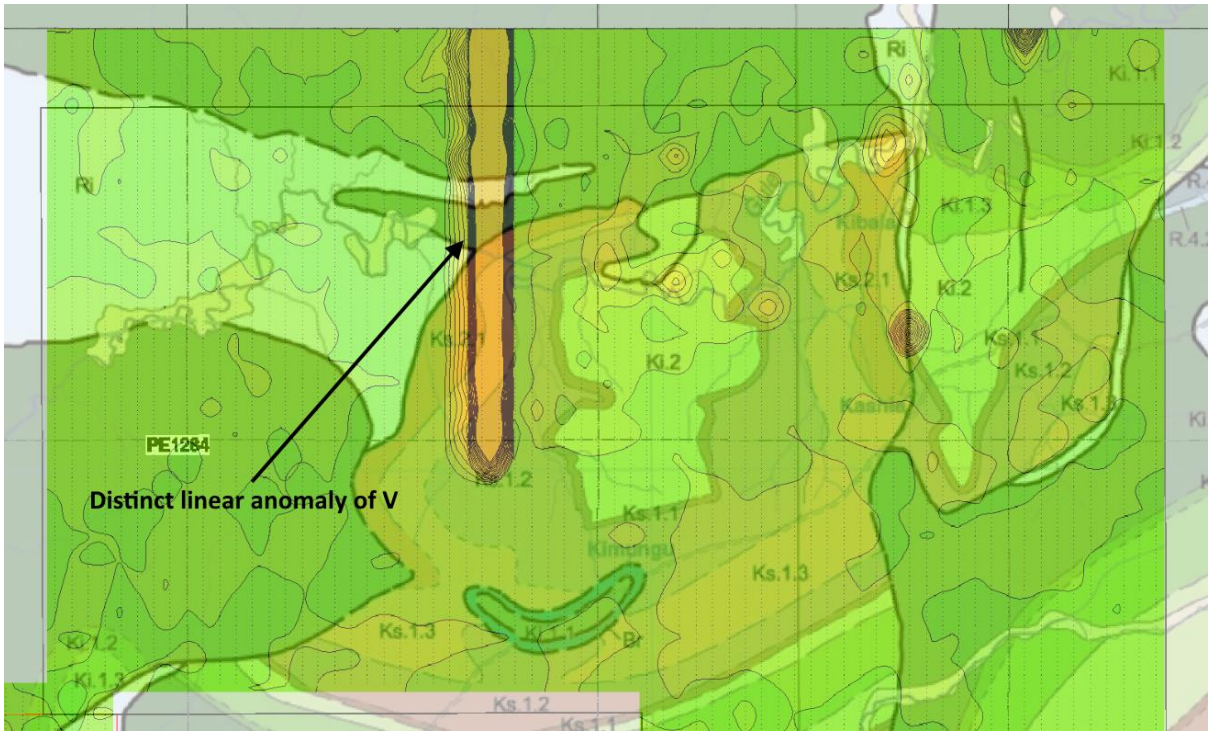

Figure 6.26*: Inflated portion of the V concentration in soil map from Figure 6.8, showing a pronounced linear anomaly of V which is likely to be a data-artefact created by error. See Figure 6.8 for key.*

The four multi-element indexes also suffer from the various data-inconsistencies which plague their constituent elements.

Given the low skewness, lack of anomalies, geometric patterns of variance and failure to correspond with similar datasets collected in the same area, it is concluded that the Comide soil database, with the exception of Cu and Ti, is unusable for the kind of exploration techniques which this study has attempted to investigate. This study was not provided with the full details of the methods of sampling and data-collection utilised in the creation of the Comide database, but it seems clear that errors have been made in the process, and/or the XRF method used for data collection was not sensitive enough, or was calibrated improperly to analyse for elements other than Cu. Standard XRF techniques are widely known to be unsuitable for the analysis of cobalt in particular; "The portable X-ray fluorescence (pXRF) technique is a widely used geochemical field tool. The assessment of cobalt using standard pXRF factory calibrations will significantly under-or-over-report concentrations due to interferences of Fe and Co peaks in the XRF spectrum" (https://www.pxrfs.com.au/portable-tools-rapid-assessment-cobalt-resources/ - retrieved: 09/10/2018).

Geometric inconsistencies in the data may be caused by differing methods of sample collection, or contamination of samples from a particular region. However, the low skewness and lack of anomalies in the data point to the handheld XRF technique used to collect the data not being sensitive enough (contrary to the universal 5ppm LLOD presented for the method). Comide employees draw similar conclusions on the dataset, Cu being the only element-soil-concentration which was found to be reliable (Chimvinga, pers. comm., 2014).

To test the effectiveness of any surface mineralisation vectors other than copper, it is concluded that a more reliable sampling process, or a more sensitive measuring technique than the handheld XRF protocol which compiled the Comide database, be used in analysing for concentration of elements in soil.

6.4.4 Comparison of Regional Soil to the Top of the Mashitu South Profile

The analysis performed in this section relies on the questionable assumption that the Comide XRF soil geochemistry database is reliable enough to develop a picture of the expected background values for soil-element concentration in the region. Given the inconclusive results of element concentration in soil within the regional dataset it was decided to compare the

average regional background concentration of elements in soil to the average concentration of elements in soil above Mashitu South, to see what variation in elements might be expected above such a deposit.

The regional soil database does not show good coverage over the Mashitu South deposit, nor does the 50m x 50m sampling grid allow for many samples taken over the deposit. Rather than use the few samples available in this database, which may be limited in its reliability (see section 6.4.3), it was decided to compare the element concentration averages of the entire soil geochemistry database with the averages of the <1m depth mid-point-of-sample dataset split from the main Mashitu South borehole database (see Chapter 5). The median would ordinarily be taken for this comparison, due to the expected skewness of the distribution of many of the elements in the regional soil database. However, it was decided to compare the means of both datasets instead, because of the number of 0 values present in the regional soil data meant that the median concentration value for many elements in this dataset was calculated as 0.

Mean values for each element in both the regional soil geochemical data and the <1m Mashitu South borehole geochemical data were calculated. The average values for elements in the Mashitu South data were then divided by the average values for the corresponding elements in the regional data, to give an 'enrichment factor': a measure of the degree to which an element is concentrated in the top of the profile above Mashitu South, compared to its regional background concentration. The results of this are presented in Figure 6.27.

It should be noted that this technique suffers from a number of limitations. First, the two datasets were collected differently: one using the Comide soil sampling procedure and XRF analysis, and the other by the Comide core sampling procedure and ICP-AES analysis. Secondly, the two datasets are of wildly different size: the average for regional soil concentration is made up of 27,983 samples, whereas the average for Mashitu South <1m borehole data is made up of 43 samples. This increases the susceptibility of the Mashitu South dataset to influence by outliers. The third limitation is that the samples are assumed to be fundamentally of the same nature: although the Mashitu South <1m borehole data is theoretically from the same sampling horizon as samples collected by a typical soil sampling program, it is possible that some of the borehole data could have been taken from resistant rock which outcropped near the surface. Also, the soil-sampling procedure used by Comide

for the collection of samples is unknown to this study. Lastly, the reliability of the XRF dataset in general is questionable, as discussed in section 6.4.3.

With these limitations in mind, elements which are enriched in the soil above Mashitu South, relative to regional background levels, are as follows, in order of highest enrichment factor to lowest: Co, U, W, Mo, Ca, Ni, S, Cu, Bi, As, Pb, P, V, Sr. Elements which are depleted in the soil above Mashitu South are, in order of highest enrichment factor to lowest: Cd, Zn, K, Ag, Fe, Ti (see Figure 6.27).

Element	Ca	Fe	Cu	K	Co	Ti	S	P	V	Ni	Sr	Zn	Pb	U	W	As	Bi	Mo	Ag	Cd
Average: <1m, MSS (ICP-OES, ppm)	424.39	22024.39	542.44	6608.54	1541.46	1507.32	174.39	140.00	151.73	17.78	16.49	13.80	12.39	5.98	10.00	9.85	11.29	3.55	1.29	0.31
Average: Regional Soil (XRF, ppm)	34.10	43710.61	94.20	10122.36	13.22	5676.93	21.43	65.45	106.08	2.13	12.41	19.02	5.06	0.30	0.56	3.73	3.15	0.29	2.30	0.39

Element	Ca	Fe	Cu	K	Co	Ti	S	P	V	Ni	Sr	Zn	Pb	U	W	As	Bi	Mo	Ag	Cd
Soil enrichment factor at MSS	12.45	0.50	5.76	0.65	116.62	0.27	8.14	2.14	1.43	8.34	1.33	0.73	2.45	20.01	17.93	2.64	3.59	12.17	0.56	0.78

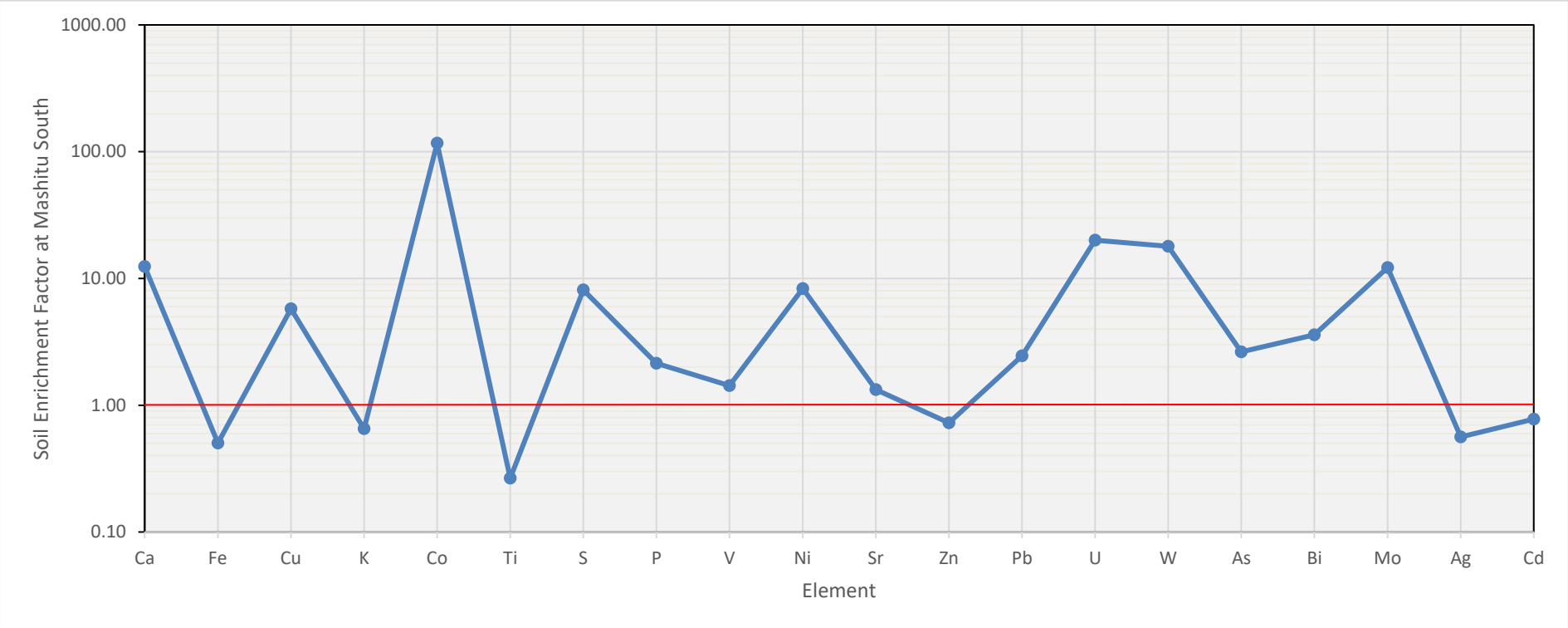

***Figure 6.27**: Table and line graph showing the enrichment factors for the concentration of elements in soil at Mashitu South (MSS), relative to the concentration of elements in the regional soil data. Values above 1 mean that an element is relatively enriched in the soil at Mashitu South compared to the regional abundance, and values below 1 mean that an element is relatively depleted at Mashitu South compared to the regional abundance in soil.*

Cobalt stands out on its own out of all the elements, being enriched in the soil above Mashitu South more than 100x relative to background levels. Molybdenum is the only other element which was predicted to be associated with Cu in the hypogene environment (see Chapter 5) and is significantly more enriched than Cu in the soil above Mashitu South, to a factor of 12.17x background.

U and W also show significant levels of enrichment, but statistical analysis shows that these elements are not directly associated with Cu in the hypogene environment, and they may be enriched somewhat coincidentally. Uranium mineralisation, certainly, is also found at Mashitu South (see Section 5.4.4) though it is not spatially associated with Cu-Co at an intra-deposit scale. Calcium is also significantly enriched in the soil above Mashitu South. This may be because the Mines Subgroup represents a relatively calcareous stratigraphic subgroup compared to the regional stratigraphy. An alternative explanation is that H^+ ions, released during the oxidation of sulphide mineralisation at depth, migrated towards the surface, dissolving carbonates along the way and producing concentrations of secondary carbonates in the soil directly above these oxidised sulphides, as per the model of Smee (1998).

Ni, S, Cu, Bi, As, Pb and P are all concentrated to moderate levels (<10x background) at the top of the Mashitu South profile, but perhaps not highly enough to form a significant geochemical anomaly on a large scale soil sampling program. Ni, S, Cu, Bi and As are shown to be associated with mineralisation in the hypogene environment (see Chapter 5). It is shown that P is associated with supergene mineralisation. Lead could be coincidentally enriched at Mashitu South, in a manner similar to U and W.

V, Sr, Cd, Zn, K and Ag show neither significant enrichment or depletion in the soil above Mashitu South. Very slight enrichment of V (1.43x) could be because the metal is predicted to co-occur with Cu in the hypogene environment.

Depletion of Fe and Ti in the surface above Mashitu South is difficult to interpret, but a similar effect can be seen above the Pungulume and Bona deposits (Figure 6.21). These siliciclastic-associated elements might be depleted above the relatively calcareous Mines Subgroup fragments.

A caveat, again, should be given on this comparative analysis. As shown in section 6.4.3, the reliability of the regional soil data on which it is based is questionable, and it should be taken as a demonstration of the feasibility of this sort of analysis more than anything else.

6.5 Conclusions from Soil Geochemistry

1. Cu concentration in soil is an effective exploration vector for certain deposits, with the Pungulume, Bona, Anticline and Kinshasa deposit groups exhibiting pronounced and focussed soil Cu anomalies.
2. Certain deposits, however, are not demarcated by appreciable anomalies of soil Cu to the scale at which exploration drilling could be directed. The Mashitu and Kalukundi groups of deposits are examples of these.
3. Anomalies of Ti have the potential to be used in a regional sense to map the surface extent of the Grand Conglomerat (Ng1.1) unit.
4. Co and Mo, which are shown to be associated with Cu in the hypogene environment at Mashitu South, are concentrated to a significantly greater degree than Cu in the surface above the deposit relative to regional background levels, making them potentially better surface vectors to Cu-Co mineralisation than Cu.
5. Ni, S, Bi and As, which are also shown to be associated with Cu in the hypogene environment at Mashitu South, are concentrated to a similar regional enrichment factor as Cu in the surface above the deposit and could potentially be used alongside Cu as surface vectors.
6. Other than Cu and Ti, the remaining elements of the Comide regional soil dataset and multi-element indexes were found to be inoperable as vectors towards surface mineralisation. This may be as a result of:
7. Inconsistencies in the variation of the Comide regional soil dataset call into question its reliability for analysing the distribution of all elements other than Cu and Ti. Whether this is as a result of sampling practice, equipment sensitivity or other aspects of data collection is unknown.

CHAPTER 7: BACILLIFORM PSEUDOFOSSILS

STATEMENT: This chapter forms the basis of a manuscript by G. Gigler et al. planned for publication in the journal 'Precambrian Research', with the working title: 'Sulphidic pseudofossils in the Cu-Co-bearing rocks of the Katangan Copperbelt, Democratic Republic of Congo'.

7.1 Introduction

During petrographic examination of a thin section cut from core sample MSSD083_16_1 (see Chapter 4: Petrography and Paragenesis), a number of sulphidic bacillus-shaped features were discovered in syn-diagenetic haematite-rutile veins. Their resemblance to bacillus-shaped prokaryotic microfossils, which are described from a diverse range of global settings from as early as the work of Barghoorn and Tyler (1965), inspired further investigation using the techniques described in this chapter. The non-genetic term 'bacilliform' was applied to the features and is used throughout this thesis to describe them. MSSD083_16_1, which comes from a depth of 173.83-173.95m within hole MSSD083, is a carbonaceous, dolomitic shale taken from the SDB unit of the Dolomitic Shales Formation (Figure 7.1). It consists of alternating greenish and dark-grey sedimentary laminations and contains visible, stratiform-disseminated pyrite (Figure 7.2). The sampling interval lies ~5m up-hole of the contact between the SDB unit and the RSC unit of the Kamoto Formation.

An ICP-AES assay taken from the 173.27-173.93m interval of hole MSSD083, which encompasses most of sample MSSD083_16_1, indicates that this interval is significantly mineralised, containing 3.5% Cu and 2.9% Co (Figure 7.1) - S, U, Ni and Bi are also found in anomalously high concentrations at this depth. The sample is situated within the hypogene 'Upper Orebody' of the deposit (see Chapters 4 and 5) and contains visible sulphide mineralisation.

Micropalaeontological research on the rocks of the Neoproterozoic Katangan Basin is scarce, and mostly limited to macro-scale analysis of stromatolitic intervals within the Roan Group (e.g. Malan, 1964). There are no microfossils yet reported in scientific literature from the well-mineralised and well-studied Mines Subgroup, despite the rocks being host to a number of biogenic features which would indicate formation by microorganisms. Studies on nearby basins of similar ages, such as the Sankuru-Mbuji-Mayi-Lomami-Lovoy Basin in the

DRC (e.g. Maithy, 1975; Baudet, 1987; Baludikay *et al.*, 2016) have revealed diverse assemblages of well-preserved prokaryotic and eukaryotic microorganisms. In this chapter, two competing arguments are assessed: that the bacilliforms identified in sample MSSD083_16_1 are either microfossils, or pseudofossils.

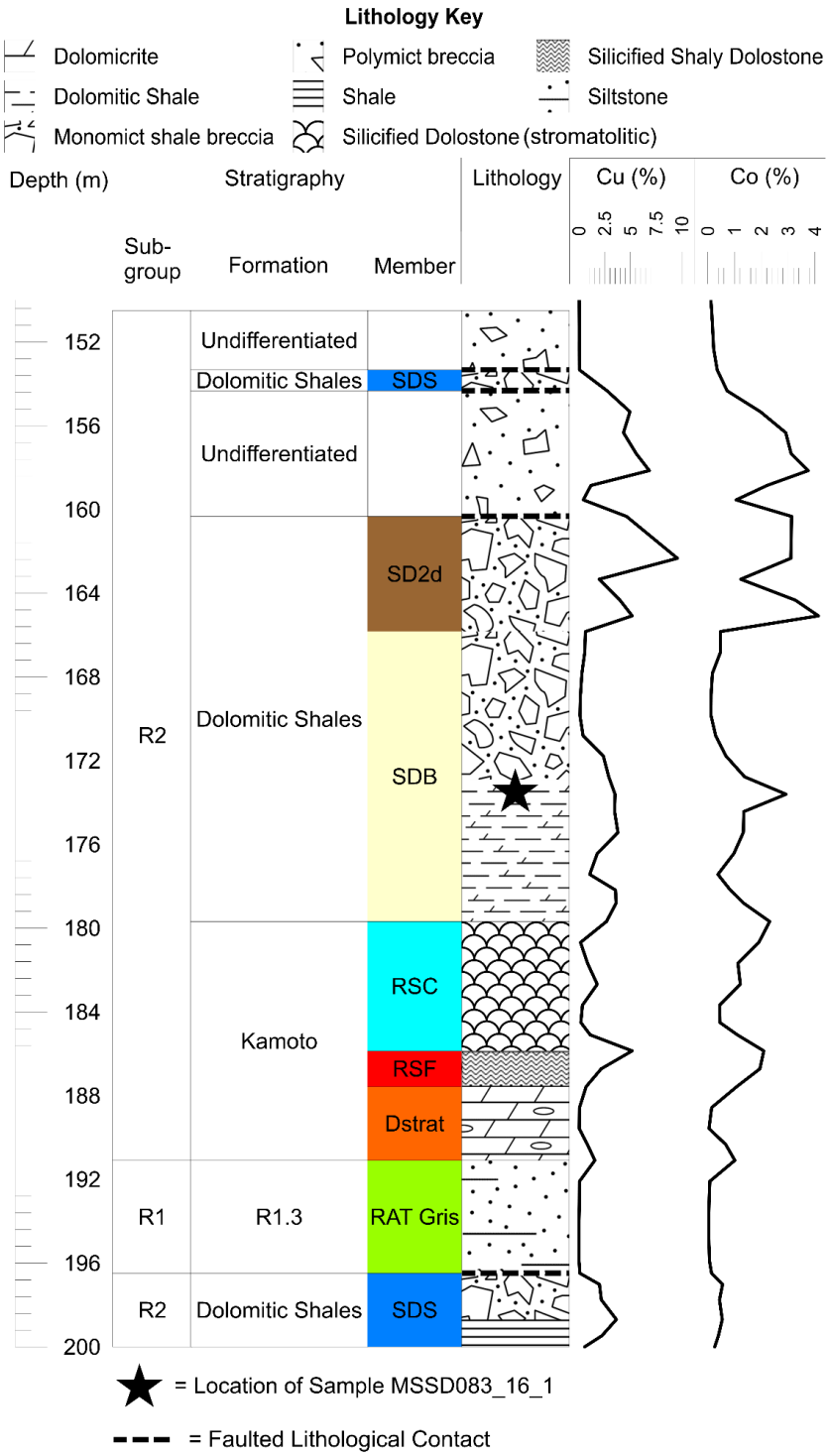

***Figure 7.1**: Lithostratigraphic column of a portion of borehole MSSD083, showing the location of sample MSSD083_16_1 and including the Cu and Co assays.*

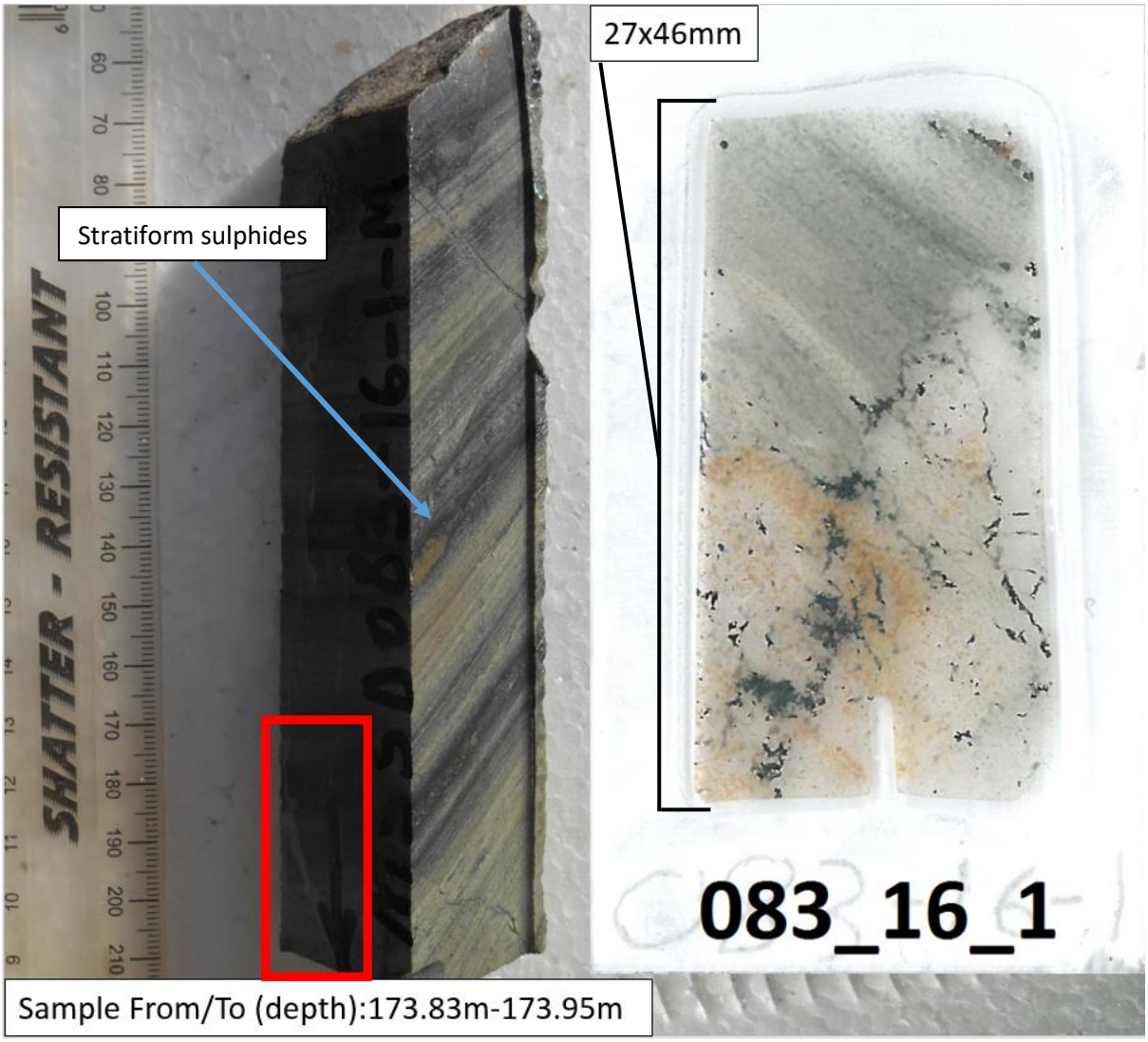

***Figure 7.2**: Photograph of sample MSSD083_16_1 and the polished original polished thin-section which was cut from it. The thin section is taken from the corner of the sample indicated by the red rectangle*.

7.2 Methods

Out of the 105 quarter-core samples examined in the petrographic study of Mashitu South (see Chapter 4: Petrography and Paragenesis), 'bacilliforms', or suspected microfossils, were discovered only in MSSD083_16_1, from which five polished thin sections were cut and subjected to various forms of analysis. These sections were made by technicians at the rock preparation laboratory of the School of Geosciences, University of the Witwatersrand, South Africa. A Struers Discoplan-TS rock saw was used to cut section blocks of each sample, which were affixed to a glass slide using EpoFix epoxy resin, and ground and polished to a thickness

of ~28-32µm using 'Aka-Paste' diamond paste and a Struers Planopol-V automatic grinder. The study material is summarised in Figure 7.3.

Sample Name	Borehole	Depth Start (m)	Depth End (m)	Description	Lithology	Stratigraphic Unit
MSSD083_16_1	MSSD083	173.83	173.95	Green-grey, laminated, carbonaceous, dolomitic argillite containing stratiform pyrite and silica bands and cross-cut by quartz-dolomite veins.	Shale	S.D.B.

Section Name	Comments
MSSD083_16_1_A	Original section in which bacilliforms were identified. Carbon-coated for electron microscopy.
MSSD083_16_1_B	Section cut from same interval as 'A' to replicate bacilliform find
MSSD083_16_1_C	Section cut from same interval as 'A' to replicate bacilliform find
MSSD083_16_1_D	Section cut from same interval as 'A' to replicate bacilliform find
MSSD083_16_1_E	Section of pyrite band ~3cm up-hole from sections A-D

Figure 7.3*: Summary of the material used in this study.*

7.2.1 Optical Microscopy:

A description of the optical microscopy methodology used in this study can be found in Section 4.2.1.

7.2.2 Scanning Electron Microscopy (SEM):

A description of the SEM methodology used in this study can be found in Section 4.2.2.

7.2.3 Raman Spectroscopy:

Sections MSSD083_16_1_B, C, and D were subjected to Raman spectroscopic analysis at the MMU, University of the Witwatersrand, primarily to detect the possible presence of kerogen in the suspected microfossils but also to confirm the identification of other mineral species. Spectra were acquired using the 514.5nm line of a Lexel Model 95 argon ion laser and a Horiba LabRAM-HR Raman spectrometer with an Olympus BX41 microscope attachment, the latter of which was used to take reflected light images to accompany the acquired spectra. The beam was focused onto the sample using a 100x objective (numerical aperture = 0.90) and the backscattered light was dispersed onto a liquid nitrogen-cooled Charge-Coupled Device (CCD) detector via a 600 lines/mm grating. The spot diameter for beam analyses was ~1µm. Laser power at the sample was approximately 0.4mW to prevent localised heating by the laser beam. A 60 second acquisition time was used for solitary spot analyses whereas a 20 second acquisition time was used for mapping analyses. Raman maps were created of selected portions of the slides, by selecting bandwidths corresponding to the relevant phases and colour-coding the image proportionally to the intensity of the selected bandwidth at the point of each spot analysis. When mapping an area for carbonaceous material, only the bandwidth of the G (graphite) mode of carbon (~1600 Δ cm^{-1}) was used to create the image, to prevent imaging overlap between the similarly placed 'D' (disorder) mode of carbon (~1350 Δ cm^{-1}) and the haematite disorder mode (~1320 Δ cm^{-1}), in line with the recommendations of Marshall and Marshall (2013). LabSpec v5 software was used to perform cosmic ray removal, baseline correction and band-intensity normalisation of the acquired spectra. 'Aka-paste' diamond paste and the EpoFix epoxy resin used during the thin section preparation process were both mounted on glass slides and their Raman spectra analysed, to eliminate the possibility that these substances could mimic the spectra of kerogenous carbon.

7.3 Results

7.3.1 Groundmass Mineralogy

The groundmass of sample MSSD083_16_1 is predominantly fine-grained detrital quartz, muscovite mica and clay minerals with minor (<10%) carbonaceous material, chlorite, rutile and sulphides. Intergranular, authigenic dolomite is also common, as are nodules or bands of crystalline quartz. Quartz nodules and elongated minerals in the groundmass define a bedding foliation. Authigenic sulphides account for ~5% of the total area of the slides from sample MSSD083_16_1 and are preferentially distributed in lateral bands or nodules, although they may be found disseminated throughout the rock. Pyrite is the most abundant and first-precipitated of the sulphides, occurring in poorly-formed framboidal clusters, occasional lone, subhedral crystals and in cm-scale bands associated with earlier-formed crystalline quartz. Where the pyrite occurs in bands, it has a macro-scale massive appearance, but microscopic inspection reveals it to be para-framboidal (Figure. 7.4A). Pyrite is rimmed and mantled by anhedral chalcocite and both these phases are themselves rimmed and mantled in succession by anhedral carrollite (Figure. 7.4B). All of the sulphides can be described as groundmass-disseminated with a stratiform preferential orientation.

7.3.2 Vein Mineralogy

Section MSSD083_16_1_A is host to a thick (max. ~2cm wide) quartz-dolomite vein which cross-cuts all of the other features in the section, has entrained portions of the groundmass, has caused localised silicification at the vein margins and is host to chalcocite mineralisation. Sections MSSD083_16_1_B, C, D and E are also cross-cut by thin (<2mm wide), discontinuous veins which are variously composed of rutile and apatite along their length (Figure 7.4C). These veins show slight displacement and deformation on either side of sedimentary laminations, quartz bands and pyrite bands. However, they do not appear to cross-cut mineralisation, as where they are composed of rutile, the rutile crystals are mantled and overgrown by chalcocite and carrollite (Figure 7.4D). At their thinnest and most constricted (<50µm), the veins are composed solely of euhedral-to-subhedral lath-shaped rutile crystals

ranging in length from a few microns to ~200µm, often preferentially orientated in the direction of the vein. Where the veins are dilated to ~500µm they are composed primarily of radial-fibrous apatite. Within the dilated apatite portion of the veins can be found µm-scale 'cavities' which are partially filled with a very finely 'stippled' haematite nanotexture, as well as botryoids of haematite. These cavities are also host to the 'bacilliforms' which are the subject of this paper.

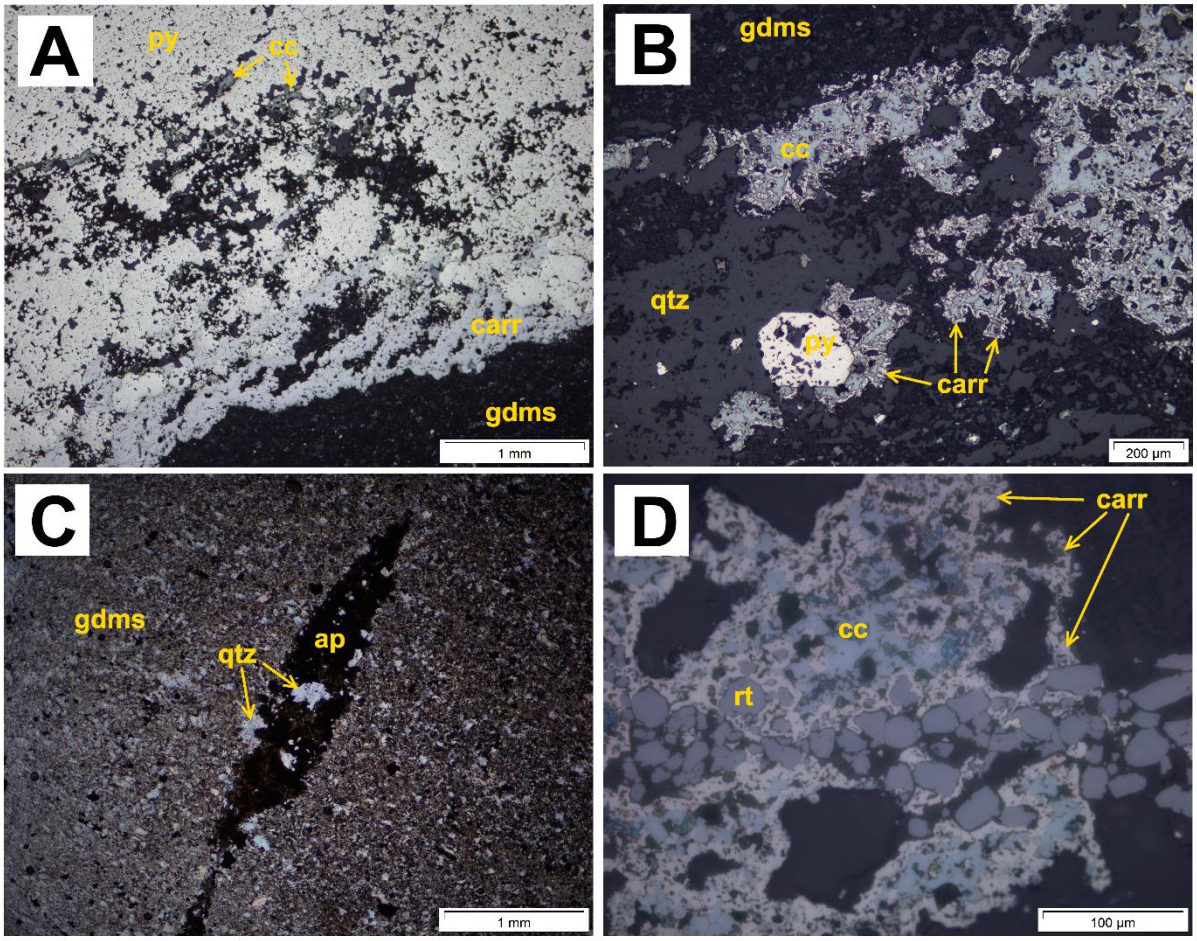

Figure. 7.4. *Optical photomicrographs of groundmass and vein mineralisation textures in thin sections cut from sample MSSD083_16_1 (A, B and D: reflected PPL; C: transmitted PPL). A: Para-framboidal pyrite band mantled by chalcocite and carrollite. B: Early subhedral pyrite within a quartz-rich band of groundmass, mantled by chalcocite, which is itself rimmed by carrollite. C: dilated portion of apatite-rutile vein which cuts through the siliciclastic groundmass of MSSD083_16_1. These dilated portions of apatite-rutile veins are host to bacilliforms. D: Rutile from a constricted portion of an apatite-rutile vein, overgrown by groundmass-hosted chalcocite and carrollite. Py=pyrite, cc=chalcocite, carr=carrollite, gdms=groundmass, qtz=quartz, ap=apatite and rt=rutile.*

7.3.3 Bacilliforms

Reflected light microscopy revealed a distinct class of micro-features, identified in all of the sections (MSSD083_16_1_A, B, C, D and E, hereby referred to as Sections A, B, C, D and E) which were assigned the non-genetic term 'bacilliforms'. They are composed of sulphides; primarily carrollite, and comprise a carrollite rim with an internal region of chalcocite (Figure. 7.5A) or a carrollite rim with a hollow internal cavity (Figures. 7.5B and 7.5C) which, in a few examples, hosts a single crystal of pyrite (Figure. 7.5D). Raman spectroscopy suggests that trace amounts of the minerals covellite, molybdenite and brookite may be present within some of the bacilliform rims together with carrollite which is predominant. The features have a distinct 'bacillus' (rod) shape from which their name is derived. Some bacilliforms are straight, while others display some form of curvature, often defined by where they come into contact with another mineral surface (Figsures. 7.5D, 7.5E and 7.5F). In Sections B, C, D, and E, bacilliforms were discovered in apatite-vein-cavities filled with the stippled haematite nanotexture. In Section A, one such cavity which contained numerous bacilliforms was discovered within a portion of the slide that experienced heavy silicification. Many similarly-sized features were identified which do not have an exact bacilliform morphology. In some cases, these features take on the appearance of clusters of bacilliforms (Figures. 7.5G and 7.5H); in others, they have the same sulphide mineralogy and elongate dimensions, but are more angular in shape. Within the internal cavities of several of the bacilliforms, Raman spectroscopy shows traces of disordered carbon corresponding optically to dark patches (Figure 7.6). No examples of bacilliforms have been identified within the groundmass of the rock.

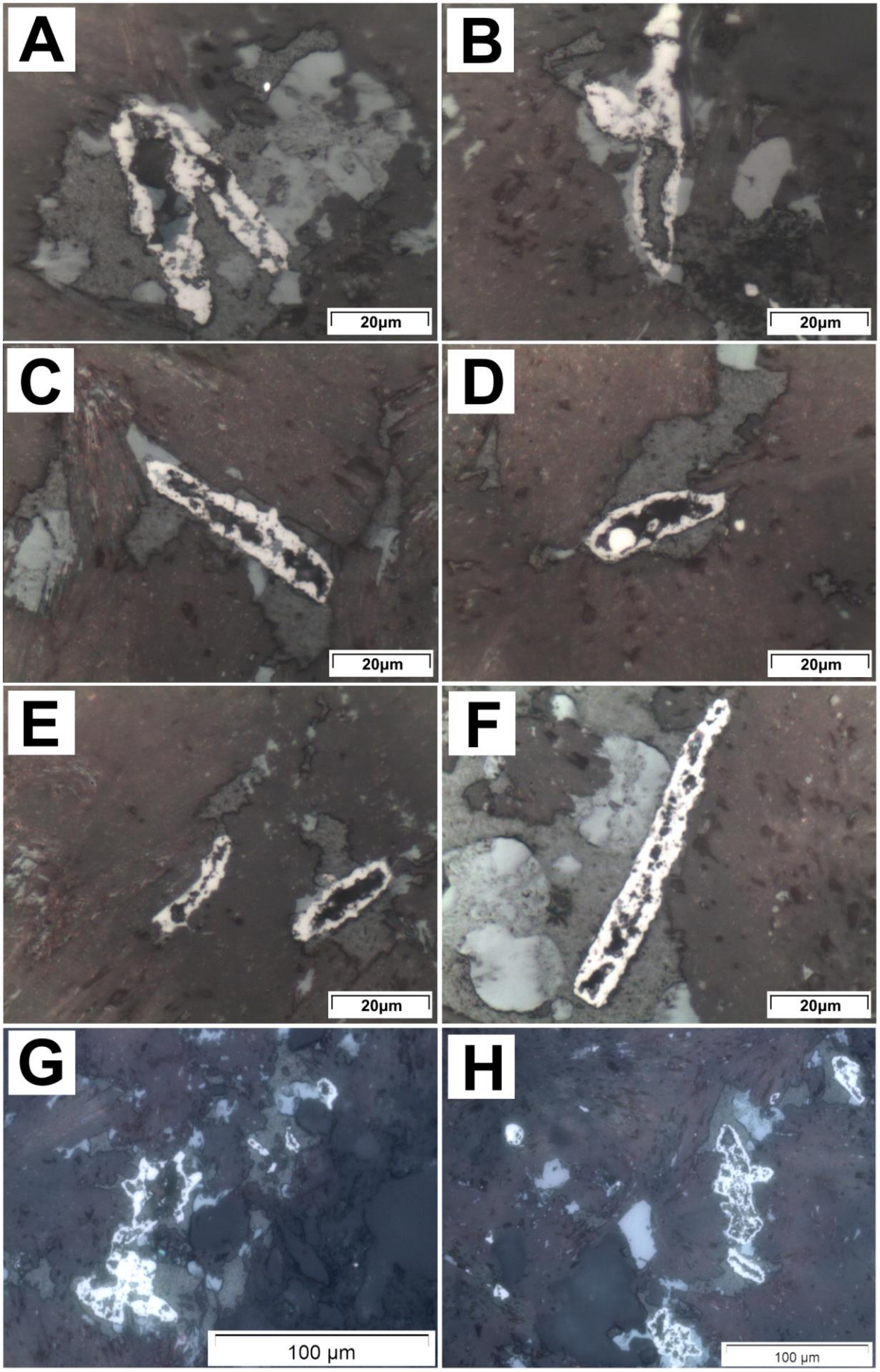
A
20µm
B
20µm
C
20µm
D
20µm
E
20µm
F
20µm
G
100 µm
H
100 µm

***Figure 7.5**. Optical photomicrographs of bacilliforms within sample MSSD083_16_1; all images taken in reflected PPL. A: two conjoined bacilliforms composed of a central chalcocite region (navy blue-grey) and an external carrollite rim (white). B, C: hollow bacilliforms consisting of just a carrollite rim. D: Pyrite crystal (bright yellow-white) within the internal cavity of a hollow carrollite bacilliform. E, F: bacilliforms exhibiting curvature against the contacting apatite substrate. G,H: clusters of conjoined bacilliforms.*

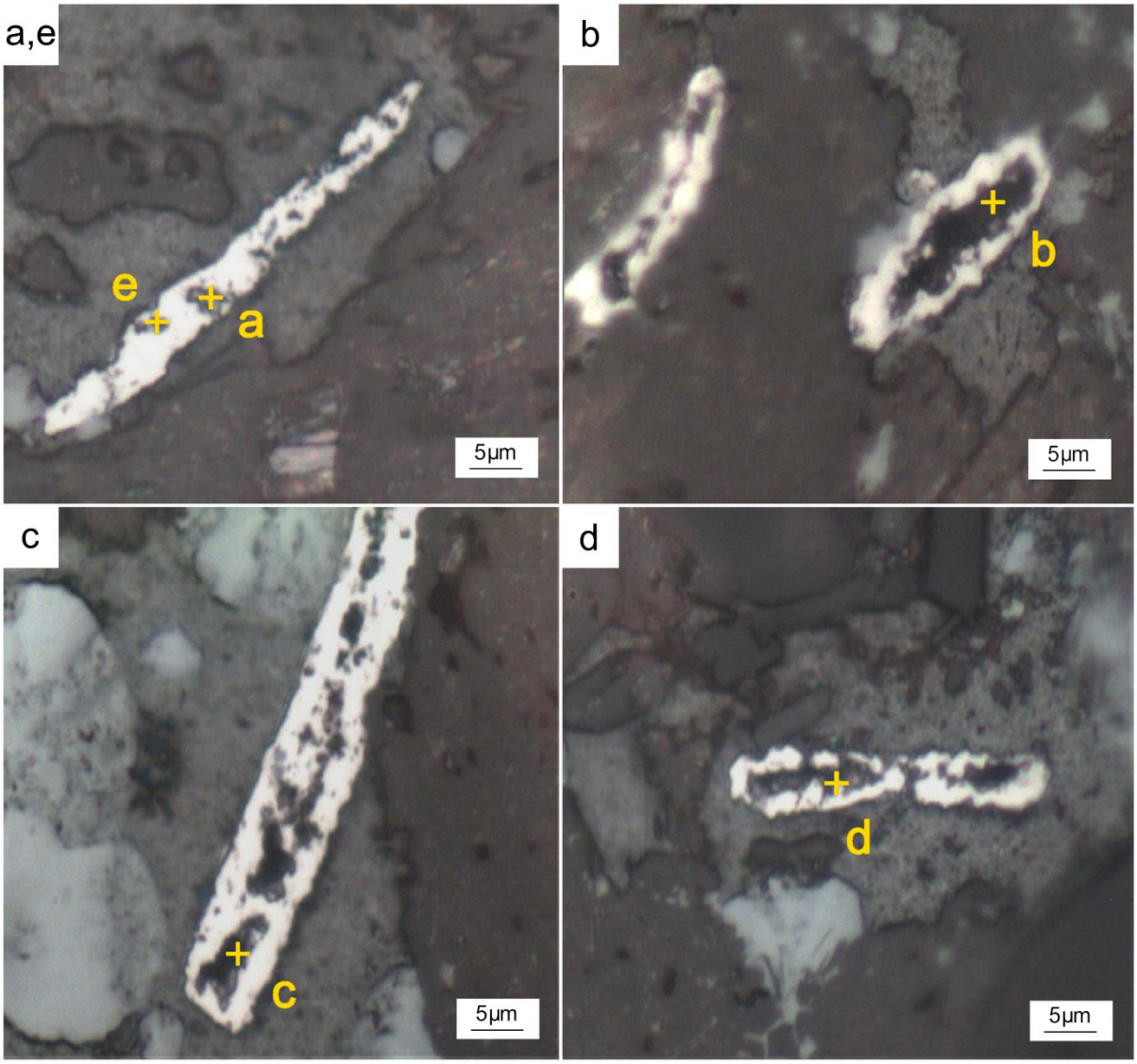

***Figure 7.6A.** Optical photomicrographs of bacilliforms taken in reflected PPL, showing the spot analysis locations for the corresponding spectra (a, b, c, d and e) in Figure 7.6B. Figure provided by Sośnicka (pers. comm., 2016) and reproduced with permission.*

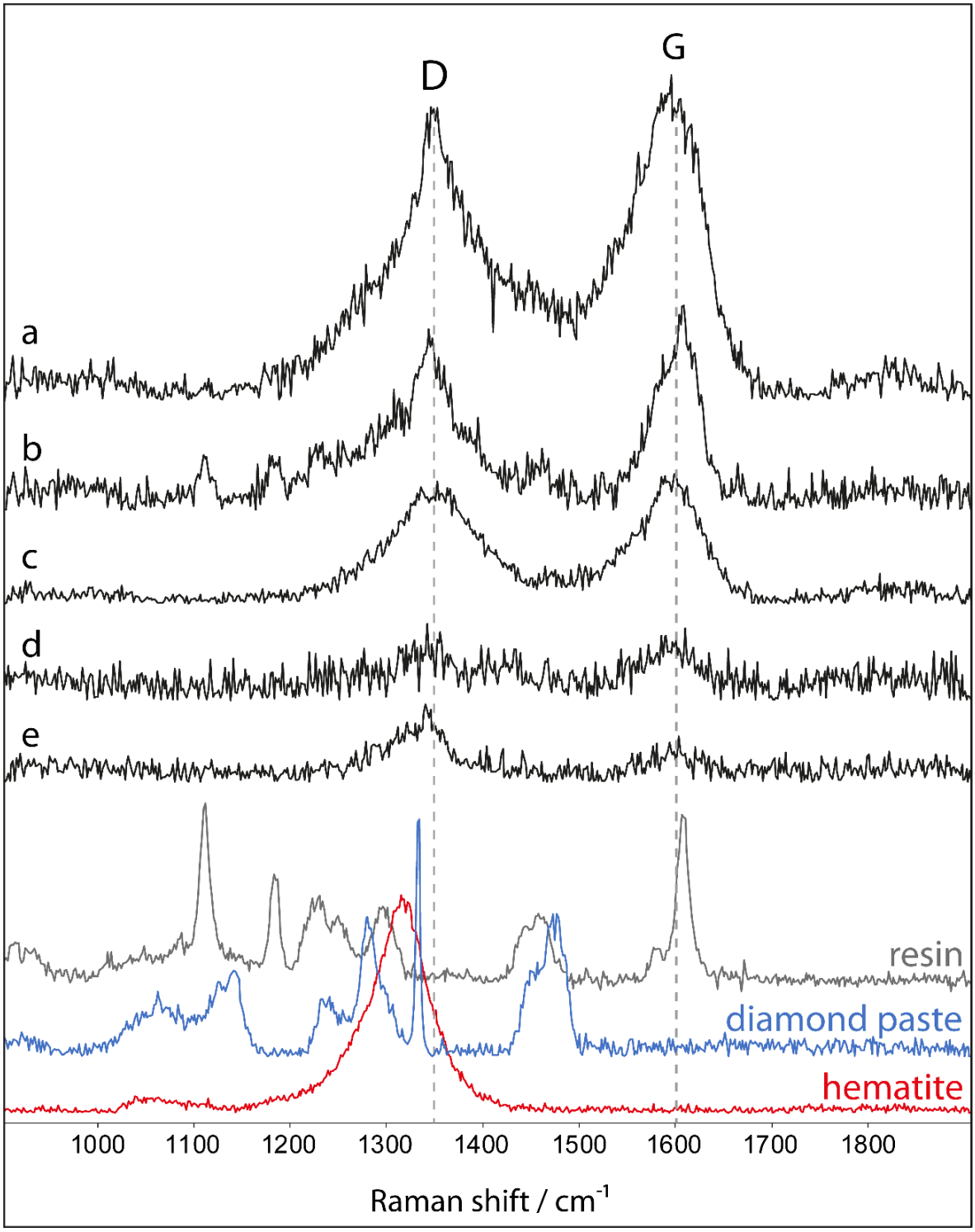

Figure 7.6B. *Band-intensity-normalised Raman spectra corresponding to the spot analysis locations denoted in Figure 7.6A (a, b, c, d and e), together with spectra collected for Epofix resin, Akapaste diamond paste and haematite from sample MSSD083_16_1 for comparative purposes. The 'D' and 'G' markers denote the position of, respectively, the disorder (~1350 Δ cm^{-1}) and graphite (~1600 Δ cm^{-1}) modes of elemental carbon. All 5 spectra indicate traces of relatively disordered carbonaceous material at the site of analysis. Figure provided by Sośnicka (pers. comm., 2016) and reproduced with permission.*

To assess the size distribution of these features, their length and width in pixels were measured from the relevant photomicrographs and converted to µm using the inset scale bar. A population of 64 bacilliforms from all five thin sections were counted, using the criteria that to be counted as a bacilliform, the feature must be 1). elongate in shape, 2). rounded on at least one of its two ends and 3). distinguishable as a separate feature, i.e. not merged significantly into a cluster of similar features (such as in Fig. 4H). These criteria were developed by the author as part of this study to distinguish bacilliforms from abiogenic, often amorphous carrollite and chalcocite crystals which are clearly abiogenic and found throughout the Mashitu South deposit. Length is defined as the greatest possible distance measured along the longest axis of the feature, and width is defined as the greatest possible distance measured along the axis of the feature perpendicular to length. It should be noted that these criteria for recording a feature as a bacilliform are somewhat subjective. Additionally, they assume that all such features will have been sectioned parallel to their length, whereas it is likely that the features have been sectioned in a variety of orientations relative to the slide. Nonetheless, the metrics give an approximate picture of the size distribution of the bacilliforms.

Of the 64 counted bacilliforms, 25 were identified in Section A, 15 in Section B, 14 in Section C, 9 in Section D and 1 in Section E. They ranged in length from ~86µm to ~5µm and in width from ~10µm to ~2µm, having a length:width ratio between ~10:1 to ~2:1. The mean length and width of all the features is ~21µm by ~5µm. The bacilliforms in Section A have a narrower size distribution and are smaller on average than those in Sections B, C, D and E, with a mean length of ~12µm and mean width of ~4µm. The variance in length for the total population is much greater than that of width, and the distribution of the length, width and length:width ratio of the population is positively skewed (see Figure 7.7).

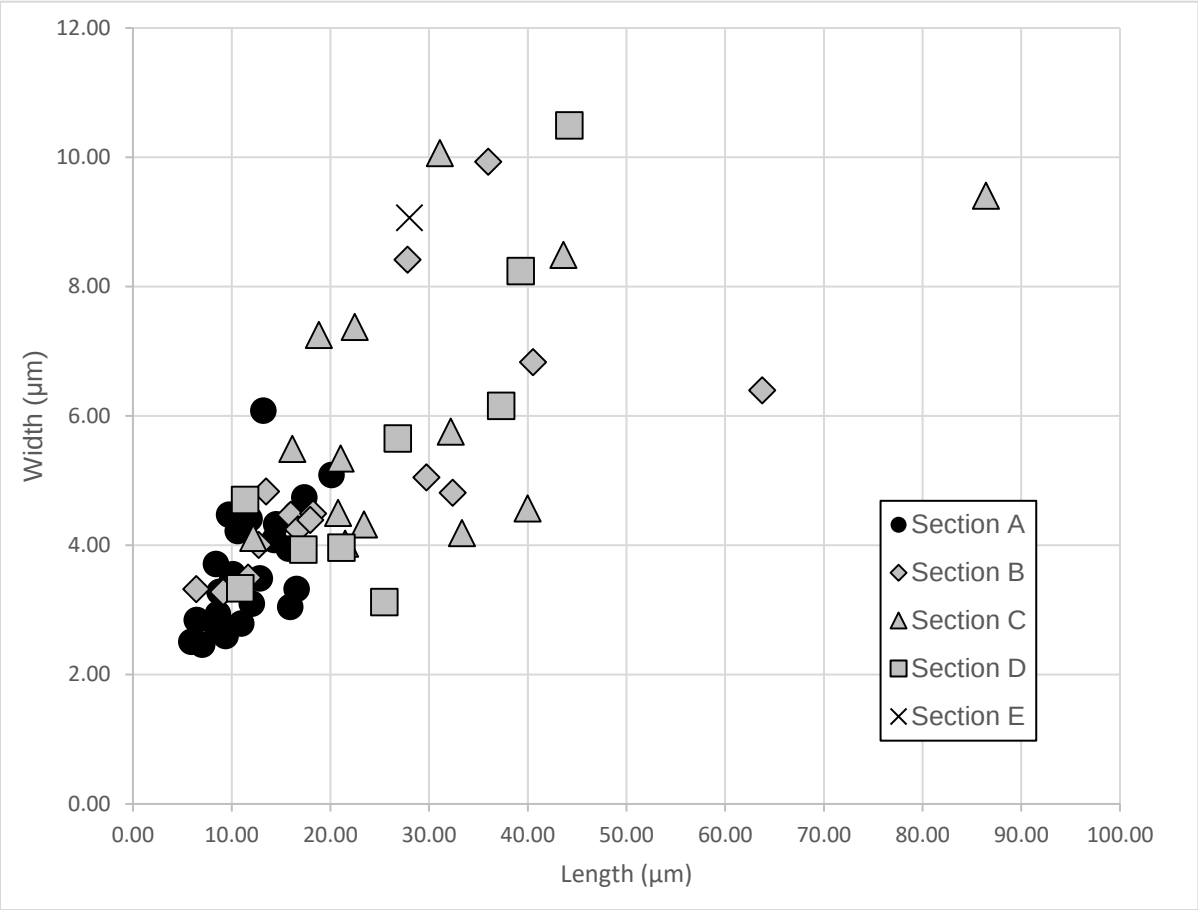

***Figure 7.7**. Size distribution of the population of 64 counted bacilliforms shown by which section cut from sample MSSD083_16_1 they were identified in.*

7.4 Discussion

7.4.1 Rock History

The groundmass of MSSD083_16_1 (16_1) reveals a sequence of siliciclastic deposition followed by diagenesis and Cu-Co mineralisation. Fine-grained detrital quartz, mica, clay minerals and carbonaceous material were deposited during the sedimentation of sample 16_1. According to Bull *et al*. (2010) this occurred during a period of progressive deepening in a transgressive systems tract, with the SDB unit representing slightly basin-ward facies from the stromatolitic 'barrier reef' of the RSC, the transition from which occurs only ~2m down-hole below sample 16_1 (Figure 7.1). Sedimentation and burial was followed by the authigenic growth of rutile, then pyrite, quartz, chlorite, stratiform chalcocite, stratiform

carrollite, and finally dolomite. A syn-diagenetic age for these stratiform sulphides is inferred and the mineralisation attributed to the Early Hydrothermal SSC Stage, with the para-framboidal pyrite equated to the Py1 phase, the stratiform chalcocite to the Cc1 phase, and the stratiform carrollite to the Car1 phase (see Chapter 4: Petrography and Paragenesis).

Rutile from the apatite-haematite-rutile veins is very similar in form to the groundmass-disseminated authigenic rutile, and there is a diffuse distribution of rutile crystals at the vein-ends away into the groundmass. This indicates that the vein-hosted and groundmass-disseminated rutile formed at the same time. Within the veins, rutile appears to have formed first, followed by apatite, crystals of which terminate against and mantle the rutile, and then haematite, which fills in spaces between well-formed crystals of apatite. Stratiform pyrite, chalcocite and carrollite also abut against and mantle both vein-and-groundmass-disseminated rutile (Figure 7.4D), as well as the vein apatite, and therefore post-date the formation of veins and groundmass-hosted rutile. These observations indicate that the apatite-haematite-rutile veins formed during diagenesis and before the stratiform Cu-Co mineralising event. Syn-diagenetic veins (and cavities later filled with minerals), formed before final lithification, are well documented in literature (e.g. Labaume *et al*., 1991; de Joussineau *et al*., 2005; Billi *et al*., 2017).

Authigenic chlorite in the groundmass is un-foliated and frequently found as inclusions within dolomite and stratiform sulphides. Together with dolomite, chlorite precipitation is viewed as part of a regional syn-diagenetic magnesian metasomatic event described by Hitzman *et al*. (2010) which accompanied or pre-dated stratiform Cu-Co mineralisation, rather than being metamorphic in origin. An absence of other possible metamorphic indicators suggests that the SDB unit at Mashitu South was exposed to sub-greenschist-facies metamorphism during the Lufilian Orogeny, if it was metamorphosed at all. Ramsay and Ridgway (1977) state that the Katangan portion of the Copperbelt generally experienced a lower grade of regional metamorphism than the Zambian portion, never reaching higher temperatures and pressures than lower greenschist facies.

The thick quartz-dolomite vein in section 16_1_A cross-cuts all previously mentioned features and is considered post-diagenetic in timing. It is accompanied by localised, pervasive silicification around the vein margins and the vein itself hosts anhedral chalcocite mineralisation, ascribed to the late-hydrothermal mineralisation stage at Mashitu South (see Chapter 4: Petrography and Paragenesis).

Although it is a common feature of rocks at Mashitu South, there is no evidence for considerable supergene alteration in sample MSSD083_16_1.

7.4.2 Prokaryotic Microfossils?

A direct biogenic origin for the bacilliforms, in that they are prokaryotic microfossils, was considered by this study. To assess this possibility, the hierarchical recognition criteria suggested by Buick (1990) for distinguishing potential microfossils from contaminants and abiogenic pseudofossils were applied to the features. These criteria require proof of two properties for a candidate microfossil to be considered as such: antiquity and biogenicity.

7.4.2.1 Antiquity

Antiquity of the bacilliforms is indicated by three criteria defined by Schopf and Walter (1983). First, there must be a clearly defined age to the host rocks. Although radiometric dating has not been carried out at Mashitu South, the rocks of the deposit have been confidently assigned to the Roan Group by stratigraphic correlation (Seibel *et al*., 2013; Gigler and Kinnaird, 2017). The Roan Group is constrained to a maximum age of 883±10 Ma (Armstrong *et al*., 2005) and a minimum age of either ~770 Ma (Key *et al*., 2001) or ~712 Ma (Bull *et al*., 2011). Within this period, the exact age of the SDB unit is uncertain, but given that it occurs within the lower-middle part of the Roan Group succession, it is likely to have been deposited and undergone diagenesis between~850-800 Ma. Secondly, the bacilliforms are embedded in the rock matrix (within the apatite-haematite-rutile veins), eliminating the possibility that they are modern surface contaminants. The third criteria for antiquity is that the suspect microfossils were emplaced during deposition, rather than being ancient contaminants. This is not the case for the bacilliforms, which are found in veins, indicating that they were emplaced post-depositionally. However, paragenetic relationships between the vein minerals and the groundmass, and the preservation of the bacilliforms in pyrite, chalcocite and carrollite indicate a diagenetic timing of emplacement. Certainly, the pyrite and carrollite components of the bacilliforms show at least that they were preserved in the hypogene environment, as these minerals do not readily form in the low pH, high Eh conditions typical of the supergene environment (Takeno, 2005).

7.4.2.2 Biogenicity

Buick (1990) posits seven sub-criteria for the recognition of biogenicity, which are all met by the bacilliforms, the first being that they occur in petrographic thin sections. This negates the risk that they may be surface artefacts created by sample preparation. Secondly, the bacilliforms occur in a low-grade meta-sedimentary rock, with the SDB at Mashitu South considered to have been exposed to sub-greenschist facies levels of temperature and pressure. Levels of metamorphism higher than lower greenschist facies have a tendency to destroy microfossils. Third, the bacilliforms exist well within the size range of extant free-living microorganisms. With a mean length and width of 21µm by 5µm, the bacilliforms are on the large side for bacteria or archaea; much larger than the smallest extant nanobacteria (~50-200nm: Kajander and Çiftçioglu, 1998) but significantly smaller than the largest discovered extant bacteria (~100-750µm: Schulz *et al*., 1999). Buick (1990)'s fourth criteria for biogenicity is that the features must be composed of kerogen. Some of the hollow bacilliforms display traces of amorphous carbon within their internal cavities (Figure 7.6), which may be kerogenous. The fact that the features are not preserved totally as organic kerogen fossils does not significantly hinder the argument for biogenicity; Westall (1999) emphasises the prevalence of mineral replacement in the microfossil record, and the bacilliforms, while originally composed of organic matter, could have induced later precipitation of and replacement by metal sulphides. Fifth, the bacilliforms occur in groups with others of a similar morphology (Figure 7.8A), particularly in Section A (Figure 7.8B), rather than being isolated occurrences. Sixth, many of the bacilliforms are hollow, a common feature of microfossils. Those bacilliforms that are not hollow are filled with chalcocite or contain crystals of pyrite, which may represent earlier stages of mineral replacement. The last, and hardest criteria to fulfil of Buick (1990) is that the objects must display cellular elaboration. Several properties of the bacilliforms are reminiscent of this. Some are linked at their ends in a manner suggestive of cell division (Figures 7.8C and 7.8D). Others are curved against the apatite substrate (Figures 7.5B, 7.5C, 7.5D and 7.5F), which would be expected if the feature was originally a soft-bodied organism. The grouped and occasionally clustered distribution of many of the bacilliforms (Figures 7.9A and 7.9B) is reminiscent of bacterial colonies. All of the above criteria are used as indicators of cellular complexity by Westall (1999) in a review of microfossil recognition.

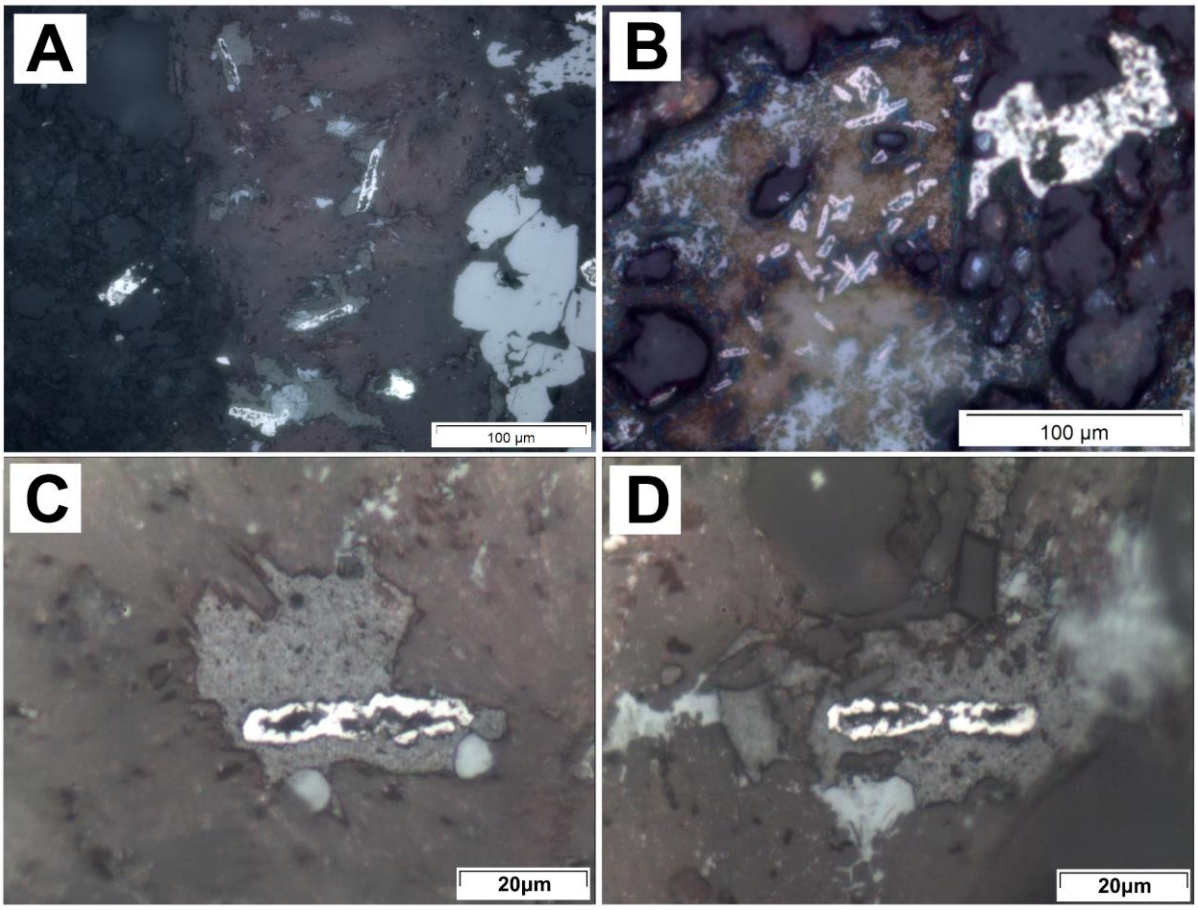

***Figure 7.8**. Optical photomicrographs of bacilliforms from sample MSSD083_16_1, taken in reflected PPL. A: several bacilliforms occupying different cavities within an apatite vein. B: a number of bacilliforms occupying a single partially-haematite-filled cavity. C, D: examples of bacilliforms conjoined at the ends in a manner reminiscent of cell division.*

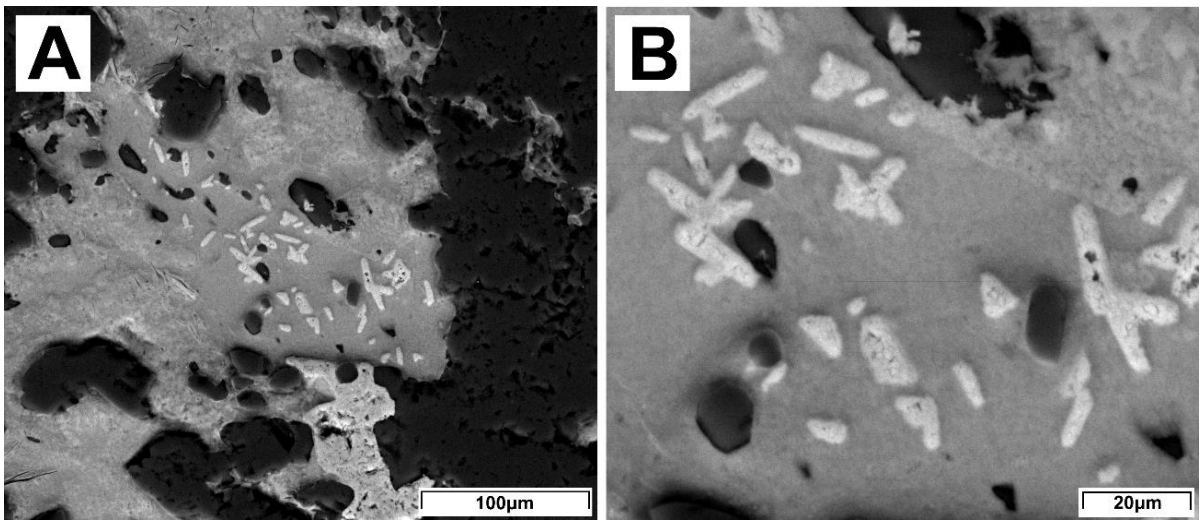

***Figure 7.9**. Back-Scattered-Electron (BSE) electron microscopy images of a number of bacilliforms existing within a cavity in slide 16_1_A. B shows a magnified portion of the field of view in A, with both images taken of roughly the same area of the slide shown by the photomicrograph in Fig. 7.8B.*

Schopf *et al*. (2010) discussed the additional need for candidate filamentous microfossils to be cylindrical, to exhibit a sinuosity correlating with their size and for the features to exhibit a uniform diameter along their length. Whereas the bacilliforms tend to have relatively uniform diameters along their lengths, their sinuosity falls short of these model characteristics, with the majority of bacilliforms being relatively straight-edged and with no distinct correlation existing between curvature and size. The cylindricity of the features has not been assessed due to the lack of 3D imaging options available to this study.

7.4.2.3 Potential mode of life and preservation:

The bacilliforms were emplaced within syn-diagenetic veins, before the main stratiform mineralising event, and can therefore be inferred to be between ~875-765Ma in age based on age limits for stratiform mineralisation at comparable deposits around the Copperbelt (Key *et al*., 2001; Armstrong *et al*., 2005; Selley *et al*., 2006; Decree *et al*., 2014). These veins would have originally been fissures or micro-faults within the lithifying host sediments and would have been the centres of diagenetic fluid flow. By the time of emplacement, apatite and haematite had already begun to crystallise, forming a radial acicular texture in the case of apatite and a botryoidal texture in the case of haematite (Figure 7.10), which indicate open-space environments of growth for both minerals. In a study of marine sandstones, Porten *et al*. (2015) found that diagenetic apatite forms at a temperature of over ~90°C, generally corresponding to a depth in the sedimentary pile in excess of >1km, depending on the geothermal gradient. They concede, however, that in an arid sedimentary environment, where evaporation causes supersaturation of the groundwater, it is possible for apatite to be precipitated at much lower temperatures, closer to the sediment surface. Given an arid, marginal marine, sabkha-like setting for the deposition of the Mines (R2) Subgroup (Bull *et al*., 2010) it seems likely that the apatite in the veins was deposited at a lower temperature and at a shallower depth in the sedimentary pile. Additionally, the open-space growth textures of the apatite and haematite indicate that the lithostatic pressure was not high enough to close the fractures in which they formed. The exact depth at which the apatite-haematite-rutile veins formed and at which the bacilliforms were emplaced is therefore uncertain, perhaps ranging from tens to hundreds of metres in the deep subsurface environment. A supergene origin for the formation of the bacilliforms is ruled out because of

their preservation in pyrite and carrollite, which do not readily form in the low pH, high Eh conditions typical of the supergene environment (Takeno, 2005). Within the veins, rutile crystallised first, then apatite, leaving (probably interconnected) cavities in the veins which were partially filled by haematite. It was after or during this initial haematite crystallisation, but before the formation of botryoidal haematite, that the bacilliforms were formed.

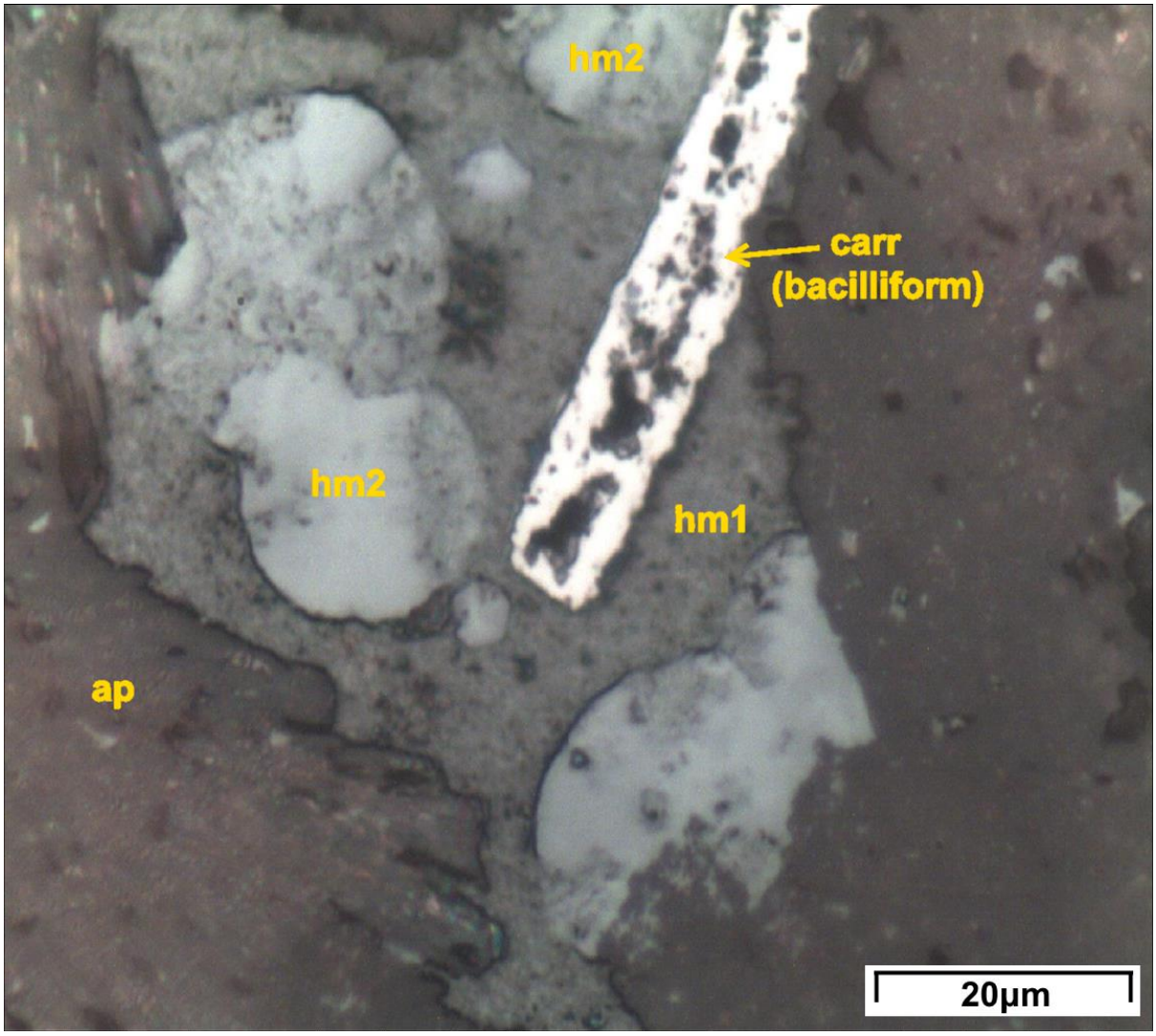

Figure 7.10. *Optical photomicrograph of a bacilliform-hosting cavity within an apatite vein, taken in reflected PPL. Cavities within the apatite (ap) were coated, but not totally filled by an early phase of haematite (hm1). The carrollite (carr) bacilliform then grew/was emplaced, followed by a second phase of botryoidal haematite (hm2) which abuts against the bacilliforms.*

Assuming that the bacilliforms are microfossils, the fracture-hosted, deep subsurface environment in which they were emplaced implies that they represent a community of chasmoendoliths, while their bacillus-shape suggests that they were prokaryotes. Clusters of

what appear to be merged bacilliforms may be interpreted as microbial colonies. Whether this community could have been mono or multi-specific is unknown, given the less-than-exceptional state of preservation. Organisms in this anaerobic, acidic, high temperature and pressure environment are typically chemolithoautotrophic (Rothschild and Mancinelli, 2001) and archaea are more typical of this extremophilic environment than bacteria (Rampelotto, 2013).

Two features of the bacilliforms suggest that, if they are biogenic, that the organisms which produced them were iron reducing. This first is their occurrence in cavities which are partially filled by haematite. The non-botryoidal haematite which lines the margins of these cavities is pitted and very finely stippled (Figure 7.10), a common texture in minerals that have been subject to 'grazing' by lithotrophic bacteria (Barker *et al*., 1997). *Extracellular Polymeric Substances* (EPS) secreted by bacteria frequently have acidic properties (Welch *et al*., 1999; Vu *et al*., 2009) and aid in the digestion of Fe^{3+} bearing compounds such as haematite, leaving the remaining substrate with this characteristic nanotexture.

The second feature of the bacilliforms which could indicate an iron-reducing metabolism is the presence of pyrite crystals within some of them (Figure 7.5D) and their preservation by Cu-Co sulphides. In anaerobic environments, iron-reducing bacteria expel Fe^{2+} at the cell wall interface or at the margins of associated EPS (Schoonen, 2004; Pósfai *et al*., 2013). Fe^{2+} reacts abiotically with available H_2S in passing diagenetic fluids to form pyrite, leading to extracellular Biologically Induced Mineralisation (BIM) and encrustation of the organism (Konhauser *et al*., 2008), or, less commonly, intracellular BIM (Glasauer *et al*., 2002; Frankel and Bazylinski, 2003; Edwards and Bazylinski, 2008). Bacillus-shapes are common for iron-reducing bacteria and encrustation would lead to a build-up of pyrite in a bacillus-shaped cast surrounding the original cell and perhaps, due to intracellular BIM, within the original cell. Later, the surface of these minerals may then act as sites of nucleation and abiogenic pyrite growth, potentially creating features which bear only a passing resemblance to the shape of the original cell (Weiner and Dove, 2003). Encrustation would have eventually resulted in the death of the cells as nutrient channels to the cell surface were blocked off, beginning the fossilisation process. A second generation of botryoidal haematite then formed in the host cavities, abutting against and growing around the bacilliforms (Figure 7.10).

The presence of pyrite within the cells could also hint at the possibility of Bacterial Sulphate Reduction (BSR) processes in the metabolic function of the bacilliforms. Jensen and

Dechow (1962) and Dechow and Jensen (1965) implicate BSR, forming abundant early, framboidal pyrite and other stratiform sulphides, as being widespread in the Katangan Copperbelt. During BSR, bacteria living in the host sediment convert dissolved seawater sulphate into sulphides, frequently pyrite. This process is an important source of sulphur in SSC deposits worldwide (Brown, 2014).

Within the groundmass of MSSD083_16_1 and at the Mashitu South deposit in general, pyrite is frequently replaced by chalcocite and carrollite. The present-day mineralogy of the bacilliforms, primarily chalcocite and carrollite, could therefore exist as the result of mineral replacement by ore-forming fluids of originally BIM-formed pyrite, or by replacement of pyrite which itself replaced earlier carbonaceous microfossils. This is supported by the remnants of pyrite and even disordered carbon found within the bacilliforms. The combination of extracellular BIM and replacement by later sulphides could have both altered the original shape of the bacilliforms and exaggerated their original size, through the nucleation of mineral growth on the original encrusting cast developed around the cell. Replacement of EPS by pyrite (and subsequently chalcocite/carrollite) may have also led to the distortion of the original cell shape. Wacey *et al*. (2013) make similar observations of a mixed assemblage of carbonaceous and pyritised Gunflintia and Huniosporia microfossils from the ~1.9 Ga Gunflint Chert from north-western Ontario, Canada, with the cell walls of the pyritised microfossils being significantly thicker and more altered from a typical bacillus morphology than the carbonaceous varieties. Incidentally, the filamentous Gunflintia microfossils from the assemblage described by Wacey *et al*. (2013) bear a strong superficial resemblance to the bacilliforms described by this study, both in terms of dimensions and morphology.

7.4.3 Abiogenic Pseudofossils?

The hollow nature of many of the bacilliforms, which Buick (1990) cites as a criterion for biogenicity in that only the outer cell wall is likely to be preserved during the fossilisation process, could be simulated abiotically if the shapes were originally composed of chalcocite and then subjected to partial ‘outside-in’ replacement by carrollite. Internal ‘cores’ of chalcocite surrounded by external ‘rims’ of carrollite are seen in most of the bacilliforms from Section MSSD083_16_1_A and traces of chalcocite were detected by Raman in several of the

bacilliforms from Sections B, C and D. Later dissolution of the chalcocite, but not the carrollite, could then produce a hollow shape.

Another consideration which casts doubt on an organic origin is uncertainty regarding the Raman spectra which show the presence of carbon within the hollow centre of some of the bacilliforms (Figure 7.6). Sośnicka (*pers. comm.,* 2016) found fluid inclusions in dolomite-aragonite veins at Mashitu South which contain carbonaceous solids, indicating that some of the hydrothermal fluids which passed through the deposit may have precipitated graphite, or amorphous carbon of an inorganic nature. The broad double peaks and pronounced 'D' (Disorder – 1354cm^{-1}) bands relative to the G (Graphite – 1603cm^{-1}) bands in the spectra (Figure 7.6B) suggest a more disordered, amorphous rather than graphitic nature to the carbonaceous material in the features (Wopenka and Pasteris, 1993; Keleman and Fang, 2001; Beyssac *et al*., 2003), which would support a kerogenous interpretation (Wopenka and Pasteris, 1993). However, the similarity in spectra to the carbonaceous solids in fluid inclusions at the deposit (Sośnicka, *pers. comm.,* 2016), together with the innate difficulties in distinguishing the Raman spectra of biogenic and abiogenic amorphous carbon (Pasteris and Wopenka, 2003) make it impossible to say for certain whether the carbonaceous material within the bacilliforms is true, residual kerogen rather than hydrothermally precipitated carbon.

Raman mapping was conducted of the bacilliforms and their immediate environs. This mapping, confirmed by longer-count spot analyses of relevant areas (Figure 7.11), found that the carbon signature is not solely limited to the bacilliforms themselves, but that traces of disordered carbon may be detected within a few µm of the features too. These carbon traces were found within the haematite-filled cavities and corresponded optically with micron-to-sub-micron scale dark patches. It is possible that this carbon could be kerogenous remnants of some other life form, fragments of cells which were not sulphidised, or that carbon may have been deposited hydrothermally alongside microfossils by coincidence. However, hydrothermal precipitation/redeposition of disordered carbon both within and outside of the bacilliforms at some stage after preservation seems to more simplistically explain the presence of carbon, and agrees with the presence of carbonaceous solids in fluid inclusions found elsewhere at Mashitu South (Sosnick, *pers. comm.,* 2016). Horodyski (1981) shows that microfossil-like objects can be formed by inorganic processes from organic kerogen, with 'biological' $\delta^{13}C$ values. In-situ carbon isotope analysis of the amorphous carbon within the

bacilliforms would therefore not produce conclusive evidence for a biological origin, however if such an analysis were to find inorganic $\delta^{13}C$ values it could preclude a biological origin for the amorphous carbon within them.

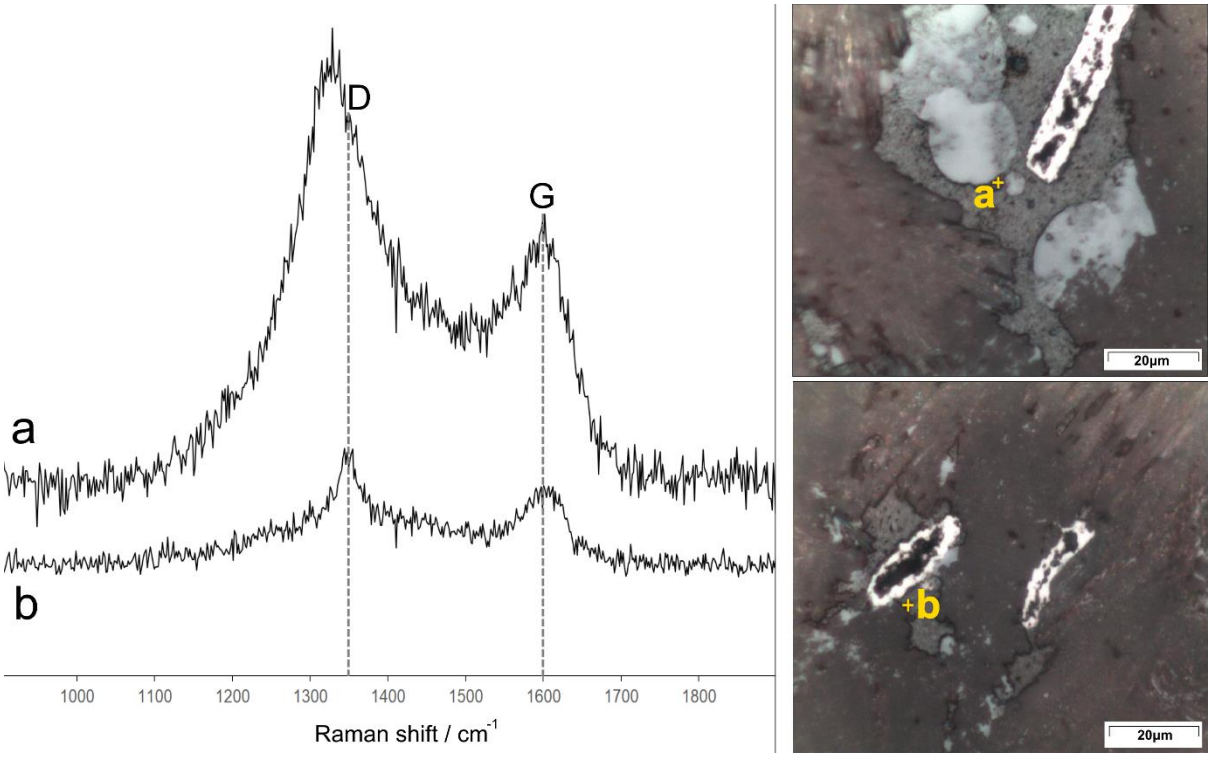

***Figure 7.11**. Band-intensity-normalised Raman Spectra of spot analyses made in close proximity to bacilliforms within sample MSSD083_16_1. Spectra a and b correspond to the respective points on the reflected PPL photomicrographs. The 'D' and 'G' markers denote the position of, respectively, the disorder (~1350 Δ cm^{-1}) and graphite (~1600 Δ cm^{-1}) modes of elemental carbon. Both spectra show the presence of carbonaceous material outside of the boundaries of the bacilliforms themselves (in spectrum a the 'D' carbon mode is obscured by the disorder mode of haematite at ~1320 Δ cm^{-1}).*

The final factor which questions the biogenicity of the bacilliforms is the positive skew, high variance and high coefficient of variance in the size distribution of the community of 64 counted bacilliforms (Figure 7.7). Schopf (1976) suggests that monospecific biogenic assemblages are likely to have a close-to-normal size distribution with a low coefficient of variance. However, Buick (1990) refutes this criterion, citing that many abiogenic crystal assemblages have close to normal size distributions, that many modern monospecific bacterial assemblages do not have a normal size distribution, and that a fossilised bacterial assemblage may not necessarily be monospecific despite similarities in form (Knoll *et al.*, 1978, Strother and Barghoorn, 1980). If some of the features included were pseudofossils of similar appearance to true microfossils, erroneously counted (i.e. the population represents

a mix of pseudofossils and microfossils), this would also produce a higher skew and variance in the size distribution than expected for a population of monospecific, normally-distributed microfossils. Additionally, when considering a microfossil assemblage in 2D, the assumption of a normal size distribution does not take into account the effect of cross-sectioning an assemblage of variably-orientated microbes (or pseudofossils) with an irregular bacillus shape.

The most likely abiogenic explanation for the creation of the bacilliforms is through replacement of euhedral-to-subhedral crystals. Distinct angularity in some of the bacilliforms suggests a crystalline rather than biogenic origin (Figure 7.12A). Euhedral rutile in particular forms lath-shaped crystals which may be somewhat rounded at the ends to produce a 'bacillus' shape (Figure 7.12B); apatite, too, can form acicular crystals which, given the right cross-section, could be misinterpreted as bacillus shaped. Isolated incidents of carrollite and chalcocite replacing both of these minerals (Figures 7.12C and 7.12D) were detected in MSSD083_16_1, raising the possibility that euhedral-to-subhedral crystals of these minerals could have been replaced by these sulphides to form pseudofossils. Indeed, spectra from one bacilliform which resembles an acicular apatite crystal (spectra a and e, Figure 7.6; Figure 7.12C) even display traces of disordered carbon, supporting the possibility that disordered carbon may find its way into the internal cavities of the bacilliforms through abiogenic means, rather than being in-situ kerogen. It should be noted that here is a degree of uncertainty in the interpretation of a cylindrical bacillus-shape for an object from a 2D image, and it is suggested that high-resolution 3D imaging of the features (e.g. by Focused Ion Beam (FIB) Transmission Electron Microscopic (TEM) tomography – see Wacey *et al*., 2013) would help to elucidate their true shapes, including their degree of angularity or cylindricity.

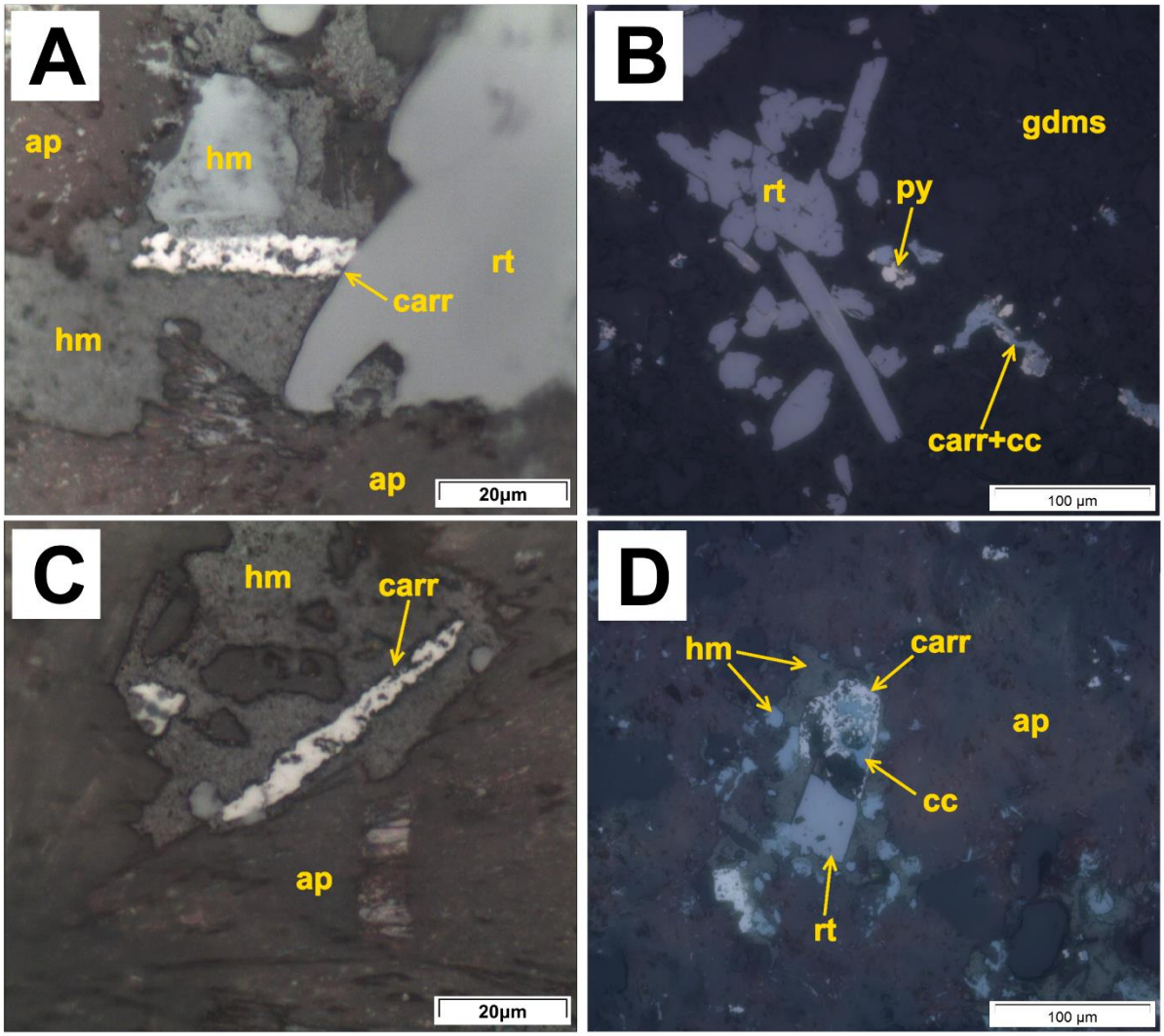

***Figure 7.12**. Optical photomicrographs of abiogenic features within MSSD083_16_1, taken in reflected PPL. A: an angular carrollite bacilliform in contact with a rutile crystal. B: lath-shaped elongate rutile crystals within the groundmass, some of which are sub-rounded at their ends. C: an acicular carrollite bacilliform, the long end of which runs parallel to a radial trend of fibrous apatite crystals, suggesting that the carrollite may be a pseudomorph of an apatite crystal. D: chalcocite and carrollite appearing to replace a lath-shaped crystal of rutile within an apatite vein. Ap= apatite, hm=haematite, carr=carrollite, rt=rutile, py=pyrite, gdms=groundmass and cc=chalcocite.*

7.4.4 Pseudofossils or Microfossils?

Many of the bacilliforms arguably tick all three of the criteria of Schopf and Walter (1983) for antiquity and the seven criteria of Buick (1990) for biogenicity (see section 7.4.2). The age of the host rocks is defined, the features are embedded in the rock matrix and paragenetic relationships show that they were formed during diagenesis. The features occur in a petrographic thin section, in a low-grade meta-sedimentary rock, are well within the size range of extant free-living microorganisms, contain disordered carbon (which could be

interpreted as kerogen), occur within groups of features with a similar morphology, are hollow and can be interpreted to display cellular elaboration. It would be possible to pick certain bacilliforms out of the total assemblage and define them as biogenic microfossils, according to the criteria of Buick (1990), which would suggest the preservation of a community of chasmoendolithic, chemolithoautotrophic prokaryotes.

However, the biogenic interpretation is questioned by angularity in the form of many of the counted bacilliforms (Figsure 7.12A and 7.12C) and evidence for replacement of abiogenic crystals by the minerals from which the bacilliforms are composed (Figure 7.12D). Additionally, most of the features do not meet the conditions for sinuosity and cylindricity of candidate microfossils espoused by Schopf *et al*. (2010), nor those pertaining to statistical parameters of an expected biogenic size distribution. With these factors considered, only a few of the features out of a counted community of 64 could be argued, on an individual basis, to me*et al*l of the proposed criteria for biogenicity considered by this study. Given that a few of the bacilliforms me*et al*l of the biogenicity criteria, whereas others appear demonstrably abiogenic, the possibility exists that the bacilliforms represent a mixed community of syngenetically-formed microfossils and pseudofossils. A simpler and less extraordinary explanation, however, is that the features are all pseudofossils, some of which coincidentally mimic the characteristics of biogenicity. With only ambiguous evidence for their biogenicity, the hypothesis that the bacilliforms represent fossilised Neoproterozoic prokaryotes should be discounted.

A more probable explanation for the bacilliforms is that they are sulphidic pseudomorphs of earlier-formed, euhedral-to-subhedral elongate crystals, which grew syn-diagenetically in an open-space environment. The majority of these original crystals were likely to have been rutile, which forms sub-rounded, lath-shaped crystals capable of mimicking a bacillus shape (Figure 7.12B). Apatite crystals could also have been replaced (Figure 7.12C). Crystal aggregates of these minerals, linked at their ends, could explain conjoined bacilliforms (Figures 7.5A, 7.8C and 7.8D) which are similar in appearance to dividing cells. These crystals were subsequently replaced by sulphides, including pyrite, chalcocite and carrollite (Figures 7.5D and 7.12D). Chalcopyrite has also been shown to replace rutile at the Kakanda Cu-Co deposit (Sośnicka, *pers. comm.,* 2016) and the decomposition of rutile in a reducing environment at the nearby Musoshi Cu-Co deposit is documented by Cailteux and Dimanche (1973). Within Polish Kupferschiefer ores, Kucha *et al*.

(1981) reports the replacement of rutile containing high Fe concentrations in its crystal lattice by chalcocite and bornite, again in a reducing environment. It is possible that the same thing occurred within the apatite-rutile veins of MSSD083_16_1, resulting in carrollite-chalcocite pseudomorphs of the replaced rutile crystals. This rutile would have to have been a later (perhaps more Fe-rich) generation of the mineral than the extant rutile in the apatite veins, which appears to have formed before the apatite (see section 7.4.1). The hollow nature of many of the bacilliforms could be explained if they were replaced by chalcocite and then carrollite, with chalcocite at the centre (see Figures 7.5A and 7.12D), as observed in the groundmass-hosted mineralisation (Figures 7.4B and 7.4D). Subsequent dissolution of the chalcocite, but not the carrollite by later hydrothermal fluids would leave a hollow carrollite 'shell'. Disordered carbon found within the internal cavities of the bacilliforms may have been precipitated by later hydrothermal fluids, as supported by fluid inclusion studies at the deposit (Sośnicka, *pers. comm.,* 2017).

7.5. Conclusions from Bacilliform Pseudofossils

This study considers the bacilliforms found within sample MSSD083_16_1 to be pseudofossils, comprising carrollite-chalcocite pseudomorphs of euhedral-subhedral rutile crystals. The features show an extensive range of biogenicity indicators, with some features, considered individually, meeting the complete set of biogenicity criteria for microfossils defined by Buick (1990). However, a holistic study which includes mineral paragenesis, Raman mapping (rather than just spot analyses) and assesses the features as a community, shows that the bacilliforms are likely to be abiogenic. Such lessons should be carefully considered by micropalaeontological studies of the rocks of the Katangan Supergroup; a sceptical viewpoint, holistic methodology and thorough scientific procedure for any investigation of suspect microfossils is recommended. Although the features reported in this study are volumetrically minor, the possibility of rutile replacement by Cu-Co sulphides raises the question as to whether rutile distribution exerts any significant control on the distribution of Cu-Co sulphide ore at the Mashitu South deposit, or across the wider Copperbelt.

CHAPTER 8: DISCUSSION AND SYNTHESIS

8.1 Structure of the Mashitu South Deposit

Results of logging (Chapter 3) confirm that the Mashitu South deposit is a 'fragment' of Mines (R2) Subgroup stratigraphy which overlies the RAT (R1) Subgroup. The uppermost fragment has apparently been thrust above a lower fragment towards the eastern margin of the deposit. In many cases, this R2-R1 contact is marked by the development of a few metres of heterogeneous, but frequently polymictic and matrix-supported breccia, usually several metres down from the top of the RAT. This breccia is equated to a regional predisposition for such a breccia layer to be located in the upper RAT, considered to be of halokinetic origin by Hitzman (2015b), and it may have accommodated a great degree of regional movement. The RAT unit is thought to have been the original site of chemo-sedimentary deposition for thicknesses of evaporite on the scale of hundreds of metres (Jackson *et al.*, 2013; Hitzman, 2015b). Certainly, breccias in the RAT appear to form structures in places which show that it acted fluidly (Figure 3.5). Also, the abundance of minerals in the R1 and R2 Subgroups which indicate Mg-K metasomatism such as chlorite, magnesite, muscovite, and biotite, together with sulphates and halides such as barite, gypsum/anhydrite, celestine and even halite (see Chapter 4) are suggestive that evaporites previously existed in the sequence (Kampunzu *et al.*, 2005).

However, the breccia is not present in all of the drill holes through the R1-R2 transition, and is not polymictic and matrix-supported in all cases. In several drill holes the R2 appears to conformably overlie the R1, and in others only a vein-supported, monomictic 'proto-breccia' exists between the two units. Also, the position and number of breccia units within the RAT is highly variable between different drill holes. This suggests that in places, the Mines Subgroup and RAT contact one another conformably, in-situ, and that the location of the breccia is not controlled strictly by stratigraphy. On this basis, the previous existence of hundreds of metres of laterally continuous evaporite in the RAT below Mashitu South is considered unlikely.

Mapping by Cheshire (2014) indicates that many of the breccias cross-cut the basin-and-dome folding of the Mashitu Principal and Mashitu South fragments, which could have

formed during the Lufilian-orogenic constrictional D2 deformation event of Kampunzu and Cailteux (1999). This suggests that they post-date the formation of these structures, which formed during the early stages of the Lufilian orogeny. The dome-and-basin folding of the fragments could also, however, have formed during the passage of halokinetic diapirs.

One piece of evidence for an early/syn-orogenic timing for the Mashitu Complex brecciation is found in the Type 2 veins at Mashitu South, host to the 'Late Hydrothermal Ore' Stage of mineralisation. This mineralisation stage is equated to the 'vein-type' mineralisation type of Dewaele *et al.* (2006) and resembles early/syn-orogenic mineralisation described at other deposits in the Central African Copperbelt (e.g. Selley *et al.*, 2005; El Desouky *et al.*, 2009). Type 2 veins contain abundant barite and rare halite, suggesting that they were formed by high-salinity fluids, which could have been produced during the large-scale mobilisation of evaporites during the early stages of the Lufilian orogeny.

A recent structural study by Byrne (2017) indicates that the breccias of the Mashitu Complex were formed primarily as the result of extensional-phase diapirism. While the observations of Mashitu South made by this study do not wholly agree with this conclusion, interpretational concession must be made for the more focussed and extensive structural work done by Byrne (2017). It is possible that early diapirism may have been overprinted by a later tectonic brecciation fabric, or that the dome-and-basin folding observed in the Mashitu South and Mashitu Principal Mines Subgroup fragments were formed during diapiric passage rather than during the D2 tectonic deformation event of Kampunzu and Cailteux (1999).

8.2 Stratigraphy and Sedimentology of the Mashitu South Deposit

This study finds the current consensus of interpretation of the stratigraphy at Mashitu South to be largely accurate. The basal RAT Subgroup, a quartzo-chloritic siliciclastic sequence of mudstones, shales, siltstones and sandstones with occasional dolomitic units, is inferred to be the result of a typical syn-rift continental-clastic depositional environment. Brecciation in the unit, as well as rare gypsum/anhydrite and celestine trapped in authigenic quartz (Figure 4.62), suggest that the RAT once hosted a number of thin evaporite units which have since been migrated and dissolved out of the system. This sequence of lithology may be indicative of deposition in a sabkha-like environment (Dalton, pers. comm., 2015). At the top of the unit,

a green-grey discolouration (known as the RAT Gris) is thought to be an alteration of the primary lithology, which is sedimentologically identical to the RAT Rouge, except for 'enterolithic' quartz-dolomite textures (Figure 3.13) which are indicative of former evaporite layers. The entire RAT sequence contains primary, authigenic haematite which is thought to have formed during diagenesis in an oxidising environment. Geochemically, when compared to the rest of the stratigraphy, the RAT Rouge is extremely depleted in S, and is also somewhat depleted in K. There is a slight elevation of Ba at the top of this unit, in the RAT Gris (Chapter 5). As a siliciclastic unit, the RAT Rouge shows elevated concentrations of Ti, Al and Sc, with extremely low Sr:Sc ratios.

The Kamoto Formation, which occurs immediately above the RAT, consists of a series of dolomites that show evidence of abundant algal/cyanobacteria growth in the form of wavy laminations and stromatolites, followed by early diagenetic, layer-parallel silicification. Laminar, 'nodular' microcrystalline silica in the lowermost DStrat unit is considered to be boudinaged layers of chert. Evidence of soft-sediment deformation is abundant in the whole formation and Type 1 veins are common (Chapter 3). The RSF unit is finely laminated and contains an appreciable amount of laminar, dark material which EDS spectra suggest may be carbonaceous, and both the RSF and DStrat contain disseminated sub-framboidal and cubic pyrite (Chapter 4) which is thought to be authigenic and diagenetic. The RSC is characterised by stromatolitic laminations (Figures 3.16 and 3.60) which are heavily silicified. The sedimentological environment in which the Kamoto Formation was deposited is thought to have been reducing, organic-rich and marginal-marine in nature. The formation was deposited during the transition from the lowstand systems tract which prevailed during RAT deposition, into a transgressive systems tract which prevailed during Kamoto Formation deposition (Bull *et al.*, 2010). At Mashitu South this formation is roughly 25-30m thick. Because of the degree to which these units have been silicified, they do not contain particularly high concentrations of Ca and Mg, however the high Sr:Sc ratios show that they were deposited as calcareous rocks (Chapter 5).

The 'Dolomitic Shales' or 'SD' Formation at Mashitu South is expressed as a thick sequence of dolomitic argillites: shales, mudstones and sometimes siltstones, which is roughly 70-80m in thickness. The formation is relatively homogeneous at Mashitu South, and unit distinction is only drawn between the upper SDS unit and the lower SDB unit, which are separated by an intervening, roughly 5m thick black shale designated as the SD2d unit. The

SD as a whole contains both authigenic, disseminated haematite and pyrite, indicating that redox conditions varied between oxidising and reducing during its deposition. The SD2d black shale, however, contains abundant carbonaceous material and pyrite and was clearly deposited in anoxic conditions. Although it contains appreciable concentrations of Ca and Mg, it also contains high Ti, Al and Sc. An abundance in the groundmass of rounded, detrital quartz and clay composition, together with low Sr:Sc ratios, indicates that this unit is a primary siliciclastic argillite unit which has been dolomitised by later alteration. The high concentration of K in the Dolomitic Shales, especially in the SD2d unit, is also thought to be due to alteration. The Dolomitic Shales Formation was deposited in marine conditions and represents the continuation of the transgressive systems tract in which the Kamoto Formation was deposited, up to the deposition of the SD2d, which marks the beginning of a highstand systems tract (Bull *et al.*, 2010).

The Kambove Formation (or CMN), which is the uppermost stratigraphic unit at Mashitu South, is interbedded with a dolomitic argillite at the base, in contact with the SD. It then becomes a thick, highly variable unit of carbonaceous dolomitic micrite, which is locally silicified, locally stromatolitic, and contains locally distributed 'cauliflower' or 'chicken wire' evaporite textures (Figure 3.24). Like the Kamoto Formation, it has an abundance of Type 1 veins and is highly calcareous, containing the highest average concentrations of Ca and Mg of any unit, and having high ratios of Sr:Sc (Chapter 5). It is, however, more variable, more carbonaceous, and generally less silicified than the Kamoto Formation. Mineralogically, the abundance of carbonaceous material and the presence of sub-framboidal and cubic pyrite suggest that the bulk of the unit was deposited in reducing environmental conditions. The Kambove Formation is the thickest out of the three formations in the Mines Subgroup, being more than 100m thick in MSSD075, 080 and 083, but, being the highest unit in the local stratigraphy, its thickness is constrained by the erosional surface. According to Bull *et al.* (2010) the Kambove Formation represents a sea-level regression from the highstand systems tract of the SDS into a sequence of deep and then supra-tidal carbonates. There is a minor transgression which deposited sub-tidal carbonates in the middle of the unit, followed by a regression and a return to supra-tidal carbonates in the upper parts of the formation.

8.3 Metasomatic Alteration at the Mashitu South Deposit

Several alteration types were distinguished by this study. The earliest alteration event is likely to have been very early-diagenetic/burial silicification of stromatolitic and algal-laminated units such as the RSC and RSF. Silicification is easily identifiable during core logging, but it is also shown in trends on the ACF diagram with data plotting towards lower values of C, with no corresponding change in A or F values (Figure 5.56). The early-diagenetic/burial silica-fixing properties of cyanobacteria could explain the association of silicification with wavy-algal-laminated or stromatolitic units (Hitzman *et al.*, 2010b; Kremer *et al.*, 2012), although later, minor microcrystalline silicification events may also have occurred, particularly in the CMN/Kambove Formation (Chapter 3) which is equated with the post-mineralisation silicification described by Fay and Barton (2012), as shown in Figure 2.7.

Magnesian and potassic alteration events have also occurred at Mashitu South. According to Hitzman *et al.* (2010b), a potassic alteration event commonly affected the Mines Subgroup in Congo, and occurred before a magnesian alteration event. No convincing or consistent paragenetic relationships between minerals assigned to the two alteration types have been identified by this study, but the order of the two alteration types is assumed from the comparison to literature, with Mg metasomatism preceded by K metasomatism. Potassic alteration in the Mines Subgroup is mostly restricted to the Dolomitic Shales Formation, which shows a large degree of K enrichment compared to the other units (Figure 5.59). The highly mineralised SD2d unit in particular contains the highest concentration of K out of all of the SD. Mineralogically, this appears to be expressed by the development of muscovite and biotite in the groundmass of the Dolomitic Shales (Figures 4.55 and 4.56).

Magnesian alteration is exhibited by all stratigraphic units present at Mashitu South and is detectable by several different trends in the geochemical data (Chapter 5). The magnesian alteration event has caused the development of dolomite, chlorite and limited quantities of magnesite in the groundmass of all of the Mines Subgroup units, and has thoroughly dolomitised the Dolomitic Shales formation. It is also likely to have coincided with the development of Type 1 dolomite veins throughout the stratigraphy (Chapter 4). The presence of inclusions of metasomatic chlorite within sulphides of the Early Hydrothermal SSC stage (Figure 4.67) indicates that Mg-metasomatism occurred before the end of

stratiform mineralisation at Mashitu South. A second magnesian alteration event appears to have occurred during the development of Type 2 veins, which routinely contain magnesite and chlorite as well as dolomite. Whether this event caused the development of alteration minerals in the groundmass too is unknown.

The last alteration type to occur which was positively identified at Mashitu South is argillic, and advanced argillic supergene alteration, caused by the action of meteoric fluids on labile mineral phases. Aluminosilicate minerals are broken down into clay, and carbonate minerals are dissolved in proximity to the surface, and wherever meteoric fluids can percolate through the rock, such as in proximity to breccias and the RSC unit. Argillic alteration is almost ubiquitous at the top of the depth profile in the region and is responsible for the development of saprolitic soils, in which only the most resistant elements are left undepleted in concentration. It appears that the concentrations of Mg, Ca, Cu, K, S, P, Ba, Ni, Sr, Zn, U, As, Be and Cd are depleted by the action of supergene leaching. However, these elements may be concentrated by supergene processes elsewhere in the profile. Al, Fe, Co, Ti, Mn, Na, V, La, Pb, W, Sc, Bi, Mo and Ag show relative enrichment by the action of supergene processes and argillic alteration (Section 5.4.2.4). The action of meteoric fluids is also responsible for causing the Early and Late Supergene Stages of mineralisation (section 8.4.4 and 8.4.5).

8.4 Mineralisation at the Mashitu South Deposit

Mineralisation at the Mashitu South deposit occurred in 4 distinct stages, preceded by a 'Pre-Ore Diagenetic Stage' of pyrite and haematite formation, which span almost 900 Ma of Earth history. A paragenetic timeline for the various mineralisation stages present at the deposit is given as Figure 8.1, and a conceptual model for deposit genesis is given as Figure 8.2. The ages given for various mineralisation stages are inferred purely on paragenetic and distribution similarities to mineralisation or geodynamic events dated at other Copperbelt deposits, and should be treated as speculative. No absolute dating work has been carried out on any material from Mashitu South as part of this study.

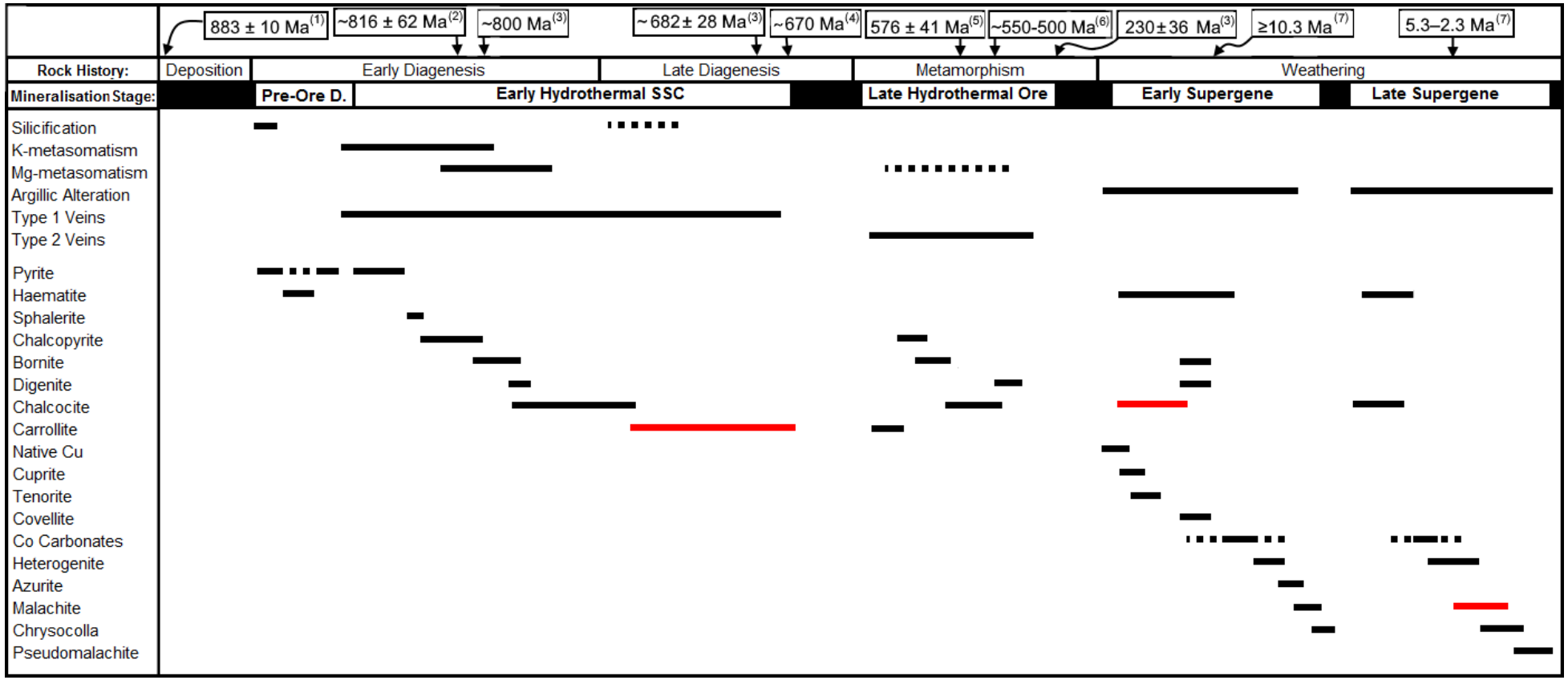

Figure 8.1: *Paragenesis table for the various mineralisation-related phases and alteration types at Mashitu South. Speculative ages are by reference to the literature as follows: (**1**): Maximum age of Roan depositions by age of detrital zircons from the Nchanga granite (Armstrong et al., 2005). (**2**): Re-Os date for stratiform sulphides at Konkola, Zambia (Barra et al., 2004). (**3**): Re-Os dates for stratiform and stratiform-remobilised hypogene sulphides at the Kamoto deposit (Muchez et al., 2015). (**4**): End of a period of U (and likely, other metals) circulation in the Katangan Copperbelt (Decree et al., 2014). (**5**): Re-Os date for vein-type sulphides at Konkola, Zambia (Selley et al., 2005). **(6):** Age of syn-metamorphic Cu-U mineralisation in the Domes Region, Zambia (Eglinger et al., 2014a; Turlin et al., 2015). **(7):** Age of two periods of supergene heterogenite formation in Katanga (Decree et al., 2010). The three phases indicated in red (Car1, Cc3 and Mal2 – see Chapter 4) are those which have contributed most significantly to the formation of high-grade Cu-Co ore at Mashitu South.*

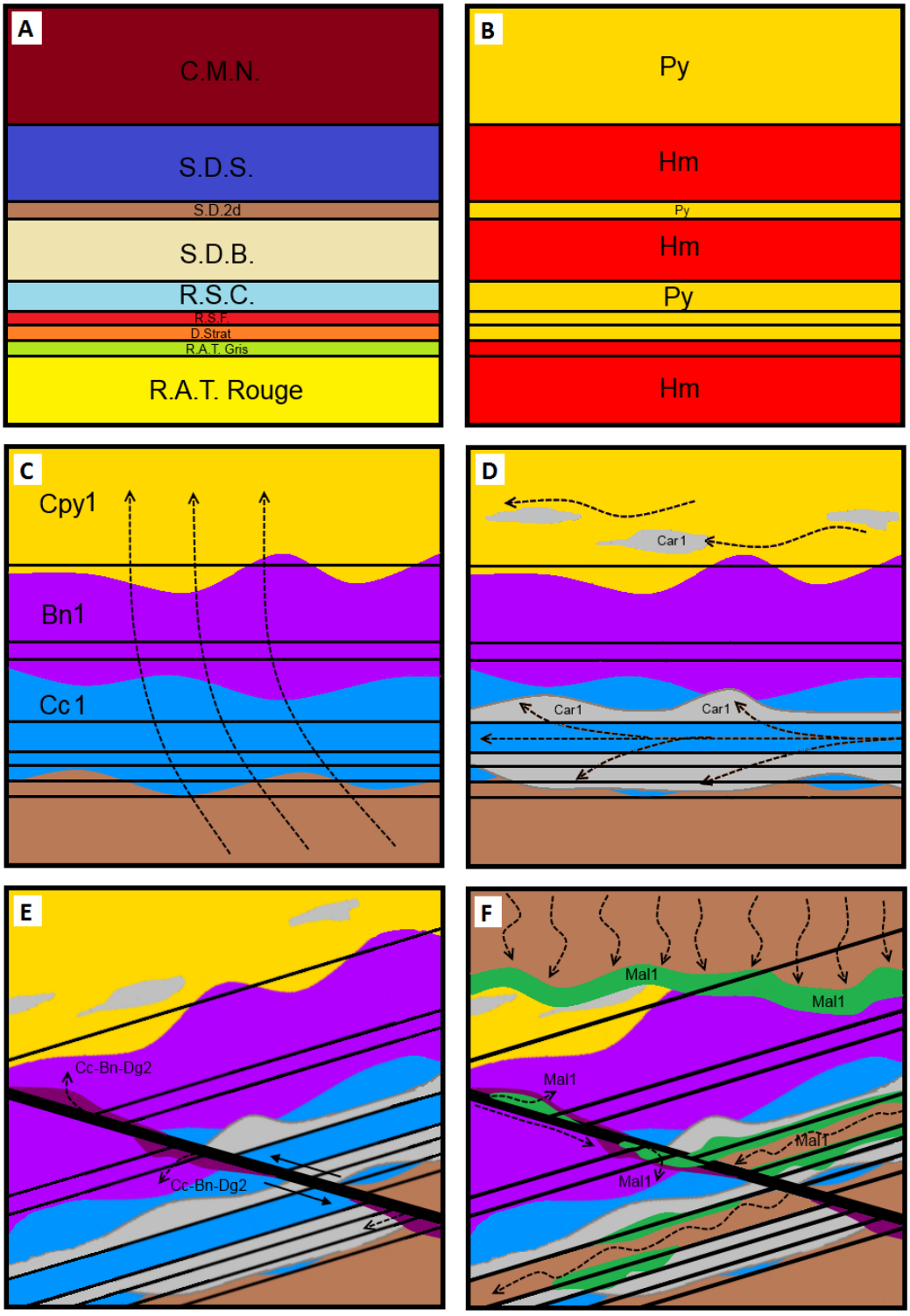

Figure 8.2: *Conceptual model for the development of each of the mineralisation stages present at Mashitu South.* ***A****: Deposition of the R1 and R2 units.* ***B****: Development of Py in reducing and Hm in oxidising environments of deposition, as part of the Pre-Ore Diagenetic Stage.* ***C****: Formation of zoned, stratiform Cu-sulphides during the Early Hydrothermal SSC stage.* ***D****: RSC-focussed distribution of stratiform carrollite in the later part of the Early Hydrothermal SSC stage.* ***E****: Development of Type 2 vein-hosted sulphides of the Late Hydrothermal Ore Stage, focussed along faults and breccias.* ***F****: Formation of supergene oxides and sulphides of the Early and Late Supergene Stages: at the top of the profile, along breccias, and along the RSC unit.*

8.4.1 The Pre-Ore Diagenetic Stage

Early diagenetic disseminated pyrite, both sub-framboidal and recrystallised-cubic in form, is found within the units of the Mines Subgroup which were deposited in reducing conditions, including the DStrat, RSF, RSC, SD2d, parts of the SD, and parts of the CMN. Fine grained specular haematite laths were formed within units which were deposited in oxidising conditions, including the RAT and parts of the SD (Figure 8.2B). These minerals were deposited from formation waters sometime shortly after the sedimentation of the rock, before the circulation of Cu-Co bearing fluids or the occurrence of Mg and K metasomatism through the Mines Subgroup. Similar phases of pyrite and haematite have been reported from other deposits in the region (Love and Amstutz, 1966; Bartholomé and Katekesha 1971; Annels, 1974; Dejonghe and Ngoyi, 1995; Dewaele *et al.*, 2006a; Selley *et al.*, 2005).

8.4.2 The Early Hydrothermal SSC Stage

The Early Hydrothermal SSC (Sedimentary-hosted Stratiform Copper) stage is the primary hypogene mineralisation event at Mashitu South, and is the stage during which the greatest hypogene concentration of Cu and Co occurred. Mineralisation of this phase is primarily stratiform and broadly resembles the SSC type deposit model described by Brown (2014). This stage is equated with the 'stratiform' regional mineralisation type described by Dewaele *et al.* (2006a).

Studies from other stratiform deposits in the region show that the mineralising fluids from this stage became metalliferous when saline, low temperature fluids circulated through the basement and the oxidised red beds of the RAT (Dejonghe and Ngoyi, 1995; Koziy *et al.*, 2009; van Wilderode *et al.*, 2014), stripping Cu and other metals from labile minerals within them and possibly remobilising pre-Katangan mineralisation in the basement (Sillitoe *et al.*, 2015). These oxidised Cu-bearing fluids would then have been transported towards the surface and focussed along extensional faults (Selley *et al.*, 2010) where they hit redox horizons such as the RAT – Mines Subgroup boundary (Figure 2.6). At these boundaries, metal ions in solution would be reduced, sourcing sulphur from bacterial sulphate reduction (BSR) and early diagenetic pyrite and precipitating Cu-sulphides with a syn-diagenetic timing (e.g. Jensen and Dechow, 1962; Dechow and Jensen, 1965; Hitzman *et al.*, 2010; Hitzman *et al.*,

2012). El Desouky *et al.* (2009) analyse fluid inclusions from the Kamoto and Luiswishi deposits to show that this stage of mineralisation was formed by mineralising fluids at a moderate-to-low temperature (115 to 220 °C or less) and salinity (11.3 to 20.9 wt.% NaCl equiv.).

At Mashitu South, this mineralising event resulted in the formation of anhedral, intergranular, stratiform-disseminated and Type 1 vein-hosted sulphides, which display a pattern of zonation and paragenesis typical of SSC deposits (Figure 4.49). A third generation of pyrite is the first phase of this stage to form, which, in contrast to the first and second generations of the Pre-Ore Diagenetic phase, contains trace concentrations of Co. This was followed by chalcopyrite, bornite and then chalcocite, which are distributed in a pattern of zonation from the first redox horizon at the base of the Mines Subgroup: chalcopyrite is most abundant in the Kambove Formation, bornite in the Dolomitic Shales Formation, and chalcocite in the Kamoto Formation (Figure 8.2C). These sulphides frequently mantle each other and earlier pyrite, and are most concentrated in highly carbonaceous units such as the RSF, SD2d, and locally within the lower CMN. Volumetrically minor sphalerite and digenite are also associated with the Early Hydrothermal SSC Stage.

Stratiform-disseminated and Type 1 vein-hosted anhedral, intergranular carrollite is the last sulphide phase of this stage to form, frequently occurring as rims to and replacing all other sulphide phases from this stage. It is one of the most abundant sulphide phases at the Mashitu South deposit, and is a significant component of the majority of the analysed samples which came from regions of core containing high-grade (>1%) Cu mineralisation recorded by the Comide database geochemical assays (Figure 4.73). This phase of carrollite does not fit in with the distribution zonation and order of paragenesis of the other sulphides of the Early Hydrothermal SSC Stage, nor does it conform to the regional model for stratiform carrollite, which usually forms early and is distributed distally relative to the other stratiform sulphides (e.g. Oosterbosch and Schuiling, 1951; Chartrand and Brown, 1984; Dejonghe and Ngoyi, 1995; Broughton and Rogers, 2010; van Langendonck *et al.*, 2013). Rather, carrollite is the last stratiform phase to form at Mashitu South, and has a distinct predilection for the stratigraphic units above and below the RSC and stromatolitic, silicified horizons in the lower CMN (Figure 8.2D). It is the only stratiform sulphide to be found within the RSC itself. This indicates a distribution pattern in which the RSC and similar horizons, through previous dolomite dissolution, became a lateral fluid conduit for mineralising fluids as per the model of Fay and Barton (2012) as indicated in Figure 2.5. To get significant lateral transport along these units,

carrollite mineralisation would have had to have occurred before the tectonic / halokinetic / olistrosomic dismemberment of the Mines Subgroup.

Chalcopyrite at Mashitu South occasionally forms tiny inclusions within authigenic quartz and carbonate, which authors working on other Congolese Copperbelt deposits, have interpreted to indicate that mineralisation occurred syn-diagenetically (e.g. Bartholome *et al.*, 1971). The presence of Early Hydrothermal SSC mineralisation in antitaxial Type 1 veins (Figure 4.15) certainly means that they formed during a period in which extensional stress fields operated (Bons and Montenari, 2005), making a pre-orogenic, syn-Katangan-rift timing the most obvious candidate for their timing of formation. Inclusions of chlorite in chalcocite and carrollite from this stage (Figure 4.67) show that Mg metasomatism occurred before the end of the Early Hydrothermal SSC stage.

The Co-Ni-bearing geochemical signature of carrollite is unusual for typical SSC deposits. This, combined with the relatively late paragenetic timing of stratiform carrollite and differing mode of distribution, indicate that carrollite mineralisation may have occurred slightly later than other stratiform phases. The timing of this mineralisation phase may perhaps coincide with a renewed period of Katangan-Basin rifting, which initiated the deposition of the Nguba group. Magmatism and hydrothermal circulation initiated by this rifting could have supplied the Co-Ni geochemical signature of carrollite (Annels *et al.*, 1983; Annels & Simmonds, 1984; Unrug, 1988; Annels, 1989; Koziy *et al.*, 2009; Muchez and Corbella, 2012).

A gradual evolution of metal source, fluid chemistry, transport conduits and mode of distribution for the Early Hydrothermal SSC stage is envisaged, with the early sulphide phases deposited in a more typical SSC-type environment, and the later phases being progressively more influenced by Nguba magmatism and RSC-focussed lateral distribution until the final deposition of carrollite.

A very limited sulphur isotope dataset at Mashitu South (see Figure 4.68 and Section 4.3.4) is lacking in negative $\delta^{34}S$ values for the ore sulphides of this stage. This would appear to contradict a Bacterial Sulphate Reduction (BSR) origin for the source of sulphur which is inferred by many authors for early stratiform sulphides in the region (e.g. Jensen and Dechow, 1962; Dechow and Jensen, 1965), perhaps suggesting Thermochemical Sulphate Reduction (TSR) of evaporites as an alternative sulphur source. However, the very limited sample size of

this isotope study is not enough to draw robust conclusions from, and further sulphur isotope work is recommended to investigate this topic.

Selley *et al.* (2005) report data from Barra *et al.* (2004), where through Re-Os dating of stratiform sulphides, an age of ~816±62 Ma is determined for early mineralisation at Konkola. Muchez *et al.* (2015) also use Re-Os isotopes to date the first stratiform mineralisation at Kamoto to ~800 Ma. Decree *et al.* (2014) find evidence for early diagenetic U mobilisation at Shinkolobwe and Kambove in two periods around ~876 and~823 Ma. The conditions in which Cu could have circulated were likely to have been similar to those which would mobilise U (Brown, 2014) and it is likely that secondary U mineralisation at Mashitu South (see Section 5.4.4) is remobilised from a primary U mineralising event accompanying Cu mineralisation, which occurred at a number of deposits in the region (Cailteux *et al.*, 1983; Loris *et al.*, 2003). An age of 846±19 Ma (Kampunzu *et al.*, 1991) is given for the initiation of Katangan-Rift magmatism and implicitly the acceleration of basin subsidence, which may have instigated the deposition of carbonates (which act as the redox boundary and host rocks for mineralisation in the Mines Subgroup). Heat flow from this magmatism may also have expedited the circulation of basinal fluids. Therefore, this date (846±19 Ma) is considered a maximum for the deposition of the Early Hydrothermal SSC Stage. Kampunzu *et al.* (2000) place the Nguba age magmatism which is supposed to have assisted in the formation of carrollite between around 760-720 Ma, and Decree *et al.* (2014) identified a period of U circulation from inherited heterogenite U-Pb ratios soon after this period (between ∼720 to ∼670 Ma). This age also coincides with a period of remobilisation of stratiform mineralisation at Kamoto (682±28 Ma) identified by Muchez *et al.* (2015). U and Co are mobile under similar hydrothermal conditions (Brown, 2014) and therefore, if Nguba magmatism is indeed the metal source for Co and Ni, the ∼720 to ∼670 Ma age for U circulation would also seem a probable age for the circulation of Cu-Co-Ni rich fluids and the deposition of stratiform carrollite.

In total, the Early Hydrothermal SSC stage is thought to have spanned a protracted, and perhaps punctuated time period between ∼850 and ∼670 Ma, during which the bacilliform pseudofossils described in Chapter 7 are also interpreted to have formed. This model developed for Mashitu South generally agrees with prevailing models of SSC ore genesis in the Katangan Copperbelt (see Dewaele et al., 2006a; Hitzman et al., 2012). However, the distinction of carrollite (Car1) deposition as a late sub-phase of the Early

Hydrothermal SSC stage, having a mode of distribution and paragenetic order disparate to that of stratiform carrollite described from other stratiform Copperbelt deposits, suggests an unrecognised mode of mineralisation hitherto undescribed in the region.

Hypogene mineralisation at Mashitu South is shown to have a geochemical association of Cu + Co + Bi + Ni + V + S ± Mo ± As ± Fe ± Zn (Section 5.4.3.2). The possible mineralogical accommodation of this association will be discussed in the following section.

8.4.3 The Late Hydrothermal Ore Stage

The sulphides of the Late Hydrothermal Ore Stage are hosted in Type 2 veins, and are volumetrically minor compared to the sulphides of the Early Hydrothermal SSC Stage. They are equated to the 'vein-type' mineralisation described by Dewaele *et al.* (2006a). Many of the same sulphide species occur in Type 2 veins of the Late Hydrothermal Ore Stage as occur in the groundmass and Type 1 veins of the Early Hydrothermal SSC Stage, but in a different relative paragenetic order, frequently with a different form and associated with different gangue minerals. In places, vein-hosted mineralisation of the Late Hydrothermal Ore Stage can be seen to cross-cut groundmass-hosted mineralisation of the Early Hydrothermal SSC Stage.

Sulphides associated with this stage occur in the following order of paragenesis: euhedral-subhedral carrollite, chalcopyrite, bornite, chalcocite and digenite, of which bornite and chalcocite are the most abundant. The veins in which they are hosted are stratabound and cross cutting to earlier stratiform mineralisation (Figures 3.49, 4.24 and 4.63), showing no stratigraphic control on their distribution within the Mines Subgroup. A fluid inclusion study by El Desouky *et al.* (2009) shows the mineralising fluids from 'vein-type' mineralisation of Dewaele *et al.* (2006) to be of relatively high salinity and temperature (270 to 385 °C and 35 to 45.5 wt.% NaCl equiv.) compared to mineralising fluids from the stratiform stage at Kamoto and Luiswishi. This agrees with the inference of high salinities for the mineralising fluids of this stage at Mashitu South, based on the presence of barite, halite, magnesite and chlorite in Type 2 veins. Due to the high Mg-composition of Type 2 veins, it seems likely that the Late Hydrothermal Ore Stage was accompanied by a magnesian alteration event. According to studies by El Desouky *et al.* (2010) and van Wilderode *et al.* (2014), the hydrothermal fluids responsible for vein-type mineralisation were unlikely to have added

metals into the system, rather they resulted in remobilisation of metals which were emplaced into the Mines Subgroup by the earlier-occurring Early Hydrothermal SSC Stage. As stated by Dewaele *et al.* (2006a), the location of faults and tectonic breccias is probably the main control on the distribution of the hypogene mineralisation from this stage (Figure 8.2E).

Re-Os dating of sulphides from vein-type mineralisation at the Nkana and Mindola deposits in the Zambian Copperbelt give an age of 576 ± 41 Ma (Selley *et al.*, 2005), corresponding to Katangan Basin inversion and the early stages of the Lufilian orogeny; additionally, El Desouky *et al.* (2007) puts a maximum age to similar mineralisation in the Lufukwe anticline of the Lufilian Foreland of 573 ± 5 Ma – the date given by Master *et al.* (2005) for the end of deposition of the Kundelungu Group, through which faults cut which host the described mineralisation. However, Eglinger et al. (2014b) and Turlin et al. (2015) date syn-orogenic Cu-U mineralisation in the Domes Region to a period of ~550-500 Ma, and Muchez et al. (2015) date one stratiform-mineralisation-remobilising event at Kamoto to as late as 230±36 Ma. A wide range of dates is therefore possible for the timing of the Late Hydrothermal Ore Stage.

Without more sensitive elemental analysis of the sulphides than that conducted in this study, it is impossible to distinguish a separate element association for the Late Hydrothermal Ore Stage from the element association indicated for hypogene mineralisation in general at Mashitu South: Cu + Co + Bi + Ni + V + S ± Mo ± As ± Fe ± Zn (Section 5.4.3.2). This element association is therefore inferred to be representative of mineralisation from the Early Hydrothermal SSC Stage *combined* with mineralisation from the remobilised sulphides of the Late Hydrothermal Ore Stage.

Although the exact mineralogical accommodation of the hypogene element association (Cu + Co + Bi + Ni + V + S ± Mo ± As ± Fe ± Zn) cannot be ascertained by this study, the literature offers clues as to which minerals might host the trace elements of the association. Pyrite, sphalerite, chalcopyrite, bornite, chalcocite, digenite and carrollite have been reported from mineralised zones. Cu, Fe and S are almost certainly accommodated primarily by the sulphides chalcopyrite, bornite, digenite and chalcocite. Fe may be found in ore-associated pyrite as well as chalcopyrite and bornite. Rare sphalerite associated with the Early Hydrothermal SSC Stage (Figure 4.9) may account for the weak association of Zn with Cu in the whole-rock geochemistry. Carrollite, $Cu(Co,Ni)_2S_4$, forms a series with linnaeite, siegenite and polydimite,

and Ni can substitute for both Cu and Co in the mineral, although substitution for Co is more common (Wagner and Cook, 1999). Analysis of the correlations of Co and Ni reveal that in most datasets (e.g. Figure 5.18), Co and Ni correlate better with each other than with any other element, strongly suggesting that carrollite is responsible for the accommodation of both elements as no other Co-Ni species is reported from the deposit. Within the 'most hypogene' >200m depth interval dataset, there is a Co:Ni ratio of 32:1. If carrollite is indeed the only mineral in the hypogene environment which hosts Co and Ni, it can be assumed that the carrollite at Mashitu South is a Co-rich, Ni-poor variety. Regardless, carrollite is likely to accommodate some of the Cu and S, and most of the Co and Ni, which forms part of the hypogene geochemical association. Some Co may also be accommodated by rare 'cobaltoan pyrite' (Figures 4.18, 4.19 and 4.28).

The remaining elements in the hypogene association: Bi, V, Mo, and As are not found in high concentrations at Mashitu South. Within the >200m depth interval, these elements have an average concentration of V: 94ppm, As: 9ppm, Bi: 3ppm and Mo: 3ppm. The highest whole-rock concentrations exhibited by these elements in a sample are: V: 828ppm, Mo: 71ppm, Bi: 63ppm and As: 57ppm. This, combined with the fact that no other sulphide species are reported from the deposit, makes it likely that these elements are primarily incorporated as traces in Cu sulphides, rather than forming discrete minerals of their own.

A study by McGoldrick *et al.* (2010) details trace element concentrations found in samples of pyrite, chalcopyrite, bornite, chalcocite and carrollite at the Kolwezi, Ruashi and Etoile Cu-Co mines in the Katangan Copperbelt. In this study, Bi was found to be most concentrated in bornite and chalcocite, with some concentrations >1000ppm. The mineral in this study which hosted the highest portion of V was chalcocite, with a range of up to 180ppm. However, this is not a high enough concentration to explain the highest V grade sample from Mashitu South containing 828ppm V. As was found to be most concentrated in carrollite and pyrite, with some carrollite samples containing up to 1% As. Mo, similarly, is also mostly hosted in carrollite and pyrite, with samples up to 1450ppm. As, and Mo, where found in elevated concentrations, tended to occur together within carrollite or pyrite. It is therefore suggested that, in the hypogene environment at Mashitu South, Bi and V are mostly hosted by bornite and chalcocite, and that As, and Mo mostly occur as trace elements within pyrite and carrollite.

8.4.4 The Early Supergene Stage

Native copper, cuprite, tenorite, chalcocite, bornite, digenite, covellite, haematite, cobaltoan carbonate, heterogenite, azurite, malachite and chrysocolla are all developed, in that order of paragenesis, as part of the first of two stages of supergene mineralisation. It is likely that secondary uranium minerals (Figure 3.36 and Section 5.4.4) also formed during this stage of mineralisation. These minerals are mostly concentrated in the upper 100m of the boreholes at Mashitu South. However, supergene mineralisation at greater depths is common, particularly in proximity to the RSC or breccia units (Figure 8.2F), which appear to have acted as conduits allowing meteoric fluids from the surface to percolate downward into the stratigraphy as per the model of Fay and Barton (2012). Native copper and secondary uranium minerals were only found within the RSC unit during this study (Chapter 3).

Leaching of hypogene mineralisation by these acidic, oxidising meteoric fluids is the cause of supergene alteration, which also causes argillic alteration in gangue assemblages. Depending on the strength of the leaching, hypogene mineralisation may be oxidised and altered in situ, or may be dissolved, remobilised and reprecipitated deeper in the profile by the downwards-travelling meteoric fluids in 'para-exotic' deposits, where redox conditions become favourable for the reprecipitation of the metals. This often creates a pattern of zonation consisting of a leached zone, a secondary oxide zone, a secondary sulphide zone, and finally a primary hypogene zone with increasing depth (Figure 2.9).

Most of the surviving mineralisation of the Early Supergene Stage of Mashitu South consists of secondary minerals which have been developed in situ, particularly chalcocite and haematite. These minerals form replacive rims around earlier, hypogene sulphides. This is likely to have happened at the margins of the secondary sulphide and hypogene zones, where fluids are oxidising/acidic enough to mobilise sulphur, but not the metals with which sulphur has combined. The result is the conversion of minerals with a low Cu:S ratio, such as chalcopyrite, into minerals with a high Cu:S ratio, such as chalcocite, plus haematite. The residual, in-situ mineralisation may be upgraded by metals which have been dissolved from further up in the profile under more oxidising, acidic conditions, which are removed from solution by reduction in proximity to residual sulphides. Chalcocite of the Early Supergene Stage appears to play an important role in upgrading the metal tenor of pre-existing sulphide mineralisation, and the highest grades of Cu ore in the Mines Subgroup tend to consist of a

combination of hypogene, stratiform carrollite rimmed by supergene chalcocite of this stage (Figure 4.73).

There is an apparent paragenetic order of the minerals containing the greatest concentration of copper precipitating early (e.g. native copper) and minerals which contain less copper by wt.% precipitating later (e.g. malachite). This reflects a general trend from more reducing Eh, more alkaline/neutral pH conditions towards more oxidising and acidic Eh/pH conditions during the progression of supergene alteration, which is illustrated as Path 1 in Figure 4.74. A second trend: Path 2, exists, which is also illustrated in Figure 4.74. This path reflects the paragenetic order of the supergene sulphides which appear to form *after* native copper. Path 2 appears to be formed by a trend towards more acidic pH conditions, without much corresponding increase in Eh.

Gangue phases which are associated with the Early Supergene Stage include dolomite, quartz, barite and apatite. A mass of supergene barite, apatite and haematite occurring in the RSC is shown in Figure 4.60, which appears to have precipitated in the paragenetic order of barite → haematite → apatite. The heterogenite phase is also associated with supergene quartz and apatite, with which it is commonly intergrown at a very fine scale (Figure 4.36).

The Early Supergene Stage is equated to the first of two stages of supergene heterogenite growth dated by Decree *et al.* (2010) and is inferred to be representative of a regional supergene alteration event. This first stage was formed by a period of regional uplift during the Miocene (Lavier *et al.*, 2001), which caused enhanced erosion and exhumation of the rocks of the Katangan Supergroup and exposed hypogene mineralisation such as that found in the Mines Subgroup to circulating meteoric fluids. According to U-Pb dating of heterogenite from this stage by Decree *et al.* (2010), this occurred at or before 10.3 Ma.

8.4.5 The Late Supergene Stage

The Late Supergene Stage is distinguished from the Early Supergene Stage by consisting of a paragenetic repetition of many of the mineral phases observed in the Early Supergene Stage. The constituent phases of the Late Supergene Stage, precipitated in the following order, are: chalcocite, haematite, cobaltoan carbonate, heterogenite, malachite, chrysocolla and pseudomalachite. These phases show paragenetic relationships with supergene phases from the Early Supergene Stage which identify them as a temporally distinct stage of mineralisation

(Figure 4.38). The abundance of the low-Cu mineral phases such as malachite and chrysocolla is higher in this stage of supergene mineralisation, in contrast to the Early Supergene Stage in which high-Cu mineral phases such as chalcocite are more abundant. This indicates that during the progression of the Late Supergene Stage, Eh-pH conditions were more likely to follow Path 1 than Path 2 in Figure 4.74. An additional difference between the stages is that the mineral phases of the Late Supergene Stage are less frequently encountered in proximity to hypogene sulphide mineralisation than mineral phases of the Early Supergene Stage, and it seems that the latter stage is characterised more by dissolution, remobilisation and reprecipitation rather than in-situ oxidation. Due to the relative lack of oxide phases which are attributed to the Early Supergene Stage, it is inferred that the second period of supergene oxidation during the Late Supergene Stage has largely remobilised these minerals and redeposited them as Late Supergene Stage oxide minerals.

The distribution (Figure 4.49), textures, gangue-phase relationships, and contribution to high grades of ore (Figure 4.73) are similar between the Early and Late Supergene Stages in the Mines Subgroup of Mashitu South and it is acknowledged that the two formed under very similar conditions. Both stages are preferentially distributed in the upper stratigraphy, near the top of the holes, and are associated with similar gangue phases.

In terms of contribution to ore, however, it is noteworthy that the para-exotic mineralisation encountered in the RAT Rouge of MSSD140 is considered to be part of the Late Supergene Stage, consisting of the malachite and pseudomalachite phases (Figures 4.45, 4.47 and 4.48). This RAT-hosted para-exotic supergene mineralisation is high grade, abundant, and of considerable economic importance (Chimvinga, pers. comm., 2014). The highest grades of Cu at Mashitu South are, on average, encountered in the 10-50m depth interval (Figures 5.49 and 5.50), and this is attributed to the abundance of oxide ores from the Late Supergene Stage at this depth.

As discussed in Chapter 3, the three main controlling factors for the development of this kind of ore appear to be the availability of metals, the permeability of the host rock, and the depth/strength of oxidation. As a result, brecciated portions of the RAT Rouge in the 10-50m depth range make the perfect host rock for para-exotic Cu mineralisation of the Late Supergene Stage: most breccia makes for a permeable host lithology, metals are available to the RAT Rouge from the leaching of hypogene mineralisation in the overlying, eroded Mines Subgroup, and the 10-50m depth range, which may have been the location of the palaeo-

water table (Robertson, pers. comm., 2014), provides the perfect Eh-pH conditions for the precipitation of oxide ore.

The Cu + Be + P ± Zn geochemical association (Chapter 5) is attributed to the para-exotic malachite-chrysocolla-pseudomalachite dominated ore of the Late Supergene Stage, the position of which in the core from hole MSSD140 (see Appendix 3d) corresponds well to high concentrations of Cu, Be and P (Figure 5.75). This geochemical association is the result of the dissociation of Cu with Co, Bi, Ni, V, S, Mo, As and Fe, which co-occur with Cu in the hypogene environment. Cu then combines with P in pseudomalachite in these ores, and a trend of positive correlation between Cu and P with a 5:1 Cu:P ratio (Figure 5.74) suggests that some other phase with this 5:1 Cu:P elemental ratio may also occur. The mineralogical accommodation of Be and Zn in supergene ore is not well understood. Sulphur, which is more mobile than Cu in meteoric fluids, is dissolved easily from hypogene mineralisation, where it is only reprecipitated again much deeper in the profile, probably as supergene sulphates such as barite, and secondary sulphides like chalcocite. The remaining elements of the hypogene association are less easily leached than Cu and remain concentrated higher in the depth profile, within the 'leached zone' above Cu mineralisation (Figures 5.49, 5.50, 5.51, 5.52 and 5.53).

The fate of Co above Cu deposits is the best understood out of these elements. Co forms 'caps' of heterogenite above supergene Cu deposits (Decree *et al.*, 2010), which are often residual and the result of in-situ oxidation of Cu-Co minerals such as carrollite. With progressively more/stronger leaching, Co will also be remobilised downwards, but will precipitate as heterogenite at a lesser depth than Cu reprecipitates as malachite-chrysocolla-pseudomalachite orebodies (Decree and Pourret, 2013). The elements Co, Bi, Ni, V, and Mo, which have the strongest associations with Cu in the hypogene environment (Figure 5.71), were found to be concentrated in the top 1m of the profile at Mashitu South in the following order of enrichment, compared to the average at the deposit (Figure 5.53): Bi → Mo → V → Co → Ni. Bismuth stands out on its own being twice as enriched in the <1m data than Mo, the nearest-most surface-enriched of the hypogene-Cu-associated elements. The residual, surface enriched nature of Bi, Mo, V, Co and Ni, combined with their affiliation with Cu in the hypogene environment, theoretically make them surface vectors to heavily leached, Late Supergene Stage Cu mineralisation. Depending on the various mobilities of Bi, Mo, V, Co and Ni in the supergene environment (Chapter 5), a pattern of vertical zonation of these elements

would be expected to occur over a supergene Cu deposit, with the most mobile elements descending to be concentrated at depth, and the least mobile remaining near the surface as trace elements in residual phases such as haematite. Figure 8.3 shows a conceptual model for the development of such a vertical zonation.

The Late Supergene Stage is equated with the second stage of Katangan supergene heterogenite growth dated by Decree *et al.* (2010) to the Pliocene at 5.3–2.3 Ma. According to Decree *et al.* (2010), there was a transition to a warmer, wetter regional climate in Katanga at this time (Alexandre, 2002; Giresse, 2005; Miller *et al.*, 2010). This change initiated a renewed period of leaching and supergene alteration, which is inferred by this study to have resulted in the creation of the Late Supergene Stage.

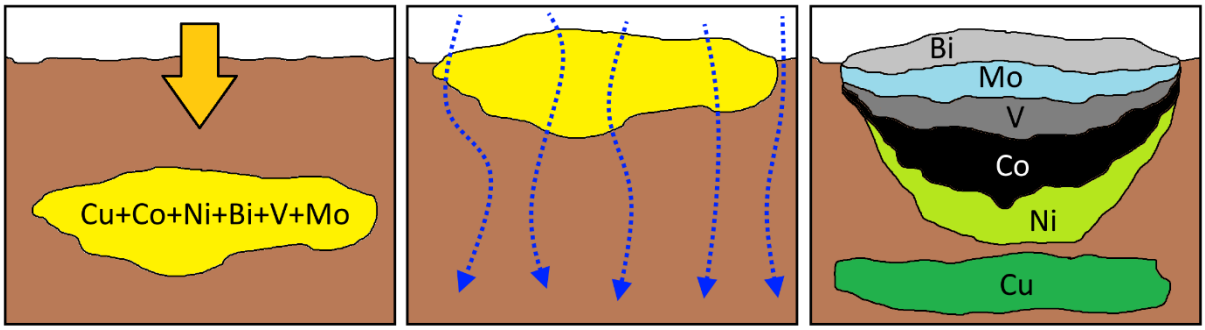

Figure 8.3: *Conceptual model for the dissociation of hypogene ore-associated elements during supergene alteration at Mashitu South. A hypogene orebody with an association of Cu+Co+Ni+Bi+V+Mo (left) is exposed to the surface environment and meteoric fluids (middle), producing a vertical pattern of enrichment zonation (right) based on the relative mobility of each element in meteoric fluids. Data from Mashitu South shows that Cu, the most mobile metal of the association, descends to a depth of between 10-50m where it is enriched as Late Supergene malachite-pseudomalachite ore, whereas Bi, the least mobile, is most enriched within the top <1m of the profile, remaining behind as a trace element in some residual phase such as haematite.*

The 5 combined stages of mineralisation at Mashitu South are summarised into a paragenesis table in Figure 8.1, and a conceptual model of deposit genesis is given as Figure 8.2, both of which are found at the start of section 8.4.

8.4.6 Implications for the Surface Geochemistry of Cu-Co Deposits

Supergene alteration, in particular that of the Late Supergene Stage (section 8.4.5), is predicted to have an effect on the geochemistry of residual, lateritic soils which overlie Cu-Co deposits. This effect is theorised to be particularly pronounced in the soils above para-exotic, supergene Cu + (Be + P ± Zn) malachite-chrysocolla-pseudomalachite deposits. The production of vertical patterns of element zonation by the action of supergene leaching, as shown in Figure 8.3, offers the possibility of using vectors other than Cu in the geochemical exploration for Cu deposits. As well as vertical zonation, a lateral zonation of elements may also occur where there is lateral transport of metals by meteoric fluids, such as where topography is pronounced or where Cu is carried by surface water (see Figure 8.4). Section 6.4.1 shows that, although Cu in soil is capable of predicting the locations of many Cu deposits in the region, it is not found in concentrations which are anomalous enough to site a drilling program over the Mashitu and Kalukundi deposit complexes.

The lack of significant Cu enrichment in the soil above the Mashitu and Kalukundi deposits is attributed to an effective leaching process, which has removed Cu from the leached zone and re-concentrated it further down in the profile as supergene oxide orebodies, creating attractive mining prospects. This leaching process has perhaps been more effective than at deposits with a strong surface Cu anomaly such as Pungulume, Anticline and Kinshasa. The reason for this postulated disparity in the effectiveness of leaching between deposits is unknown, but it is probably controlled by factors which pre-date supergene alteration. These factors may include differences in lithostratigraphy, structure, deposit geochemistry and the hydrological and topographic architecture of a deposit. For example, Pungulume Principal may show a higher surface Cu anomaly than Mashitu South because it is so much more topographically elevated than its surroundings, with copper able to leach 'downhill' into the soils surrounding Pungulume hill. Pungulume is also thought to be hosted by Dipeta Subgroup rocks while Mashitu South is hosted in the Mines Subgroup (Chimvinga, pers. comm., 2014).

The results of the analysis of borehole data at Mashitu South (Chapter 5) explore the zonation of elements with depth (Figures 5.16, 5.49, 5.50, 5.51, 5.52 and 5.53). These results indicate that, of the hypogene ore associated elements of Cu + Co + Bi + Ni + V + S ± Mo ± As ± Fe ± Zn, Bi, Mo, V, Ni and Co are more concentrated at the top of the profile than Cu at

Mashitu South, which is probably due to their resistance to supergene mobilisation. This study demonstrates the utility of conducting empirical, deposit-scale analysis of element variation by depth at polymetallic deposits in metallogenic regions affected by supergene weathering. It presents the average-normalisation method described in Chapter 5 as a method for achieving this, predicting that anomalies of Bi, Mo, V, Ni and Mo would be found over Cu-Co deposits in the region.

In Chapter 6 the regional soil distribution of these elements was investigated, using the prediction from Chapter 5 that Bi, Mo, V, Ni and Co would be found over known Cu-Co deposits, perhaps with more pronounced expression than Cu anomalies over these deposits. The regional soil geochemistry was mapped and analysed for any spatial correspondence between these elements and known Cu-Co deposits, however, no such correspondence was found (section 6.3). The lack of spatial correspondence of these elements over known Cu-Co deposits was probably due to the unsuitability of the data acquisition methods used by Comide for this type of analysis (see section 6.4).

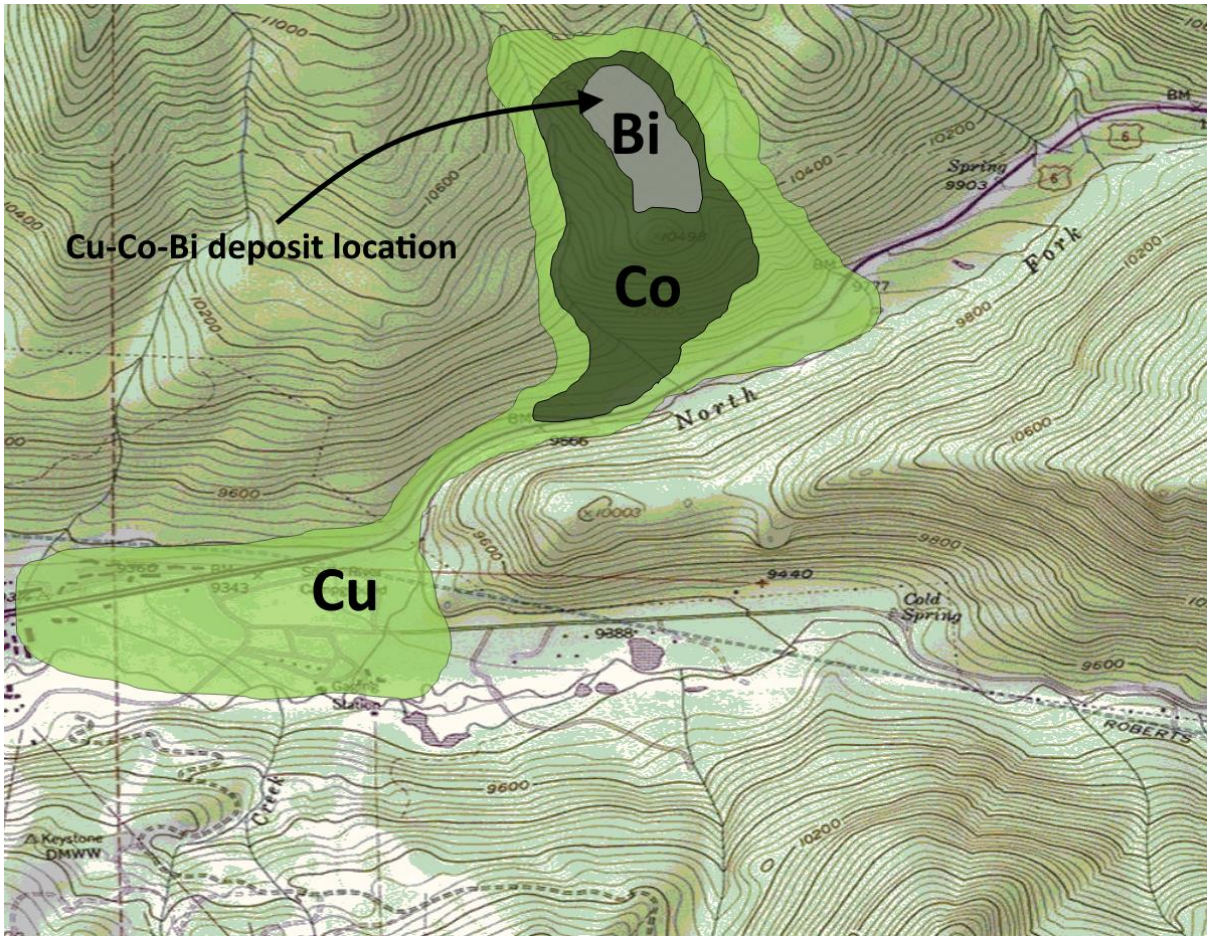

Figure 8.4: *Conceptual model for the development of lateral element zonation around a fictional Cu deposit with a Cu-Co-Bi hypogene association. Bi, the least mobile element in meteoric fluid, remains proximal to the location of the orebody, while the more mobile Co and Cu are redistributed and enriched hydrologically and topographically downstream of the deposit in accordance with their mobility. Topographic map is from Apollo Mapping (2016) and is only used for conceptual purposes.*

Another form of analysis was attempted to ascertain which elements would be found in anomalous concentrations above the Mashitu South deposit, when compared to their average concentrations in regional soil (section 6.4.4). There was poor coverage of XRF soil data over Mashitu South so ICP-OES borehole assays with mid-point depths of >1m from Mashitu South were compared to the XRF regional soil data. It was found that Co was concentrated above the Mashitu South deposit by an enrichment factor of >100x the regional average. Mo, also associated with Cu in the hypogene environment, had an enrichment factor of >12x the regional average. Ni, S, Bi, As and Cu, all found co-mineralised at depth at Mashitu South, were found to be enriched compared to the regional average by a factor of between 2

and 10. U, W and Pb are not found to be directly associated with Cu-Co mineralisation, but are also significantly enriched over the Mashitu South deposit.

Unfortunately, the Comide regional XRF data for Co, Bi, Ni, V and Mo was found to be full of spatial inconsistencies, the technique being either marred by procedural errors and/or lacking the sensitivity to analyse for the quantities of these elements present in the regional soils. Encouraging results of nearby Africo Resources soil geochemistry mapping (Siebel *et al.*, 2013), in which spatial variation between Cu and Co similar to that shown by Figure 8.4 is seen above the Anticline and Mashitu South deposit clusters (Figure 5.76), suggests that this method of exploration using surface vectors other than Cu may still work. Other studies in the region, such as that by Halley *et al.* (2016), have shown that the concentration of certain 'gangue elements' can be used to effectively map the underlying geology in leached, highly saprolitic terrain. This could prove effective in identifying near-surface Mines Subgroup fragments that were missed by regional mapping, which would have obvious application to Cu-Co exploration. However, any of these techniques would require a multi-element soil-concentration dataset which is more robust and covers a fuller range of elements than the one provided to this study by Comide.

8.5 Further Work: Exploration Considerations

1. The first unanswered question of this study is: How are the trace elements of the hypogene (Cu + Co + Bi + Ni + V + S ± Mo ± As ± Fe ± Zn) and supergene (Cu + Be + P ± Zn) geochemical associations accommodated? Attempts were made to investigate this using EDS analysis (Chapter 4), however it was found that this technique was not sensitive enough for an in-depth study of the concentrations of different trace elements in the various mineralisation-related phases. It is suggested that Laser Ablation – Induced Coupled Plasma Mass Spectrometry (LA-ICP-MS) could provide important information on the accommodation of mineralisation-related trace elements, and could help with the distinction of particular stages or phases of mineralisation using whole rock geochemistry. A similar LA-ICP-MS study by McGoldrick *et al.* (2010) was able to achieve an understanding of trace element distribution at the Kolwezi, Ruashi and Etoile deposits.

2. A second useful study would be to use 3D modelling software to investigate the spatial distribution of mineralisation-related elements other than Cu and Co, to confirm their co-occurrence with mineralisation, or with particular stratigraphic units which are prone to hosting mineralisation such as the RSF and SD2d. In particular, it is suggested that uranium be subjected to 3D modelling at the deposit, as the element attains significant concentrations at depth towards the far eastern side of the Mashitu South Mines Subgroup fragments. An unforeseen abundance of U could be deleterious to the exploitation of the Cu-Co orebody.
3. Re-Os dating of the sulphide phases would greatly strengthen the temporal deposit model inferred by this study, which has so far relied on correlation to literature examples of mineralisation based on the form, textures and chemistry of mineralisation. Absolute dating of sulphide phases at Mashitu South would provide a robust model for the age(s) of mineralisation present, which could assist in the geological understanding of the deposit and add value to the exploration model.
4. Analysis of the present Comide soil database has shown that it is unusable for the kind of soil-geochemistry analysis advocated by this study in the search for surface vectors. Cu concentration, for which the soil database appears to be relatively reliable, is shown not to produce significant anomalies over all of the known Cu-Co deposits in the region (notably, not the Mashitu and Kalukundi deposit groups). Data trends in borehole geochemistry at Mashitu South are highly suggestive that Co, Ni, Bi, V, Mo and possibly other elements may act as surface vectors to Cu, given the right method of analysis, and may prove useful in the discovery of new, highly supergene-altered Cu-Co deposits. To test this, it is recommended that a low-investment pilot study be conducted. A soil sampling program which systematically analyses and compares a limited number of soil samples from above deposits which are known to be Cu-Co mineralised, and from above areas from which no mineralisation is known, could lend empirical evidence to the case for using leaching-resistant refractory elements as surface vectors towards supergene Cu. These soil samples should be analysed by a more sensitive and accurate procedure than the XRF technique used to collect the current database, in order to fully utilise the trace element concentrations. 'Wet' geochemistry lab-based techniques such as ICP-AES may be necessary for this, which may be costlier, but such a pilot study could provide an exploration technique which

would be regionally useful in the location of Cu-Co orebodies, throughout the Copperbelt.

5. At an intra-deposit scale, the element associations for particular stratigraphic units (Chapters 5 and 6) could be used in borehole and soil geochemistry to aid in the mapping and geological modelling of Mines Subgroup deposits.

CHAPTER 9: CONCLUSIONS

9.1 Structure

The Mashitu South deposit is confirmed as a domal fragment of Mines (R2) Subgroup, which is thrust over another, deeper Mines Subgroup fragment on the eastern flank of the deposit. Both fragments sit atop the RAT (R1) Subgroup, in a conformable manner in places. The dome-and-basin structure of Mashitu South and the neighbouring Mashitu Principal fragments are surrounded and cross-cut by typical Katangan 'megabreccias', which are complex in form and origin and appear multi-generational. Most of the brecciation appears to cross-cut and therefore post-date the dome-and-basin folding of the Mashitu South and Principal fragments.

9.2 Sedimentology and Stratigraphy

Each stratigraphic unit at the deposit appears to have a distinct geochemical signature, which could be used to help identify and map units where a lithostratigraphic identification is difficult. These geochemical signatures, relative to the Average Concentration of Elements at Mashitu South (ACEMS) are: **CMN**: elevated Ca, W and Ag. **SD**: elevated K. **RSC**: slightly elevated U, depleted in K. **RSF**: elevated Bi. **DStrat**: elevated As and Mo. **RAT Gris**: elevated Ba and Mo. **RAT Rouge:** depleted in S. Some of these geochemical signatures may be sedimentary, others may have been inherited through alteration.

Additionally, the Sr/Sc concentration ratio of a sample dataset was found to be useful as an indicator of calcareous: siliciclastic input in the original depositional environment of sedimentary rocks at Mashitu South. This can be used to discriminate between original vs. dolomitised bulk-composition-carbonate rocks.

9.3 Mineralogy and Alteration

Gangue mineral phases present at Mashitu South which were confirmed by petrography include (in approximate order of abundance): dolomite, quartz, clay minerals, chlorite, muscovite, apatite, biotite, magnesite, rutile, barite, monazite, zircon, halite, gypsum/anhydrite and celestine. Some of these gangue minerals have a sedimentary origin but many have been formed by diagenesis, metasomatism or metamorphism.

Geochemical, petrographic and observational evidence for magnesian alteration, potassic alteration, silicification and argillic alteration exists at Mashitu South. Magnesian alteration is widespread throughout the Mines Subgroup and RAT and has caused the development of chlorite, dolomite and magnesite throughout the sequence. Potassic alteration, which caused the development of muscovite and biotite, is preferentially concentrated in the SD Formation. Silicification appears to be associated with stromatolitic or wavy-laminated units such as the RSC and RSF, as well as local horizons of this type within the lower CMN. Argillic alteration at Mashitu South is caused by Tertiary weathering, is controlled by depth and proximity to permeable lithologies, and results in oxidation, leaching of labile minerals, and development of clay. Although there are associations between alteration types and mineralisation, none of the alteration types make reliable vectors towards hypogene or supergene mineralisation.

9.4 Mineralisation

There are four Cu-Co mineralisation stages at Mashitu South. These four stages are preceded by the *Pre-Ore Diagenetic Stage*, characterised by the early diagenetic formation of disseminated pyrite and haematite, which formed before the circulation of Cu-Co-bearing fluids. The age ranges inferred for these mineralisation stages are based purely upon comparison to similar mineralisation stages and geodynamic events dated from elsewhere in the Copperbelt, and should be considered as speculative. No absolute dating has been carried out on any material from Mashitu South.

The first is the *Early Hydrothermal SSC Stage*, the age of which spans from early-late diagenesis. It resulted in the formation of stratiform-disseminated and Type 1 vein-hosted

pyrite, sphalerite, chalcopyrite, bornite, digenite, chalcocite and carrollite. Chalcopyrite, bornite and chalcocite from this stage show an upwards pattern of zonation typical of SSC-type deposits, with chalcocite most abundant in the lower Mines Subgroup DStrat and RSF units, bornite most abundant in the SD, and chalcopyrite most abundant in the uppermost CMN unit. Carrollite is the latest and most abundant sulphide of this stage to form, and is preferentially concentrated above and below the RSC unit, and similar stromatolitic horizons within the lower CMN. Studies on equivalent mineralisation elsewhere in the Central African Copperbelt (Kampunzu *et al.*, 1991; Kampunzu *et al.*, 2000; Barra *et al.*, 2004; Decree *et al.*, 2014) suggest that this happened over a protracted period between ~850 and ~670 Ma. The bacilliform pseudofossils described in Chapter 7 are interpreted to have formed during this mineralisation stage.

The *Late Hydrothermal Ore Stage* is the second hypogene mineralisation stage, consisting of early/syn-orogenic, Type-2 vein-hosted carrollite, chalcopyrite, bornite, chalcocite and digenite. These phases show no signs of stratigraphic distribution control, and it is likely that the stage formed in proximity to faults and stratabound breccias. Sulphides of this stage are volumetrically minor compared to those of the Early Hydrothermal SSC Stage. They are thought to have resulted from the remobilisation of metals from earlier mineralisation, rather than from a new input of metals into the system. Similar vein-type mineralisation in the Zambian Copperbelt is dated at 576 ± 41 Ma (Selley *et al.*, 2005).

The two hypogene mineralisation stages at Mashitu South have a combined geochemical association of: Cu + Co + Bi + Ni + V + S ± Mo ± As ± Fe ± Zn.

The *Early and Late Supergene Stages* formed during Tertiary weathering of the region and are equated to two periods of supergene heterogenite formation in the Katanga region, which have been dated by Decree et al. (2014) to at or before ~10.3 Ma (Early Supergene Stage) and ~5.3–2.3 Ma (Late Supergene Stage).

Native copper, cuprite, tenorite, chalcocite, bornite, digenite, covellite, haematite, cobaltoan carbonates, heterogenite, azurite, malachite and chrysocolla are recognised from the Early Supergene Stage, and the surviving minerals from this stage mostly exhibit textures indicating that they formed by the in-situ oxidation of earlier mineralisation. There is also RSC-hosted secondary U mineralisation at depth, toward the eastern edge of Mashitu South, which is ascribed to having formed during this stage.

The Late Supergene Stage resulted in the formation of void-filling chalcocite, haematite, cobaltoan carbonate, heterogenite, malachite, chrysocolla and pseudomalachite. Many of the minerals of the Late Supergene Stage appear to have been remobilised, in contrast to the prevalence of in-situ oxidation in the Early Supergene Stage.

Supergene mineralisation has a Cu + Be + P ± Zn geochemical association. The two most important controlling factors on the distribution of supergene mineralisation are metal availability and rock permeability. Breccias, the RSC unit and the RAT (where it was overlain by leached and eroded Mines Subgroup) are identified as good fluid conduits and hosts for supergene mineralisation.

While this study finds that mineralisation at Mashitu South follows generally accepted models of mineralisation for stratiform, vein-type and supergene Cu-Co deposits across the Copperbelt (e.g. Dewaele et al., 2006a; Hitzman et al., 2012), it recognises the disparity in the distribution and paragenetic order of stratiform carrollite at Mashitu South compared to stratiform carrollite found at other Copperbelt deposits. The late-diagenetic, permeable-horizon-distributed model of stratiform carrollite mineralisation proposed by this study may represent a hitherto-undescribed mode of mineralisation in the Copperbelt. Follow-up work to confirm and further constrain this model for Mashitu South, and to investigate its possible application at other deposits, is recommended.

Orebodies and high-grade mineralisation at Mashitu South are as follows.

1. Anhedral, intergranular carrollite of the Early Hydrothermal SSC Stage, which usually rims appreciable quantities of chalcocite and minor bornite and chalcopyrite, is the primary constituent of the stratiform-disseminated, primarily RSF-hosted hypogene orebody at Mashitu South. Between a depth of 150-50m, grades of this mineralisation are frequently upgraded by the in-situ development of chalcocite from the Early Supergene Stage, which is concentrically banded or intergrown with haematite.
2. High grades (>1%) of anhedral, intergranular, stratiform-disseminated chalcopyrite-bornite are found in the SD2d black shale unit and this unit may locally form minor hypogene orebodies. All hypogene mineralisation at Mashitu South is associated with abundant, early pyrite.

3. Late Supergene, para-exotic oxide orebodies are also present at Mashitu South. These orebodies are characterised by space-filling malachite with minor chrysocolla and pseudomalachite. They are primarily found in brecciated portions of the RAT, beneath leached or eroded Mines Subgroup units, and at a depth of between 10 and 50m.

9.5 Surface Geochemistry

During the supergene alteration of hypogene ore, the hypogene geochemical association of Cu + Co + Bi + Ni + V + S ± Mo ± As ± Fe ± Zn breaks down. Sulphur, which is more mobile than Cu in the supergene environment, descends to much greater depths, and forms supergene sulphides and sulphates. Cu is also leached from the surface at Mashitu South during supergene alteration. It is re-concentrated at a depth of around 10-50m, forming the high-grade supergene oxide orebodies of the Late Supergene Stage. However, the degree of leaching can be so great that in some instances, including at the Mashitu and Kalukundi deposit groups, no appreciable Cu-in-soil anomaly can be detected above the host rocks, when compared with the broad enrichment of Cu-in soil above the Roan Group.

The remaining elements of the hypogene assemblage have a variety of resistances to leaching and this results in a pattern of vertical zonation above supergene Cu deposits, with different elements enriched at different levels in the depth profile, the most resistant being found at the top of the profile and the least resistant being enriched at greater depth. Depending on the strength of weathering and the resistance-to-leaching of the element in question, an element may be residually enriched, or enriched through dissolution and reprecipitation (as is the case for Cu in supergene oxide ores).

Co, Bi, Ni, V and Mo, which are strongly associated with Cu in the hypogene environment, are found to have a higher affinity for the surface environment. This is due to a greater resistance to leaching by meteoric fluids than Cu. It is hypothesised that these elements would form stronger, less laterally and vertically dispersed geochemical anomalies than Cu in the soil above leached Cu-Co deposits of a similar nature to Mashitu South in Katanga. In this way, they could be used as surface vectors towards supergene and hypogene Cu-Co mineralisation, and may prove more effective than Cu in locating deposits that have experienced a high degree of leaching.

It was not possible to investigate the regional distribution of Co, Bi, Ni, V and Mo in soil as part of this study, as the Comide regional soil database was found to be unreliable in analysing the spatial variation of all elements except for Cu and Ti. It is predicted that Co, Bi, Ni, V and Mo soil concentrations would show good spatial correspondence with known Cu-Co deposits in a more reliable soil geochemistry dataset.

Suggestions for further work and Cu-Co exploration considerations are presented in section 8.5.

REFERENCES

Alexandre, J., 2002. *Les cuirasses latéritiques et autres formations ferrugineuses tropicales: Exemple du Haut Katanga méridional*. Annales du Musée Royal de l'Afrique Centrale, Sciences Géologiques 107: p.p. 118

ALS Global, 2016. ALS Global website: http://www.alsglobal.com/ Retrieved: 31/01/2016

Anderson, J.A., 1982. Characteristics of leached capping and techniques of appraisal. *In:* Titley, S.R., *(ed.),* Advances in geology of the porphyry copper deposits, southwestern North America: Tucson, University of Arizona Press, p.p. 275–295.

Annels, A.E., 1974. Some aspects of the stratiform ore deposits of the Zambian Copperbelt. *In* Bartholomé, P., *ed*., Gisement stratiformes et provinces cuprifères: Société Géologique de Belgique, 235–254

Annels, A.E., 1989. Ore genesis in the Zambian Copperbelt with particular reference to the Northern Sector of the Chambishi Basin. *In:* Boyle, R.W., Brown, A.C., Jefferson, C.W., Jowett, E.C. & Kirkham, R.V. (*eds*), Sediment-hosted Stratiform Copper Deposits. Geological Association of Canada Special Paper, **36**: 427-452.

Annels, A.E., Vaughan, D.J. and Craig, J.R., 1983. Conditions of ore mineral formation in certain Zambian Copperbelt deposits with special reference to the role of cobalt. *Mineralium Deposita*, **18**: 71-88.

Annels, A.E., and Simmonds, J.R., 1984. Cobalt in the Zambian Copperbelt. *Precambrian Research*, **25**: 75-98.

Apollo Mapping, 2016. Apollo Mapping website: https://apollomapping.com/2012/June/14%20-%20G-FAQ/Keystone_anime.gif Retrieved: 26/02/2016

Armstrong, R.A., Master, S. and Robb, L.J., 2005. Geochronology of the Nchanga Granite, and constraints on the maximum age of the Katanga Supergroup, Zambian Copperbelt. *Journal of African Earth Sciences*, **42**: 32-40

Auger, F., 1975. Manifestations volcaniques dans le Roan inferieur et dans la Serie des Mines du Shaba (Zaire). *Annals de la Facultie de Science de Lubumbashi (Zaire),* **1**: 35-42.

Baker, D.M., Lillie, R.J., Yeats, R.S., Johnson, G.D., Yousuf, M. and Zamin, A.S.H., 1988. Development of the Himalayan frontal thrust zone: Salt Range, Pakistan. *Geology,* **16**: 3-7.

Baludikay, B.K., Storme, J.-Y., François, C., Baudet, D. and Javaux, E.J., 2016. A diverse and exquisitely preserved organic-walled microfossil assemblage from the Meso–Neoproterozoic Mbuji-Mayi Supergroup (Democratic Republic of Congo) and implications for Proterozoic biostratigraphy. *Precambrian Research*, **281**: 166–184

Bargoorn, E.S. and Tyler, S.A., 1965. Microorganisms from the Gunflint Chert. *Science*, **147**: 563-575

Barker, W.W., Welch, S.A., and Banfield, J.F., 1997. Biogeochemical weathering of silicate minerals. *In:* Banfield, J.F. and Nealson, K.H. (*eds.*) Geomicrobiology: interactions between microbes and minerals, vol. 35. Mineralogical Society of America, Washington, DC, p.p. 391–428

Barra, F., Broughton, D., Ruiz, J., and Hitzman, M., 2004. Multi-stage mineralization in the Zambian Copperbelt based on Re-Os isotope constraints [abs.]: Geological Society of America Abstracts with Program, 36: 516

Bartholomé P., 1958. *On the paragenesis of copper ores.* Studia Universitatis 'Lovanium', Faculte´ des Sciences, Leopoldville (Kinshasa) 4: 5–31.

Bartholomé, P., 1962. *Les minerais cupro-cobaltiferes de Kamoto (Katanga-Ouest).* Institute de Petrographie: Kinshasa, Zaire, Studia Universite de Lovanium, Faculte de Science, 14, p.p. 40

Bartholomé, P., 1974. On the diagenetic formation of ores in sedimentary beds, with special reference to Kamoto, Shaba, Zaire. *In*: Bartholomé, P., *(ed.),* Gisements stratiformes et provinces cupriferes. Liege, Geologique Societe Belgique, p.p. 203-213.

Bartholomé, P. and Katekesha, F., 1971. Cobalt zoning in microscopic pyrite from Kamoto, Republic of the Congo (Kinshasa). *Mineral Deposita*, **6**: 167-176

Bartholomé, P., Evrard, P., Katekesha, F., Lopez-Ruiz, J., and Ngongo, M., 1972. Diagenetic ore-forming processes at Kamoto, Katanga, Republic of the Congo. *In:* Amstutz, G.C., and Bernard, A.J., (*eds.*) Ore in sediments. New York, Springer-Verlag, pp. 21–41.

Bartholomé, P., Evrard, P., Katekesha, F., Lopez Ruiz, J., and Ngongo, M., 1973. Diagenetic ore-forming processes at Kamoto, Katanga, Republic of the Congo. *In:* Amstutz, G. C., and Bernard,A . J. (*eds.)* Ores in sediments. Berlin, Springer-Verlag, p.p. 21-41.

Baudet, D., 1987. Implications of a palynological study in the Upper Precambrian from eastern Kasai and northwestern Shaba, Zaire. G*eological Journal*: **22**, 121–137

Behr, H.J., Ahrendt, H., Schmidt, A. and Weber, K., 1981. Saline horizons acting as thrust planes along the southern margin of the Damaran Orogeny (Namibia/SW-Africa). *Special Publications of the Geological Society of London*, **9**: 167-1 72.

Behr, H.J., Ahrendt, H., Porada, H. and Weber, K., 1983. The Sole Dolomite at the base of the Naukluft Nappe Complex. *Special Publications of the Geological Society of South Africa*, **11**: 185-197.

Bell, R.T., 1989. *A Conceptual Model for Development of Megabreccias and Associated Mineral Deposits in Wernecke Mountains, Canada, Copperbelt, Zaire, and Flinders*

Range, Australia. IAEA Techincal Document 500, Geological Survey of Canada contribution 31487.

Beyssac, O., Goffé, B., Petitet, J.-P., Froigneux, E., Moreau, M. and Rouzaud, J.-N., 2003. On the characterization of disordered and heterogeneous carbonaceous materials by Raman spectroscopy. *Spectrochimica Acta*, **59**: 2267-2276

Billi, A., Berardi, G., Gratier, J-P., Rossetti, F., Vignaroli, G., Baykara, M.O., Bernasconi, S.M., Kele, S., Soligo, M., De Filippis, L. and Shen, C-C., 2017. First records of syn-diagenetic non-tectonic folding in quaternary thermogene travertines caused by hydrothermal incremental veining. *Tectonophysics*, **700**: 60-79

Binda, P.L and van Eden, J., 1972. Sedimentological evidence on the origin of the Precambrian Great Conglomerate (Kundelungu Tillite), Zambia. *Palaeogeography, Palaeoclimatology, Palaeoecology*, **12**:151-168

Binda, P.L. and Porada, H., 1995. Observations on the Katangan breccias of Zambia. *In:* Wendorff, M., Tack, L. (*eds*.), Late Proterozoic Belts in Central and Southwest Africa. Annales Sciences Geologiques Musee Royal de I'Afrique Centrale, Tervuren 101, pp. 49-62

Birgul, O., 1981. Scandium-iron correlation in clay minerals. *Earth and Planetary System Science Letters*, **55**: 450-452

Bons, P.D. and Montenari, M., 2005. The formation of antitaxial calcite veins with well-developed fibres, Oppaminda Creek, South Australia. *Journal of Structural Geology*, **27**: 231–248

Brininstool, M., 2014. *Copper*. U.S. Geological Survey, Mineral Commodity Summaries 2014

Broughton, D., 2014. *Geology and Ore Deposits of the Central African Copperbelt*. Unpublished PhD Thesis, Colorado School of Mines.

Broughton, D., and Rogers, T., 2010. Discovery of the Kamoa copper deposit, Central African Copperbelt, D.R.C.. *Society of Economic Geologists Special Publication*, **15**: 287–298.

Broughton, D.W., Hitzman, M.W., and Stephens, A.J., 2002. Exploration history and geology of the Kansanshi Cu-(Au) deposit, Zambia. *Society of Economic Geologists Special Publication*, **9**: 141–153.

Brown, A.C., 2009. A process-based approach to estimating the copper derived from red beds in the sediment-hosted stratiform copper model. *Economic Geology*, **104**: 857–868

Brown, A.C., 2014. Low-Temperature Sediment-Hosted Copper Deposits. *In:* Scott, S.D. (ed.) *Treatise on Geochemistry, 2nd Edition*, 13.10, p.p. 251-271

Buick, R., 1990. Microfossil Recognition in Archean Rocks: An Appraisal of Spheroids and Filaments froma 3500 M.Y. Old Chert-Barite Unit at North Pole, Western Australia. *Palaios:* **5**, 441-459

Bull, S., Selley, D. and Hitzman, M., 2010. A sequence- and chemo-stratigraphic interpretation of the Central African Copperbelt. *CODES-CSM/AMIRA P872: Sediment-hosted copper deposits of Congolese, Zambian and central Australian basin systems.* p.p. 1-31

Bull, S., Selley, D., Broughton, D., Hitzman, M., Cailteux, J., Large, R., and McGoldrick, P. 2011. Sequence and carbon isotopic stratigraphy of the Neoproterozoic Roan Group strata of the Zambian Copperbelt. *Precambrian Research*, **190**: 70–89

Byrne, G., 2017. Geometries and genesis of breccias within the Halokinetic Kalukundi Diapir at the Mashitu Mine, Katanga, Democratic Republic of Congo. Unpublished MSc Thesis, Colorado School of Mines.

Cahen, L. and Snelling, N.J., 1984. *The geochronology and evolution of Africa*. Clarendon Press, Oxford. 512 p.p.

Cailteux, J., 1983. Le Roan shabien dans la région de Kambove (Shaba-Zaïre). Etude sédimentologique et métallogénique. Unpublished PhD Dissertation, University of Liège, Belgium, 232 p.p.

Cailteux, J., 1994. Lithostratigraphy of the Neoproterozoic Shaba-type (Zaire) Roan Supergroup and metallogenesis of associated stratiform mineralization. *Journal of African Earth Sciences*, **19**: 279–301.

Cailteux, J. and Dimanche, F., 1973. Examen des oxydes de fer et titane dans l'environment du gisement du cuivre de Musoshi (Shaba, Republique du Zaire). *Bulletin de la Société Française de Minéralogie et de Cristallographie*: **96**, 378-382

Cailteux, J., Binda, P. L. Katekesha, W.M., Kampunzu, A.B., Intiomale, M.M., Kapenda, D., Kaunda, C., Ngongo, K., Tshiauka, T., and Wendorff, M., 1994. Lithostratigraphical correlation of the Neoproterozoic Roan Supergroup from Shaba (Zaire) and Zambia, in the central African copper-cobalt metallogenic province. *Journal of African Earth Sciences*, **19**: 265–278.

Cailteux, J. and Kampunzu, A.B., 1995. The Katangan tectonic breccias in the Shaba Province (Zaire) and their genetic significance. *In*: Wendorff, M., Tack, L.(eds.) *Late Proterozoic Belts in Central and Southwest Africa*. Annales Sciences Geologiques Musee royal de l'Afrique Centrale 101, Tervuren. pp 49-62.

Cailteux, J.L.H., Kampunzu, A.B., Lerouge, C., Kaputo, A.K., and Milesi, J.P., 2005. Genesis of sediment-hosted stratiform copper-cobalt deposits, Central African Copperbelt. *Journal of African Earth Sciences,* **42**: 134–158.

Cailteux, J.LH., Kampunzu, A.B., and Lerouge, C., 2007. The Neoproterozoic Mwashya-Kansuki sedimentary rock succession in the central African Copperbelt, its Cu-Co mineralization and regional correlations. *Gondwana Research*, **11**: 414–431.

Cailteux J.L.H., Muchez, P., De Cuyper, J., Dewaele S. and De Putter, T., 2018. Origin of the megabreccias in the Katanga Copperbelt (D.R.Congo). *Journal of African Earth Sciences*, **140**: 76-93

Capistrant, P.L., Hitzman, M.W., Wood, D., Kelly, N.M., Williams, G., Zimba, M., Kuiper, Y., Jack, D., and Stein, H., 2015. Geology of the Enterprise hydrothermal nickel deposit, North-Western Province, Zambia. *Economic Geology*, **110**: 9–38

Cathles, L.M. III, Oszczepalski, S., and Jowett, E.C., 1993. Mass balance evaluation of the late diagenetic hypothesis for Kupferschiefer Cu mineralization in the Lubin basin of southwestern Poland. *Economic Geology*, **88**: 948–956

Chabu, M., 1990. Metamorphism of the Kipushi Carbonate Hosted Zn–Pb–Cu deposit, Shaba, Zaire. *In:* Spry, P.G., Bryndzia, L.T. *(eds.),* Regional Metamorphism of Ore Deposits. Proceedings of 28th International Geological Conference, VSP, p.p. 27–47

Chartrand, F.M. and Brown, A.C., 1984. Preliminary comparison of diagenetic stratiform copper mineralization from Redstone, NW Territories, Canada, and Kamoto, Shaban copperbelt, Zaire. *Journal of the Geological Society of London*, **141**: 291-297

Cheshire, P., 2014. Personal Communication.

Cheshire, P., 2014. *Cataclasite–Breccia Zones, Mashitu & Kakanda Pits, DRC Copperbelt, Preliminary Field Description & Comments.* E.R.G. Internal Communication.

Chimvinga, J., 2014. Personal Communication.

Condie, K.C., 2003. Supercontinents, superplumes and continental growth: the Neoproterozoic record. *In*: Yoshida, M., Windley, B.F. and Dasgupta, S. (eds.) *Proterozoic East Gondwana: Supercontinent Assembly and Breakup*. Geological Society of London, pp 1-23.

Cooke, D.R., 2003. Zambian Copperbelt geochemical modelling: implications for mineralising processes*. ARC/AMIRA P544 Final Report*, 21B.1-21B.6

Cosi, M., De Bonis, A., Gosso, G., Hunziker, J., Martinotti, G., Moratto, S., Robert, J.P. and Ruhlman, F., 1992. Late Proterozoic thrust tectonics, high-pressure metamorphism and uranium mineralization in the Domes area, Lufilian arc, northwest Zambia. *Precambrian Research*, **58**: 215-240.

Coward, M.P. and Daly, M.C., 1984. Crustal lineaments and shear zones in Africa: their relationships to plate movements. *Precambrian Research*, **24**: 27-45.

Cox, S.F., 2005. Coupling between deformation, fluid pressures, and fluid flow in ore-producing hydrothermal systems at depth in the crust, *In*: Hedenquist J. W., Thompson J.F.H., Goldfarb R.J. and Richards J.P., *(eds.),* Economic Geology 100th Anniversary Volume 1905–2005: Littleton, Colorado, Society of Economic Geologists, 39–75

Cox, D.P., Lindsey, D.A., Singer, D.P., Moring, B.C., and Diggles, M.F., 2007. *Sediment-hosted copper deposits of the world: Deposit models and database*. U.S. Geological Survey Open File Report 03-107, 53 pp.

Craig, R.R. and Vaughan, D.J., 1994. *Ore Microscopy and Ore Petrography, 2nd Edition*. Jon Wiley and Sons, Inc. New York. 434 p.p.

Craig J. R., Vokes, F. M. and Solberg, T. N., 1998. Pyrite: physical and chemical textures. *Mineralium Deposita*, **34**: 82-101

Dalton, K., 2015. Personal Communication.

Daly, M. C., 1986. The intracratonic Irumide Belt of Zambia and its bearing on collision orogeny during the Proterozoic of Africa. *In*: Coward, M.P. and Ries, A.C. (eds.) *Collision tectonics*. Geological Society Special Publication 19, pp 321-328.

Darnley, A.G., Horne, J.E.T., Smith, G.H., Chandler, T.R.D., Dance, D.F., and Preece, E.R., 1961. Ages of some uranium and thorium minerals from east and central Africa, *Mineralogical Magazine*, **32**: 716–724.

Dawson, G., 2002. *Initial SHRIMP geochronology of xenotime and monazite from Mufulira, Konkola North, Ndola East and Chambishi*. AMIRA P554 internal communication, available at: http://www.utas.edu.au/codes/publications/past-amira-reports

Dechow, E. and Jensen, M.L., 1965. Sulphur isotopes of some central African sulphide deposits. *Economic Geology*, **60**: 894-941

Decree, S., Deloule, E., Ruffet, G., Dewaele, S., Mees, F., Marignac, C., Yans, J. and De Putter, T., 2010. Geodynamic and climate controls in the formation of Mio–Pliocene world-class oxidized cobalt and manganese ores in the Katanga province, DR Congo. *Miner Deposita*, **45**: 621-629

Decree, S., Deloule, E., De Putter, Th., Dewaele, S., Mees, F., Yans, J. and Marignac, C., 2011. SIMS U–Pb dating of uranium mineralization in the Katanga Copperbelt: constraints for the geodynamic context. *Ore Geology Reviews*, **40**: 81–89

Decree, S. and Pourret, O., 2013. *Origin of heterogenite (CoOOH) as illustrated by rare earth element fractionation*. Goldschmidt 2013 Conference Abstracts.

Decree, S., Deloule, E., De Putter, T., Dewaele, S., Mees, F., Baele, J. and Marignac, C., 2014. Dating of U-rich heterogenite: New insights into U deposit genesis and U cycling in the Katanga Copperbelt. *Precambrian Research*, **241**: 17– 28

Dejonghe, L., 1997. Features and origin of the strata-bound siliciclastic hosted Kinsenda copper deposit in the Roan of south-east Shaba, Zaire. *In:* Charlet, J.-M. *(ed.),* International Cornet Symposium Strata-Bound Copper Deposits and Associated Mineralizations. Royal Academy of Overseas Sciences, Brussels, pp. 145–158.

Dejonghe, L. and Ngoyi, K., 1995. The Kinsenda Ore Deposit (SE Shaba, Zaïre): a stratabound copper concentration in the siliciclastic formations of the Roan (Upper Proterozoic). *Chronique de la recherche miniere,* **521**: 19-37

de Joussineau, G., Bazalgette, L., Petit, J-P. and Lopez, M., 2005. Morphology, intersections, and syn/late-diagenetic origin of vein networks in pelites of the Lodève Permian Basin, Southern France. *Journal of Structural Geology*, **27**: 67-87.

Delvaux, D. and Sperner, B., 2003. New aspects of tectonic stress inversion with reference to the TENSOR program. *In*: Nieuwland, D.A. *(ed.) New Insights into Structural Interpretation and Modelling*. Geological Socitey of London Special Publications 212, 75-100.

De Magnee, I. and Francois, A., 1988. The Origin of the Kipushi (Cu, Zn, Pb) Deposit in Direct Relation with a Proterozoic Salt Diapir. Copperbelt of Central Africa, Shaba, Republic of Zaire. *In:* Freiderich, G.H. and Herzig, P.M. *(eds.)* Base Metal Sulfide Deposits in Sedimentary and Volcanic Environments. Springer Berlin Heidelberg, p.p. 74-93

de Maret, P., 1982. Rock art. In: Van Noten F. (ed.) *The Archaeology of Central Africa*. Graz: Akademische Drücku.Verlagsanstalt. pp 97–9

de Maret, P., 1986. The Ngovo Group: an industry with polished stone tools and pottery in Lower Zaïre. *The African Archaeological Review*, **4**: 103–33

Demesmaeker, G., Francois, A. and Oosterbosh, R., 1963. La tectonique des gisements cuprif~res stratiformes du Katanga. *In*: Lombard, J. and Nicolini, P. (eds.) *Gisements stratiformes de cuivre en Afrique,* 2~me partie Paris. pp 47-115.

De Putter, T., Mees, F., Decree, S., Dewaele, S., 2010. Malachite, an indicator of major Pliocene Cu remobilization in a karstic environment (Katanga, Democratic Republic of Congo). *Ore Geology Reviews*, **38**: 90–100

Dewaele, S., Muchez, P. and Banks, D.A., 2004. Fluid evolution along multistage composite fault systems at the southern margin of the Lower Palaeozoic Anglo-Brabant fold belt, Belgium. *Geofluids*, **4**: 341-356

Dewaele, S., Muchez, P., Vets, J., Fernando-Alonzo, M. and Tack, L., 2006a. Multiphase origin of the Cu-Co ore deposits in the western part of the Lufilian fold and thrust belt, Katanga (Democratic Republic of the Congo). *Journal of African Earth Sciences*, **46**: 455-469

Dewaele, S., Muchez, P., Heijlen, W., Boutwood, A., Lemmon, T. and Tyler, R., 2006b. Reconstruction of the hydrothermal history of the Cu-Ag vein-type mineralisation at Dikulushi, Kundelungu foreland, Katanga, D.R. Congo. *Journal of Geochemical Exploration*, **89**: 376-379.

Douglas, G.B., Butt, C.R.M., Gray, D.J., 2003. Mulga Rock Uranium and Multi-Element Deposit, Officer Basin, W.A. In: Butt, C.R.M., Cornelius, M., Scott, K.M. and Robertson, I.D.M. *(eds.)* Regolith Expression of Australian Ore Systems, a monograph of geochemical case histories and conceptual dispersion, process and exploration models. CRC LEME, available at: http://www.crcleme.org.au/Pubs/Monographs/RegExpOre.html

Edwards, J.K. and Bazylinski, D.A., 2008. Intracellular minerals and metal deposits in prokaryotes. *Geobiology*: **6**, 309 – 317

Eglinger, A., 2013. *Cycle de l'uranium et évolution tectono-métamorphique de la ceinture orogénique Pan-Africaine du Lufilien (Zambie).* Unpublished PhD thesis, Université de Lorraine, France.

Eglinger, A., Ferraina, C., Tarantola, A., André-Mayer, A.S., Vanderhaeghe, O., Boiron, M.C., Dubessy, J., Richard, A., Brouand, M., 2014a. Hypersaline fluids generated by high-grade metamorphism of evaporites: fluid inclusion study of uranium occurrences in the Western Zambian Copperbelt. *Contributions to Mineralogy and Petrology*, **167**: 967–994.

Eglinger, A., Tarantola, A., Durand, C., Ferraina, C., Vanderhaeghe, O., André-Mayer, A-S., Paquette, J.L., Deloule, E., 2014b. Uranium mobilization by fluids associated with Ca–Na metasomatism: A P–T–t record of fluid–rock interactions during Pan-African metamorphism (Western Zambian Copperbelt). *Chemical Geology*, **386**: 218–237.

Eglinger, A., Vanderhaeghe, O., André-Mayer, A-S., Goncalves, P., Zeh, A., Durand, C. and Deloule, E., 2016. Tectono-metamorphic evolution of the internal zone of the Pan-African Lufilian orogenic belt (Zambia): Implications for crustal reworking and syn-orogenic uranium mineralizations. *Lithos*, **240**: 167-188

El Desouky, H.A., Muchez, P., Dewaele, S., Boutwood, A. and Tyler, R., 2007. The stratiform copper mineralisation of the Lufukwe Anticline, Lufilian Foreland, Democratic Republic of Congo. *Geologica Belgica*, **10**: 148-151

El Desouky, H.A., Muchez, P., Dewaele, S., Boutwood, A. and Tyler, R., 2008a. Postorogenic Origin of the Stratiform Cu Mineralization at Lufukwe, Lufilian Foreland, Democratic Republic of Congo. *Economic Geology*, **103**: 555-582

El Desouky, H.A., Muchez, P. and Tyler, R., 2008b. The sandstone-hosted stratiform copper mineralization at Mwitapile and its relation to the mineralization at Lufukwe, Lufilian foreland, Democratic Republic of Congo. *Ore Geology Reviews*, **34**: 561–579

El Desouky, H.A., Muchez, P. and Cailteux, J., 2009. Two Cu-Co sulphide phases and contrasting fluid systems in the Katanga Copperbelt, Democratic Republic of Congo. *Ore Geology Reviews*, **36**: 315-332

El Desouky, H.A., Muchez, P., Boyce, A.J., Schneider, J., Cailteux, J.L.H., Dewaele, S. and von Quadt, A., 2010. Genesis of sediment-hosted stratiform copper–cobalt mineralization at Luiswishi and Kamoto, Katanga Copperbelt (Democratic Republic of Congo). *Miner Deposita*, **45**: 735-763

Ellerbeck, B., 2011. *Preliminary Mineralogy Report No: 12/462: Detailed Mineralogical Testwork on Twenty-one Copper-cobalt Ore Samples from Democratic Republic of Congo (DRC) (Phase 2*). S.G.S. report commissioned for Comide Mining (ENRC).

El Shazly, A.K. and Al Belushi, M., 2004. Petrology and Chemistry of Metasomatic Blocks from Bawshir, Northeastern Oman. *International Geology Review*, **46**: XXX-XXX.

Enders, S., Knickerbocker, C., Titley, S.R. and Southam, G., 2006. The Role of Bacteria in the Supergene Environment of the Morenci Porphyry Copper Deposit, Greenlee County, Arizona. *Economic Geology*, **101**: 59–70

Eskola, P., 1915. On relations between the chemical and mineralogical composition in the metamorphic rocks of the Orijarvi region. *Bulletin de la Commission géologique de Finlande*, **44**: 109-143

Fay, I. and Barton, M.D., 2012. Alteration and ore distribution in the Proterozoic Mines Series, Tenke-Fungurume Cu–Co district, Democratic Republic of Congo. *Miner Deposita*, published online

François, A., 1973. *L'extrémité occidentale de l'Arc cuprifere shabien.* Étude Géologique: Bureaux d'Études Géologiques, Gécamines-Exploitation, Likasi, Zaire, pp. 65.

François, A., 1974. Stratigraphy, tectonique et minéralisations dans l'arc cuprifière du Shaba (Républic du Zaire). *In* Bartholomé, P. (ed.), *Gisements stratiformes et provinces cuprifières*. Liège, Belgium, Centenaire de la Sociéte Géologique de Belgique, 79-101.

François, A., 1987. Synthese geologique sur 1'Arc cuprifere du Shaba (Rep.du Zaire). *Centenaire de la Sociéte Géologique de Belgique*, 15-65

François, A., 1993. La structure tectonique du Katanguien dans la region de Kolwezi (Shaba, Republique du Zaire). *Annals de la Sociéte Géologique de Belgique*., **116**: 87-104.

François, A., 2006. *La partie centrale de l'Arc cuprifère du Katanga: étude géologique.* Tervuren, Musée royal de l'Afrique centrale.

Frankel, R.B. and Bazylinski, D.A., 2003. Biologically Induced Mineralisation by Bacteria. *Reviews in Mineralogy and Geochemistry*: **54**, 95 – 114

Garlick, W.G., 1962. Geology of Chibuluma mine. *In:* Lombard, J., Nicolini, P. (*eds*.), Gisements stratiformes de cuivre en Afrique. Association des Services Geologiques Africains, pp. 137–149.

Gasse, F., 2006. Climate and hydrological changes in tropical Africa during the past million years. *Comptes Rendus Academie de la Science Palevol*, **5**: 35–43

Gauthier, G. and Deliens, M., 1999. Cobalt minerals of the Katanga Crescent, Congo. *Mineralogical Record*, **30**: 255-267

Gee, E.R., 1983. Tectonic problems of the sub-Himalayan region of Pakistan. *Kashmir Journal of Geology*, **1**: 11-18.

Gigler, G.M. and Kinnaird, J.A., 2017. Element mobility in the weathering environment and surface vectors to mineralisation—A case study from the Mashitu South Cu-Co deposit, Katanga, Democratic Republic of Congo. *Journal of Geochemical Exploration*, **183**, 127-137.

Giresse, P., 2005. Mesozoic-Cenozoic history of the Congo Basin. *Journal of African Earth Science*, **43**: 301–315

Glasauer, S., Langley, S., Beveridge, T.J., 2002. Intracellular iron minerals in a dissimilatory iron-reducing bacterium. *Science*: **295**, 117 – 119

Graham, D.J. and Midgley, N.G., 2000. Graphical representation of particle shape using triangular diagrams: an Excel spreadsheet method. *Earth Surface Processes and Landforms*, **25**: 1473-1477. TRI-PLOT Excel spreadsheet available for download at http://www.lboro.ac.uk/microsites/research/phys-geog/tri-plot/index.html

Gribble, C.D. and Hall A.J., 1992. *Optical mineralogy, principles and practice.* UCL Press, London. 302 p.p.

Grujenschi, C., 1978. Quelques observations sur la position stratigraphique de la "Serie des Mines" au Shaba. *Annals de la Sociéte Géologique de Belgique*, **101**: 1-11

Haest, M., Muchez, P., Jerome, C.J. Petit and Vanhaecke, F., 2009a. Cu isotope ratio variations in the Dikulushi Cu-Ag deposit, D.R.C.: of primary origin or induced by supergene reworking? *Economic Geology*, **104**: 1055-1064

Haest, M., Muchez, Ph., Dewaele, S., Boyce, A.J., von Quadt, A. and Schneider, J., 2009b. Petrographic, fluid inclusion and isotopic study of the Dikulushi Cu-Ag deposit, Katanga (D.R.C.): implications for exploration. *Mineralium Deposita*, **44**: 505–522

Halley, S.W., Wood, D., Stoltze, A., Godfroid, J., Goswell, H. and Jack., D., 2016. Using Multielement Geochemistry to Map Multiple Components of a Mineral System: Case Study from a Sediment-Hosted Cu-Ni Camp, NW Province, Zambia. *SEG Newsletter*, **104**: 1-21

Hanson, R.E., Wilson, T.J. and Munyanyiwa, H., 1994. Geologic evolution of the Neoproterozoic Zambesi Orogenic Belt in Zambia. *Journal of African Earth Science*, **18**: 135-150.

Heijlen, W., Banks, D.A., Muchez, P., Stensgard, B.M. and Yardley, B.W.D., 2008. The nature of mineralizing fluids of the Kipushi Zn-Cu deposit, Katanga, Democratic Republic of Congo: Quantitative fluid inclusion analysis using laser ablation ICP-MS and bulk crush-leach methods: *Economic Geology*, **103**: 1459–1482

Hitzman, M.W., 2000. Source basins for sediment-hosted stratiform Cu deposits: implications for the structure of the Zambian Copperbelt. *Journal of African Earth Sciences*, **30:** 855-863.

Hitzman, M.W., 2010a. Significant findings and exploration significance of P872. *CODES-CSM/AMIRA P872: Sediment-hosted copper deposits of Congolese, Zambian and central Australian basin systems.* pp. 385-388

Hitzman, M.W., 2010b. Alteration associated with sulfide mineralization at the Lupoto and Kasonta copper deposits, southern Congolese Copperbelt, Democratic Republic of Congo. *CODES-CSM/AMIRA P872: Sediment-hosted copper deposits of Congolese, Zambian and central Australian basin systems.* pp. 301-324

Hitzman, M.W., 2015a. Personal Communication.

Hitzman, M.W., 2015b. *Geology of Sedimentary rock-hosted stratiform copper deposits*. Short-course presentation for E.N.R.C., 15/04/2015

Hitzman, M.W., Kirkham, R., Broughton, D., Thorson, J. and Selley, D., 2005. The sediment-hosted stratiform copper ore system. *Economic Geology 100th Anniversary Volume*: 609–642

Hitzman, M.W., Selley, D., and Bull, S., 2010. Formation of Sedimentary Rock-Hosted Stratiform Copper Deposits through Earth History. *Economic Geology*, **105**: 627-639

Hitzman, M.W., Broughton, D., Selley, D., Woodhead, J., Wood, D., Bull, S., 2012. The Central African Copperbelt: Diverse Stratigraphic, Structural, and Temporal Settings in

the World's Largest Sedimentary Copper District. *S.E.G. Special Publication*, **16**: pp. 487-514

Hitzman, M.W. and Broughton, D.W., 2017. Discussion: Age of the Zambian Copperbelt by Sillitoe et al. (2017) Mineralium Deposita. *Mineralium Deposita*, **52**: 1273–1275

Hoffmann, K.-H., Condon, D. J., Bowring, S. A. and Crowley, J. L., 2004. U–Pb zircon dates for the Neoproterozoic Ghaub Formation, Namibia: constraints on Marinoan glaciation. *Geology*, **32**: 817–820.

Hofmann, H.J., 1972. *Precambrian remains in Canada: Fossils, dubiofossils and pseudofossils*: Proceedings of the 24th International Geological Congress, Section 1, p.p. 20-30.

Horodyski, R.J., 1981. Pseudomicrofossils and altered microfossils from a middle Proterozoic shale, Belt Supergroup, Montana: *Precambrian Research*: **16**, 143-154.

Hoy, L.D., and Ohmoto, H., 1989. Constraints for the genesis of redbed associated stratiform Cu deposits from sulphur and carbon mass balance relations. *In:* Boyle, R.W., Brown, A.C., Jefferson, C.W., Jowett, E.C., Kirkham, R.V. (*eds.),* Sediment-hosted Stratiform Copper Deposits. Geological Association of Canada, Special Paper 36, pp. 135–149.

Iain, S. and Chassé, M., 2016. Scandium. *In*: White, W.M. (*ed*.) Encyclopedia of Geochemistry. Springer International Publishing Switzerland, pp.1-4.

Intiomale, M.M. and Oosterbosch, R., 1974. Géologie et géochimie du gisement de Kipushi–Zaire. *In:* Bartholome, P. *(ed.)* Gisements stratiformes et provinces cupifères: Centenaire de la Société Géologique Belgique de Liège, 123–164.

Jackson, M.P.A., Warin, O.N., Woad, G.M. and Hudec, M.R., 2003. Neoproterozoic allochthonous salt tectonics during the Lufilian orogeny in the Katangan Copperbelt, central Africa. *Geological Society of America Bulletin*, **115**: 314-330

Jensen, M.L. and Dechow, E., 1962. The bearing of sulphur isotopes on the origin of the Rhodesian copper deposits. *Transactions of the Geological Society of South Africa*, **65**: 2-17

Jobin-Bevans, S., Lotriet, M.P., Heili, C., Meintjes, A. and Naismith, A., 2006. *Amended Technical Report for Kamoto Copper Company Kolwezi, Katanga Province, Democratic Republic of the Congo*. McIntosh RSV LLC.

John, T., 2001. *Subduction and continental collision in the Lufilian Arc-Zambesi Belt orogen: A petrological, geochemical, and geochronological study of eclogites and whiteschists (Zambia).* PhD dissertation, Christian-Albrechts-Universitat.

John, T., Schenk, V., Haase, K., Scherer, E. and Tembo, F., 2003. Evidence for a Neoproterozoic ocean in south-central Africa from mid-oceanic-ridge–type geochemical signatures and pressuretemperature estimates of Zambian eclogites. *Geology*, **31**: 243-246

John, T., Schenk, V., Mezger, K., and Tembo, F., 2004. Timing and PT evolution of whiteschist metamorphism in the Lufilian arc-Zambezi belt orogen (Zambia): Implications for the assembly of Gondwana. *Journal of Geology*, **122**: 71–90.

Johnson, R.D., 2014. *Orebody characterisation and structural features that govern copper and cobalt mineralisation in the eastern limb of the Lufilian Arc, Democratic Republic of Congo*. Unpublished MSc Thesis, University of the Witwatersrand, 209 pp.

Kajander, E.O. and Çiftçioglu, N., 1998. Nanobacteria: An alternative mechanism for pathogenic intra- and extracellular calcification and stone formation. *Proceedings of the National Academy of Sciences of the United States of America*: **95**, 8274–8279

Kampunzu, A.B., Kapenda, D. and Manteka, B., 1991. Basic magmatism and geotectonic evolution of the Pan African belt in Central Africa: evidence from the Katangan and West Congolian segments. *Tectonophysics*, **190**: 363-371

Kampunzu, A.B. and Cailteux, J., 1999. Tectonic Evolution of the Lufilian Arc (Central Africa Copper Belt) During Neoproterozoic Pan African Orogenesis. *Gondwana Research*, **2,** 401-421

Kampunzu, A.B., Tembo, F., Matheis, G., Kapenda, D. and Huntsman-Mapila, P., 2000. Geochemistry and Tectonic Setting of Mafic Igneous Units in the Neoproterozoic Katangan Basin, Central Africa: Implications for Rodinia Break-up. *Gondwana Research*, **3**: 125-153

Kampunzu, A.B., Cailteux, J.L.H., Moine, B., and Loris, H.N.B.T., 2005. Geochemical characterization, provenance, source and depositional environment of 'Roches Argilo-Talqueuses' (R.A.T.) and Mines Subgroups sedimentary rocks in the Neoproterozoic Katangan belt (Congo): Lithostratigraphic implications. *Journal of African Earth Sciences*, **42**: 119–133

Kampunzu, A.B., Cailteux, J.L.H., Kamona, A.F., Intiomale, M.M. and Melcher, F., 2009. Sediment hosted Zn-Pb-Cu deposits in the Central African Copperbelt. *Ore Geology Reviews*, **35**: 263-297

Katsikopoulos, D., Fernandez-Gonzalez, A., Prieto, A. and Prieto, M., 2008. Cocrystallization of Co (II) with calcite: Implications for the mobility of cobalt in aqueous environments. *Chemical Geology*, **254**: 87–100

Kazadi Banza, S., 2012. *Structural geology of the Kinsevere Copper Deposit, DRC*. Unpublished MSc thesis, University of Pretoria, 204 pp.

Keleman, S.R. and Fang, H.L., 2001. Maturity Trends in Raman Spectra from Kerogen and Coal. *Energy and Fuels*, **15**: 653-658.

Kenyon, K., 2014. Personal Communication.

Key, R. M., Liyungu, A. K., Njamu, F. M., Somwe, V., Banda, J., Mosley, P. M. and Armstrong, R. A., 2001. The western arm of the Lufilian Arc in NW Zambia and its potential for copper mineralization. *Journal of African Earth Sciences*, **33**: 503–528.

Kipata, L. M., Delvaux, D., Sebagenzi, M. N., Cailteux, J. and Sintubin, M., 2013. Brittle tectonic and stress field evolution in the Pan-African Lufilian arc and its foreland (Katanga, DRC): from orogenic compression to extensional collapse, transpressional inversion and transition to rifting. *Geologica Belgica*, **16**: 1-17

Kirkham, R.V., 1989. The distribution, settings and genesis of sediment-hosted stratiform copper deposits. *In*: Boyle, R.W. et al. (*eds*.) Sediment-Hosted Stratiform Hosted Deposits. Geological Association of Canada Special Paper, 36, 3-38

Klein, C., Beukes, N.J. and Schopf, J.W., 1987. Filamentous microfossils in the early Proterozoic Transvaal Supergroup: their morphology, significance, and paleoenvironmental setting. *Precambrian Research*, **36**: 81–94

Knoll, A.H., Barghoorn, E.S., and Awramik, S.M., 1978. New microorganisms from the Aphebian Gunflint Iron Formation, Ontario. *Journal of Paleontology*, **52**, 976-992

Konhauser, K.O., Lalonde, S.V., Phoenix, V.R., 2008. Bacterial biomineralization: Where to from here? *Geobiology*: **6**, 298-302

Kortman, C.R., 1972. The geology of the Zambia Broken Hill Mine, Kabwe. *Geologie en Mijnbouw,* **51**: 347–356

Koziy, L., Bull, S., Large, R. and Selley, D., 2009. Salt as a fluid driver, and basement as a metal source, for stratiform sediment-hosted copper deposits. *Geology*, **37**: 1107–1110.

Kröner, A. and Stern, R.J., 2005. Africa/Pan African Orogeny. *In*: Selley, R.C., Cocks, R.M. and Plimer, I.R. (eds.) *Encyclopedia of Geology*. Elsevier, pp 1-12

Kremer, B., Kazmierczak, J., Lukomska-Kowalczyk, M. and Kempe, S., 2012. Calcification and silicification: fossilization potential of cyanobacteria from stromatolites of Niuafo'ou's Caldera Lakes (Tonga) and implications for the early fossil record. *Astrobiology*, **6**: 535-48

Kucha, H., Mayer, W., Piestrzyński, A., Wieczorek, A., 1981. The replacement of rutile by chalcocite in the copper ores of the Fore-Sudetic Monocline. *Mineralogia Polonica*: **12**, 69-76.

Kulp, J.L., Turekian, K. and Boyd, D.W., 1951. Strontium content of limestones and fossils. *Bulletin of the Geological Society of America*, **63**: 701-716

Labaume, P., Berty, C. and Laurent, Ph, 1991. Syn-diagenetic evolution of shear structures in superficial nappes: an example from the Northern Apennines (NW Italy). *Journal of Structural Geology,* **13**, 385-398.

Lanier, W.P., 1986. Approximate growth rates of Early Proterozoic microstromatolites as deduced by biomass productivity. *Palaios,* **1**: 525–542

Large, R., McGoldrick, P. and Croaker, M., 2002. *Zambian Copper Belt Geochemistry: Part III; Preliminary assessment of chemostratigraphy and alteration geochemistry*. AMIRA P554 internal communication, available at: http://www.utas.edu.au/codes/publications/past-amira-reports

Large, R., McGoldrick, P., Bull, S., Scott R. and Selley D., 2003. Lithogeochemistry and alteration halos to stratiform mineralisation in the Chambishi Basin, Zambian Copperbelt. *ARC/AMIRA P544 Final Report*, 21A.1-21A.4

Lavier, L.L., Steckler, M.S. and Brigaud, F., 2001. Climatic and tectonic control on the Cenozoic evolution of the West African margin. *Marine Geology*, **178**: 63–80

Lefebvre, J.J., 1975. Les roches ignees dans le Katanguien du Shaba (Zaire). Le district du cuivre. *Annals de la Sociéte Géologique de Belgique*, **98**: 47-73.

Lefebvre, J.J., 1976. Phenomenes post-diagenetiques dans l'ecaille nord-est du gisement de Kabolela, Shaba, Zaire. Bulletin de la Societe Belge Geologie, **85**: 7–29

Lepersonne, J., 1974. *Carte Géologique du Zaire.* Département des Mines, République du Zaire. Musée royal de l'Afrique Central, Belgique.

Loris, N.B.T., Charlet, J.M., Kanzundu, M., Cailteux, J. and Kampunzu, A.B., 2003. Distribution of uranium in the Luishia Cu–Co stratiform deposits (Katanga, RDC) and genetic implications. *In:* Abstracts of the IGCP 450 Conference and Field Workshop, July 14–24, 2003, Lubumbashi, Democratic Republic of Congo, 108–112

Love, L. G. and Amstutz, G. C., 1966. Review of microscopic pyrite. *Fortschritte der Mineralogie,* **43**: 273-309

Maithy, P.K., 1975. Micro-organisms from the Bushimay system (Late Precambrian) of Kanshi, Zaire. *Palaeobotany*: **22**, 133–149

Malan, S.P., 1964. Stromatolites and other algal structures at Mufulira, Northern Rhodesia. *Economic Geology*, **59**: 397-415

Malavieille, J. and Ritz, J.F., 1989. Mylonitic deformation of evaporites in decollements: examples from the southern Alps, France. *Journal of Structural Geology*, **11**: 583-590.

Maree, S.C., 1963. Structural features of the Mufulira area Northern Rhodesia. *In:* Lombard, L., Nicolini, P. *(eds.),* Stratiform Copper Deposits in Africa. Association of African Geological Surveys, Paris, pp. 158–177.

Marshall, C.P. and Marshall, A.O., 2013. Raman Hyperspectral Imaging of Microfossils: Potential Pitfalls. *Astrobiology*: **13**, 920-931

Martin, A., 2014. Personal Communication.

Master, S., 1991. *The origin and controls on the distribution of copper and precious-metal mineralization at the Mangula and Norah mines, Mhangura, Zimbabwe.* Unpublished Ph.D. thesis, University of the Witwatersrand, Johannesburg, 385 pp.

Master, S., 2003. *Evidence for palaeoseismites and seismogenic high-pressure fluid expulsion related to diagenetic mineralization in stratabound sediment-hosted copper deposits: examples from the Palaeoproterozoic Magondi Copperbelt (Zimbabwe) and the Neoproterozoic central African Copperbelt.* Abstract: Third Workshop of IGCP 450: Proterozoic Sediment-hosted Base Metal Deposits of Western Gondwana. Lubumbashi, D.R. Congo, July 2003.

Master, S., 2014. Personal Communication.

Master, S., Rainaud, C., Armstrong, R.A., Phillips, D. and Robb, L.J., 2005. Provenance ages of the Neoproterozoic Katanga Supergroup (Central African Copperbelt), with implications for basin evolution. *Journal of African Earth Sciences*, **42**: 41-60

Master, S. and Wendorff, M., 2011. Neoproterozoic glaciogenic diamictites of the Katanga Supergroup, Central Africa. *In*: Arnaud, E., Halverson, G. P. and Shields-Zhou, G. (eds) *The Geological Record of Neoproterozoic Glaciations*. Geological Society, London, Memoirs, 36, 173–184.

McGoldrick, P. and Cooke, D., 2003. Zambian Copperbelt geochemistry and stable isotopes: implications for mineralising processes. *ARC/AMIRA P544 Final Report*, 10.1-10.6

McGoldrick, P., Scott, R., Selley, D. and Broughton, D., 2003. Minor element geochemistry of Zambian Copperbelt deposits. *ARC/AMIRA P544 Final Report*, 12.1-12.6.

McGoldrick, P., Meffre, S. and Selley, D., 2010. Trace elements and lead isotopes in Mines Series sulfides, Democratic Republic of Congo. CODES-CSM/AMIRA P872 Final Report: 371-384

McLaren, C.H., 2011. *Mineralogical Report No: MIN 12/462 Phase 1. Petrographic Investigation of Twenty One Cu-bearing Drill-Core Samples from the Democratic Republic of the Congo*. S.G.S. report commissioned for Comide Mining (ENRC).

Mendelsohn, F., 1961. Roan Antelope. *In:* Mendelsohn, F. *(ed.),* The Geology of the Northern Rhodesian Copperbelt. Macdonald, London, pp 351-405.

Meneghel, L., 1981. The occurrence of uranium in the Katanga System of northwestern Zambia. *Economic Geology*, **76**: 56-68

Mielke, J.E., 1979. Composition of the Earth's Crust and Distribution of the Elements. *In*: Siegel, F.R., (*ed*): Review of Research on Modern Problems in Geochemistry. Paris, International Association for Geochemistry and Cosmochemistry, Earth Science Series, 16, 13-37.

Miller, R. McG., Pickford, M., Senut, B., 2010. The geology, palaeontology and evolution of the Etosha Pan, Namibia: implications for the terminal Kalahari deposition. *South African Journal of Geology*, **113**: 307-334.

Mirnejad, H., Mathur, R., Einali, M., Dendas, M. and Alierzaei, S., 2010. A comparative copper isotope study of porphyry copper deposits in Iran. *Geochemistry: Exploration, Environment, Analysis*, **10**: 413-418.

Morse, J.W. and Bender, M.L., 1990. Partition coefficients in calcite: Examination of factors influencing the validity of experimental results and their application to natural systems. *Chemical Geology*, **82**: 265-277

Mucci, A., 1987. Influence of temperature on the composition of magnesian calcite overgrowths precipitated from seawater. *Geochmica et Cosmochimica Acta*, **51**: 1977-1984

Mucci, A. and Morse, J.W., 1990. Chemistry of low-temperature abiotic calcites: Experimental studies on coprecipitation, stability, and fractionation. *Aquatic Sciences*, **3**: 217-254.

Muchez, P., Vanderhaeghen, P., El Desouky, H., Schneider, J., Boyce, A., Dewaele, S. and Cailteux, J., 2008. Anhydrite pseudomorphs and the origin of stratiform Cu-Co ores in the Katangan copperbelt (Democratic Republic of Congo). *Miner Deposita*, **43**: 575-589

Muchez, P., Brems, D., Clara, E., De Cleyn, A., Lammens, L., Boyce, A., De Muynck, D., Mukumba, W., and Sikazwe, O., 2010. Evolution of Cu–Co mineralizing fluids at Nkana Mine, Central African Copperbelt, Zambia. *Journal of African Earth Sciences*, **58**: 457–474

Muchez, P. and Corbella, M., 2012. Factors controlling the precipitation of copper and cobalt minerals in sediment-hosted ore deposits: advances and restrictions. *Journal of Geochemical Exploration*, **118**: 38-46.

Muchez, P., André-Mayer, A-M., El Desouky, H.A. and Reisberg, L., 2015. Diagenetic origin of the stratiform Cu–Co deposit at Kamoto in the Central African Copperbelt. *Miner Deposita*, **50**: 437-447

Muchez, P., André-Mayer, A.-S., Dewaele, S. and Large, R., 2017. Discussion: Age of the Zambian Copperbelt. *Mineralium Deposita*, **52**: 1269–1271

Nelson, S.A., 2011. Triangular Plots in Metamorphic Petrology. Online resource from Tulane University: EENS 2120 Petrology module. Available at: http://www.tulane.edu/~sanelson/eens212/triangular_plots_metamophic_petrology.htm Retrieved: 01/02/2016

Nilsson, J., Simpson, R.G. and McKenzie, W., 2011. *Technical Report Expansion Feasibility Study for the Tenke Fungurume Mine, Katanga Province, Democratic Republic of Congo*. 43-101 Technical Report.

Noffke, N., 2008. Turbulent lifestyle: Microbial mats on Earth's sandy beaches—Today and billion years ago. *GSA Today*, **18**: 4-9

Oosterbosch, R. and Schuiling, H., 1951. Copper Mineralisation in the Fungurume Region, Katanga. *Economic Geology,* **46**: 121-148

Pasteris, J.D. and Wopenka, B., 2003. Necessary, but Not Sufficient: Raman Identification of Disordered Carbon as a Signature of Ancient Life. *Astrobiology*, **3**: 727-738

Peel, M. C., Finlayson, B. L. and McMahon, T. A., 2007. Updated world map of the Köppen–Geiger climate classification. Hydrological Earth System Science, **11**: 1633–1644.

Pitcairn, I.K., Craw, D., Olivo, G.R., Kerrich, R. and Brewer, T.S., 2006. Sources of metals and fluids in orogenic gold deposits: insights from the Otago and Alpine schists, New Zealand. *Economic Geology*, **101**: 1525-1546.

Pollington, N., McGoldrick, P. and Selley, D., 2002. *Zambian Copper Belt Geochemistry: Part IIa Konkola North. AMIRA P554 internal communication, available at:* http://www.utas.edu.au/codes/publications/past-amira-reports

Porada, H., 1989. Pan-African rifting and orogenesis in southern to equatorial Africa and eastern Brazil: *Precambrian Research*, **44**: 103–136.

Porada, H. and Behr, H.J., 1988. Setting and sedimentary facies of late Proterozoic alkali lake (playa) deposits in the southern Damara Belt of Namibia. *Sedimentary Geology*, **58**: 171-194.

Porada, H., and Berhost, V., 1998. Thrust tectonics in the Domes region and Copperbelt of Zambia: Outline and outlook. *Frieberger Forschungshefte, Hefte C*., **475**: 145–162.

Porada, H. and Berhorst, V., 2000. Towards a new understanding of the Neoproterozoic-Early Palaeozoic Lufilian and northern Zambesi Belts in Zambia and the Democratic Republic of Congo. *Journal of African Earth Sciences,* **30**: 727-771.

Porten, K.W., Walderhaug, O and Torkildsen, G., 2015. Apatite overgrowth cement as a possible diagenetic temperature-history indicator. *Journal of Sedimentary Research*: **85**, 1478–1491

Pósfai, M., Kasama, T. and Dunin-Borkowski, R.E., 2013. Biominerals at the nanoscale: transmission electron microscopy methods for studying the special properties of biominerals. *In:* Nieto, F. and Livi, K., (*eds.)* Minerals at the Nanoscale. European Mineralogical Union Notes in Mineralogy, Vol. 14. European Mineralogical Union and the Mineralogical Society of Great Britain & Ireland, London, p.p. 375-433

Pracejus, B., 2008. *The Ore Minerals Under the Microscope, an Optical Guide*. Elsevier, Amsterdam. 875 p.p.

Rainaud, C., Armstrong, R.A., Master, S. and Robb, L.J., 1999. A fertile Palaeoproterozoic magmatic arc beneath the Central African Copperbelt. *In*: Stanley, C.J. et al. (eds.) *Mineral Deposits: Processes to Processing, Volume 2:* A. A. Balkema, Rotterdam, pp 1427-1430.

Rainuad, C., Master, S., Armstrong, R.A. and Robb, L.J., 2003. A cryptic Mesoarchean terrane in the basement to the Central African Copperbelt. *Journal of the Geological Society*, **160**: 11-14

Rampelotto, P.H., 2013. Extremophiles and Extreme Environments. *Life*: **3**, 482-485

Ramsay, C.R. and Davidson, L.R., 1970. The Origin of Scapolite in the Regionally Metamorphosed Rocks of Mary Kathleen, Queensland, Australia. *Contributions to Mineralogy and Petrology*, **25**: 41-51

Ramsay, C.R., and Ridgway, J., 1977. Metamorphic patterns in Zambia and their bearing on problems of Zambian tectonic history. *Precambrian Research*, **4**: 321–337.

Richards, J.P., Krogh, T.E., and Spooner, E.T.C., 1988a. Fluid inclusion characteristics and U-Pb rutile age of late hydrothermal alteration and veining at the Musoshi stratiform copper deposit, Central African Copper Belt, Zaire. *Economic Geology,* **83**: 118–139.

Richards, J.P., Cumming, G.L., Krstic, D., Wagner, P.A, and Spooner, E.T.C., 1988b. Pb isotope constraints on the age of sulfide ore deposition and U-Pb age of late uraninite veining at the Musoshi stratiform copper deposit, Central African Copperbelt, Zaire. *Economic Geology*, **83**: 724–741.

Ricke, W., 1964. Praparation von Schwefeldioxid zur massenspektrometrischen Bestimmung des Schwefel-Isotopen- Verhaltnisses ($^{34}S/^{32}S$) in naturlichen Schwefelverbindungen. *Zeitschrift fur analytische Chemie*, **199**: 401-13

Robertson, J., 2014. Personal Communication.

Rose, A.W., 1976. The effect of cuprous chloride complexes in the origin of red-bed copper and related deposits. *Economic Geology*, **71**: 1036–1048.

Rose, A.W., 1989. Mobility of copper and other heavy metals in sedimentary environments. *Geological Association of Canada, Special Paper,* **36**: 97–110

Rothschild, L.J. and Mancinelli, R.L., 2001. Life in extreme environments. *Nature*: **409**, 1092–1101

Salama, W., Anand, R.R., Kidder, J., Pinchand, T., 2016a. Multi-scale detection of buried mineralization and lithology through Kalahari transported cover in NW Botswana. *In*: Conference paper number 566, 35th International Geological Congress, Cape Town, South Africa

Salama, W., Gazley, M.F., Bonnett, L.C., 2016b. Geochemical exploration for supergene copper oxide deposits, Mount Isa Inlier, NW Queensland, Australia. *Journal of Geochemical Exploration*: **168**, 72–102

Schmandt, D., Broughton, D., Hitzman, M.W., Bjorklund, P.P., Edwards, D. and Humphrey, J., 2013. The Kamoa Copper Deposit, Democratic Republic of Congo: Stratigraphy, Diagenetic and Hydrothermal Alteration, and Mineralisation. *Economic Geology*, **108**: 1301-1324

Schoonen, M.A.A., 2004. Mechanisms of sedimentary pyrite formation. *In:* Amend, J. P., Edwards, K. J. and Lyons. T. W. (*eds.)* Sulfur biogeochemistry – Past and present. Geological Society of America Special Paper, Geological Society of America, Boulder, Colorado, p.p. 117–134

Schopf, J.W., 1976. Are the oldest "fossils" fossils? *Origins of Life*: **7**, 19-36

Schopf, J.W. and Walter, M.R., 1983. Archean microfossils: New evidence of ancient microbes. *In*: Schopf, J.W., *ed*., Earth's Earliest Biosphere: Its Origins and Evolution: Princeton University Press, Princeton, p.p. 214-239.

Schopf, J.W., Kudryavtsev, A.B., Sugitani, K. and Walter, M.R., 2010. Precambrian microbe-like pseudofossils: A promising solution to the problem. *Precambrian Research*, **179**: 191–205

Schulz, H.N., Brinkhoff, T., Ferdelman, T.G., Hernández Mariné, M., Teske, A. and Jørgensen, B.B., 1999. Dense Populations of a Giant Sulfur Bacterium in Namibian Shelf Sediments. *Science*: **284**, 493-495

Seibel, G., Rust, J. and Searston, S., 2013. Africo Resources Ltd. Kalukundi Copper – Cobalt Project, Democratic Republic of Congo, NI 43-101 Technical Report on Updated Mineral Resource Estimate. Prepared by AMEC Foster Wheeler PLC.

Selley, D., Broughton, D., Scott, R., Hitzman, M., Bull, S., Large, R., McGoldrick, P., Croaker, M., Pollington, N. and Barra, F., 2005. A New Look at the Geology of the Zambian Copperbelt. *In*: Hedenquist, J.W., Thompson, J.F.H., Goldfarb, R.J., Richards, J.P. (eds.), *Economic Geology 100th Anniversary Volume*. pp. 965–1000.

Selley, D., Duffett, M., Scott, R. and Hitzman, M., 2010a. Katangan Basin evolution and architecture: controls on ore location. *CODES-CSM/AMIRA P872: Sediment-hosted copper deposits of Congolese, Zambian and central Australian basin systems*. p.p. 125-174

Selley, D., McGoldrick, P., Gilbert, S. and Scott, R., 2010b. Geochemistry of the Kolwezi ores. *CODES-CSM/AMIRA P872: Sediment-hosted copper deposits of Congolese, Zambian and central Australian basin systems.* p.p. 269-301

Seo, J.H., Lee, S.K. and Lee, I., 2007. Quantum chemical calculations of equilibrium copper (I) isotope fractionations in ore-forming fluids. *Chemical Geology*, **243**: 225-237

Serdyuchenko, D.P., 1975. Some precambrian scapolite-bearing rocks evolved from evaporites. *Lithos*, **8**: 1-7

Shedd, K.B., 2014. *Cobalt*. U.S. Geological Survey, Mineral Commodity Summaries 2014

Sibson, R.H., Robert, F., and Poulsen, K.H., 1988. High-angle reverse faults, fluid-pressure cycling, and mesothermal gold-quartz deposits. *Geology*, **16**: 551–555

Sillitoe, R.H., 1973. The tops and bottoms of porphyry copper deposits. *Economic Geology*, **68**: 799-815

Sillitoe, R.H., Perelló, J., and García, A., 2010. Sulfide-bearing veinlets throughout the stratiform mineralization of the Central African Copperbelt: Temporal and genetic implications. *Economic Geology*, **105**: 1361–1368.

Sillitoe, R.H., 2012. Copper provinces. *Society of Economic Geologists Special Publication*, **16**: 1–18

Sillitoe, R.H., Perello, J., Creaser, R.A., Wilton, J. and Dawborn, T., 2015. Two Ages of Copper Mineralisation in the Mwombezhi Dome, Northwestern Zambia: Metallogenic Implications for the Central African Copperbelt. *Economic Geology*, **110**: 1917-1923

Sillitoe, R.H., Perelló, J., Creaser, R.A., Wilton, J., Wilson, A.J. and Dawborn, T., 2017. Age of the Zambian Copperbelt. *Mineralium Deposita*, **52**: 1245–1268

Smee, B.W., 1998. A new theory to explain the formation of soil geochemical responses over deeply covered gold mineralization in arid environments. *Journal of Geochemical Exploration*, **61**: 149-172

Sośnicka, M., 2016. Personal Communication.

Spry, P.G. and Gedlinske, B.L., 1987. *Tables for the Determination of Common Opaque Minerals.* The Economic Geology Publishing Company.

Stern, R.J., 1994. Arc assembly and continental collision in the Neoproterozoic East African orogen: implications for the consolidation of Gondwanaland. *Annual Review of Earth and Planetary Sciences 1994*, **22**: 319-351

Strother, P.K., and Barghoorn, E.S., 1980. Microspheres from the Swartkoppie Formation: A Review. *In*: Halverson, H.O., and van Holde, K.E. (*eds*.) The Origins of Life and Evolution. A.R. Liss, New York, p.p. 1-18.

Sweeney, M.A. and Binda, P.L., 1989. The role of diagenesis in the formation of the Konkola Cu-Co Orebody of the Zambian Copperbelt. *Geological Association of Canada Special Paper*, **36**: 499-518.

Sweeney, M.A., Binda, P.L. and Vaughan, D.J., 1991. Genesis of the ores of the Zambian Copperbelt. *Ore Geology Reviews*, **6**: 51-56

Syamujaye, S.K., 2014. Zambia Mining website: http://www.zambia-mining.com/country.html Retrieved: 20/03/2014

Takeno, N., 2005. *Atlas of Eh-pH diagrams: intercomparison of thermodynamic databases.* Geological Survey of Japan Open File Report No.419. National Institute of Advanced Industrial Science and Technology, Research Center for Deep Geological Environments

Taylor, J.H., 1954. The lead–zinc–vanadium deposits at Broken Hill, Northern Rhodesia. *Colonial Geology and Mineral Resources*, **4**: 335–365

Taylor, R., 2011. Gossans and Leached Cappings: Field Assessment. Springer-Verlag Berlin Heidelberg, p.p. 146.

Taylor, S.R. (1964). Abundance of chemical elements in the continental crust: a new table. *Geochimica et Cosmochimica Acta*, **28**: 1273-1285

Tembo, F., Kampunzu, A.B. and Porada, H., 1999. Tholeiitic magmatism associated with continental rifting in the Lufilian Fold Belt of Zambia. *Journal of African Earth Sciences*, **28**: 403-425.

Thode, H.G., 1991. Sulphur Isotopes in Nature and the Environment: An Overview. *In:* H.R. Krouse and V.A. Grinenko (*eds*.) Stable Isotopes in the Assessment of Natural and Anthropogenic Sulphur in the Environment. John Wiley & Sons Ltd, pp 1-26.

Timmermans, E., 2015. Quantitative mineralogy of a saprolite-soil sequence on a talc and chlorite bearing substrate, Upper Katanga, D.R. Congo. Unpublished MSc. Thesis, University of Ghent.

Torrealday, H.I., Hitzman, M.W., Stein, H.J., Armstrong, R., and Broughton, D., 2000. Age and duration of mineralization at the vein-hosted Kansanshi copper deposits, northern Zambia through Re-Os and SHRIMP U-Pb methods. *Economic Geology*, **95**: 1165–1170

Turlin, F., Eglinger, A., Vanderhaeghe, O., André-Mayer, A.-S., Poujol, M., Mercadier, J., Bartlett, R., 2015. Synmetamorphic Cu remobilization during the Pan-African orogeny: Microstructural, petrological and geochronological data on the kyanite-micaschists hosting the Cu(-U) Lumwana deposit in the Western Zambian Copperbelt of the Lufilian belt. *Ore Geology Reviews*, **75**: 52-75.

Turner, E.C., Broughton, D.W., Brooks, T., 2018. Neoproterozoic carbonate lithofacies and ore distribution at the Kipushi Cu-Zn deposit, Democratic Republic of Congo, and Gayna River Zn Camp, Northwest Territories, Canada. *Economic Geology*, **113**: 779-788.

Unrug, R., 1988. Mineralization Controls and Source of Metals in the Lufilian Fold Belt, Shaba (Zaire), Zambia, and Angola. *Economic Geology*, **83**: 1247-1258

van Langendonck, S., Muchez, P. Dewaele, S., Kaputo-Kaluni, A. and Cailteux, J., 2013. Petrographic and mineralogical study of the sediment-hosted Cu-Co ore deposit at Kambove West in the central part of the Katanga Copperbelt (DRC). *Geologica Belgica*, **16**: 91-104

van Wilderode, J., El Desouky, H.A., Elburg, M.A., Vanhaecke, F. and Muchez, P., 2014. Metal sources for the Katanga Copperbelt deposits (DRC): insights from Sr and Nd isotope ratios. *Geologica Belgica*, **17**: 137-147

Vu, B., Chen, M., Crawford, R.J. and Ivanova, E.P., 2009. Bacterial Extracellular Polysaccharides Involved in Biofilm Formation. *Molecules:* **14**, 2535 – 2554.

Wacey, D., McLoughlin, N., Kilburn, M.R., Saunders, M. Cliff, J.B., Kong, C., Barley, M.E. and Brazier, M.D., 2013. Nanoscale analysis of pyritized microfossils reveals differential heterotrophic consumption in the ∼1.9-Ga Gunflint chert. *Proceedings of the National Academy of Sciences*, **110**: 8020-8024

Waggoner, B.M. 1996. Bacteria and protists from Middle Cretaceous amber of Ellsworth County, Kansas. *PaleoBios*, **17**: 20-26

Wagner, T. and Cook, N. J., 1999. Carrollite and related minerals of the linnaeite group: Solid solutions and nomenclature in the light of new data from the Siegerland District, Germany. *The Canadian Mineralogist*, **37**: 545-558

Wakefield, J., 1978. *Samba: a deformed porphyry-type copper deposit in the basement of the Zambian Copperbelt*. Transactions of the Institute of Mining and Metallurgy 87, pp 43-52

Walker, T.R., 1989. Application of diagenetic alterations in redbeds to the origin of copper in stratiform copper deposits. *In*: Boyle RW, Brown AC, Jefferson CV, Jowett EC, and Kirkham RV (*eds.)* Sediment-Hosted Stratiform Copper Deposits, Geological Association of Canada Special Paper 36, pp. 85–96. Ottawa: Geological Association of Canada.

Walsh, M.M., 1992. Microfossils and possible microfossils from the Early Archean Onverwacht Group, Barberton Mountain Land, South Africa. *Precambrian Research*, **54**: 271–292

Walsh, M.M. and Lowe, D.R., 1985. Filamentous microfossils from the 3500 Myr-old Onverwacht Group, Barberton Mountain Land, South Africa. *Nature*, **314**: 530–532

Weiner S. and Dove P.M., 2003. An overview of biomineralization processes and the problem of the vital effect. *Mineralogy and Geochemistry*: **54**, 1-29

Welch, S.A., Barker, W.W., and Banfield, J.F., 1999. Microbial extracellular polymers and plagioclase dissolution. *Geochimica et Cosmochimica Acta*: **63**, 1405–1419

Wendorff, M., 1995. Gravity emplacement of synorogenic megabreccias with Cu-Co mineralisation in the Katangan of Shaba, Zaire. *In:* Pasava, J., Kribek, B., Zak, K. *(eds.),* Mineral Deposits: From Their Origin to Their Environmental Impacts (Addendum: Late Contributions). Balkema, Rotterdam, pp. 28-29.

Wendorff, M., 2000. Genetic aspects of the Katangan megabreccias: Neoproterozoic of Central Africa. *Journal of African Earth Sciences*, **30**: 703-715

Wendorff, M., 2003. Stratigraphy of the Fungurume Group – evolving foreland basin succession in the Lufilian fold-thrust belt, Neoproterozoic-Lower Palaeozoic, Democratic Republic of Congo. *South African Journal of Geology*, **106**: 17-34.

Wendorff, M., 2005. Sedimentary genesis and lithostratigraphy of Neoproterozoic megabreccia from Mufulira, Copperbelt of Zambia. *Journal of African Earth Sciences*, **42**: 61–81.

Westall, F., 1999. The nature of fossil bacteria: A guide to the search for extraterrestrial life. *Journal of Geophysical Research*: **104**, 16437-16451

White, D.E., 1968. Environments of generation of some base-metal ore deposits. *Economic Geology*, **63**: 301–335

White, W.S., 1971. A paleohydrologic model for mineralization of the White Pine copper deposit, northern Michigan. *Economic Geology*, **66**: 1–13,

Winfield, O. and Robinson, I.C., 1963. The structures of Chibuluma mine. *In:* Lombard, J., Nicolini, P. *(eds.),* Stratiform Copper Deposits in Africa. Association of African Geological Surveys, Paris, pp. 192–202.

Winter, D., 2016. WebElements website: http://www.webelements.com/periodicity/atomic_weight/ Retrieved: 01/02/2016

Wopenka, B. and Pasteris, J.-D., 1993. Structural characterisation of kerogens to granulite-facies graphite: Applicability of Raman microprobe spectroscopy. *American Mineralogist*, **78**: 533-557

Wood, D., Halley, S., Stoltze, A., Goswell, H., Godfroid, J., Hitzman, M., Jack, D. and Meighan, C., 2014. *Using Multi-Element Geochemistry to Map Multiple Components of a Mineral System. Case Study From a Sediment Hosted Cu-Ni Camp, NW Province Zambia*. SEG 2014 Conference

Woodcock, N.H. and Mort, K., 2008. Classification of fault breccias and related fault rocks. *Geological Magazine Rapid Communication*, **145**: 435-440

Woodhead, J., 2013. *The Neoproterozoic Roan Group in the Zambian Copperbelt: Sequence Stratigraphy, Alteration and Mineralization*. Unpublished PhD thesis, Colorado School of Mines.

Yeldar, R., 2012. *Eurasian Natural Resources Corporation PLC – Annual Report and Accounts 2012*

APPENDICES

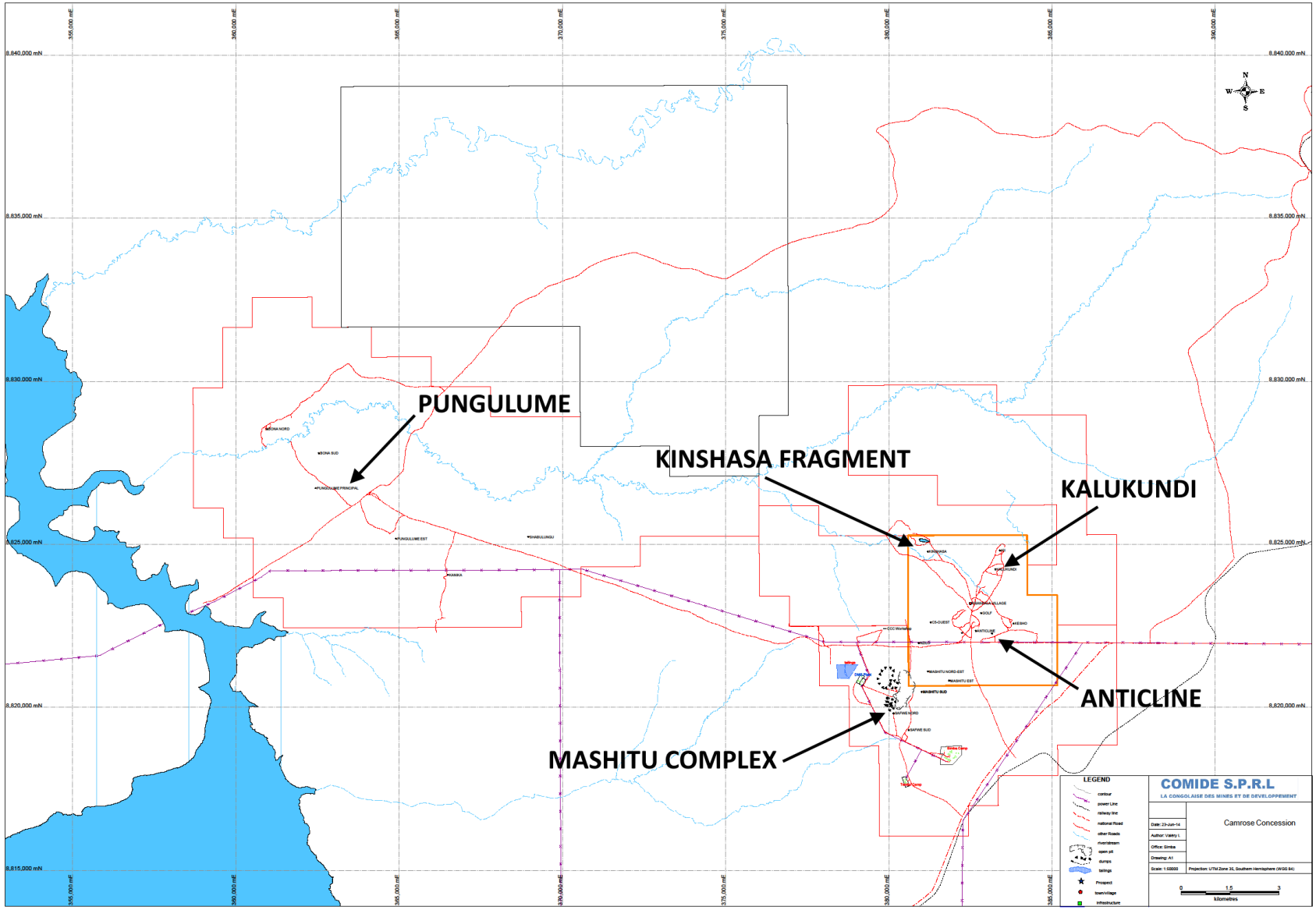

***Appendix 1**: Regional infrastructure map of the Camrose concession licence of Comide S.P.R.L., showing the location of known deposits and prospects. Image provided by Comide and modified by the author.*

Stratigraphic Column for the Shaba systeme									
SUBDIVISIONS					local name	System stratigraphy	Colours adopted by Gecamines		
Systeme	Series	Formation		level			Small Scale 1/20000 and less		large scale 1/500 to 1/200000
SHABA SYSTEM	KUNDELUNGU KS	3 plateaux	33		Plateau Sandstone and conglomerate	Fine medium or coarse grain arkose, Mica abundant in finely coarse crystalline beds. Red, pink or Lilac. Massive texture or finely laminated, generally irregular. Grevish Arkosic Orthoconglomerate. clasts inferior to 4 mm.	245	245	245
			32						
			31						
		2 Kiubo	22			Sandy shale alternating with clay shale and fine carbonated micro Sandstone. Due to alteration, sandy shale or Red clay, lilac or purple.	10	10	60
			21	132	Kiubo Sandstone	micro Sandstone alternating with feldspatic sandy shale (pink grey) and clayey shale (purple grey)		10	
			13	131	Pink Oolitic Limestone	Thinly impure limestone, pink grey, with sometimes small flattened oolite	50	50	
			12	122		Northern facies : clayey or sandy shales, carbonated, non-micaceous, gey green or grey purple Southern facies : Calcareous shales with steady lamination		50 60	
				121	Pink Limestone	Thinly calcareous dolomite, pink to clear grey.		60	
			11		Petit Conglomerat	Tillite with clayey shales or sandy dolomitic tills, massive, grey purple. 0.1 to 3cm clasts.	80	80	80
	NGUBA KI	2 Monwezi	22			Not very micaceous sandy dolomitic shales, green grey or purple. Yellow or red lilac due to alteration	35	35	
			21			Coarse dolomitic shale, none or finely micaceous, green grey or purple and yellow grey or lilac grey after alteration.		35	
		1 Likasi	13			Northern facies: Massif shale, not very dolomitic, with finely arkosic layers Southern Facies: Micro sandy non micaceous shale, non stratified, purple grey to lilac grey.	65	65	
			12	122	Katontwe Limestone	Northern facies: fine to coarse crystalline impure dolomite, pinkish with Chlorite joints Or fine to coarse crystalline pure calcareous dolomite, grey to blackish Southern facies: Dolomite and blue limestone		141	
				121		Northern facies: black grey clayey shales alternating with finely laminated sandy shale, gey, brown or lilac. Southern facies: fine shales non micaceous. Red, brown, yellow or clear lilac.		59	
			11		Grand Conglomerat	Tillite with clayey shales or sandy dolomitic tills, unstratificated, grey to greenish grey. 1mm to 50 cm clasts.	49	49	49
	ROAN "R"	R4	42		Upper Mwashya	Clayey shale, finely laminated, clear green grey lilac	100	100	100
			41		Lower Mwashya	Green grey or black red coarse Clayey shales alternating with alterated dolomite in silicaceous rock		120	120
		R3	32		Mofa and Upper Dipeta	Massive macrocrystalline dolomite in thick layers. White, beige or	140	140	140
			31		R.G.S. or Lower Dipeta	sandy shales or micro sandstone, thinly feldspathic, massive, clear grey to purple grey.			140
		R2	23	232	Upper C.M.N.	Massive impure microcrystalline dolomite or well stratified, Clear grey or clear pink, with clear grey conglomeratic dolomitic sandstone. Micro crystals of pyrite disseminated.	180	160	90
				231	Lower C.M.N	From bottom to top. Felspatic dolomitic sandstone, medium grained, grey. Carbonaceous dolomitic shales layers. Then impure talc dolomite with chlorite and sericite alternating with clayey dolomitic carbonaceous shales (grey to black).Micro crystals of pyrite disseminated.			
			22		Upper S.D.	Upper dolomitic shales, subdivided as follows: SD. 3b Finely laminated black carbonaceous sandy and strongly dolomitic shale. Pyrite finely disseminated. SD. 3.a α β Clear voided silicic dolomite. 50 cm. (White dolomite). SD 3a Finely laminated and strongly dolomitic micro sandstone, clear green grey. Micro crystals of pyrite present SD. 2d Finely laminated sandy graphitic Shale, black or grey, weakly dolomitic. Pyrite and sometimes chalcopyrite disseminated. SD 2c Finely laminated sandy dolomitic shale, clear green. SD 2b Micro to medium grained weakly impure dolomite, clear grey dolomite. Presence of some thick stromatolitic beds SD 2a Micro sandstone and dolomitic graphitic clayey shale, finely laminated, lightly irregular for the sandstone.			65 65 65 65
					S.D 1.b or BOMZ	SD 1b BOMZ (Black Ore Main Zone) blue-grey, crystalline dolomite			59
					S.D. 1.a or S.D.B.	Sandy Shale, strongly dolomitic, Finely and regularly laminated. Cd, Cr and Br abundant. Clear to black grey			59
			21	213	R.S.C	Massive siliceous dolomite with some sandy clayey shale layers. Rare Stromatolite. Grey			171
					R.S.F	Siliceous, dolomitic shales, micaceous, light-grey weathering whitish, extremely finely laminated			80
				212	D STRAT	argilitic dolomite. well bedded to laminated, light-grey to light-brown, yellow weathering, chert horizons, nodule layer towards top			30
				211	RAT Grises	argillitic sandstones, massive and dolomitic, light-grey. talc present in varying quantities			249
		R1			R.A.T. 2	argillitic siltstones, dolomitic, banded to well bedded containing beds of dolomitic sandstone and occasionally beds of stromatolitic dolomite	249	249	240
					R.A.T.1	upper portion: silty argillite, red and bedded. Lower portion unknown			
					Basal Pudding stone	Unknown formation, transgression conglomerate and arkoses in other localities	159	159	159

***Appendix 2**: Stratigraphic column for the Katangan Supergroup as used by Gecamines. Image provided by Comide.*

Appendix 3*: Scanned lithostratigraphic logs of Comide diamond drill-core from holes MSSD075, MSSD080, MSSD083 and MSSD140 at Mashitu South, compiled by the author.*

***Appendix 3a**: Log of MSSD075*

SUMMARY DIAMOND DRILLING LOG

By: GMG
Date: 05/06/14

Hole: MSSD075
Page 1 of 5

Depth (m)	Interp	Lith1	Lith2	Graphic Log (mm) (mud, 0.5, 2, 8, 32, 64, max)	Summary Description	Mineralisation %	Style	Mi
2, 4, 6, 8, 10, 12, 14, 16, 18		CLY			Red brown orange clay. Roots in top 5m.			
20		CLY	BRE		Clay rich reddish-brown breccia. Clasts of quartz + blue + red dolomite supported by a clay matrix.			
22, 24		CLY	SND		Grey-brown course sandy clay rich layer, broken into chunks at top. Haematite, goethite and possibly Mn oxides	~10%		Mn? Fe?
26		ARG	CLY		Bedded, highly weathered pink argillite with haematite veins. Brecciated towards base.			
28		CLY	SND		Grey brown coarse sandy clay rich layer.	~10%		Mn? Fe?
30, 32		ARG	CLY		Bedded, highly weathered pink argillite with haematite veins in fractures. Some quartz fragments.			
		ARG	BRE		Brecciated argillite, whitish.			
34		CLY	BRE		Black brownish clay rich breccia, polymictic with black layer in middle. Argillite clasts + quartz			
36		ARG			Whitish yellow fractured argillite, intense argillic alt.			
38, 40		BRE	ARG		Yellow to blue to red brecciated argillitic dolomite. Gravel to pebble sized clasts, perhaps in situ. Some Mn oxides visible.	~1%		Mn?
42, 44, 46, 48		DOL	ARG		Dark blue-black graphitic dolomitic argillite. Variable lithologies from graphitic laminar siltstone/mudstones to beds of quartz pebbles/pseudomorphs, often tectonically deformed, to nodular dolomite beds. Over the metre scale variation. Intruded by 'dolo-dykes' which host Cu-sulphides occasionally. (Sometimes Cu oxides too)			

SUMMARY DIAMOND DRILLING LOG

By: GMG
Date: 05/06/14

Hole: MSSD075
Page 2 of 5

Depth (m)	Interp	Lith1	Lith2	Graphic Log (mm) (mud, 0.5, 2, 8, 32, 64, max)	Summary Description	Mineralisation %	Mineralisation Style	Mineralisation Min
52–92		DOL	ARG		Sometimes wavy laminations may indicate algal sedimentation, but soft-sediment / tectonic deformation is definitely apparent. Some sigmoidal quartz clasts.			
52–54						~0.001	vein	Cpy? Bo? Mal.
94–98		DOL			Blue-grey coarsely crystalline dolomite. Evidence of significant dolomitisation and silicification.			

SUMMARY DIAMOND DRILLING LOG

By: GMG
Date: 05/06/14

Hole: MSSD075

Depth (m)	Interp	Lith1	Lith2	Graphic Log (mm) (mud, 0.5, 2, 8, 32, 64, max)	Summary Description	Mineralisation %	Mineralisation Style	Mineralisation Min
102, 104, 106, 108, 110, 112, 114, 116, 118, 120, 122		DOL	ARG		Dark-blue-black graphitic dolomitic argillites. Similar to 2nd unit above but less graphitic shales apparent.			
124, 126, 128, 130, 132, 134, 136, 138, 140, 142, 144, 146, 148		DOL	ARG		Massive (but occasionally bedded) red-green patchy dolomitic argillite. Haematisation in red alteration patches. Intruded by dolo-dykes and well sorted. Dolo-dykes are occasionally mineralised with Cu sulphides and there is some stratiform Py, usually haematised.	0.001	Vein Strat.	Cpy? Py FeO

SUMMARY DIAMOND DRILLING LOG

By: GMG
Date: 05/06/14

Hole: MSSD075
Page 4 of 5

Depth (m)	Interp	Lith1	Lith2	Graphic Log (mm) (mud, 0.5, 2, 8, 32, 64, max)	Summary Description	Mineralisation %	Mineralisation Style	Mineralisation Min
152				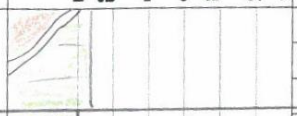				
154 156 158		SHA		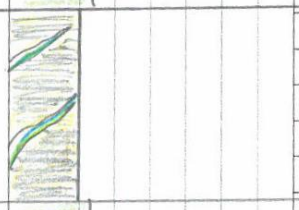	Yellowish, laminated shale. Highly altered and fissile in places. Significant alteration along what look like relict dolo dykes, Malachite in fractures and along dolo dyke relics.	~0.5%	Vein + Frac	Mal.
160 162 164 166 168 170 172 174 176 178 180 182 184 186		DOL	ARG	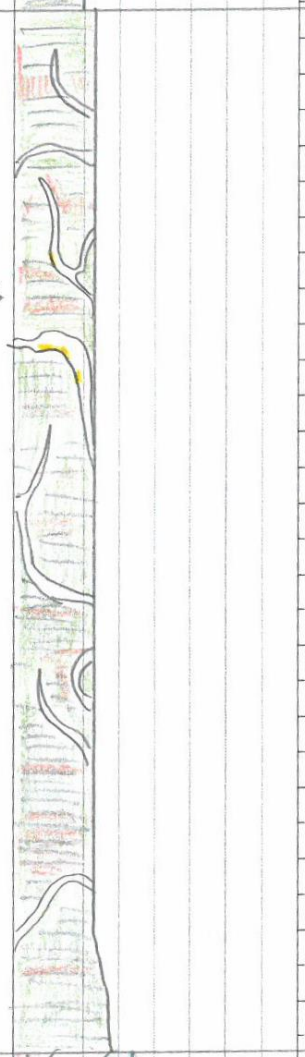	Bedded red-green patchy dolomitic argillite. Haematization mostly along bedding planes. Intruded by dolo-dykes which sometimes host mineralisation in the form of Cu-sulphide.	~0.01	Vein	Cpy
188 190 192 194 196 198		DOL			Coarsely crystalline massive pink-red-blue dolomite. Highly dolomitised and in places, silicified. Vuggy. Pervasive malachite, Co. dolomite and disseminated chalcocite, (pyolusite?), maybe heterogenite? Veins at margins (look like dolo-dykes hosting Co. dol.)	~3%	Perv. Diss. Vein.	Mal Co. Dol. Cha Het Pyr Co. dol.

SUMMARY DIAMOND DRILLING LOG

By: GMG
Date: 05/06/14

Hole: MSSD075
Page 5 of 5

Depth (m)	Interp	Lith1	Lith2	Graphic Log (mm) (mud, 0.5, 2, 8, 32, 64, max)	Summary Description	Mineralisation %	Mineralisation Style	Mineralisation Min
202 – 204 – 206		DOL	ARG		Blue-grey laminated dolomitic argillite, silicified in contact with above unit. Not particularly vuggy or mineralised, nor is it intruded by dolo-dykes.			
208 – 210		DOL	ARG	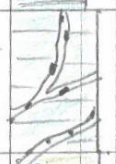	Bedded, grey green-blue dolomitic argillite, intruded by dolo-dykes hosting carrollite and chalcocite.	~2%	vein.	Car. Cha.
212		DOL	ARG		Massive greenish dolomitic argillite, intruded by dolo-dykes hosting cobaltian dolomite + haematite.	~0.5%	vein	Co. dol.
214 – 216		SIL			Massive sandy siltstone with whitish vein/nodules. Intruded by dolo-dykes. Reddish.			
218					Poorly sorted polymictic matrix supported rounded pebble conglomerate, sand to pebble clasts.			
220					Reddish sandy siltstone brecciated by dolo-dykes.			
222 – 224 – 226 – 228 – 230					E.O.H.			

***Appendix 3b**: Log of MSSD080.*

SUMMARY DIAMOND DRILLING LOG

By: GMG
Date: 04/06/2014

Hole: MSSD080
Page 1 of 6

Depth (m)	Interp	Lith1	Lith2	Graphic Log (mm) (mud, 0.5, 2, 8, 32, 64, max)	Summary Description	Mineralisation %	Mineralisation Style	Mineralisation Min
2, 4, 6, 8, 10, 12, 14, 16, 18, 20		CLY			Reddish - orange clay. Organic brown material + rootlets in top metre. Becomes more rubbly towards base.			
22, 24, 26, 28, 30, 32, 34, 36, 38, 40		CLY			Whitish clay with mottled black mineral - appears to be intense argillic alteration. Towards the bottom pebble - gravel sized clasts of rock are apparent, some quartz clasts, others are altered completely to clay + fragmented, some clasts of dolomite.			
42		CLY			Black clay rich layer, heavily fragmented.	~10%	Mas.	Mn?
44, 46, 48		CLY	BRE		Clay rich whitish breccia, polymictic, with clasts of dolomite + quartz, pebble to gravel sized. Heavy argillic alteration. Rounded fragments.			

SUMMARY DIAMOND DRILLING LOG

By: GMG
Date: 04/06/2014

Hole: MSSD080

Depth (m)	Interp	Lith1	Lith2	Graphic Log (mm) (mud, 0.5, 2, 8, 32, 64, max)	Summary Description	Mineralisation %	Mineralisation Style	Mineralisation Min
		DOL	BRE		Grey laminated dolomite - brecciated, silicified and argillic alteration. Silty.			
52 – 64		BRE	DOL	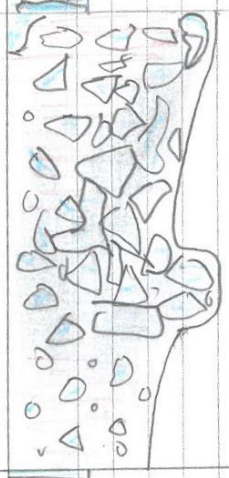	Reddish - blue breccia with clasts of dolomite (blue) - sub angular clasts, many proto breccia. Intense argillic alteration, haematisation + silicification of dolomite clasts. Finer clasts towards base.			
66 – 68		DOL	ARG		Blue-grey laminated dolomitic argillite. Brecciated in places. intense argillitic alteration.			
70 – 72		CLY	BRE	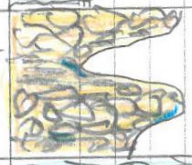	Yellowish clay rich rock, fragmented into gravel sized clasts, intense argillitic alteration and chrysocolla mineralisation towards base.	~0.5	Diss.	Cry
74 – 82		DOL	BRE	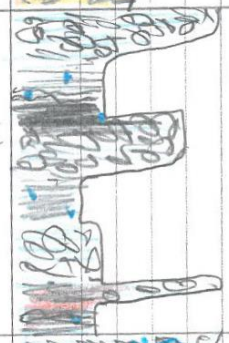	Blue grey wavy laminated (algal?) dolomitic argillite with fine veins. Intense argillic alteration, brecciated into clays and gravels in places (one horizon black (Mn?) and one horizon red (Fe?)) Sporadic chrysocolla mineralisation.	~0.5	Diss.	Cry Mn? Fe?
84 – 90		DOL	ARG	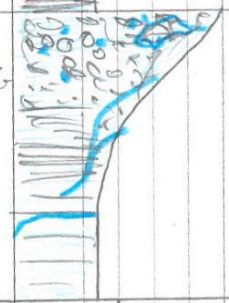	Blue grey layered dolomitic argillite, coarse crystalline dolomitisation in places. Brecciated to clasts, often gravel sided, more towards top. Argillic alteration. Abundant disseminated and fracture coating chrysocolla, as well as dendritic Mn oxides.	~3%	Diss + Frac.	Chry Mn?
92 – 96		DOL		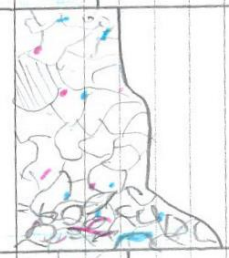	Blue coarsely crystalline dolomite, some relict bedding structures. Patches of silicification and brecciated to gravel towards base. Disseminated + fracture filling chrysocolla + cobaltian dolomite.	~0.01	Diss + Frac.	Cry Co. Dol.
98				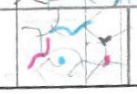				

SUMMARY DIAMOND DRILLING LOG

By: GMG
Date: 04/06/2014

Hole: MSSD080
Page 3 of 6.

Depth (m)	Interp	Lith1	Lith2	Graphic Log (mm) (mud, 0.5, 2, 8, 32, 64, max)	Summary Description	Mineralisation %	Mineralisation Style	Mineralisation Min
102 – 104		DOL		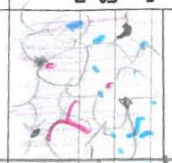	Reddish blue coarsely crystalline silicified dolomite. Vuggy with voids infilled by chrysocolla, cobaltian dolomite + chalcocite	~0.5	Diss. + Frac.	Chry Co. Dol. Cha
104 – 134		DOL			Blue-grey medium-fine crystalline dolomite with relict bedding towards top of profile. Intense dolomitisation + silicification, protobreccia - chaotic breccia and intruded by dolo-dykes in upper half. Lower half more massive + without relict bedding. Disseminated + vein chalcocite, bornite, malachite and chrysocolla. Cobaltian dolomite rare.	~1%	Diss + Vein	Cha Bo Cry Mal
134 – 148		DOL	ARG		Green-red bedded dolomitic argillite. Intruded by dolo-dykes + altered to red colour in patches. More bedding towards base			

SUMMARY DIAMOND DRILLING LOG

By: GMG
Date: 04/06/14

Hole: MSSD080
Page 4 of 6

Depth (m)	Interp	Lith1	Lith2	Graphic Log (mm) (mud, 0.5, 2, 8, 32, 64, max)	Summary Description	Mineralisation %	Mineralisation Style	Mineralisation Min
152, 154, 156, 158, 160, 162, 164, 166, 168, 170, 172, 174, 176, 178, 180, 182								
184, 186, 188, 190		DOL	BRE		Chaotic - mod. breccia of the green dolomitic argillite. Silicified in places and significantly intruded by dolo-dykes. Fracture controlled malachite mineralisation.	~0.1%	Frac.	Mal.
192, 194, 196, 198		DOL	ARG		Green-red bedded dolomitic argillite intruded by dolo dykes.			

SUMMARY DIAMOND DRILLING LOG

By: GMG
Date: 04/06/14

Hole: MSSD080

Depth (m)	Interp	Lith1	Lith2	Graphic Log (mm)	Summary Description	Mineralisation %	Mineralisation Style	Mineralisation Min
202, 204, 206, 208, 210, 212		DOL	ARG					
214, 216, 218		SHA			Black finely laminated graphitic shale. Occasional beds of very fine grained stratiform pyrite, associated with chalcocite.	~0.5%	Strat.	Py Cha
220, 222, 224, 226, 228, 230, 232, 234, 236, 238, 240, 242, 244, 246, 248		DOL	ARG		Green-red dolomitic argillite, intruded by dolodykes. Occassionally disseminated + dolo-dyke hosted chalcopyrite + chalcocite ↓ Mostly towards base.	~0.01	Diss. + Vein	Cpy? Cha?

SUMMARY DIAMOND DRILLING LOG

By: GMG
Date: 04/06/14

Hole: MSSD 080

Depth (m)	Interp	Lith1	Lith2	Graphic Log (mm)	Summary Description	Mineralisation %	Mineralisation Style	Mineralisation Min
252–260		DOL	ARG			~0.1%	Diss + Vein	Cpy Cha
262–274		DOL		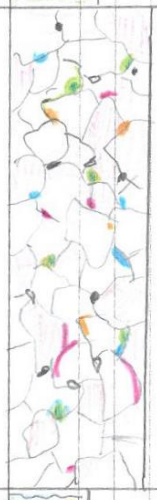	Massive red-white vuggy coarsely crystalline dolomite. Silicified in places. Vugs filled with Malachite, chrysocolla, chalcocite, Native Cu, possible carrollite (brighter silver than chalcocite). Also some Co. dolomite	~2%	Diss.	Mal Cry Cha Nat. Cu Car? Co. Dol.
276–280		DOL	ARG	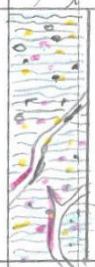	Blue-grey wavy laminated (algal?) dolomitic argillite - vuggy and intruded by dolo-dykes. Dolo-dykes + vugs host Chalcopyrite, chalcocite, bornite, carrollite + cobaltoan dolomite.	~5%	Diss + Vein	Cpy Cha Bo Car Co. Dol
282–286		DOL	ARG	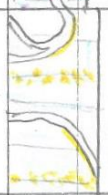	Blue-grey bedded dolomitic argillite, intruded by dolo-dykes, often silicified, evidence of tight isoclinal folding (offset by dolo-dykes). Stratiform and vein-related chalcopyrite.	~2%	Strat. + vein.	Cpy
288–292		DOL	ARG		Green grey massive dolomitic argillite, intruded by dolodykes and host to heavy talc alteration			
294–296		SIL			Red-green sandy siltstone, massive with alteration spots, intruded by dolodykes			
298		BRE			Chaotic breccia of red-green sandy siltstone matrix of dolomite, mostly + clay.			

E.O.H.

SUMMARY DIAMOND DRILLING LOG

By: GMG
Date: 30/05/2014

Hole: MSSD083
Page 1 of 7

Depth (m)	Interp	Lith1	Lith2	Graphic Log (mm) (mud, 0.5, 2, 8, 32, 64, max)	Summary Description	Mineralisation %	Mineralisation Style	Mineralisation Min
2, 4, 6, 8, 10		CLY			Red-brown earthy clay with roots in the first ½ meter. Well sorted but small quantities of yellowish rock fragments are present			
12, 14		CLY			Grades into yellowish-ochre coloured gritty/sandy poorly sorted clay with occasional gravel-sized clasts of pale, soft rock, streaked with patches of reddish clay and contains tiny grains of specular haematite.			
16, 18, 20, 22, 24, 26, 28, 30, 32, 34		CLY	BRE		Grey-white-yellow argillitic polymictic breccia - predominantly whitish clay with sub-rounded to sub angular clast of varying colours. Occasional areas of fine grained disseminated specular haematite and black mineral (more along veins/ fractures than black mineral. Rock seems to have undergone intense argillic alteration. Clast supported, with some matrix supported areas			
36		BRE	CLY		3 layers of fine grained black material amongst breccia. Mn? Fe? Oxides?			Mn? Fe?
38, 40, 42, 44		BRE	CLY	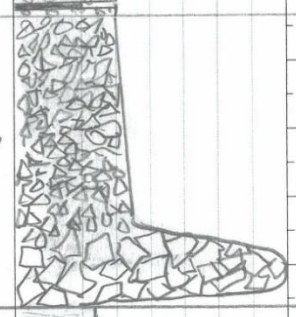	Yellow to grey white to red brecciated rock. Angular clasts at base grading to sub rounded at top. Clasts are mostly argillite + quartz, poorly sorted (gravel → boulders). Clasts at base have thin veins of haematite (red) running through and dendritic black mineral (Mn oxide pyrolusite?) and yellow streaks. Intense argillic alteration. Mostly chaotic breccia			
46, 48		DOL	SHA		Stylolitic calcareous argillite. Grey blue in colour. Wavy interbedded dark and light layers that seem tectonically disturbed. Some dark layers are nodular and seem wildly deformed. Some appear quartz rich. All layers are intruded/brecciated by dolomite dykes			

SUMMARY DIAMOND DRILLING LOG

By: GMG
Date: 30/05/2014

Hole: MSSD083

Depth (m)	Interp	Lith1	Lith2	Graphic Log (mm) (mud, 0.5, 2, 8, 32, 64, max)	Summary Description	Mineralisation %	Mineralisation Style	Mineralisation Min
52, 54, 56, 58, 60, 62, 64, 66, 68, 70, 72, 74, 76, 78, 80, 82, 84, 86, 88, 90, 92, 94, 96, 98		DOL	SHA	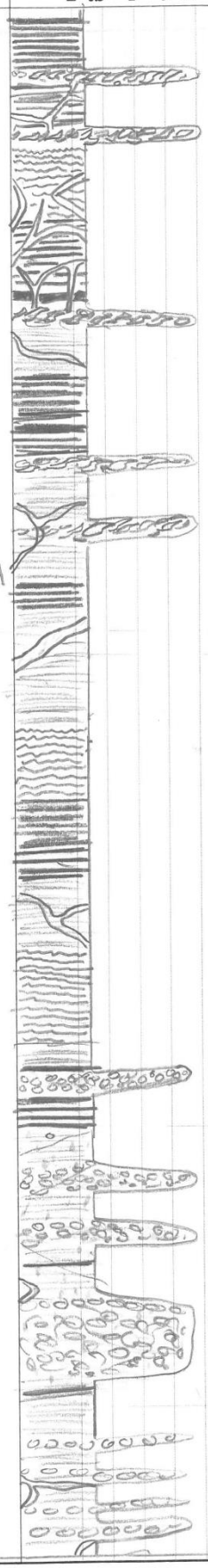	These dykes appear to exhibit little deformation. Towards top and middle of the unit the dolomite is highly carbonaceous with black shales in laminations with dolomite shales. These carbonaceous layers, where thicker, are highly susceptible to brittle fracturing by the dolomite dykes. In the middle of the unit are multiple beds ~ 50 cm thick of gravel sized rounded quartz clasts in a matrix of fine grained dark material. These often exibit tectonic deformation in the form of S-C fabrics and sigmoidal quartz clasts. The dolomite dykes may intrude along tension gashes. Some layers appear to have wavy algal laminations, others appear to exhibit soft sediment deformation. Some of the dolomite dykes appear to be syn-sedimentary, 'pushing up' through layers of sediment and deforming them. young young young These syn-sedimentary structures seem to contain very fine grained metallic yellow sulphides (Syn sedimentary pyrite?). Occasional layers of calcitic, apparently preserved, carbonate. Fragmental angular matrix supported breccia of carbonate clasts, with dropstones suggesting younging direction @ 84.94m. young Inconsistent younging directions and structural deformation suggests folding, but most young downwards. Algal layers young down. Partial overturning? More intense massive dolomitisation, breccias (sedimentary?) and less carbonaceous material from 86m downwards. • Chalcopyrite min. in dolomite dykes @ 70.63, for 60cm. • Disseminated and dolomite-vein hosted Cu sulphides + silver cubic sulphides (carrollite?) from 75.93m to 95m	~3%	Vein	Cpy?
						~0.3%	Diss. Vein.	Cpy? Car?

SUMMARY DIAMOND DRILLING LOG

By: GMG
Date: 31/05/2014

Hole: MSSD083

Depth (m)	Interp	Lith1	Lith2	Graphic Log (mm) (mud, 0.5, 2, 8, 32, 64, max)	Summary Description	Mineralisation %	Mineralisation Style	Mineralisation Min
102–116		DOL		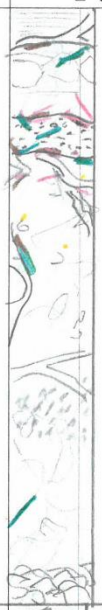	Blue-grey-white dolomitic argillite, intense dolomitisation and silicification. Brecciated in places. Massive + crystalline in some places. 'Dolo-dykes' less prevalent than above unit. Some relict sedimentary textures seen to remain - algal bedding maybe. Disseminated silver mineral (cerrolite?) with some disseminated copper sulphide minerals. Dark grey brown mineral, green mineral (malachite?) and pink mineral (cobaltian dolo./erythrite) hosted along fractures. Brecciated frequently. Some haematisation along veins.	~1%	Vein Diss	Mal? Ery? Het? Cha? Bo? Car? Cha?
118–120		DOL	ARG		Blue-grey dolomitic argillite, intruded by 'dolo-dykes'			
120–128		DOL			Red-white-blue-green massively crystalline dolomite with breccias. Pervasive red haematisation overprinting protolith - disseminated silver minerals and vein-hosted pink erythrite/cobaltian dolomite. Some original sedimentary structures left e.g. wavy algal bedding.	~1%	Diss Vein	Car? Ery?
130–134		DOL	ARG		Bedded green-grey dolomitic argillite. Intruded by dolo-dykes which host pink erythrite/cobaltian dolomite. Protocataclastic at base + occasional silver minerals. Spots of reddish alteration. (Haematite?)	~1%	Vein	Car? Ery?
136		BRE		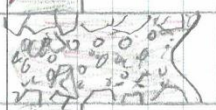	Reddish greenish, polymictic, matrix supported breccia with sub rounded clasts of argillite. Finer towards middle.			
138–148		DOL	ARG		Bedded green grey dolomite argillite. Intruded by dolo-dykes which host pink erythrite/cobaltian dolomite. Protocataclastic throughout. Spots of reddish alteration.			
		BRE						

SUMMARY DIAMOND DRILLING LOG

By: GMG
Date: 31/05/2014

Hole: MSSD083
Page 4 of 7

Depth (m)	Interp	Lith1	Lith2	Graphic Log (mm) (mud, 0.5, 2, 8, 32, 64, max)	Summary Description	Mineralisation %	Mineralisation Style	Mineralisation Min
152		BRE		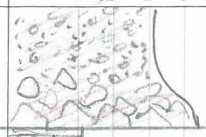	Reddish greenish polymictic, matrix supported breccia with sub rounded clasts of argillite. Finer towards middle. Minor argillic alteration to matrix. Some vein-hosted pink mineral (Eny?)	~0.5%	vein	Eny?
154		DOL	ARG		Bedded grey green dolomitic argillite	~1%	vein	Eny?
156 158 160 162 164 166 168		BRE	DOL		Intensely broken green-grey-red breccia. Matrix supported in places and clast supported crackle-chaotic breccia in others. Slightly polymictic. Intense dolomitisation with pink cobaltoan dolomite pervasive. Sub rounded to sub angular. Haematisation pervasive. ↑ + dolomitisation	~4%	Diss.	Co Dol?
170 172 174 176 178		DOL	ARG		Grey blue to greenish banded dolomitic argillite. Some layers have white dolomitic nodules (occassionally replaced by silver mineral). Some evidence for wavy algal bedding. From 168m → 173m rock is a proto-breccia, with blue botryoidal Cu mineral (Chrysocolla?) and haematite. Silver mineral disseminated below this in sediment. ↓ And brownish mineral - Chalcanite? ↓ Heterogenite?	~2% ~0.5%	Vein Diss.	Cry? Het? Cha? Car?
180 182 184 186		DOL			Massive, locally brecciated silicified dolomite. Occasionally vuggy - silica dominant. Vugs and veins frequently infilled by cobaltoan dolomite and silver mineral (Cerolite?) Reddish tinge to rock. Native copper dissem.	~2%	Diss.	Nat. Cu. Car? Co. dol.?
188		DOL	ARG		Grey blue banded dolomitic argillite. Dolo-dykes and replaced nodules (with some yellow sulphides	~0.1%	Diss.	Cpy?
190 192 194		DOL			Massive grey green finely crystalline dolomite, with red alteration patches, intruded by 'dolo-dykes'. Dolomite nodules and occasional cryptic banding (white).			
196 198		BRE	DOL	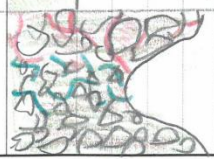	Brecciated massively crystalline dolomite, reddish green, monomictic (green argillite clasts). Locally vuggy. Abundant chrysocolla and cobaltoan dolomite. Angular fragments, chaotic breccia with protobreccia to sides (pink above blue min)	~4%	Vein	Cobd? Cry?

SUMMARY DIAMOND DRILLING LOG

By: GMG
Date: 31/05/2014

Hole: MSSD083

Depth (m)	Interp	Lith1	Lith2	Graphic Log (mm) (mud, 0.5, 2, 8, 32, 64, max)	Summary Description	Mineralisation %	Mineralisation Style	Mineralisation Min
202–236		DOL			Massive red-green patchy finely crystalline dolomite. Red alteration patches pervasive, sometimes associated with dark, slightly silvery minerals. Fractures host occasional cobaltoan dolomite and Mn oxide (dendritic). Cut throughout by 'dolo-dykes'. Cu sulphide mineralisation in the top 2 and bottom 5m.	0.01	Diss.	Cpy?
234–236						~1%	Diss.	Cpy?
238–242		SHA			Carbonaceous black shale, fine grained. Cut by dolo-dykes hosting a range of Cu-sulphide + oxide mineralisation. Mineralisation apparently contemporaneous with dykes. Fine grained pyrite within laminations. (Thick vein @ 240.53)	~5%	Vein Strat.	Cpy? Bo? Cha? Mal? Py
242–248		DOL	ARG		Red green patchy argillaceous dolomite. Grades from massive at top towards bedded at the bottom. Pervasive red alteration. Fractures bring haematisation. Cu sulphides in top 10m. Cut by dolo-dykes. ↓ and from 274-279m.	~0.1%	Diss.	Cpy?

SUMMARY DIAMOND DRILLING LOG

By: GMG
Date: 31/05/2014

Hole: MSSD083
Page 6 of 7

Depth (m)	Interp	Lith1	Lith2	Graphic Log (mm) (mud, 0.5, 2, 8, 32, 64, max)	Summary Description	Mineralisation %	Mineralisation Style	Mineralisation Min
252–284		DOL	ARG		Progressively less haematisation downwards.			
276–278						~0.1%	Diss + Vein	Cpy?
284–298		DOL			Coarse Crystalline siliceous dolomite. Chaotic crystal textures, patches of red, white + grey crystals (is grey original colour/texture?). Vuggy throughout, particularly in bottom 5m. At the basal portion these vugs are filled by pink cobaltous dolomite, a bright yellow, soft powdery mineral (UO_x?) and a dark silvery mineral. A brighter silvery mineral is found throughout. Heavy silicification + maybe potassic alteration is apparent.	~0.5%	Diss.	Car? Co. Dol. UO_x (Soe?)

SUMMARY DIAMOND DRILLING LOG

By: GMG
Date: 01/06/2014

Hole: MSSD083
Page 7 of 7

Depth (m)	Interp	Lith1	Lith2	Graphic Log (mm) (mud, 0.5, 2, 8, 32, 64, max)	Summary Description	Mineralisation %	Mineralisation Style	Mineralisation Min
302 304 306		DOL	ARG		Grey-white alternating laminated silicified dolomitic argillite. Dissolution of darker (grey) layers causing vugs in places. Mineralisation throughout of Cu sulphides and silver minerals as well as pink cobaltoan dolomite along fractures and in vugs.	~2%	Diss.	Cha? Cpy? Bo? Co. DOL.
308 310 312		DOL	ARG	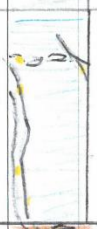	Bedded argillaceous dolomite, blue grey, cut by 'dolo-dykes'. Not as fine laminations as above. Occasional sigmoidal clasts/boudinaged layers of quartz - Cu sulphides hosted in pressure shadows of these and in 'dolo-dykes'.	~0.5%	Diss. + Vein	Cpy? Bo? Cha?
314 316		ARG	DOL		Green-red orange partially crystalline dolomitic argillite. Intruded by dolo-dykes and chaotically brecciated towards base. Green layers that are soft and soapy to the touch. (Talc).			
318 320		SLT	SST		Sandy-siltstone, poorly sorted, red-orange. Intruded by dolo-dykes and brecciated locally.			
				E.O.H.				
322 324 326 328 330 332 334 336 338 340 342 344 346 348								

SUMMARY DIAMOND DRILLING LOG

By: GMG
Date: 29/05/2014

Hole: MSSD140
Page 1 of 2

Depth (m)	Interp	Lith1	Lith2	Graphic Log (mm) (mud, 0.5, 2, 8, 32, 64, max)	Summary Description	Mineralisation %	Mineralisation Style	Mineralisation Min
	Topsoil	CLY	SIL		Brown-red clay-ey friable material - clay and argillic. Angular chunks of silicic material - in situ? Frag rock @ base			
2–6	Silicified laminated dolomite	ARG	DOL		Grey-white fragile laminated rock - dark and light bands of wavy argillite. Silicic grey bands in places, carbonate (scratches with penknife) in others. Light bands always scratch. Tiny cross cutting veins of black and red material, fine grained. Becomes more silicic and vuggy in non-silicic bands towards base. Lots of rounded vugs.			
6–8		BRE	CLY		Highly fragmented rock - red clay at top, to gravel-sized angular fragments of siliceous dolomite. Abundant development of black (Mn?) minerals, reddish alteration and clay. Grades to reddish clay at base, with fragments of black veined monomineralic argillite	~3	Diss + Vein	(Mn?) (Hae?)
8–12		ARG	BRE		Fractured chunks of fine grained whitish argillite, some relict laminations reminiscent of laminated dolomite above. (Limonite + haematite/goethite?) Iron oxides and black oxides around fractures. Matrix is very soft → argillic - advanced argillic alteration. Highly fragmented towards base, vuggy throughout. Pinkish colour.			Fe? Mn?
12–20		BRE	CLY		Poorly sorted, gravel to clay breccia with pervasive development of iron + Mn oxides. Angular fragments. Protolith unknown. Advanced argillic alteration. Clast supported chaotic breccia. Pinkish colour.			Fe? Mn?
20–32		ARG	BRE		Highly fragmented pale pink argillite with fractured breccia zones throughout. Pervasive development of Fe + Mn oxides. Very fragile, clay rich rock suggests argillic - advanced argillic alteration. Specular haematite throughout and Cu-oxides developed towards base of the unit. ↓ Malachite...			Fe? Mn? Cu (Mal)
32–48		ARG			Pink argillite. Occasionally bedded with wavy layers of pink and whitish yellow material. Red layers contain abundant nodules of white mineral, that scratches with penknife but not fingernail. Weak dissolution of powder in acid (dolomite). Some nodules replaced (↑ but not crystals) partially (or fully) with specular haematite. Nodules further up the core (to a depth of 53m) seem to be dissolved and have left vugs, again often filled by haematite. Nodules seem to follow bedding. Abundant cross-cutting veins of white material (scratches with knife, not nails, effervesces very weakly as a powder, euhedral in places - dolomite) and minor specular haematite brecciate the rock. Vein-fluid breccias with clasts of country rock. To a depth of 45m, these dolomite veins seem to have been dissolved, leaving cavities filled by euhedral malachite (botryoidal) with cavity infill textures → significant Cu mineralisation. Rare cross cutting veins of haematite, few mm thick. No veins from ↓ 45m → 54m in a brecciated zone	~3-5% 0%		Cu (Mal)

SUMMARY DIAMOND DRILLING LOG

By: GMG
Date: 29/05/2014

Hole: MSSD140

Depth (m)	Interp	Lith1	Lith2	Graphic Log (mm) (mud 0.5 2 8 32 64 max)	Summary Description	Mineralisation %	Mineralisation Style	Mineralisation Min
52				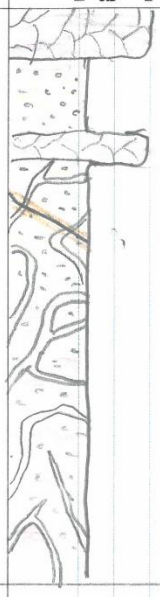	Tiny haematite veins that cross cut rock + dolomite veins, with haematisation/argillic alteration halo.			
54								
56								
58								
60								
62								
64								
66								

Notes

- Laminated silicified dolomite, underlain by some sort of cataclastic breccia, with a more massive red argillite at the base.

  RSF
  Bre
  RAT ?

- Supergene enrichment at base of the weathering profile. Mn (+ Co?) oxides appear to be left further up profile towards surface.
- Apparently late haematite veins cross-cut all and cause argillic/haematite alteration.
- Malachite in the enrichment zone appears to exploit cavities caused by dissolution of dolomite veins.

Appendix 4*: Descriptions of assay techniques used by Comide contractors.*

ALS Minerals

GEOCHEMICAL PROCEDURE

ME- ICP61

TRACE LEVEL METHODS USING CONVENTIONAL ICP- AES ANALYSIS

SAMPLE DECOMPOSITION

HNO_3 -$HClO_4$ -HF-HCl digestion, HCl Leach (GEO-4ACID)

ANALYTICAL METHOD

Inductively Coupled Plasma - Atomic Emission Spectroscopy (ICP - AES)

A prepared sample (0.25 g) is digested with perchloric, nitric, hydrofluoric and hydrochloric acids. The residue is topped up with dilute hydrochloric acid and the resulting solution is analyzed by inductively coupled plasma-atomic emission spectrometry. Results are corrected for spectral interelement interferences.

NOTE: Four acid digestions are able to dissolve most minerals; however, although the term *"near- total"* is used, depending on the sample matrix, not all elements are quantitatively extracted.

ELEMENT	SYMBOL	UNITS	LOWER LIMIT	UPPER LIMIT	DEFAULT OVER-LIMIT METHOD
Silver	Ag	ppm	0.5	100	Ag-OG62
Aluminum	Al	%	0.01	50	
Arsenic	As	ppm	5	10,000	
Barium	Ba	ppm	10	10,000	
Beryllium	Be	ppm	0.5	1,000	
Bismuth	Bi	ppm	2	10,000	
Calcium	Ca	%	0.01	50	
Cadmium	Cd	ppm	0.5	500	
Cobalt	Co	ppm	1	10,000	Co-OG62
Chromium	Cr	ppm	1	10,000	
Copper	Cu	ppm	1	10,000	Cu-OG62
Iron	Fe	%	0.01	50	
Gallium	Ga	ppm	10	10,000	
Potassium	K	%	0.01	10	
Lanthanum	La	ppm	10	10,000	
Magnesium	Mg	%	0.01	50	
Manganese	Mn	ppm	5	100,000	

ALS Minerals

ME- ICP61

ELEMENT	SYMBOL	UNITS	LOWER LIMIT	UPPER LIMIT	DEFAULT OVER-LIMIT METHOD
Molybdenum	Mo	ppm	1	10,000	Mo-OG62
Sodium	Na	%	0.01	10	
Nickel	Ni	ppm	1	10,000	Ni-OG62
Phosphorus	P	ppm	10	10,000	
Lead	Pb	ppm	2	10,000	Pb-OG62
Sulphur	S	%	0.01	10	
Antimony	Sb	ppm	5	10,000	
Scandium	Sc	ppm	1	10,000	
Strontium	Sr	ppm	1	10,000	
Thorium	Th	ppm	20	10,000	
Titanium	Ti	%	0.01	10	
Thallium	Tl	ppm	10	10,000	
Uranium	U	ppm	10	10,000	
Vanadium	V	ppm	1	10,000	
Tungsten	W	ppm	10	10,000	
Zinc	Zn	ppm	2	10,000	Zn-OG62

ELEMENTS LISTED BELOW ARE AVAILABLE UPON REQUEST

ELEMENT	SYMBOL	UNITS	LOWER LIMIT	UPPER LIMIT	DEFAULT OVER-LIMIT METHOD
Lithium	Li	ppm	10	10,000	
Niobium	Nb	ppm	5	2,000	
Rubidium	Rb	ppm	10	10,000	
Selenium	Se	ppm	10	1,000	
Tin	Sn	ppm	10	10,000	
Tantalum	Ta	ppm	10	10,000	
Tellurium	Te	ppm	10	10,000	
Yttrium	Y	ppm	10	10,000	
Zirconium	Zr	ppm	5	500	

ALS Minerals

ASSAY PROCEDURE

ME- OG62

ORE GRADE ELEMENTS BY FOUR ACID DIGESTION USING CONVENTIONAL ICP- AES ANALYSIS

SAMPLE DECOMPOSITION

HNO_3-$HClO_4$-HF-HCl Digestion (ASY-4A01)

ANALYTICAL METHOD

Inductively Coupled Plasma - Atomic Emission Spectroscopy (ICP - AES)*

Assays for the evaluation of ores and high-grade materials are optimized for accuracy and precision at high concentrations. Ultra high concentration samples (> 15 -20%) may require the use of methods such as titrimetric and gravimetric analysis, in order to achieve maximum accuracy.

A prepared sample is digested with nitric, perchloric, hydrofluoric, and hydrochloric acids, and then evaporated to incipient dryness. Hydrochloric acid and de-ionized water is added for further digestion, and the sample is heated for an additional allotted time. The sample is cooled to room temperature and transferred to a volumetric flask (100 mL). The resulting solution is diluted to volume with de-ionized water, homogenized and the solution is analyzed by inductively coupled plasma - atomic emission spectroscopy or by atomic absorption spectrometry.

***NOTE:** ICP-AES is the default finish technique for ME-OG62. However, under some conditions and at the discretion of the laboratory an AA finish may be substituted. The certificate will clearly reflect which instrument finish was used.

ELEMENT	SYMBOL	UNITS	LOWER LIMIT	UPPER LIMIT
Silver	Ag	ppm	1	1,500
Arsenic	As	%	0.01	30
Bismuth	Bi	%	0.01	30
Cadmium	Cd	%	0.0001	10
Cobalt	Co	%	0.001	20
Chromium	Cr	%	0.002	30
Copper	Cu	%	0.001	40
Iron	Fe	%	0.01	100
Manganese	Mn	%	0.01	50
Molybdenum	Mo	%	0.001	10
Nickel	Ni	%	0.001	30
Lead	Pb	%	0.001	20
Zinc	Zn	%	0.001	30

	Cu	Sr	Ti	V	W	Zn	Co	Ca	Ni	Fe	Ag	Al	As	Ba	Be	Bi	Cd	K	La	Mg	Mn	Mo	Na	P	Pb	S	Sc	U
Cu		-0.017	-0.062	0.178	-0.007	0.162	0.343	-0.092	0.206	0.100	0.009	-0.001	0.158	-0.004	0.267	0.332	0.028	0.017	0.035	-0.080	-0.032	0.090	0.015	0.266	0.022	0.198	0.095	0.031
Sr	-0.017		-0.031	-0.040	-0.030	-0.087	-0.033	0.442	0.009	-0.192	-0.009	-0.134	0.012	0.369	-0.184	-0.024	0.001	0.050	0.043	0.170	0.001	-0.006	0.098	-0.014	0.004	0.131	-0.142	0.021
Ti	-0.062	-0.031		0.399	-0.053	0.208	-0.055	-0.229	0.046	0.327	-0.017	0.800	0.096	0.115	0.432	-0.007	0.035	0.601	0.291	0.076	0.081	0.081	0.250	0.295	0.027	0.092	0.696	-0.014
V	0.178	-0.040	0.399		-0.029	0.122	0.271	-0.314	0.338	0.243	-0.013	0.316	0.216	0.085	0.323	0.230	0.012	0.329	0.244	-0.272	0.060	0.222	0.141	0.179	0.068	0.065	0.397	0.081
W	-0.007	-0.030	-0.053	-0.029		0.038	-0.008	-0.053	0.041	0.011	0.249	-0.063	0.005	-0.016	0.005	-0.006	0.069	-0.039	-0.006	-0.040	0.069	0.030	-0.008	-0.027	-0.002	-0.023	-0.021	-0.004
Zn	0.162	-0.087	0.208	0.122	0.038		0.068	-0.242	0.163	0.315	0.000	0.311	0.065	0.007	0.455	0.014	0.225	0.048	0.045	0.092	0.145	0.077	0.163	0.211	0.102	-0.076	0.318	0.014
Co	0.343	-0.033	-0.055	0.271	-0.008	0.068		-0.124	0.473	-0.031	-0.006	-0.083	0.138	0.031	0.132	0.332	-0.001	-0.068	-0.041	-0.185	0.117	0.109	0.045	0.064	0.028	0.256	0.027	0.114
Ca	-0.092	0.442	-0.229	-0.314	-0.053	-0.242	-0.124		-0.106	-0.436	-0.014	-0.376	-0.012	0.084	-0.456	-0.106	-0.065	0.001	-0.193	0.412	-0.119	-0.049	-0.036	-0.076	-0.017	0.201	-0.409	0.018
Ni	0.206	0.009	0.046	0.338	0.041	0.163	0.473	-0.106		0.082	0.300	0.074	0.075	0.097	0.203	0.110	0.026	-0.070	-0.041	-0.009	0.011	0.061	0.061	0.073	0.055	0.166	0.088	0.339
Fe	0.100	-0.192	0.327	0.243	0.011	0.315	-0.031	-0.436	0.082		0.002	0.629	0.166	-0.055	0.528	0.026	0.121	0.164	0.253	0.122	0.197	0.139	0.046	0.168	0.033	-0.005	0.654	-0.021
Ag	0.009	-0.009	-0.017	-0.013	0.249	0.000	-0.006	-0.014	0.300	0.002		-0.020	0.002	-0.004	-0.008	-0.004	0.006	-0.010	-0.004	-0.019	0.007	0.006	-0.004	-0.011	-0.001	-0.006	-0.015	0.000
Al	-0.001	-0.134	0.800	0.316	-0.063	0.311	-0.083	-0.376	0.074	0.629	-0.020		0.053	0.050	0.614	-0.054	0.089	0.440	0.343	0.303	0.085	0.045	0.166	0.324	0.020	0.030	0.860	-0.027
As	0.158	0.012	0.096	0.216	0.005	0.065	0.138	-0.012	0.075	0.166	0.002	0.053		0.027	0.118	0.156	0.046	0.136	0.048	-0.068	0.071	0.177	0.051	0.157	0.045	0.142	0.109	0.083
Ba	-0.004	0.369	0.115	0.085	-0.016	0.007	0.031	0.084	0.097	-0.055	-0.004	0.050	0.027		0.012	-0.015	-0.013	0.092	0.030	0.017	0.058	0.000	0.157	0.050	0.008	0.073	0.035	0.052
Be	0.267	-0.184	0.432	0.323	0.005	0.455	0.132	-0.456	0.203	0.528	-0.008	0.614	0.118	0.012		0.037	0.097	0.235	0.205	0.089	0.091	0.078	0.095	0.619	0.038	-0.050	0.637	0.010
Bi	0.332	-0.024	-0.007	0.230	-0.006	0.014	0.332	-0.106	0.110	0.026	-0.004	-0.054	0.156	-0.015	0.037		0.020	0.053	0.096	-0.221	0.032	0.096	0.044	0.035	0.021	0.124	0.043	0.023
Cd	0.028	0.001	0.035	0.012	0.069	0.225	-0.001	-0.065	0.026	0.121	0.006	0.089	0.046	-0.013	0.097	0.020		-0.013	0.015	0.052	0.063	0.029	0.024	0.045	0.043	-0.003	0.109	0.003
K	0.017	0.050	0.601	0.329	-0.039	0.048	-0.068	0.001	-0.070	0.164	-0.010	0.440	0.136	0.092	0.235	0.053	-0.013		0.376	-0.260	0.028	0.058	0.285	0.255	0.028	0.196	0.427	-0.015
La	0.035	0.043	0.291	0.244	-0.006	0.045	-0.041	-0.193	-0.041	0.253	-0.004	0.343	0.048	0.030	0.205	0.096	0.015	0.376		-0.117	0.095	0.046	0.168	0.129	0.018	-0.019	0.351	-0.017
Mg	-0.080	0.170	0.076	-0.272	-0.040	0.092	-0.185	0.412	-0.009	0.122	-0.019	0.303	-0.068	0.017	0.089	-0.221	0.052	-0.260	-0.117		-0.105	-0.066	-0.112	0.065	-0.021	0.050	0.131	-0.008
Mn	-0.032	0.001	0.081	0.060	0.069	0.145	0.117	-0.119	0.011	0.197	0.007	0.085	0.071	0.058	0.091	0.032	0.063	0.028	0.095	-0.105		0.055	0.002	0.000	0.020	-0.093	0.242	-0.014
Mo	0.090	-0.006	0.081	0.222	0.030	0.077	0.109	-0.049	0.061	0.139	0.006	0.045	0.177	0.000	0.078	0.096	0.029	0.058	0.046	-0.066	0.055		0.021	0.041	0.071	0.056	0.100	0.030
Na	0.015	0.098	0.250	0.141	-0.008	0.163	0.045	-0.036	0.061	0.046	-0.004	0.166	0.051	0.157	0.095	0.044	0.024	0.285	0.168	-0.112	0.002	0.021		0.096	0.053	0.072	0.134	-0.007
P	0.266	-0.014	0.295	0.179	-0.027	0.211	0.064	-0.076	0.073	0.168	-0.011	0.324	0.157	0.050	0.619	0.035	0.045	0.255	0.129	0.065	0.000	0.041	0.096		0.022	0.065	0.348	0.000
Pb	0.022	0.004	0.027	0.068	-0.002	0.102	0.028	-0.017	0.055	0.033	-0.001	0.020	0.045	0.008	0.038	0.021	0.043	0.028	0.018	-0.021	0.020	0.071	0.053	0.022		0.000	0.039	0.046
S	0.198	0.131	0.092	0.065	-0.023	-0.076	0.256	0.201	0.166	-0.005	-0.006	0.030	0.142	0.073	-0.050	0.124	-0.003	0.196	-0.019	0.050	-0.093	0.056	0.072	0.065	0.000		0.000	0.086
Sc	0.095	-0.142	0.696	0.397	-0.021	0.318	0.027	-0.409	0.088	0.654	-0.015	0.860	0.109	0.035	0.637	0.043	0.109	0.427	0.351	0.131	0.242	0.100	0.134	0.348	0.039	0.000		-0.019
U	0.031	0.021	-0.014	0.081	-0.004	0.014	0.114	0.018	0.339	-0.021	0.000	-0.027	0.083	0.052	0.010	0.023	0.003	-0.015	-0.017	-0.008	-0.014	0.030	-0.007	0.000	0.046	0.086	-0.019	

Appendix 5: Correlation matrix for all 12,058 geochemical samples from drill core at Mashitu South. Colour coding: black for a correlation (R-value) =1; red for 1 > R ≥ 0.8; orange for 0.8 > R ≥ 0.6; yellow for 0.6 > R ≥ 0.4, white (no colour) for 0.4 > R > -0.4; light blue for -0.4 ≥ R > -0.6; dark blue for -0.6 ≥ R > -0.8; and indigo for -0.8 ≥ R ≥ -1.

N	LITHO-STRAT	Mg	Al	Ca	Fe	Cu	K	Co	Ti	S	Mn	P	Na	Ba	V	Ni	Sr	Zn	La	Pb	U	W	Sc	As	Bi	Mo	Be	Ag	Cd
24	(Undiff Bx) Monomict Breccia (and)	1.32	0.97	2.60	0.84	0.56	1.52	1.29	1.08	1.60	1.08	1.19	1.16	1.01	0.81	1.34	1.02	0.99	0.48	0.54	0.79	0.70	0.93	1.30	0.39	1.06	0.95	0.28	1.15
125	(Undiff Bx) Composite/Polymict Breccia (and)	1.28	1.19	1.78	1.10	1.12	1.25	1.79	1.24	1.56	1.24	1.02	1.31	2.07	1.27	1.39	1.55	1.42	1.36	0.98	1.18	0.58	1.21	1.18	1.40	1.19	1.05	0.50	1.05
204	(SDS) Dolomite (and)	1.25	1.15	2.36	0.55	0.82	2.25	1.65	1.29	2.57	0.77	1.24	1.11	1.32	0.66	0.66	1.23	0.72	0.61	0.39	0.70	0.58	0.98	0.88	0.85	0.70	0.67	0.23	0.85
6	(SDS) Breccia (mono+polymict)	1.26	1.28	1.56	1.19	1.33	1.42	0.90	1.51	2.75	1.10	1.94	1.05	2.66	1.53	1.47	1.05	1.38	0.59	0.65	1.71	0.58	1.44	1.69	1.28	1.34	1.50	0.23	1.84
683	(SDS) Shale (and)	1.05	1.34	1.81	0.78	0.43	3.04	0.39	1.66	1.75	0.90	1.47	1.26	1.34	0.85	0.67	1.02	1.21	0.64	0.55	0.59	0.59	1.24	1.09	0.53	0.65	1.01	0.29	1.09
24	(SDB) Clay (and)	0.53	1.70	0.14	1.68	0.44	4.16	0.44	2.27	0.07	1.02	2.07	1.94	1.38	1.42	0.85	0.73	1.68	1.93	0.68	0.54	0.70	1.56	1.66	0.87	1.05	1.90	0.51	0.80
182	(SDB) Dolomite (and)	1.21	1.15	2.42	0.59	0.54	2.36	1.28	1.38	5.13	0.89	1.47	1.16	1.40	0.71	0.95	1.17	0.68	0.67	0.40	1.26	0.58	1.01	0.88	0.50	0.57	0.81	0.23	0.81
1489	(SDB) Shale (and)	0.85	1.53	1.00	1.20	0.81	3.04	0.99	1.87	2.39	1.16	1.70	1.81	1.36	1.32	1.15	0.94	1.08	1.77	1.84	1.13	0.59	1.42	1.24	1.24	1.13	1.44	0.29	0.92
41	(SDB) Siltstone	0.72	1.59	0.92	0.95	1.50	3.48	0.91	1.81	0.40	0.98	1.87	2.12	1.27	1.32	1.10	1.59	0.85	3.34	0.79	0.65	0.58	1.58	1.20	1.62	0.99	1.40	0.23	0.83
514	(RSF) Dolomite (and)	0.37	0.39	0.78	0.69	2.05	0.62	1.92	0.50	1.06	0.86	0.82	1.29	1.32	1.19	1.66	1.06	0.84	1.28	1.53	2.29	0.83	0.54	1.06	2.36	1.18	0.62	0.71	0.91
14	(RSF) Mudstone	0.02	0.46	0.01	1.20	0.07	0.70	0.64	0.59	0.09	1.21	0.25	1.08	0.30	0.98	0.57	0.42	0.59	0.95	1.12	0.54	21.98	0.70	0.97	2.14	1.87	0.26	31.44	1.49
11	(RSF) Shale (and)	0.11	0.34	0.01	0.54	1.08	0.49	1.82	0.50	0.06	1.10	0.65	1.03	0.36	0.92	0.24	0.38	1.07	1.68	2.22	0.54	0.58	0.61	0.74	2.28	0.97	0.79	0.27	0.80
98	(RSF) Silicic Rock (and)	0.25	0.35	0.53	0.54	2.98	0.54	2.84	0.48	0.83	1.02	0.56	1.08	0.44	0.96	1.21	1.28	1.12	1.06	1.40	0.60	0.86	0.56	0.90	3.38	0.62	0.48	0.79	1.14
334	(RSF) Siltstone	0.32	0.40	0.68	0.65	1.61	0.71	1.56	0.53	0.75	0.82	0.72	1.32	0.48	1.10	1.05	0.99	0.61	1.43	0.94	0.59	1.04	0.57	0.99	2.93	1.16	0.65	0.39	0.93
881	(RSC) Dolomite (and)	0.33	0.22	0.66	0.42	0.73	0.06	1.57	0.31	0.29	0.94	0.46	0.76	1.15	1.10	1.50	0.93	0.63	0.32	1.00	2.97	0.76	0.46	0.71	1.03	0.69	0.63	0.46	0.89
8	(RSC) Mudstone (and)	0.33	0.72	0.09	0.62	1.35	0.14	2.18	0.93	0.05	0.84	0.55	1.34	0.20	1.17	0.57	0.50	0.47	5.79	0.71	0.54	6.46	0.66	1.08	3.23	0.30	0.70	3.15	0.80
7	(RSC) Saprolite	0.03	0.53	0.01	1.03	0.04	0.19	0.47	0.76	0.03	0.49	0.25	0.81	0.27	1.20	0.34	0.34	0.42	0.58	0.90	0.54	0.58	0.67	1.35	1.89	0.74	0.13	0.23	0.80
1186	(RSC) Silicic Rock (and)	0.26	0.21	0.48	0.43	0.91	0.07	1.65	0.30	0.17	0.94	0.46	0.73	0.68	0.96	1.03	0.66	0.64	0.40	0.63	0.56	0.88	0.45	0.69	1.08	0.50	0.55	0.66	0.89
266	(RATRouge) Breccia (and)	1.24	1.43	1.08	1.81	1.39	1.64	0.76	1.18	0.29	1.59	1.13	1.64	1.21	0.81	1.06	1.79	1.55	1.65	0.70	0.69	0.69	1.30	0.64	0.50	0.47	1.35	0.37	1.15
762	(RATRouge) Clay (and)	1.45	1.59	0.22	1.78	0.98	0.26	0.74	1.03	0.05	1.18	1.14	0.65	0.60	0.85	1.12	0.55	1.22	1.35	0.42	0.56	0.61	1.49	0.57	0.57	0.25	1.52	0.28	1.08
310	(RATRouge) Dolomite (and)	1.46	1.36	0.73	1.47	0.75	0.21	0.55	1.12	0.07	0.94	1.08	0.89	0.71	0.79	1.07	0.88	1.20	1.02	0.44	0.59	0.60	1.25	0.54	0.39	0.28	1.25	0.34	0.91
906	(RATRouge) Mudstone (and)	1.48	1.61	0.15	1.79	1.01	0.17	0.56	1.07	0.06	1.05	1.31	0.60	0.39	0.87	1.17	0.51	1.23	1.17	0.42	0.58	0.68	1.51	0.64	0.46	0.24	1.52	0.32	1.14
705	(RATRouge) Sandstone (and)	1.49	1.63	0.19	1.75	1.11	0.25	0.66	1.05	0.06	1.09	1.01	0.65	0.42	0.83	1.12	0.52	1.41	1.36	1.66	0.63	0.60	1.47	0.67	0.57	0.30	1.38	0.28	1.25
6	(RATRouge) Siltstone (and)	1.47	1.83	0.08	1.32	0.37	0.27	0.21	1.57	0.10	0.75	1.58	2.73	0.62	0.85	1.10	1.55	0.73	1.73	0.09	0.54	0.58	1.38	1.06	0.28	0.22	1.33	0.23	1.68
73	(RATGris) Clay	1.44	1.64	0.66	0.89	0.66	0.16	1.08	2.04	1.05	1.16	1.08	0.67	3.31	1.64	1.37	1.44	1.20	0.93	1.60	1.61	0.77	1.52	1.22	0.75	2.47	1.16	0.76	1.02
153	(RATGris) Dolomite	1.60	1.46	0.93	0.79	0.99	0.11	0.94	1.78	0.95	0.70	1.34	0.80	4.33	1.15	1.20	1.47	1.18	0.77	1.38	1.79	0.59	1.22	1.42	0.62	1.50	1.20	0.35	1.01
478	(RATGris) Sandstone	1.56	1.69	0.48	0.97	0.63	0.20	0.82	1.97	0.64	0.75	1.23	1.03	1.84	1.39	1.18	0.98	1.27	0.91	1.67	1.00	0.65	1.43	1.34	0.72	3.35	1.27	0.40	1.06
75	(RATGris) Siltstone	1.62	1.63	0.59	0.91	1.16	0.12	0.64	1.91	0.94	0.74	1.46	1.05	0.79	1.23	1.16	0.72	1.01	0.52	1.06	0.86	0.63	1.34	1.18	1.01	1.22	1.33	0.26	0.93
11	(Dstrat) Clay	0.33	0.87	0.02	1.78	0.56	0.12	1.72	1.02	0.05	3.47	0.46	0.46	0.32	2.04	1.16	0.28	0.77	0.97	3.50	1.28	2.80	1.54	2.57	2.35	6.34	0.73	2.21	1.06
580	(Dstrat) Dolomite (and)	0.84	0.63	1.23	1.10	1.43	0.51	1.00	0.68	1.42	1.40	0.82	0.52	0.56	1.27	0.69	1.33	0.94	0.56	1.79	1.16	0.81	0.76	2.27	1.19	3.59	0.72	0.52	1.06
11	(Dstrat) Monomict Breccia and Dolomite	1.12	0.53	1.97	0.95	0.58	0.12	1.26	0.60	0.49	1.76	1.86	0.38	0.58	1.23	0.76	0.92	0.82	0.27	2.01	1.13	0.58	0.81	2.67	0.40	13.95	0.99	0.29	1.94
21	(Dstrat) Shale, Mudstone, Siltstone (and)	0.45	0.81	0.01	1.24	0.95	0.53	1.02	0.99	0.04	1.06	0.34	0.39	0.17	1.60	0.53	0.18	0.85	0.62	2.64	0.85	3.46	0.97	2.28	1.18	4.57	0.66	1.19	1.14
3	(Dstrat) Silicic Rock (and)	0.07	0.56	0.01	1.23	2.65	1.27	0.72	0.76	0.07	1.49	0.22	0.77	0.27	1.23	0.26	0.15	0.78	0.27	1.01	0.54	0.58	0.76	1.50	0.46	2.60	0.49	0.34	0.80
12	(CMN) Breccia (mono + polymict)	0.81	0.82	0.06	1.17	0.29	0.60	0.62	0.71	0.09	1.17	0.45	1.22	0.42	0.80	0.47	0.60	1.65	0.50	0.54	0.54	10.60	1.15	1.13	0.57	1.73	1.08	17.58	1.04
79	(CMN) Clay, Saprolite (and)	1.31	0.71	0.08	1.04	1.25	0.27	0.40	0.64	0.05	2.50	0.53	0.75	0.99	0.70	0.58	0.59	1.69	1.09	0.92	0.54	15.66	0.84	1.05	0.65	2.30	1.16	13.66	1.17
1041	(CMN) Dolomite (and)	1.56	0.20	2.82	0.35	0.55	0.13	0.35	0.19	0.98	0.71	0.33	0.51	0.66	0.21	0.18	1.82	0.68	0.37	0.36	0.62	1.85	0.26	0.90	0.72	0.38	0.37	1.22	0.95
16	(CMN) Mudstone (and)	0.74	0.47	0.63	1.02	0.28	0.06	0.58	0.47	0.03	1.56	0.34	0.80	0.54	0.56	0.62	0.66	1.61	0.43	0.65	0.54	23.92	0.72	1.00	0.88	1.25	0.90	18.96	1.76
7	(CMN) Sandstone (and)	0.81	0.16	0.39	0.59	0.67	0.02	0.61	0.15	0.10	1.46	0.21	0.39	0.25	0.30	0.43	0.33	2.16	0.27	0.40	0.54	3.98	0.52	0.66	0.67	0.46	1.18	6.23	1.15
272	(CMN) Shale (and)	1.44	0.67	2.32	0.67	0.61	0.95	0.36	0.72	0.94	0.93	0.69	1.14	0.77	0.66	0.44	1.66	1.32	0.52	0.95	0.71	0.80	0.68	1.02	0.60	0.63	0.67	0.55	0.89
141	(CMN) Silicic Rock (and)	0.92	0.15	2.26	0.39	0.35	0.05	0.37	0.12	0.53	0.64	0.19	0.45	0.43	0.18	0.53	1.03	0.51	0.28	0.22	0.54	2.36	0.19	0.70	0.50	0.43	0.29	29.96	0.93
10	(SD2d) Dolomite, Dolomite and Sandstone	0.22	1.79	0.32	0.89	4.79	6.79	0.64	2.40	1.71	0.16	1.63	1.80	1.43	3.83	0.30	0.97	0.74	3.16	0.60	0.86	0.58	1.71	0.78	1.40	3.62	1.38	0.26	0.80
42	(SD2d) Shale and Dolomite	0.58	1.72	0.78	1.11	4.75	5.25	3.69	1.97	12.44	0.35	1.68	3.04	1.79	2.75	0.92	1.57	0.79	1.31	0.85	0.86	0.58	1.56	1.92	2.66	2.76	1.30	0.25	1.02
181	(SD2d) Shale	0.27	1.89	0.41	1.55	3.16	5.81	1.32	2.21	3.02	0.32	1.90	2.30	2.22	3.55	0.98	1.20	0.93	3.44	1.30	0.73	0.58	1.94	2.53	2.31	3.36	1.67	0.25	0.92

***Appendix 6**: ACEMS-normalised mean concentrations for all of the lithostratigraphically split datasets. Orange and yellow are anomalously high values while blue and purple denote anomalously low values (see Section 4.2.8 for a full explanation of the colour coding).*

Appendix 7*: Scatterplots of Cu-vs-other-element-concentration in the entire geochemistry dataset for Mashitu South.*

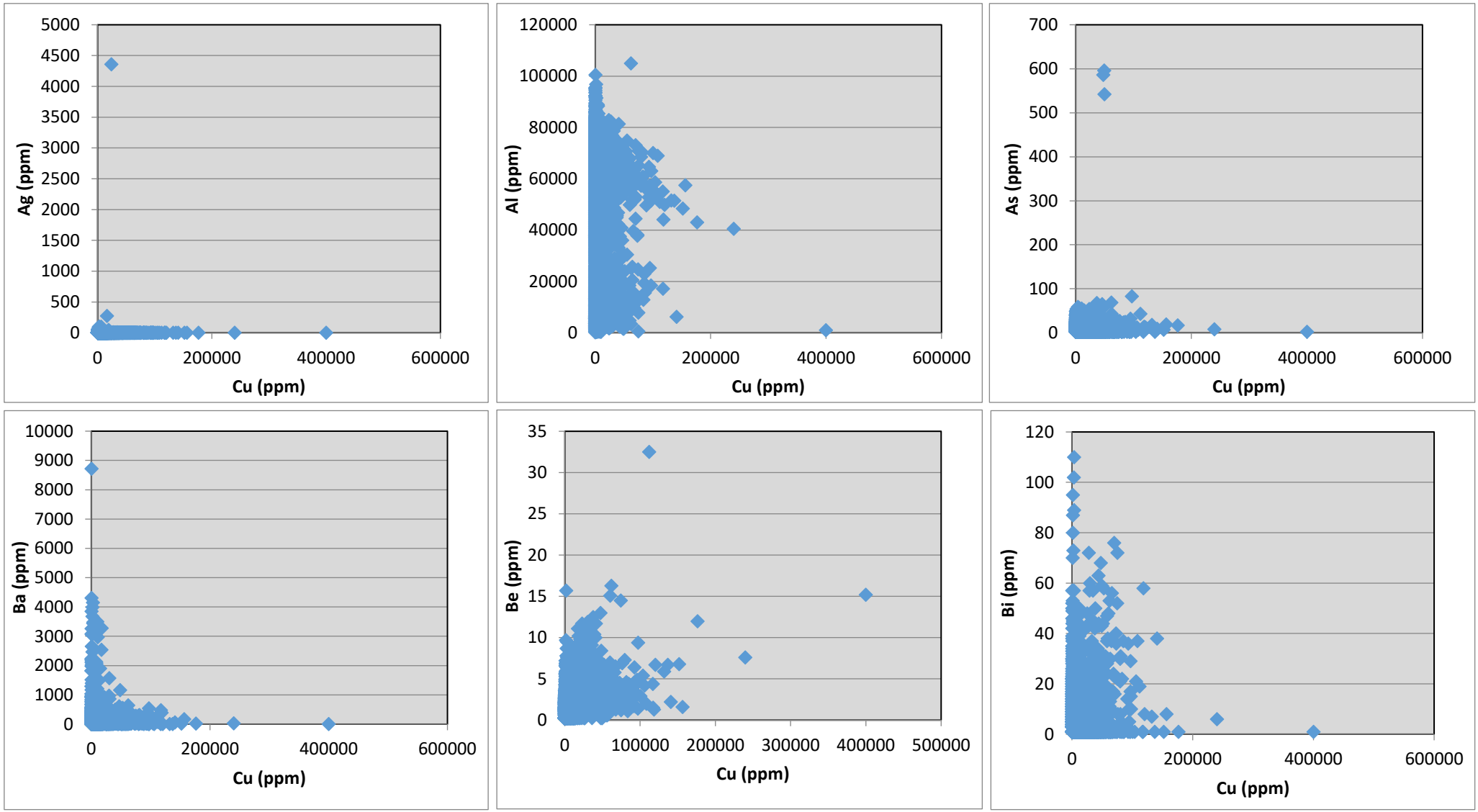

***Appendix 7**: Scatterplots of concentrations the other 27 elements analysed in the samples of the Mashitu South combined database vs concentration of Cu in ppm. Number of samples = 12,058.*

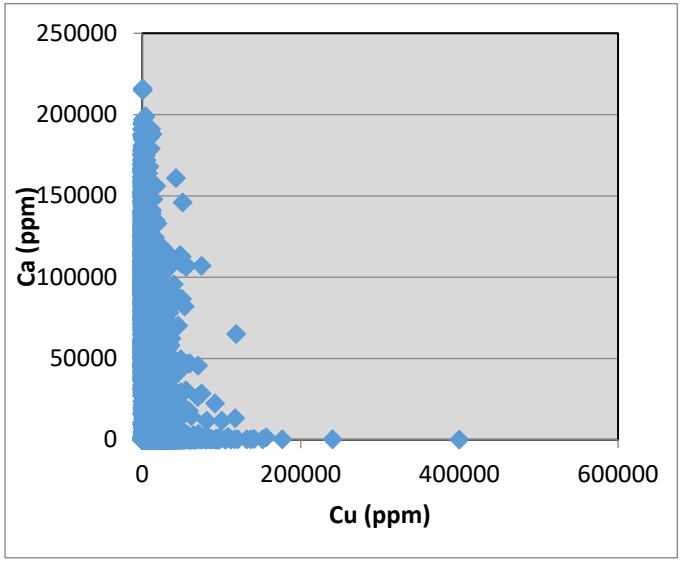

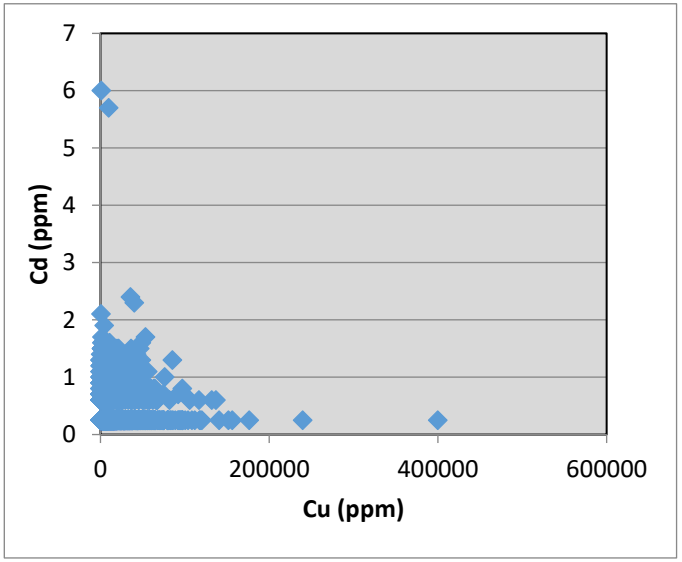

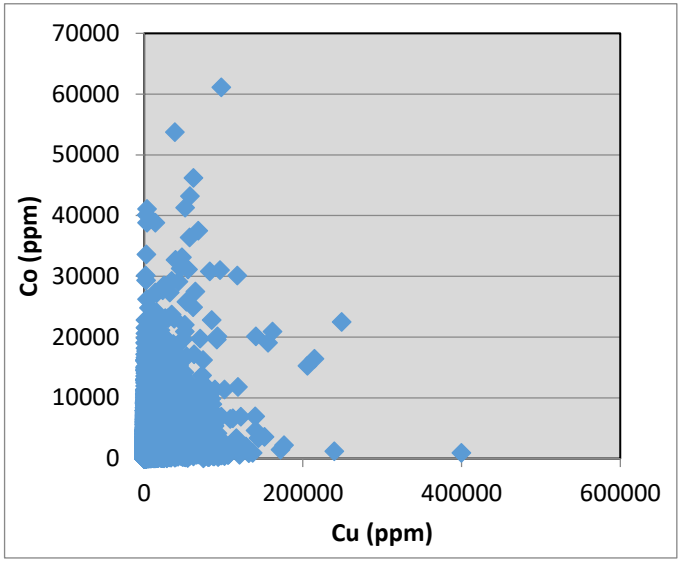

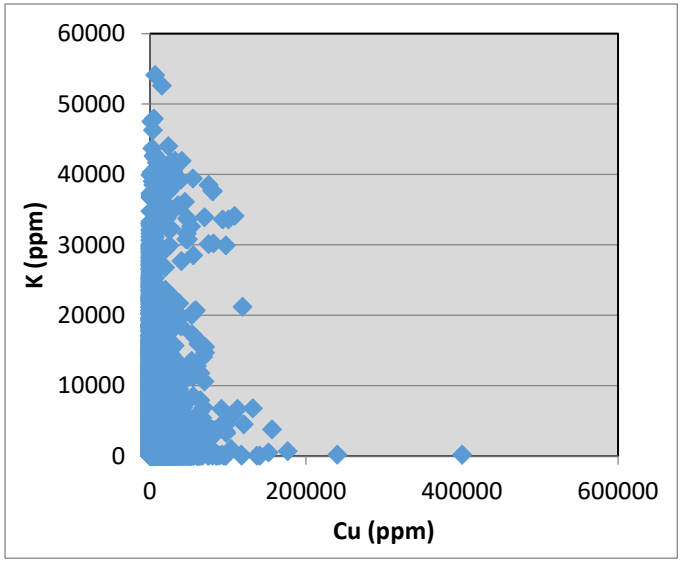

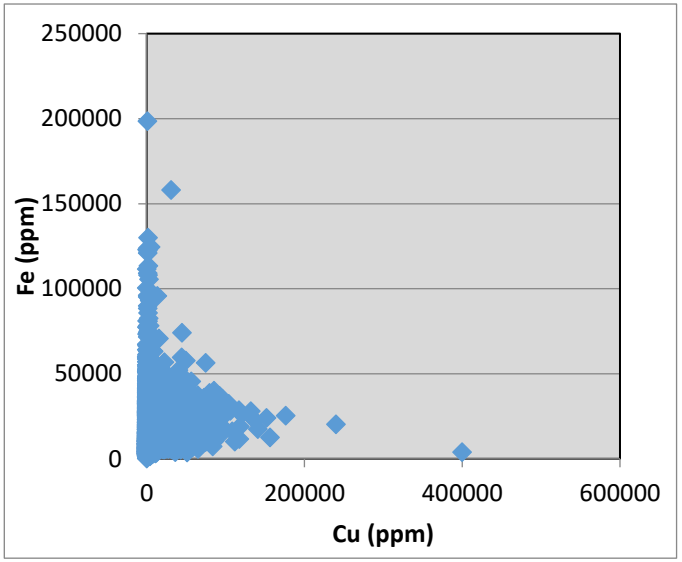

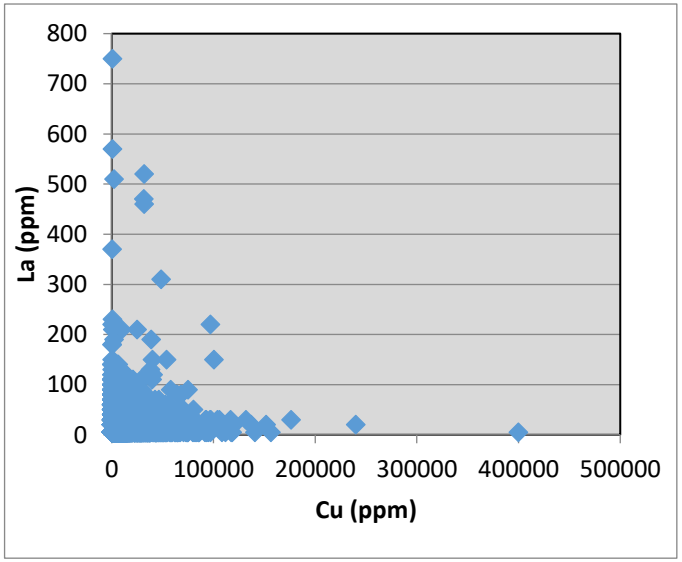

***Appendix 7 (continued)**: Scatterplots of concentrations the other 27 elements analysed in the samples of the Mashitu South combined database vs concentration of Cu in ppm. Number of samples = 12,058.*

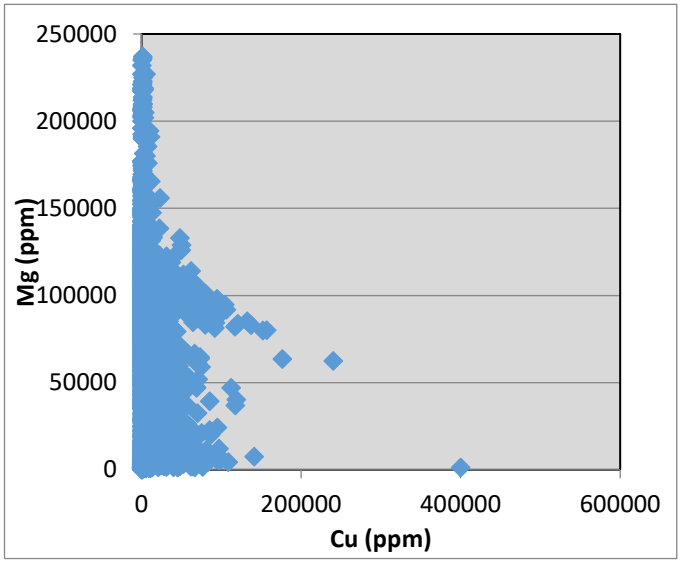

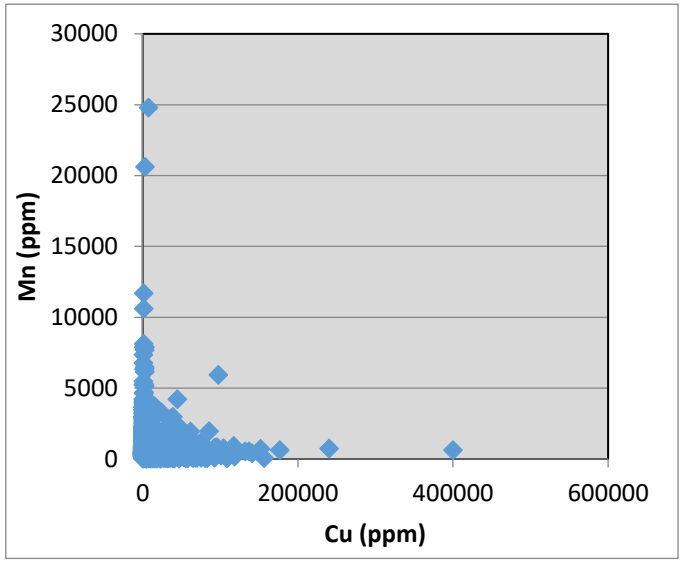

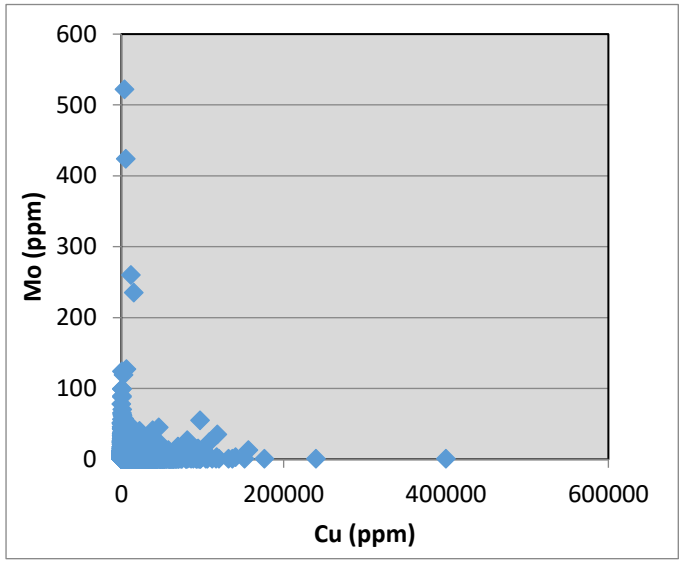

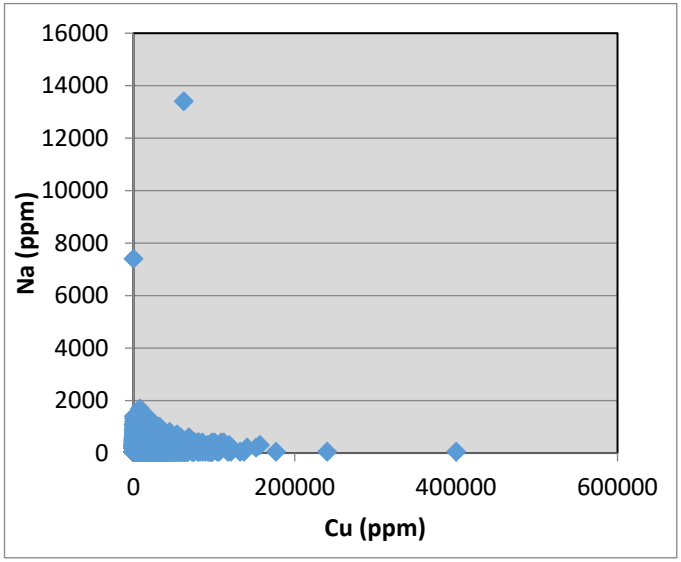

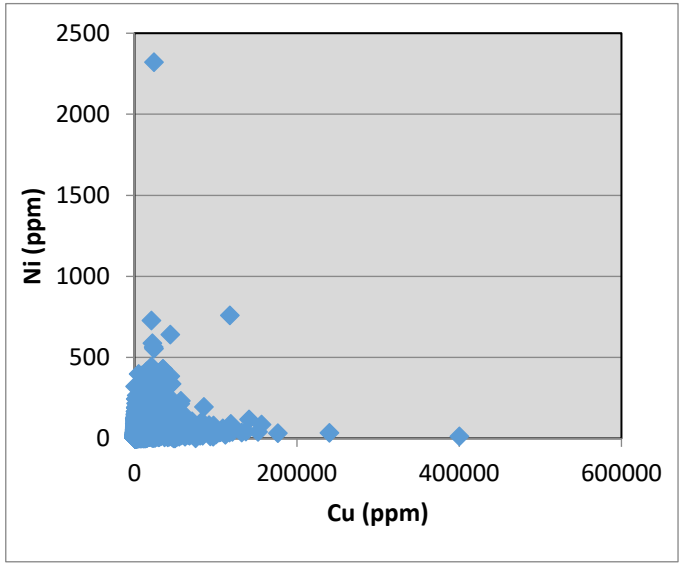

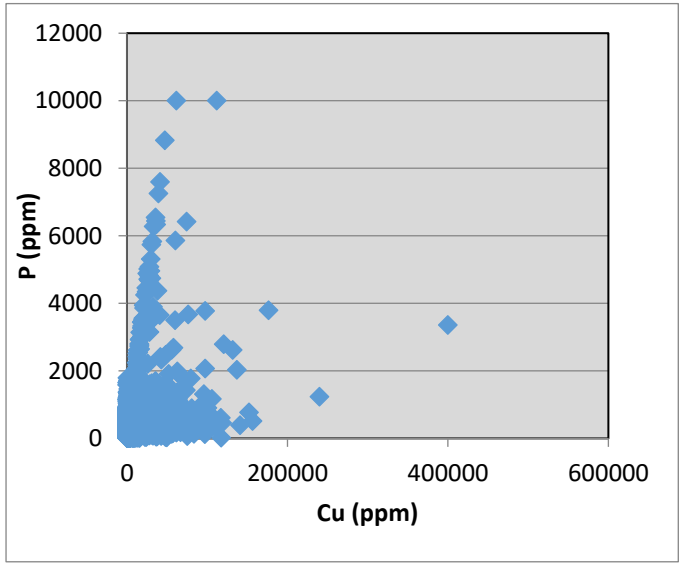

***Appendix 7 (continued)**: Scatterplots of concentrations the other 27 elements analysed in the samples of the Mashitu South combined database vs concentration of Cu in ppm. Number of samples = 12,058.*

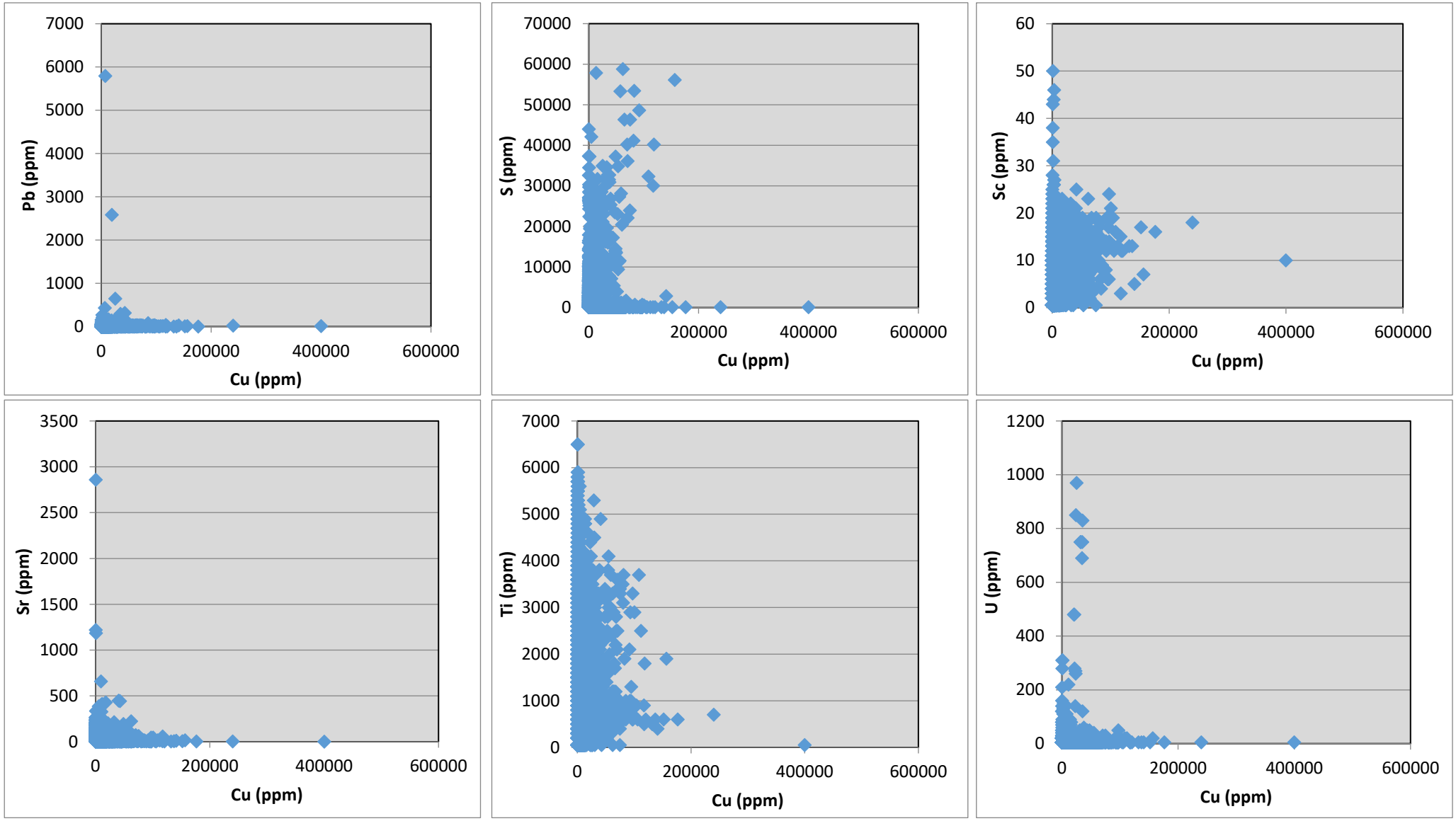

***Appendix 7 (continued)**: Scatterplots of concentrations the other 27 elements analysed in the samples of the Mashitu South combined database vs concentration of Cu in ppm. Number of samples = 12,058.*

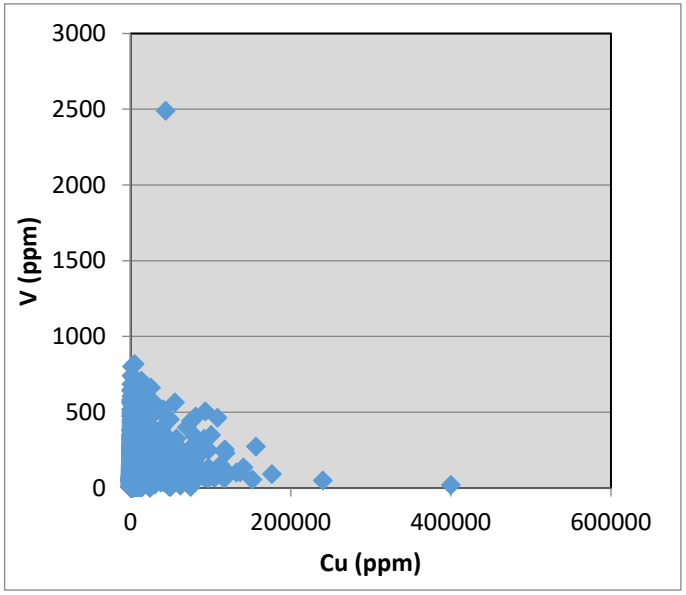

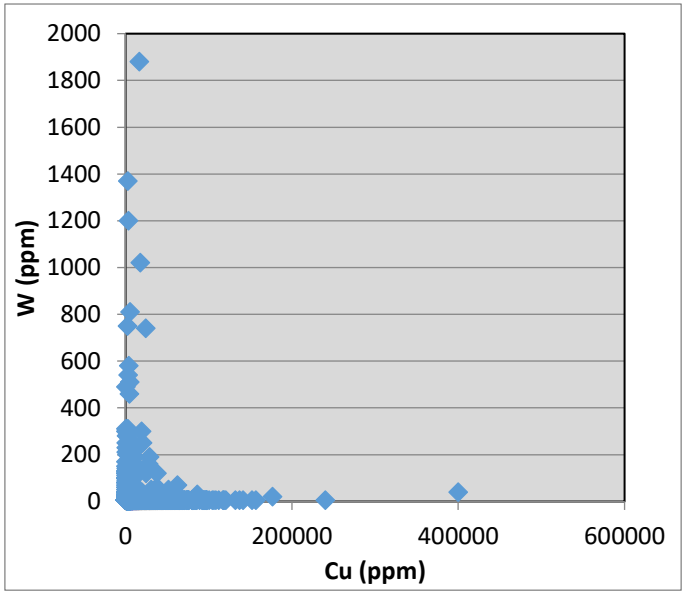

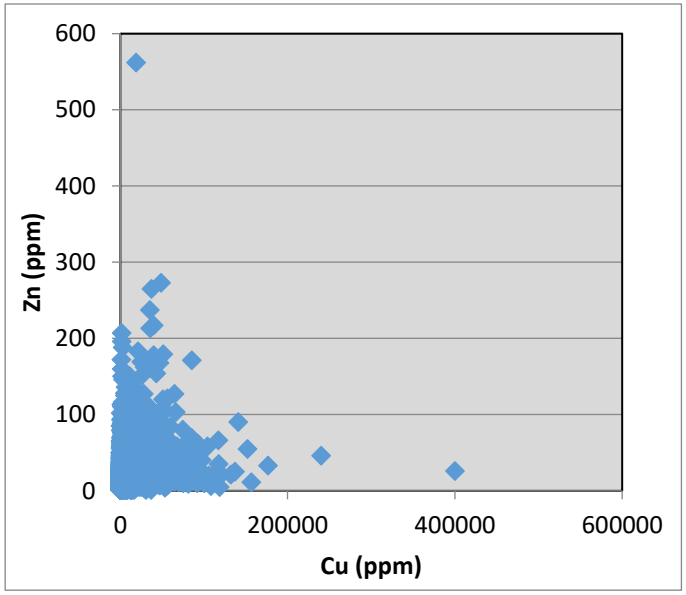

***Appendix 7 (continued)**: Scatterplots of concentrations the other 27 elements analysed in the samples of the Mashitu South combined database vs concentration of Cu in ppm. Number of samples = 12,058.*

Appendix 8*: List of samples taken from boreholes MSSD075, 080, 083, 140 for use in this study, with brief descriptions.*

MSSD075					
Number	Sample Name	Depth Start (m)	Depth End (m)	Interpreted Unit	Comments
1	MSSD075_11_1_M	53.02	53.2	CMN	Laminated argillite with disseminated sulphides
2	MSSD075_11_2_U	59.85	59.99	CMN	Dark organic shale
3	MSSD075_11_3_U	61.41	61.56	CMN	Deformed white grains/crystals?
4	MSSD075_11_4_U	69.21	69.36	CMN	Massive-thickly bedded dark grains/crystals
5	MSSD075_11_5_U	79.15	79.3	CMN	Laminated deformed and veined by dolomite
6	MSSD075_12_1_U	93.7	93.85	CMN	Massive crystalline silicified dolomite
7	MSSD075_13_1_U	111.05	111.2	CMN	Bedded dark shale
8	MSSD075_14_1_U	129.2	129.35	SDS	Green bedded argillite
9	MSSD075_14_2_M	136.2	136.35	SDS	Iron altered argillite veined by dolomite, disseminated oxidised sulphides?
10	MSSD075_15_1_U	153.35	153.5	SDB/SDS	Transition marker black shale, altered
11	MSSD075_16_1_U	172.3	172.45	SDB	Argillite
12	MSSD075_16_2_M	180.6	180.75	SDB	Bedded argillite, dolomite vein hosted chalcocite(?)
13	MSSD075_16_3_M	186.8	186.95	SDB	Dolomite vein hosted cobaltoan carbonate, with open space fibrous malachite
14	MSSD075_17_1_M	191.8	191.93	RSC	Vuggy silicification, disseminated pyrolusite(?)
15	MSSD075_17_2_M	187.75	187.9	RSC	Silicified crystalline dolomite, with disseminated chalcocite(?) and fracture-hosted heterogenite?
16	MSSD075_18_1_U	203.63	203.78	RSF	Laminated argillite, disseminated/stratiform sulphides
17	MSSD075_18_2_M	206.26	206.41	RSF	Laminated argillite, with grey lath shaped scapolite(?)
18	MSSD075_19_1_M	208.47	208.61	Dstrat	Deformed bedded argillite, stratiform and pressure-shadow hosted yellow sulphides
19	MSSD075_19_2_M	209.2	209.35	Dstrat	Argillite with dolomite vein-hosted chalcocite
20	MSSD075_19_3_U	210.47	210.57	Dstrat	Argillite
21	MSSD075_19_4_M	210.6	210.75	Dstrat	Bedded argillite with vein hosted carrollite and disseminated chalcocite(?)
22	MSSD075_19_5_M	211.43	211.58	Dstrat	Argillite with disseminated chalcocite(?)
23	MSSD075_20_1_U	213.17	213.32	RAT gris	Argillite
24	MSSD075_20_2_M	212.8	212.9	RAT gris	Argillite with dolomite-vein-hosted cobaltoan carbonate
25	MSSD075_21_1_U	214.46	214.61	RAT lilac	Argillite cut by dolomite vein
26	MSSD075_21_2_M	218.02	218.17	RAT lilac	Argillite with typical whitish alteration mineral
27	MSSD075_22_1_U	219.02	219.17	Breccia	Clastic polymict breccia(?) with rounded clasts
28	MSSD075_22_2_M	217.3	217.45	RAT lilac	Green-orange alteration texture (and brecciation?)
29	MSSD075_23_1_M	220.09	220.24	RAT lilac	Argillite with typical dolomite vein mosaic brecciation

MSSD080					
Number	Sample Name	Depth Start (m)	Depth End (m)	Interpreted Unit	Comments
1	MSSD080_10_1_M	82.7	82.85	CMN	Crystalline dolomite contact with silicification
2	MSSD080_10_2_M	88.3	88.45	CMN	Crystalline dolomite cut by dolomite veins and blue Cu mineral
3	MSSD080_11_1_M	91.5	91.65	CMN	Crystalline dolomite with disseminated chalcocite(?), heterogenite(?) and surficial blue Cu mineral
4	MSSD080_12_1_M	100.83	100.98	CMN	Crystalline dolomite with disseminated chalcocite(?), heterogenite(?) and vein-hosted cobaltoan carbonate
5	MSSD080_13_1_M	110.9	111.05	CMN	Dolomitic argillite with dolomite-vein hosted chalcocite(?) and minor green-blue Cu mineral
6	MSSD080_13_2_U	115.22	115.37	CMN	Finely crystalline dolomite
7	MSSD080_14_1_M	143.83	143.98	SDS	Dolomitic argillite with dolomite-vein-hosted weathered chalcocite(?)
8	MSSD080_14_2_M	151.14	151.29	SDS	Dolomitic massive argillite with surficial(?) dendritic pyrolusite(?)
9	MSSD080_14_3_U	158.32	158.47	SDS	Dolomitic argillite with weathering spots (previously disseminated Cu mineralisation?
10	MSSD080_15_1_U	213.75	213.9	SDS/SDB	Laminated black shale with stratiformly-elongate black minerals
11	MSSD080_16_1_M	226.74	226.89	SDB	Iron (?) altered dolomitic argillite with dolomite-vein-hosted cobaltoan carbonate and Cu oxides
12	MSSD080_16_2_U	229.91	230.06	SDB	Dolomitic argillite with unmineralised dolomite vein
13	MSSD080_16_3_U	239.07	239.22	SDB	Dolomitic argillite with unmineralised dolomite vein - seems to have entrained surrounding argillite
14	MSSD080_18_1_M	260.86	260.99	RSC	Silicified crystalline dolomite with native Cu, blue Cu oxides and dark coloured minerals (vein hosted?)
15	MSSD080_18_2_U	266.22	266.37	RSC	Silicified (brecciated?) crystalline dolomite with feldspar(?) alteration
16	MSSD080_19_1_M	278.51	278.66	RSF	Laminated, silicified dolomitic argillite cut by cobaltoan carbonate vein, hosting carrollite(?) and chalcocite(?)
17	MSSD080_19_2_U	279.57	279.72	RSF	Laminated, silicified dolomitic argillite with perhaps disseminated chalcocite(?) and pervasive cobaltoan dolomite
18	MSSD080_20_1_U	284.33	284.48	Dstrat	Massive dolomitic argillite
19	MSSD080_20_2_M	284.9	285.05	Dstrat	Bedded dolomitic argillite - disseminated chalcocite(?) and stratiform fine grained yellow sulphides
20	MSSD080_21_1_U	286.82	287.02	RAT gris	Partially dolomitic green argillite
21	MSSD080_22_1_U	293.33	293.48	RAT lilac	Massive red argillite with pale white and green alteration spots
22	MSSD080_23_1_U	296.3	296.42	RAT lilac	Green-orange alteration texture of argillite
23	MSSD080_23_2_U	298.22	298.37	RAT lilac	Mosaic-brecciated red argillite

***Appendix 8a**: List of samples taken from Mashitu South boreholes MSSD075 and MSSD080.*

MSSD083					
Number	Sample Name	Depth Start (m)	Depth End (m)	Interpreted Unit	Comments
1	MSSD083_06_1_U	48.41	48.58	CMN	Laminated dolomitic argillite contact with black-spotted rock
2	MSSD083_06_2_M	52.48	52.63	CMN	Dolomitic argillite with chalcopyrite(?) hosted in dolomite vein
3	MSSD083_06_3_U	54.13	54.28	CMN	Bedded/laminated dolomitic argillite
4	MSSD083_06_4_U	65.1	65.12	CMN	Deformed quartz clasts(?) in fine laminated dolomitic argililte matrix, cut by dolomite veins
5	MSSD083_06_5_M	86.62	86.82	CMN	Crystalline dolomite with disseminated chalcopyrite(?)
6	MSSD083_07_1_M	99.93	100.1	CMN	Crystalline dolomite with dolomite-vein-related chalcocite(?) heterogenite and green Cu-oxide. Whitish (feldspar?) alteration.
7	MSSD083_07_2_U	108.48	108.6	CMN	Crystalline (iron altered?) dolomite
8	MSSD083_07_3_M	116.46	116.66	CMN	Crystalline dolomite with cryptic-fracture-hosted chalcocite(?)
9	MSSD083_08_1_M	118.68	118.88	CMN	Bedded/laminated dolomitic argillite with stratiform copper sulphides
10	MSSD083_09_1_M	121.09	121.23	CMN	Crystalline dolomite with disseminated chalcocite(?) and iron alteration
11	MSSD083_10_1_M	132.72	132.87	SDS	Laminated dolomitic argillite with disseminated chalcocite(?)
12	MSSD083_11_1_M	134.71	134.86	SDS/breccia	Contact between green dolomitic argillite and brown monomictic clast supported breccia. Iron alteration and cobaltoan carbonate in dolomite veins
13	MSSD083_12_1_U	141.63	141.78	SDS	Massive dolomitic argillite. Iron alteration along veins
14	MSSD083_13_1_U	151.29	151.44	Breccia	Polymictic breccia with clasts of massive green dolomitic argillite
15	MSSD083_14_1_M	154.68	154.83	SDS?	Bedded dolomitic argillite with stratiform and disseminated chalcocite(?)
16	MSSD083_15_1_M	157.5	157.65	Breccia	Polymictic breccia with intense iron alteration, pervasive cobaltoan carbonate and disseminated chalcocite(?)
17	MSSD083_16_1_M	173.83	173.95	SDB?	Laminated dolomitic argillite with stratiform green alteration and yellow sulphides (pyrite? chalcopyrite?)
18	MSSD083_17_1_M	180.33	180.48	RSC?	Silicified crystalline dolomite with beige feldspar(?) alteration and pervasive/fracture filling cobaltoan carbonate
19	MSSD083_17_2_M	185.62	185.74	RSC? RSF?	Silicified dolomite with disseminated chalcocite, green alteration
20	MSSD083_18_1_M	187.81	187.93	RSF? Dstrat?	Dolomitic argillite with pressure-shadow-hosted and stratiform chalcopyrite(?)
21	MSSD083_19_1_U	193.48	193.63	RAT gris?	Massive green-red argillite with whitish alteration spots
22	MSSD083_19_2_U	195.39	195.59	RAT gris?	Massive green-grey argillite with wavy nodular white layers
23	MSSD083_20_1_U	196.43	196.58	Breccia	Brecciated rock with green-red alteration, dolomite veins and possible disseminated Cu sulphides
24	MSSD083_21_1_M	214.73	214.88	SDS	Green red dolomitic argillite with dolomite veins, associated red-pink alteration, and disseminated chalcocite(?)
25	MSSD083_21_2_U	219.53	219.64	SDS	Massive green dolomitic argillite
26	MSSD083_21_3_U	232.02	232.14	SDS	Bedded green dolomitic argillite with stratiform grey lath shaped minerals (scapolite?) cut by dolomite vein
27	MSSD083_21_4_M	236.39	236.59	SDS/SDB	Laminated black shale with dolomite-vein-hosted chalcopyrite(?)
28	MSSD083_22_1_M	238.99	239.09	SDS/SDB	Laminated black shale with stratiform yellow sulphides (pyrite?)
29	MSSD083_22_2_M	240.09	240.24	SDS/SDB	Laminated black shale with dolomite-vein-hosted sulphides
30	MSSD083_23_1_M	244.51	244.66	SDB	Bedded green dolomitic argillite with disseminated chalcopyrite(?)
31	MSSD083_23_2_U	244.85	245.02	SDB	Bedded/laminated green dolomitic argillite
32	MSSD083_23_3_U	251.52	251.67	SDB	Bedded green dolomitic argillite, with red iron(?) alteration
33	MSSD083_23_4_M	277.28	277.42	SDB	Bedded dolomitic argillite with disseminated sulphides
34	MSSD083_24_1_M	291.69	291.84	RSC	Silicified crystalline dolomite with beige feldspar(?) alteration and pervasive cobaltoan carbonate
35	MSSD083_24_2_M	298	298.15	RSC	Silicified crystalline dolomite with disseminated carrollite(?), chalcocite(?) and beige feldspar(?) alteration
36	MSSD083_25_1_M	303.92	304.04	RSF	Wavy laminated silicified dolomitic argillite with vein hosted cobaltoan dolomite
37	MSSD083_26_1_M	309.16	309.31	Dstrat	Bedded dolomitic argillite with pressure-shadow hosted sulphides
38	MSSD083_26_2_M	313.18	313.33	Dstrat	Crystalline green dolomite with dolomite-vein-hosted multiple sulphides
39	MSSD083_27_1_U	314.68	314.83	RAT gris	Massive red-orange altered argillite with green alteration spots
40	MSSD083_27_2_U	317.13	317.28	RAT gris	Brecciated(?) argillite with dolomite veins, red and green alteration
41	MSSD083_28_1_U	319.67	319.82	RAT lilac	Crackle brecciated (dolomite veins) red argillite

MSSD140					
Number	Sample Name	Depth Start (m)	Depth End (m)	Interpreted Unit	Comments
1	MSSD140_07_1_M	40.55	40.7	RAT lilac	Massive red argillite with supergene malachite(?) vein
2	MSSD140_07_2_U	51.95	52.1	RAT lilac	Massive red argillite with white alteration(?) spots
3	MSSD140_07_3_U	56.5	56.6	RAT lilac	Bedded red-orange argillite with bedding parallel alteration(?), cut by and entrained into dolomite vein
4	MSSD140_07_4_U	63.8	63.9	RAT lilac	Massive red argillite cut by haematite vein, around which there is an orange-beige alteration halo
5	MSSD140_07_5_M	82.44	82.59	RAT lilac	Massive red argillite with disseminated haematite(?) and orange alteration around dolomite vein
6	MSSD140_07_6_U	83.13	83.28	RAT lilac	Massive red argillite with disseminated haematite(?) and orange and white alteration spots
7	MSSD140_08_1_U	99.85	100	RAT (?)	Laminated grey-orange-white argillite with orange alteration and intruded by dolomite vein
8	MSSD140_08_2_U	100.4	100.55	RAT (?)	Laminated orange-grey-white argillite with wavy bedding
9	MSSD140_08_3_U	101.58	101.73	RAT (?)	Deformed laminated grey-orange-white argillite, deformed (growth faults?) and nodular vugs
10	MSSD140_09_1_U	105.8	105.95	RAT lilac	Near homogenous red argillite - tiny alteration spots and haematite/dolomite veins

***Appendix 8b**: List of samples taken from Mashitu South boreholes MSSD083 and MSSD140.*

Appendix 9*: Photo-scans of all the thin-sections examined during this study taken from the samples described in Appendix 8.*

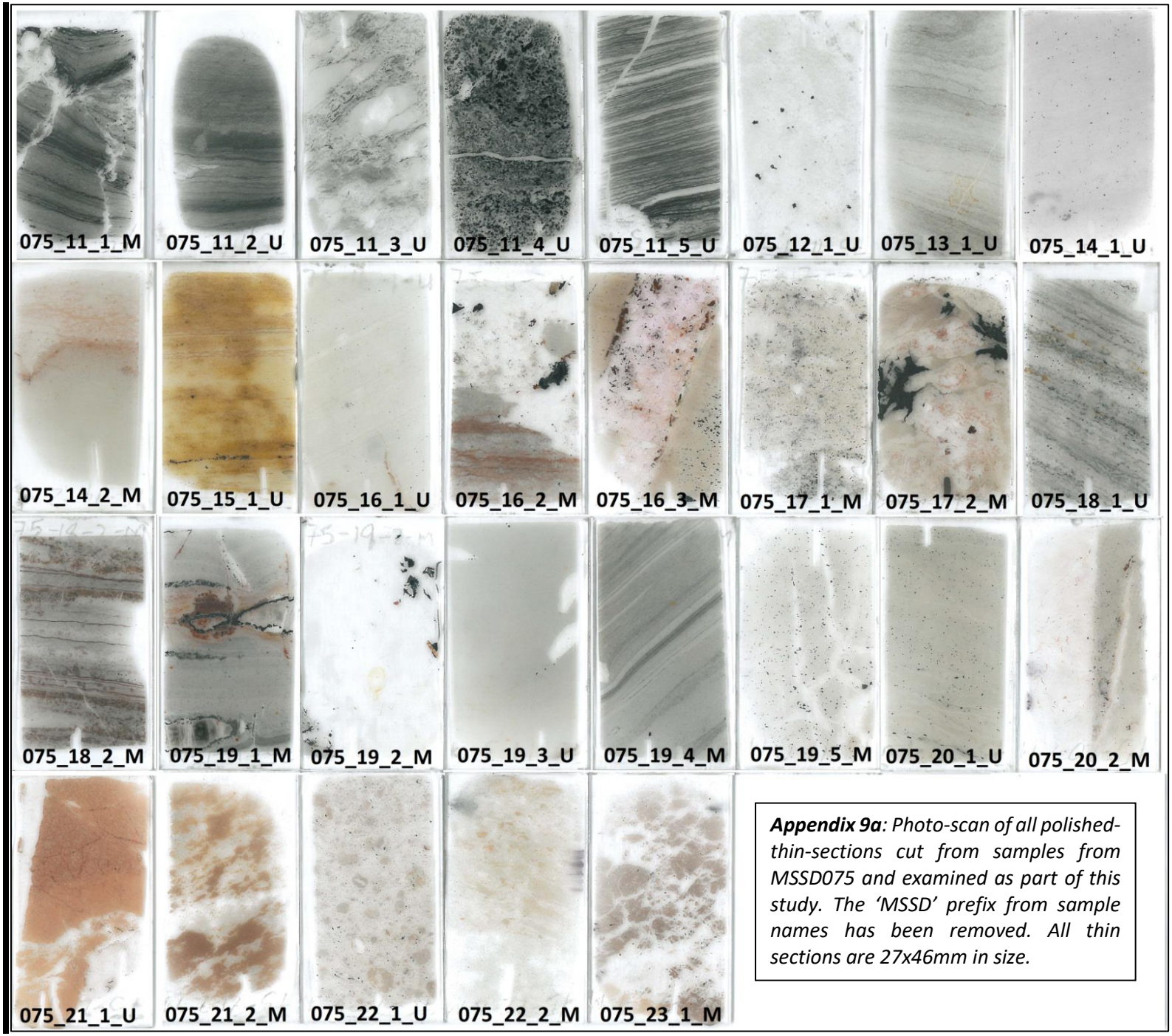

***Appendix 9a**: Photo-scan of all polished-thin-sections cut from samples from MSSD075 and examined as part of this study. The 'MSSD' prefix from sample names has been removed. All thin sections are 27x46mm in size.*

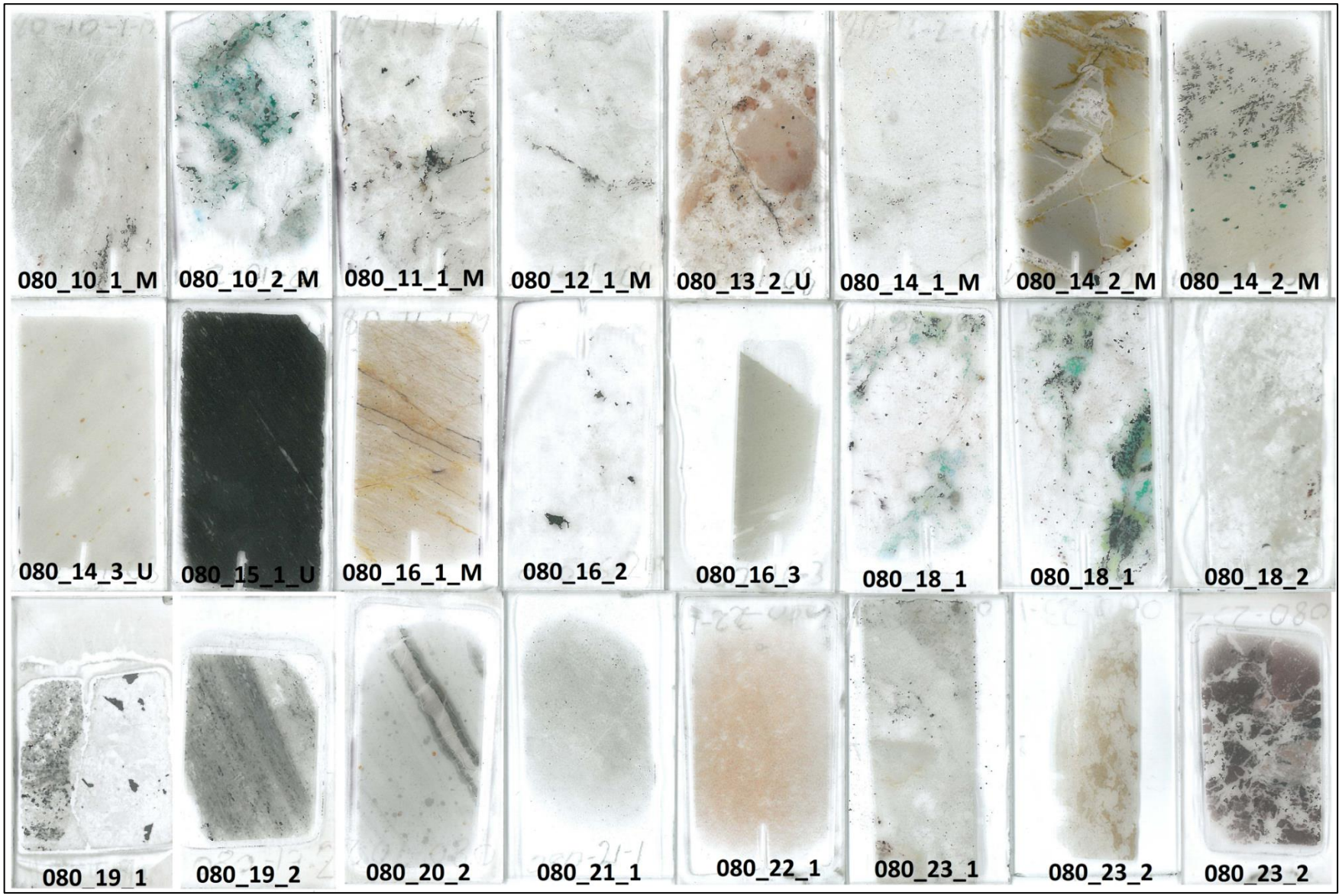

Appendix 9b: *Photo-scan of all polished-thin-sections cut from samples from MSSD080 and examined as part of this study. The 'MSSD' prefix from sample names has been removed. All thin sections are 27x46mm in size.*

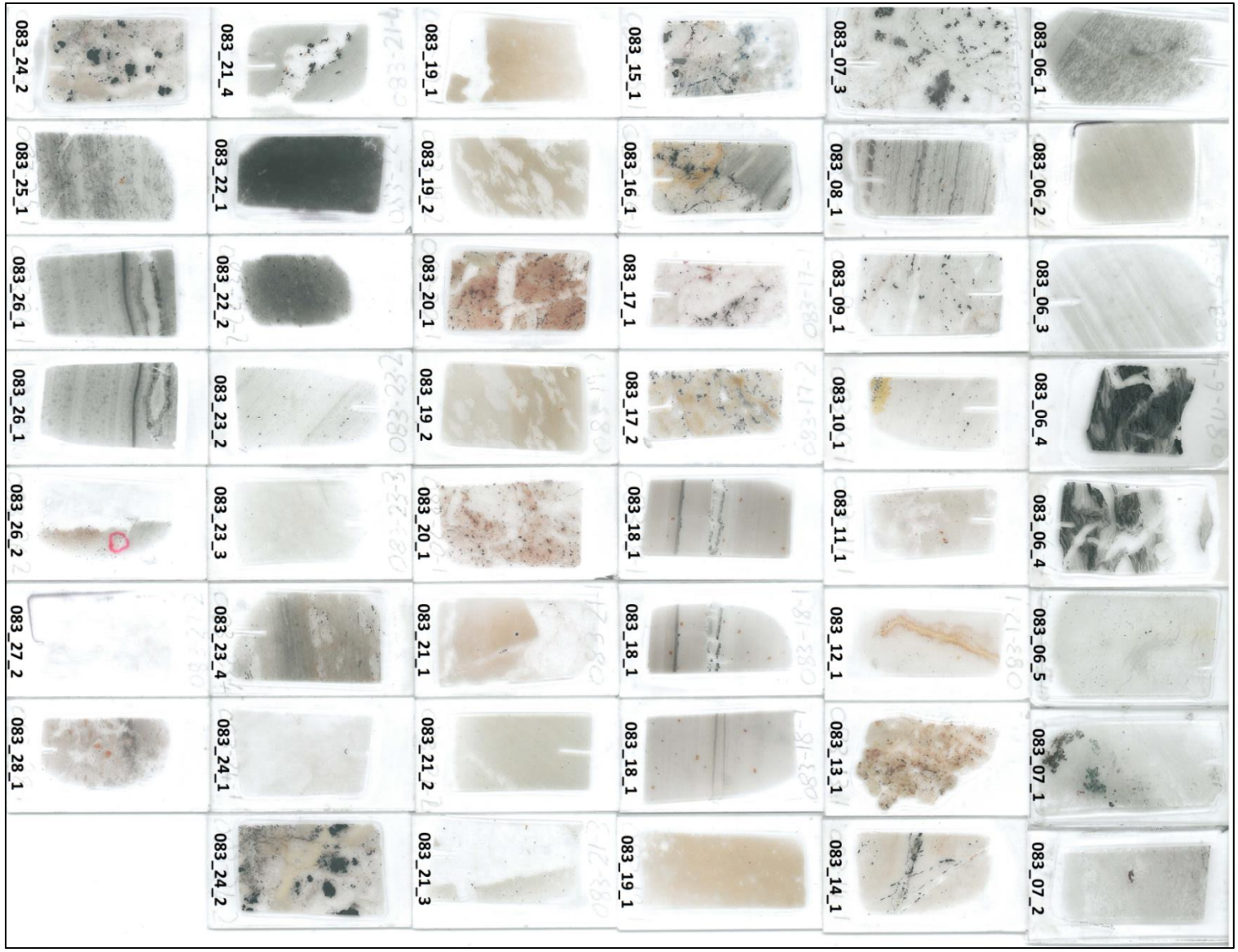

Appendix 9c: *Photo-scan of all polished-thin-sections cut from samples from MSSD083 and examined as part of this study. The 'MSSD' prefix from sample names has been removed. All thin sections are 27x46mm in size.*

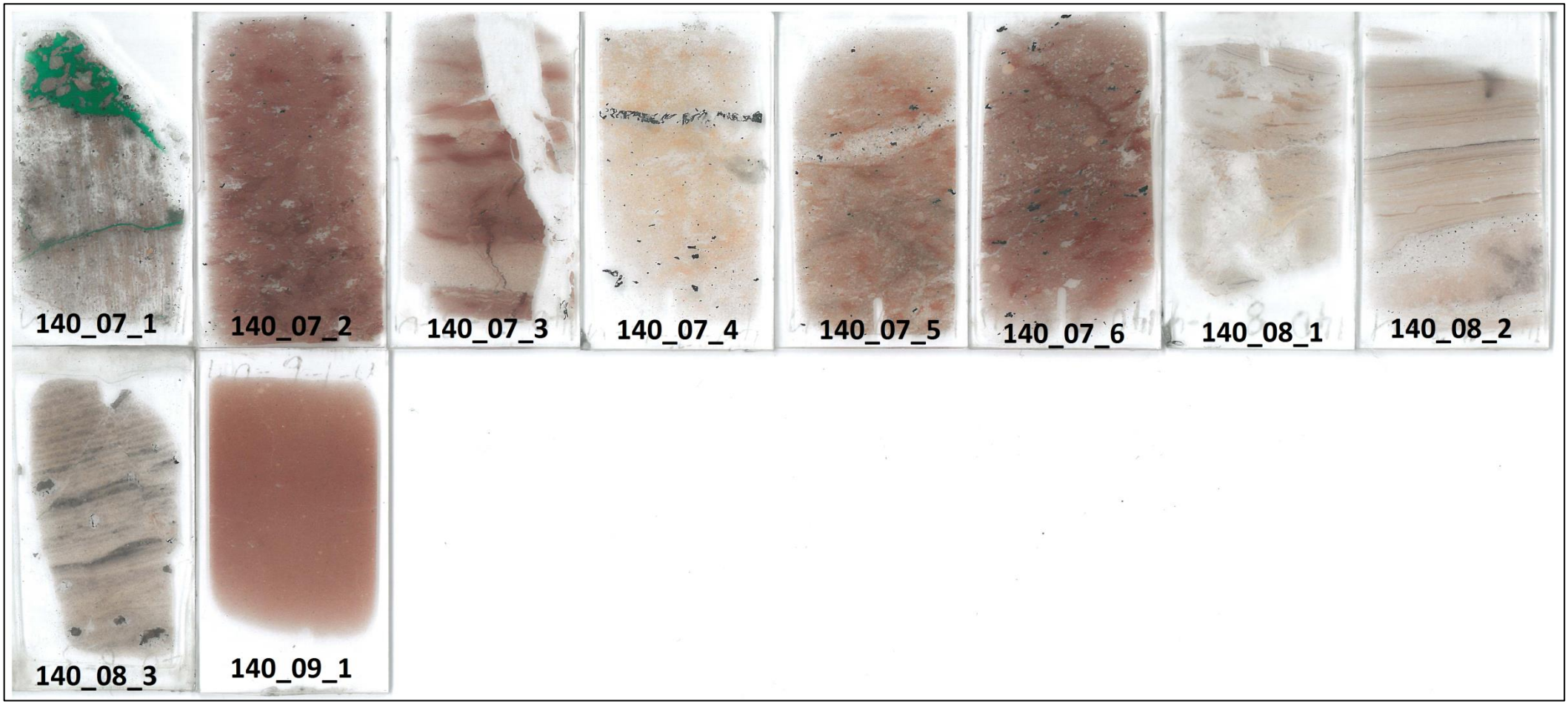

Appendix 9d: *Photo-scan of all polished-thin-sections cut from samples from MSSD140 and examined as part of this study. The 'MSSD' prefix from sample names has been removed. All thin sections are 27x46mm in size.*

Appendix 10*: Paragenesis matrix for all mineralised thin-sections from holes MSSD075, 080 and 083.*

MSSD075		1	2	3	4	5	6	7	8	9	10	11	12	13	14	15
	Stage →	Pre-ore diagenetic			Early hydrothermal SSC							Late hydrothermal ore stage				
Stratigraphic Unit ↓	Sample Name ↓ Phase →	Pyrite 1	Haematite 1	Pyrite 2	Pyrite 3	Sphalerite 1	Chalcopyrite 1	Bornite 1	Digenite 1	Chalcocite 1	Carrollite 1	Carrollite 2	Chalcopyrite 2	Bornite 2	Chalcocite 2	Digenite 2
CMN	11_1						Cpy									
	12_1						Cpy				Car					
SDS	14_1			Py												
SD2d	15_1						Cpy									
SDB	16_1						Cpy					Car				
	16_2				Py			Bn		Cc	Car					
	16_3															
RSC	17_1															
	17_2									Cc						
RSF	18_1										Car					
	18_2										Car					
DStrat	19_1				Py										Cc	
	19_2	Py			Py								Cpy	Bn	Cc	Dg
	19_3				Py					Cc	Car					
	19_4										Car					
	19_5											Car				
RATGris	20_1			Py							Car					
	20_2											Car				

MSSD075		16	17	18	19	20	21	22	23	24	25	26	27	28	29	30	31	32	33
	Stage →	Early Supergene											Late Supergene						
Stratigraphic Unit ↓	Sample Name ↓ Phase →	Native Copper 1	Cuprite 1	Tenorite 1	Chalcocite 3	Bn-Dg-Cov 3	Haematite 2	Cobaltoan Carbonate 1	Heterogenite 1	Azurite 1	Malachite 1	Chrysocolla 1	Chalcocite 4	Haematite 3	Cobaltoan Carbonate 2	Heterogenite 2	Malachite 2	Chrysocolla 2	Pseudomalachite 1
CMN	11_1												Cc						
	12_1				Cc														
SDS	14_1																		
SD2d	15_1				Cc	Bn													
SDB	16_1				Cc														
	16_2																		
	16_3				Cc	Bn									CoCarb		Mal		
RSC	17_1												Cc	Hm		Het			
	17_2													Hm		Het			
RSF	18_1																		
	18_2																		
DStrat	19_1																		
	19_2				Cc		Hm												
	19_3																		
	19_4																		
	19_5																		
RATGris	20_1				Cc														
	20_2				Cc	Bn								Hm	CoCarb				

Appendix 10a: *Paragenesis matrix for all mineralised samples within MSSD075. The presence of a mineral phase in a particular sample is indicated by the abbreviated mineral name (see List of Abbreviations and Terminology) in the row for that sample. Columns represent the relative timing of each mineral phase, with earlier-formed phases towards the left and later phases towards the right. The phases and stages were interpreted after all of the relative timings for minerals were correlated.*

MSSD080		1	2	3	4	5	6	7	8	9	10	11	12	13	14	15
	Stage →	Pre-ore diagenetic			Early hydrothermal SSC							Late hydrothermal ore stage				
Stratigraphic Unit ↓	Sample Name ↓ Phase →	Pyrite 1	Haematite 1	Pyrite 2	Pyrite 3	Sphalerite 1	Chalcopyrite 1	Bornite 1	Digenite 1	Chalcocite 1	Carrollite 1	Carrollite 2	Chalcopyrite 2	Bornite 2	Chalcocite 2	Digenite 2
CMN	10_1									Cc	Car					
	10_2											Car				
	11_1											Car	Cpy			
	12_1														Cc	
	13_1															
	13_2						Cpy				CoPy					
SDS	14_1											Car	Cpy		Cc	
	14_2															
	14_3															
SD2d	15_1										Car					
SDB	16_1															
	16_2						Cpy									
	16_3											Car				
RSC	18_1										Car					
	18_2															
RSF	19_1											Car			Cc	
	19_2										Car					
Dstrat	20_2				Py				Dg	Cc	Car					
RATGris	21_1	Py										Car				

MSSD080		16	17	18	19	20	21	22	23	24	25	26	27	28	29	30	31	32	33
	Stage →	Early Supergene											Late Supergene						
Stratigraphic Unit ↓	Sample Name ↓ Phase →	Native Copper 1	Cuprite 1	Tenorite 1	Chalcocite 3	Bn-Dg-Cov 3	Haematite 2	Cobaltoan Carbonate 1	Heterogenite 1	Azurite 1	Malachite 1	Chrysocolla 1	Chalcocite 4	Haematite 3	Cobaltoan Carbonate 2	Heterogenite 2	Malachite 2	Chrysocolla 2	Pseudomalachite 1
CMN	10_1				Cc							Cry		Hm			Mal	Cry	
	10_2				Cc	Dg+Cov	Hm				Mal	Cry					Mal	Cry	Psm
	11_1				Cc	Dg+Cov	Hm										Mal	Cry	
	12_1						Hm								CoCarb		Mal		
	13_1												Cc	Hm					
	13_2				Cc														
SDS	14_1			Ten							Mal			Hm			Mal		
	14_2				Cc	Cov								Hm		Het	Mal		
	14_3												Cc						
SD2d	15_1												Cc						
SDB	16_1						Hm												
	16_2																		
	16_3																Mal		
RSC	18_1	Cu	Cup	Ten	Cc		Hm		Het	Azu							Mal	Cry	
	18_2													Hm					
RSF	19_1				Cc		Hm								CoCarb				
	19_2				Cc														
Dstrat	20_2																		
RATGris	21_1						Hm						Cc						

Appendix 10b: *Paragenesis matrix for all mineralised samples within MSSD080. The presence of a mineral phase in a particular sample is indicated by the abbreviated mineral name (see List of Abbreviations and Terminology) in the row for that sample. Columns represent the relative timing of each mineral phase, with earlier-formed phases towards the left and later phases towards the right. The phases and stages were interpreted after all of the relative timings for minerals were correlated.*

MSSD083		1	2	3	4	5	6	7	8	9	10	11	12	13	14	15
	Stage →	Pre-ore diagenetic			Early hydrothermal SSC							Late hydrothermal ore stage				
Stratigraphic Unit ↓	Sample Name ↓ Phase →	Pyrite 1	Haematite 1	Pyrite 2	Pyrite 3	Sphalerite 1	Chalcopyrite 1	Bornite 1	Digenite 1	Chalcocite 1	Carrollite 1	Carrollite 2	Chalcopyrite 2	Bornite 2	Chalcocite 2	Digenite 2
CMN	06_1						Cpy				Car					
	06_2			Py												
	06_3	Py		Py			Cpy									
	06_4			Py												
	06_5										Car		Cpy	Bn		Dg
	07_1												Cpy			
	07_2				Py										Cc	
	07_3											Car				
	08_1									Cc	Car					
	09_1			Py								Car				
SDS	10_1															
	12_1	Py														
	13_1												Cpy			
	14_1										Car		Cpy	Bn	Cc	
SDB	15_1											Car				
	16_1		Hm		Py					Cc	Car					
RSC	17_1														Cc	
RSF	17_2										Car				Cc	
DStrat	18_1	Py			Py					Cc						
RATGris	19_2		Hm													
RATRouge	20_1				Py		Cpy				Car					
SDS	21_1															
	21_2															
	21_3			Py									Cpy			
SD2d	21_4		Hm		Py	Sph	Cpy	Bn	Dg		Car					
	22_2	Py	Hm	Py			Cpy	Bn								
SDB	23_2		Hm	Py			Cpy	Bn		Cc	Car					
	23_3			Py												
	23_4				Py											
RSC	24_2										Car					
RSF	25_1				Py						Car				Cc	
DStrat	26_1				Py		Cpy	Bn		Cc	Car					
RATGris	26_2				Py		Cpy	Bn		Cc		Car			Cc	Dg
RATRouge	28_1		Hm													

Appendix 10c: *Paragenesis matrix for hypogene phases of all mineralised samples within MSSD083. Supergene phases are presented in Appendix 10c (continued), overleaf, for layout formatting purposes. The presence of a mineral phase in a particular sample is indicated by the abbreviated mineral name (see List of Abbreviations and Terminology) in the row for that sample. Columns represent the relative timing of each mineral phase, with earlier-formed phases towards the left and later phases towards the right. The phases and stages were interpreted after all of the relative timings for minerals were correlated.*

MSSD083		16	17	18	19	20	21	22	23	24	25	26	27	28	29	30	31	32	33
	Stage →	Early Supergene											Late Supergene						
Stratigraphic Unit ↓	Sample Name ↓ Phase →	Native Copper 1	Cuprite 1	Tenorite 1	Chalcocite 3	Bn-Dg-Cov 3	Haematite 2	Cobaltoan Carbonate 1	Heterogenite 1	Azurite 1	Malachite 1	Chrysocolla 1	Chalcocite 4	Haematite 3	Cobaltoan Carbonate 2	Heterogenite 2	Malachite 2	Chrysocolla 2	Pseudomalachite 1
CMN	06_1				Cc	Dg													
	06_2																		
	06_3																		
	06_4																		
	06_5																		
	07_1				Cc									Hm			Mal		
	07_2						Hm												
	07_3				Cc			CoCarb											
	08_1																		
	09_1				Cc		Hm												
SDS	10_1				Cc		Hm												
	12_1				Cc		Hm												
	13_1						Hm												
	14_1																		
SDB	15_1				Cc													Cry	
	16_1												Cc	Hm					
RSC	17_1						Hm	CoCarb							CoCarb				
RSF	17_2																		
DStrat	18_1																		
RATGris	19_2																		
RATRouge	20_1				Cc		Hm						Cc						
SDS	21_1				Cc		Hm												
	21_2				Cc														
	21_3																		
SD2d	21_4																		
	22_2																		
SDB	23_2																		
	23_3				Cc														
	23_4																		
RSC	24_2				Cc			CoCarb											
RSF	25_1														CoCarb				
DStrat	26_1																		
RATGris	26_2																		
RATRouge	28_1																		

Appendix 10c (continued): *Paragenesis matrix for supergene phases of all mineralised samples within MSSD083. Hypogene phases are presented on the first page of Appendix 10c, for layout formatting purposes. The presence of a mineral phase in a particular sample is indicated by the abbreviated mineral name (see List of Abbreviations and Terminology) in the row for that sample. Columns represent the relative timing of each mineral phase, with earlier-formed phases towards the left and later phases towards the right. The phases and stages were interpreted after all of the relative timings for minerals were correlated.*

***Appendix 11**: 'Element mobility in the weathering environment and surface vectors to mineralisation—A case study from the Mashitu South Cu-Co deposit, Katanga, Democratic Republic of Congo'. This 2017 paper by Gigler and Kinnaird was published in the Journal of Geochemical Exploration and is based on work presented in Chapter 4: Geochemistry and Geostatistics.*

Journal of Geochemical Exploration 183 (2017) 127–137

Contents lists available at ScienceDirect

Journal of Geochemical Exploration

journal homepage: www.elsevier.com/locate/gexplo

Element mobility in the weathering environment and surface vectors to mineralisation—A case study from the Mashitu South Cu-Co deposit, Katanga, Democratic Republic of Congo

Gruffudd M. Gigler*, Judith A. Kinnaird

University of the Witwatersrand, Richard Ward, 1 Jan Smuts Ave, Braamfontein, Johannesburg 2000, South Africa

ARTICLE INFO

Keywords:
Copper
Cobalt
Weathering
Supergene
Mineral exploration
Democratic Republic of Congo

ABSTRACT

The Cu-Co deposits of the Katangan Copperbelt are affected by a deep chemical weathering regime. Meteoric fluids leached mobile elements from the near-surface environment and have redistributed them further down, forming remobilised supergene Cu deposits at a depth of ~30–50 m which are highly economic. The same process has caused residual enrichment of less mobile elements such as Co, forming 'cobalt caps' in the near-surface above such supergene Cu deposits. Elements which are associated with hypogene Cu-Co mineralisation, but which are relatively immobile during supergene alteration, can make effective surface vectors to buried supergene Cu deposits; especially where these deposits have experienced a high degree of leaching and where high regional background Cu concentrations obscure surface Cu anomalies.

This study uses an average-normalisation technique, applied to a large whole-rock-geochemistry database, to assess the variation in geochemistry between different depth intervals at the Mashitu South Cu-Co deposit. Geochemical variation by depth acts as an empirical proxy for element mobility during weathering, with the average concentrations of more mobile elements being depleted in the near surface profile.

Of the major and trace elements which are known to be associated with hypogene mineralisation at Mashitu South, Cu, Ni, S and Zn are depleted in the near-surface environment, whereas Co, Bi, V, Mo, As and Fe experienced residual enrichment due to supergene alteration. Indeed, Bi and V exhibit an even greater degree of residual enrichment than Co, which is known as a surface pathfinder to Cu deposits in Katanga. It is suggested that Bi, V and Co would make effective surface vectors to Katangan Cu-Co deposits that have experienced a high degree of leaching; deposits which may evade detection by exploration solely for Cu surface anomalies. The average-normalisation technique utilised by this study can be used to identify immobile surface vectors to any polymetallic deposit which has been significantly affected by chemical weathering.

1. Introduction

The Mashitu South Cu-Co deposit (referred to as Mashitu Sud in Belgian literature), part of the 'Mashitu Complex' of deposits, lies approximately 25 km east of the city of Kolwezi in the Katanga Province of south-eastern Democratic Republic of Congo (DRC). It is situated within the Katangan Copperbelt, part of the Central African Copperbelt (CAC) (Fig. 1), a metallogenic province that contains ~6% of the world's known Cu reserves and ~48% of the world's known Co reserves (USGS, 2016), with remarkably high average Cu-Co grades relative to other global sources.

The exploitation of Cu-Co deposits in Katanga has, to date, mostly focussed on oxidised, supergene ores (Hitzman et al., 2012) which are economically attractive due to their high average grades, ease of mineral processing and proximity to the surface. Mining of these oxidised ores dates to at least the 4th Century CE (de Maret, 1982, 1986) and artisanal diggings, abundant in the area, have offered an easy guide for colonial and post-colonial era exploration. More recently, regional and local soil geochemical surveys have also met with success in locating Cu-Co deposits, through the targeting of Cu surface anomalies (Chimvinga, pers. comm., 2014). However, many Cu-Co deposits do not exhibit a discernible Cu anomaly at surface when compared to the regionally high background soil Cu concentrations, largely due to intense weathering in the region and high mobility of Cu in the near-surface environment. Soil samples taken from over Mashitu South, for example, have an average Cu concentration of ~192 ppm. While this is above the average Cu-in-soil concentration for a regional study carried out by Eurasian Resources Group (ERG) comprising a ~300 km^2 licence area

* Corresponding author at: School of Geosciences, University of the Witwatersrand, Private Bag 3, 2050 Wits, South Africa.
E-mail address: griffgigler@yahoo.com (G.M. Gigler).

http://dx.doi.org/10.1016/j.gexplo.2017.10.002
Received 5 May 2017; Received in revised form 8 September 2017; Accepted 3 October 2017
Available online 07 October 2017
0375-6742/ © 2017 Published by Elsevier B.V.

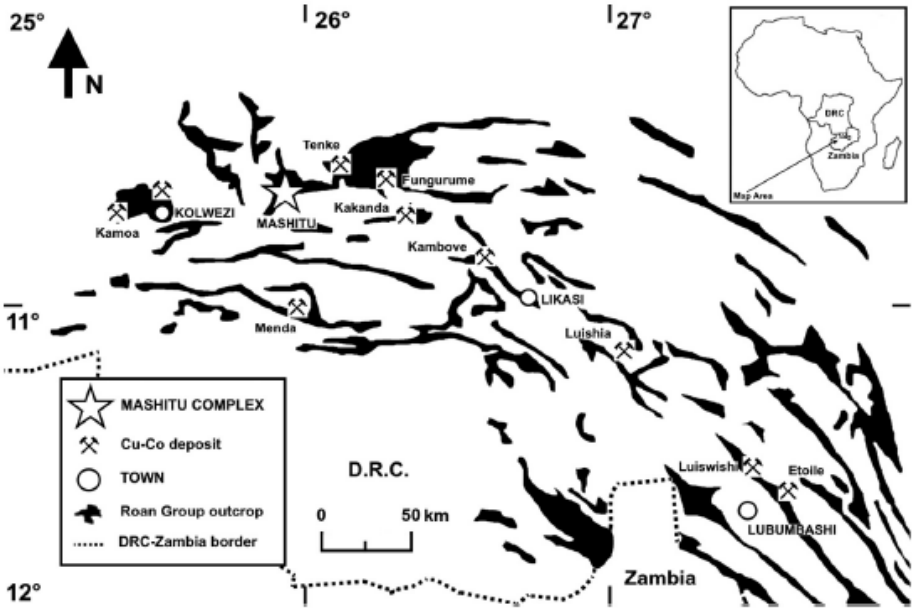

Fig. 1. Location map of the Mashitu Complex showing its position within the Katangan Copperbelt and outcrops of Roan Group metasedimentary rocks. After François (1974).

(~94 ppm Cu), it is not significantly above the average for a smaller, ~25 km^2 portion of this region (~163 ppm Cu) which comprises prospective stratigraphy in which Mashitu South is situated. Indeed, only values of > 720 ppm Cu for the larger, ~300 km^2 licence area and > 360 ppm Cu for the smaller, ~25 km^2 prospective stratigraphy portion are statistically indicated to be 'anomalously high', making the ~192 ppm Cu-in-soil-average of Mashitu South easy to overlook as a target for further exploration (Gigler, 2016).

The targeting of Co anomalies is well known as an alternative to targeting Cu as a means of exploration for Cu-Co deposits. In Katanga, Co is frequently associated with Cu mineralisation in stratiform, hypogene deposits, however the two metals are known to decouple during supergene alteration (Gauthier and Deliens, 1999; Decrée et al., 2010; Fay and Barton, 2012). Cobalt is less mobile than Cu in the oxidising environment and remains near the surface residually, or travels a short distance downwards to form remobilised Co-oxide deposits, usually as heterogenite – CoOOH (Decrée et al., 2015). By contrast, Cu tends to leach more efficiently from the oxidised zone, travelling downwards to the water table where it precipitates primarily as malachite ($Cu_2CO_3(OH)_2$) in voids (De Putter et al., 2010). This results in 'cobalt caps' of 'black earth' which overlie supergene copper deposits (Decrée et al., 2010). Over such deposits, one would expect the Co surface anomaly to be stronger and more easily discernible than the Cu anomaly.

Although Cu and Co are the primary products of mining in the Central African Copperbelt, many deposits are polymetallic, with economic concentrations of Ni, Zn, Pb, Ag, Au, Ge and U as well as subeconomic concentrations of As, V, Mo, Bi, Ga, Pt and Pd closely associated with hypogene copper mineralisation (Torrealday et al., 2000; Broughton et al., 2002; McGoldrick et al., 2003; Dewaele et al., 2006a; Kampunzu et al., 2009; McGoldrick et al., 2010; Selley et al., 2010; Halley et al., 2016). At Mashitu South, hypogene mineralisation has been shown to have a geochemical association of Cu + Co + Bi + Ni + V + S ± Mo ± As ± Fe ± Zn, while supergene Cu-oxide mineralisation has a geochemical association of Cu-Be-P ± Zn (Gigler, 2016).

In this study, analysis of massed drill-core assay data from Mashitu South is used to characterise the geochemical variation of major and trace elements through the depth profile of the deposit. This variation in geochemistry empirically reflects the mobility of these different elements under oxidising, leaching conditions. Identifying elements which are associated with hypogene Cu mineralisation, but which are less mobile than Cu in the supergene environment, can lead to the development of surface pathfinder elements to buried supergene Cu deposits. The approach developed in this paper can be applied to identify surface pathfinder elements to any polymetallic mineral deposit which has been heavily leached through chemical weathering.

2. Geological setting

The Cu-Co deposits of the Katangan Copperbelt are hosted in rocks of the Katangan Supergroup, which were deposited between ~880 Ma (Armstrong et al., 2005) and ~573 Ma (Master et al., 2005). The rocks of the lowermost Roan Group host the majority of regional mineralisation and are made up of a sequence of siliciclastic argillites and arenites (the Roches Argilo-Talqueuse – 'RAT' Subgroup) which transition upwards into a sequence of dolostones and dolomitic shales (the Mines Series Subgroup). The Mines Series comprises (from bottom to top): The Dolomies Stratifiées (DStrat), Roches Siliceuses Feuilletées (RSF) and Roches Siliceuse et Cellulaire (RSC) units (the Kamoto Formation), the Shales Dolomitique (SD) unit (the Dolomitic Shales Formation) and the Calcaire à Minéraux Noire (CMN) unit (the Kambove Formation). The primary regional mineralisation event occurred between ~875 and ~750 Ma (Key et al., 2001; Selley et al., 2006; Muchez et al., 2010; Decrée et al., 2014), forming *syn*-diagenetic, stratiform Cu-Co sulphides (Dewaele et al., 2006b) hosted mainly in the Mines Series Subgroup. Subsequent to the deposition and stratiform mineralisation of the Mines Series, the Roan Group experienced an episode of tectonic disruption wherein the strata were deformed and fragmented into 'megabreccias'. This disruption created 'megaclasts' or 'rafts' of intact stratigraphy, often several cubic km in volume, which lie in a 'matrix' of heterogeneous breccias and smaller megaclasts. The most widely-accepted explanation for this disruption is that it was caused by halokinetic diapirism of thick evaporite units previously located in the RAT and Dipeta Subgroups of the Roan Group (Bell, 1989; Jackson et al., 2003; Hitzman et al., 2012). The sedimentary rocks of the Katangan Supergroup were also deformed by the Lufilian Orogeny, from which peak metamorphism is dated to ~540–535 Ma (Kröner and Stern, 2005), reaching maximum P/T conditions of lower greenschist facies in Katanga (Ramsay and Ridgway, 1977). A second, 'vein-type' hypogene mineralisation event is distinguished in the region by Dewaele et al. (2006b), which formed vein-hosted Cu-Co sulphides and

is dated to a wide range of ages in different locations around the Copperbelt, spanning from ~615–470 Ma (Richards et al., 1988a, 1988b; Dawson, 2002; Selley et al., 2006; Torrealday et al., 2000). Pre, syn and post-folding structural relationships are identified in the host veins, indicating that multiple post-lithification hydrothermal events contributed to the formation of this stage of mineralisation. It should be noted that compared to stratiform Cu-Co mineralisation, vein-hosted Cu-Co mineralisation in the Katangan Copperbelt tends to be volumetrically and economically minor (Sweeney et al., 1991; Sweeney and Binda, 1994; Dewaele et al., 2006b).

The post-Lufilian geological history of Katanga is dominated by uplift, erosion, weathering and supergene mineralisation. Decrée et al. (2010) discerned two periods of supergene mineralisation in the region, dated to the Late Miocene, at or before ~10.3 Ma, and the Pliocene (~5.3–2.3 Ma), respectively. The Miocene period coincided with epeirogenic uplift initiated by the reactivation of the West African tectonic margin (Lavier et al., 2001), which excavated Roan Group stratigraphy and exposed rocks that hosted hypogene mineralisation to the action of meteoric fluids. The Pliocene supergene ore-formation event coincided with a regional transition to a more humid climate (Alexandre, 2002; Giresse, 2005; Miller et al., 2010) during which weathering processes were accelerated by warmer, wetter, more tropical conditions than those that prevailed in the Miocene or today (Gasse, 2006; Peel et al., 2007; Miller et al., 2010). It is possible, however, that earlier supergene events may have occurred which have since been overprinted; Hitzman (pers. comm., 2016) relates an incidence of supergene enrichment at the nearby Kolwezi deposit which is covered by Karoo Supergroup rocks, indicating a possible Mesozoic or even Palaeozoic age for enrichment. Today, there is a deep saprolite over much of the Katangan substratum, with around 10 m of clay, often kaolinite ($Al_2Si_2O_5(OH)_4$), developed at the surface (Giresse, 2005; Timmermans, 2015). This attests to a deep weathering regime which influenced the considerable supergene alteration to the Cu-Co deposits in the region (Dewaele et al., 2006b). Supergene Cu-Co deposits in Congo typically occur at a depth of < 100 m (Ngongo, 1975) however supergene alteration may occur at depths of > 1 km (Hitzman et al., 2012), particularly where there is a fluid pathway such as a breccia or a permeable stratigraphic unit to facilitate downwards migration of meteoric fluids (Fay and Barton, 2012). Elements which are more mobile under weathering conditions are depleted from the near surface environment, and enriched at depth due to re-precipitation under favourable Eh-pH conditions.

The Mashitu South deposit is situated roughly 25 km east of the city of Kolwezi, within a roughly triangular structure of heterogenous, brecciated Roan Group stratigraphy, informally termed the 'Kalukundi Diapir' by Hitzman (pers. comm., 2015). The deposit is a domal fragment of Mines Series Subgroup rocks which is bounded by RAT Subgroup rocks, heterogenous breccias and another underlying fragment of Mines Series along the eastern margin. It lies amongst a cluster of several other fragments of Mines Series and Cu-Co deposits termed the 'Mashitu Complex' (Fig. 2). The regolith at Mashitu South is deep and almost exclusively residual, and there is almost no surface expression to the Mines Series Subgroup fragment on which the deposit is centred. There is typically a ~10 m thick ferruginous pedolith at the top of the profile which retains none of the fabric of the original rock from which it formed. Below this is a ferruginous-pallid mottled zone of variable thickness and a kaolinitic saprolite which extends to ~50 m depth. Saprock may be found to a depth of between ~100–200 m before striking unweathered bedrock. The thicknesses of the zones of the regolith profile are highly variable and dependent upon the primary lithologies which have been weathered; saprock and unweathered bedrock are generally found at shallower depths in the siliciclastic RAT Subgroup rocks, whereas the primarily calcareous Mines Series Subgroup rocks tend to have a thicker and more well-developed saprolitic zone. In addition, weathering was enhanced in the vicinity of permeable breccias and stratigraphic units such as the RSC, and by the presence of sulphides in the weathering rocks (Gigler, 2016).

The Mashitu South fragment has been extensively delineated by drilling between 2005 and 2012. There are three main types of orebody at Mashitu South (Gigler, 2016). The first is a stratiform-disseminated chalcocite (Cu_2S) – carrollite ($CuCo_2S_4$) orebody hosted in the silicified, dolomitic Kamoto Formation, equivalent to the 'Lower Orebody' of regional literature (Hitzman et al., 2012). The second is a stratiform-disseminated chalcopyrite ($CuFeS_2$) – bornite (Cu_5FeS_4) dominated orebody developed in the ~5 m thick SD2d stratigraphic unit, a carbonaceous shale within the Dolomitic Shales Formation. The third type of orebody is supergene in origin, hosted in the RAT Subgroup and is dominated by void-filling malachite. This type of orebody generally occurs within 30-50 m of the surface and within the lower saprolite or upper saprock, beneath the former position of leached and eroded Mines Series stratigraphy.

Gigler (2016) distinguished four discrete mineralising events at Mashitu South. The stratiform orebodies in the SD2d and the Kamoto Formation were created *syn*-diagenetically in a protracted event equated with the main stratiform mineralisation stage in the region. A 'vein-type' second mineralisation stage is also evident; however, this did not significantly remobilise or re-concentrate ore at Mashitu South and is not responsible for the present-day distribution of any of the orebodies. The third and fourth mineralisation stages are both supergene and are equated to the Miocene-Pliocene events described by Decrée et al. (2010). The most recent of these supergene events is interpreted to have controlled the distribution of the RAT-hosted malachite orebodies, which are of significant economic importance.

3. Methods

3.1. Data capture

A geochemical assay database provided by Comide S.P.R.L. was the source of data for this study. This database was compiled from assays on half-core, < 1 m long samples from diamond drill core of varying thicknesses drilled at the Mashitu South deposit. These samples were selected by Comide employees from areas containing visible Cu-Co mineralisation, stratigraphic intervals which were expected to host mineralisation, and the broad environs of each (Chimvinga, pers. comm., 2014). Once selected, the samples were split, crushed and sent to ALS Global Laboratories. Copper and cobalt were assayed using the 'ME-OG62' technique: 'Ore-grade elements by four acid digestion using conventional inductively coupled plasma - atomic emission spectroscopy (ICP-AES) analysis', and Ag, Al, As, Ba, Be, Bi, Ca, Cd, Fe, K, La, Mg, Mn, Mo, Na, Ni, P, Pb, S, Sc, Sr, Ti, U, V, W and Zn were assayed using the 'ME-ICP61' technique: 'Trace level methods using conventional ICP-AES analysis'. Both methods involve four-acid-digestion of the samples followed by ICP-AES analysis of the resultant solutions. More information on these techniques can be found on the ALS Global website (ALS Global, 2009a, 2009b).

These two assay techniques for the 28 elements were used respectively in the amended final database because they had the lowest associated margins of error and Lower Limit of Detection (LLOD), out of the variety of assay techniques conducted on the samples in the original database provided by Comide. Only samples which had a full suite of ICP-AES results for the 28 elements mentioned above and which were coded as belonging to the MSS deposit were included in the final amended database. The database was then 'cleaned' by removing values below the LLOD and replacing them with half the LLOD, to remove spuriously low values and to give non-zero values for statistical analysis. The detection limits for each elemental analysis are given below in Table 1.

Additionally, in order to create discrete depth values for each sample, a mid-point depth was calculated for each, by averaging the 'depth from' and 'depth to' attributes as logged by Comide employees. Stratigraphy, lithology and Hole I.D. attributes were then added to each

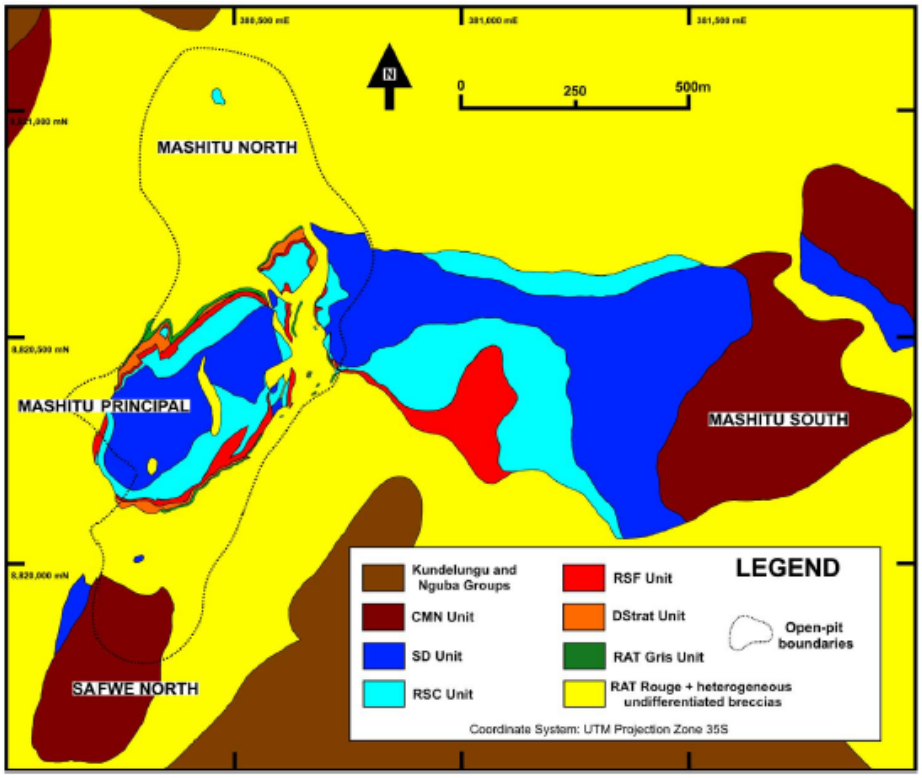

Fig. 2. Local geology map showing the four deposits of the Mashitu Complex, Mashitu North, Mashitu Principal, Mashitu South and Safwe North. CMN: Calcaire à Minéraux Noire Unit, SD: Shales Dolomitique Unit, RSC: Roches Siliceuse et Cellulaire Unit, RSF: Roches Siliceuses Feuilletées Unit, DStrat: Dolomies Stratifiées Unit, RAT: Roches Argilo-Talqueuse, i.e. RAT Gris and RAT Rouge units. Data provided by Eurasian Resources Group (ERG).

Table 1
LLOD (Lower Limit Of Detection) values for the ME-ICP61 and ME-OG62 assay techniques on the 28 different elements considered in this study, supplied by Comide S.P.R.L. and ALS Global.

Element	Assay technique	LLOD (ppm)
Ag	ME-ICP61	0.5
Al	ME-ICP61	100
As	ME-ICP61	5
Ba	ME-ICP61	10
Be	ME-ICP61	0.5
Bi	ME-ICP61	2
Ca	ME-ICP61	100
Cd	ME-ICP61	0.5
Co	ME-OG62	10
Cu	ME-OG62	10
Fe	ME-ICP61	100
K	ME-ICP61	100
La	ME-ICP61	10
Mg	ME-ICP61	100
Mn	ME-ICP61	5
Mo	ME-ICP61	1
Na	ME-ICP61	100
Ni	ME-ICP61	1
P	ME-ICP61	100
Pb	ME-ICP61	2
S	ME-ICP61	100
Sc	ME-ICP61	1
Sr	ME-ICP61	1
Ti	ME-ICP61	100
U	ME-ICP61	10
V	ME-ICP61	2
W	ME-ICP61	10
Zn	ME-ICP61	2

sample by comparison of the geochemical assay and geological databases provided by Comide. The final product was a Microsoft Excel database of 12,058 samples from almost 200 drill holes at Mashitu South, each with 32 attributes: Hole ID, depth, stratigraphy, lithology, and assay values for each of the 28 elements considered in this study.

3.2. Normalisation techniques

In order to assess the relative concentration of different elements at different depth intervals, a self-normalisation method was conceived. This involved first calculating the average concentration of each element within the amended final database, by calculating the mean concentration out of the 12,058 samples for each element. This gave values dubbed the 'Average Concentration of Elements at Mashitu South', or ACEMS values. The ACEMS values were then used to normalise split datasets by dividing concentration values from a particular sample, or average concentration values from a split dataset, by the ACEMS values for each element. The ACEMS values are given in Table 2.

By normalising to ACEMS, an immediate picture is obtained of whether any element is concentrated or depleted within a particular sample or dataset, relative to the average concentration of that element for the 12,058 samples in the amended final Mashitu South database.

To assess the variation in element geochemistry by depth caused by weathering, samples were split into different sub-databases using the 'DEPTH' attribute in the amended final database: for example, 0–10 m, 10–50 m and 50–100 m sub-databases were created. Mean concentration values for each of these depth intervals were then calculated and normalised to ACEMS, to give an idea of the relative depletion or enrichment of these elements at each given depth interval.

The amended final database was primarily split simply by depth intervals, with a view to providing a general idea of element variation by depth irrespective of lithology or stratigraphy. However, the database was also split into sub-databases for each stratigraphy, which were themselves split into sub-databases by depth, to assess the weathering mobility of elements in different types of mineralised stratigraphic units.

4. Results

The ACEMS-normalised element plot for the < 10 m, 10–50 m,

Table 2
Table of ACEMS (average concentration of elements at Mashitu South) values, calculated by taking the mean concentration of all 12,058 samples in the amended final database and used as normalising factors.

Element	ACEMS value (ppm)
Mg	70,189.53
Al	39,312.94
Ca	36,095.20
Fe	19,676.71
Cu	6388.14
K	5204.34
Co	1623.43
Ti	1498.93
S	1429.81
Mn	651.96
P	401.62
Na	238.29
Ba	139.64
V	103.64
Ni	42.80
Sr	34.08
Zn	24.31
La	18.35
Pb	10.59
U	9.25
W	8.61
Sc	8.31
As	7.09
Bi	3.63
Mo	2.31
Be	2.25
Ag	1.09
Cd	0.31

50–100 m, 100–200 m and > 200 m depth intervals at Mashitu South (Fig. 3) shows that the concentrations of most of the 28 elements analysed vary significantly between each depth interval. These depth intervals were chosen to give a near surface, maximally weathered portion roughly equivalent to the ferruginous pedolith (< 10 m), an interval which corresponds to the saprolite, in which most of the remobilised supergene mineralisation is observed in core logs at the deposit (10-50 m), an interval generally comprised of saprock (50-100 m), a depth interval in which the weathering zone classification varies considerably between saprock and 'fresh' bedrock in different drill-cores (100–200 m) and a minimally weathered portion comprised almost exclusively of unweathered bedrock (> 200 m). It should be noted that the correspondence of these depth intervals with weathering zone classifications is highly approximate and the accuracy varies considerably between the > 200 drill-cores from Mashitu South analysed as part of this study, for reasons discussed in Section 2: Geological setting.

Four trends in element concentration vs. depth are observable at Mashitu South. Calcium, sulphur, strontium, magnesium, barium and uranium all display a pattern of progressively higher concentrations with increasing depth intervals, suggesting that they are depleted by surficial processes. Conversely, the elements La, W, Bi, Mo, Co, V and Ag are progressively more concentrated towards the surface. The concentrations of Al, Ti, Sc, Na, Pb, Cd and Mn show very little variation throughout the profile. Copper, beryllium, phosphorous, nickel, potassium, zinc, arsenic and iron have inconsistent patterns of increases or decreases in concentration by depth interval.

The variation in geochemistry by depth is reflected at multiple scales. Fig. 4 shows the ACEMS-normalised concentration of three groups of elements at 10 m intervals to a depth of 100 m, a portion encompassing the pedolith, saprolite and saprock weathering zones at Mashitu South and containing most of the leached, oxide and mixed

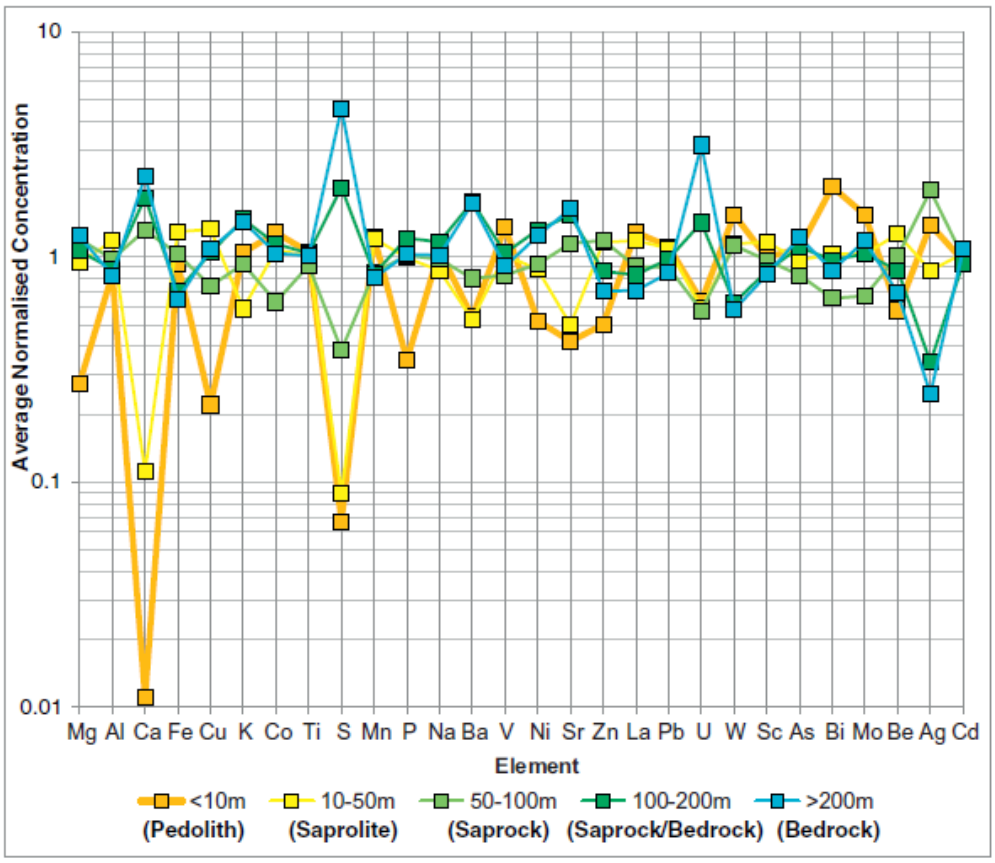

Fig. 3. ACEMS-normalised average concentration of elements within the < 10 m (Pedolith), 10–50 m (Saprolite), 50–100 m (Saprock), 100–200 m (Saprock/Bedrock) and > 200 m (Bedrock) depth intervals at Mashitu South.

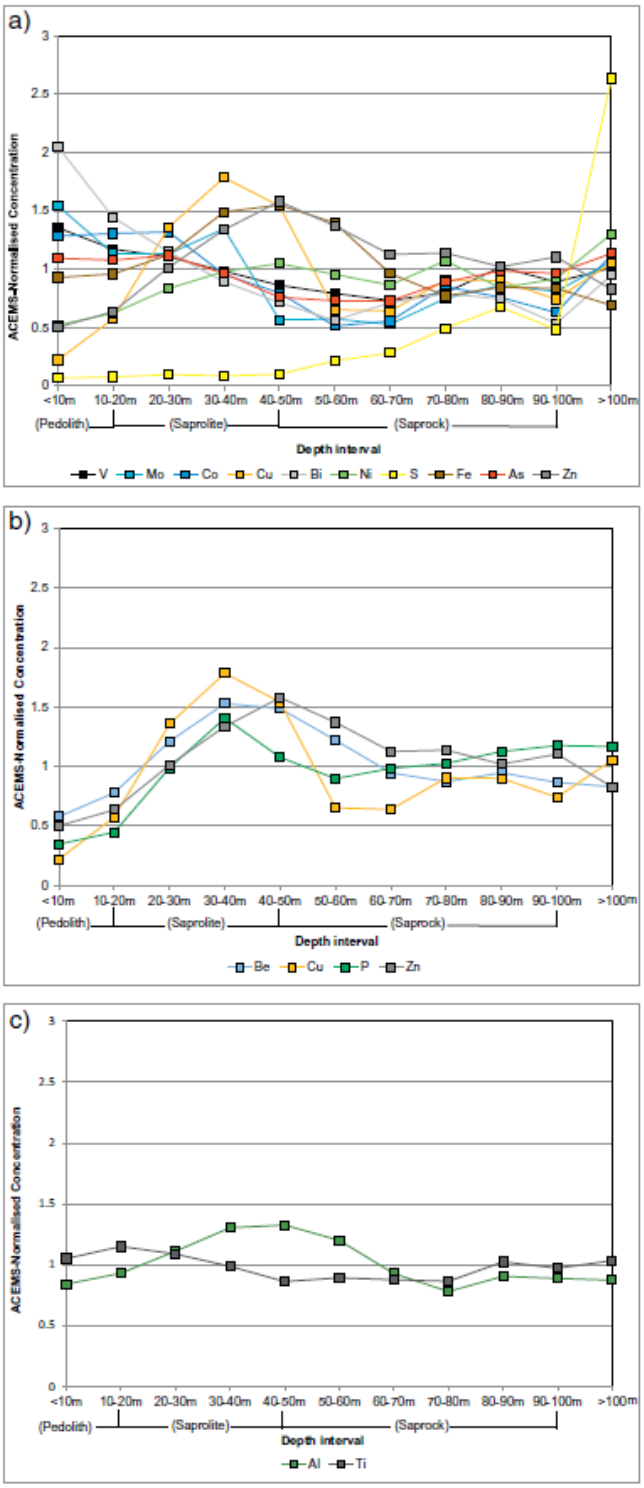

Fig. 4. a: ACEMS-normalised average concentration of the hypogene-mineralisation-associated elements within the top 100 m of the profile at Mashitu South, presented in 10 m increments. The < 10 m interval corresponds to the pedolith weathering zone, the 10-50 m interval corresponds to the saprolite weathering zone and the 50-100 m interval corresponds to the saprock weathering zone.
b: ACEMS-normalised average concentration of elements associated with supergene Cu-oxide mineralisation, within the top 100 m of the profile at Mashitu South, presented in 10 m increments. The < 10 m interval corresponds to the pedolith weathering zone, the 10–50 m interval corresponds to the saprolite weathering zone and the 50–100 m interval corresponds to the saprock weathering zone.
c: ACEMS-normalised average concentration of 'immobile' elements within the top 100 m of the profile at Mashitu South, presented in 10 m increments. The < 10 m interval corresponds to the pedolith weathering zone, the 10–50 m interval corresponds to the saprolite weathering zone and the 50–100 m interval corresponds to the saprock weathering zone.

oxide-sulphide mineralisation zones at the deposit. Fig. 4a presents elements from the hypogene mineralisation association: Cu + Co + Bi + Ni + V + S ± Mo ± As ± Fe ± Zn, Fig. 4b presents elements from the supergene mineralisation association: Cu-Be-P ± Zn and Fig. 4c presents the 'immobile' elements Al and Ti for comparison.

Fig. 5 shows the geochemical variation between elements of the hypogene mineralisation association at 1 m intervals in the < 10 m, near surface portion of the deposit, to give a picture of the transition to surface geochemistry.

5. Discussion

The variation of average element concentration at different depth intervals is primarily due to depth-dependant geological processes. Querying such a large database smooths out variation in element geochemistry caused by varying stratigraphy, lithology, or mineralisation. All stratigraphic units of the Mines Series at the deposit are represented in the final amended MSS dataset (Table 3). Additionally, the domal structure of Mashitu South, together with the stratiform manner of primary mineralisation means that most stratigraphic units, including the mineralised ones, are found both near the surface and at great depth. It should be noted that, as discussed in the methods section, drill-core sampling was not systematic and targeted only areas of visible mineralisation. Therefore, interpretations drawn from this study contain a degree of bias towards well mineralised areas.

At Mashitu South, elements which would be expected to be relatively immobile during weathering, such as Al and Ti, show very little variation in ACEMS-normalised concentration between different depth intervals when compared to elements which would be expected to be mobile during weathering such as Ca and S (Figs. 3, 4a and c). These patterns of element distribution support the hypothesis that variation in average element geochemistry by depth at Mashitu South is primarily influenced by weathering.

5.1. Redistribution of elements in the profile

The varying average concentrations of the elements associated with hypogene mineralisation at different depth intervals (Figs. 3, 4a) indicate that these elements dissociate spatially in the supergene environment and are redistributed according to their mobility in meteoric fluids.

5.1.1. Copper distribution

Copper displays the highest average concentrations between 30 and 50 m depth. The other elements which make up the supergene mineralisation association, Be, P and Zn, also show high average concentrations relative to ACEMS at this depth (Fig. 4b). The reason for this is the presence of large supergene orebodies in the RAT unit beneath leached and eroded fragments of Mines Series at Mashitu South, which have significant economic potential (Chimvinga, pers. comm., 2014). These oxide-zone orebodies consist of malachite – chrysocolla ($(Cu,Al)_2H_2Si_2O_5(OH)_4 \cdot nH_2O$) – pseudomalachite ($Cu_5(PO_4)_2(OH)_4$) dominated, void-filling mineral assemblages (Gigler, 2016), and are 'exotic' in the sense that they formed from copper-bearing solutions leached from the Mines Series. These solutions then migrated downwards and precipitated copper oxides below the original position of hypogene ore where Eh-pH conditions were more reducing. At Mashitu this occurred at around 30-50 m depth, roughly coincident with the position of the present-day water table (Robertson, pers. comm., 2014),

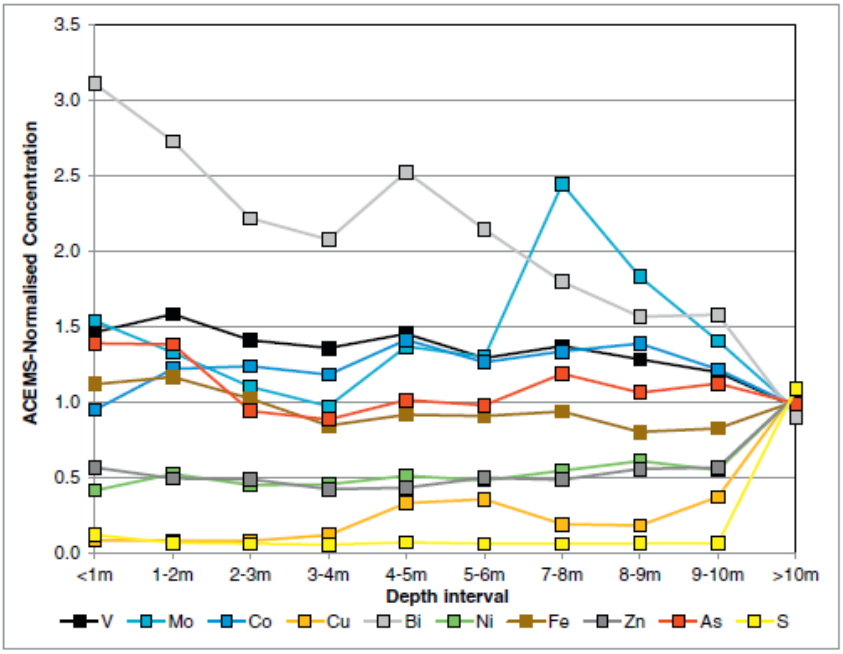

Fig. 5. ACEMS-normalised average concentration of hypogene-mineralisation-associated elements within the top 10 m of the profile (roughly equivalent to the pedolith) at Mashitu South, presented in 1 m increments.

Table 3
Number of samples (N) in the Final Amended MSS (Mashitu South) database taken from each stratigraphic unit. CMN: Calcaire à Minéraux Noire Unit, SD: Shales Dolomitique Unit, RSC: Roches Siliceuse et Cellulaire Unit, RSF: Roches Siliceuses Feuilletées Unit, DStrat: Dolomies Stratifiées Unit, RAT: Roches Argilo-Talqueuse, i.e. RAT Gris and RAT Rouge units.

Stratigraphic Unit	N
CMN	1568
SD	2880
RSC	2085
RSF	977
DStrat	629
RAT Gris	781
RAT Rouge	2955
Undifferentiated Breccia	183
Total	12,058

which is a common site of deposition for remobilised malachite in Katanga (De Putter et al., 2010). The secondary ore at Mashitu is hosted in the mostly siliciclastic RAT unit and primarily occupies the pore spaces of arenaceous units, fills porous regions of breccias, and occurs in cavities where dolomite veins have dissolved. Within these orebodies, P is mineralogically accommodated by pseudomalachite and supergene apatite – $Ca_{10}(PO_4)_6(OH,F,Cl)_2$ (Gigler, 2016). The source of Be and Zn within the supergene association is unknown, but it is possible that they substitute for Cu within the structure of copper oxide minerals.

5.1.2. Cobalt distribution

Cobalt shows the highest average concentrations in the 20–30 m depth range, although it is also highly concentrated in the 10–20 m and < 10 m depth ranges. Copper and cobalt are closely associated in the hypogene environment and the spatial disparity in their concentrations in the near surface environment is an indicator of the dissociation of these two elements through supergene alteration. Such dissociation is well documented in Katanga, with Co-oxides frequently forming 'cobalt caps' in the near-surface environment above supergene copper deposits (Gauthier and Deliens, 1999; Decrée et al., 2010). At Mashitu South, near surface Co is accommodated primarily by heterogenite, which is frequently residual and is hosted at or near the site of original hypogene mineralisation (Gigler, 2016). Cobalt has a high affinity for Mn and Fe oxides and may also be accommodated within such minerals, particularly within soil at the top of the profile (Pourret et al., 2015). Fig. 6, a downhole element profile for hole MSSD140, shows an example of high cobalt concentrations at a depth of ~7 m in the RSF and DStrat units, where Cu-Co hypogene ore is commonly present in rocks which have not experienced supergene alteration. This zone of residual Co enrichment overlies a large, remobilised, supergene Cu orebody hosted in the RAT unit at a depth of ~30–50 m.

5.1.3. Trace element and sulphur distribution

All of the other elements of the hypogene mineralisation association except for sulphur show higher ACEMS-normalised average concentrations than Cu in the top 20 m of the profile (Fig. 4a). In the < 10 m interval, S, Cu, Ni and Zn are significantly depleted relative to ACEMS, levels of Fe and As are roughly equal to ACEMS levels, while Co, V, Mo and Bi are significantly enriched relative to ACEMS (Fig. 4a). The average concentration of Bi in particular is over twice that of ACEMS in the < 10 m interval, and this concentration increases progressively in 1 m increments, such that Bi shows more than three times the average concentration in the < 1 m interval relative to ACEMS (Fig. 5). From this, it can be inferred that while S, Cu, Ni and Zn are depleted from the near-surface environment by chemical weathering, Co, V, Mo and particularly Bi experience residual, relative enrichment due to the same process. Spikes in the concentration of Co, V, Mo and Bi at the stratigraphic position of the RSF-DStrat 'lower orebody', within 10 m of the surface, are observable in hole MSSD140, shown in Fig. 6. Cu concentration at this depth is negligible by comparison.

After leaching and depletion from the surface, Cu and Zn migrated downwards and became enriched within oxide zone ores at around 30–50 m depth (Fig. 4b; Section 4.1.1). Sulphur leached from the surface may have contributed to the development of supergene Cu sulphides and sulphates deeper in the profile. However, S has not been reconcentrated at a particular depth level like Cu and there is no true 'chalcocite blanket' at Mashitu South (Gigler, 2016). Average sulphur concentrations increase progressively with depth (Fig. 3), indicating that there is net leaching of sulphur down to a depth of at least 200 m. The fate of Ni leached from the surface is unknown as no secondary Ni-

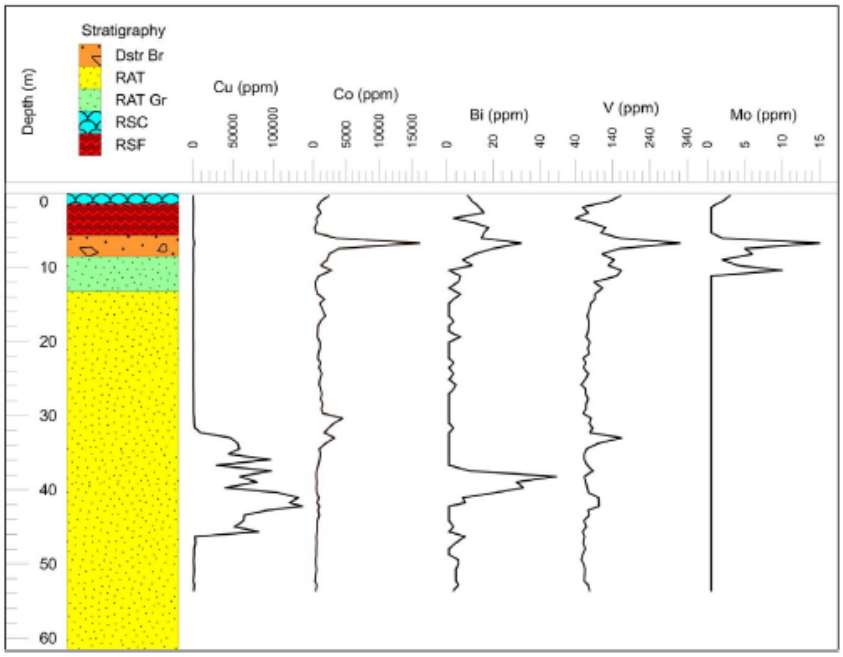

Fig. 6. Near-surface downhole concentration plot for selected elements of the hypogene-mineralisation-association: Cu, Co, Bi, V and Mo, in hole MSSD140 at Mashitu South. Stratigraphic abbreviations: RSC: Roches Siliceuse et Cellulaire Unit, RSF: Roches Siliceuses Feuilletées Unit, DStrat Br: brecciated Dolomies Stratifiées Unit, RAT Gr: Roches Argilo-Talqueuse Grises Unit, RAT: Roches Argilo-Talqueuse Rouge Unit. Note that Cu no longer exists in appreciable concentrations at the expected stratigraphic position of the hypogene 'lower orebody': within the RSF and DStrat units. Instead it has been leached into a supergene orebody within the RAT Rouge unit, while the less mobile elements associated with hypogene mineralisation have mostly remained behind (with the exception of Bi, which is also concentrated within the orebody).

bearing minerals were identified in the petrological study of Gigler (2016), although it may have been fixed within supergene Cu sulphides.

As discussed earlier, Co in the near surface environment is mostly present as residual heterogenite. The accommodation of V, Mo and Bi is less certain: these elements are present in concentrations of no more than tens to hundreds of ppm in any sample and no V, Mo or Bi-bearing minerals have been identified at Mashitu South. However, heterogenite is also a possible source as it commonly forms complex admixtures with Fe-Mn-Cu-Ni oxides, which are enriched in a number of trace elements and REE (Decrée et al., 2010; Decrée et al., 2015). High correlations between the concentrations of Co, and those of V, Mo and Bi in samples from the top 50 m of the profile also suggest that heterogenite may accommodate these trace elements.

5.2. The effect of weathering on orebody geochemistry

To demonstrate how weathering changes the geochemistry of mineralised units at Mashitu South, the ACEMS-normalised geochemistry of the depth intervals from two units which commonly host contrasting styles of Cu-Co mineralisation are compared here: the RSF unit (Fig. 7a), which frequently hosts the majority of the stratiform, hypogene Cu + Co + Bi + Ni + V + S ± Mo ± As ± Fe ± Zn 'lower orebody', and the RAT Rouge unit, part of the RAT Subgroup, which only hosts remobilised, supergene, oxide zone Cu-Be-P ± Zn type mineralisation (Fig. 7b). The contrasting variation in geochemistry by depth between the RSF and RAT Rouge units illustrates their predisposition to hosting hypogene and supergene mineralisation respectively.

In the RSF, Cu, S, and Ni are all greatly enriched relative to ACEMS in the > 200 m depth interval, being more concentrated here than at any depth. They also display significant depletion in the < 10 m depth interval, together with Zn. Cobalt also shows the highest ACEMS-relative enrichment at the greatest depth and the lowest at the shallowest depth interval. However, even in the < 10 m interval Co is still slightly enriched relative to ACEMS in the RSF, suggesting that it is slightly mobile within the RSF in the near-surface environment, but not to the same degree as Cu. Iron concentration is lower than ACEMS at all depth intervals but does not vary significantly between intervals. Arsenic, molybdenum and vanadium are slightly enriched in the RSF relative to ACEMS, but again with little variation between depth intervals. Bismuth displays high concentrations relative to ACEMS at all depth intervals, however the highest concentrations are to be found in the < 10 m interval (at 4 × the ACEMS Bi value on average). This suggests surficial, residual enrichment of bismuth in the RSF unit.

The geochemistry of the RAT reflects the propensity of that unit to host supergene, rather than hypogene mineralisation. Most of the elements of the hypogene mineralisation association display average concentration values which are significantly below or roughly equal to the ACEMS values, except for in the < 10 m interval where Mo and V appear to display slight residual enrichment. Cobalt also displays slight enrichment in this interval, which may reflect limited downward migration of Co from the Mines Series to form remobilised near-surface heterogenite in alkaline pH conditions (Decrée et al., 2015). Copper is depleted relative to ACEMS in all intervals within the RAT Rouge except for the 10–50 m depth interval, where it displays relative enrichment, owing to the presence of the malachite-chrysocolla-pseudomalachite supergene orebodies discussed in Section 4.1.1. Beryllium is also slightly enriched at this interval compared to other intervals, but P and Zn do not appear to show preference for the 10–50 m compared to other intervals in the RAT Rouge, indicating that the RAT may be a source of these trace elements for supergene Cu-Be-P ± Zn ores.

5.3. Implications for geochemical exploration

The hypogene ore association of Cu + Co + Bi + Ni + V + S ± Mo ± As ± Fe ± Zn can be split into two groups of elements. Copper, nickel, sulphur and zinc are depleted from the surface by weathering, and Co, Bi, V, Mo, As and Fe experience residual enrichment in the near-surface. Fig. 5 shows that average concentrations of the latter group of elements remain high relative to ACEMS throughout the top 10 m of the depth profile, right to the < 1 m depth interval. It is therefore suggested that components from this group of elements would produce surface geochemical anomalies over leached, supergene Cu deposits which are greater in magnitude and more focussed than Cu itself, in cases where weathering has been severe, such as at Mashitu South. These anomalies would be expected in proximity to surface expressions of units which were originally host to hypogene ore, such as the RSF. Cobalt, bismuth and vanadium would be of

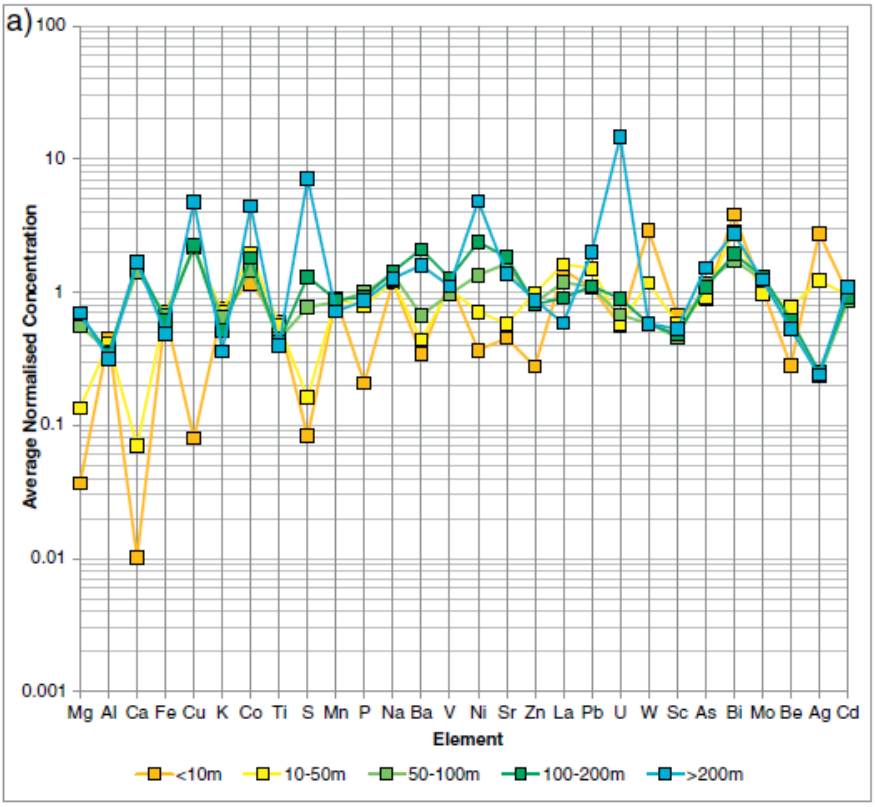

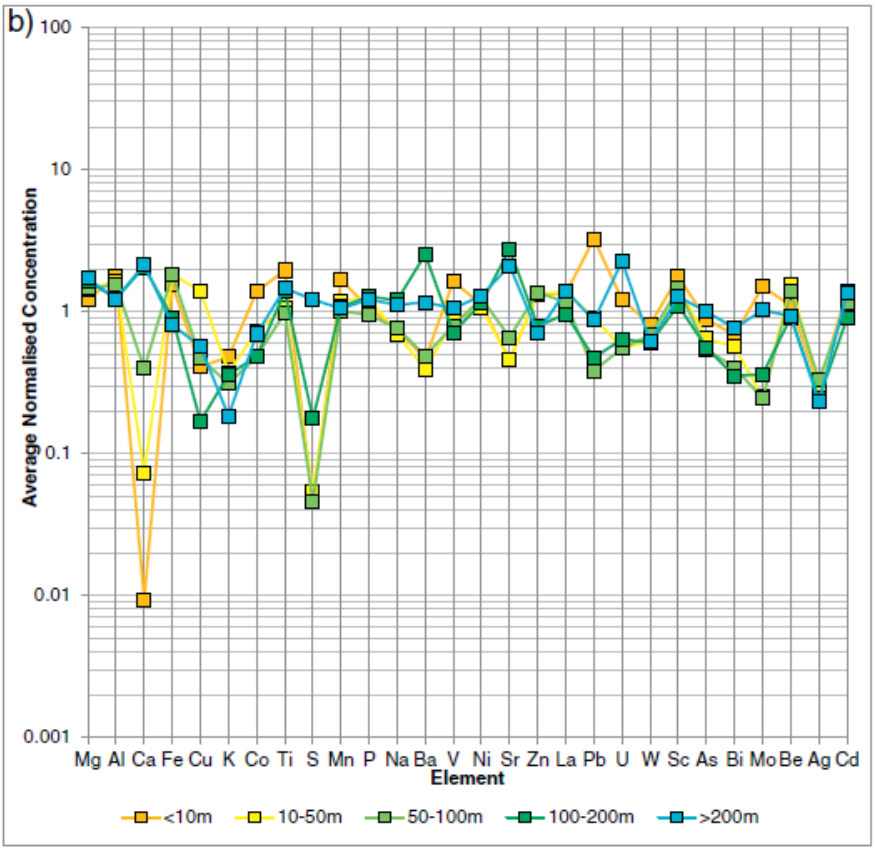

Fig. 7. a: ACEMS-normalised average concentration of elements within the < 10 m, 10–50 m, 50–100 m, 100–200 m and > 200 m depth intervals of the RSF (Roches Siliceuses Feuilletées) stratigraphic unit at Mashitu South.
b: ACEMS-normalised average concentration of elements within the < 10 m, 10–50 m, 50–100 m, 100–200 m and > 200 m depth intervals of the RAT (Roches Argilo-Talqueuse) Rouge stratigraphic unit at Mashitu South.

particular use, as they are proven to be associated more exclusively with the hypogene mineralisation present at Mashitu South than Mo, As and Fe (Gigler, 2016), while still being more residually concentrated than the other elements of the association. It should be noted that, when using the average-normalisation technique presented in this paper to determine surface pathfinder elements to mineralisation, one must have a solid understanding of the major and trace elements which may be confidently associated with hypogene mineralisation of the type being explored for. This is important to exclude the erroneous use of elements as pathfinders which are simply enriched in the surface profile without being enriched in the rocks by hypogene mineralisation processes. At Mashitu South, the hypogene geochemical association of Cu + Co + Bi + Ni + V + S ± Mo ± As ± Fe ± Zn was determined by geostatistical and petrological studies of 'fresh' rock intervals known to be host to hypogene mineralisation, with minimal alteration by supergene processes (Gigler, 2016).

Exploring for 'cobalt caps' is a well-known method of prospecting for supergene Cu in the region (Gauthier and Deliens, 1999; Decrée et al., 2010). However, near-surface element concentrations (Fig. 5) suggest that Bi and V make even better surface vectors than Co, as they are more residually enriched. Bismuth in particular should form the strongest, most localised anomalies directly over the position of former hypogene orebodies as it displays the most residual enrichment, at over 3 × the ACEMS concentration in the top < 1 m of the profile. Indeed, a comparison of the near-surface element profile of the generally 'hypogene-mineralised' RSF and the 'hypogene-barren' RAT Rouge units highlights the usefulness of Bi as a surface vector. In the < 10 m depth interval of the RSF (Fig. 7a), Bi displays an average concentration of 3.8 × ACEMS, compared to 0.1 × ACEMS for Cu and 1.2 × ACEMS for Co. By comparison, the typically 'hypogene-barren' RAT Rouge (Fig. 7b) has an average Bi concentration at < 10 m depth of 0.7 × ACEMS, an average Cu concentration of 0.4 × ACEMS and an average Co concentration of 1.4 × ACEMS. The high average concentration of Bi in the near-surface profile of hypogene-mineralised units, such as the RSF, compared to its low average concentration in hypogene-barren units, such as the RAT-Rouge, recommends it as a surface vector to leached hypogene orebodies where Cu is not found in appreciable near-surface quantities. The use of residually-concentrated trace elements associated with Cu-mineralisation as surface pathfinders, including Bi and Mo, has also been recommended at the supergene Cu deposits of the Mount Isa Inlier, NW Queensland, Australia by recent research (Salama et al., 2016a). Additionally, lateral migration of elements in the near-surface environment could encourage the formation of a 'bullseye' geochemical target, with more mobile elements such as Cu displaying broad, diffuse anomalies and less mobile elements such as Co and Bi displaying localised, intense anomalies directly above a supergene orebody beneath the centre of the 'bullseye'.

Soil concentrations of Cu have proven adequate for locating many Cu-Co deposits in the region (Chimvinga, pers. comm., 2014). However, the soil concentrations of Bi, Co and V, or multi-element concentrations of these three elements, could prove useful in locating hitherto undiscovered deposits which have been subjected to a high degree of chemical weathering, like Mashitu South. Pit sampling or shallow drilling of the pedolith, followed by high-precision 'wet-geochemistry' assay methods are recommended for use in this type of exploration. XRF analysis of soil samples may not be accurate enough to produce conclusive assay results for trace elements present in such low concentrations as Bi and V (Gigler, 2016). In their study of supergene Cu mineralisation at the Mount Isa Inlier, Salama et al. (2016a) find that Bi and V are effectively concentrated above Cu-sulphide deposits in ferruginous lag (> 7.6 mm size fraction) and in termitaria. Given a similar weathering regime between the two study areas, these materials are also recommended as sampling media in detecting highly residual surface pathfinders such as Bi and V while exploring for Cu-Co mineralisation in Katanga. Cobalt, which is slightly more mobile in the near-surface than Bi and V (Fig. 5), is enriched in ferruginous duricrusts at the Mount Isa Inlier along with Cu and Ni (Salama et al., 2016a), so it is recommended that this medium be used as a sampling material when using these elements as pathfinders. When using Co and even Cu as surface pathfinders, it is recommended to normalise the concentration data against Mn in order to exclude false positives produced by scavenging of these metals by Mn oxides in the near-surface, which has been demonstrated to occur in Cu exploration over the buried Katangan Supergroup of NW Botswana (Salama et al., 2016b).

6. Conclusions

Splitting a large whole-rock-geochemistry dataset into sub-databases, then normalising average concentration values within those sub-databases to average values for the entire database, is an effective tool for assessing geochemical variation between datasets. This geochemical variation between different depth intervals at Mashitu South primarily reflects the effects of weathering. From the hypogene ore element association at the deposit of Cu + Co + Bi + Ni + V + S ± Mo ± As ± Fe ± Zn, two groups of elements are distinguished: those which are depleted in the near-surface environment by weathering (Cu, Ni, S and Zn) and those which are residually enriched by weathering (Co, Bi, V, Mo, As and Fe). These residually enriched elements would be expected to be present in highly anomalous concentrations in the near-surface environment proximal to the original position of hypogene Cu-Co orebodies, even where Cu has been leached efficiently from the surface and no significant Cu anomaly exists. In such cases of extreme leaching, Cu is commonly re-concentrated at depth into supergene orebodies with high economic potential. It is therefore suggested that surface concentrations of Co, V and particularly Bi would be effective surface vectors to the position of similar supergene Cu orebodies in Katanga. The average-normalisation technique presented in this paper could be used to assess element variation by depth in large geochemistry databases from any polymetallic deposit which has undergone significant chemical weathering.

Acknowledgements

Access to data, samples and the Mashitu South site was provided by Eurasian Resources Group (ERG) S.A.R.L. and Comide S.P.R.L. The authors would like to thank M. Sośnicka for a critical review of this manuscript and M. Bevelander for permission to publish.

Funding

This study was supported financially by Eurasian Resources Group (ERG) S.A.R.L. and the Centre of Excellence for Integrated Mineral and Energy Resource Analysis (CIMERA).

References

Alexandre, J., 2002. Les cuirasses latéritiques et autres formations ferrugineuses tropicales: Exemple du Haut Katanga méridional. Annales du Musée Royal de l'Afrique Centrale. Sciences Géologiques 107, 118.

ALS Global, 2009a. Assay Procedure; ME-OG62; Ore grade elements by four-acid-digestion using conventional ICP-AES analysis. (Revision 03.04. Available at www.alsglobal.com. Retrieved 05/01/2017).

ALS Global, 2009b. Geochemical Procedure; ME-ICP-61; Trace level methods using conventional ICP-AES analysis. (Revision 06.02. Available at www.alsglobal.com. Retrieved 05/01/2017).

Armstrong, R.A., Master, S., Robb, L.J., 2005. Geochronology of the Nchanga Granite, and constraints on the maximum age of the Katanga Supergroup, Zambian Copperbelt. J. Afr. Earth Sci. 42, 32–40.

Bell, R.T., 1989. A Conceptual Model for Development of Megabreccias and Associated Mineral Deposits in Wernecke Mountains, Canada, Copperbelt, Zaire, and Flinders Range, Australia. (IAEA Techincal Document 500, Geological Survey of Canada contribution 31487).

Broughton, D.W., Hitzman, M.W., Stephens, A.J., 2002. Exploration history and geology of the Kansanshi Cu-(Au) deposit, Zambia. 9. Society of Economic Geologists, pp. 141–153 Special Publication.

Dawson, G., 2002. Initial SHRIMP geochronology of xenotime and monazite from

Mufulira, Konkola North, Ndola East and Chambishi. AMIRA P554 internal communication, available at. http://www.utas.edu.au/codes/publications/past-amira-reports.
de Maret, P., 1982. Rock art. In: Van Noten, F. (Ed.), The Archaeology of Central Africa. Akademische Drücku.Verlagsanstalt, Graz, pp. 97–99.
de Maret, P., 1986. The Ngovo group: an industry with polished stone tools and pottery in Lower Zaïre. Afr. Archaeol. Rev. 4, 103–133.
De Putter, T., Mees, F., Decrée, S., Dewaele, S., 2010. Malachite, an indicator of major Pliocene Cu remobilization in a karstic environment (Katanga, Democratic Republic of Congo). Ore Geol. Rev. 38, 90–100.
Decrée, S., Deloule, E., Ruffet, G., Dewaele, S., Mees, F., Marignac, C., Yans, J., De Putter, T., 2010. Geodynamic and climate controls in the formation of Mio–Pliocene world-class oxidized cobalt and manganese ores in the Katanga province, DR Congo. Mineral. Deposita 45, 621–629.
Decrée, S., Deloule, E., De Putter, T., Dewaele, S., Mees, F., Baele, J., Marignac, C., 2014. Dating of U-rich heterogenite: new insights into U deposit genesis and U cycling in the Katanga Copperbelt. Precambrian Res. 241, 17–28.
Decrée, S., Pourret, O., Baele, J.-M., 2015. Rare earth element fractionation in heterogenite (CoOOH): implication for cobalt oxidized ore in the Katanga Copperbelt (Democratic Republic of Congo). J. Geochem. Explor. 159, 290–301.
Dewaele, S., Muchez, P., Heijlen, W., Boutwood, A., Lemmon, T., Tyler, R., 2006a. Reconstruction of the hydrothermal history of the Cu-Ag vein-type mineralisation at Dikulushi, Kundelungu foreland, Katanga, D.R. Congo. J. Geochem. Explor. 89, 376–379.
Dewaele, S., Muchez, P., Vets, J., Fernando-Alonzo, M., Tack, L., 2006b. Multiphase origin of the Cu-Co ore deposits in the western part of the Lufilian fold and thrust belt, Katanga (Democratic Republic of the Congo). J. Afr. Earth Sci. 46, 455–469.
Fay, I., Barton, M.D., 2012. Alteration and ore distribution in the Proterozoic Mines Series, Tenke-Fungurume Cu–Co district, Democratic Republic of Congo. Mineral. Deposita (published online).
François, A., 1974. Stratigraphy, tectonique et minéralisations dans l'arc cuprifière du Shaba (Républic du Zaire). In: Bartholomé, P. (Ed.), Gisements stratiformes et provinces cuprifières. Centenaire de la Sociéte Géologique de Belgique, Liège, Belgium, pp. 79–101.
Gasse, F., 2006. Climate and hydrological changes in tropical Africa during the past million years. C. R. Acad. Sci. Palevol. 5, 35–43.
Gauthier, G., Deliens, M., 1999. Cobalt minerals of the Katanga Crescent, Congo. Mineral. Theatr. Rec. 30, 255–267.
Gigler, G.M., 2016. The Transition From Hypogene to Supergene Mineralisation at the Mashitu South Cu-Co Deposit. University of the Witwatersrand, Katanga, Democratic Republic of Congo Unpublished MSc Thesis. (491 pp.).
Giresse, P., 2005. Mesozoic-Cenozoic history of the Congo Basin. J. Afr. Earth Sci. 43, 301–315.
Halley, S.W., Wood, D., Stoltze, A., Godfroid, J., Goswell, H., Jack, D., 2016. Using Multielement Geochemistry to Map Multiple Components of a Mineral System: Case Study From a Sediment-hosted Cu-Ni Camp, NW Province, Zambia. 104. SEG Newsletter, pp. 1–21.
Hitzman, M.W., Broughton, D., Selley, D., Woodhead, J., Wood, D., Bull, S., 2012. The Central African Copperbelt: Diverse Stratigraphic, Structural, and Temporal Settings in the World's Largest Sedimentary Copper District. 16. S.E.G, pp. 487–514 Special Publication.
Jackson, M.P.A., Warin, O.N., Woad, G.M., Hudec, M.R., 2003. Neoproterozoic allochthonous salt tectonics during the Lufilian orogeny in the Katangan Copperbelt, central Africa. Geol. Soc. Am. Bull. 115, 314–330.
Kampunzu, A.B., Cailteux, J.L.H., Kamona, A.F., Intiomale, M.M., Melcher, F., 2009. Sediment hosted Zn-Pb-Cu deposits in the Central African Copperbelt. Ore Geol. Rev. 35, 263–297.
Key, R.M., Liyungu, A.K., Njamu, F.M., Somwe, V., Banda, J., Mosley, P.M., Armstrong, R.A., 2001. The western arm of the Lufilian Arc in NW Zambia and its potential for copper mineralization. J. Afr. Earth Sci. 33, 503–528.
Kröner, A., Stern, R.J., 2005. Africa/Pan African Orogeny. In: Selley, R.C., Cocks, R.M., Plimer, I.R. (Eds.), Encyclopedia of Geology. Elsevier, pp. 1–12.
Lavier, L.L., Steckler, M.S., Brigaud, F., 2001. Climatic and tectonic control on the Cenozoic evolution of the West African margin. Mar. Geol. 178, 63–80.
Master, S., Rainaud, C., Armstrong, R.A., Phillips, D., Robb, L.J., 2005. Provenance ages of the Neoproterozoic Katanga Supergroup (Central African Copperbelt), with implications for basin evolution. J. Afr. Earth Sci. 42, 41–60.
McGoldrick, P., Scott, R., Selley, D., Broughton, D., 2003. Minor Element Geochemistry of Zambian Copperbelt Deposits. ARC/AMIRA P544 Final Report. pp. 12.1–12.6.
McGoldrick, P., Meffre, S., Selley, D., 2010. Trace Elements and Lead Isotopes in Mines Series Sulfides, Democratic Republic of Congo. CODES-CSM/AMIRA P872 Final Report. pp. 371–384.
Miller, R. McG, Pickford, M., Senut, B., 2010. The geology, palaeontology and evolution of the Etosha Pan, Namibia: implications for the terminal Kalahari deposition. S. Afr. J. Geol. 113, 307–334.
Muchez, P., Brems, D., Clara, E., De Cleyn, A., Lammens, L., Boyce, A., De Muynck, D., Mukumba, W., Sikazwe, O., 2010. Evolution of Cu–Co mineralizing fluids at Nkana Mine, Central African Copperbelt, Zambia. J. Afr. Earth Sci. 58, 457–474.
Ngongo, K., 1975. Sur la similitude entre les gisements uranifères (type Shinkolobwe) et les gisements cuprifères (type Kamoto) au Shaba, Zaïre. Ann. Soc. Geol. Belg. 98, 449–462.
Peel, M.C., Finlayson, B.L., McMahon, T.A., 2007. Updated world map of the Köppen–Geiger climate classification. Hydrol. Earth Syst. Sci. 11, 1633–1644.
Pourret, O., Lange, B., Houben, D., Colinet, G., Shutcha, M., Faucon, M.-P., 2015. Modeling of cobalt and copper speciation in metalliferous soils from Katanga (Democratic Republic of Congo). J. Geochem. Explor. 149, 87–96.
Ramsay, C.R., Ridgway, J., 1977. Metamorphic patterns in Zambia and their bearing on problems of Zambian tectonic history. Precambrian Res. 4, 321–337.
Richards, J.P., Cumming, G.L., Krstić, D., Wagner, P.A., Spooner, E.T.C., 1988a. Pb isotope constraints on the age of sulfide ore deposition and U-Pb age of late uraninite veining at the Musoshi stratiform copper deposit, Central African Copperbelt, Zaire. Econ. Geol. 83, 724–741.
Richards, J.P., Krogh, T.E., Spooner, E.T.C., 1988b. Fluid inclusion characteristics and U-Pb rutile age of late hydrothermal alteration and veining at the Musoshi stratiform copper deposit, Central African Copper Belt, Zaire. Econ. Geol. 83, 118–139.
Salama, W., Anand, R.R., Kidder, J., Pinchand, T., 2016a. Multi-scale detection of buried mineralization and lithology through Kalahari transported cover in NW Botswana. In: Conference paper number 566, 35th International Geological Congress, Cape Town, South Africa.
Salama, W., Gazley, M.F., Bonnett, L.C., 2016b. Geochemical exploration for supergene copper oxide deposits, Mount Isa Inlier, NW Queensland, Australia. J. Geochem. Explor. 168, 72–102.
Selley, D., Broughton, D., Scott, R., Hitzman, M., Bull, S., Large, R., McGoldrick, P., Croaker, M., Pollington, N., Barra, F., 2006. A New Look at the Geology of the Zambian Copperbelt. In: Hedenquist, J.W., Thompson, J.F.H., Goldfarb, R.J., Richards, J.P. (Eds.), Economic Geology 100th Anniversary Volume, pp. 965–1000.
Selley, D., McGoldrick, P., Gilbert, S., Scott, R., 2010. Geochemistry of the Kolwezi ores. In: CODES-CSM/AMIRA P872: Sediment-hosted copper deposits of Congolese, Zambian and central Australian basin systems, pp. 269–301.
Sweeney, M.A., Binda, P.L., 1994. Some constraints on the formation of the Zambian Copperbelt deposits. J. Afr. Earth Sci. 19, 303–313.
Sweeney, M.A., Binda, P.L., Vaughan, D.J., 1991. Genesis of the ores of the Zambian Copperbelt. Ore Geol. Rev. 6, 51–56.
Timmermans, E., 2015. Quantitative Mineralogy of a Saprolite-soil Sequence on a Talc and Chlorite Bearing Substrate, Upper Katanga, D.R. Congo. Unpublished MSc. Thesis. University of Ghent.
Torrealday, H.I., Hitzman, M.W., Stein, H.J., Armstrong, R., Broughton, D., 2000. Age and duration of mineralization at the vein-hosted Kansanshi copper deposits, northern Zambia through Re-Os and SHRIMP U-Pb methods. Econ. Geol. 95, 1165–1170.
USGS (U.S. Geological Survey), 2016. Mineral Commodity Summaries 2016. U.S. Geological Surveyhttp://dx.doi.org/10.3133/70140094. (202 pp.).